JOURNAL OF

METALS

IN 3 SECTIONS - SECTION 1

January 1955

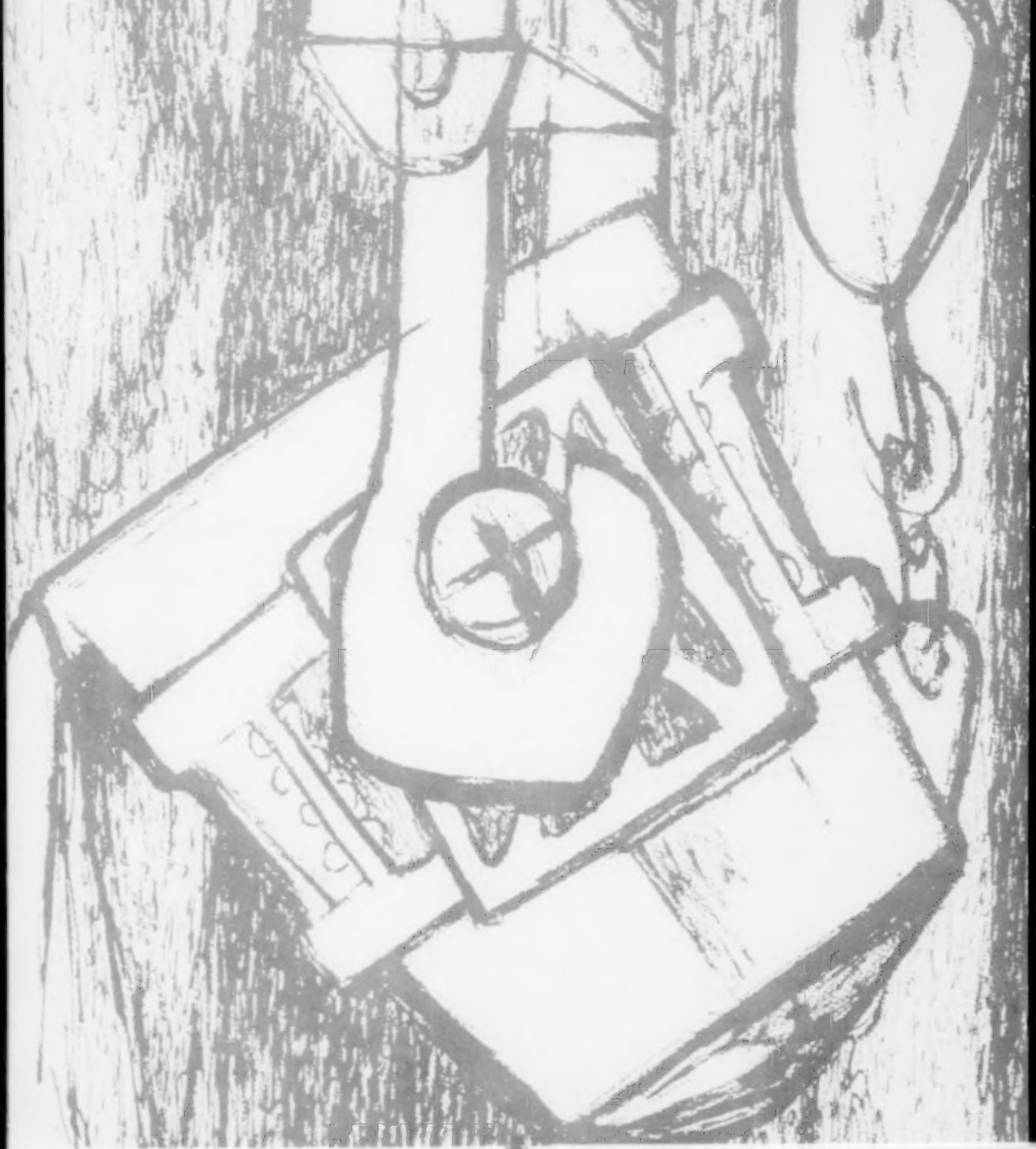

NATIONAL PITCH-RESERVOIR NIPPLES*

TRADE-MARK

THE NEW PITCH-RESERVOIR NIPPLE, an exclusive "National" product, is another major contribution by National Carbon Company to more efficient electric furnace operation. You can now be sure that tight joints will stay tight under normal load and service conditions.

"NATIONAL" PITCH-RESERVOIR NIPPLES, designated Type PR-F, are now available for electrode diameters from 14" to 24". Thoroughly proved in service, they are identical in strength, size, shape, tolerances, composition and quality to our standard, tapered, graphite nipples. Talk it over soon with your National Carbon Company electrode representative.

***PATENTS PENDING**
EXCLUSIVE DESIGN

HERE'S HOW IT WORKS:

Reservoirs near each end of the nipple contain pitch. As the electrode column becomes hot in service, the pitch flows from the reservoirs into the threaded sections of the joint and cokes out, cementing and locking the threads of the nipple and sockets together.

FOR ELECTRODES AND ELECTRODE SERVICE...
Rely on NATIONAL CARBON COMPANY!

The term "National" is a registered trade-mark of Union Carbide and Carbon Corporation

NATIONAL CARBON COMPANY
A Division of Union Carbide and Carbon Corporation
30 East 42nd Street, New York 17, N. Y.

Sales Offices: Atlanta, Chicago, Dallas, Kansas City, Los Angeles, New York, Pittsburgh, San Francisco. *In Canada:* Union Carbide Canada Limited, Toronto

JOURNAL OF

METALS

Published to provide a continuing, authoritative, and up-to-date record of technological, engineering, and economic progress in all branches of the metals industry by the Metals Branch American Institute of Mining and Metallurgical Engineers, Inc. 29 West 39th Street, New York 18

• • •

ALVIN S. COHAN
Manager of Publications
Editor, JOURNAL OF METALS
EDWIN M. WEISS
Associate Editor

• • •

M. A. MATZKIN M. SNEDEKER
G. M. ZILL
Assistant Editors
GRACE PUGSLEY Production Manager
W. J. SEWING Asst. Prod. Mgr.

• • •

METALS BRANCH COUNCIL

R. R. McNaughton Chairman
E. O. Kirkendall Secretary
J. H. Scaff IMD Chairman
J. S. Marsh ISD Chairman
P. T. Stroup EMD Chairman
M. Cohen R. D. Parks
T. J. McLoughlin D. S. Eppelsheimer

EDITORIAL ADVISORY COMMITTEE

J. S. Smart, Jr. Chairman
W. A. Dean Evan Just
J. C. Kinnear, Jr. John Marsh
T. D. Jones M. Tenenbaum

TECHNICAL PUBLICATIONS COMMITTEES

Robert Aborn AIME Chairman
M. A. Jones ISD Chairman
S. J. Dickinson EMD Chairman
W. R. Hibbard, Jr. IMD Chairman
E. J. Kennedy, Jr. Secretary

• • •

WARREN V. SMITH
Eastern Advertising Manager
BOB WILSON
Western Advertising Manager
84 E. Randolph St., Chicago

• • •

The AIME Publishes:
Journal of Metals
Mining Engineering
Journal of Petroleum Technology

VOL. 7, NO. 1 JANUARY, 1955

COVER

Predictions for increased steel production during the coming year influenced the theme for Harry Brocke's cover this month.

NEWS

Meet the Authors	4	Trends	10
Books for Engineers	6	Drift of Things	12
Employment Service	7	Reporter	15
Industrial Notes	8	AIME News	65
Coming Events	8	Personals	70
Annual Meeting Program			28

TECHNICAL FEATURES

Hydro-Arc Control Reduces Costs in Electric Furnace Operation — Joseph Seymour — 17

History of Iron Ore Sintering Recalls Variety of Experimentation — M. O. Holowaty — 19

Reusable Hot Tops Proven Successful in Ingot Pouring Practice — J. C. Carpenter — 24

Progress in European Vacuum Melting Described — M. H. Scholefield — 25

TRANSACTIONS

Canadian Copper Refiners Ltd. Electric Furnace Melting Practice — W. A. Sheaffer — 33

Some Factors Affecting Open-Hearth Practice — D. J. Carney, J. J. Oravec, E. Van Meter — 39

Electrolytic Production of Hydrometallurgical Reagents for Processing Manganese Ores — J. B. Clemmer, C. Rompacek, P. E. Churchward — 51

Equilibrium Between Titanium in Liquid Iron and Titanium Oxides — R. L. Hadley, G. Derge — 55

Sulphur Pressure Measurements of Molybdenum Sesquisulphide in Equilibrium with Molybdenum — C. L. McCabe — 61

TECHNICAL NOTE

Martensite Formations in Powders and Lump Specimens of Ti-Fe Alloys — D. H. Polonis, J. G. Parr — 64

This issue of JOURNAL OF METALS is in three Sections:
Section 1—Magazine Section 2—Transactions Section
Section 3—Index

Published the first day of each month by the American Institute of Mining and Metallurgical Engineers, Inc., 29 West 39th Street, New York 18, N. Y. Telephone: PEnnsylvania 6-9220. Subscription $8 per year for non-AIME members in United States and North, South and Central America; $10, foreign; $6 for AIME members, or $4 additional in combination with a subscription to "Mining Engineering" or "Journal of Petroleum Technology." Single copies, 75 cents; single copies foreign, $1.00; special issues, $1.50.... The AIME is not responsible for any statement made or opinion expressed in its publications.... Copyright 1955 by the American Institute of Mining and Metallurgical Engineers, Inc.... Registered cable address, AIME New York.... Indexed in Engineering Index, Industrial Arts Index and Chemical Abstracts.... Reentered as second-class matter Sept. 27, 1949, at the post office at New York, N. Y., under the Act of March 3, 1879. Additional entry established at Manchester, N. H.

Major Advance ..

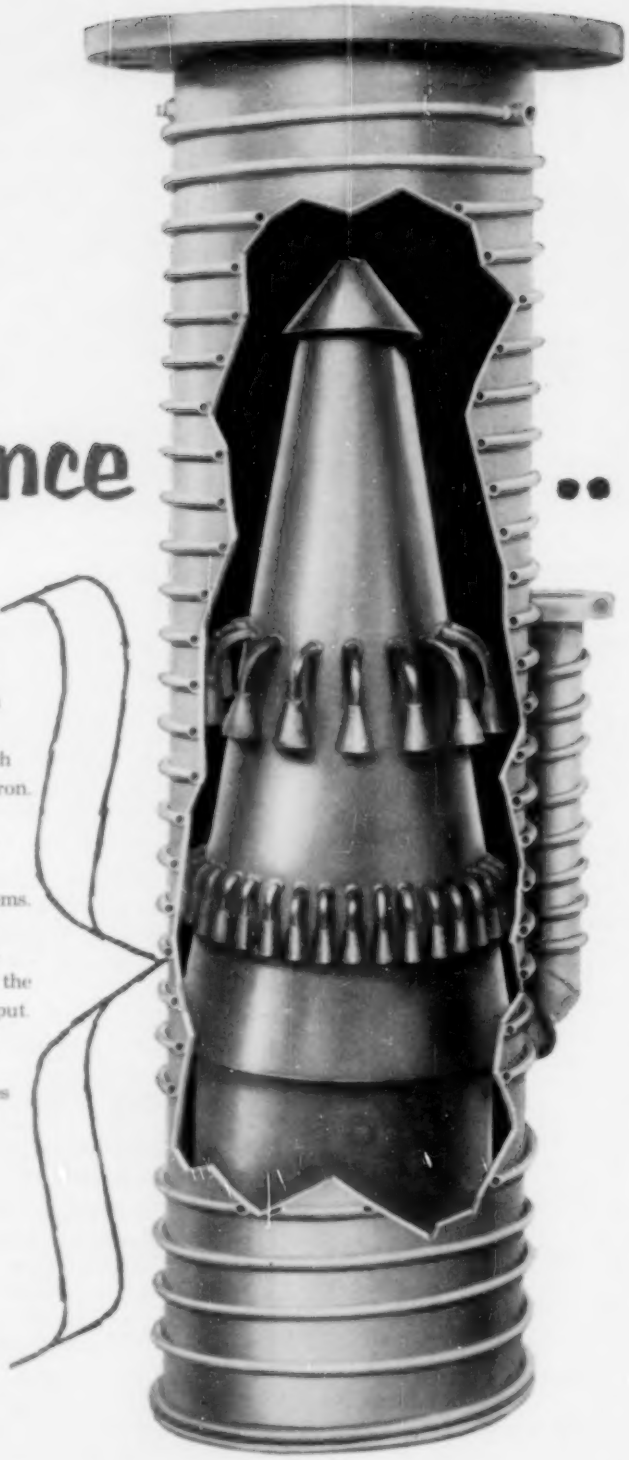

Higher Pumping Speeds in Critical Ranges. Examples: the 6-inch booster exhausts 760 cfm at 50 microns, 1400 cfm at 15 microns, with an ultimate pressure of .06 microns. The 16-inch diffusion pump exhausts 11,000 cfm at 1 micron.

Shorter Pumping Cycles for all high vacuum processing equipment including vacuum metallizers, vacuum furnaces and exhaust systems.

Higher Forepressures. Examples: at blankoff, 2.4 mm. for the 6-inch booster; 0.35 mm. for the 16-inch diffusion pump, both at normal heat input.

Sizes Available NOW:

Diffusion Pumps: 4, 6, 10, 14 and 16 inches
Booster Pumps: 4, 6, 10 and 16 inches

Use the Coupon (upper right) to request specifications and performance curves.

STOKES MAKES: High Vacuum Equipment, Vacuum Pumps and Gages / Industrial

F. J. STOKES MACHINE COMPANY
5500 Tabor Road, Philadelphia 20, Pa.

Please send me complete specifications and performance curves on:

☐ Diffusion Pumps ☐ Booster Pumps

Application_____

NAME_____

COMPANY_____

ADDRESS_____

CITY_____ STATE_____

.in DIFFUSION PUMPS

The NEW Stokes RING-JET Diffusion and Booster Pumps Increase Pumping Capacity More Than 50%

The revolutionary design of the new Stokes Ring-Jet* Diffusion and Booster Pumps is a major development in diffusion pump techniques. It is a high point of achievement in Stokes' 50 years of experience in building high vacuum equipment.

Here, briefly, is a description of the old and the new . . . the development which has given Stokes Ring-Jet Pumps such high pumping capacity. Diffusion pumps have as one limiting factor the cross section of the air flow path. A second limiting factor is the distance from the jet to the condensing surface.

The new Stokes Ring-Jets replace the conventional jet cone with a *ring of jets*. This increases the cross-sectional area of the air flow path without increasing the distance to the condensing surface. The effect is to increase pumping speeds on some models more than 50%.

Increased pumping speeds, shorter pumping cycles, smaller mechanical pumps, operation against higher forepressures, are outstanding advantages of the new Stokes Ring-Jet Pumps. Fill out the coupon for full information.

STOKES

*Patents Pending

Tabletting, Powder Metal and Plastics Molding Presses / Pharmaceutical Equipment

Meet The Authors

D. H. Polonis (p. 64) is currently working for his Ph.D. in metal physics at the University of British Columbia. Mr. Polonis received his B.A.Sc. from the University of British Columbia in 1951 and his M.A.Sc. from the University of Toronto in 1953. For a short time he was employed by the Steel Co. of Canada, Ltd., Hamilton, Ont., Canada. He holds membership in AIME and his hobbies include reading and music appreciation.

J. C. Carpenter (p. 24) has been associated with the Ferro Engineering Co. since 1936, with the exception of several years in the Army. From 1942 to 1945 he was a captain, Ordnance Corps, and 1951 to 1952 he was a major, Ordnance Corps. Prior to joining Ferro, Mr. Carpenter had been a staff metallurgist at Battelle Memorial Institute. From 1929 to 1935 he was associated with the Chase Brass & Copper Co., as an assistant metallurgist at the Cleveland plant. Mr. Carpenter was born at East Cleveland and graduated from Case Institute of Technology. In his spare time he does amateur radio work.

J. Bruce Clemmer (p. 51) joined the U. S. Bureau of Mines in January 1929. He is presently chief of the metallurgical div., Region IV, Salt Lake Experiment Station, Salt Lake City. Mr. Clemmer was born at Coon Rapids, Iowa and graduated from the South Dakota State School of Mines and Missouri School of Mines. He is a member of the AIME Salt Lake Local Section and American Chemical Society.

J. B. CLEMMER

E. VAN METER

E. Van Meter (p. 39) a native of Columbus, Ohio, is an investigation analyst for the research laboratory of the U. S. Steel Corp., Chicago. In 1949 he had been associated with the Republic Steel Corp. From 1950 to 1952 Mr. Van Meter was a graduate student in the Chrysler Corp. Institute of Engineering. Mr. Van Meter enjoys hunting as his hobby. He is also a member of the Chicago Local Section of AIME.

Carl Rampacek (p. 51) is a graduate of Creighton University, Omaha, Neb. Following graduation he was engaged in graduate work at the Missouri School of Mines. In 1939 he joined the Phillips Petroleum Co., Bartlesville, Okla., as a research chemist. He became a mineral technologist for the Bureau of Mines in 1941 and later held positions as physical chemist and metallurgist. Mr. Rampacek is presently chief of process development and research branch, metallurgical div., Region IV, Tucson, Ariz. He is a member of AIME and American Chemical Society.

J. J. Oravec (p. 39), a graduate of Ohio State University is presently with the metallurgical research dept. of the U. S. Steel Corp., Chicago. He was born at Youngstown, Ohio and received his degree from Ohio State in 1942. For four years Mr. Oravec was in the Army and in 1946 joined U. S. Steel.

J. J. ORAVEC

J. SEYMOUR

Joseph Seymour (p. 17) has been metallurgist and melting supervisor for Kensington Steel Co., Kensington, Ill. for approximately 10 years. He was a chemist for seven years and then held the position as night supervisor, melting dept. for the same firm. Mr. Seymour was born in Chicago and attended the Illinois Institute of Technology. His hobbies include photography and woodworking.

P. E. Churchward (p. 51) is a metallurgist with the Bureau of Mines located at Salt Lake City, Utah. Mr. Churchward has been associated with the Bureau since 1939. He is a graduate of University of Washington, B.S., M.S. From 1928 to 1934 he was a chemist with Crown Willamette Paper Co., Camas, Wash. Prior to joining the Bureau of Mines, Mr. Churchward was an instructor in chemistry and physics at Grays Harbor Junior College.

M. O. Holowaty (p. 19) is presently chief of raw materials, research and development dept., Indland Steel Co., East Chicago, Ind. Dr. Holowaty was born in the Ukraine and graduated from the University of Breslau. He is a member of AIME.

M. O. HOLOWATY

R. L. HADLEY

R. L. Hadley (p. 55) is a native of Warren, Ohio and attended Purdue University and Carnegie Institute of Technology. Dr. Hadley was an officer in the field artillery during World War II. He joined General Electric Co. in 1949 as a research associate in the laboratory. At present he is engineering manager, metallurgy and ceramics, major appliances laboratories.

PROFESSIONAL SERVICES

Limited to AIME members, or to companies that have at least one AIME member on their staffs. Rates $40 per year per inch.

OXYGEN IN METALS
By Wet Procedure
(Accuracy at one-half current prices)
LEDOUX & COMPANY
Metallurgical Chemists—Spectroscopists
359 Alfred Ave., Teaneck, New Jersey

DR. B. EGEBERG
Metallurgical Consultant
Reg. Prof. Engr.
Steel & Metals
Operations — Research
Meriden, Conn.

HANS NEUBERT
PRECISE PROMPT
TECHNICAL TRANSLATIONS FROM GERMAN, SPANISH, FRENCH INTO ENGLISH. $1.00 per 100 WORDS OF THE ENGLISH TRANSLATION.
31 Hilltop Ave. Clark-Rahway, N.J.

MAX STERN
Consulting Engineer
Expert for Scrap Recovery and Shipwrecking — Modernization of Plants and Yards for Ferrous and Nonferrous Metal Scrap
149 Broadway New York 6, N. Y.

H. L. TALBOT
Consulting Metallurgical Engineer
Extraction and Refining of Base Metals
Specializing in Cobalt and Copper
Room 331, 84 State St., Boston 9, Mass.

Compact, versatile x-ray inspection unit

goes where the job is

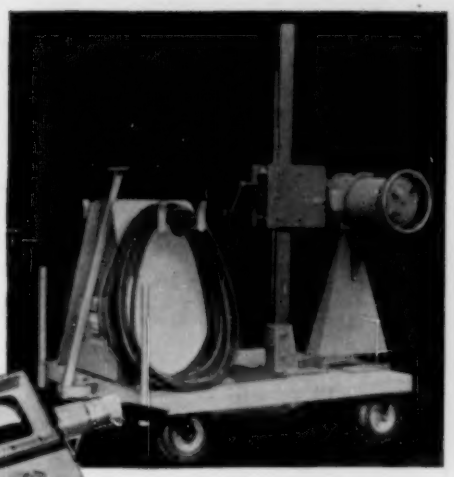

Here's one of the ten mounts available for OX-175. It's a mobile truck with elevating tube stand.

•

Sturdy control cabinet measures 18 x 18 x 14 inches . . . features large, easy-to-read dials, pinpoint accuracy of operation.

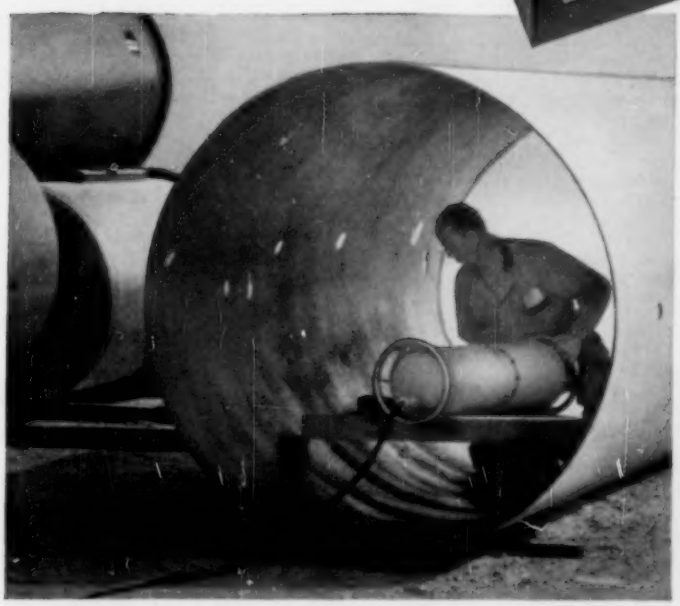

Shown here is inside-out x-ray inspection of a vessel weld.

General Electric OX-175 can help you cut costs . . . improve quality

Opening new horizons for industry in the use of x-ray inspection is General Electric's new OX-175. This rugged, lightweight apparatus handles the widest working range ever covered by a single x-ray unit.

The OX-175 can be easily moved from one job to the next, and its 200 feet of cable gives it extra portability. Highly versatile, the OX-175 can be equipped with angle-target tube for 60° field of radiation. With flat-target tube it will produce a 360° field of radiation that will radiograph an entire circumferential weld in one exposure. This also permits simultaneous radiographing of a large number of castings or assemblies by grouping these around the tube head.

In addition, the small size of the tube head makes it ideal for inside-out radiography . . . giving greater radiographic coverage, better radiographs, and reducing protective needs.

Get all the facts from your G-E x-ray representative. Or write X-Ray Department, General Electric Company, Milwaukee 1, Wisconsin, for Pub. AY14.

Progress Is Our Most Important Product

GENERAL ELECTRIC

Available Now . . .

NICKEL in IRON and STEEL

By A. M. HALL,
Battelle Memorial Institute

The second publication in the Alloys of Iron Research
NEW MONOGRAPH SERIES
Frank T. Sisco, Director and Editor

Modern metallurgy's most important alloying metal receives skillful and thorough treatment in this monograph. Taking the occurrence and refining of nickel ores as a starting point, the book delves into such important topics as: the thermal and physical properties of steels containing nickel, the structure and heat treatment of wrought and cast nickel steels, and the effect of nickel on all the important engineering properties of steel, at normal, high, and low temperatures.

The corrosion of nickel steel in the atmosphere, water, soils, and other media is completely covered, and the book provides a reliable guide for selecting the proper steel for a particular purpose. The many effects of nickel on the constitution and properties of cast iron are also included. Each chapter is concluded with a summary which spotlights important considerations.

Nickel in Iron and Steel brings you a wealth of reliable, useful information in concise, compact form. Before publication, the book was given a final stamp of approval by the Iron and Alloys Committee of the Engineering Foundation. As an index to past findings and a foundation for future research, it is the only book of its kind in existence.

1954

595 pages

Illustrated

$10.00

Mail for your ON-APPROVAL copy
JOHN WILEY & SONS, Inc.
440 Fourth Ave., New York 16, N. Y.

Please send me a copy of NICKEL IN IRON AND STEEL to examine ON APPROVAL. Within ten days I will either return the book and owe you nothing or will remit $10.00, plus postage.

Name

Address

City Zone State

( ) SAVE POSTAGE! Check here if you ENCLOSE $10.00, in which case we pay postage. Same return privilege. (JM-15)

Books for Engineers

ORDER YOUR BOOKS THROUGH AIME—Address Irene K. Sharp, Book Department. Ten pct discount given whenever possible.

Physical Chemistry and Metal Extraction, by D. W. Hopkins. *J. Garnet Miller Ltd.*, approx. $4.80, 232 pp., 1954—The book has been prepared for the use of students of extractive metallurgy, research workers in the field of physical chemistry as applied to reactions between metallic compounds, metals and slags, and technical personnel controlling or developing metal extraction processes. Theoretical basis of the subject is treated to extent needed for an adequate understanding of the practical applications. Special emphasis is placed on development from fundamental definitions along simple mathematical lines.

Deterioration of Materials, edited by Glenn A. Greathouse and Carl J. Wessel. *Reinhold Publishing Corp.*, $12.00, 835 pp., 1954—The book has been prepared with the collaboration of 24 specialists and describes and analyzes the causes of deterioration of materials and presents proven techniques for prevention or retarding such deterioration. The publishers state that this is the first book to bring under one cover a full discussion of the subject covering a wide variety of materials. The volume covers in detail the climatic, physical, chemical, and biological agents of deterioration; materials such as metals, wood, paper, textiles, cordage, leather, plastics and rubber, paints, varnishes, lacquers and enamels; electrical, electronic and other equipment; dehumidification; storage and packaging; and toxilogical aspects of preservatives used.

FBI Register of British Manufacturers, 27th edition. *Iliffe & Sons Ltd.*, approx. $5.88, 1089 pp., 1954—An important new feature of the 1955 edition of the Register is the French, German, and Spanish, Glossaries. Each glossary gives a translation of every heading in the buyer's guide. There are eight sections in the new Register, each one having a reinforced index card for ease of reference. About 6800 FBI member firms are listed under more than 5000 trade headings in the buyer's guide.

Product Directory of the Refractories Industry in the United States. *The Refractories Institute*, $2.00, 157 pp., 1954—Purpose of the directory is to list in convenient form for reference the names and addresses of manufacturers of refractories in the U. S., locations of plants, the product divisions, and the brand or trade name under which the products are sold. The book is cross indexed.

Engineering Metallurgy, by E. M. H. Lips. *Philips' Technical Library*, $6.25, 246 pp., 1954—For both the metallurgist and the practical engineer, this volume brings the study of metals into direct relationship with present day construction techniques. Latest metal data is presented in such a way as to make it easy for the engineer to find the information he needs to deal with a specific situation. It presents such things as values of the characteristics of materials he plans to use, or what particular treatment is needed to produce the physical properties he wants in these materials. Available in U.S., through Elsevier Press, Inc.

A Dictionary of Electronic Terms, edited by Gordon R. Partridge. *Allied Radio Corp.*, 25¢, 72 pp., 1954—The collection contains more than 3500 terms used in television, radio, and industrial electronics. Definitions cover mostly modern techniques and equipment, but range from many words no longer in general use to the new language of color television and electronics of nuclear physics.

Textures of the Ore Minerals and Their Significance, second edition, by A. B. Edwards. *Australasian Institute of Mining and Metallurgy*, 242 pp., 1954—The book consists of a series of lectures delivered to graduate students in the geology dept. of the University of Melbourne. While not claiming to be comprehensive, it attempts to bring together the significant ideas relating to the origin of mineral textures and their applications to geological and metallurgical problems. The approach, in the main, is genetic.

Metal Statistics, 42nd annual edition, *Metallgesellschaft A. G.*, 199 pp., 1954—The work presents statistical tables on aluminum, lead, copper, zinc, tin, cadmium, magnesium, nickel, mercury, and silver. Production and consumption statistics are presented for various countries.

Physics Literature, by Robert H. Whitford. Scarecrow Press, $5.00, 223 pp., 1954. A guide at the college level, this book describes the types and forms of literature available, lists a selected working collection, and outlines briefly the use of books and libraries. There are both author and subject indexes.

Behavior of Metals Under Impulsive Loads, by John S. Rinehart and John Pearson. *American Society for Metals*, $5.50, 256 pp., 1954. This book discusses the character of impulsive loading, conditions under which such loading develops, and the main phenomena involved when materials are subjected to rapidly applied loads of short duration. It includes treatment of loads and forces generated by impacts and explosions, and of fundamental aspects of failure under impulsive loads.

—Personnel Service—

THE following employment items are made available to AIME members on a non-profit basis by the Engineering Societies Personnel Service Inc., operating in cooperation with the Four Founder Societies. Local offices of the Personnel Service are at 8 W. 40th St., **New York 18;** 100 Farnsworth Ave., **Detroit;** 57 Post St., **San Francisco;** 84 E. Randolph St., **Chicago 1.** Applicants should address all mail to the proper key numbers in care of the New York office and include 6c in stamps for forwarding and returning application. The applicant agrees, if placed in a position by means of the Service, to pay the placement fee listed by the Service. AIME members may secure a weekly bulletin of positions available for $3.50 a quarter, $12 a year.

MEN AVAILABLE

Metallurgical Engineer, 34. Seven years responsible experience in development, customer service and technical supervision with specialty steel and aircraft engine manufacturers. Desires association with smaller manufacturer, fabricator or producer in technical sales or supervision. M-133.

POSITIONS OPEN

Engineers. (a) Junior metallurgist, under 30, will engage in research in the high temperature and wear resistant materials field. Salary, $4500 to $5400 a year. (b) Chief metallurgist or assistant director of research, 35 to 45, experienced in powder metallurgy and refractory metallurgy; in the fields of high temperature alloys, cements, cemented carbides and tool steels. Will take charge of a small group of young and progressive graduate metallurgists and chemical engineers. Salary, about $9000 a year. Location, Westchester County, N. Y. W774.

Metallurgist with experience in mechanical metallurgy and materials investigation covering ferrous and nonferrous alloys for high temperature applications. Salaries open. Location, Ohio. W757(c).

Metallurgical Engineer for welding, material testing. Salary, $4200 to $5400 a year. Location, New York State. W751(c).

Engineers. (a) Assistant director of research, 40 or over, graduate metallurgist, with some experience in powder metallurgy. If qualified will eventually become director of research into some advanced powdered metallurgy centered on the carbides. Salary to start about $10,000 a year. (b) Production engineer, 40 or younger, graduate metallurgist, able to steer a large laboratory operation into a pilot plant line and then into a full production line for powdered metal products. Salary to start about $10,000 a year. Location, East. W683.

Metallurgical Engineer, to take charge of the metallurgical problems of a mining operation. Should have thorough knowledge of flotation, cyanidation, lixiviation and if possible, have some knowledge of running a sulphuric acid plant. Accommodations for man and wife only. Salary open. Location, Chile. F172.

Mining Engineer, 30 to 40, minimum of 5 years experience in metal mining (not coal) practices and knowledge of metal mining and exploration. Will keep abreast of developments in mining department and keep executive concerned informed; will organize and present studies on operating results and special mining projects; follow up special projects requiring knowledge of mining and exploration procedures and familiarity with sources of information. Some traveling. Headquarters, New York, N. Y. W762.

Junior Engineer, mining or civil engineering graduate, for field work on gold dredging project. Must be single. Two-year contract. Salary, $3600 a year plus room and board. Location, Columbia. F44-S.

METALLURGICAL ENGINEER—BS degree plus 1 to 3 years experience with interest in welding application and development of welding materials and processes of special alloys including Titanium, Zirconium, etc. Location, Ohio. Please include complete description of work experience, present salary, etc., in reply.
Box A-5M AIME
29 W. 39th St., New York 18

METALLURGICAL ENGINEER—BS degree plus 1 to 3 years experience for research and process development in special alloys having Atomic Energy application. Location, Ohio. Please include complete description of work experience, present salary, etc., in reply.
Box A-4M AIME
29 W. 39th St., New York 18

Metallurgical or Chemical Engineering Graduate wanted to assist Melting Department metallurgist in steel mill making high speed, tool, stainless, specialty steels and high-temperature alloys. Reply giving details of education, experience, age, references, etc.
Box A-1M AIME
29 W. 39th St., New York 18

Metallurgist for laboratory work in steel mill making high-temperature alloys, high speed, tool, stainless and specialty steels. Work will include metallurgical examination of materials, writing of reports, conducting investigations of mill problems involving a large variety of alloys. Good opportunity for graduate with 1 to 3 years experience. Reply giving education, experience, age, references, etc.
Box A-3M AIME
29 W. 39th St., New York 18

Metallurgical graduate with several years experience for process development in steel mill making high-temperature alloys, high speed, tool, stainless and specialty steels. Duties would involve development of processing procedures for new alloys as well as the improvement of processes for established alloys under direction of Process Development Metallurgist. Reply giving details of education, experience, age, references, etc.
Box A-2M AIME
29 W. 39th St., New York 18

METALLURGISTS

Alloy Development—includes composition development for high temperature and magnetic alloys, phase diagrams, creep, precipitation hardening, vacuum melting and other techniques. Development experience in physical metallurgy or alloy systems, background in theoretical physical metallurgy and knowledge of solid state physics useful; M.S. or Ph.D. in Metallurgical Engineering. For application write to

Westinghouse Electric Corporation
Educational Department
East Pittsburgh, Pa.

COLUMBIA UNIVERSITY
SCHOOL OF MINES
HENRY KRUMB SCHOLARSHIPS
WILLIAM CAMPBELL FELLOWSHIPS
KENNECOTT SCHOLARSHIP

Applications for the above awards are now invited for the academic year 1955-56. They are available to degree candidates in Mining, Mineral Engineering and Metallurgy.

The Henry Krumb Scholarships, in the amount of $1000 a year, are awarded to B.S., M.S., and professional engineering degree candidates.

The William Campbell Fellowships, with the value of $1800-$2100 a year, are awarded for graduate study leading to the M.S. or doctoral degree, or for post-doctoral work.

The Kennecott Scholarship is an undergraduate scholarship, restricted to mining students, and has the value of $1000 a year.

In addition to these departmental offerings other University and Engineering School scholarships and fellowships are available to students in the School of Mines.

Application blanks and further information may be obtained from the Office of University Admissions, Columbia University, New York, 27, N. Y. The closing date for applications is February 21, 1955.

Industrial Notes

• National Precision Casting Corp., Clifton Heights, Pa. is investment casting spacer blocks used to support the skins at the leading edge of aircraft inboard flaps for the Glenn L. Martin Co. The blocks were formerly machined from 75S-T6 aluminum alloy bar stock. Investment casting has cut costs per block by about 50 pct. In addition to eliminating the numerous machining steps, the investment cast parts need no additional polishing.

• *E. I. duPont de Nemours & Co. reduced prices for ductile titanium sponge for the second time in 1954. New prices are: Grade A-1 ductile titanium metal sponge, containing a maximum of 0.3 pct iron, $4.50 per lb, a reduction of 22¢; Grade A-2 ductile sponge, with a top iron content of 0.5 pct, $4.00 per lb, a reduction of 46¢. Greater volume and plant expansion were given as the reasons for the price drop.*

• **Naresco Equipment Corp. has put a new 30 lb induction heated vacuum furnace on the market. The equipment sales subsidiary of National Research Corp. states that furnace is available with either a vertical or horizontal shell. The furnace is completely self contained, has a co-axial power feed-through, and has facilities for adding additional charge or alloying material during melt without loss of vacuum.**

• Chemurgic Process Corp. has developed an efficient, low cost process for removing industrial odors and fumes and recovering valuable vapors from plant exhausts. The process, Siftaire, makes use of lung protecting principles of the gas mask.

• A new research and product development center has been opened in Denver, Colo. by Micro Switch, a div. of Minneapolis-Honeywell Regulator Co. The new center will supplement research activities at the division's main office and factory in Freeport, Ill. Wilbert Martin, assistant director of product research and development will be in charge of the new facility.

• *With its first nonferrous metals casting clinic a success, Federated Metals Div., American Smelting & Refining Co., plans to hold similar sessions in other parts of the country. The first clinic was held at the company's New Jersey laboratories in October. The first clinic attracted 85 foundry supervisors and metallurgists from about 45 nonferrous foundries in the metropolitan New York and Philadelphia areas.*

• **Tabor Mfg. Co., 70 year old manufacturers of foundry molding machines and equipment, has become a division of Turbo Machine Co., Lansdale, Pa. Turbo announced that the complete Tabor line will be made in Lansdale. Purchase involved business name trademark, inventories, patents, and licenses, but did not include remaining assets, principally fixed assets, which will be sold at auction.**

• U. S. Gypsum Co. has launched a campaign to call attention to its new Hydroperm, a casting plaster for nonferrous metals. The firm believes the product answers requirements for a product giving a mold with the smoothness of plaster and the permeability of sand.

• *Dow Chemical Co. formed a research and development section in the market research dept. Primary job will be analyzing specific industrial fields as a means of forecasting long range trends and needs. Dow will use the information to develop new products.*

• **Battelle Memorial Institute is planning a $1.53 million expansion of its nuclear energy research facilities. Funds have already been appropriated by the Institute's trustees. On the program is the construction of a nuclear reactor, a reactor development laboratory, and a nuclear fuels laboratory, and installation of a large cobalt-60 source.**

• Pennsylvania Salt Mfg. Co. has acquired all patents and assets of the Gilron Products Co. of Cleveland, Ohio. One of the products featured by Gilron is Drawcote, a light drawing compound widely used in the automotive, appliance, and munitions industry.

• **Jones & Laughlin Corp. plans to spend $50 million for improvement and expansion of plant and equipment in 1955. Most important of the projects involved are: additional equipment for producing new joist sections at the 14 in. bar mill at the Aliquippa, Pa. Works. Additional facilities at Aliquippa for production of high strength and special seamless tube products used in the oil industry; an electric-weld pipe mill at Aliquippa designed to produce pipe for the oil industry and broaden market scope; improved and additional wire and wire specialty manufacturing facilities; and a continuous sheet galvanizing line at Pittsburgh.**

• A new vacuum melting and casting furnace for moderate-size production of high-purity metals or for experimental and pilot plant work has been developed by F. J. Stokes Machine Co., Philadelphia, Pa. The new furnace has a melting capacity of 50 lb of steel or other metals. Chamber of the furnace is a horizontal cylinder 4 ft in diam and 4 ft long.

Coming Events

Feb. 3-5, 1955, Colorado Mining Assn., annual meeting, Denver, Colo.

Feb. 8-9, Midwest Welding Conference, Armour Research Foundation, Illinois Institute of Technology, Chicago.

Feb. 10, AIME, Cleveland Local Section, American Room, Manger Hotel, Cleveland.

Feb. 14-17, AIME, annual meeting, Hotel Conrad Hilton, Chicago, Ill.

Feb. 21-24, American Concrete Institute, annual convention, Hotel Schroeder, Milwaukee, Wis.

Mar. 9, AIME, Connecticut Local Section, Bridgeport, Conn.

Mar. 10, AIME, Cleveland Local Section, American Room, Manger Hotel, Cleveland.

Mar. 10-11, Porcelain Enamel Institute, Pacific Coast conference, Biltmore Hotel, Los Angeles, Calif.

Mar. 14-15, Steel Founders' Society of America, annual meeting, Drake Hotel, Chicago, Ill.

Mar. 15, Society for Applied Spectroscopy, Philadelphia Section, Philadelphia, Pa.

Mar. 16, AIME, Connecticut Local Section, annual meeting, Statler Hotel, Hartford, Conn.

Mar. 20-23, American Institute of Chemical Engineers, Kentucky Hotel, Louisville, Ky.

Mar. 28-Apr. 1, Western Metal Exposition, Western Metal Congress; Pan-Pacific Auditorium, Ambassador Hotel, Los Angeles, Calif.

Apr. 13, Material Handling Institute, spring meeting, Drake Hotel, Chicago, Ill.

Apr. 14, AIME, Cleveland Local Section, joint meeting with American Ceramic Society, NACA Laboratories, Cleveland Hopkins Airport.

Apr. 18-19, Third National Air Pollution Symposium, Pasadena, Calif.

Apr. 18-20, AIME, Blast Furnace, Coke Oven and Raw Materials and National Open Hearth Steel Conferences, Bellevue-Stratford Hotel, Philadelphia.

Apr. 19-21, Canadian Institute of Mining and Metallurgy, annual meeting, Royal York Hotel, Toronto.

Apr. 28-30, AIME, Pacific Northwest Conference, Spokane, Wash.

May 1-4, American Institute of Chemical Engineers, Shamrock Hotel, Houston, Texas.

May 2-6, Electrochemical Society, Sheraton-Gibson Hotel, Cincinnati, Ohio.

May 6, American Assn. of Spectrographers, annual conference, Chicago.

May 14-22, Chemical Engineering & Equipment Exhibition, Frankfort am Main, Germany.

May 18-20, Porcelain Enamel Institute, mid-year div. conference, Edgewater Beach Hotel, Chicago.

May 30-June 1, Chemical Institute of Canada, annual conference, Quebec, Canada.

June 1-18, Joint Metallurgical Societies, European meeting.

Heroult ELECTRIC MELTING FURNACES

TOPS FOR PRODUCTION OF HIGH GRADE STAINLESS, ALLOY AND RIMMING STEELS

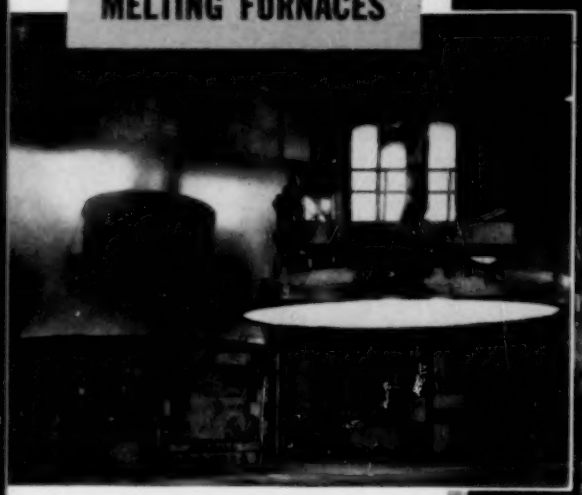

World's Largest Electric Furnaces

. . . now in operation!

INSTALLED in the ultra-modern mill of McLouth Steel Corporation, in Detroit, these giant *200-Ton* Heroults are the largest electric melting furnaces ever built. With an inside shell diameter of 24'6", they have a rated charge capacity of 400,000 pounds, and each is designed for efficient operation on 25,000 to 33,000 KVA transformer capacity. Featuring a swing-type roof, these furnaces are equipped with the finest, most up-to-date mechanism and electrical controls available.

McLouth's adoption of electric furnaces of this size sets a precedent. It is a "first" which should conclusively prove that, in addition to closer control, higher uniformity, better performance, and greater safety, large capacity Heroult Electric Furnaces are an economically sound investment—even for high tonnage steel-making.

We welcome an opportunity to help you select and install the furnace best suited to your particular requirements.

ASK FOR NEW CATALOGUE. *Contains latest information on modern electric furnaces—types, sizes, capacities, rating, etc. Write Pittsburgh Office for free copy.*

AMERICAN BRIDGE DIVISION, UNITED STATES STEEL CORPORATION
GENERAL OFFICES: 525 WILLIAM PENN PLACE, PITTSBURGH, PA.

Contracting Offices in New York, Philadelphia, Chicago, San Francisco and other principal cities.
United States Steel Export Company, New York

USS

UNITED STATES STEEL

Journal of Metals

AFTER a rather dismal beginning last year, the steel industry closed out 1954 with a sudden, healthy upsurge that for the most part could be traced to the widespread public acceptance of the 1955 automobile models. Several steel industry spokesmen interpreted the rise in production as a good sign of better days in 1955. On another, probably more significant front, steel men were encouraged by what appears to be an improvement in the broad base of consumer demand.

Generally speaking, most conservative prophets are apt to go slowly with highflown predictions, but the usual rash of year's end forecasts ran the gamut. Significantly, though, two leading steel executives predicted that production this year will jump about 10 to 14 million net tons over last year. Even the less encouraging statements were couched in terms that promise that this will be a good year for the steel industry. Construction, enjoying its greatest boom, appears to be headed for another good year. If business continues to improve as it has, public confidence may even require a revision upward of current projected plans. Defense outlays, at the very least will be equal to 1954 and some experts think they will be even greater.

Inventory during 1954 fell well below normal minimums. Thus replacements will be one of the important factors this year. How intense replacement will be is a matter for speculation at this point, the economists feel. A number of orders have come into sales offices with *urgent* written all over them, suggesting that until now many buyers have been buying on the basis of last minute needs.

Some forecasts place production at an average of 84 pct of capacity during 1955. With only a 16 pct production reserve on hand, buyers will have to take a good look at policy. The reserve would not mean a similar percentage available in terms of steel products.

The general feeling for the first quarter of this year is that the current demand for finished products will continue without abatement. Another group, only slightly less conservative, feels that the first half of 1955 should be better than the similar period last year. Another facet to be considered is the expected government aid to railroads which may stimulate car buying and other replacements on the roads. Railroads have been spending in relation to income—not good for the steel industry. But no recovery in railroad buying is expected which will match recovery in other areas of the economy.

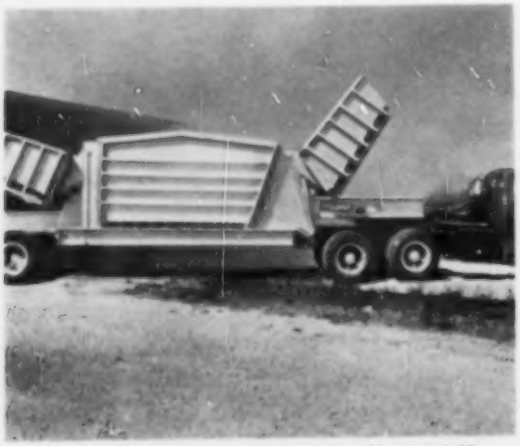

Dominion Foundries & Steel Ltd. is using this special 35-ton Fruehauf carryall with Phil Wood hot ingot carrying body to transport hot ingots from soaking pits to rolling mill. Use of the special conveyor eliminates ingot reheating.

◆◆◆◆◆◆

DESPITE all the talk about the coming substitution for materials used in the tin can, one American Can Co. representative thinks that it will be some time before the tin can is completely replaced with anything else. J. M. Jackson, manager of the American Can Co.'s Maywood, Ill. laboratory told the Senate Subcommittee on Minerals and Metals that some substitutes have been found for certain products, but no overall replacement has been developed.

There is possibly nothing more prosaic than the tin can. Yet, when the magnitude of the can industry's growth is taken into account, from only 2 million cans in 1900 to 35 billion cans in 1953, its place in American economic life is impressive. Some 4,003,692 tons of sheet metal were used in 1953. Right now intensive research is being directed toward finding a substitute for tin itself in the manufacture of the containers. Organic coatings (chemical treatment) and metallic coatings are under study. Additional use of steel, synthetic rubber, resins, and drying oils have reduced the amount of tin essential for some cans.

Mr. Jackson told the Senate group that projects underway to reduce the amount of soldering include application of metal coatings on margin areas of the steel to facilitate soldering with tin-free solder, electric welding, and replacement of metallic solders with cements of higher bonding strength and sealing efficiency.

Work toward development of new organic coatings to protect steel surfaces from corrosion has been encouraging, but still requires a great deal of research to lower costs and improve effectiveness. It is hoped that eventually steel sheets can be protected by special can enamels without the benefit of chemical pretreatment.

◆◆◆◆◆◆

CHEMICAL nickel plating appears to offer some definite advantages over the electrolytic method and American Locomotive Co. spokesmen seem to be sold on the processes' future. However, there are still several unanswered questions that only the future can solve. Right now, Alco, under license from General American Transportation Corp.,

Trends

owners of the patents on the Kanigen process, has installed the largest capacity plant for commercial application of chemical nickel plating in industry. Alcoplate incorporates some significant pre-plating and post-plating operations, along with experimentation, laboratory testing, and quality control.

One of the largely unanswered questions concerning Alcoplate is its cost vs that of electrolytic plating. Company officials agree that cost is probably no more, and quite probably will prove to be less, for chemical plating. Right now there is still insufficient data for a final conclusion.

The product to be plated is immersed, after suitable surface pretreatment, in a 180°F alkali cleaner for 10 min. After rinsing in cold water, the piece is pickled for 10 min in muriatic acid at room temperature. A second cold water rinse precedes reimmersion in the alkali cleaner. In the actual plating process geometry of the piece to be plated is no problem. Plating is evenly executed over any area—despite irregularities of surface or shape. Alco also claims that thickness of plating is uniform, and even in the thinnest plating thicknesses zero porosity is guaranteed. The bond is intermolecular. Plated steel shows no flaking or spalling even when pulled to the yield point. Hardness averages about 500 Vickers or 49 Rc and can be increased by post-plating heat treatment to 950 Vickers or 63 Rc.

Alco is conducting investigations that are expected to disclose the practical limitations of chemical nickel plating. The process is being offered for those products where definite test information has shown the soundness of the application.

One of the stranger aspects of the process is its original discovery in 1844. Until 1916 it remained a laboratory and classroom curiosity. The U. S. Bureau of Standards, under the direction of Abner Brenner and Grace Riddel, have been performing pioneering work since 1916. A patent for such a process was issued by the U. S. to Roux during that year and many others have followed. General American now holds most of the patents.

In recent months Alco has actually used the new process to plate more than 200 million sq ft of transmission equipment for the Atomic Energy Commission. Chemicals for plating are mixed in 8 ft diam make-up tanks. Solution is transferred through plastic pipe to the surge tank of the process loop. From the surge tank solution is pumped through a pre-heater into the main heater, where temperature is raised to 215°F and then introduced into the work to be plated. Plating takes place by catalytic reduction of nickel by sodium hypophosphite at the elevated temperatures. From the product, the spent nickel passes through flash evaporators to the generation tank. Flash evaporators are used to drop solution temperature rapidly and to remove accumulated condensate from the main heater. In the generation tank concentrated solutions of caustic, nickel sulphate, and sodium hypophosphite are introduced by an automatic proportioning pump to restore the solution to optimum concentration. Alcoplate will plate almost any material except glass. Thus, glass pipe and glass linings are used for all parts of the system from the preheater to the flash evaporators. Recently, it has been found that with proper preparation, even plastics may be coated with nickel. The chemical composition of Alcoplate is 93 pct nickel and 7 pct phosphorus. After plating, products are dipped in a rinse water solution at room temperature and then immersed in a hot alkaline solution for 10 min, followed by a final rinse.

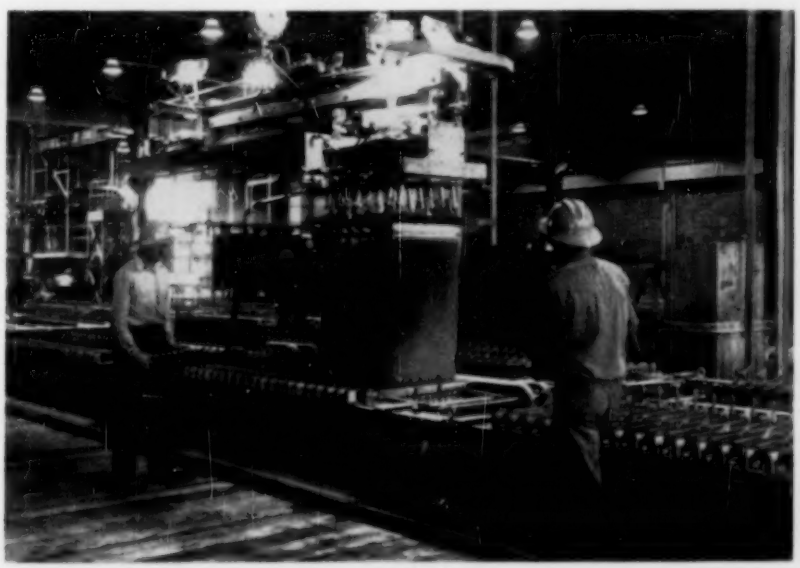

This is the cell room of Electro Metallurgical Co.'s new electrolytic manganese plant at Marietta, Ohio. Plant output is expected to be about 6000 tons a year when electrolytic units are in full operation.

Drift of Things

SEVERAL times in the course of a year, the subject of the shortage of engineers is reopened for discussion. The latest word on the subject is that the Russians are graduating increasing numbers of engineers and technicians, and in a short time will have more trained technical manpower than that available in the U. S. Engineering school enrollment here has dropped steadily until this year, with but slight increases predicted for the next few years, despite the demand for engineers and scientists. This low enrollment has been blamed on many factors, ranging from the reported poor quality of secondary school training and guidance, to the draft.

Perhaps one of the most important, but least spoken of factors, is that in the Soviet Union the scientific and engineering occupations are the highest paid. In addition, as AIME President Leo Reinartz pointed out in a recent talk, the Russian engineer is the national hero.

We have failed someplace—applicants for medicine schools far exceed the facilities available, law schools are crowded, business administration is increasing in popularity, but engineering and teaching are lagging. It is probably true that the low salaries are responsible for the dearth of teachers, but except for a few incidences, this does not apply to engineering. For the most part, we cannot control the high schools, selective services, salaries, etc., but there remains much that we can do.

Metallurgy and metallurgical engineering can and should be popularized, to attract prospective students. All the aspects of popularization exist—glamour, the challenge, the tremendous unknown. When talking to high school students and the public in general, we must appeal to them in terms that they can understand—not in terms with which we are familiar. The word must be spread, and that is within the power of every engineer.

Many companies, usually large organizations, have excellent public relations, student guidance, and scholarship programs. They have found that these are not merely philanthropic ventures, but actually pay interest in the form of interested and trained individuals that eventually take their place in industry and are able to contribute to the profession. More companies, the small as well as the large, are needed to adopt this forward outlook—the companies that require engineering talent have the most at stake.

Mr. Reinartz has suggested that AIME Local Sections, or individual members, adopt a *big brother* policy—taking under their guidance one or more high school or college students interested in engineering. Metallurgical engineering students would welcome the opportunity to be taken to AIME meetings as guests, and to be introduced to various leaders in the field for inspiration and information.

ACCORDING to the report of the Engineering Societies Library for the fiscal year ended Sept. 30, 1954, 16,817 visitors were served, and 21,278 nonvisitors. Orders for photoprints increased to 4704. Close to 10,000 telephone inquiries were answered and some 4800 written replies to inquiries. A total of some 260,000 words were translated. The number of borrowers decreased owing to a discontinuance of lending periodicals.

The Library now consists of 170,787 volumes, 16,301 maps, and 5,457 searches. One third of the new accessions were gifts, and the Director, Ralph H. Phelps, will welcome offers of books that may be desirable additions. Approximately 1400 periodicals are currently being received. Special note in the report is made of the greatly increased number of Japanese technical periodicals now being received, nearly 50 of which are in the field of the Library, all either wholly in English or with English summaries.

Library hours are now from 10 am to 9 pm except Saturdays, 1 to 6 pm; closed Sundays and the principal holidays. (E.H.R.)

MEMBERS of AIME are urged by Orville T. Colby, chief, technology div., Office of Technical Services, Dept. of Commerce, Washington 25, D. C. to make more use of the growing stock of research reports released by the Federal Government through his office. He states that the Government is conducting or sponsoring scientific and technical research at a rate of $2 billion a year, mostly for military purposes. By far the largest share represents applied research and development. The research generates a large amount of nonconfidential technical information available to those interested in developing new production processes, in making technological improvements, and in avoiding duplication of research efforts. Even ideas for new products have been sparked by these reports.

Some 350 such reports are described each month in *U. S. Government Research Reports*, (formerly *Bibliography of Technical Reports*), available from the Superintendent of Documents, Government Printing Office, Washington 25, D. C., or from any of the U. S. Dept. of Commerce field offices, for $6 per year. (E.H.R.)

ANOTHER big season of meetings has just begun, and a few words of advice are in order. To begin with, if you contemplate attending any out-of-town meeting, you would be wise to make hotel reservations well in advance. We cannot overemphasize the importance of early reservations, and you have only to observe the proceedings in a hotel lobby the day of a big meeting and see the people being turned away to impress this upon yourself. When an AIME meeting is held, the Institute arrangements with the headquarters hotel require that the hotel set aside a certain minimum number of rooms for registrants, and that the hotel give preference to reservations specifying the meeting. It is your individual responsibility to obtain a room. All reservations, including those for special luncheons, are on a first come-first served basis.

Many AIME members attending a meeting have been annoyed by telephone calls from photographers who claim to be *official* photographers. If any *official* photographs are to be scheduled, you will be so notified by a staff member of the Institute. When the Publications Dept. does employ a photographer for meeting photographs, no attempt is made to sell the photographs—they become the property of the Institute. Quite often a hotel will permit photographers to take overall group photographs of banquets, but the individual is under no obligation to purchase a copy.

A. S. Cohan

MAKE YOUR ELECTRODES STOP LOAFING!

Let your men see and hear *The Electrode Story* — a shop-level informational program aimed at developing optimum electrode service for electric steel producers.

This series of four illustrated talks — developed especially for melt shop personnel — gives the men-on-the-furnace a better knowledge and understanding of electrode handling and joint assembly.

***The Electrode Story* was developed to help effect important economies in electrode utilization, and thus contribute to the advancement of the electric steel industry as a whole. It is being made available to electric furnace steel producers without charge or obligation. This forward-looking program can help your company get optimum service from electrodes and substantially reduce electrode costs.**

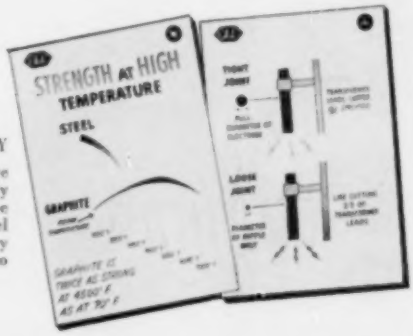

Typical Panels From THE ELECTRODE STORY

Two of the many informative panels that dramatize simply yet forcefully the importance of electrodes in electric steel making, and the reasons why proper shop practice is so important.

Inquiries about *The Electrode Story* are most cordially invited. Write to . . .

ELECTRODE DIVISION

Great Lakes Carbon Corporation

GLC

18 EAST 48th STREET • NEW YORK 17, NEW YORK

JOIN THIS RAPIDLY GROWING GROUP OF ELECTRIC STEEL PRODUCERS who have benefited from *The Electrode Story* informational program.

Allegheny Ludlum Steel Corporation
Copperweld Steel Company
Crucible Steel Company of America
Firth Sterling Inc.
Fort Pitt Steel Casting Co.
Jessop Steel Company
McQuay-Norris Manufacturing Co.
National Malleable and Steel Castings Company
Newport Steel Corporation
Northwestern Steel & Wire Company
Rotary Electric Steel Company
St. Louis Steel Casting Company
Sterling Steel Casting Co.
. . . and many others

HERE'S WHAT ELECTRIC STEEL PRODUCERS SAY ABOUT *The Electrode Story*

". . GLC is setting the pace on education within the industry."
". . brings home to the men the importance of proper handling of materials."
". . the improvements were very noticeable."
". . is proving helpful in reducing consumption."
". . has shown marked improvements in the Melting Department."
". . one of the best things that ever happened to educate the men on the furnace."
". . the results of the lectures are noticeable daily in the extra care taken in handling and assembling electrodes."
". . a model of the use of visual aids and of conference and discussion techniques."
". . the men are more careful now."
". . proved very beneficial in better handling of electrodes."

"Great Lakes takes the long-range view that it is better to sell an extra carload of electrodes because a customer has added another furnace, than because he is getting less-than-optimum service out of his existing equipment"— from an article in STEEL.

USS "T-1", A Nickel Alloy Steel, Helps Save Money

Lips of Nickel Alloy Steel show 11 times the life of the previous material used . . . in Clamshell Bucket

T-1 steel not only replaced a more expensive material here, but also outlasted it by 11 to 1. In this application, T-1 is still on the job after 11 months, handling open hearth sinter, whereas a wear resisting steel cracked and failed in 30 days under abrasion, impact and operating temperatures of 500 to 600°F.

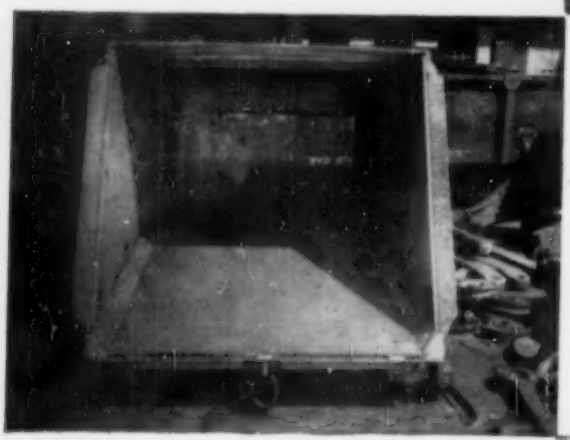

4 to 1 Better Service than carbon-manganese steel . . . in Skip Car Bottoms, Sides and Bail Plates

On skip cars handling coke, ore and limestone, T-1 steel bottoms, sides and bail plates are saving money. So far they have outlasted carbon-manganese steel 4 to 1. This four-fold longer life means more use per dollar for T-1 steel even though its initial cost is about twice that of the steel it replaced.

Unmatched Performance under heat and wear . . . in Blooming Mill Conveyor Chain

Here's a 40" blooming mill conveyor chain for lifting hot slabs at U. S. Steel's Ohio Works. Various materials used for chain failed under the severest impact conditions imaginable, caused by falling or jammed hot slabs. Notice the good appearance of the present chain made from T-1 steel. This product has far outlasted all previously used materials.

These applications in U. S. Steel's Ohio Works show how T-1 steel can reduce your maintenance, operating and repair expenses under like conditions. Write for complete details.

INCO
TRADE MARK

THE INTERNATIONAL NICKEL COMPANY, INC.

67 WALL STREET
NEW YORK 5, N. Y.

A lump-sum contract to design, build, and test operate a prototype package nuclear power plant for military use has been awarded to the American Locomotive Co. The project is designed to develop a power reactor plant with components transportable by air, which can be used at remove bases. The Atomic Energy Commission will share the contract price of $2,096,753 with the Dept. of the Army. The prototype will have a capacity of about 2000 kw.

It has been estimated that aluminum production for 1954 reached 2.9 million lb. Production stayed at record levels for most of the year.

The Air Force is planning to build a $5.75 million atomic research laboratory in Middletown, Conn. The project may eventually employ about 2500 people and will operate in connection with the Pratt & Whitney Div. of United Aircraft Corp. The original price tag covers land acquisition and laboratory construction. Recent estimates predict an additional cost of $4.25 million.

Wisconsin Centrifugal Foundry, Inc., has uncovered what is said to be the first successful method for the centrifugal casting of titanium. Casting must be conducted in a vacuum or inert atmosphere to prevent oxidation and other chemical action. Armour Research Foundation participated in the development.

Climax Molybdenum raised the price of molybdic oxide about 10 pct and other refined products proportionately. Molybdic oxide now costs $1.25 per lb of contained molybdenum. The last price change was made in December 1950.

Silicate coating, similar to porcelain enamel, which fuses to metal at temperatures from 900° to 1200°F has been produced by Poor & Co. and Youngstown Sheet & Tube Co. Coating is applied like paint, water is evaporated and the object fired in a furnace. Basic ingredient is sand from northern Michigan.

A new pump that works on an electromagnetic principle can move liquids within cooling or heating systems, according to Callery Chemical Co., Callery, Pa. An electric current is passed through the metal in a direction perpendicular to a magnetic field surrounding the metal, producing a force that sets the metal in motion within the pumping section. The pump can also be used to force liquid into die casting forms.

It has been reported that India rejected a bid by British investors to build a million ton steel plant in association with Indian businessmen. However, it is reported that the project may be approved if the British interests agree to give the Indian Government the controlling share of the company. India is also said to be talking over the possibility of a half million and a million ton steel plant with the USSR.

Announcing . . .

ELECTROLYTIC MANGANESE

99.9% PURE

Now available from ELECTROMET in tonnage quantities. For all uses where a high purity manganese is required, including:

. *Low-Carbon Stainless Steels*
. *High-Temperature Alloys*
. *Non-Ferrous Alloys*
. *Electrical Resistance Alloys*

Electrolytic manganese is now being produced in tonnage quantities at ELECTROMET's new Marietta, Ohio, plant. ELECTROMET's new manufacturing process produces manganese of very high purity with 99.9 per cent minimum manganese.

Additional information about electrolytic manganese and other ELECTROMET ferro-alloys and metals will be gladly furnished on request. The ELECTROMET office in your area will be pleased to answer your inquiry.

The term "Electromet" is a registered trade-mark of Union Carbide and Carbon Corporation.

ELECTRO METALLURGICAL COMPANY
A Division of Union Carbide and Carbon Corporation
30 East 42nd Street UCC New York 17, N. Y.
OFFICES: Birmingham • Chicago • Cleveland • Detroit
Houston • Los Angeles • New York • Pittsburgh • San Francisco
In Canada: Electro Metallurgical Company, Division of Union Carbide Canada Limited, Welland, Ontario

Electromet
TRADE MARK
Ferro-Alloys and Metals

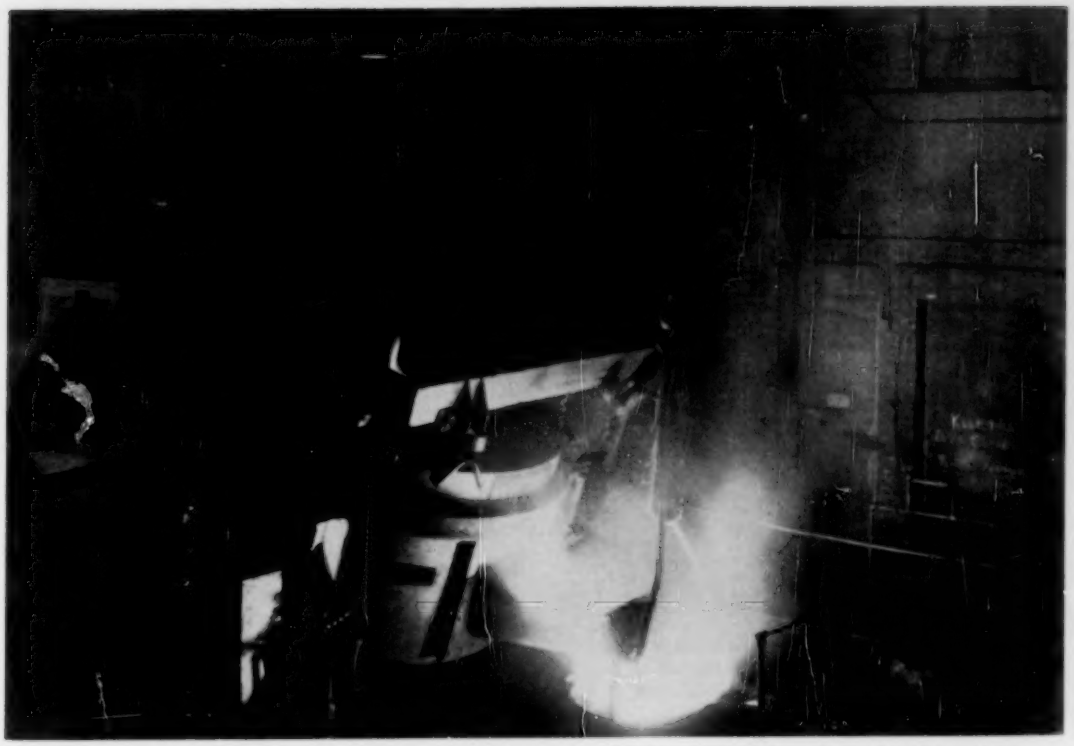

Hydro-arc control was installed on an 8MT furnace which has an 8-ft shell diam. Graphite electrodes are 8-in. diam and are energized by an 1800-kva transformer.

Hydro-Arc Control Reduces Costs In Electric Furnace Operation

by Joseph Seymour

A NEW hydro-arc control was installed by Kensington Co. to obtain experimental data under production conditions. The control was used in connection with the hydro-arc basic practice furnace which is used to manufacture Hadfield manganese steel castings.

The new control was installed in such a manner that it could be changed to the original control in approximately one minute if anything went wrong. With this set-up it was possible to give the new control very severe service, within the limits of the rest of the equipment, without fear of stopping the production operation of the furnace.

The original equipment used with the Whiting hydro-arc furnace was the hydraulic electrode positioning equipment using reversing electrode motors energized by a current contactor type of furnace regulator. An 1800 kva furnace transformer used on an old furnace was replaced by the new furnace. The tap settings on the transformer used are given in Table I.

The new equipment consists of an air counterbalanced hydraulic differential energized directly from the furnace bus. The electrode motors do not reverse. They operate in one direction only. One motor runs at constant speed while another runs at a variable speed according to what the furnace demands. The same transformer is still used with the same tap settings. The furnace, which is a size 8MT having an 8-ft shell diam using 8-in. graphite electrodes, could be energized with a larger transformer.

Operations and Savings

When the control was first installed, some bottom trouble was encountered because the electrodes bored through the charge so rapidly that there was not an adequate pool of metal formed under them when they reached the bottom. Also, when the heat

J. SEYMOUR is Chief Metallurgist, Kensington Steel Co., Kensington, Ill. This paper was presented at the AIME Electric Furnace Steel Conference, Pittsburgh, Dec. 1 to 3, 1954.

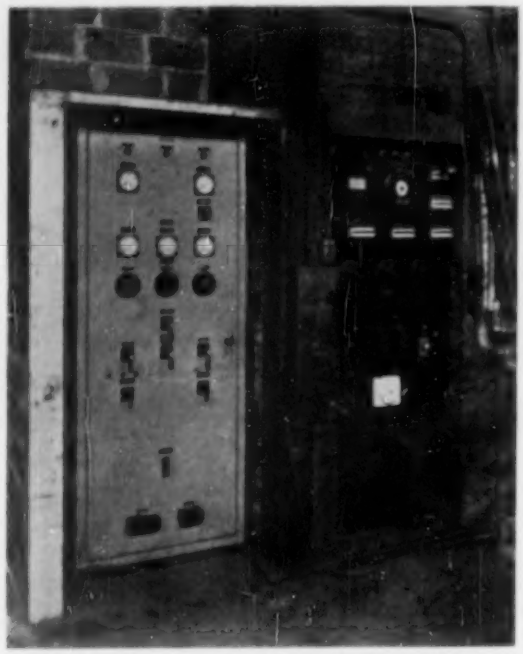

Location of new panel board for hydro-arc control with respect to original board makes it possible to change from one control to the other in approximately 1 min.

should have been melted down, according to time, there still remained quite a bit of unmelted scrap clinging to the banks and sidewalls. This was caused by the extreme concentration of the heat of the arc straight down and not spreading enough. Correction was accomplished by simply taking reactance out of the circuit and making the arc wilder. More reactance could have been removed but the old control, which was maintained in operating condition during these tests, would not operate satisfactorily with so much removed from the circuit. Removing this reactance from the system has increased the power factor and changed what was a boring machine into a melting tool. This displaced enough metal to cover the bottom refractories sufficiently to eliminate the bottom refractory problem. The arc heat was spread to reach unmelted scrap at the sidewalls without damaging sidewall refractories.

The electrodes operate at a speed of approximately 4 ft per min as before, but it is believed that with the rapid response to the arc signal now obtained that the electrode speed could be increased to approximately 6 ft per min or more and still maintain a steady arc.

Because of the rapid response of the electrodes and their ability to hold the arc no great surging was experienced. The elimination of this surging, along with the reduction of the reactance, has helped to keep the transformer operating at a lower temperature. Actually it was found that the transformer temperature runs approximately 10 to 15 deg cooler with the new control.

Refractory cost was also reduced by about 10 to 12 pct. This, it is believed, was due to the rapid response and speed of the electrodes.

Another saving has been in kilowatt hour consumption. Consumption has been reduced by about 5 to 6 pct. The old control averaged between 520 kwh per ton to 530 kwh per ton, and with the new control the average is between 485 kwh per ton to 495 kwh per ton. Electrode consumption has remained about the same with both controls approximately 7 lb per ton. This is very good and would be hard to improve upon.

Facilities in the plant limit the ability to take full advantage of the speed available with this control. However, there have been occasions when only one furnace was operating for a full day. Using the furnace with the new control during these times melting time was reduced from tap to tap by about 15 pct and averaged 489 kwh per ton.

On another occasion a failure of the tap changing mechanism made it impossible to get off the first tap. This was no fault of the new control. The furnace continued to operate on first tap for the balance of the heat by cutting back the rheostats as the heat progressed. The heat was tapped within the regular time and at the proper temperature without any increase in kilowatt hours per ton and with no noticeable damage to the roof or sidewalls.

Table I. Tap Setting on Furnace Transformer

Tap	Volts	Amp
No. 1	214	6850
No. 2	160	6270
No. 3	108.5	5520
No. 4	86	6270

New and Old Maintenance

Experience in the past with the old furnace control showed that it required approximately 2 to 3 hr every week to clean and check the contactors, springs, and other movable parts.

After about seven months of fairly steady use of the new control none of the equipment has been cleaned with the exception of the front of the operator's panel. This was done to see just how long the equipment would operate before it failed and then try to determine what caused the failure. This is not recommended as a regular practice although in all that time only two fuses were replaced. These blew shortly after the equipment was installed. Slightly heavier fuses were used and no further difficulties have been encountered.

The only other problem which developed, and this was due to the temporary set-up of the testing equipment, was that one of the hydraulic connections leading from one of the pumps failed and sprayed oil around the transformer room. The failure of this connection was, it is believed, caused by vibration of the platform on which the equipment was installed. Because of the crowded conditions in the transformer room the new control was installed on a steel platform standing on legs about 10 ft high and not too rigidly braced. At this time the equipment is being relocated in a cabinet mounted solidly against the wall outside the transformer room and down at floor level. This should eliminate any vibration and also improve the efficiency of the equipment by reducing the head of oil to the pumps and lengths of pipe needed.

Reference

[1] Charles W. Vokac: New Developments in Electric Furnace Design and Operation. *Proc. Electric Furnace Steel Conference*, AIME (1953) **11**, p. 174.

History of Iron Ore Sintering Recalls Variety of Experimentation

Numerous methods were invented to solve the problem of agglomeration of flue dust and other kinds of ore fines. Methods tried on a large scale were: sintering, briquetting, blocking, and nodulizing. The sintering process introduced in 1900 has developed into the most efficient and economical of these processes.

by Michael O. Holowaty

FIRST mention of a steelmaking process that included a step of ore agglomeration is to be found in a description of the ancient Catalan or Corsican furnaces. In these processes carbon fuel was intimately mixed with ore, heated, and charged into a shaft furnace. The first stage of the reduction was characterized by fusion of ore particles together in a hard clinker like mass.

The following centuries of metal making show little changes in iron ore handling and treating methods. Even the introduction of reverberatory furnaces in the copper and lead smelting industries, and the gradual development of modern high capacity, iron producing blast furnaces did nothing to improve the situation created by the mounting piles of ore fines and flue dust.

The first steps leading to the final solution of the problem were made in England and Germany about the middle of the nineteenth century. English copper foundries used a battery of small sintering (blast roasting) pots to agglomerate copper sulphide fines. The performance of the battery was apparently satisfactory since the battery was in continuous use for over 25 years.[1] German lead smelters at Freidberg in Saxony were well acquainted with blast roasting of ores as sintering was called in those days.[2] They operated two small horizontal updraft sintering pots for lead sulphide fines.

James W. Neill, an American mining engineer, is credited with the first recorded commercial sintering operation of iron ore.[3] After ten years of experimenting, Neill built two regular sintering pots in 1892 at Bingham Canyon, Colo. The pots were constructed of cast iron plates and measured 6x4 ft. In the course of this process Neill sintered several hundred tons of −1 in. pyrite ore and pyrite iron concentrates from the old Jordan Mining Co. Neill's process was abandoned about 1902 or 1903 and substituted with newer, more efficient sintering methods.

The commercial sintering processes were first developed and accepted for the sintering of copper sulphides because the profit margin was more favorable in this metal industry than in any other at that time. Gradually, however, sintering was accepted by the lead, zinc, and finally the iron industry.

M. O. HOLOWATY is Research Metallurgist, Research and Development Dept., Indiana Harbor Works, Inland Steel Co., East Chicago, Ind.

Modern sintering industry was developed and practically applied by the nonferrous industry. Sintering processes are closely interrelated and have frequently used identical equipment for agglomeration of ferrous as well as nonferrous materials. Commercial sintering processes fall generally into one of the two basic classes of sintering methods: A—updraft sintering, and B—downdraft sintering.

Updraft Sintering

The Huntington-Heberlein pot sintering process was introduced to the U. S. in 1905 by the American Smelting & Refining Co. which held the patent rights for the U. S.[4] The primary objective of this process was to agglomerate lead sulphide fines which could not be used directly in the blast furnace. The pots used in the process were made of cast iron and equipped with a stationary grate. The pots were square, 9x11 ft long and 15 in. to 36 in. deep. The joints between the cast walls of the pot and between the grate and the pot were air tight with asbestos cord. Usually one 5 or 8-in. air pipe was attached to a hopper welded to the lower part of each pot. The capacities of the sintering pots ranged from 10 to 25 tons per day depending on the size of the pot and the characteristics of the ore. The sintering plants of the lead industry usually employed batteries of Huntington-Heberlein pots consisting of 14 pots arranged in one line. Sintering of galena fines lowered the sulphur content of the product by about 50 pct. Because the high sulphur content of the material no other fuel was required in the sintering operation. The Huntington-Heberlein process has been also applied to the agglomeration of blast furnace flue dust. The resulting material was of more or less cellular structure. The surface of the material was glazed by the silicates and consequently undesirable for use in the blast furnace.

The Savelsberg process was originated in Sweden.[5] Its application in the U. S. was limited to sintering lead sulphide concentrates, and in a modified form to the agglomeration of copper bearing fines.

A typical Savelsberg installation was used at St. Joseph Lead Co. at Flat River, Mo. for desulphurizing and agglomerating galena concentrates. The installation consisted of 18 pots placed in two rows. The pots were 8.5 ft diam and 4.5 ft deep. The average daily production of each pot was about 20 tons. The mixing of the charge was done mechanically.

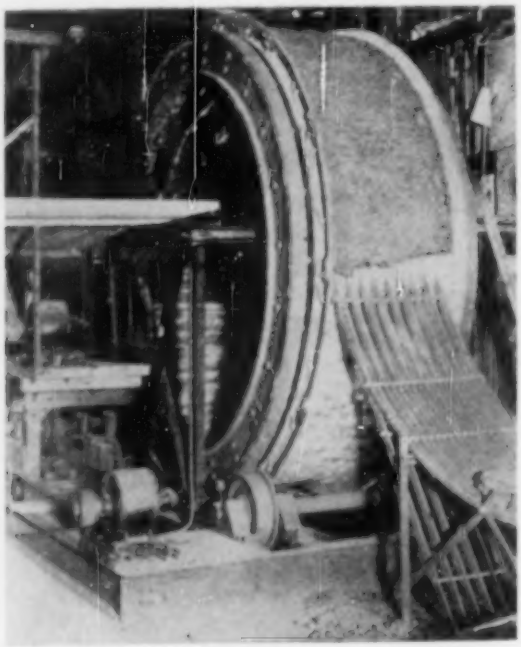

Fig. 1—Early drum type Dwight-Lloyd sintering machine consisted of a horizontal cylinder 11 ft 4 in. in diam and 3 ft wide.

The charging of the pots, however, was done by hand. The sintered block was broken up with sledge hammers. The material was then screened and the —½-in. fines were recirculated. The St. Joseph Lead Co. investigated also the possibility of sintering blast furnace flue dust. The investigation was apparently sponsored by a steelmaking firm. The results were discouraging and consequently the Savelsberg process was never used for agglomeration of flue dust or ore fines.

The Tintic Smelter at Salt Lake City, Utah had a battery of Kelley sintering pots. These were tilting tray shaped steel vessels, 8 ft long, 4 ft wide and 14 in. deep. The battery was used in sintering lead sulphide ore. Robinson blast roasters were installed in 1905 at the Bingham Junction, Utah plant of the U. S. Smelting, Refining & Mining Co.[6] Pots of the Robinson process were 8 or 10 ft square pans. These were replaced in 1908 by smaller pans 6 ft square and 3 ft deep having a cast iron bottom perforated by ⅝-in. holes. The plant used a battery of 20 pans. Charging and discharging of the vessels was done mechanically. A pusher ram similar to those used in pushing coke from horizontal coke ovens was installed for discharging ore sinter and was reported to give good service.

The leading process of Australia was the Carmichael-Bradford pot roasting process used on lead and copper ores.[7, 8] The process was almost identical with the Huntington-Heberlein process. Unfavorable market conditions caused the shut down of many smelters in Australia, and the sintering of ore in Carmichael pans were discontinued in 1909. Around the turn of the century blast roasting was the common name for sintering. The reason for this was that the process of agglomeration was intended to remove certain amounts of sulphur as well as to improve the physical structure of the ore.

Sintering with updraft pots was accompanied by several disadvantages. The main ones were:

A—The ore was exposed for a long time to the influence of hot gases which resulted in an uneven sintering of the product.

B—The pots required constant attention in charging, blowing, and discharging.

C—Handling of fines and updraft flowing through the bottom caused excessive losses of material.

D—The process was intermittent.

E—The cost of operation and maintenance was exceedingly high.

Downdraft Sintering

The disadvantages of pot sintering seem to have been overcome by the continuous sintering process introduced by Dwight-Lloyd in the early 1900s.[9, 10]

This sintering process was the outcome of a series of experiments carried out by Dwight and Lloyd in the plant of the Cananea Consolidated Copper Co.[11]

The first description of the process is contained in an article published by Dwight in 1908. According to Hoffman the first installations of sintering machines operating on the principle of Dwight and Lloyd were made before 1908. To these belong the sintering machines of the Cerro de Pasco Mining Co. in Peru, and one used by the American Smelting & Refining Co. at Maurer, N. J.[12] Both machines were installed in 1907 for treatment of sulphide ores. The process as first evolved was not satisfactory for iron ores. Further experimentation resulted in an application for a patent on June 17, 1911, but this was not issued until Jan. 27, 1918.

Early reports on the process show that three types of Dwight-Lloyd machines were in operation in the first stage of commercial sintering. They are as follows: A—The drum machine, B—The horizontal tray machine, and C—The straight line machine.

The drum machine shown in Fig. 1 consisted of a horizontal cylinder 11 ft 4 in. diam and 3 ft wide made up of a pair of circular pieces of iron, carrying cast iron herring bone grates with an effective width of 30 in. The drum structure rested on two pairs of friction rollers, one of which was driven by an electric motor. Inside the drum was a stationary suction box occupying the top quadrant of the circle. The ore fed mechanically upon the rising grate was ignited by gasoline jets, and then travelled over the suction box. The sintered product was discharged from the grate surface by the points of an upturned grizzly.

Two companies are known to have used this type of sintering machine. The American Smelting & Refining Co. of Maurer, N. J., and the Baltimore Copper Smelting & Rolling Co. of Baltimore.

The horizontal tray machine resembled a horizontal rotating picking table in which the ring shaped table was replaced by herring bone grates. The outer diameter was 15 ft, the inner diameter was 8 ft, giving a total grate area of 126 sq ft. The blowing area was about 50 sq ft. The table made

Table I. Structural Dimensions of Dwight-Lloyd Machines, 1911

Dimensions	50 Ton	100 Ton
Length, overall, ft	27	41
Width, overall, ft	7	7½
Height, to top of hopper	11 ft. 4 in.	13 ft. 9 in.
Weight of complete machine	16 ton	28 ton
Suction box, in.	30x150	42x264

the suction is applied on the bottom hopper and the

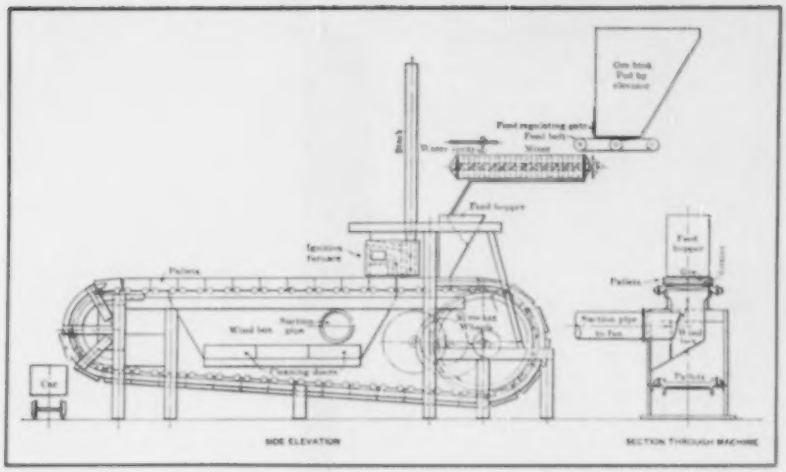

Fig. 2—Diagram of conventional Dwight-Lloyd sintering machine with Type E conveyor shows component parts.

about one revolution in 45 min. There was a stationary feed hopper and an ignition stand. The sinter was removed by means of a scraper. The machine had a capacity of approximately 30 tons a day and was considered quite satisfactory for treating lead and copper sulphide ores. This type was in use at the copper sulphide plant of the American Smelting & Refining Co. at Garfield, Utah, and at the plant of the Cerro de Pasco Mining Co. in Peru.

Experimental runs on sintering iron ores were not successful, primarily because of the small capacity of the machine. The small capacity, difficulties in maintenance, and high cost of operation caused the industry to abandon the drum machine and the horizontal tray machine in favor of the strand machine. The straight line machine became widely known as the Dwight-Lloyd sintering machine.

The prototype of the present sintering machine was known originally as the *Type E* or the conveyor type machine. A machine of this type is shown in Fig. 2. It consisted of a frame of structural steel supporting a feeding hopper, an ignition furnace, a suction box and a pair of endless track circuits to accommodate a train of sections called pallets. The pallets thus formed an endless conveyor. Any element of this conveyor could be easily removed and repaired or substituted with a new one without stopping the machine. The speed of the horizontal travel of the pallet conveyor was adjustable to meet varying requirements, with the usual range of 7 to 30 in. of linear travel per min. The charge was placed on the strand in a thin layer, 4 to 6 in. thick, through a simple funnel-shaped hopper located directly over the pallets. The front edge of the hopper acted as a scraper to form a uniform layer of the proper thickness. The stream of ore emerging from the hopper passed under an ignition stand, where fuel was ignited on the surface layer of the charge. The combustion thus started was carried downward through the mass by air, as the material passed over the suction box. The agglomeration was accomplished in a narrow high temperature zone which reached the bottom of the bed just prior to sinter discharge.

Gayley reported in 1911 that Dwight-Lloyd machines were available in two standard sizes, the so called 50 ton per day unit and the 100 ton per day unit. Table I gives the structural dimensions of the two units. Consensus is that the first machine for sintering blast furnace flue dust was put into operation in September 1911 at the E. & G. Brook Iron Co. at Birdsboro, Pa.[38]

A statement made by Gayley in 1911 seems to contradict this accepted contention. At an AIME meeting held in 1911 at Wilkes-Barre, Pa., Gayley stated: "In one plant which was in steady operation for two years, the average cost of supplies and repairs was from two to four cents per ton. A number of iron bearing materials, of different kinds were treated on this machine and in each case with satisfactory results."[38]

This would put the date of the start of iron ore sintering at somewhere between 1907 and 1909, with at least one machine positively operating in 1909. Gayley did not give the location of the sintering plant and no other references pertaining to this installation could be found in the literature.

The Birdsboro plant was put into operation on Oct. 1, 1911. Klugh[40] and Gayley[41] gave a detailed description of the Birdsboro plant only a few months after it was put into operation. Initially, the plant had one 100-ton sintering unit in operation, which processed the blast furnace flue dust collected in large piles in the blast furnace yard. Sintering of blast furnace flue dust was the main task of the newly constructed sintering plants, as ore fines were not used in the first stage of commercial sintering. Klugh and his associates, however, saw in sintering of flue dust more than only a useful way to dispose of the growing piles of the heretofore useless blast furnace flue dust.

Other steel producers quickly sensed the advantages of sintering and as the result, sintering plants were built all over the country. Fig. 3 shows the growth of the number of sinter plant installations in the U. S. since 1911.

The Dwight-Lloyd process maintained and even strengthened its position by providing advantages of operation and economy not offered by any other of the previously mentioned processes.

Batch Sintering Processes

The batch or intermittent sintering processes were developed almost simultaneously with the continuous process of Dwight-Lloyd. The first batch process was introduced by Greenawalt a few months before the Dwight-Lloyd process became known. The following years brought numerous processes of

burden on Swedish blast furnaces contains about

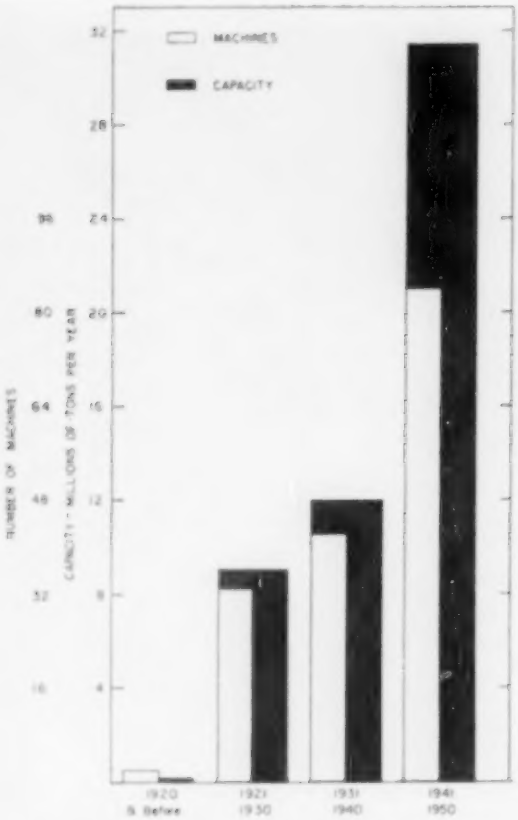

Fig. 3—Rapid acceptance of sintering process by steel producers is shown by the growth of iron ore sinter plant installations in the U. S. since 1911.

which only the original Greenawalt process survived to the present time.

The most important of the batch type processes are as follows: A—Greenawalt, B—West, C—Krom, D—Cardiff-AIB, E—Holmberg System, and F—other processes.

The original Greenawalt process employed large rectangular pans usually 8 ft wide and 14 to 20 ft long.[17] Modern installations use pans 10 ft wide, 25 ft long and up to 25 in. deep.[18] The sintering pans are equipped with pin hole grate plates or with conventional grate bars similar to those used on Dwight-Lloyd machines. The Greenawalt pan is located on top of a suction hopper so that the system is efficiently sealed against air infiltration.

The bottom hopper is connected to an air fan. Fans used in Greenawalt installations are usually equipped with two blowing compartments, each of which is connected to a separate sintering pan. Most Greenawalt plants employ an even number of pans in order to operate two sintering pans with a single air fan in a parallel arrangement.

The charging of the pan is accomplished by a charging car which moves over the sintering pans on a pair of tracks. Sinter feed material is prepared in pug mills or mixers closely resembling those used for mixing concrete. After the charging of the pan is completed an ignition car moves over the pan and ignites the bed with gas or oil flames. At this point the suction is applied on the bottom hopper and the material begins to sinter.

It is interesting to note that the air suction in Greenawalt installations frequently reaches 50 in. W.G., while on continuous machines it seldom exceeds 24 in. This may be attributed to the air leakage which is very serious in continuous systems and almost negligible in intermittent installations such as Greenawalt.[19]

After sintering has been completed, the pan is moved by an overhead crane to a discharge mechanism which trips the pan and causes the sinter to discharge into a hopper or onto a sinter pile.

The popularity of the Greenawalt type plants has been diminishing steadily over the last 30 years. As far as it is known only two installations of this type are being operated at the present time in the U. S. Only one of them is engaged in production of iron ore sinter. The basic idea of batch type sintering still has many supporters in foreign countries, particularly in England and Sweden.

The principle of Krom's sintering machine was very similar to that of Greenawalt's, with the exception that the pans used in the Krom process were of circular design about 6 ft diam. Sintering was accomplished by internal combustion of carbon contained in the sinter mix and by the air sucked through the bed. Sinter cake was removed by tilting the pan. The only known sinter plant using Krom's process was located at Helen Bess Mine near Birmingham, Ala. The plant produced sinter from Clinton hematites. It was known to be in operation in 1916 but no further reference to the process or the plant could be found in the literature available.

Although the idea of producing iron sinter in circular pans incorporated in Krom's sintering system was not popular with the American steel industry, it was revived again by Swedish iron ore industry in the late twenties. It was reported that at least one plant employed a process similar to that of Krom. The process became known as the AIB process. The data of a plant operating under a Swedish AIB license and constructed about 1927 at the Cardiff Works in Britain were published and offer some information on the AIB process.[20] The sinter plant at Cardiff employed a 12-pan unit. The pans were placed in two rows of six pans each. Each pan was 8½ ft diam, 13 in. deep and contained from 1.5 to 1.75 tons of sinter. The pans were made of four circular, ribbed steel castings machined and bolted together. Across the bottom of the pan were bolted spacer bars which supported the grate. The charging of the pans and the igniting of the feed was accomplished with separate cars, specially constructed for these purposes.

Air suction was provided by electric fans. One 135-hp motor was used to drive two double compartment fans. The exhaust gases passed through a dust collecting chamber, in which a large portion of flue dust was eliminated. From here the gases were exhausted through a stack into the atmosphere. Sintering times ranged from 1 to 1½ hr per batch, depending on the material used and air volume available. When sintering was completed the pan was conveyed by an overhead crane to a tippler gear which emptied the pan into a hopper. The Cardiff plant was in continuous operation for several years, in spite of its low production rate which averaged 230 tons per day.

The Holmberg sintering process is the dominating process of the Swedish iron ore agglomerating industry.[21] It is interesting to note that the average

burden on Swedish blast furnaces contains about 80 pct sinter. This high percentage might seem surprising in view of Sweden's excellent supply of high grade iron ore. The explanation, however, can be found in government regulations which specify that only iron ores containing less than 38 pct iron can be used for domestic steel production. All higher grade ores are being exported. Consequently, the Swedish iron industry must rely on iron ore concentrates and on sintering to obtain a satisfactory furnace charge.

The Holmberg sintering process is basically identical with the Greenawalt process, except for a few modifications and improvements which were necessitated by local conditions. There are six plants at present in Sweden operating with the Holmberg system. Their daily production ranges from 100 to 485 tons of sinter.

A typical Swedish Holmberg plant is equipped with seven sintering pans 11 ft 6 in. long x 11 ft and 6 in. wide, and having a total depth from top of the grates to top of pans of 12 in. Pan grates are made of low carbon chrome-vanadium steel. The pans obtain their charge from three raw material bins in the following order: A—Bedding material (approx 2 in.), B—Sinter mix (approx 9½ in.), and C—Charcoal or coke braize (approx ¼ in.). The charged sintering pan is placed by a crane onto a suction stool which is connected to an air fan. Placing of pan on the stool opens automatically the main air valve which starts the air flow through the bed. At this time the ignition car is brought over the pan and the charge ignited. Sintering times range from 1 to 1½ hr per pan. When the operation has ended the pan is picked up by an overhead crane and delivered to a tippler stand in which the pans are emptied into railroad cars. The pan is then brought to the filling stand, and the whole procedure is repeated.

It is apparent that Swedish industry has its sinter tailor-made in an intermittent type of operation, which cannot be accomplished in a continuous type machine of Dwight-Lloyd. The sinter which is produced from finely sized ore concentrates is, according to the available reports, highly oxidized. The main disadvantage of the Holmberg system seems to be in the intermittancy of the process, which means time losses due to changing, igniting and discharging of pans. Also the costs of labor in the Holmberg process are comparatively high. Its advantages lie in the quality of the finished product which consists mainly of hematite.

It can be seen from the description of the most important batch type processes that they are all identical in their basic principles, and very similar in the design of the plant equipment. Numerous inventors developed various batch sintering processes merely by making insignificant changes in the existing Greenawalt equipment. The literature does not reveal the names of all inventors of the batch type processes. Only a few of these names have been preserved. To these belong the names of Plock, Grasselli, and Brown. No details on their respective processes could be found in the literature. These processes seem to be completely forgotten.

West Sintering System

Development of West's stationary sintering process was first reported by its inventor in 1912.[77,78] The process was quite different from all other sintering processes in that the blast furnace flue dust was brought to fusion by the direct heat generated by two burners inserted in one wall of the sintering chamber, and not by the heat of combustion of fuel contained in the sinter feed itself. West's system consisted of a furnace with a movable bottom on which a block of fused material was being built up as fast as the action of the heat supplied by the burners agglomerated the particles together. Flue dust was fed into the sintering furnace from a hopper and then was spread mechanically to a thin layer. West reported that the product of his sintering furnace was far superior to products of all other processes used at that time. An analysis of flue dust and sinter is given in Table II. The deficiencies of the West process are as follows: A—High cost of fuel for burners, B—Waste of carbon contained in the flue dust, C—Extremely high deficiency of oxygen resulting in a highly reduced slaggy product, D—Presence of carbon in sintered product, and E—Increase of sulphur in sinter.

Table II. Analyses of Flue Dust and Sinter of West Sintering Process

Item	Flue Dust	Sinter
SiO_2	8.77	9.60
Fe	47.19	64.20
P	0.032	0.049
Mn	0.38	0.56
CaO	2.16	6.51
MgO	1.79	0.54
C	10.20	0.34
S	0.05	0.12
H_2O	12.75	—

It seems only logical that West's process could not compete with other much more efficient and economical processes. The only installation of this kind was dismantled already in 1913, and since then has become almost completely forgotten.[77]

References

[1] H. O. Hoffman: *Trans.* AIME (1911) **41**, p. 745.
[2] A. S. Dwight: *Engineering & Mining Journal* (1908) **85**, p. 649.
[3] J. W. Neill: Disc. on paper No. 1, *Trans.* AIME (1911) **41**, p. 915.
[4] Huntington-Haberlein Sintering Process, U. S. Patent 600,347 (1898).
[5] Savelsberg Sintering Process, U. S. Patent 755,598 (1904).
[6] W. R. Ingals: *Engineering & Mining Journal* (1907) **84**, p. 527.
[7] Carmichael-Bradford Sintering Process, U. S. Patent 705,904 (1902).
[8] L. S. Austin: *Mining Scientific Press* (1909) **98**, p. 195.
[9] H. O. Hoffman: *Mining Industry* (1905) **14**, p. 404.
[10] A. S. Dwight: Dwight-Lloyd Sintering Process. *Engineering & Mining Journal* (1908) **85**, p. 649.
[11] G. M. Schwartz: *Trans.* AIME (1929) **84**, pp. 34-67.
[12] *Mineral Industry* (1907) **41**, p. 380.
[13] F. A. Vogel: *Trans.* AIME (1913) **43**, p. 193.
[14] J. Gayley: *Trans.* AIME (1912) **42**, p. 180.
[15] B. G. Klugh: *Trans.* AIME (1913) **43**, p. 364.
[16] J. Gayley: *Iron Age* (1912) **89**, p. 73.
[17] W. E. Greenawalt: *Mining Science Press* (1921) **122**, pp. 81-85.
[18] J. A. Poll: *Proc. Blast Furnace, Coke Oven and Raw Materials*, AIME (1952) pp. 214-221.
[19] A. W. Robinson: *Proc. Blast Furnace, Coke Oven and Raw Materials*, AIME (1950) pp. 246-258.
[20] W. E. Simmons: *Journal of Iron and Steel Inst.* **119**, pp. 89-102.
[21] T. L. Joseph: *Proc. Blast Furnace, Coke Oven and Raw Materials*, AIME (1951) pp. 36-43.
[22] Private Communication: A. A. Nilsen and W. J. Urban, American Ore Reclamation Co.

Reusable Hot Tops Proven Successful in Ingot Pouring Practice

by Joel C. Carpenter

IN the early days of steelmaking, no attempt was made to control the shrinkage cavity and major zone of segregation in killed steel ingots. Steel which was suitable for application as prime product rarely amounted to more than 60 pct of the total ingot. The top 40 pct or so, containing the pipe cavity and major segregation zone was either scrapped, or possibly applied to orders on which substandard quality was permitted. The price which could be obtained for this top portion was either scrap value, or at most, considerably less than that which could be obtained for prime product.

To make a greater percentage of the ingot available for application as prime product has long been the aim of steel plant operators and metallurgists. During the past 50 years, innumerable ideas have been tried for controlling and relocating the shrinkage cavity, and its effect upon center soundness and internal quality of killed steel ingots. Some of these ideas have involved the use of hydraulic or mechanical pressure for squeezing out the pipe cavity, and some have employed gas generating substances to build up pressure to try to control feeling, but most ideas have been directed toward maintaining a reservoir of molten metal at the top of the ingot to feed the shrinkage cavity.

Reusable Hot Top

Several years ago, a reusable insulated low volume C&D hot top was developed by the Ferro Engineering Co., and it has been tested and proved successful in the steel industry. It consists of a cast iron casing lined with insulating fire brick and employs the usual appurtenances for protecting the bottom of the casing preventing the flow of molten steel between the mold hot top. It may be poured with only a slight hesitation to obtain a seal at the hot top-mold junction. After pouring, the supporting blocks are knocked out, so that no *hanging* of the ingot will occur.

The insulating fire brick used absorbs only 30 pct as much heat as regularly fireclay brick and has an insulating value 3.1 times as great at 2600°F. The use of this material has resulted in a notable increase in the efficiency of the hot top.

A reusable hot top requires that the refractory lining be capable of repeatedly withstanding contact with molten steel, and the abrasion incident to the stripping of the hot top from the sinkhead portion of the ingot. To protect the insulating fire brick lining from the molten steel, a refractory veneer, approximately ½ in. thick is applied to the inner face of the hot top lining before each use. This veneer is applied as a mortar, and is thoroughly dried before using, forming a monolithic surface, which resists penetration by the molten steel. Replacement of the insulating firebrick lining should only be necessary at infrequent intervals if the protective veneer is properly applied and dried.

During the past several years, tests of insulated low volume C&D hot tops, conducted at a number of steel plants making both electric furnace and open hearth steel, have shown an increase in prime product yield, when compared with that obtained with regular hot top practice. These tests were conducted using regular production ingot molds at each plant involved in the testing program. Mold cavity configurations included square, rectangular and duodecagonal cross sections, with various contours and different flutings.

Comparisons were made by substituting insulated low volume C&D hot tops for regular hot tops at certain positions in the drag of molds, usually somewhere after the first buggy of molds. The practice on molds with regular hot tops was to pour ingots with sinkheads of from 13.6 pct to 16 pct by weight, molten, depending upon the size and shape of the ingot and the grade of steel being poured. Ingots made in molds with insulated low volume C&D hot tops were usually poured at 3 pct less by weight, molten, than the comparison ingots made in molds with regular hot tops. In the case of comparison ingots, both types of hot tops were set the same distance in the mold, so that the ingot body weights would be the same. Evaluation of prime product obtained showed that the insulated low volume C&D hot top increased the yield by at least 3 pct, at a comparable quality level with that obtained with regular hot tops. Quality level was determined by macro etch tests and chemical segregation tests, made at the top of the product in accordance with accepted metallurgical testing practice.

An additional important feature of the insulated low volume C&D hot top is that it is heavy enough so that it will not float off of the ingot mold during or after pouring. Furthermore, this hot top is easily removed from the sinkhead before the ingot is loosened, and the sinkhead has a chance to cool sufficiently to be hard enough to be gripped by stripper crane bits without collapsing. In actual practice, no difficulty has been experienced in handling ingots made with these hot tops, although the sinkheads are somewhat smaller than those made with regular hot tops.

Reference

[1] J. W. Mueller: A Progress Report on Hot Top Research. *Proc. National Open Hearth Conference*, AIME (1949) **32**, pp. 120-126.

J. C. CARPENTER is a Metallurgical Engineer, Ferro Engineering Co., Cleveland. This is an abstract of a paper presented at the AIME Electric Furnace Steel Conference, Pittsburgh, Dec. 1 to 3, 1954.

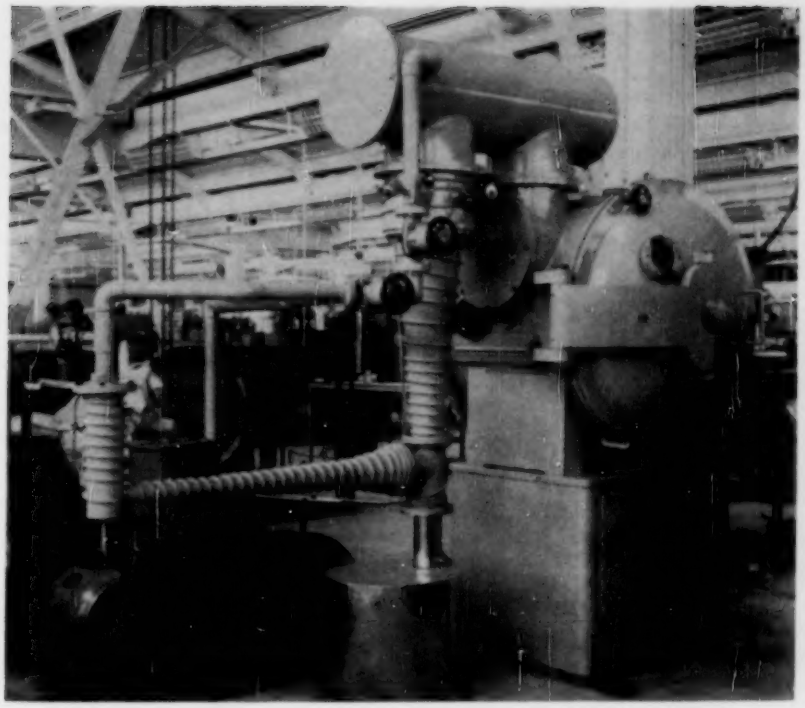

Degassing unit shown at W. Edwards & Co. Ltd., London, is pumped by a 1883 booster pump in conjunction with a 3000 liter per min gas ballasted rotary pump.

Progress in European Vacuum Melting Described

by H. H. Scholefield

DEVELOPMENT and progress of vacuum melting on a commercial scale up to World War II is largely the result of Heraeus Vacuumschmelze A. G. activities[1, 2, 3] which commenced in the early 1920's. This is all the more surprising when it is remembered that induction heating for melting had not been evolved to a stage when it could be employed on a commercial scale until the late 1920's, so that the early furnaces developed by Heraeus Vacuumschmelze A.G., of quite large capacity, 650 lb., were resistance heated. Furthermore little was known about vacuum engineering and only mechanical rotary pumps were available. Although low frequency heating was used for a short period, from the early 1930's onwards, high frequency induction heating has been employed almost exclusively.

A comprehensive range of special alloys were produced. A series of beryllium copper alloys, particularly the 1 pct and 2 pct beryllium, but to a lesser extent the more complex copper and nickel base beryllium bearing alloys were melted under reduced pressure and, apart from the low loss of beryllium, enabled more consistent characteristics to be achieved than were then obtainable with current air melting practice. A group of the heat resisting alloys, particularly the nickel chromium alloys of the 80/20, 65/15, and 30/20 types were produced. But here, owing to the highly competitive markets, it was an economic possibility mainly for specialized applications such as for drawing wires to fine gages of the order of 0.001 in. or less. There was also the added complication of introducing rare earths *in vacuo*. Soft magnetic alloys based on nickel-iron and silicon-iron such as Mumetal and Trafoperm, melted under reduced pressure, gave a significant improvement in magnetic performance. Vacuum melted alloys for thermionic valves and for glass-to-metal seals also overcame many of the practical difficulties associated with outgassing of valves and hermetically sealed containers.

Before the World War II, Heraeus Vacuumschmelze A. G. and the Telegraph Construction & Maintenance Co. Ltd. were employing commercial vacuum melting techniques in which the heats were not only melted but poured at reduced pressures. The furnace chambers were evacuated with high

H. H. SCHOLEFIELD is Technical Manager, Metals Div., The Telegraph Construction & Maintenance Co. Ltd., London, England. This is an abstract of a paper presented at the AIME Electric Furnace Steel Conference, Pittsburgh, Dec. 1 to 3, 1954.

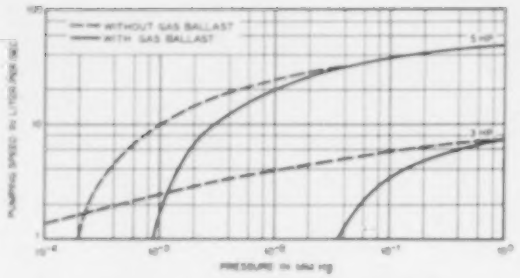

Fig. 1—Characteristics of some typical rotary pumps are shown with and without gas ballast. Geraetebau-Anstalt Balzers and E. Leybold's Nachfolger supplied the data for the graph.

capacity mechanical rotary pumps and the pressure at casting would be in the range 0.5 to 5 mm of mercury measured with a McLeod type gage, the temperatures being up to approximately 1650°C.

Pumping Equipment

During World War II vacuum pumping equipment was developed to meet demands in various fields where ultimate pressures in the range down to 10^{-4} mm of mercury were required in relatively large containers. Diffusion pumps were available long before the war but were not of adequate size to cope with the leak rate of complicated chambers.

Advantage of the developments has been taken in vacuum melting, and it is common practice today to melt and cast under pressures of the order of 10^{-4} to 10^{-1} mm of mercury. Essentially two types of pumps are employed—rotary mechanical pumps including gas ballast pumps and diffusion pumps including booster pumps. The rotary pump is considered to be the most efficient for attaining pressures down to 0.1 or 0.05 mm of mercury. However, at these pressures its free air speeds are low. In high vacuum work the rotary pump's main function is to lower the pressure of the vessel to a suitable level for a diffusion pump to take over and subsequently to provide the requisite backing pressure for its satisfactory operation. Basic principles of the pump have not altered although there have been considerable improvements in design. A rotor is mounted adjacent the periphery of a cylindrical container between inlet and outlet ports. It is fitted with spring loaded blades, and as it rotates the blades pass the inlet and outlet ports alternately drawing air from the system to be evacuated, compressing it, and discharging it through the outlet valve. In the case of permanent gases this results in no complication but when condensible vapors are present the compression may result in liquid being formed which contaminates the oil in the pump. When this oil enters the low pressure side, vapor is reformed and the efficiency of the pump decreased. The older method of overcoming this was to insert a liquid air or other cooling trap in the pumping manifold before the gas reached the pump, but more recently the gas ballast pump has been developed to avoid this complication.

In the gas ballast pump a one-way valve connects the compression side of the pump to the atmosphere. When the blades pass this valve, air is drawn into the space containing the vapor which is about to be compressed and, if enough air is present, the vapor is expelled as such through the outlet valve before its partial pressure is sufficiently high to cause condensation. Because of the work done in compressing the additional volume of air these pumps run hotter than unballasted pumps. This is, of course, an advantage as the saturation pressure of the vapor is correspondingly higher. In unit time the volume of vapor exhausted is by definition equal to the pumping speed and to a first approximation this must be compressed to the volume of the ballast air flow before the mixture attains atmospheric pressure and is discharged out of the pump. The vapor, therefore, is compressed in the ratio of the pumping speed to the air ballast flow and to avoid condensation the pressure at inlet multiplied by this compression ratio must not exceed the saturation pressure of the vapor at the temperature of operation of the pump. In practice the air ballast flow is adjusted to give some safety factor on the calculated flow required.

This type of pump operates very satisfactorily provided the vapor does not dissolve in or attack the oil. The effect of the former can be mitigated to some extent by isolating the pump and running it with gas ballast. Chlorinated and fluorinated hydrocarbon oils may be sufficiently immune to attack by reactive vapors to overcome the latter. As there is bound to be some leakage into the low pressure side of the system gas ballasting obviously affects the ultimate vacuum attainable. Normally, however, this is not of major importance as the pressure is still sufficiently low to permit efficient operation of a diffusion pump. A low ultimate vacuum can be achieved if required by using a two stage pump in which it is only necessary to gas ballast the rough stage as the compression in the fine stage is not sufficient to cause condensation. Fig. 1 shows typical characteristics of some rotary mechanical pumps with and without gas ballast.

Diffusion pumps are essential for the high pumping speeds necessary at low pressures of the order of 10^{-4} to 10^{-6} mm of mercury now being employed in vacuum melting. Here again the principles of operation of the pumps have not altered. Oil is vaporized and blows through jets pointing away from the inlet to the pump. These vapor streams cause gas molecules which have diffused into the pump to be carried away, compressed and exhausted to the backing pump while they themselves condense on the water cooled walls of the pump and run back into the boiler. Attention to design has resulted in

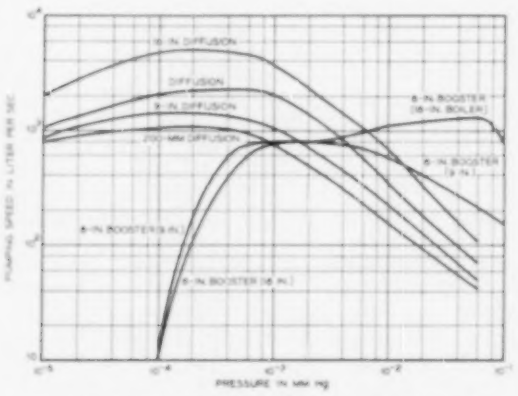

Fig. 2—Characteristics of some typical diffusion and booster pumps are shown. Data for the graph supplied by W. Edwards & Co. Ltd., London, and Geraetebau-Anstalt Balzers.

improved performance. For example with pumps of this type the possibility of oil vapor molecules migrating back into the high vacuum system due to collision with the gas molecules is bound to occur and attention to jet design[4] and the use of water cooled baffles has reduced this to a minimum.

Attention is also being directed to the layout of the jets and very high pumping speeds are being achieved by building concentric annular jets around the conventional three or four stage pump. An extended range of oils is now available for vapor pumps,[5] in particular the silicone oils which, because of high resistance to decomposition and oxidation, enable the pumping system to be exposed to the atmosphere while still hot with little or no deleterious effect.

By incorporating an oil ejector in the ejector stage of a diffusion pump, the oil ejector being fed from the boiler of the diffusion pump, the high pumping speeds of the diffusion pump have been made available in the pressure range 10^{-3} to 10^{-6} mm of mercury. Introduction of these pumps, called *booster pumps*, therefore closes the gap between the rotary pump and the diffusion pump and enables high pumping speeds to be obtained economically throughout the entire pressure range. Fig. 2 shows typical characteristics of some diffusion and booster pumps. Booster pumps are obviously of vital importance in vacuum melting. A great advantage of these pumps is their ability to work against a relatively high backing pressure. It is thus possible to operate them with a single stage gas ballasted rotary pump of moderate size and for example in the region of 10^{-4} mm of mercury a backing pressure of the order of 2 mm of mercury only is necessary and in the region of maximum throughput backing pressures of the order of 3 to 3½ mm of mercury are adequate. This combination of pumps is therefore ideal for vacuum melting requirements where water vapor and other impurities must be pumped as a result of out-gassing of refractories etc. and reactions of the melt.

To round off this description of pumping equipment in brief consideration will be given to the factors governing the selection of pump combinations.

Diffusion and booster pumps operate efficiently only when the pressure at the exit is less than the critical backing pressure, at which level the number of gas atoms is such that back diffusion occurs and the performance of the pumps is impaired. Critical backing pressures vary from say 0.2 to 3 mm of mercury. The size of the rotary pump required for any given diffusion pump is decided mainly by the two factors: A—The backing pressure must not at any time exceed the critical backing pressure, and, B—The product of pressure and volume for a gas is constant allowing for the difference in temperatures between the pumps. It is necessary, therefore, to select a rotary pump which has an adequate speed at the maximum throughput of the diffusion pump to hold the pressure below the critical backing pressure of the latter. In practice of course a reasonable factor of safety is always allowed.

Furnace Design

To take advantage of the lower pressures which had become available it was necessary to pay greater attention to furnace design. The vacuum chamber is often fabricated from stainless steel and is water cooled. In some cases it may consist of a double walled shell through which water is pumped. To avoid loss of pumping speed and facilitate cleaning, the inside of the chamber is smooth and streamlined as far as possible. The main seal of the outer casing is effected by a rubber or neoprene ring between two machined flanges, various means being employed, such as the *O* seal, to avoid excessive loading of the gasket. An induction coil and crucible, device for charging additions, thermocouple and ingot mold are housed in the chamber and a typical layout is illustrated in Fig. 3. A multi-pocket rotating hopper mounted either directly above the crucible or provided with a chute to the crucible is used for making additions to the charge as required during the melting cycle. Its capacity may be of the order of one third of the charge. The hopper is rotated by an external handle so that each compartment can be brought over the charging hole.

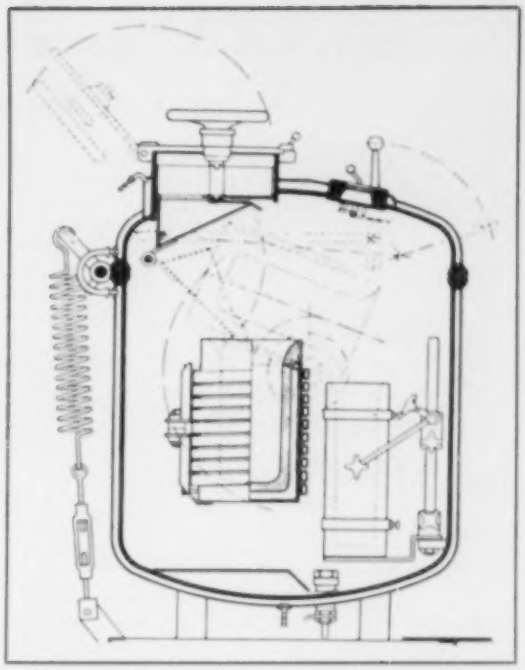

Fig. 3—Typical layout of a modern high-vacuum high-frequency melting furnace shows design features. Diagram furnished by Geraetebau-Anstalt Balzers.

Acknowledgments

The author wishes to thank Degussa-Wolfgang, W. Edwards & Co. (London) Ltd., Geraetebau-Anstalt Balzers, E. Leybold's Nachfolger, the National Physical Laboratory and Vacuumschmelze A. G. for information supplied and helpful discussions and is indebted to the directors of the Telegraph Construction & Maintenance Co. Ltd. for permission to publish the paper.

References

[1] German Patents Nos. 345,161 (Jan. 1918) and 354,218 (April 1918).

[2] W. Rohn: *Tech. Publication No. 470*, AIME (1932).

[3] W. Rohn: *Journal Institute of Metals* (1929) **42**, p. 203.

[4] L. Riddiford and R. F. Coe: *Journal of Scientific Instruments* (1954) **31**, p. 33.

[5] D. Latham, B. D. Power, and N. T. M. Dennis: *Vacuum 1 and Vacuum 2*, (1952) London.

Chicago Will Be Scene of AIME Annual Meeting

Technical and Social Meetings Highlight Varied Program

Advance registration for the Annual Meeting to be held at the Hotel Conrad Hilton can be made by writing to AIME headquarters in New York. Registration fee is $5.00 for members and $8.00 for non-members. Registration at the meeting will be held in the Grand Assembly Ballroom.

The AIME Annual Banquet will be held in the Grand Ballroom at 7:00 pm on Wednesday, February 16.

The President's Reception will be held in the Normandy Room immediately following the presentation of awards. Tickets for the banquet are priced at $12.00 per person.

Tickets for the dinner-smoker are $10.00 each. The Metals Branch Dinner will take place on Tuesday, tickets will cost $6.00. The EMD luncheon is scheduled for Wednesday, $3.50. A Powder Metallurgy Committee luncheon will be held on Thursday, $3.50.

IRON AND STEEL DIV.

MONDAY, FEBRUARY 14

9:30 am, West Ballroom

Statistical Methods in the Steel Industry

J. E. Stukel, Chairman

An Example of the Use of Linear Programing in Planning New Production Facilities on a Tin Plate Mill: K. H. Kramer

Pitfalls in the Application of Statistics to Steel Plant Data: D. S. Leckie, Republic Steel Corp., Cleveland

Experimental Planning for Rapid Determination of Optimum Process Conditions: W. A. Griffiths, New Jersey Zinc Co., Palmerton, Pa.

10:00 am

Metals Branch Council Meeting

R. R. McNaughton, Chairman

2:30 pm, South Ballroom

Thermochemistry of Slags

Physical Chemistry of Steelmaking

Physical Chemistry of Extractive Metallurgy

Joint Session with EMD

R. Schuhmann, Jr., and D. J. Girardi, Associate Chairmen

Ionic Nature of Liquid Iron-Silicate Slags: M. T. Simnad, Gerhard Derge, Carnegie Institute of Technology, Pittsburgh, Pa., and I. George, Distillers Co. Ltd., Glamorgan, South Wales, Great Britain

Surface Tension of Slags: R. Bowni, Gerhard Derge, Carnegie Institute of Technology, Pittsburgh, Pa.

Equilibrium Between Titanium in Liquid Iron and Titanium Oxides: R. L. Hadley, Gerhard Derge, Carnegie Institute of Technology, Pittsburgh, Pa.

Phase Equilibria in the System FeO-Fe_2O_3-SiO_2: Arnulf Muan, Pennsylvania State University, State College, Pa.

TUESDAY, FEBRUARY 15

9:00 am, Waldorf Ballroom

New Processes in the Industry

J. F. Elliott, Chairman

Oxygen Steelmaking in Canada: F. J. McMullin

One Year of Experiment with the International Low Shaft Furnace: P. Coheur, Centre National De Recherches Metallurgiques, Liege, Belgium

10:45 am

ISD Annual Business Meeting

A. W. Thornton, presiding

11:00 am

Howe Memorial Lecture

H. DeWitt Smith and A. W. Thornton, Associate Chairmen

The Anatomy of the Open Hearth: J. S. Marsh, assistant manager of research, Bethlehem Steel Co., Bethlehem, Pa.

12:15 pm

Luncheon Meeting, Physical Chemistry of Steelmaking Committee

J. F. Elliott, Chairman

2:00 pm, Waldorf Ballroom

Mechanical Working

Michael Tenenbaum and B. R. Queneau, Associate Chairmen

Forgeability of Steels with Varying Amount of Manganese and Sulphur: C. T. Anderson, V. V. Donaldson, R. W. Kimball, F. R. Cattoir, U. S. Bureau of Mines, Redding, Calif.

Evaluation of Soaking Pit Capacity: Robinson and Eckholm

Factors in Soaking Pit Heating: R. L. Hindson

Practical Observations on the Influence of Slab Heating and Rolling Techniques on Slab Surface: H. B. Wishart

6:00 pm

Metals Branch Cocktail Party

7:00 pm

Metals Branch Annual Dinner

WEDNESDAY, FEBRUARY 16

7:30 am

ISD Executive Committee Breakfast Meeting

J. S. Marsh, Chairman

9:00 am, P.D.R. No. 1

Sulphur and Oxygen

D. L. McBride and D. W. Murphy, Associate Chairmen

Desulphurization of Carbon Saturated Iron: Gerhard Derge, W. O. Philbrook, Carnegie Institute of Technology, Pittsburgh, Pa.

Equilibria in Systems Containing Oxygen and Sulphur: Bishop, H. N. Lander, John Chipman, and N. J. Grant, Massachusetts Institute of Technology, Cambridge, Mass.

Distribution of Sulphur Between Gas and Open Hearth Type Slags: George St. Pierre, John Chipman, Massachusetts Institute of Technology, Cambridge, Mass.

Chicago Section, NOHC, Annual All-Day Meeting

Registrants for the AIME Annual Meeting, particularly Iron and Steel Div. Members, are invited to attend this meeting at the Del Prado Hotel, 53rd & Lake Park Blvd.

9:00 am, Del Prado Hotel

Registration

9:30 am

Basic Furnaces and Refractories

T. D. Hess and D. J. Carney, Associate Chairmen

Design and Operation of All Basic Open Hearth Furnaces at Keystone Steel & Wire Co.: A. H. Sommer, Keystone Steel & Wire Co., Peoria, Ill.

Operation and Performance of all Basic Open Hearth Furnaces at U. S. Steel Corp., South Works: J. J. Oravec, J. F. O'Brien, U. S. Steel Corp., South Works, Chicago, Ill.

Behavior and Testing of Basic Refractories for Open Hearth Use: W. S. Debenham, U. S. Steel Corp., Pittsburgh, Pa.

2:00 pm, Del Prado Hotel

Structure and Segregation of Rimming Steel Ingots

M. Tenenbaum and H. Wishart, Associate Chairmen

Influence of Furnace Practice and Deoxidation on the Structure and Performance of Rim Steel: L. Fleming, U. S. Steel Corp., Gary Works, Gary, Ind.

Influence of Capping Practice on Structure and Performance of Rim Steel: R. Demeter, Youngstown Sheet & Tube Co., Indiana Harbor, Ind.

Influence of Ingot Dimensions on Segregation of Rim Steel Ingots: J. F. Elliott, Inland Steel Co., Chicago, Ill.

Influence of Pouring Technique on Surface Structure of Rimming Ingots—Movies: W. H. Mayo, U. S. Steel Corp., Pittsburgh, Pa.

Steelmaking Developments During the Past Decade: K. L. Fetters, Youngstown Sheet & Tube Co., Youngstown, Ohio.

5:30 pm, Del Prado Hotel

Cocktail Hour

Courtesy Suppliers' Committee

6:30 pm

Annual Chicago Section Dinner

Toastmaster: Oscar Pearson, U. S. Steel Corp.

Speaker: Frank Leahy, Exothermic Alloy Corp.

THURSDAY, FEBRUARY 17

9:00 am, Astoria Ballroom

High Temperature Kinetics

C. R. Taylor and C. W. Sherman, Associate Chairmen

Solid State Diffusion in the Reduction of Magnetite: J. O. Edstrom, Euskede, Stockholm, Sweden, Gust Bitsianes, University of Minnesota, Minneapolis, Minn.

Diffusion in Liquid Iron Saturated with Carbon: Gerhard Derge, Carnegie Institute of Technology, Pittsburgh, Pa.

Rate of Reduction of FeO from a Lime-Silica-Alumina Slag Over Carbon Saturated Iron: W. O. Philbrook, Carnegie Institute of Technology, Pittsburgh, Pa.

Rates of Desulphurization as Measured by Carbon Monoxide Evolution from an Iron Bath: Ramachandran, King, Grant

9:00 am, Parlor C

Steelmaking

C. F. Staley and F. O. Lemmon, Associate Chairmen

The Use of Hot Metal in the Electric Furnace: R. J. McCurdy, Republic Steel Corp., Chicago, Ill.

Preparation and Arc Melting of High Purity Iron: G. W. P. Rengstorff, H. B. Goodwin, Battelle Memorial Institute, Columbus, Ohio

Association of Temperature with Fundamental Steelmaking: C. F. Christopher, Continental Foundry & Machine Co.

Mechanical Properties of Medium Carbon Boron Steel: Kattus, Southern Research Institute,

2:00 pm, Astoria Ballroom

High Temperature Thermodynamics

Gerhard Derge and R. L. Hindson, Associate Chairmen

Solubility of Oxygen in Liquid-Iron and Iron-Nickel Alloys: H. A. Wriedt, U. S. Steel Corp., Pittsburgh, Pa., John Chipman, Massachusetts Institute of Technology, Cambridge, Mass.

Relations of Oxygen with Molten Iron-Chromium Alloys: D. C. Hilty, W. O. Forgeng, R. L. Folkman, Electro Metallurgical Co., Niagara Falls, N. Y.

Thermodynamic Activity of Sulphur in Liquid Iron-Nickel Solutions: Cordier, John Chipman

Sampling Liquid Iron for Oxygen Content: A Further Evaluation of the Bomb Technique: S. Gilbert, G. R. Bailey, U. S. Steel Corp., Pittsburgh, Pa.

EXTRACTIVE METALLURGY DIV.

MONDAY, FEBRUARY 14

10:00 am

Metals Branch Council Meeting

R. R. McNaughton, Chairman

2:30 pm, Astoria Ballroom

Aluminum

H. W. St. Clair and A. C. Byrnes, Associate Chairmen

Gas Content of Solid Aluminum by Solid Extraction and Vacuum Fusion: J. L. Brandt, N. Cochrane, Aluminum Co. of America, Aluminum Research Laboratories, New Kensington, Pa.

Production of Alumina From Anorthosite: H. W. St. Clair, U. S. Bureau of Mines, Washington, D. C.

Carbon Technology Related to Aluminum Production: S. W. Martin, Great Lakes Carbon Corp., Chicago, Ill.

Solubility and Density of Hydrated Aluminas in Sodium Hydroxide Solutions: A. S. Russell, J. D. Edwards, C. S. Taylor, Aluminum Co. of America, Aluminum Research Laboratories, New Kensington, Pa.

Coal as a Source of Power for Production of Aluminum: A. Johnson, Olin-Mathieson Corp., Alton, Ill.

2:30 pm, South Ballroom

Physical Chemistry of Extractive Metallurgy
Physical Chemistry of Steelmaking
Joint Session with ISD

R. Schuhmann, Jr., and D. J. Girardi, Associate Chairmen

Ionic Nature of Liquid Iron-Silicate Slags: M. T. Simnad, Gerhard Derge, Carnegie Institute of Technology, Pittsburgh, Pa., and I. George, Distillers Co. Ltd., Glamorgan, South Wales, Great Britain

Surface Tension of Slags: R. Bowni, Gerhard Derge, Carnegie Institute of Technology, Pittsburgh, Pa.

Equilibrium Between Titanium in Liquid Iron and Titanium Oxides: R. L. Hadley, Gerhard Derge, Carnegie Institute of Technology, Pittsburgh, Pa.

Phase Equilibria in the System FeO-Fe_2O_3-SiO_2: Arnulf Muan, Pennsylvania State University, State College, Pa.

TUESDAY, FEBRUARY 15

7:30 am

Executive Committee Breakfast Meeting

P. T. Stroup, Chairman

9:00 am, Astoria Ballroom

Hydrometallurgy-Physical Chemistry of Extractive Metallurgy

Joint Session with MBD

J. Dasher and O. Tangel, Associate Chairmen

Kinetic Study of the Oxidation of Sphalerite: J. N. Ong, Jr., M. E. Wadsworth, W. M. Fassell, Jr., University of Utah, Salt Lake City, Utah

Acid Pressure Leaching of Uranium Ores: F. A. Forward, J. Halpern, University of British Columbia, Vancouver, Canada

Reaction Rate Study of the Solution of Cuprite in Sulphuric Acid: M. E. Wadsworth, D. R. Wadia, University of Utah, Salt Lake City, Utah

Mechanism and Rate of Dissolution of Chalcocite in Acid Ferric Sulphate: C. O'Neill, N. Arbiter, Columbia University, New York

2:00 pm, West Ballroom

Physical Chemistry of Extractive Metallurgy

T. B. King and F. L. Stephens, Jr., Associate Chairmen

Electrical Conduction in Molten Cu-Fe Sulphide Mattes: G. M. Pound, Gerhard Derge, G. Osuch, Carnegie Institute of Technology, Pittsburgh, Pa.

Thermodynamics of the Cu-Fe-S System at Matte-Smelting Temperatures: W. A. Krivsky, R. Schuhmann, Jr., Massachusetts Institute of Technology, Cambridge, Mass.

Chemical Behavior of Oxygen in Liquid Mattes: H. L. Lander, R. Schuhmann, Jr., T. B. King, Massachusetts Institute of Technology, Cambridge, Mass.

Sulphur Pressure Measurements of Molybdenum Sesquisulphide in Equilibrium with Molybdenum: C. L. McCabe, Carnegie Institute of Technology, Pittsburgh, Pa.

2:00 pm, Astoria Ballroom

Hydrometallurgy

Joint Session with MBD

R. D. MacDonald and F. A. Forward, Associate Chairmen

Metal Precipitation From Salt Solution by H_2 Reduction: F. A. Schaufelberger, Chemical Construction Corp., New York

Agitation vs Process Results in a Zinc Dust Purification: L. A. Painter, R. K. Carpenter, American Zinc Co., Monsanto, Ill.

Beaver Lodge Hydrometallurgical Plant: R. W. Mancantelli, J. R. Woodward, Eldorado Mining & Refining Ltd., Saskatchewan, Canada

Nickel-Cobalt Separation by Selective Reduction: F. A. Schaufelberger, Chemical Construction Corp., New York and T. K. Roy, Jadavpur College, Calcutta, India

6:00 pm

Metals Branch Cocktail Party

7:00 pm

Metals Branch Annual Dinner

WEDNESDAY, FEBRUARY 16

9:00 am, Upper Tower

Symposium

Refractories for Processing Liquid Metals and Slags

P. T. Stroup and J. D. Sullivan, Associate Chairmen

Developments in Refractories and Their Applications for Non-ferrous Metallurgy: W. F. Rochow, C. A. Brashares, Harbison-Walker Refractories Co., Pittsburgh, Pa.

Silicon Nitride—A Refractory Material: J. F. Collins, Electro Metallurgical Co., Niagara Falls, New York and T. F. Frangos, Haynes Stellite Co., Kokomo, Ind.

"Gold" Brick and Non-ferrous Metals: B. M. Johnson, A. A. Turner and H. Schroeder, Carborundum Co., Perth Amboy, N. J.

Ceramic Coatings for the High-Temperature Protection of Metal: B. W. King, Battelle Memorial Institute, Columbus, Ohio

12:15 pm, Upper Tower

Annual EMD Stag Luncheon and Business Meeting

2:00 pm, Upper Tower

Symposium

Refractories for Processing Liquid Metals and Slags

P. T. Stroup and J. D. Sullivan, Associate Chairmen

Metallic Materials Resistant to Molten Zinc: R. M. Evans, Webster Hodge, A. F. Haskins, Battelle Memorial Institute, Columbus, Ohio

Materials Resistant to Molten Zinc Sintered Borides: Webster Hodge, R. M. Evans, A. F. Haskins, Battelle Memorial Institute, Columbus, Ohio

Life and Replacement of a Reverberatory Furnace Bottom: Harold Foard, International Smelting & Refining Co., Inspiration, Ariz.

Carbon Bonded Silicon Carbide Refractories in Non-ferrous Metallurgy: G. J. Easter, Electro Refractories & Abrasives Corp., Buffalo, N. Y.

THURSDAY, FEBRUARY 17

9:00 am, South Ballroom

Pyrometallurgy and Hydrometallurgy of Zinc and Lead

R. E. Lund and R. G. Knickerbocker, Associate Chairmen

Slag Fuming at Flin Flon: R. E. Mast, G. H. Kent, Hudson Bay Mining & Smelting Co., Ltd., Manitoba, Canada

Processing of Zinc Oxide Fume at Flin Flon: Roy Ellerman, Hudson Bay Mining & Smelting Co., Ltd., Manitoba, Canada

Laboratory Research on Germanium and Cadmium in Sphalerite Concentrates: H. Kenworthy, A. G. Starliper, A. Ollar, U. S. Bureau of Mines, Rolla, Mo.

Tank Room Acidity Control in Electrolytic Zinc Production: G. Steintveit, Det Norske Zinkkompani, Norway

9:00 am, Boulevard Room

Titanium

W. J. Kroll and N. C. Fick, Associate Chairmen

ONR Program of Research on Extractive Metallurgy of Titanium: W. C. Arsem, J. J. Harwood, Office of Naval Research, Washington, D. C.

Preparation and Chlorination of Titaniferous Slags From Idaho Ilmenites: A. H. Roberson, L. H. Banning, U. S. Bureau of Mines, Albany, Ore.

Preparation of Metallic Titanium by Film Boiling: A. W. Petersen, U. S. Signal Corps., and L. A. Bromley, University of California, Berkeley, Calif.

New Method for Casting Titanium: R. A. Beall, A. H. Roberson, F. W. Wood, U. S. Bureau of Mines, Albany, Ore.

2:00 pm, Boulevard Room

Titanium-Zirconium

S. M. Shelton and R. B. Gordon, Associate Chairmen

Preparation of High Purity Zirconium Tetrachloride From Alkali Chlorozirconates: R. V. Harrigan, Titanium Alloy Mfg. Div., National Lead Co., Niagara Falls, N. Y.

Zirconium and Hafnium Production Operations of the Carborundum Metals Corp.: W. W. Stephens, C. Q. Morrison, Carborundum Metals Corp., Akron, N. Y.

Development in the Use of a Precision Titanium Reduction Unit: A. Boozenny, D. W. Cleaves, Titanium Metals Corp. of America, Henderson, Nev.

INSTITUTE OF METALS DIV.

SUNDAY, FEBRUARY 13

7:00 pm

Publication Committee Meeting

W. R. Hibbard, Jr., Chairman

8:30 pm

Program Committee Meeting

D. J. Blickwede, Chairman

MONDAY, FEBRUARY 14

9:45 am, Waldorf Ballroom

Nuclear Metallurgy

D. W. Lillie and E. Epremian, Associate Chairmen

Study of the Radiation Stability of Austenitic Type 347 Stainless Steel: M. B. Reynolds, J. R. Low, Jr., L. O. Sullivan, General Electric Co., Schenectady, N. Y.

Embrittlement of Molybdenum by Neutron Radiation: C. A. Bruch, W. E. McHugh, R. W. Hockenbury, General Electric Co., Schenectady, N. Y.

Preferred Orientation of Cold-Rolled Uranium Foil: W. Seymour, General Electric Co., Schenectady, N. Y.

9:45 am, Parlor Room 1

Constitution

D. J. McPherson and J. P. Nielsen, Associate Chairmen

Zirconium Columbium Diagram: B. A. Rodgers, D. F. Atkins, Iowa State College, Ames, Iowa

Vanadium-Zirconium Alloy System: J. T. Williams, Iowa State College, Ames, Iowa

Gallium-Antimony System: I. G. Greenfield, R. L. Smith, Franklin Institute of the State of Pennsylvania, Philadelphia, Pa.

Magnesium-Rich Corner of the Magnesium-Lithium-Aluminum System: J. A. Rowland, Bureau of Mines, Rolla, Mo.

Curie Temperatures of Binary and Ternary Sigma Phases: M. V. Nevitt, Virginia Polytechnic Institute, Blacksbury, Va., P. A. Beck, University of Illinois, Urbana, Ill.

Structure and Magnetic Properties of Some Transition Metal Nitrides: G. W. Wiener, Westinghouse Electric Co., E. Pittsburgh, Pa., J. A. Berger, University of Pittsburgh, Pittsburgh, Pa.

10:00 am

Metals Branch Council Meeting

R. R. McNaughton, Chairman

2:30 pm, Parlor A

Recrystallization

G. Edmunds and W. R. Opie, Associate Chairmen

Temperature Dependence of Annealing Phenomena in Cold Rolled Aluminum Single Crystal: A. H. Lutts, P. A. Beck, University of Illinois, Urbana, Ill.

Relationship Between Recovery and Recrystallization in Super Purity Aluminum: E. C. W. Perryman, Aluminium Laboratories Ltd., Kingston, Ont., Canada

Microcalorimetric Investigation of the Recrystallization of Copper: Paul Gordon, Institute for the Study of Metals, University of Chicago, Chicago, Ill.

Recrystallization Characteristics of Super Purity Base Aluminum-Magnesium Alloys Containing 0 to 5 Pct Magnesium: E. C. W. Perryman, Aluminium Laboratories Ltd., Kingston, Ont., Canada

Some Aspects of the Crystallization and Recrystallization of Vapor Deposited Vitreous Selenium: N. E. Brown, F. L. Ver Snyder, General Electric Co., Schenectady, N. Y.

Effect of Zn Content on the Rolling Texture and Annealing Texture: P. A. Beck, Alfonso Merlini, University of Illinois, Urbana, Ill.

Recrystallization Textures of a Cold-Rolled Aluminum Single Crystal: Y. C. Liu, New York University, New York, W. R. Hibbard, Jr., General Electric Co., Schenectady, N. Y.

Preferred Orientations in Beta-Annealed Zirconium: J. H. Keeler, A. H. Geisler, General Electric Co., Schenectady, N. Y.

3:00 pm

JOURNAL OF METALS Editorial Advisory Board Meeting

J. S. Smart, Jr., Chairman

4:30 pm

IMD Membership Committee Meeting

J. P. Nielsen, Chairman

TUESDAY, FEBRUARY 15

7:30 am

IMD Titanium Committee Breakfast Meeting

J. H. Jackson, Chairman

9:00 to 10:30 am, South Ballroom

Deformation I

C. S. Roberts and F. L. Vogel, Associate Chairmen

Method of Measuring the Contribution of Crystal Structure to the Hardness of Metals: Walston Chubb, Battelle Memorial Institute, Columbus, Ohio

Further Observations on Yield in Single Crystals of Iron: H. W. Paxton, Carnegie Institute of Technology, Pittsburgh, Pa., I. J. Bear, C.S.I.R.O., Australia

Cold-Rolled Textures of Silicon-Iron Crystals: P. K. Koh, Allegheny-Ludlum Steel Corp., Brackenridge, Pa., C. G. Dunn, General Electric Co., Pittsfield, Mass.

High-Temperature Properties of Iron-Rich Iron-Molybdenum Alloys: S. F. Retter, Rome Fastener Corp., New Haven, Conn., W. R. Hibbard, Jr., General Electric Co., Schenectady, N. Y.

12:15 pm

IMD Executive Committee Luncheon Meeting

J. H. Scaff, Chairman

2:00 pm, South Ballroom

Deformation II

H. Y. Hunsicker and A. A. Burr, Associate Chairmen

Study of a New Mode of Plastic Deformation in Zinc Crystals: J. J. Gilman, General Electric Co., Schenectady, N. Y.

Some Aspects of Slip in Germanium: R. G. Treuting, Bell Telephone Laboratories, Inc., Murray Hill, N. J.

Plastic Deformation of Germanium and Silicon by Torsion: E. S. Greiner, Bell Telephone Laboratories, Inc., Murray Hill, N. J.

Determination of the Amount of Strain Hardening Associated with Fatigue: Rayjor Webeler, Lewis Flight Propulsion Laboratory, National Advisory Committee for Aeronautics, Cleveland, Ohio

Study of the Room-Temperature Fatigue Properties of Molybdenum: W. L. Bruckart, W. S. Hyler, Battelle Memorial Institute, Columbus, Ohio

Baushinger Effect in Creep and Tensile Tests on Copper: J. D. Lubahn, General Electric Co., Schenectady, N. Y.

Viscous Flow of Copper at High Temperatures: A. L. Pranatis, G. M. Pound, Carnegie Institute of Technology, Pittsburgh, Pa.

Creep Deformation of Magnesium at Elevated Temperatures by Non-Basal Slip: A. R. Chaudhuri, H. C. Chang, N. J. Grant, Massachusetts Institute of Technology, Cambridge, Mass.

6:00 pm

Metals Branch Cocktail Party

7:00 pm

Metals Branch Annual Dinner

WEDNESDAY, FEBRUARY 16

9:00 to 10:00 am, Boulevard Room

Transformation I

L. Seigle and H. Dixon, Associate Chairmen

Calorimetric Investigation of the Energy Relations in Alloys of Composition Cu_3Au: L. R. Rubin, J. S. Leach, Division of Industrial Cooperation, Massachusetts Institute of Technology, Cambridge, Mass., M. B. Bever, Massachusetts Institute of Technology, Cambridge, Mass.

Dispersion Hardening of Copper-Chromium Alloys: W. R. Hibbard, Jr., E. W. Hart, General Electric Co., Schenectady, N. Y.

Decomposition of Beta Titanium: F. R. Brotzen, Rice Institute, Houston, Texas, E. L. Harman, Jr., A. R. Troiano, Case Institute of Technology, Cleveland, Ohio

10:45 am

IMD Annual Business Meeting

J. H. Scaff, Chairman

11:00 am

Annual Lecture, IMD

L. F. Reinartz and J. H. Scaff, Associate Chairmen

The Impact of Magnetism Upon Metallurgy: Clarence Zener, Westinghouse Electric Corp., E. Pittsburgh, Pa.

2:00 pm, South Ballroom

Transformation II

D. Turnbull and D. J. Blickwede, Associate Chairmen

Study of the Effect of Boron on the Decomposition of Austenite: C. Simcoe, A. R. Elsea, G. K. Manning, Battelle Memorial Institute, Columbus, Ohio

Influence of Heat Treatment on the Ductile-Brittle Transition Temperature of Semikilled Steel Plate: R. H. Frazier, F. W. Boulger, C. H. Lorig, Battelle Memorial Institute, Columbus, Ohio

Isothermal Embrittlement in Chromium and Molybdenum Alloy Steel During Tempering: G. Bhat, J. F. Libsch, Lehigh University, Bethlehem, Pa.

Relation of Flake Formation in Steel to Hydrogen, Microstructure and Stress: A. W. Dana, Jr., Case Institute of Technology, Cleveland, Ohio, F. J. Shortsleeve, Union Carbon & Carbide Research Laboratories, Niagara Falls, N. Y., A. R. Troiano, Case Institute of Technology, Cleveland, Ohio

Ordering and Magnetic Heat Treatment of 50 Iron-50 Cobalt Alloy: R. C. Hall, Westinghouse Electric Corp., E. Pittsburgh, Pa., G. P. Conard, J. F. Libsch, Lehigh University, Bethlehem, Pa.

THURSDAY, FEBRUARY 17

9:00 am, Normandie Lounge

Diffusion and Powder Metallurgy

H. H. Hausner and G. T. Horne, Associate Chairmen

Diffusion of Zinc and Copper in Alpha and Beta Brasses: R. Resnick, Sylvania Electric Products, Inc., Bayside, N. Y., R. W. Balluffi, Columbia University, N. Y.

Grain Boundary Diffusion of Nickel into Copper: S. Yukawa, General Electric Co., Schenectady, N. Y., M. J. Sinnott, University of Michigan, Ann Arbor, Mich.

Relation of Strength, Composition and Grain Size of Sintered WC-Co Alloys: J. Gurland, P. Bardzil, Firth Sterling, Inc., Pittsburgh, Pa.

Study of the Microstructure of Titanium Carbide: Herman Blementhal, Ronald Silverman, American Electro Metal Corp., Yonkers, N. Y.

An Evaluation of Dissociated Ammonia and Hydrogen Atmosphere for Sintering Stainless Steel: H. S. Kalish, E. N. Mazza, Sylvania Electric Products, Inc., Bayside, N. Y.

9:00 am, Waldorf Ballroom

Research in Progress

F. H. Wilson and M. Steinberg, Associate Chairmen

12:15 pm

IMD Powder Metallurgy General Luncheon

H. H. Hausner, Chairman

2:00 pm, Normandie Lounge

Powder Metallurgy Symposium

A. J. Shaler, Chairman

Interaction Between Metals and Atmospheres During Sintering: John Norton, Massachusetts Institute of Technology, Cambridge, Mass.

Panel Discussion: F. N. Rhines, Carnegie Institute of Technology, Pittsburgh, Pa., N. J. Grant, John Norton, Massachusetts Institute of Technology, Cambridge, Mass., A. J. Shaler Pennsylvania State University, State College, Pa.

2:00 pm, Waldorf Ballroom

Oxidation and Melting

H. R. Ogden and J. Everhart, Associate Chairmen

High Pressure Oxidation of Metals—Molybdenum in Oxygen: R. C. Peterson, W. M. Fassell, Jr., University of Utah, Salt Lake City, Utah

Kinetics and Mechanism of the Oxidation of Molybdenum: M. Simnad, A. Spilners, Carnegie Institute of Technology, Pittsburgh, Pa.

Oxidation of Cobalt Metal: R. E. Carter, Canada Dept. of Mines and Technical Survey, Ottawa, Canada, F. D. Richardson, Nuffield Research Group in Extractive Metallurgy, Kinsington, London, England

Conditions Governing the Instability of a Smooth Solid Liquid Interface During the Solidification of Metals: D. Walton, W. A. Tiller, J. W. Rutter, W. C. Winegard, University of Toronto, Canada

Contribution to the Mathematics of Zone Melting: Leslie Burris, Jr., Argonne National Laboratory, Lemont, Ill., C. H. Stockman, Special Scientific Employee on Loan from B. F. Goodrich Co., Research Center, Brecksville, Ohio, I. G. Dillon, Argonne National Laboratory, Lemont, Ill.

Continuous Multistage Separation by Zone Melting: W. G. Pfann, Bell Telephone Laboratories, Inc., Murray Hill, N. J.

Molybdenum Deposition on Titanium: Sam Tour, George Fischer, Andre Styra, Sam Tour & Co., Inc., New York

Canadian Copper Refiners Ltd.

Electric Furnace Melting Practice

by Warren A. Sheaffer

Electric furnace installation and tough-pitch copper-casting operation at Canadian Copper Refiners Ltd. are described. General layout, power supply and control, refractories, induction pour hearth, casting equipment, metal temperature control, and oxygen-content control are discussed.

ELECTRIC furnace at Canadian Copper Refiners Ltd. was put into operation in August 1949. The installation was designed primarily to melt electrolytic copper cathodes and to produce vertically cast tough-pitch shapes. To meet emergencies during reverberatory furnace shut-downs, provision was made for casting horizontal tough-pitch wire bars. Due to the ease with which metal temperatures, melting rates, oxygen content, and casting hours can be altered to suit production demands, the electric furnace has met the requirements admirably.

General Layout

The plant has been described by H. S. McKnight[1] and by J. H. Schloen and E. M. Elkin.[2] Since these papers were written, the electric furnace has been installed in a 140 ft extension of the original casting building. The extension, 264 ft in width, is divided into one 24 ft and four 60 ft bays, each a continuation of similar bays in the older building. Fig. 1, a partial floor plan of the extension, shows the location of major equipment.

Power Supply and Control

Power for the electric furnace and its auxiliary equipment is delivered by Quebec Hydro over two 12 kv three-phase, 60 cycle pole lines. One line is in use, while the second serves as an emergency standby. Connections for the electric furnace from these lines, which also feed the refinery power house, are made to a substation on Canadian Copper Refiners Ltd. property. Connections between this substation and the furnace transformer room are in underground conduit. The arc-furnace transformer, 550 v auxiliary-equipment transformer, and 12 kv switchgear are in the transformer room near the furnace.

Stepdown from 12 kv to arc-furnace voltages is done by a 7500 kva oil-immersed water-cooled three-phase 60 cycle transformer. This unusually high kva rating is available because the arc furnace and transformer were adapted from a steel-melting unit. Secondary voltages are available in 16 steps between 251 and 95 v (across phases). A four-position tap changer, operated from the furnace switchboard is connected to taps yielding 199, 164.5, 127, and 115 v, respectively. The transformer primary feeder is equipped with a General Electric Magne-Blast circuit breaker.

The pour hearth, casting wheel, bosh conveyor, and other auxiliary equipment are fed by a 12 kv to 550 v, 750 kva three-phase 60 cycle transformer.

Graphite electrodes, 14 in., with tapered nipples are held in the arc-furnace electrode arms with steel wedges. The arms, fed from the transformer secondary busbars by flexible cable bundles, are actuated by winch cables. Direct-current motors operating the winches are supplied by a 250 v motor-generator set.

Power input to the furnace is controlled from the furnace switchboard. The board has the usual combination of remote controls for the 12 kv breaker and transformer tap changer, meters, overload relays, automatic and manual electrode motion controls, switchgear, etc.

When power is on the furnace, automatic electrode feed is used; the power draw on a given voltage tap then is governed by current-limiting rheostats. The rheostats work through a Westinghouse balanced-beam control circuit which, in turn, operates reversing contactors in the winch motor circuits.

Arc Furnace

The arc furnace is a standard-type NT Pittsburgh Lectromelt with inside shell diameter 12 ft 3¾ in. By hydraulic-lift cylinders, the furnace can be tilted forward to 39½° and backward to 5° from horizontal. A roof-swing cylinder is also installed but not used. Fig. 2 shows refractory-lining details.

With the lining as shown, operating life between repairs is 6 to 9 months of two-shift casting operation. Charge slot, skim door, and roof refractories then are replaced completely, and any necessary repairs made to side walls. Bottom life is longer and the original under courses are still in service, while the top course was replaced in October 1951.

The launder is lined with high chrome-magnesite trough brick backed by fireclay and insulating brick. The trough is covered with fireclay brick and asbestos sheet. At intervals, openings 12x8 in. are left in the permanent covering. These are covered with

W. A. SHEAFFER is associated with Canadian Copper Refiners Ltd., Montreal East, Quebec, Canada.

Discussion of this paper, TP 3850D, may be sent, 2 copies, to AIME by Mar. 1, 1955. Manuscript, Feb. 4, 1954. New York Meeting, February 1954.

The Transactions papers appearing in the Journal of Metals during 1955 will subsequently appear in AIME Transactions Volume 203, and may be permanently referenced to that volume.

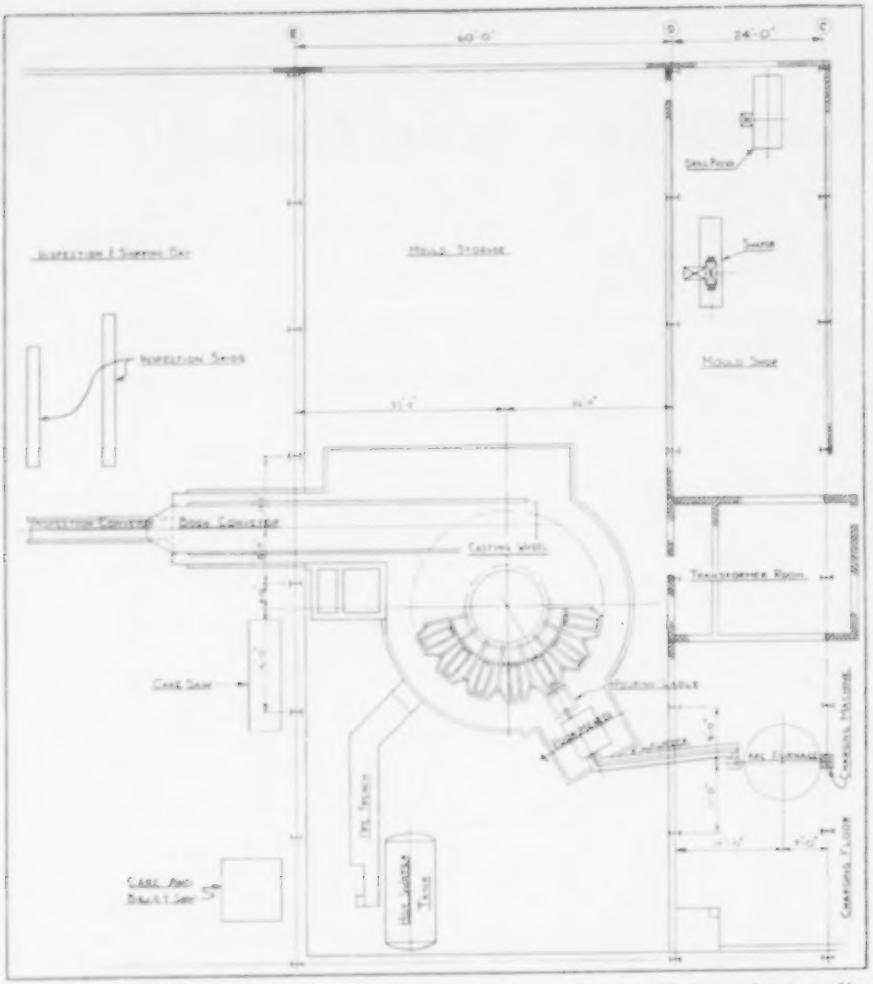

Fig. 1—Partial floor plan of the extension showing the location of major equipment. The electric arc furnace is installed in the 140 ft extension of the original casting building at Canadian Copper Refiners Ltd. The new section, 264 ft wide, is divided into one 24 ft and four 60 ft bays, each a continuation of similar bays in the older building.

loose bricks and permit heating of the launder with oil burners prior to casting.

The furnace is charged by a tilting roller-bed table hinged to the charge-slot framing. Tilting is effected by an air cylinder mounted on the under side. Fig. 3 shows the device in operation.

Gases are removed from the furnace through a 10 in. diam opening in the roof refractory. A suspended bonnet conducts the gases to a flue system which connects through a dust-recovery unit to a 6000 cfm constant-speed draft fan.

Flue dust is collected in a four-section Dracco-type vibrating bag house, each section containing 25 wool bags, 7 in. diam. Gas temperature entering the bag house is limited to 250°F by admitting cold air to the flue. This air admission also is used to make minor furnace-draft adjustments. Approximately 6 lb of dust, running 86 pct Cu, is recovered per ton of cathodes melted. Dust is used in the manufacture of Noranda-brand copper sulphate.

Pour Hearth

The pour hearth was designed to act as a holding vessel between the arc furnace and pouring ladle. Containing 4½ to 5 tons of melt, it serves to smooth out temperature fluctuations in the arc furnace. The unit was built by Ajax Engineering Co.

The hearth is a refractory-lined steel cylinder inclined at 1½ in. per ft to the horizontal. Inlet and outlet tubes are on an axis parallel to the principal axis of the hearth. The furnace rests in a cradle which rotates about the inlet-outlet axis, this providing a means of adjusting the rate of discharge.

The 60 cycle inductor unit, rated at 125 kw, bolts to a flange on the under side of the hearth shell. The case of the unit is of welded-steel construction and is provided with a high permeability core and a glass tape-insulated primary coil. Cooling of core, primary coil, and refractory lining around the primary is done by two 1000 cfm blowers.

The hearth is lined with 4½ in. of chemically bonded magnesite brick backed by fireclay brick, insulating brick, and asbestos board. The inductor unit and connecting throat in the hearth are gunrammed with sillimanite. Refractory life has been excellent; an inductor replaced in May 1953 had been in service for 41 months. At the same time, the hearth lining which had been in use for 45 months was renewed also although still serviceable.

Pour-hearth electrical-control equipment is housed in a cubicle at the arc-furnace switchboard. Power is supplied to the cubicle by the 550 v auxiliary-equipment transformer. The cubicle contains the usual switchgear, auto-transformer, interlocked high

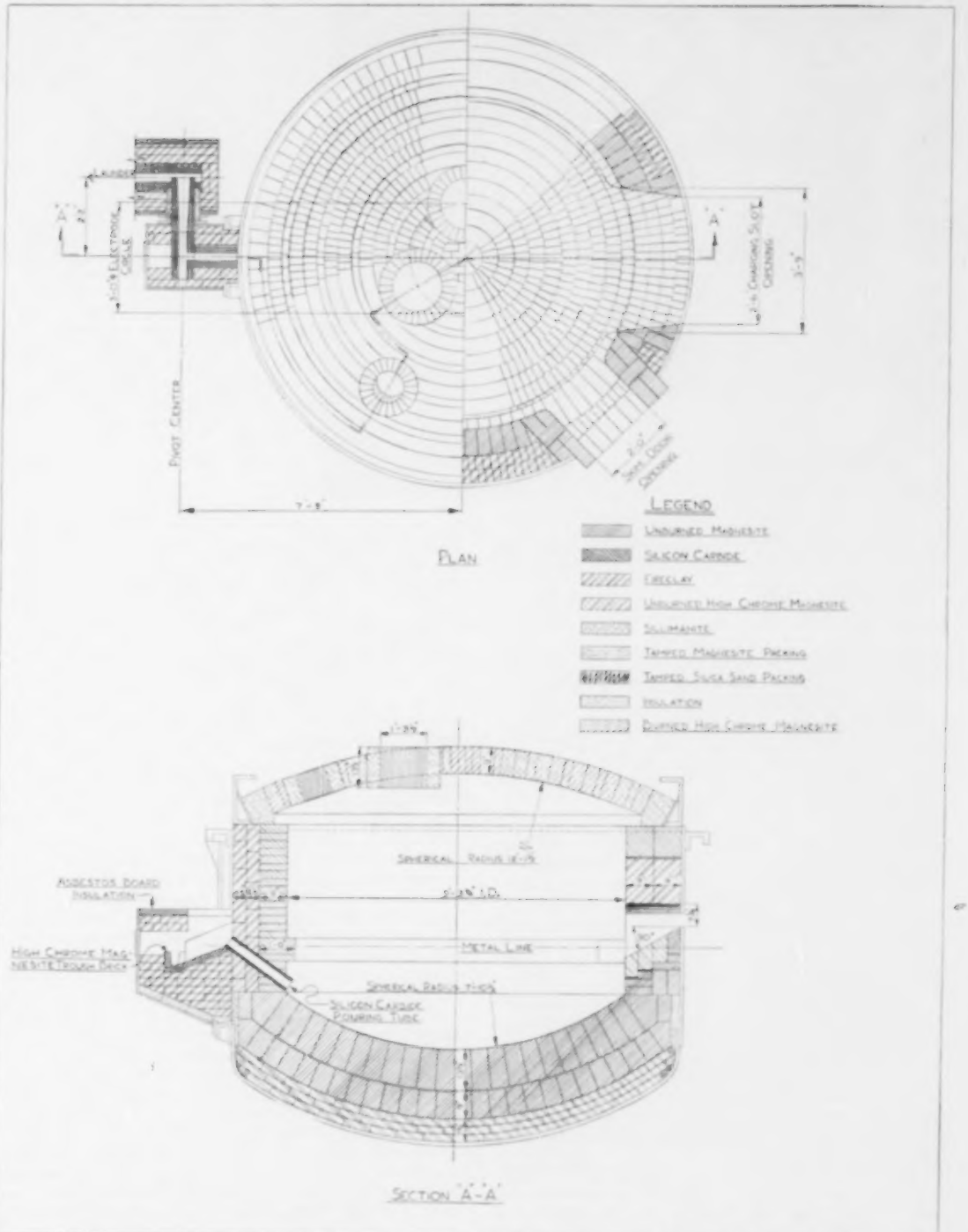

Fig. 2—Diagrams of the electric arc furnace showing refractory-lining details. Operating life between repairs for the lining as described is 6 to 9 months of two-shift casting operation. After this period, charge slot, skim door, and roof refractories are replaced completely and any repairs necessary are made to side walls. Bottom life is longer. Launder lining is high chrome-magnesite trough brick backed by fireclay and insulating brick.

and low power contactors, and power-factor compensating capacitors. Five voltage taps supply nominal draws of 10, 20, 30, 70, and 110 kw, respectively. Manual selectors permit connecting the 10, 20, or 30 kw taps to the "low" power contactor and the 70 or 110 kw taps to the "high" power contactor. High or

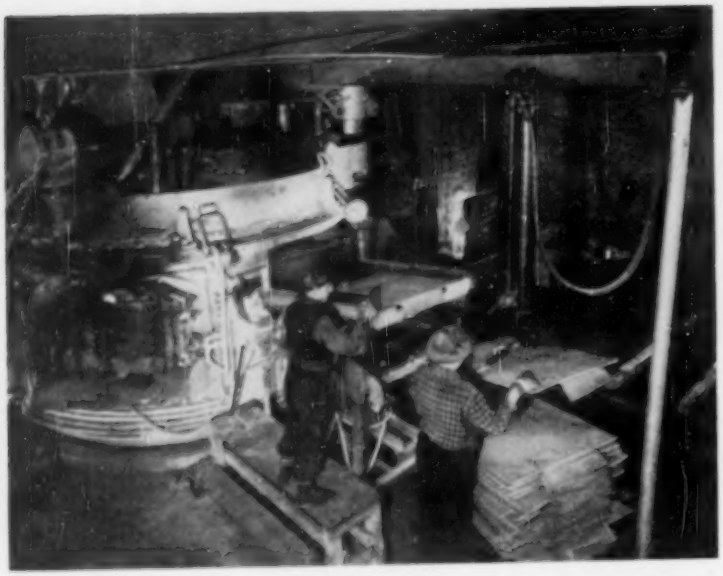

Fig. 3—Arc-furnace charging machine: a tilting roller-bed table hinged to the charge-slot framing. Tilting is effected by an air cylinder mounted on the under side. Photograph shows the equipment in operation.

low power selection can then be made by a selector switch. Also, by this switch, the furnace can be put on automatic temperature control.

For holding during layover periods, the furnace is placed on auto-control and held by a controlling recorder to within 10°F of desired temperature. Temperature measurement is made by a Rayotube sighting on a closed-end silicon-carbide target tube partially immersed in the melt. The recorder, by mercury switching, places the inductor on either high or low power according to temperature.

The pour hearth is normally operated on the 30 and 70 kw taps. Holding power is 52 kw at 2150°F and load power factor, 40 pct.

Casting Equipment and Operation

Wire bars and vertically cast cakes are cast from a conventional bowl-type ladle, using either one or two lips as required. The steel shell is lined with fireclay brick covered by a ½ in. protective coating of Portland cement. Lips are made from fireclay trough brick. The ladle is tilted by a hydraulic cylinder working through a cable system.

Vertically cast billets are poured in pairs from a brick-lined cylindrical two-lipped oil-fired distributor. Metal is poured from the cylinder by rotation about the principal axis. Additional pouring control is provided by tilting this axis and by forward and sidewise motions. The streams from the lips are directed into the molds by fireclay-brick funnels.

The two pouring operations are illustrated in Figs. 4 and 5.

The 28 ft casting wheel has 14 positions providing for a maximum of 28 molds. Pipes entering and leaving the wheel through a central distributing hub provide water for circulation through the water-cooled vertically cast molds. The cooling bosh is equipped with an 8 ft wide steel-lagged conveyor which elevates shapes to the inspection floor.

Molds are cast from tough-pitch copper. Those for horizontal wire bars are prepared for use by air hammering the pocket faces until smooth. Castings for vertically cast cake and billet molds are transferred to the mold shop where pocket faces are machined and water-cooling channels drilled. The cooling system consists of a series of holes which allows water to enter headers near the bottom of the molds, rise in vertical channels parallel to the pocket faces, and leave by headers near the top.

Cooling water for cake and billet molds is pumped to the casting wheel at 1500 gal per min, 55 to 65 psi, and 185° to 195°F. Water returns from the wheel to a 5000 gal storage tank which serves as a head tank for the circulating pump. Cooling-water temperature is controlled by a resistance thermometer in the return line and is recorded by a pneumatic-type recording controller which, operating through an air-actuated valve, admits cold water to the return line as required. A 5 psi overflow valve on the storage tank drains excess water to the sewer.

In general, furnace operation consists of four major steps: charging, melting, mold preparation, and casting. These steps are governed to produce non-porous castings with smooth, inclusion-free surfaces, and set surfaces which meet accepted standards. Metal temperature, oxygen and sulphur contents, mold conditions, and pouring procedure are factors to be controlled. Successful operation requires a balance between these factors. Working procedures have been designed to produce this balance while maintaining satisfactory equipment life.

Cathodes to be melted in the arc furnace are selected with regard to structure of the deposit. Sulphate inclusions in nodulated or deeply striated cathodes lead to casting difficulties; hence, smooth uniform deposits are preferred. Surface sulphates are removed by rinsing. Cathodes are spray-washed with hot water immediately after leaving the electrolytic cells. They are then transported to the furnace charge floor in three to four ton industrial carloads where each load is dip-washed in hot water to remove sulphates trapped in suspension loops, stacked, and allowed to dry before charging. Cathodes are charged singly at calculated time intervals according to desired melting rate.

Casting procedures and equipment for all shapes have been adjusted to give casting rates from 9 to 12 tons per hr. In this range, the 127 v tap is used for

melting. Power consumption, while melting, averages 250 kw-hr per ton at 75 pct power factor.

Pouring temperatures for vertically cast shapes are limited to 2050 ± 10°F at the pouring-ladle lip. Temperatures throughout the system must be controlled to yield this requirement. The control is effected largely in the arc furnace by adjusting conditions according to taphole temperature. The ideal arrangement is to charge at the required casting rate and adjust power input to give the desired taphole temperature, maintaining this balance through the casting period. However, deviations from this procedure are caused by other considerations such as start-up and shut-down when operating with one or more holding shifts and by minor variations due to electrode slipping, charge-slot cleaning, casting interruptions, etc. Compensation for such variations is made by altering power input or charge rate.

The pour hearth, acting as a capacitor, cushions the effect of arc-furnace surges on casting temperature. Rapid cooling in the pour hearth is done by charging cathode cuttings. Also, under normal operating conditions, a 125 lb tough-pitch slab cast in a 250 lb horizontal wire-bar mold is fed continuously into the pouring-ladle bowl. However, if low pour-hearth melt temperatures, and hence low casting temperatures, are encountered, this slab is removed to provide a casting-temperature increase. After corrective measures have been taken in the arc furnace and pour hearth, the slab is replaced in the ladle bowl.

At 15 min intervals during the casting period, temperatures are measured at the arc-furnace taphole using a chromel-alumel immersion-type pyrometer. Pour-hearth temperature is recorded continuously by the Rayotube installation. Ladle-lip temperatures are estimated by the furnace operator although frequent checks are made with the immersion pyrometer.

Fig. 6 graphically illustrates temperatures at the arc-furnace taphole, pour-hearth melt, and pouring-ladle lip for a typical single-shift casting period.

Accurate oxygen-content control is essential if acceptable set surfaces are to be produced on tough-pitch shapes. With the simultaneous melting and casting procedure, this becomes a problem of balancing oxygen pickup against copper melted.

Except for a small pickup where the metal stream drops into and out of the pouring ladle, oxygen must be obtained by air admission to the arc furnace, pour hearth, or pouring ladle. To limit this admission primarily to one location and, hence, simplify control, a charcoal-briquette cover is maintained in the pour hearth and pouring ladle. Launder openings are covered by loose bricks. As a result, oxygen pickup is confined essentially to the arc furnace.

Air enters the arc furnace as cathodes are charged. Also, a 6 in. square opening is left in the work door. Control is effected by altering furnace draft and, when necessary, the work-door opening. Under normal conditions, satisfactory control is obtained by this method. Where additional pickup is desired, air can be admitted by opening the loose launder cover or by removing portions of the charcoal-briquette cover in the pour hearth. Limited reduction in the oxygen content of the metal is effected by working the pouring-ladle cover into the melt.

Samples for optical estimation of oxygen content are taken from the arc-furnace taphole and the pouring-ladle lip at 1 hr intervals during the cast. The samples, measuring ⅝ in. diam by 3½ in. long are cut, polished, etched, and examined at 60 diam. Results are used for control purposes and as a check on oxygen content of the shapes.

Typical average oxygen-content distribution through the system is shown in Table I.

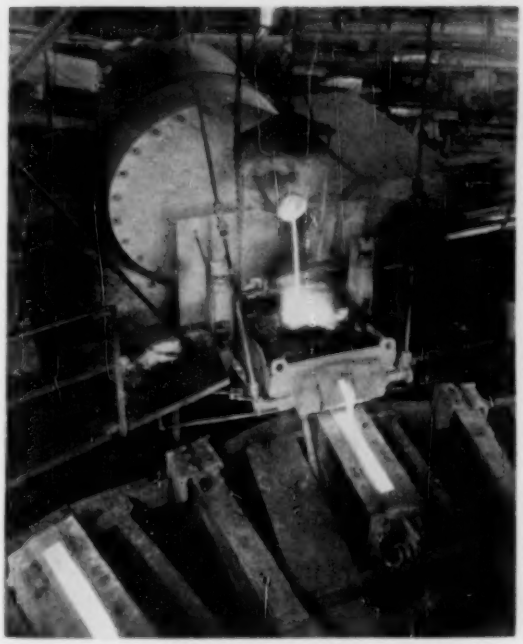

Fig. 4—Coke pouring ladle in operation. Wire bars and vertically cast cakes are poured from the conventional bowl-type ladle, as illustrated, using either one or two lips as required.

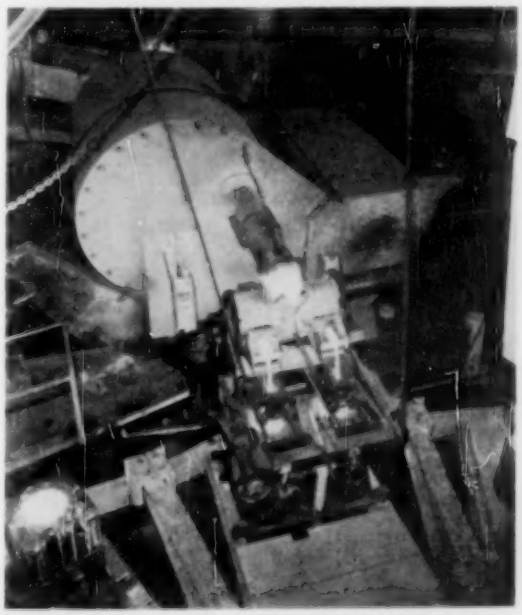

Fig. 5—Billet distributor, showing how vertically cast billets are poured in pairs from the brick-lined cylindrical two-lipped oil-fired distributor. Metal is poured from the cylinder by rotation about the principal axis. Streams from the lips are directed into the molds by fireclay-brick funnels.

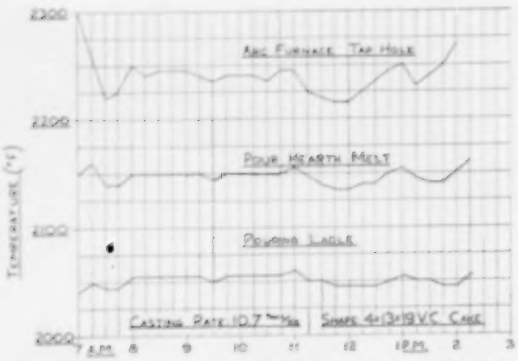

Fig. 6—Copper temperature distribution for a typical single-shift casting period.

Molds are dressed by applying a thin layer of bone ash. The thickness, uniformity, and adherence of this coating largely determine the surface quality of the castings.

When casting horizontal wire bars, a 10°Be slurry is sprayed onto the mold pocket. Mold temperature is kept at 270° to 310°F.

For vertically cast shapes, a more extensive procedure has been adopted. Mold temperatures prior to dressing are kept at 185° to 195°F by circulating water as described previously. Pocket faces are gently rubbed with a soft woolen swab to remove discolored material from the residual coating. New dressing is applied by flowing on a bone-ash slurry using a 1¼x1/16 in. nozzle operating under a 4 ft head. The nozzle is held against the top edge of the mold face and passed slowly around the perimeter. Specific gravity of the slurry depends on shape dimensions and varies from 15° to 26° Be.

Accurate oxygen-content control must be supplemented by correct pouring technique if acceptable set surfaces are to be produced. Depending on dimensions, each shape is poured during a given time interval. However, for vertically cast shapes, the interval is not divided uniformly along the vertical center line. The pouring rate is diminished considerably for the top 3 in. of the casting. In practice, the total pouring time is measured and the correct distribution of this interval obtained by personnel training.

Splashes, shot, cold-sets, seams, etc., must also be avoided. Vertically cast cakes are floated in the usual manner. Vertically cast billet-mold doors are cupped to diminish splashing.

Silver-bearing tough-pitch shapes, with silver contents between 8 and 25 oz per ton according to specification, are made by adding electrolytic silver sand. In preparation for a silver-bearing cast, the pour-hearth melt is brought to required content during an off shift. The required weight of silver then is added to the copper stream in the launder as each shape is poured during the cast. The procedure utilizes the pour-hearth inductor agitation and melt weight to keep variations to within ±1 oz per ton of any specified content.

Table I. Average Oxygen Contents During Casting Period, Pct

Shape	Arc-Furnace Tap-hole	Pour-Hearth Melt	Ladle Lip	In Shape
4x13x19 in. vertically cast cake	0.025	0.030	0.033	0.035
4x16x30 in. vertically cast cake	0.030	0.035	0.035	0.040
3½x25x38 in. vertically cast cake	0.035	0.040	0.045	0.050
7 13/16 in. diam by 52 in. long vertically cast billet	0.025	0.025	0.025	0.030
250 lb horizontal wire bar	0.030	0.030	0.030	0.030

Table II. Vertically Cast Copper Analysis

Cu	99.945 pct
Ag	0.40 oz per ton
Au	0.02 oz per ton
Se	0.0003 pct
Te	0.0002 pct
As	0.0001 pct
Sb	0.0001 pct
Pb	0.0002 pct
Fe	0.0008 pct
S	0.0016 pct

Sampling and Inspection

One electrical conductivity test is made for each casting period. For this test, a sample is taken from the pouring-ladle lip and cast into a billet 1⅝ in. diam by 5¾ in. long. The billet is skinned, forged to ½ in. rod, and cold drawn to 12 gage wire. The wire then is annealed and conductivity determined. Average conductivity is between 100.30 and 101.10 pct, based on International Annealed Copper Standard.

For each 8 hr casting shift, one shape is selected as a sample. The sample is drilled and the drillings sent to the Canadian Copper Refiners Ltd. laboratory for analysis. Typical results are shown in Table II.

From the bosh conveyor, all vertically cast shapes are transferred to inspection skids where they are examined for defects. Principal causes for rejection are the inability of set surfaces to meet accepted standards, deep-seated surface inclusions, sweat, and casting seams due to splashing. Shallow inclusions are removed by grinding and ends are cropped to eliminate mechanical bruises, shallow seams, and slightly low set surfaces. Where subsurface porosity is suspected, set surfaces are also cropped. Sawn shapes are reinspected and rejected if any defects are visible. Horizontal wire bars are similarly inspected but no cropping equipment is available. All rejected shapes are sent to reverberatory furnaces for remelt.

During layover periods, bath temperature in the arc furnace is held at approximately 2250°F by applying power at 30 min intervals. Holding power is 180 kw. Oxygen content is kept at 0.030 to 0.040 pct by the electrodes and by adding hard-wood brands. To aid gas elimination prior to casting, oxygen content is increased to 0.5+ pct by venting and then reduced to casting requirements by poling.

The pour hearth is held at 2150°F by the Rayotube control unit. Oxygen content is maintained at 0.030 pct by charcoal-briquette additions.

The Canadian Copper Refiners Ltd. electric furnace is equipped, at present, to cast the following tough-pitch shapes: 250, 265, 275, and 300 lb horizontal wire bars: 4x13x18, 4x13x19, 4x16x25, 4x16x30, 3½x25x22, 3½x25x38, 5x12x32, and 5x14x32 in. vertically cast cakes; and 7 13/16 in. diam by 52 in. long vertically cast billets.

References

[1] H. S. McKnight: Montreal East Plant of Canadian Copper Refiners Limited. *Trans.* AIME (1933) **106**, pp. 352-368.

[2] J. H. Schloen and E. M. Elkin: Canadian Copper Refiners Montreal East Plant. *Trans.* Canadian Institute of Mining & Metallurgy (1946) **49**, pp. 143-190.

Some Factors Affecting Open-Hearth Performance

by D. J. Carney, J. J. Oravec, and E. Van Meter

A study was made of combustion-air temperatures and factors affecting air temperatures in the open-hearth regenerative systems. Air-temperature surveys in the regenerative system revealed marked thermal gradients in the air above the checkers. The design of the fantail-uptake region plays a prominent part in increasing the heat recovery of the regenerative system.

THE efficiency of the open-hearth regenerative system is one of the most important factors affecting open-hearth performance. Until recently, this factor has not received the attention in the literature given to many other items affecting performance, such as the type of charge, speed of charging, and the mechanical equipment of the open hearth. J. S. Marsh[1] emphasized the importance of the flame temperature and its dependence upon the combustion-air temperature. By means of measured air temperatures in open-hearth furnaces, data were presented which showed a remarkable degree of correlation between production rate and combustion-air temperature. This correlation was extremely good in view of the numerous factors, other than air temperature, which affect open-hearth production rates. In Marsh's work, a 100°F increase in air temperature reduced the heat time by approximately 45 min.

Realizing the importance of combustion-air temperature, it is desirable to know which factors control the regenerative efficiency of the open-hearth furnace. B. M. Larsen recently discussed this subject.[2] The present paper illustrates a few of the more important items that affect regenerative efficiency and combustion-air temperature.

In the latter part of 1951, a study of open-hearth combustion-air temperatures was begun at the South Works of the United States Steel Corp. In the initial work at open-hearth shop *X*, which produces low carbon steel products, temperatures were measured in the uptake in a manner similar to that used by Marsh[1] and the results obtained were very similar to the Bethlehem data. When it was decided to expand the study of combustion-air temperatures, open-hearth shop *Y* was selected because of the greater variety of furnace-design features, types of steel produced, and firing rates used. With the use of aspirating thermocouples, continuous gas analyzers, thermocouple and optical pyrometers, a study was made of: 1—effect of combustion-air temperature on open-hearth production rate, 2—thermal gradients present in various zones of the regenerative system, 3—effect of furnace-design variations on air temperature and heat recovery, 4—effect of furnace-operating variables on heat recovery, and 5—variation in heat recovery with furnace age during the normal furnace campaign.

Data collected on individual heats at 15 min intervals included air-flow rate, firing rate, checker temperature, combustion-air temperature, and furnace pressure. These data were collected on approximately 230 heats of steel. In addition, information was obtained at random on air infiltration and combustion-gas compositions. The data gathered have shown the desirability of closer control of open-hearth firing practices, a need for reducing air infiltration in the uptake zones, and a need for further study of design of checkers and of uptake-fantail areas.

Equipment

Air is practically a nonradiating medium. Consequently, in the measurement of air temperatures, the principle of heat conduction must be used rather than heat radiation. For this reason, aspirating-type thermocouple pyrometers normally are used to measure air temperatures. With these devices, air

D. J. CARNEY, Member AIME, J. J. ORAVEC, Associate Member AIME, and E. VAN METER are Chief Development Metallurgist, Physicist, and Metallurgical Analyst, respectively, South Works Research Laboratory, United States Steel Corp., Chicago.

Discussion on this paper, TP 3852C, may be sent, 2 copies, to AIME by Mar. 1, 1955. Manuscript, Nov. 11, 1953. Open Hearth Conference, April 1954.

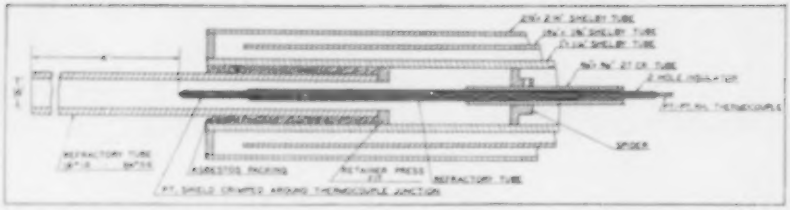

Fig. 1—Front end of the aspirating-thermocouple assembly.

is drawn over the hot junction of a thermocouple at a high velocity by means of an aspirator. In the open hearth, since the refractories are always hotter than the air and since the brick gives off heat by radiation, the thermocouples used to measure air temperature must be protected from the radiated heat of the brick. In addition to the foregoing requirements, the aspirating thermocouple for the open hearth must be durable and capable of accurate temperature measurement for a reasonable period of usage. The design of the aspirating pyrometer which was used in the present study was developed and calibrated by the Kearny Research Laboratory of the United States Steel Corp.[5] The thermocouple hot-junction section of this instrument is shown in Fig. 1 and a photograph of the assembled equipment is shown in Fig. 2. Shielding from radiation is accomplished by a refractory open-end tube rather than by nickel tubes which were used in the Bethlehem study. A platinum foil covers the hot junction of the thermocouple to promote conductivity and also to act as a further shield from radiated heat. A 1-in. Schütte-Koerting ejector with a controllable compressed-air flow was used as the aspirating device to control the hot-air flow over the thermocouple. The desired flow of combustion air passing by the thermocouple hot junction was obtained by increasing the compressed-air flow of the ejector to the point at which further increases in air supply caused no discontinuity in the temperature record.

Cities Service Heat Provers were used to obtain waste-gas analyses. These instruments operate on the principle of rapid combustion of gases and yield a continuous record of oxygen and combustibles. Additional equipment used included thermocouples, potentiometers, and optical pyrometers.

Procedure

Except for the special studies which are discussed individually in this report, the normal procedure followed in the investigation of combustion-air temperatures was as follows:

The aspirating-thermocouple equipment was assembled at one end of the furnace and the thermocouple was inserted through a small hole in the end wall at the sill level of the rear uptake. The unit was inserted at the beginning of each air cycle and removed at the end of the air cycle. A continuous record of the air-temperature variation during each air-reversal cycle thereby was obtained. A complete chronological heat log was kept which included not only the combustion-air temperature but also the fuel-firing rate, air-flow rate, steam pressure, furnace pressure, checker temperatures, and furnace additions. In addition, a record was kept of the heat number, grade of steel, charging time, hot-metal analysis, melt carbon, furnace age from reline to reline, and all other furnace data which seemed pertinent. A typical log is shown in Table I. The maximum (start) and minimum (finish) temperatures of each air cycle were noted. The mean temperature for each air reversal was derived by taking the arithmetic mean of the highest and lowest recorded air temperatures. This simplification eliminated the necessity of integrating the area under each air temperature-time curve to determine the true mean air temperature for each cycle. The relationship of the true and the arithmetic mean temperature was investigated for a number of heats. In general, the true mean temperatures were slightly higher than the arithmetic mean temperatures but the difference was reasonably uniform and not large enough to be of great significance in this work. The mean temperatures of each air cycle from the end of lime boil to the time of tap were averaged and used as an index of the furnace performance. Also, for comparison purposes, the average checker temperatures for each cycle, as measured by four chromel-alumel thermocouples inserted through the checker bulkheads into the zone above the checkerwork, were averaged over the same period of the heat.

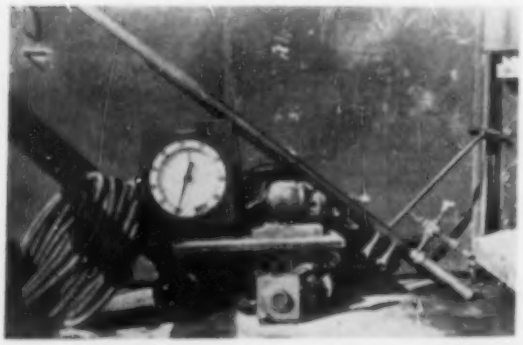

Fig. 2—Aspirating pyrometer and complementary equipment.

In addition to this standard procedure, certain special studies were made. One of these studies involved the measurement of air temperatures in other parts of the regenerative system. In this study, two aspirating thermocouples were used simultaneously. The positions selected for study were 1—furnace uptake at sill level, 2—checker bridgewall, and 3—checker bulkhead. In all furnaces but one, the checker area was divided into two sections, called the air checker and gas checker, respectively. The air-temperature measurements usually were taken in both the bridgewall and bulkhead zones. In one of the furnaces studied, the all-basic, the checker chamber was not divided. Variations in the air temperatures were recorded at the checker bulkhead and checker bridgewall, both vertically and horizontally. After determining the temperature variations at these position, the standard position selected for most studies was approximately 6 ft from the checker inner wall and 15 in. above the top of the checkers for silica furnaces and 9 in. above the top for the all-basic furnace. For correlation purposes, the measured checker air temperatures were compared with optical-pyrometer readings at the bridge-

wall and with checker-thermocouple readings in the bulkhead.

Studies were made also by taking air-temperature measurements at sill-plate level on both ends of the same furnace when checkers were balanced thermally and when checkers were out of balance. When temperatures were measured in only one uptake of the furnace, data were collected only when the checkers were in reasonable thermal balance.

Other variations from the normal procedure involved the use of heat provers to obtain waste-gas analysis simultaneously with the air-temperature measurements. For the study of combustion, the heat provers were inserted in the same positions as the thermocouples at the sill level in the uptake at the opposite end of the furnace. For the study of air infiltration, two heat provers were used simultaneously, one at sill level and one in the checker flues. Other variations from normal procedures involved the use of major variations in air-flow rates during short-time intervals and a study of the effect of various furnace pressures on air temperature.

In order to study changes in furnace design, emphasis was placed on obtaining data from five particular furnaces at open hearth shop *Y*. These five 130 ton furnaces are described in Table II and may be differentiated briefly as follows: 1—Furnace *A* is an all-basic furnace which has suspended basic brick in the roof, port slope, uptake walls, and fantail zone. The double uptake area is 43 sq ft. 2—Furnace *B* is representative of suspended basic-refractory construction in the uptake walls and fantail zone with a silica main roof. The uptake area is 43 sq ft. 3—Furnace *C* is an extended-hearth furnace with a single uptake construction 40 sq ft in area. 4—Furnaces *D* and *E* are conventional silica-roof construction and are typical of 11 of the 14 furnaces in this shop. These furnaces have double uptakes 50 sq ft in area. In addition, furnace *E* uses a slightly different firing practice than furnace *D*.

These variations are particularly well suited for analysis, since these furnaces are all located in the same shop and are producing the same products. Some of the similar features of these furnaces are as follows: 1—All furnaces, with the exception of *A*, have identical types of checkers and checker roofs. The all-basic furnace has a single checker chamber with a flat suspended checker roof as compared to the divided chamber and double-arch roof of the other furnaces. 2—All furnaces, with the exception of *C*, have the same hearth area and bath depth. 3—Each furnace has basic end walls, forced-air fans, waste-heat boilers, manual reversing controls, fuel oil, and natural-gas firing facilities with steam atomization. 4—Furnaces *A* and *C* are equipped with facilities for the use of compressed air for flame enrichment. The importance of some of these features will be discussed in a later section.

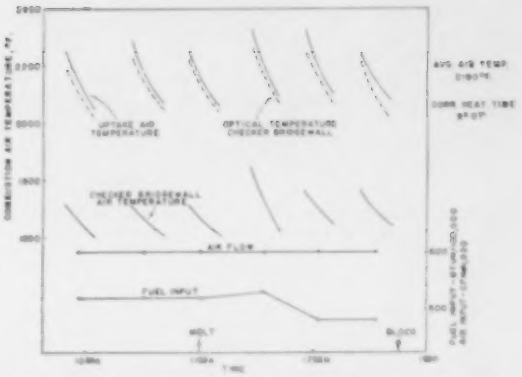

Fig. 3—Graphical presentation of data obtained on a representative heat.

Results and Discussion

Results of a Typical Heat: Before beginning a discussion of the results which out of necessity have been condensed greatly, the results of a portion of an individual heat are shown graphically in Fig. 3 and in detail in Table I. Fig. 4 illustrates the variation in combustion-air temperature during a single air cycle. These data are typical for the regenerative system at open-hearth shop *Y* when using the normal air-flow and firing rates. With the average reversal time of 15 min and manual control, the temperature will fall approximately 180°F during an air cycle. These results compare favorably with the single-pass checker-system data illustrated by Marsh.[1] It should be remembered that in this report the average air temperature of each cycle is used rather than the maximum air temperature of the cycle or the temperature after 5 min elapsed time, which criteria have been used by various authors. Fig. 3 illustrates the variation of the average air temperature for each

Table I. Log* of Heat Presented Graphically in Fig. 3

Time		Sill-Level Air Temperature				Air Checker Bridgewall Air Temperature				Air Checker Bridgewall Optical-Pyrometer Temperature			Firing Practice				
Start	Finish	Start	Med.	Finish	Half	Start	Med.	Finish	Half	5 Min after Reversal	Half Reversal	Finish Reversal	Oil, Million Btu per Hr	Gas, Million Btu per Hr	Air, Thousand Cu Ft per Hr	Steam, Psi	Furnace Pressure, In. H2O
9:50 am	10:05 am	2250	2150	2050	2140	1710	1655	1600	1640	2190	2100	2020	40	12	600	115	0.07
10:25 am	10:40 am	2280	2175	2070	2160	1710	1660	1610	1650	2230	2075	2050	40	12	600	115	0.08
10:55 am	11:10 am	2250	2155	2060	2160	1710	1660	1610	1660	2220	2095	2045	40	12	600	110	0.08
11:27 am	11:42 am	2320	2205	2090	2180	1840	1680	1620	1670	2265	2135	2075	40	13	600	110	0.06
11:56 am	12:11 pm	2320	2210	2100	2200	1760	1700	1640	1680	2250	2125	2075	39	09	600	115	0.05
12:25 pm	12:40 pm	2240	2160	2080	2160	1760	1700	1640	1675	2215	2110	2025	39	09	600	105	0.05

Furnace Additions

10:30 am: 1200 lb limestone
11:00 am: melt, 0.71 pct C
11:05 am: 1500 lb lump ore
11:25 am: 2400 lb limestone
11:30 am: 1000 lb lump ore
11:45 am: 0.40 pct C
11:55 am: bath temperature, 2850°F
12:05 pm: 1200 lb limestone
12:10 pm: 0.22 pct C
12:20 pm: 1200 lb limestone
12:30 pm: 900 lb burnt lime
12:40 pm: 0.10 pct C
12:45 pm: block
1:05 pm: lite
1:15 pm: tapped

* The following data pertain to the log chart: date, Jan. 1, 1953; grade of steel, Triten; firing, north end; heat no. 1001; tap carbon, 0.10 pct; stations, sill level and checker bridgewall; charging, from 3:10 am to 4:45 am; charging time, 1 hr 35 min; hot metal, 6:00 am and 6:15 am, 1.16 pct Si and 0.050 pct S; melt, 11:00 am, 0.71 pct C; block, 12:45 pm; and begin charge-to-block, 9 hr 35 min.

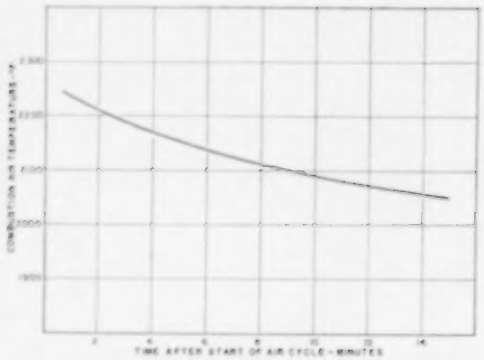

Fig. 4—Air-temperature variation throughout a typical air cycle.

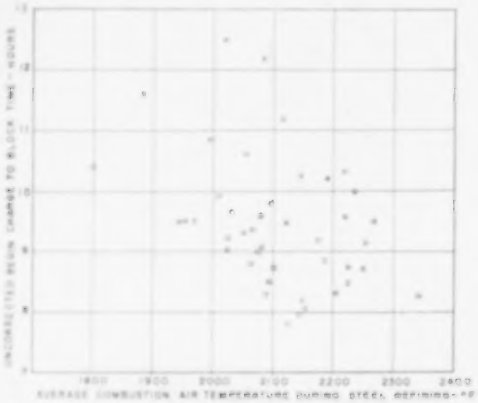

Fig. 5—Effect of combustion-air temperature on uncorrected begin charge-to-block time on standard silica furnaces.

cycle during the latter portion of a single heat. The average air temperature of this heat from melt to tap was 2185°F and the corrected heat time was 9 hr 07 min. Data of this nature were used to evaluate the effect of combustion-air temperature on production rate. These findings will be discussed in the next section.

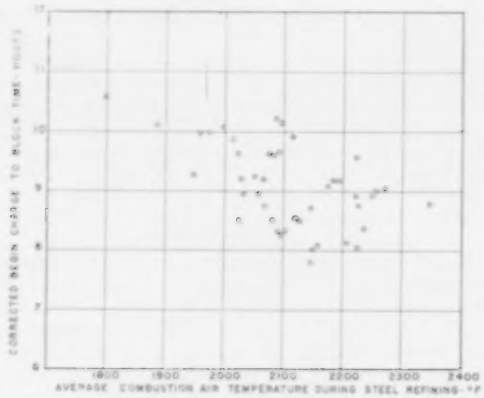

Fig. 6—Effect of combustion-air temperature on corrected begin charge-to-block time on standard silica furnaces.

Effect of Combustion-Air Temperature on Open-Hearth Production Rate: For each heat studied, the average combustion-air temperature from melt-to-tap or furnace block was obtained as described above. These data then were compared with the open-hearth heat time as measured in hours from begin charge-to-tap or block. Fig. 5 illustrates the correlation of combustion-air temperature and heat time for the open hearth shop Y silica furnaces. Each point represents one individual heat. It can be seen that there is a fair correlation between heat time and the combustion-air temperature. However, since this shop produces a variety of steel products ranging from 1.00 to 0.05 pct C, all of the heat-time data were corrected to a constant tap carbon and charging time by means of factors developed by the Industrial Engineering Dept. The heats were corrected to a 0.20 pct C content at tap and further corrections were applied if the charging time was over 1 hr. Fig. 6 illustrates the same data as Fig. 5 except that corrections have been made for tap carbon and charging time. It is readily apparent that there is considerably less scatter of the points when these corrections were applied, and a much stronger correlation exists between combustion-air temperature

Table II. Specifications of No. Y Open-Hearth Furnaces

	No. A	No. B	No. C	Standard Silica
Hearth dimensions at fireplate level:				
length, ft	38.0	38.0	44.0	38.0
width, ft	14.25	14.25	14.25	14.25
area, sq ft	542	542	627	542
Zone area* at furnace center line (above fireplate, elevation 32 ft 2 in.), sq ft	87.0	95.2	95.2	95.2
Uptake dimensions (each end):				
number of uptakes	2	2	1	2
uptake zone area, sq ft	43.2	43.2	39.8	49.2
zone area under burner arch, sq ft	188.0	188.0	—	156.7
Zone area under fantail arch, sq ft	133.7	133.7	72.0	72.0
Zone area at checker bridgewall, sq ft	84.0	62.2	62.2	62.2
Checker-chamber dimensions (each end):				
number of checker chambers	1	2	2	2
volume of checkers, cu ft	5550	4160	3927	3927
height of checkers, ft	10.0	8.5	8.0	8.0
Refractories:				
main roof	Basic	Silica	Silica	Silica
port slopes	Basic	Silica	Silica	Silica
end walls	Basic	Basic	Basic	Basic
fantails	Basic fireclay	Basic fireclay	Fireclay	Fireclay
checker roof	Fireclay	Fireclay	Fireclay	Fireclay
Reversing valve type	Blaw-Knox straight-line	Dybliet butterfly	Dybliet butterfly	Dybliet butterfly
Flame-enrichment available	Yes	No	Yes	No
Manual reversing controls	Yes	Yes	Yes	Yes
Forced-air fans	Yes	Yes	Yes	Yes

* Zone area: area of a section perpendicular to the direction of gas travel.

and the corrected heat time. In all future data in this report, the heat times plotted have been corrected in this manner.

In Figs. 7 and 8 are shown the correlation of air temperature and heat time for *A* (all-basic) furnace at open-hearth shop *Y* and for the silica furnaces at the open-hearth shop *X*. Fig. 9 illustrates the differences observed over the period of study for the various furnaces at the open-hearth shop *Y*. The line drawn for each furnace design is the average curve obtained from measurements on approximately 35 heats during the course of several furnace campaigns. The data for these furnaces have been plotted individually in order to demonstrate that an open-hearth furnace does tend to possess individualistic performance characteristics. In these cases, however, these furnaces did vary somewhat in design and operation.

The explanation offered for the major differences observed between the furnaces illustrated in Fig. 9 is as follows: Furnace *A* (all-basic) has an average of 1 hr shorter heat time than the shop silica furnaces largely because of the use of a 10,000,000 Btu per hr increased firing rate as compared to other shop furnaces. A higher firing rate necessitated a larger air-flow rate on furnace *A* which, in turn, resulted in somewhat lower air temperature but faster heat times. For a given fuel and air-flow rate, increased air temperatures resulted in shorter heat times.

In summary, it can be seen that, considering all the variables that affect open-hearth heat time, there exists a very strong correlation between heat time and average combustion-air temperature.

Effect of Furnace Age on Open-Hearth Air Temperature and Furnace Performance: It is known generally that furnace efficiency and production rates decline throughout the progress of furnace campaigns. This efficiency loss results from changes in the overall thermal efficiency of the regenerative system. Some factors contributing to the decline in heat efficiency are: 1—deposition of dirt and oxide in the regenerative system, 2—increased air infiltration, and 3—heat loss through the refractories resulting from refractory deterioration.

The degree of air infiltration at any given stage in a particular campaign is not consistent with age but varies with details of construction, the method of furnace operation early in the campaign, and refractory conditions at the various stages of the campaign. From the air-infiltration studies on furnaces at open-hearth shop *Y*, a general trend is evidenced in air-infiltration changes throughout a furnace campaign. On the first few heats subsequent to relining, the typical shop furnace with conventional uptake design has an air infiltration of the order of 25 pct. After mechanical sealing of the furnace ends and of the regenerative-system bulkheads during the first few heats and the natural sealing by fluxing of refractory hot faces, the air infiltration is decreased to approximately 15 to 20 pct after the accumulation of 30 to 60 heats. Measurements on heats throughout the rest of the campaign indicate that air infiltration gradually increases to approximately 20 to 25 pct near the end of the campaign. A sharp change in air infiltration and heat losses frequently occurs in the latter heats of a campaign when the refractories are in relatively poor condition. This type of change is noticeable particularly in the furnaces with sections of suspended-basic bricks.

The supposition that combustion-air temperature is a measure of many undeterminable factors present in normal open-hearth furnace operation is substantiated in Figs. 10 and 11. In these charts, both heat time, expressed as the corrected begin charge-to-block time, and average combustion-air temperature are plotted against the furnace age.

It is evident in these plots that heat time throughout a campaign parallels the changes in heat losses and air infiltration. Performance peaks in the campaigns are indicated by high combustion-air temperature and lowest begin charge-to-block times at

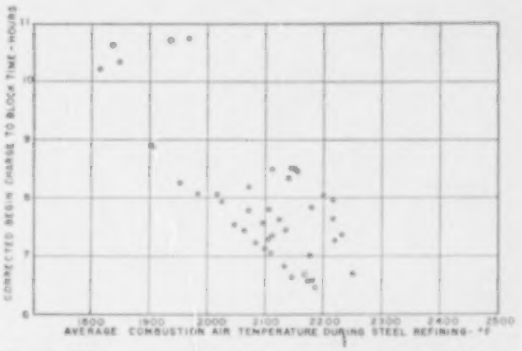

Fig. 7—Effect of combustion-air temperature on corrected begin charge-to-block time on No. *A* furnace.

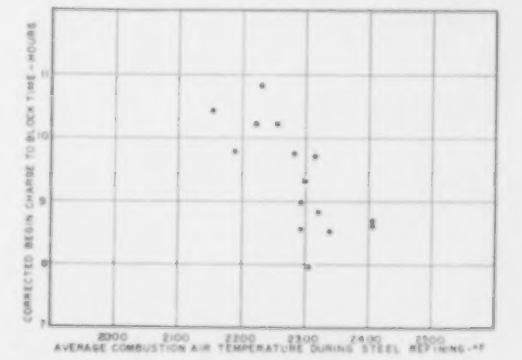

Fig. 8—Effect of combustion-air temperature on corrected begin charge-to-block time on 200 ton silica furnaces (No. *X* open-hearth shops).

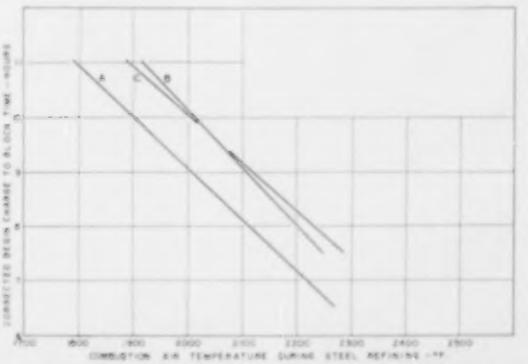

Fig. 9—Characteristic effect of combustion-air temperature during steel refining on corrected begin charge-to-block time for Nos. *A*, *C*, and shop silica furnaces. *A* is No. *A* all-basic; *B*, No. *C* extended hearth; and *C*, average of shop silica.

approximately 50 heats. After this peak, there is a general decrease in combustion-air temperature which is approximately 30°F for each additional 50 heats accumulated.

The accelerated deterioration of refractories and resultant decline in combustion-air temperature near the end of a campaign is most evident in the data for the eighth campaign of the *A* (all-basic) furnace shown in Fig. 11. This effect is the result of rapid changes in efficiency of the regenerative system, as structural changes occur in the suspended-basic roofs and ends near the close of their usefulness. This deterioration results in air infiltration and excessive heat losses.

These charts of the relationship between campaign life and combustion-air temperature indicate that air-temperature measurement is a reliable index to furnace performance. The fact that an exact relationship is not obtained can be explained somewhat by variations in furnace-operation technique. The effects of melting-chamber pressure and of fuel and air-flow rates on air temperature will be discussed later. Other factors inherent in the process could not be evaluated. However, in spite of all these variables, the air temperature-campaign life relationship is very satisfactory and, by interpolation of the data, it may be concluded that inefficiency results if a furnace campaign is extended to the ultimate life of the refractories.

Air-Temperature Survey in the Regenerative System: In the course of the present study, it became apparent that air-temperature surveys should be made in various sections of the regenerative system. To begin this phase of the investigation, a survey was made of the air-temperature variation in the uptake at sill level both in a lateral and longitudinal direction. Measurements were made on several heats on each of several furnaces. When the aspirating thermocouple was moved both laterally and longitudinally in the uptake zone, it was observed that the temperature of the air-flow stream in the uptake was substantially uniform. This observation is similar to those previously made by Marsh.[2] Following this observation, a standard procedure was adopted for locating the pyrometer hot junction near the center of the pit-side uptake well. To insure the reliability of air-temperature measurements on only one side of the regenerative system, measurements were made with the use of aspirating pyrometers on each end of the furnace. In this manner, the air temperatures of all the air cycles throughout the steel-refining period were obtained. These results showed that, in the last 2 hr of the heat, only a minor difference in air temperature (10°F) was observed from one end of the furnace to the other. These measurements were made, of course, when the checker systems were in reasonable thermal balance. From these results, it was concluded that the average air temperature obtained in the uptake on one end of the furnace during the steel-refining period yielded a temperature representative of the average for both ends, provided that uniform reversal times were maintained and that checker temperatures were similar. These latter requirements were adhered to for the majority of heats included in this study.

Very informative air-temperature surveys were made in the checker system. In the early part of the present study, a comparison of the measured air temperatures in the uptake with optical-pyrometer measurements taken at the checker bridgewall indicated that it was both necessary and desirable to measure air temperatures in the checker system with an aspirating thermocouple rather than with an optical pyrometer or standard thermocouple. It seemed obvious that, if it were necessary to use aspirating thermocouples to obtain accurate air-temperature measurements in the uptake zone, it would be equally necessary to use these same instruments to obtain accurate air temperatures in the checker chambers. Access to the checker-bridgewall zone was provided by the installation of refractory pull-blocks midway between the top of the checker bridgewall and the roof skew channel of the air-checker chamber. The pyrometer used for checker-temperature measurements was 9.5 ft long to facil-

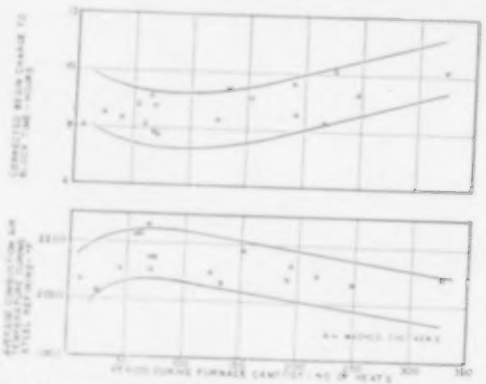

Fig. 10—Variations in combustion-air temperature and corrected begin charge-to-block time during a furnace campaign, No. *D* silica furnace.

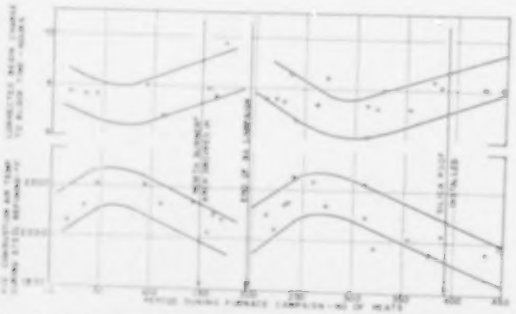

Fig. 11—Variations in combustion-air temperature and corrected begin charge-to-block time during the eighth all-basic campaign, No. *A* furnace.

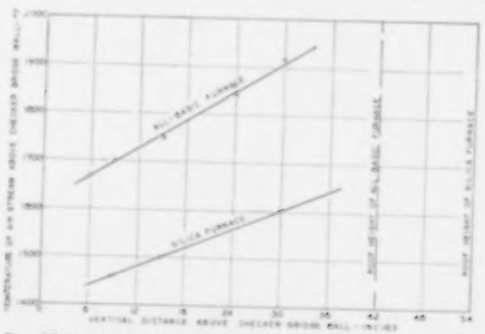

Fig. 12—Variation of air temperature measured at various heights above checker bridgewalls of all-basic and silica furnaces.

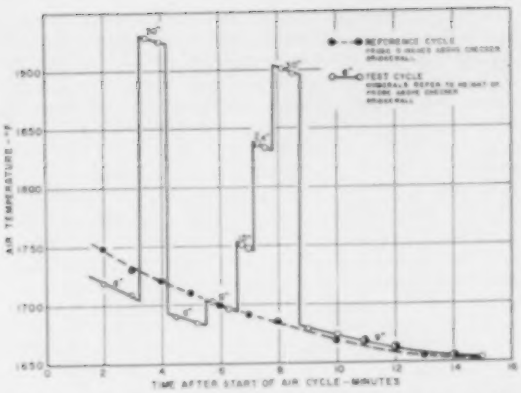

Fig. 13—Variation of air temperature measured at various heights above checker bridgewall of all-basic furnace.

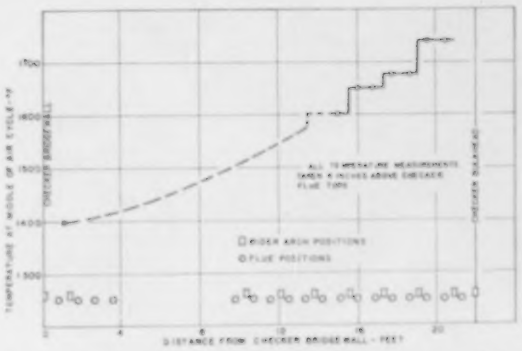

Fig. 14—Variation of air temperature in different zones of the air-checker chamber of silica furnace.

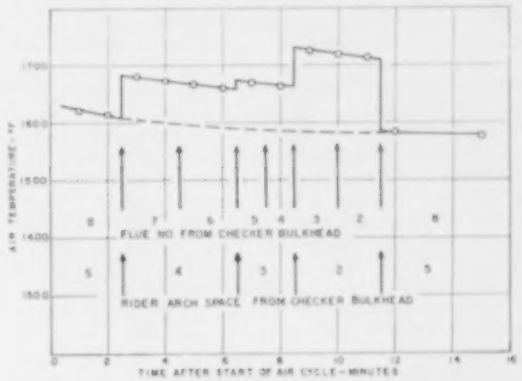

Fig. 15—Variation of air temperature with distance from the checker bulkhead showing the effect of rider arches on temperature distribution.

itate temperature measurement near the center of the air-checker chambers which were 13 ft wide. When the pyrometer was inserted, a seal around the thermocouple was made with asbestos packing.

A study was made of the air-temperature segregation in the checker-bridgewall zone. The pyrometer was moved in a vertical plane at different distances from the checker sidewall. In all cases, large increases in air temperature were observed as the pyrometer was moved vertically toward the checker roof. The most representative temperature-stratification data were accumulated on the all-basic furnace which had a flat suspended checker roof and presented a uniform cross-sectional area. The relationship obtained between air temperature and vertical distance above the checkers at the checker bridgewall is shown in Fig. 12 for both the all-basic furnace and the average silica furnace. These curves reveal an air-temperature variation of from 350° to 400°F from the tops of the checkers to the roof at the bridgewall. These data also demonstrate that at this location the air temperature in the all-basic furnace is approximately 200°F hotter than the air temperature in the silica furnaces. This difference is largely the result of the fact that the checker volume of *A* furnace is 41 pct greater than that of the silica furnaces. This increase was obtained by making the checkers deeper rather than longer. Further discussion of the differences observed in the regenerative systems of the all-basic furnace and the shop silica furnaces is given in the next section.

The method by which the data illustrated in Fig. 12 were obtained is shown in Fig. 13. Air temperatures were measured at the different distances above the checker bridgewall for one air cycle. Temperature levels obtained were compared with the temperatures taken at the distances involved on a preceding air cycle. Reproducibility was established by the fact that the two separate curves overlapped at the same time in the air cycle for the same distances above the checker bridgewall. Similar vertical thermal gradients were noted on all the furnaces studied. Only minor temperature stratification was observed at any given height above the checkers between the checker sidewalls and center of the checkers.

Following the survey conducted at the checker bridgewall, temperatures also were measured near the checker bulkheads to determine the longitudinal variation in air temperature above the checkers. These readings were taken through holes in the checker bulkhead near the center of the air chamber at 2 ft and at 4 in. above the checker. The longitudinal thermal segregation observed in this manner is demonstrated for the silica furnaces in Fig. 14. These data show that, for a given distance above the top of the checkers, the air coming out of the checkers at the bulkhead is approximately 400°F hotter than the air arising from the checkers at the checker bridgewall. Again, this difference was noted on all the furnaces studied.

In Fig. 15 is presented the method used to develop data for Fig. 14. One interesting observation from Figs. 14 and 15 is that the air coming out of the checkers above each flue arch was relatively constant within each arch but increased markedly as each arch was passed in the direction of the checker bulkhead. Observations of the position of the couple in the checker chamber were made during the traverse by means of a second hole in the bulkhead.

It was observed that the vertical thermal segregation at the checker bulkhead was very minor as compared to vertical segregation at the checker bridgewall. Fig. 16 schematically shows the temperature differences observed simultaneously in the various parts of the regenerative system studied for the *A* (all-basic) furnace. The explanation offered for this stratification of air temperatures above the checker flues is as follows: With the long shallow single-pass checker system, the majority of waste gases tend to move to the rear to the checker bulk-

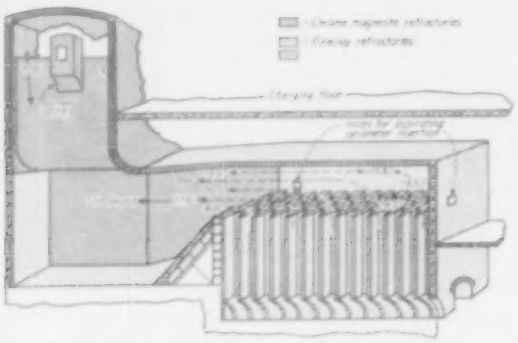

Fig. 16—Regenerative system of No. *A* all-basic furnace showing temperature variations encountered in the various zones.

head and down through this end of the checker system, thereby transferring most of their heat to the checkers at this position. On the other hand, the major portion of the incoming air, because of the checker design, tends to come forward to the checker bridgewall and up through the checkers at this point. Also, the air probably passes through the checkers in this position at a greater velocity. Further, since this part of the checker system has not received as much heat from waste gases, the air above the checkers at this point is not heated as much as the air which arises through the checkers at the bulkheads. The measurements presented in this report substantiate the line of reasoning offered before, which fact has been suspected by other writers on this subject. These data lead to the conclusion that, for open-hearth regenerative systems, shorter and deeper checkers are preferable to long and shallow checkers. Furthermore, any method by which greater turbulence can be imposed upon the incoming air stream and outgoing gas stream would appear to be desirable. In this respect, a two-pass design checker should perform more efficiently than a single-pass design having the same checker volume.

Effect of Furnace Design on Heat Transfer in the Uptake-Fantail Zone: It was noted in the present study that, although the all-basic furnace had a 41 pct larger checker volume and as a result had higher air temperatures above the checkers, the combustion-air temperature at sill level was almost the same as that observed for the shop silica furnaces. This observation led to a number of simultaneous observations of combustion-air temperatures at the checker bridgewall and in the uptake at sill level. Since the air temperature was not constant in the zone above the checker bridgewall, all air-temperature measurements in this phase of the work were made at a distance above the top of the checkers of 15 in. for silica furnaces and of 9 in. for the all-basic furnace; the horizontal displacement from the checker-sidewall hot face was 6 ft in all cases. These positions were selected as the most representative after a study of the data obtained in the previous section. Although there may be some disagreement as to whether the position selected is the most representative, it appeared to be adequate for the purpose of the present study which compared four furnaces of slightly different design.

In Table III are listed the average air temperatures measured at the sill and checker bridgewall for the individual furnaces studied. The line in this table listed "Relative heat recovery . . ." was derived as follows

$$\text{Pct Uptake-Fantail Regeneration} = \frac{T_s - T_{sw}}{T_s - T_a}$$

where T_s is the mean air temperature in uptake at sill level, T_{sw} is the mean air temperature in checker-bridgewall zone, and T_a is the ambient air temperature. It should be noted first that there is a large increase in combustion air temperature in the uptake-fantail zone of the furnace. Theoretical calculations based on the brick volume and temperatures in these zones revealed that the actual increases are theoretically possible. Further, the increases measured are very similar to those recently reported by Larsen.[1] It is important to remember that the uptake-fantail region of the furnace is as important a part of the regenerative system as the checkers themselves.

It was observed that a relatively constant percentage of increase in air temperature occurred in the uptake-fantail region for the individual furnaces studied regardless of the temperature obtained at the sill level. It was reasoned that this temperature increase should be related partly to the ratio of the refractory hot-face area in this furnace zone to the contained volume of this zone. That such a relationship did exist is shown in Fig. 17. The *A* (all-basic) furnace, although having a relatively small area in the uptake well, has an extremely large fantail zone, making the overall ratio of brick area-to-volume of the uptake-fantail small. The *B* furnace, which is also of suspended-basic construction below sill level, has a somewhat larger ratio than the *A* furnace and

Table III. Comparison of Heat Recovery, Refractory Hot-Face Area, and Contained Volume in the Uptake-Fantail Zones of Various Furnaces in the Open-Hearth Shop *Y*

	No. A	No. B	No. C	Standard Silica
Average sill-level combustion-air temperature (T_s), °F	2065	2180	1980	2140
Average air temperature above checker bridgewall (T_{sw}), °F	1730	1675	1395	1515
Air-temperature difference ($T_s - T_{sw}$), °F	335	505	585	625
Relative heat recovery in uptake-fantail zone, pct	16.7	23.3	30.5	30.2
Hot-face surface area of uptake-fantail zone, sq ft	1318	1456	1340	1307
Contained volume of uptake-fantail zone, cu ft	2513	2584	2121	1937
Surface-to-volume ratio of uptake-fantail zone, ft^{-1}	0.524	0.562	0.631	0.778

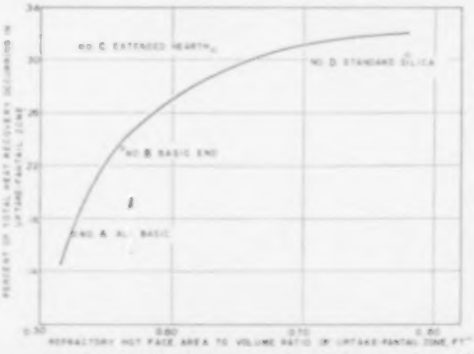

Fig. 17—Relationship between surface/volume ratio and heat-recovery efficiency in uptake-fantail zones of various open-hearth furnaces.

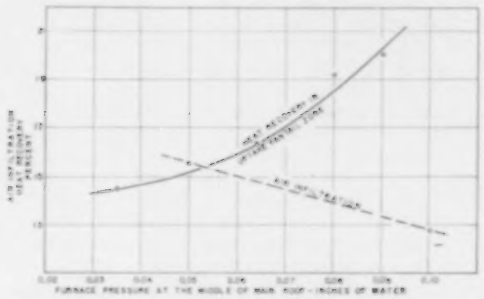

Fig. 18—Effect of furnace pressure on the percentage of heat recovery in the uptake-fantail zones and on the percentage of air infiltration, No. *A* furnace.

a smaller ratio than the shop silica furnaces, also because of the larger fantail region. It was observed that when the brick area-to-volume ratio in the uptake fantail region was high, the percentage of heat recovery in this zone increased, and tended to level off at a ratio above 0.60 for the furnaces studied in this investigation.

The importance of this finding is illustrated in the case of the all-basic furnace. Although the air infiltration for *A* furnace was generally low (15 pct) and the air temperature above the checkers was 200°F hotter by reason of a larger checker volume, the actual combustion-air temperature at sill level was the same as that for the silica furnaces, since less heat was delivered to the air in the uptake-fantail zone. The explanation offered for the effect of the surface area-to-volume ratio on heat recovery is as follows: Air cannot be heated by radiation but must be heated by convection, consequently the air must be brought into contact with the hot-brick surfaces to accomplish heat transfer. The narrower fantail-uptake regions of the silica furnaces not only allow more brick surface to be exposed in relation to volume but also, by increasing the velocity of the air, tend to increase turbulence and thereby increase heat recovery of combustion air. As in the previous section which indicated a need for improved design of checkers, the data illustrated in this section indicate a need for greater consideration of the optimum design of the fantail-slag pocket-uptake regions of open-hearth furnaces.

Effect of Furnace-Operating Practice on Air Temperature and on Open-Hearth Production: **Furnace Pressure:** One of the operating tools available to the open-hearth furnace shop melters and first helpers is the control of melting-chamber pressure. There is considerable disagreement among various operators as to how and when high and low furnace pressures should be used. In the present work, a study was made of the effect of furnace pressure on combustion-air temperature and on open-hearth production rate. The all-basic furnace was used for most of this study. This furnace was operated at various gage pressures from 0.02 to 0.15 in. of water during the refining period. The various heats studied were grouped according to furnace pressures of 0.02 to 0.05, 0.05 to 0.08, 0.08 to 0.09 and over 0.09 in. of water. For this grouping of furnace pressures, air-temperature readings were taken at the checker bridgewall and in the furnace uptake. In this manner the percentage of heat recovery in the uptake-fantail area was averaged for the 14 heats studied. The correlation of heat recovery and furnace pressure is presented in Fig. 18. Also on this same figure are plotted measurements of air infiltration taken on heats operated at very low and very high furnace pressures. The data in Fig. 18 show a marked increase in relative heat recovery with increased furnace-operating pressure. That this increase in heat recovery is associated with the decrease in air infiltration in the uptake-fantail zone of a furnace is shown by the infiltration data plotted. It is also possible that there are some changes in the velocity of the combustion air in this region when the furnace is operated at high pressures. It should be noted also that the air infiltration obtained on the all-basic furnace is of the order of 14 to 18 pct which is somewhat less than that normally observed on the shop silica furnaces. This may be associated with the flat checker-roof construction of the *A* furnace in place of the arch construction used on the shop silica furnaces. Fig. 18 reveals a reduction of approximately 18 pct in air infiltration on the *A* furnace by increasing furnace pressure from 0.05 to 0.10 in. of water. Similar studies made on silica furnaces in the open-hearth shop *Y*, when operating with various furnace pressures, indicate that an increase of pressure from 0.05 to 0.10 in. of water reduces air leakage 17 to 20 pct.

To illustrate the effect of furnace pressure on open-hearth production rates, two heats were made on *A* furnace when operating with a pressure of about 0.09 to 0.12 in. of water which corresponds to flame puffing from 4 to 5 doors. The heat times and air temperatures observed on these heats are compared with heat times and air temperatures of heats made at normal furnace pressure of 0.05 in. in Fig. 19. It can be seen that, with the same combustion-air temperature, shorter heat times were obtained with higher furnace pressures. Waste-gas analyses were obtained continuously during these two heats so that approximately 1 pct O and 0 pct combustibles were obtained throughout the working of the heats. It was observed that, to meet this waste-gas requirement with the increased furnace pressure, considerably more metered air (100,000 cu ft per hr) had to be drawn through the furnace for the same fuel-flow rate. This increased air-flow rate was an indication of the amount of air that leaked into the furnace through the doors and uptakes when the furnace was operated at normal pressures.

In summary, it can be stated that increased furnace pressure sometimes can effectively reduce air infiltration and increase open-hearth production

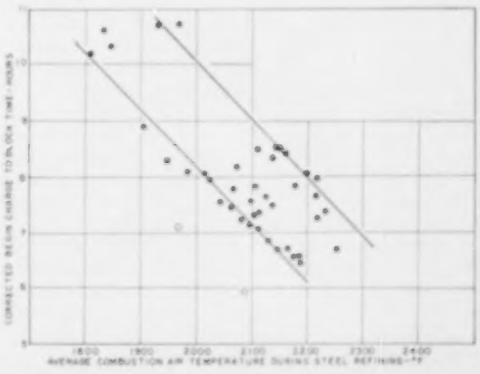

Fig. 19—Effect of combustion-air temperature on corrected begin charge-to-block time on No. *A* furnace. Closed circle is furnace pressure, 0.04 to 0.07 in. of water; open circle is furnace pressure above 0.09 in. of water.

Fig. 20—Effect of air flow rate on air temperature in the uptake at foreplate level and above the checker bridgewall. *A* is air temperature measured in the uptake at foreplate level, *B* is air temperature measured 9 in. above the center of the checker bridgewall.

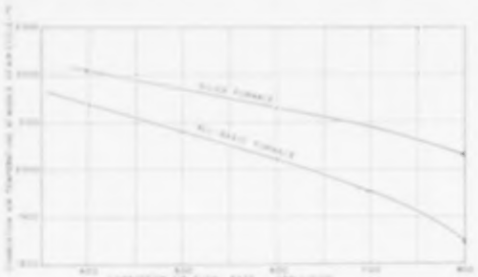

Fig. 21—Effect of air flow rate on combustion-air temperature at the middle of the air cycle.

rates. However, the use of extremely high pressures lowers refractory life quite markedly, particularly if insufficient air is drawn through the checkers to efficiently burn fuel within the melting chamber. The use of high pressure with the present furnace equipment therefore is limited by the refractory life, particularly of frontwalls and doors and by the ability of the drafting system to supply sufficient air for the high firing rates and bath-reaction rates.

Firing and Air-Flow Rates: Various firing rates were used on the furnaces studied in this report. It was noted in general that, for furnaces of the same size in the same shop, those operated at the higher firing rates tended to have somewhat lower average combustion-air temperatures and still shorter heat times. Since increased air flow must be used with higher firing rates, a study was made of the effect of air-flow rate on combustion-air temperatures. The normal air flow in this shop when operating with 60,000,000 Btu fuel per hr was 680,000 cu ft air per hr. In individual air cycles, the air-flow rate was varied for short-time intervals from 400,000 to 800,000 cu ft per hr. Fig. 20 illustrates the data obtained in this manner on *A* (all-basic) furnace both at the checker bridgewall and in the uptake. It can be seen that, upon decreasing the air-flow rate from 680,000 to 400,000 cu ft per hr, the air temperature increased approximately 200°F instantaneously. This effect was observed on numerous other occasions both on *A* furnace and the silica furnaces. A demonstration of the effect of air-flow rate on combustion-air temperature for the two types of furnaces is presented in Fig 21. These data were obtained in a manner similar to that shown in Fig. 20. It is understood, of course, that the magnitude of the effect of air-flow rate on combustion-air temperature will not be as great as that indicated in Fig. 21 if the furnaces were operated for long periods throughout the heat at a high and a low air-flow rate and the corresponding fuel rate.

Further examples of the effects of air and fuel-flow rate in the working of open-hearth heats is shown schematically in Fig. 22. It can be seen from this figure that there is a marked and instantaneous effect of air and fuel flow on the combustion-air temperature. The heat pattern followed by combustion-air temperature closely approximates the fuel/air ratio and the air-flow rate.

It was illustrated previously in Fig. 9 that, for a given combustion-air temperature, the all-basic furnace had shorter heat times than did the shop silica furnaces. This was attributed to the higher firing rate on the *A* furnace as compared to the shop silica furnaces. In the case of the *A* furnace, although a higher air-flow rate was maintained than for the shop silica furnaces, the combustion-air temperature was approximately the same as that of the shop silica furnaces, largely because of the increased checker volume of *A* furnace. The *E* (silica) furnace was operated recently at approximately the same firing rate as the *A* furnace. In this case, the combustion-air temperatures of *E* were generally somewhat lower than the shop silica furnaces and the *A* furnace. This lower air temperature was caused by the higher air-flow rate which was required for the higher fuel rate. Even so, for the same combustion-air temperature, shorter heat times were achieved by the use of the higher firing rates on the *E* furnace. That the firing rate and air-flow rate throughout the heat did appear to affect combustion-air temperature and heat time is illustrated in Fig. 23. In this case it can be seen that the data for both the *A* (all-basic) furnace and the *E* (silica) furnace tend to fall on the same curve of combustion-air temperature vs heat time when both were operated at 60,000,000 Btu per hr in the refining period. The data obtained on the *E* furnace appeared

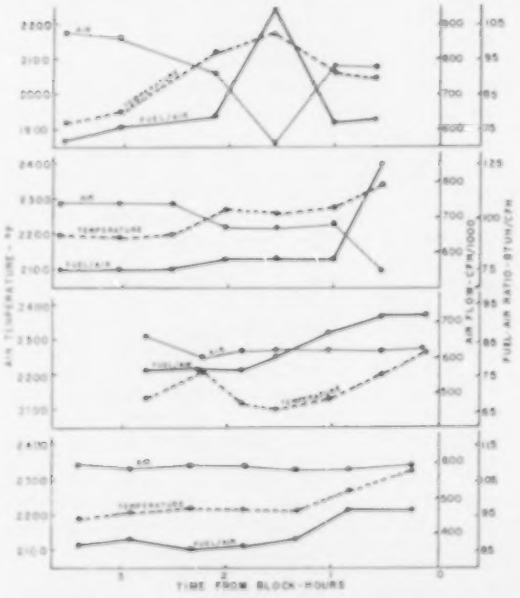

Fig. 22—Effect of air flow and fuel-air ratio on combustion-air temperature.

Table IV. Examples of Waste-Gas Analysis Measured in Uptakes throughout Open-Hearth Heats

Heat No.	Time	Period of Heat	Air Temperature, °F	Fuel Input, Million Btu per Hr	Air-flow Rate, Thousand Cu Ft per Hr	Pressure, H_2O	Waste Gas	
							O_2, Pct	Combustibles, Pct
A	9:30 am	Charging	1880	66	820	0.08	4.0	0.0
	9:50 am	Charging	1880	65	720	0.08	1.8	0.0
	10:20 am	Hot metal added	1860	66	830	0.09	1.1	0.8
	10:50 am	—	1930	66	810	0.09	1.0	0.5
	11:20 am	—	1940	66	810	0.10	0.3	1.5
	11:50 am	—	1965	66	810	0.11	0.5	0.5
	12:20 pm	Melt	1960	65	750	0.09	1.3	0.2
	1:50 pm	—	1950	65	790	0.10	0.5	0.5
	2:20 pm	—	2005	66	780	0.09	0.5	0.5
	2:50 pm	Tap	—	—	—	—	—	—
B	9:50 am	Charging	1830	67	790	0.08	0.2	0.4
	10:20 am	Charging	1850	67	820	0.07	0.5	0.2
	11:10 am	Hot metal added	2010	68	820	0.07	0.0	8.0
	11:40 am	—	2080	63	820	0.08	0.0	2.0
	12:10 pm	—	2040	63	820	0.08	0.0	1.0
	12:40 pm	—	2115	63	810	0.09	0.0	2.5
	1:10 pm	Melt	2070	63	750	0.08	0.5	0.0
	1:40 pm	—	2110	63	780	0.08	1.0	0.0
	1:50 pm	Tap	—	—	—	—	—	—
C	11:40 am	Charging	1970	57	780	0.04	0.5	0.5
	12:10 pm	Hot metal added	1910	53	770	0.06	1.0	0.4
	12:40 pm	—	1880	55	780	0.06	0.5	0.9
	1:10 pm	—	1930	55	780	0.06	0.4	0.5
	1:40 pm	—	1950	57	780	0.06	1.5	0.0
	2:30 pm	—	1980	59	780	0.06	1.5	0.0
	3:00 pm	—	1930	55	760	0.06	2.0	0.0
	3:20 pm	—	1870	55	780	0.06	2.0	0.0
	3:30 pm	Melt	—	—	—	—	—	—

to be an extension of the lower portion of the curve for *A* furnace (lower air temperature, longer heat times).

In summary, the data obtained for the furnaces studied at the open-hearth shop *Y* indicated that the use of higher firing rates generally resulted in somewhat lower combustion-air temperatures and still shorter heat times. However, the overall efficiency of operation with high firing rates must be evaluated.

Combustion Efficiency: It is agreed generally that an ideal waste-gas analysis for operating an open-hearth furnace consists of approximately 1 pct O and 0 pct combustibles. This composition of waste gases is used as an aim in determining the proper fuel/air ratio for each furnace at the open-hearth shop *Y*.

In the course of the present work, waste-gas analyses were measured throughout the working of a few open-hearth heats. One such heat is shown in Table IV. These data illustrate the general observation that considerable fuel arises from the bath during various periods of the heat and air must be made available to burn this fuel. Consequently, for efficient combustion, it is necessary to vary the fuel/air ratio throughout the working of an open-hearth heat. This observation regarding fuel from the bath has also been made by Larsen[4] and considerable discussion was given to the importance of having sufficient air to burn the bath fuel at all times. The necessity of obtaining efficient combustion was noted in the present study and some examples of the effects of furnace operation with excess fuel and excess air are given as follows:

In Fig. 24 are illustrated three specific examples of heats made within the same time period which typify furnace operation with normal fuel/air ratios as well as fuel/air ratios higher and lower than normal. The upper curves in Fig. 24 present the data for operation with a fuel/air ratio which was considered normal for this particular furnace at this particular time. The middle series of curves portray a similar heat with a lower than normal fuel/air ratio and the lower series of curves a higher than normal fuel/air ratio. The heat made with the highest fuel/air ratio (excess fuel) had a high combustion-air temperature and yet heat time was longer than that of the normal heat. The heat produced with the lowest fuel/air ratio (excess air) had the lowest combustion-air temperature and a slightly longer heat time than that of the normal heat.

These data illustrate only the period from melt-to-tap. A few heats were observed in which a constant fuel/air ratio was used for the period from hot metal-to-tap. In these cases, the combustion-air temperature increased in the period of hot metal-to-melt, since considerable combustibles were coming from the bath and being burned by the excess combustion air. After melt, when using the same fuel/air ratio, the air temperature tended to decrease as a result of more combustion air than required to burn both the fuel and bath combustibles.

Fig. 24 illustrates the effect of combustion efficiency on three specific heats. Some general trends regarding combustion efficiency were also noted in this work. For example, in Fig. 23 a distinction was made in the case of the *E* furnace for operation in two different time periods with quite different air-flow rates and but the same fuel-flow rate. In this case, it can be seen readily that the heats produced with lower than required fuel/air ratio (excess air)

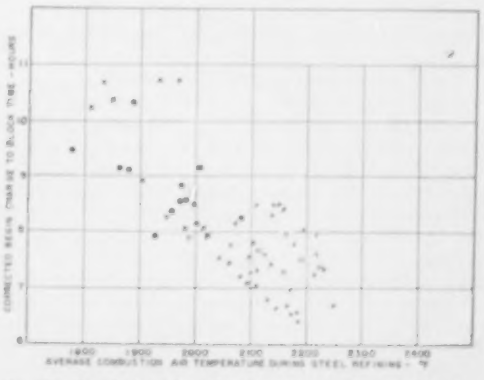

Fig. 23—Correlation of combustion-air temperature with corrected begin charge-to-block time for Nos. *A* and *E* furnaces. X represents No. *A*; closed circle, high air flow, No. *E*; and open circle, low air flow, No. *E*.

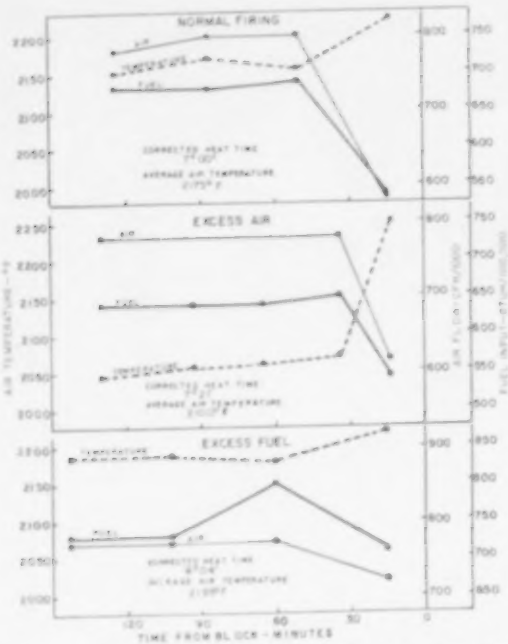

Fig. 24—Typical examples of combustion efficiency and its effect on air-temperature and production rates.

had lower air temperatures and longer heat times than the heats produced with the lower air-flow rate which was adequate for this furnace. As further evidence, *D* furnace purposely was operated in the period with a higher than recommended fuel/air ratio (excess fuel) and the average air temperatures of approximately 20 such heats were higher than normal; yet the corresponding heat times were either normal or longer than normal.

It appears from this study that one of the most important tools that could be made available for the first helper is a sturdy reliable continuous waste-gas analyzer. The proper use of this analyzer to adjust the fuel/air ratio throughout the working of an open-hearth heat would result in considerable savings in open-hearth heat time, since operation with either excess fuel or excess air is harmful. Of the two evils, excess air is somewhat preferable, since the open-hearth process is an oxidizing one and, in this respect, somewhat like the bessemer operation.

Summary and Conclusions

Effect of Combustion-Air Temperature on Open-Hearth Heat Time: An inverse relationship was observed between combustion-air temperature and open-hearth heat time. For the heats studied, an increase of 100°F in combustion-air temperature reduced heat time from 40 to 60 min for a given firing practice.

Effect of Furnace Age on Combustion-Air Temperature and Furnace Performance: Combustion-air temperature reached a maximum and open-hearth heat time a minimum after approximately 50 heats following a complete furnace reline. For each additional 50 heats produced following the peak performance, combustion-air temperature decreased approximately 30°F and open-hearth heat time increased proportionately. The combustion-air temperature decrease near the end of the campaign on the all-basic furnace was greater than the decrease found for the silica furnaces.

Air-Temperature Survey in the Regenerative System: Aspirating-pyrometer measurements of combustion-air temperatures at various positions throughout the regenerative system revealed that marked thermal gradients exist in the air above the checkers. At the checker bridgewall, a progressive increase of air temperature of approximately 300°F was observed from the top of the checkers to the checker roof. Further, at a given level above the top of the checkers, air temperatures near the checker bulkhead were approximately 400°F hotter than air temperatures at the checker bridgewall. Steplike increases in air temperatures were observed as each flue arch was traversed in the direction of the checker bulkhead. In many cases, relatively poor correlations were observed between checker-thermocouple temperatures and actual preheat temperature and between optical-pyrometer readings and preheat-air temperatures in the checker system.

Effect of Furnace Design on Heat Transfer in the Uptake-Fantail Zone: A series of simultaneous aspirating-pyrometer readings was made at the checker bridgewall and the sill level in the uptake. Marked air-temperature increases occurred in the uptake-fantail region. A relationship between the uptake-fantail brick surface to contained volume ratio and, the percentage of heat recovery in this zone was found to exist, i.e., increasing uptake-fantail surface to volume ratios caused an increased heat recovery in the uptake-fantail zone.

Effect of Furnace-Operating Practice on Combustion-Air Temperature and Heat Time: 1—Furnace pressure: Data were obtained which illustrated that increased furnace pressure reduced air infiltration, increased heat recovery in the uptake-fantail region, and reduced open-hearth heat time. The correlation of combustion-air temperature and open-hearth heat time was affected by furnace pressure.

2—Firing rate: For the furnaces studied in this report, the use of higher firing rates generally resulted in somewhat lower combustion-air temperatures and still shorter open-hearth heat times.

3—Combustion efficiency: A summary of all the data obtained in regard to the fuel/air ratio indicated the following: Heats produced on a given furnace with a higher fuel/air ratio than required had higher than normal combustion-air temperature and somewhat longer than normal open-hearth heat times. Heats produced with a lower fuel/air ratio than required had somewhat lower than normal combustion-air temperatures and had normal or somewhat longer open-hearth heat times. On individual heats, a close correlation was observed between the fuel/air ratio and the combustion-air temperature.

Acknowledgment

The authors would like to express their appreciation for the assistance and the fine cooperation of the Open Hearth Div., Fuel and Power Div., and the Instrument Laboratory of the South Chicago Works of the United States Steel Corp.

References

[1] J. S. Marsh: Significance of Air Temperature in Open Hearth Operations. Yearbook American Iron & Steel Institute (1951) pp. 185-200.

[2] B. M. Larsen: Regenerator Efficiency and Air Preheat in the Open Hearth. Trans. AIME (1954) **200**, p. 129; Journal of Metals (February 1954).

Electrolytic Production of Hydrometallurgical Reagents for Processing Manganese Ores

by J. Bruce Clemmer, Carl Rampacek, and P. E. Churchward

A cyclic method for processing manganese ores using sodium sulphate as the basic reagent is described. Sodium sulphate is electrolyzed in a diaphragm cell to give an anolyte-containing sulphuric acid and a catholyte-containing caustic soda, a part of which is carbonated in a cyclic manner to form soda ash. The reduced ore is leached with the anolyte to dissolve the manganese and the impurities are precipitated by addition of catholyte. Manganese in the pregnant solution is precipitated as synthetic rhodochrosite with a carbonated catholyte, and sodium sulphate is regenerated. Calcining the manganese carbonate gives a high grade product and the carbon dioxide is returned to the carbonation step. The results of laboratory tests using cells equipped with synthetic-fiber diaphragms and permselective membranes, which permit transfer of anions or cations during electrolysis, are described.

A METHOD which has been considered for processing manganese ores under emergency conditions to recover a product suitable for smelting to ferromanganese involves reductive roasting of the ore for leaching with dilute sulphuric acid followed by precipitation of the manganese from the purified pregnant solution with sodium carbonate. Although the process is operable and involves no novel or untried steps, it is noncyclic in regard to reagents. Research seemed warranted to determine if a cyclic process could be developed by electrolyzing the sodium sulphate formed during precipitation of the manganese with soda ash to regenerate sulphuric acid and sodium hydroxide. Reduced ore would be leached with acid anolyte to dissolve the manganese. The iron, alumina, and other dissolved impurities would be precipitated with the caustic catholyte, and the manganese in the purified pregnant solution would be precipitated as artificial rhodochrosite with carbonated catholyte to regenerate simultaneously sodium sulphate for electrolysis. Waste boiler gas and CO_2 from calcining the manganese precipitate would be recycled for carbonation of the caustic catholyte.

There is a surprising lack of data in the technical literature on diaphragm electrolysis of sodium sulphate. One of the more comprehensive papers, by Atwell and Fuwa,[1] describes the problem involved in electrolyzing byproduct sodium sulphate from the viscose process with particular regard to the design and operation of asbestos diaphragm cells. Frisk[2] also investigated electrolysis of sodium sulphate from viscose-spinning baths to recover caustic soda and sulphuric acid. The objective in these investigations was to produce, by electrolysis and evaporation, a concentrated caustic-soda solution and a sulphuric-acid solution low in sodium sulphate. Because of these requirements, the process was not too attractive despite a favorable yield of caustic and acid with a reasonable power consumption. Because strong acid and base are not required for processing manganese ores and nonelectrolyzed sodium sulphate is not objectionable in either reagent, the present problem was somewhat simpler than that of these investigators.

The purpose of this report is to summarize briefly the results of laboratory electrolysis of commercial sodium sulphate in diaphragm cells of different types and the application of the acid and caustic for processing manganese ores in a cyclic manner.

Electrolysis in Permeable Diaphragm Cells

The principal problem in electrolyzing sodium sulphate in a permeable diaphragm cell is to prevent mixing of the acid and base formed in the anode and cathode compartments. It is not enough to separate the anolyte and catholyte by a single diaphragm. A three-compartment cell in which the sodium-sulphate solution is fed to the center compartment and flows through the permeable diaphragms to the anode and cathode compartments is more efficient electrically. Diaphragms should be porous enough to allow flow of solution to outer compartments but tight enough to prevent gross mixing of the anolyte and catholyte. In addition to being resistant to acid and alkali, the diaphragms should offer minimum resistance to the flow of current. It is also important that the electrolyte contain a high concentration of sodium sulphate to furnish an abundance of sodium and sulphate ions and thereby decrease the current carried by hydrogen and hydroxyl ions. A practical limitation of sodium-sulphate concentration is imposed by the decreased solubility of sodium sulphate with decreasing temperature. At 20°C, a concentration of 200 g per liter sodium sulphate can be maintained. Little is gained in conductivity by using a concentration greater than 200 g per liter.

The small-scale continuous electrolysis tests were made in a 12x12 in. open-top bakelite cell equipped

J. B. CLEMMER, Member AIME, is Chief, Metallurgist Div., Region IV, United States Bureau of Mines, Salt Lake City; C. RAMPACEK, Member AIME, is Supervising Metallurgist, United States Bureau of Mines, Tucson, Ariz.; and P. E. CHURCHWARD is Chemist, Salt Lake Experiment Station, United States Bureau of Mines, Salt Lake City.

Discussion on this paper, TP 3867BD, may be sent, 2 copies, to AIME by Mar. 1, 1955. Manuscript, Feb. 11, 1954. New York Meeting, February 1954.

Papers by authors on the Bureau of Mines Staff are not subject to copyright.

An abstract of this paper will appear in MINING ENGINEERING.

Table I. Electrolysis of Na_2SO_4 in a Three-Compartment Cell with Permeable Diaphragms

Diaphragm Material	Feed Rate, Ml per Min	Cell Voltage	Temperature, °C	Current Density,* Amp per Sq Ft	G per Liter		Lb per Kw-Hr		Current Efficiency, Pct
					NaOH	H_2SO_4	NaOH	H_2SO_4	
Vinyon 101 N	15	4.65	65	70	73.0	93.6	0.57	0.69	81.3
Vinyon 101 N	30	4.82	60	70	45.2	54.2	0.63	0.75	92.6
Vinyon 101 N	30	5.70	70	125	68.5	85.6	0.48	0.59	84.6
Vinyon 101 N	30	6.40†	70	125	64.3	84.5	0.43	0.52	85.3
Vinyon 101 N	30	6.85	70	175	89.7	119.6	0.37	0.45	77.9
Vinyon 101 N	50	5.90	70	125	46.2	58.5	0.49	0.60	89.9
Nylon 220	30	6.30	40	125	64.2	90.0	0.44	0.53	85.0
Nylon 220	30	5.90	70	125	80.7	85.9	0.45	0.56	83.2
Dynel 162	30	5.75	40	125	71.1	94.8	0.49	0.61	88.6

* Current density based on immersed area of diaphragm.
† Two-inch electrode spacing; other tests were made with one-inch spacing.

with a perforated sheet lead anode and a perforated stainless-steel cathode using thin asbestos diaphragms to form the third or feed compartment. Gross area of each electrode and diaphragm was 72 sq in. Sodium-sulphate solution was fed to the bottom of the center compartment at a uniform rate from a constant-head siphon feeder. The anolyte and catholyte were removed from the bottom of the compartments through an adjustable overflow tube. A hydrostatic head of solution was maintained in the feed compartment to overcome resistance of the diaphragms to solution flow. Liquid-level gages allowed observation of the solution level in each compartment. By adjusting the overflow tubes, the quantity of anolyte and catholyte could be varied to control the relative strengths of the acid and base.

The tests made, using long-fiber asbestos diaphragms, confirmed findings of Atwell and Fuwa[1] and showed that electrolysis of a 20 pct sodium-sulphate solution at 50°C would give an anolyte containing 5 to 7 pct sulphuric acid and a catholyte containing 4 to 6 pct sodium hydroxide, with a current efficiency of about 80 pct. The diaphragms, however, were fragile and developed pinholes after short use. Subsequent tests were made using synthetic-fiber diaphragms made of such material as Vinyon, nylon, Dynel, or Saran. In addition to being more durable, these diaphragms were more permeable than asbestos and permitted a higher solution-feed rate but were tight enough to prevent mixing of the anolyte and catholyte.

The results of a few pertinent tests showing the influence of feed rate, cell temperature, and current density on yield and concentration of acid and base are summarized in Table I. Data also are included from similar tests made using different diaphragm materials. The recorded tests were from 6 to 8 hr duration, of which 3 hr was required for the cell to reach equilibrium.

These tests were made on 200 g per liter sodium-sulphate solutions prepared from technical-grade material substantially free of sodium chloride. Except for an accelerated corrosion of the anode, electrolysis of a commercial salt cake gave similar results. Sodium chloride in the salt cake could be adequately removed by washing the crystals with a saturated solution of the sodium sulphate. The magnesia content of the feed material also is critical, since it precipitates in the feed compartment during the electrolysis and plugs the diaphragm. The technical-grade sodium sulphate used in these tests contained less than 0.01 pct MgO, whereas pregnant leach solutions in cyclic tests generally contained about 0.3 g per liter MgO derived from the ore. Final treatment of the regenerated sodium-sulphate solutions with 0.5 to 1 g per liter of sodium hydroxide to give a pH of 11 precipitates the magnesia and alleviates the difficulty.

These and other tests show that conditions for electrolysis of sodium sulphate are not too critical. As might be expected, the concentration of acid and base varies with both feed rate and current density. The highest current efficiency is obtained when the weakest reagents are produced. For a particular feed rate, increasing the current density gave a stronger acid and base but decreases the yield both by reducing the current efficiency and increasing the voltage. Under good operating conditions, about 0.5 lb of caustic soda and 0.6 lb of acid can be made per kw-hr at an average current efficiency of 85 pct when operating the cell at current density as high as 125 amp per sq ft. On this basis, a cell containing 17 2x3 ft anodes and 18 cathodes of similar size should produce a ton of acid and 1625 lb of caustic per day.

In all tests, the feed compartment became alkaline as the run progressed. The caustic concentration at cell equilibrium varied from 2 to 10 g per liter depending upon the solution feed rate; the higher the feed rate, the lower was the caustic concentration. It is apparent that more hydroxyl than hydrogen ions were transferring into the feed compartment. This may be attributed to the high concentration of hydroxyl ion in the catholyte, whereas the hydrogen-ion concentration in the anolyte was relatively low because of the buffering action of the sodium sulphate and possible formation of HSO_4 ions.

The harmful effect of chlorides on anode corrosion has been mentioned. Exploratory tests showed that lead anodes containing 1 pct Ag were more resistant to corrosion than lead or Pb-Te anodes. Corrosion

Table II. Electrolysis of Na_2SO_4 in Three-Compartment Cell with Permselective Diaphragms

Feed Rate, Ml per Min		Cell Voltage	Temperature, °C	Current Density,* Amp per Sq Ft	G per Liter		Lb per Kw-Hr		Current Efficiency, Pct
Anode	Center				NaOH	H_2SO_4	NaOH	H_2SO_4	
15	15	9.9	50	125	68.0	94.0	0.25	0.31	76
10	10	6.6	50	75	61.8	76.8	0.41	0.49	81
8	8	5.1	50	50	52.8	74.6	0.54	0.64	82
5	5	5.0	50	50	70.8	89.2	0.47	0.59	72
4	6	5.0	50	50	58.8	99.4	0.48	0.62	76
3.5	2	4.1	50	25	56.6	92.7	0.58	0.70	71
10	10	5.2†	52	50	57.2	65.8	0.53	0.69	85
10	20	6.8†	52	100	63.4	111.0	0.39	0.46	78
20	20	7.0†	53	100	66.8	63.9	0.39	0.49	84

* Current density based on immersed area of diaphragm.
† 2.25 in. electrode spacing; other tests were made with one-inch spacing.

of the Pb-Ag anode over a period of 11,000 amp-hr of intermittent operation was about 4.5 mg Pb per amp-hr. Manganese dioxide and graphite anodes failed in service. Black iron cathodes appeared to be as suitable as stainless steel.

The laboratory electrolysis results were sufficiently encouraging to warrant larger-scale continuous tests at the Boulder City station. Several cell designs were tried. The best results were obtained with a multiple-electrode press-type cell with closed compartments provided with solution and gas outlets. Although the work was recessed temporarily owing to the urgency of more pressing problems, the cell was operated for a number of 10 day campaigns and gave results almost as good as the laboratory tests. This work will be described in a later report.

Electrolysis in Permselective Diaphragm Cells

Ion-permeable membranes were used as cell diaphragms for sodium-sulphate electrolysis. These membranes are ion-exchange resins in sheet form and have the property of being selectively permeable to ions of one sign, while offering greater resistance to the passage of the ions of opposite sign. These membranes are less permselective with respect to hydrogen and hydroxyl than to other ions. The function and properties of Amberplex anion and cation-permeable membranes, which were used as diaphragms, are described in a trade publication of the Rohm and Haas Co. Use of these membranes obviates solution flow through the diaphragm, thereby eliminating plugging, and also permits feeding the compartments at a desired rate so as to control the concentration of acid and base.

Electrolysis tests were made in the three-compartment cell using either anion or cation diaphragms to separate the center anode compartment from the outer cathode compartments. The compartments were fed individually and the cell was equipped with perforated Pb-Ag and stainless-steel electrodes. This cell design gave a low current efficiency; the anion diaphragm allowed free transfer of hydroxyl ions from the catholyte to the anolyte, and the cation diaphragm allowed transfer of hydrogen ions from the anolyte to the catholyte. In order to obtain high current efficiency and produce acid and caustic of the desired concentration, the design was changed to separate the center compartment from the anode with an Amberplex anion-permeable diaphragm and from the cathode by an Amerplex cation-permeable diaphragm. As in the tests with fabric diaphragms, the center compartment became alkaline; therefore, it was connected in series to feed the cathode compartment. The center and anode compartments were fed separately at a desired rate using a 200 g per liter solution of sodium sulphate. The results of typical tests with this cell are summarized in Table II. Included also are results from several tests made in an 18x10 in. rectangular cell of similar design using an electrode spacing of 2.25 in.

These tests demonstrated that acceptable acid and caustic could be made in the permselective diaphragm cell with a moderately good current efficiency. Best results were obtained by operating the cell at a current density of 50 amp per sq ft at the 2.25 in. electrode spacing; 0.53 lb of caustic soda and 0.69 lb of sulphuric acid were produced per kw-hr at a current efficiency of 85 pct. The yield of acid and base at high current densities was somewhat less than with permeable fabric diaphragms because of the increased voltage required to overcome ohmic resistance of the membranes. It seems likely that better results could be obtained by using a thinner membrane of lower resistance even though some permselectivity would be sacrificed.

Exploratory tests were made in a two-compartment permselective diaphragm cell for direct precipitation in the cathode compartment of manganese from anolyte-leach solutions while electrolyzing sodium sulphate in the anode compartment to form acid for the leaching step. An anion-permeable membrane was used to separate the compartments and allow the transfer of sulphate ions from the catholyte to the anolyte to form acid. Since the hydroxyl-ion concentration in the cathode compartment was low because of precipitation of manganese hydroxide, a single diaphragm sufficed. In continuous operation, the sodium sulphate remaining in the catholyte would be returned to the anode compartment for acid making after filtration to remove the manganese-hydroxide precipitate. A current efficiency of 92 pct was obtained when making an anolyte containing 50 g per liter of sulphuric acid. The permeable membranes appear to have considerable merit for this application. This phase of the electrolysis study is not yet completed and will be described in a later paper.

Cyclic Processing of Manganese Ore

A series of four cyclic leaching and precipitation tests were made on reduced Artillery Peak manganese ore starting with anolyte and catholyte from electrolyzing technical-grade sodium sulphate. The data from these tests are summarized in Table III and the flowsheet in Fig. 1.

The reduced ore was ground to 65 mesh and pulped with enough anolyte to give an initial slurry containing about 50 pct solids for agitation leaching. Additional anolyte was added over a period of 60 min to give a final pH of 2.0; slow addition minimized dissolution of silica and alumina. The average

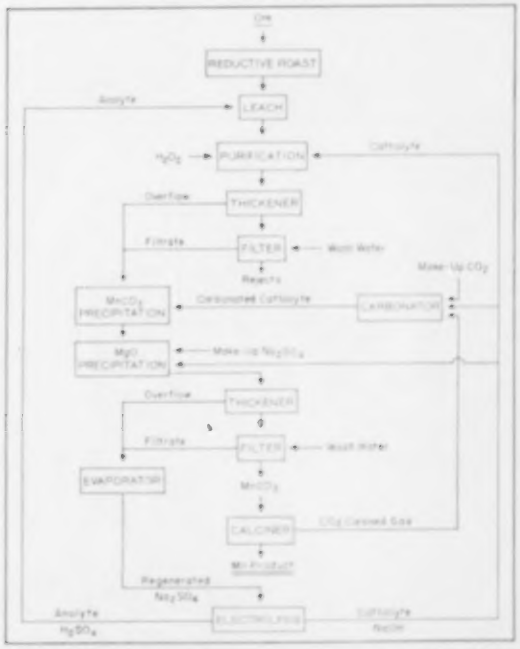

Fig. 1—Flowsheet for processing manganese ores by the sodium-sulphate process.

extraction in the four cycles was 88.8 pct of the total manganese or 95.7 pct of the acid-soluble manganese in the reduced ore.

The leached slurry was treated with hydrogen peroxide to oxidize the iron for precipitation at a pH of 5.5 with caustic catholyte. Most of the dissolved silica and alumina precipitated with the ferric hydroxide. The partly neutralized slurry then was thickened for filtration and two-stage displacement washing, using 1.5 lb of water per lb of dry solids.

The thickener overflow, filtrate, and wash liquors were combined for precipitation of the manganese with carbonated catholyte to obtain a product easy to handle. The catholyte was carbonated to a pH of 10 with bottle gas in a flotation cell. The carbonated catholyte was added over a period of 30 min to precipitate the manganese at a pH of 7.8. Natural catholyte then was added to raise the pH to 11 to precipitate the dissolved magnesia in the manganese product and give a regenerated sodium sulphate suitable for electrolysis.

The carbonated precipitate was thickened to about 36 pct solids for filtration and displacement washing with 2 lb of water per pound of dry product. The manganese carbonate, after drying at 110°C, assayed 47.8 pct Mn, 0.54 pct S, 0.37 pct MgO, and less than 0.01 pct P. Calcining at 850°C gave a product that assayed 64.5 pct Mn, 0.73 pct S, 0.5 pct MgO, and less than 0.01 pct P. The overall recovery was 92.6 pct of the acid-soluble manganese in the reduced ore.

The regenerated sodium-sulphate solution was evaporated to about 200 g per liter of sodium sulphate for return to electrolysis. Approximately 7.7 lb of water had to be evaporated per pound of manganese recovered. No difficulty was experienced in electrolyzing the regenerated sodium sulphate. The concentrations of acid and caustic, current efficiencies, and power requirements in the four cycles were nearly the same as for electrolyzing technical-grade sodium sulphate. About 0.2 lb of makeup sodium sulphate was required per pound of manganese recovered. There was no apparent buildup of impurities in the cyclic tests. Corrosion of the anode was about 6.6 lb per ton of recovered manganese. Had the cyclic tests been continued, however, anode corrosion might have increased because of chlorides from the ore or from failure of the protective oxide coating on the anode.

The average power consumed for making acid and caustic in the cyclic tests was 3.9 kw-hr per lb of recovered manganese.

Table III. Cyclic Processing of Reduced Artillery Peak Ore

	Total	Acid-soluble
Roasting		
Ore roasted 4 min at 800°C with natural gas-reduced ore assay, pct Mn	15.33	14.25
Leaching		
Total weight of ore leached, g	11,500	
Average extraction, pct of total Mn	88.8	
Average extraction, pct of acid-soluble Mn	95.7	
Acid used (43,320 ml analyte containing 83.5 g per liter H_2SO_4), g	3,534	
Weight of manganese leached, g	1,568	
H_2SO_4 per lb Mn leached, lb	2.25	
Weight of Mn recovered, g	1,517	
H_2SO_4 per lb Mn recovered, lb	2.33	
Purification of Leach Liquor		
H_2O_2 used, g	42.3	
H_2O_2 per lb Mn recovered, lb	0.028	
NaOH used (4,526 ml catholyte, 68.9 g NaOH per liter), g	203	
NaOH per lb Mn recovered, lb	0.20	

Pregnant Liquor Assay

	G per Liter						
	Mn	SiO_2	Al_2O_3	Fe_2O_3	MgO	H_2SO_4	pH
Before purification	37.8	3.29	1.47	2.69	0.3	3.2	2.0
After purification	34.8	0.09	0.29	0.20	0.8	—	5.5

Precipitation		
Carbonated catholyte used, equivalent to NaOH, g	2,185	
NaOH per lb Mn recovered, lb	1.44	
Final pH Establishment		
Catholyte equivalent to NaOH, g	235	
NaOH per lb Mn recovered, lb	0.17	

MnCO₃ Product

	Assay, Pct						
	Mn	SiO_2	Al_2O_3	S	CaO	MgO	P
Dried at 110°C	47.8	0.28	0.02	0.54	1.25	0.37	<0.01
Ignited at 850°C	64.5	0.33	0.03	0.73	1.70	0.5	<0.01

Recovery of acid-soluble Mn in ore, pct	92.6

Regenerated Na_2SO_4

	Analysis, G per Liter						
	Mn	SiO_2	R_2O_3	MgO	Cl	S	Specific Gravity
First cycle	0.008	0.010	0.030	Trace	0.016	44.65	1.162
Fourth cycle	0.006	0.015	0.015	Trace	0.025	44.50	1.165

Reagent and Power Requirements per Lb Mn Recovered

Reagents made by electrolysis:	
NaOH, lb	1.92
H_2SO_4, lb	2.33
Power required (total), kw-hr	3.9
Other Reagents:	
H_2O_2, lb	0.028
Na_2SO_4 (makeup), lb	0.2
CO_2 (makeup), lb	Not determined

Thickening, Filtering, and Washing

	Area, Sq Ft per Ton Dry Solids per Day	Lb per Lb of Dry Solids	Pct Solids: Feed	Pct Solids: Underflow
Residue:				
Thickening (No flocculant)	10.9		18.3	40.8
Filtration and washing	1.25		40.8	65
Wash water		1.5		
Precipitate:				
Thickening (No flocculant)	13.3		3.7	35.5
Filtration and washing	0.75		35	54
Wash water		2.0		

The small-scale continuous electrolysis tests showed that about 0.5 lb caustic soda and 0.6 lb of sulphuric acid could be made per kilowatt-hour in a three-compartment permeable diaphragm cell. Anode corrosion was not severe and no difficulty was experienced from plugging of the diaphragms, provided magnesia was first removed.

The cyclic tests showed that the anolyte and the catholyte could be used for leaching and precipitation of manganese from reduced Artillery Peak ore. No difficulty was encountered in the handling steps. It is apparent, however, that the process would be costly, particularly in regard to equipment. It does not seem likely that the cost would be less than for that of a plant for electrolytic manganese. The power consumed in making the reagents for cyclic processing of manganese ores was 3.9 kw-hr per lb Mn recovered as a manganese-carbonate product. The power is nearly the same as for electrolytic manganese and the end product is less valuable. On the other hand, solution purity is less critical, cell operation is easier to control, and the reagent cost is less in sodium-sulphate electrolysis.

Summary and Conclusions

References

[1] H. V. Atwell and Tyler Fuwa: The Electrolytic Production of Acid and Alkali from Sodium Sulfate Solutions. *Industrial and Engineering Chemistry* (1923) **15**, pp. 617-620.

[2] P. W. Frisk: Electrolyzing Sodium Sulfate Waste from Spinning-Bath Recovery in Viscose Process. *Rayon Textile Monthly* (1948), **29**, No. 2, pp. 51-53.

Equilibrium between Titanium in Liquid Iron And Titanium Oxides

by R. L. Hadley and G. Derge

The amounts of oxygen in liquid iron-titanium alloys up to 50 pct Ti were measured and the oxide phases in equilibrium with these alloys were determined by using TiO_2 crucibles. A minimum of about 0.003 pct O occurs at less than 1 pct Ti. The various liquid and solid oxide phases can be arranged on a ternary isotherm.

THREE characteristics of titanium contribute to the interesting aspects of its reaction with oxygen in liquid iron: 1—It forms a number of stable oxides. 2—All oxides have large negative free energies of formation. 3—The pure metal exhibits high solubility for oxygen.

In addition, the use of titanium as a stabilizing and strengthening element in alloys suggests a need for investigation of its reactions in amounts greater than those normally required for deoxidation. These higher compositions are also of interest because they occur during the addition of ferroalloys and produce deoxidation products before dilution is achieved.

Titanium Deoxidation in the Literature

While the use of titanium as an alloying element and deoxidizer has been common for several decades, the first detailed study of its deoxidizing characteristics was carried out by Wentrup and Hieber[1] in 1939. These authors determined the extent of deoxidation possible with titanium and identified, by microscopic examination, the products formed. They found that titanium in excess of 0.2 pct did not reduce the oxygen content of iron below 0.004 pct at 1600°C. They identified the spinel $FeO \cdot TiO_2$ at low titanium concentrations and Ti_2O_3 in melts containing more than 0.2 pct Ti.

A portion of the area surveyed by Wentrup and Hieber has been investigated recently by Evans and Sloman[2] using X-ray diffraction for inclusion identification. They concurred in general with the findings of Wentrup and Hieber, but reported the existence of Ti_3O_5 as a deoxidation product in the range near 0.1 pct Ti.

Comstock, Urban, and Cohen[3] discussed the deoxidation of iron with titanium, correlating the data of Wentrup and Hieber with free-energy data for the titanium oxides. Scatter at high titanium values was considered attributable either to the formation of an oxide exhibiting high solubility in liquid iron or to the entrainment of solid oxide particles leading to high apparent solubility.

Chipman[4] has calculated the deoxidation curves for titanium based on free-energy data for titanium oxides. These calculations (Fig. 1) and those of Comstock, Urban, and Cohen involve assumptions as to the activity coefficients of oxygen and titanium in liquid iron, since such data have not been determined.

Investigation of the deoxidizing characteristics of chromium[5] and vanadium[6] have shown that these elements decrease the activity coefficient of oxygen in liquid iron, leading to a tendency toward relatively high oxygen values and experimental scatter in highly alloyed melts.

Experimental

This investigation involved two major objectives: 1—determination of the composition of the oxide phases in equilibrium with liquid Fe-Ti alloys, and 2—establishing the pattern of oxygen solubility in liquid Fe-Ti alloys at titanium concentrations in excess of that required for attainment of minimum oxygen content.

Raw Materials

Ingot iron was used having the following composition: 0.02 pct C, 0.017 pct Mn, 0.01 pct Si, 0.02 pct S, 0.006 pct P, and 0.03 pct O. The titanium used

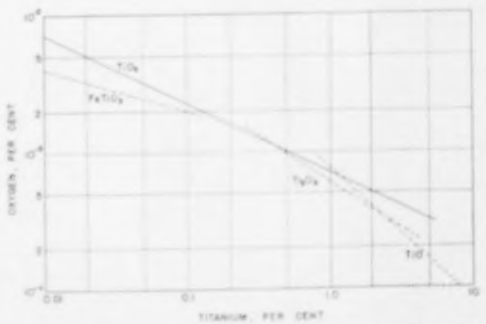

Fig. 1—Percentage of oxygen in metal vs titanium in metal, as calculated by Chipman[4] for various deoxidation products.

R. L. HADLEY, formerly Graduate Fellow, Dept. of Metallurgical Engineering, Carnegie Institute of Technology, is now Engineering Manager, Metallurgy and Ceramics, Major Appliance Div. Laboratory, General Electric Co., Louisville, and G. DERGE, Member AIME, is Jones & Laughlin Professor of Metallurgical Engineering, Carnegie Institute of Technology, Pittsburgh.

Discussion on this paper, TP 3827C, may be sent, 2 copies, to AIME by Apr. 1, 1955. Manuscript, Apr. 9, 1954. Chicago Meeting, February 1955.

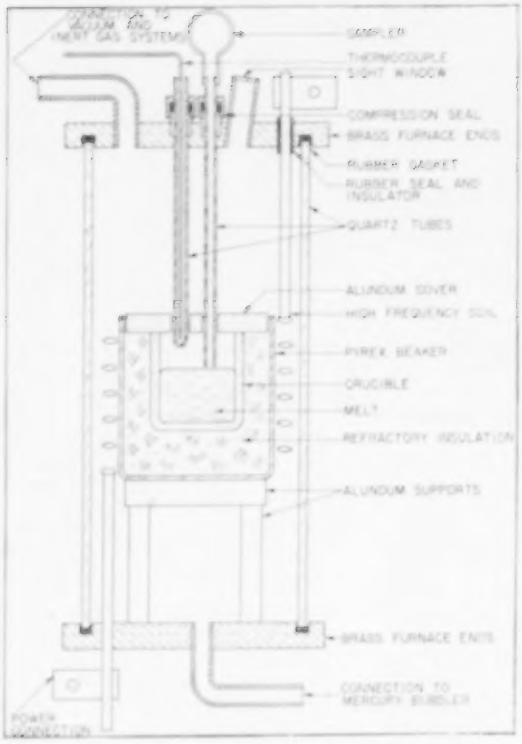

Fig. 2—Diagram of inert-atmosphere melting furnace.

was pressed sponge with the following analysis: 0.13 pct C, 0.05 pct Si, 0.1 pct O, and 0.05 pct Fe.

The high degree of reactivity of titanium at liquid iron temperatures required maintenance of close control of the melting atmosphere and container. To avoid contamination, TiO_2 was selected as a crucible material for the bulk of the melting experiments. While it was sometimes possible to melt successfully in unsupported crucibles, the best results were obtained using a crucible assembly consisting of a pyrex beaker containing the crucible in a bed of granular MgO or TiO_2. The granular material was fired at a temperature of 1200°C and kept in a desiccator until used.

The furnace assembly is shown in Fig. 2. The melting procedure included the following: 1—loading of crucible with approximately 200 g of iron and titanium, the latter being surrounded by iron; 2—evacuation of the furnace to about 0.02 mm Hg; 3—introduction of helium; 4—melting, using a 20 kw spark-gap high-frequency converter; 5—immersion of thermocouple and temperature adjustments; 6—holding at temperature for 20 to 30 min; 7—sampling if required; and, 8—cooling in helium stream.

Solidification ordinarily took place within 1 min. In some heats, samples were sucked into quartz tubes for comparison of rapidly chilled metal with the more slowly cooled ingot.

Evaluation

When cool, the crucible and ingot were removed from the furnace and samples prepared for analysis.

Cubes were cut from solid portions of the ingot for analysis of oxygen content by vacuum fusion. Drillings were taken for titanium analyses. The reaction zone between ingot and crucible was separated for determination of iron and titanium contents. X-ray diffraction patterns also were obtained on this material, which tended to form easily separable layers representing different stages of oxidation between TiO and the oxide phase in equilibrium with the metal.

Metal samples were analyzed for titanium content and oxide phases for titanium and, in some cases, for iron. In a few cases, carbon analyses were carried out on the ingots.

The procedure for determination of oxygen and nitrogen involved the use of conventional vacuum-fusion apparatus, an iron bath, and addition of tin to the bath between samples.[7] Most consistent results were obtained when the analysis was started with the bath at 1550° to 1600°C and the temperature increased gradually to 1800°C as gas evolution proceeded.

The pertinent data from the experimental heats are shown in Table I.

Table I. Experimental Heats

Heat Number	Metal			Oxide		Crucible	Temperature, °C
	Pct Ti	Pct O	Pct N	Pct Ti	Pct Fe		
71	0.002	0.024	0.0004	50.3	17.53	TiO_2	1580
75	0.003	0.027	0.0018	50.2	18.37	TiO_2	1565
76	0.014	0.027	0.0016	51.6	15.82	TiO_2	1585
92	0.016	0.0078	0.0041	59.1	2.66	TiO_2	1615
68	0.03	0.019	0.0059	47.9	—	TiO_2	1600
72	0.04	0.027	0.0006	50.8	14.62	TiO_2	1575
90	0.07	0.0223	—	32.4	10.57	TiO_2	1665
89	0.071	0.014	0.0037	57.3	4.76	TiO_2	1570
93	0.10	0.0019	0.0026	62.3	1.26	TiO_2	1590
81	0.11	0.0021	—	61.0	—	TiO_2	1550
74	0.16	0.009	0.0010	62.5	—	TiO_2	1600
80	0.22	0.0021	—	61.8	—	TiO_2	1590
94	0.25	0.0011	0.0022	55.7	1.12	TiO_2	1545
91	0.27	0.0016	0.0016	58.2	2.24	TiO_2	1595
97	0.36	0.0022	0.0010	61.8	0.91	TiO_2	1600
67	0.37	0.0049	0.0014	53.7	—	TiO_2	1605
96	0.46	0.0027	0.0008	60.7	0.98	TiO_2	1615
82	0.83	0.015	—	63.0	—	TiO_2	1540
66	0.87	0.0043	0.0012	52.0	—	TiO_2	1605
99	0.88	0.0023	0.0040	63.8	0.56	TiO_2	1650
98	1.12	0.003	0.0017	63.7	0.56	TiO_2	1610
65	1.37	0.0085	0.0035	—	—	TiO_2	1620
73	2.88	0.0045	0.0009	0.3	—	TiO_2	1575
83	4.06	0.0084	—	59.9	—	TiO_2	1585
107	7.84	0.015	0.0008	—	—	TiO_2	1585
69	8.61	0.015	0.0016	56.9	—	TiO_2	1590
70	12.93	0.026	0.0005	62.8	—	TiO_2	1650
121	29.76	0.362	—	—	—	TiO_2	1590
122 I	0.18	0.0064	0.0008	—	—	TiO_2	—
II	0.04	0.016	0.0012	57.8	3.92	TiO_2	1605
124 I	0.54	0.0039	0.0007	—	—	—	—
II	0.13	0.0032	0.0007	—	—	—	—
III	0.016	0.021	0.0014	59.6	4.48	TiO_2	1650
125 I	0.065	0.0033	0.0007	—	—	—	—
II	0.007	0.025	0.0012	56.9	5.51	TiO_2	1600
101	0.14	0.0020	0.0051			MgO	1595
86	0.15	0.022	0.0054			MgO	1670
108	0.20	0.0033	0.0008			MgO	1600
85	0.84	0.013	0.0065			MgO	1510
84	0.89	0.012	0.0062			MgO	1510
87	1.80	0.0064	0.0027			MgO	1630
88	9.0	0.029	0.0026			MgO	1640
100	15.96	0.0892	0.0061			MgO	1620
64	1.30	0.0028	0.0009			Al_2O_3	1590
118	5.00	0.0078	0.0013			Al_2O_3	1665
119	3.35	0.0156	0.0009			Al_2O_3	1660
111	0.16	0.0032	0.0012			ZrO_2	1600
90	0.37	0.0012	0.0016			ZrO_2	1590
113	2.40	0.0053	0.0012			ZrO_2	1580
110	16.08	0.073	0.0020			ZrO_2	1585

Discussion of Results

The results of this study consist of the following: 1—melting observations, 2—analyses and micrographs of alloys and deoxidation products, and 3—graphical representation of relationships in the Fe-Ti-O system.

Melting Observations: The products of the experimental heats consisted of an alloy ingot with a slag or oxide coating continuous with a layered reaction zone extending into the crucible. The ingot assumed the shape of the crucible at low and high titanium contents but was partially supported by

the oxide film on its surface when the titanium content was between 0.1 and 5 pct.

The standard melting procedure, in which individual elements were charged without preliminary melting of a titanium master alloy, was selected after comparison of the two practices. No difference was apparent in either ingot or crucible reaction zone. Both practices require a holding period to establish equilibrium with the TiO_2 crucible, since the first liquid to melt, being high in titanium, could have reduced the crucible surface to a lower oxide than would be stable at equilibrium.

In general, reaction with the crucible appeared to be rapid and no heats held over 10 min exhibited localized color variations which would distinguish inhomogeneities in the oxide layer. Alloys which were sufficiently low in titanium to be in equilibrium with a liquid oxide phase attacked the crucible very rapidly. Consistent oxygen values were not obtained at low titanium contents although it was anticipated that the system would equilibrate with the TiO_2 crucible in equilibrium with a TiO_x-saturated liquid slag.

Where solid oxide phases were stable, the surface scale retained the upper part of the melt, giving an irregular lapped appearance. The thinness of the film was believed to be responsible for the absence of the effect at high titanium content.

Despite precautions to avoid oxidation by refractory components and atmosphere, loss of titanium to the amount of a few tenths of one percent occurred on most of the heats. The oxygen content of the charge exceeded the amount soluble in the liquid alloy in all melts containing less than 15 pct Ti. Losses in titanium could be expected because of reaction with the excess oxygen and, in the case of concentrations of titanium too high to be in equilibrium with TiO_x, reaction with the crucible.

Temperature measurement was somewhat better than temperature control. For purposes of evaluation, heats equilibrated at temperatures between 1580° and 1620°C are regarded as being at 1600°C. A calibrated Pt—Pt-10 pct Rh thermocouple gave temperature values within 3° but drifting occurred

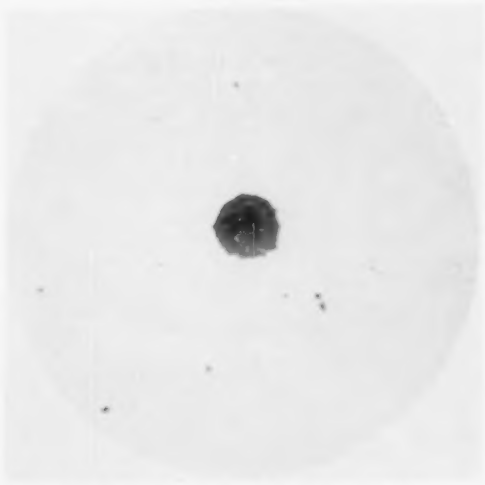

Fig. 3—Heat 91, 0.27 pct Ti. Unetched. X250.

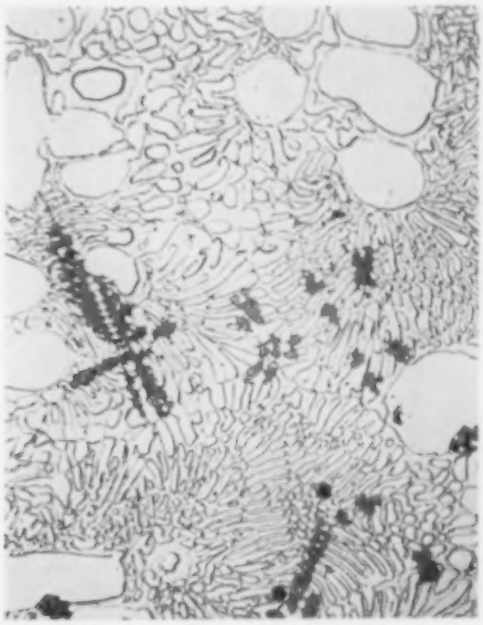

Fig. 5—Heat 110, 16.08 pct Ti. Nital etch. X500. Area reduced approximately 15 pct for reproduction.

Fig. 4—Heat 83, 4.06 pct Ti. Unetched. X250. Area reduced approximately 25 pct for reproduction.

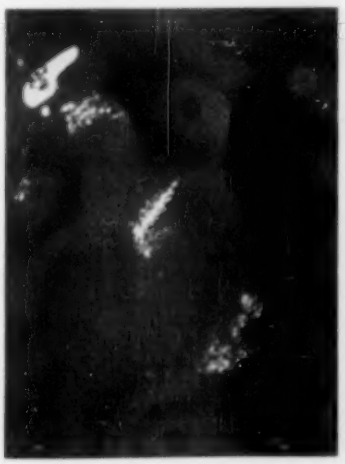

Fig. 6—(Inclusions) heat 121, 29.76 pct Ti. X100. Area reduced approximately 20 pct for reproduction.

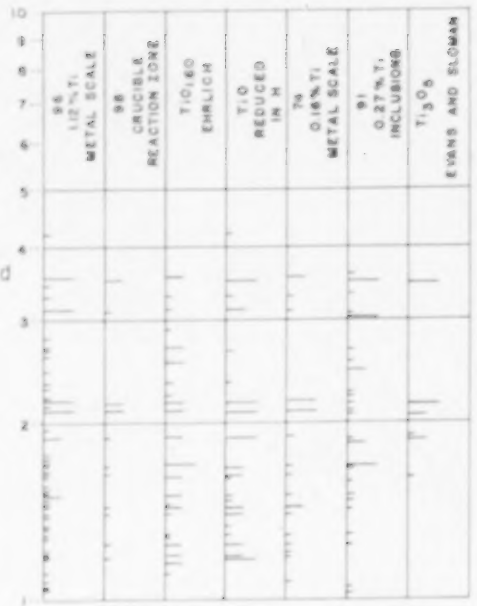

Fig. 7—X-ray diffractions patterns: TiO range.

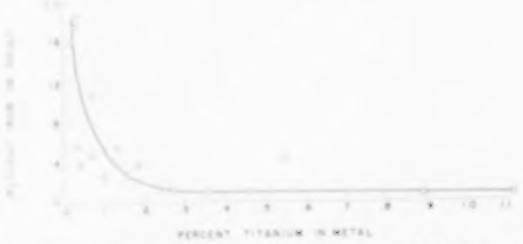

Fig. 8—Percentage of iron in oxide vs percentage of titanium in metal.

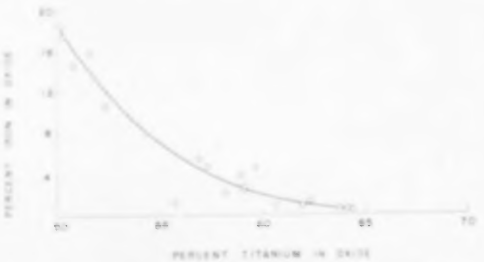

Fig. 9—Percentage of iron in oxide vs percentage of titanium in oxide.

during the holding period, causing some scatter in temperatures.

Analyses and Micrographs of Alloys and Deoxidation Products: Nonmetallic inclusions found in the alloys fall into three general groups: Two-phase gray-black inclusions. These were round at lowest titanium contents, becoming irregular in outline with increasing titanium. These are evidently identical with those reported by Wentrup and Hieber[1] and by Evans and Sloman[2] in the range below 1 pct Ti. An example is shown in Fig. 3. Gray-bronze rods and plates appearing as an eutectic were found in alloys containing 1.5 to 5 pct Ti. This type is

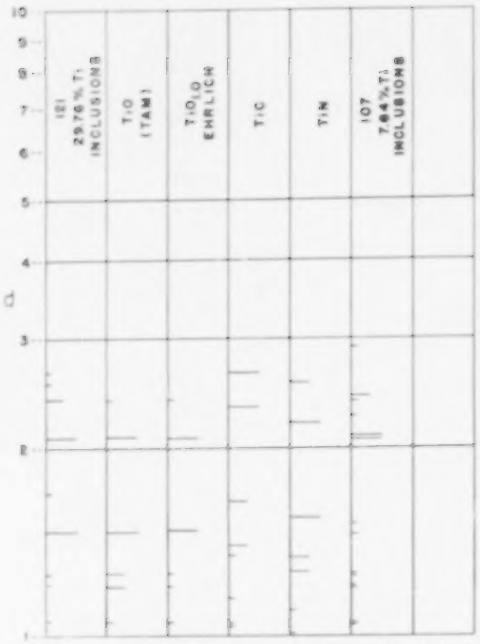

Fig. 10—X-ray diffraction patterns: reduced TiO_2 range.

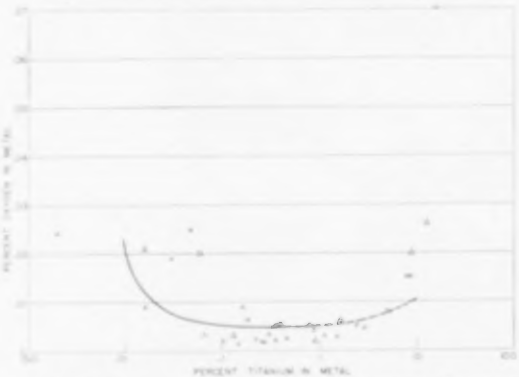

Fig. 11—Percentage of oxygen in metal vs percentage of titanium in metal at 1600° and 1650°C. Circle represents 1600°C; triangle, 1650°C; and solid line, data of Wentrup and Hieber (1600°C).[1]

shown in Fig. 4. Gold dendritic inclusions appeared when titanium content exceeded 7 pct, Fig. 5.

Chemical analyses of ingots for titanium revealed relatively large amounts of residue insoluble in the 1:1 hydrochloric-acid solution used in dissolving samples. In an effort to determine the nature of this "insoluble titanium," some residues were re-examined metallographically and samples were prepared for X-ray diffraction. Fig. 6 shows the extracted residue in the case of an alloy containing 29.76 pct Ti. This appears to be the yellow dendritic-inclusion type observed metallographically in high titanium alloys. X-ray diffraction patterns for this material and for the residue from a 7.84 pct Ti alloy are tabulated in Fig. 7. Patterns obtained for TiO, TiC, and TiN are shown for comparison.

At titanium contents below 2 pct, the oxide layer in contact with the metal exhibited sufficient thickness to permit both chemical and X-ray analyses. The substantial solution of iron in this layer is

shown as a function of the titanium content of the alloy in Fig. 8. The relation between iron and titanium contents of the oxide layer is shown in Fig. 9.

Ehrlich[4] has shown that X-ray diffraction patterns exhibit substantial variation within ranges of composition over which the various titanium oxides are stable. Presence of iron oxide, as shown in Fig. 9, further complicates identification of the oxides present. A tabulation of "d" values characteristic of oxide phases in contact with the ingot is shown in Fig. 10, together with some data available from the literature. Reduced TiO_2 was obtained by selecting the inner layer of a TiO_2 bar which had been partially reduced in dry hydrogen to yield three layers, the outer two corresponding to TiO and Ti_2O_3. This sample resembles the pattern attributed to Ti_4O_7 by Evans and Sloman.[3]

No patterns close to the compounds $FeO \cdot TiO_2$ and $FeO \cdot Ti_2O_3$ were observed. No analyzed oxides contained more than 18 pct Fe. $FeO \cdot TiO_2$ contains 36.8 pct Fe, an indication that the composition in equilibrium with the liquid alloy is well removed from the stoichiometric compound. Evans and Sloman[3] report the presence of $FeO \cdot TiO_2$ in the case of one low titanium ingot in their study of inclusions.

The relation between oxygen and titanium in liquid iron is shown in Figs. 11 and 12. The data at 1600° and 1650°C are not distinguishable. Inconsistent results at 1550°C led to the conclusion that experimental conditions did not permit attainment of equilibrium and separation of deoxidation products. There was no measurable difference in the Ti-O relationship in alloys melted in TiO_2, MgO, Al_2O_3, and ZrO_2 crucibles.

In an effort to study the point at which a visible shift from solid to liquid oxide occurred, sampling experiments were run. Samples were sucked into quartz tubes during step-wise removal of titanium from the melt by oxidation. A liquid oxide phase was found to appear when a rapid increase in oxygen solubility occurred.

The increase in oxygen solubility at titanium contents in excess of approximately 5 pct is reflected in Fig. 11. In order to establish the existence of increased solubility as opposed to oxide entrainment, a series of alloys were arc-melted in a water-cooled copper crucible in argon. These alloys are described in Table II.

Low oxygen iron and titanium were used, and in two instances (heat Nos. 130 and 135), oxygen was added as increments of TiO in order to determine an approximate solubility limit. While the temperature distribution was not investigated, the solubility at 25 pct Ti was found to be of the order of 0.03 pct O, in rough agreement with Fig. 11. The 46 pct Ti alloy (FeTi) dissolved 1.60 pct O before a second phase appeared on the surface.

The solubility of nitrogen did not appear to show a minimum in the range studied although a less detailed study was made. The total nitrogen analyses obtained are shown in Fig. 13. No controlled additions of nitrogen were made at high titanium con-

Fig. 12—Percentage of oxygen in metal vs percentage of titanium in metal at titanium content above 5 pct at 1600° and 1650°C.

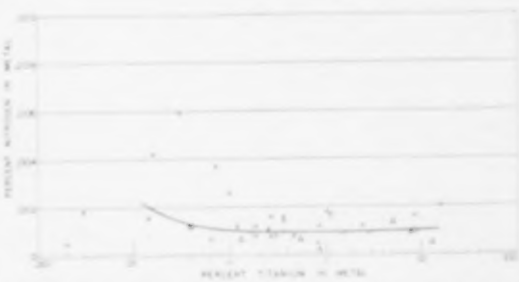

Fig. 13—Percentage of total nitrogen in metal vs percentage of titanium in metal at 1600° and 1650°C.

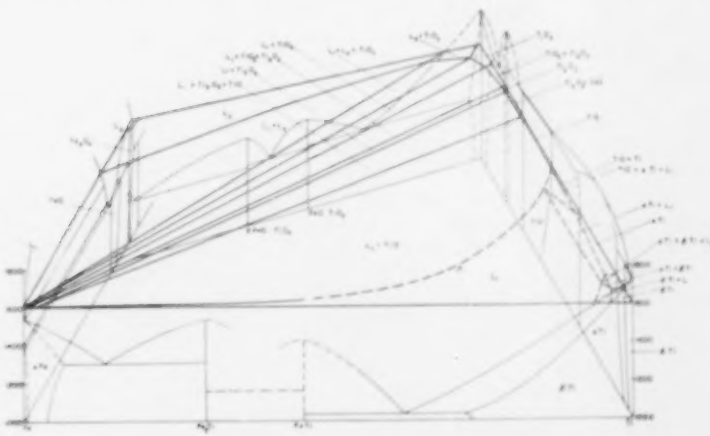

Fig. 14—1600°C isotherm in the system Fe-Ti-O, condensed phases.

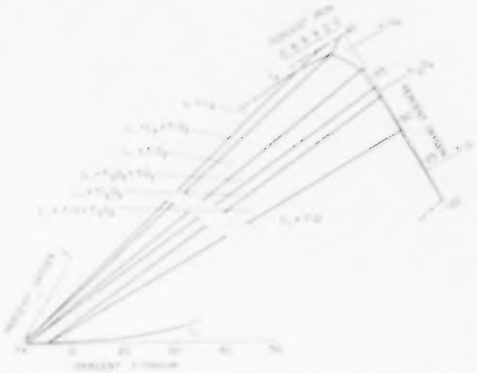

Fig. 15—Composition of phases in equilibrium at 1600°C in the system Fe-Ti-O.

tents nor was the analytical technique verified as to recovery of nitrogen.

On the basis of binary diagrams available for the systems Fe-Ti,[3,4,5] Fe-O,[6] FeO-TiO,[7] and Ti-O,[8-10] an approximate isotherm for the Fe-Ti-O system at 1600°C has been constructed, Fig. 14. A more detailed drawing of the area of this investigation is shown in Fig. 15. In view of the incomplete evidence for the existence of Ti_2O, and variation in X-ray data as a function of iron content of the oxide, only TiO_2, Ti_2O_3, and TiO are shown.

Liquid Structure and the Position of the Oxygen-Solubility Minimum: It is interesting to consider possible reasons for the existence of the oxygen solubility minimum at a low percentage of titanium. A rationalization is possible, based on the high free energy of solution which has been estimated for titanium in iron,[2] the high free energy of formation of titanium oxide, and information on the structure of liquid metals.

Sauerwald[11] has compiled available data on the coordination numbers characteristic of liquid metals. For cubic and hexagonal metals, each atom has, on the average, 11 nearest neighbors. The high heat of solution anticipated for titanium in iron would be expected to lead to a configuration in dilute solutions in which titanium atoms would be surrounded by iron. The deoxidation curve is not far from that calculated (see Fig. 1) from oxide free-energy considerations in this range.

However, the high oxygen solubility exhibited by liquid titanium requires the observed trend toward high oxygen solubility with increasing amounts of titanium in iron. Although it cannot be calculated from thermodynamic data, this trend would be expected to appear as the titanium approached a concentration such that insufficient iron atoms were present, on the average, to fill the coordination shell of the titanium atoms. This would occur at an atom ratio of 11 Fe to 1 Ti or approximately 5 wt pct Ti. The qualitative picture appears to be in good agreement with observation.

Table II. Arc-Melted Alloys

Heat	Ti, Pct	Appearance
131	0	Heavy purple scale, gold film
132	5	Heavy purple scale, gold film
133	6	Purple-gold scale
134	7	Purple-gold scale
126	8	Gold flecks
127	10	Few gold flecks, blue film
128	15	Few gold flecks
129	20	Shiny
130	25	Shiny
135	46	Shiny

Conclusions

1—The solubility of oxygen in iron at 1600°C decreases to a minimum of 0.002 to 0.004 wt pct in the presence of 0.1 to 1.0 pct Ti.

2—Increase in titanium content beyond 5.0 pct leads to rapidly increasing solubility for oxygen.

3—The Fe-Ti-O system at 1600°C can be represented by a ternary isotherm in which the metal phase is in equilibrium with an oxide phase which decreases in iron and increases in titanium as the titanium content of the iron increases: 0 to 0.5 pct Ti (metal)—liquid FeO-TiO_2 solution (oxide); 0.05 to 1.0 pct Ti (metal)—solid reduced TiO_2 containing FeO (oxide); 1.0 to 5.0 pct Ti (metal)—Ti_2O_3 (oxide); and 5.0 pct Ti (metal)—TiO (oxide).

Acknowledgments

The authors wish to express their appreciation to the Titanium Alloy Manufacturing Div., National Lead Co. for its support of this investigation in the form of a graduate fellowship, analytical service, and supplying of the titanium sponge and the TiO_2 and ZrO_2 crucibles used. Particular thanks are due Dr. Stephen F. Urban, Director of Research, for his counsel and assistance.

References

[1] H. Wentrup and G. Hieber: Concerning the Equilibrium Between Oxygen and Titanium in Liquid Iron. *Tech. Mitteilungen Krupp A, Forschungsbechte* (1939) **2**, p. 47.

[2] E. L. Evans and H. A. Sloman: Deoxidation of Iron by Titanium. *Journal* Iron & Steel Institute (1953) **174**, p. 318.

[3] G. F. Comstock, S. F. Urban, and M. Cohen: *Titanium in Steel.* (1949) p. 32. New York. Pitman Publishing Corp.

[4] J. Chipman: *Basic Open Hearth Steelmaking.* (1951) p. 670. New York. AIME.

[5] H. M. Chen and J. Chipman: Vanadium-Oxygen Equilibrium in Liquid Iron. *Trans.* ASM (1947) **38**, p. 110.

[6] J. Chipman and H. M. Dastur: Vanadium-Oxygen Equilibrium in Liquid Iron. *Trans.* AIME (1951) **191**, p. 111; JOURNAL OF METALS (February 1951).

[7] G. Derge: Analysis of Oxygen in Titanium. *Trans.* AIME (1949) **185**, p. 31; JOURNAL OF METALS (January 1949).

[8] P. Ehrlich: Phase Relations and Magnetic Behavior in the System Titanium-Oxygen. *Ztsch. für Elektrochemie* (1939) **45**, p. 362.

[9] H. W. Worner: The Constitution of Titanium-Rich Alloys of Iron and Titanium. *Journal* Institute of Metals (1951) **79**, p. 173.

[10] R. J. Van Thyne, H. D. Kessler, and M. Hansen: The System Titanium-Chromium and Titanium-Iron. *Trans.* ASM (1952) **44**, p. 974.

[11] L. S. Darken and W. Gurry: The System Iron-Oxygen. *Metals Handbook.* (1948) p. 1212. Cleveland. ASM.

[12] J. Grieve and J. White: The System FeO-TiO_2. *Journal* Royal Technical College, Glasgow, Scotland (1939) **4**, p. 441.

[13] E. S. Bumps, H. D. Kessler, and M. Hansen: Titanium-Oxygen Systems. *Trans.* ASM (1953) **45**, p. 1008.

[14] P. H. Morton and W. N. Baldwin: The Scaling of Titanium in Air. *Trans.* ASM (1952) **44**, p. 1004.

[15] O. Kubaschewski and E. L. Evans: *Metallurgical Thermochemistry.* (1951) p. 188. New York. Academic Press, Inc.

[16] F. Sauerwald: Systematic Relationship of the Properties of Molten Metals and Alloys III. *Ztsch. für Metallkunde* (1950) **41**, p. 214.

Sulphur Pressure Measurements of Molybdenum Sesquisulphide in Equilibrium with Molybdenum

by C. Law McCabe

It has been established that molybdenum sesquisulphide, not molybdenite, is in equilibrium with molybdenum metal and sulphur vapor in the vicinity of 1100°C. The S_2 pressure for this system has been obtained using the Knudsen orifice method and the standard free energy for the dissociation of S_2.

THIS work was undertaken to help in determining the thermodynamic properties of the molybdenum sulphide which is in equilibrium with metallic molybdenum and sulphur vapor in the temperature range 1025° to 1150°C. From the results of Montoro[1] and of Parravano and Malquori[2] molybdenite would be expected to be in equilibrium with molybdenum metal, while the results of Guichard[3] indicate that a lower sulphide must be in equilibrium with the metal. Thus it was concluded that the problem warranted reconsideration, especially in view of the suspiciously low temperature independent term for the standard free-energy function for the reaction $MoS_2 \rightleftarrows Mo + S_2$. The reaction was calculated and duly noted as being low by Richardson and Jeffes,[4] using the data of Parravano and Malquori.[2]

Experimental Method

The general method used in this investigation is that of the Knudsen orifice method for the determination of equilibrium pressure. The apparatus and technique are similar to those described for the determination of the vapor pressure of silver.[5] However, a closed-end McDanel tube instead of fused silica was used to maintain the vacuum, a molybdenum effusion cell with a replaceable lid was employed instead of a silica cell, and a titanium getter maintained at run temperature was used to assure that no oxidation of the molybdenum or molybdenum sulphide was taking place. All runs were made at a residual pressure less than 10^{-5} mm Hg. The data are given in Table I. Runs 1 through 13 were obtained using molybdenite, analyzed 98.5 pct, from the Molybdenum Corp. of America. The remaining runs were done with a sample from the Climax Molybdenum Corp. which was their grade No. 3 and analyzed 59.87 pct Mo.

The weight loss of the cell during heating up and cooling down was subtracted from the total weight loss of the cell during the run. Also, when the temperature was changed, the Knudsen cell was placed in the vacuum chamber and heated at temperature for several hours in order to allow the sulphide and the metal to adjust their compositions to the equilibrium values, to desorb or adsorb gases into or from the molybdenum cell itself, and to desorb any water from the molybdenum sulphide or molybdenum powder inside the cell. Water may have been adsorbed inside the cell because, after each run, the top of the cell was removed and the material in the cell was stirred to insure that a layer of molybdenum metal would not build up and obstruct the passage of sulphur vapor into the gas phase. It was established that the molybdenum cell alone decreased in weight an inappreciable amount when heated at the highest run temperature for long periods of time.

There are two questions to be answered before the data in Table I can be used to calculate thermodynamic functions: 1—Which molybdenum sulphide is in equilibrium with molybdenum metal and sulphur vapor? 2—What sulphur species are present in the vapor phase? It can be assumed safely that no molybdenum is vaporized, since its vapor pressure is almost negligible at these temperatures. It will be shown subsequently that no sulphide of molybdenum is volatile.

Question 1 was answered in the following way: The especially purified molybdenite, obtained from the suppliers mentioned previously, was charged

Table I. Summary of Experimental Data

Run Number	Orifice Area, Cm	Duration of Run, Min	T	Weight Loss of Cell, Grams
3	0.01497	955	1423	0.0300
6	0.0069	1182	1423	0.0176
7	0.00693	978	1425	0.0154
11	0.01497	5603	1327	0.0196
13	0.00693	5820	1373	0.0302
18	0.00693	2530	1397	0.0200
19	0.00693	2475	1397	0.0185
26	0.00777	2450	1383	0.0207
27	0.00777	2631	1395	0.0250
28	0.00777	2550	1383	0.0238
29	0.00777	4035	1351	0.0139
30	0.01497	5558	1303	0.0095
31	0.01497	3950	1327	0.0111
32	0.01497	3903	1327	0.0120

C. L. McCABE, Junior Member AIME, is Assistant Professor of Metallurgical Engineering, Carnegie Institute of Technology, Pittsburgh.

Discussion on this paper, TP 3832D, may be sent, 2 copies, to AIME by Apr. 1, 1955. Manuscript, Feb. 1, 1954. Chicago Meeting, February 1955.

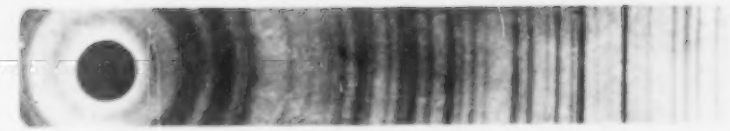

Fig. 1a—Debye-Scherrer patterns of molybdenite as-received.

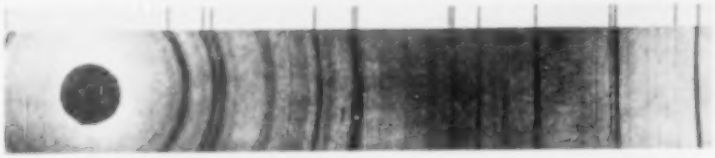

Fig. 1b—Pattern of the residue after equilibrium established between sulphur vapor, molybdenum, and the sulphide. The lines marked are those of molybdenum.

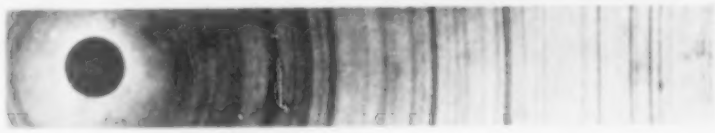

Fig. 1c—Pattern after molybdenum metal was dissolved from sample whose pattern is shown in b.

in the molybdenum effusion cell. Debye-Scherrer patterns of the two original samples were identical. Subsequent experiments on each sample gave identical pressures. Several runs were required to obtain constant weight losses per unit time. After several additional runs were made, the material in the cell was removed and a powder pattern was run. Fig. 1 shows the X-ray patterns described. The Debye-Scherrer patterns were obtained with unfiltered Cu radiation; exposure times were 6 hr; and the camera diameter was 114.6 mm. The patterns in Fig. 1 are the back-reflection half of the film. Molybdenum lines (see pattern *B*) were very strong and, in addition, weak lines, not those of molybdenite, were visible. The molybdenum was dissolved out of the sample with dilute aqua regia, and a Debye-Scherrer pattern and a chemical analysis of the material which did not dissolve was obtained. The Debye-Scherrer pattern (see pattern *C*) was totally different from that of molybdenite and the chemical analysis was 66.0 pct Mo and 32.0 pct S. Using elementary methods, this corresponds to the chemical formula $Mo_{1.96}S_3$. Whether this apparent nonstoichiometry is real or not is problematical, but it is certain that the molybdenum sulphide in equilibrium with sulphur vapor and molybdenum metal from 1025° to 1150°C is molybdenum sesquisulphide, Mo_2S_3.

The second question to be answered, that of the constitution of the sulphur vapor, can be estimated only with fair accuracy at the present time because of the uncertainty of the heat of dissociation of sulphur.[6] Incidentally, a value for this heat of dissociation can be obtained when good gas-equilibria data are available for the reaction $Mo_2S_3 + 3H_2 \rightleftarrows 2Mo + 3H_2S$. This data and the Knudsen data reported here will allow the calculation to be made. A paper on this method will be forthcoming from work in progress on effusion measurements of iron sulphide in equilibrium with iron. For the present, the value selected by Richardson and Jeffes[5] for the equilibrium constant for the reaction

$$S_2 \rightleftarrows 2S. \qquad [1]$$

will be taken. From the data reported by Richardson and Jeffes,[5] it can be shown that no sulphur species other than S_2 and S will be present in appreciable concentration in the gas phase.

One further point to be clarified is to determine whether a molybdenum sulphide is volatile. To establish this, a 0.5002 g sample of molybdenite containing 59.2 pct Mo was placed in an open zircon crucible and placed in a vacuum at 1150°C for two days. It was found that 0.3333 g of material was left in the cell and it analyzed 86.9 pct Mo. Thus, 97.8 pct of the molybdenum was still in the cell. In view of the uncertainty of quantitative removal of the material from the cell, errors in analysis, and other possible losses, it was concluded these data show no volatilization of MoS, or Mo_2S_3. Thus, the entire weight loss of the cell during the effusion runs was due to the loss of sulphur.

Table II. Summary of Experimental Data

Run Number	Pressure of S_2 in Atm	Log of p_{S_2}	T	1/T x10⁴
5	1.77x10⁻⁴	−3.752	1433	7.027
6	1.80x10⁻⁴	−3.737	1423	7.027
7	1.94x10⁻⁴	−3.712	1425	7.019
11	1.38x10⁻⁴	−3.860	1327	7.536
13	6.12x10⁻⁴	−4.213	1277	7.292
18	9.19x10⁻⁴	−4.037	1397	7.158
19	8.51x10⁻⁴	−4.070	1397	7.158
26	6.81x10⁻⁴	−4.055	1393	7.179
27	1.02x10⁻³	−3.990	1395	7.168
28	1.01x10⁻³	−3.995	1393	7.179
29	3.50x10⁻⁴	−4.456	1351	7.402
30	7.77x10⁻⁴	−4.110	1393	7.675
31	1.32x10⁻³	−3.879	1327	7.536
32	1.45x10⁻³	−3.839	1327	7.536

Calculations

In order to set up the standard free energy for the reaction

$$4/3\,Mo\,(solid) + S_2\,(gas) \rightleftarrows 2/3\,Mo_2S_3\,(solid) \qquad [2]$$

it is necessary to obtain the partial pressure of S_2 from the effusion measurements and the equilibrium constant for reaction 1.

On reasonable assumptions that equilibrium between S_2 and S is maintained in the gas phase, that S_2 and S effuse independently and without interaction, and that ideal gas behavior is obeyed, the following equation is derived easily from the fundamental Knudsen-cell equation[7]

$$M_{S_2}^{1/2}\,p_{S_2} + K^{1/2}\,M_S^{1/2}\,p_{S_2}^{1/2} - \frac{W\,L}{A} = 0 \qquad [3]$$

where p_{S_2} is the pressure of S_2 in atmospheres in the gas phase, M is the molecular weight of the species

in question, W L is the weight loss in grams of the cell per minute, A is equal to 2658 times the area of the orifice in square centimeters times the duration of the run in minutes divided by the square root of the absolute temperature, and K is the equilibrium constant for reaction 1.

Using Eq. 3, the pressure of S_2 has been calculated for the data given in Table I and these values have been listed in Table II. The data in Table II have been plotted in Fig. 2. The best line selected for this data is

$$\log p_{S_2} = \frac{-21{,}200}{T} + 9.13. \qquad [4]$$

Unfortunately, the entropy data needed to perform other thermodynamic calculations are not available. However, the standard free energy for reaction 2 can be calculated and is

$$\Delta F^\circ = -96{,}800 + 41.8T. \qquad [5]$$

This equation is valid in the region 1300° to 1425°K. Due to the present uncertainty in the standard free energy for reaction 1, the accuracy, according to the system of Richardson and Jeffes,[4] will be accuracy C or ±10 kcal.

Using the nomenclature of C. I. Whitman,[5] the value of L/r for the molybdenum cell used in this investigation is 2.9; $W_s = 1$, since the orifice had knife edges, and f was 0.011 for the largest orifice. This gives a value of $K = 0.99$. On the assumption that $\alpha = 1$, the pressure for S_2 reported above should be reduced by 1 pct. The value for α in this case is unknown, but, in view of the fact that the observed pressures were not a function of orifice size, it is concluded that any correction for $K \neq 1$ and $\alpha \neq 1$ is unwarranted in this case. The correction would be a small fraction of the estimated accuracy.

Discussion

From the results presented, it is obvious that either hydrogen does not reduce MoS_2 directly to molybdenum as reported by Parravano and Malquori[2] or, if it does, the standard free energy of the reaction Mo (s) + S_2 (g) ⇄ MoS_2 (s) cannot be determined from gas-equilibria measurements. This latter statement is true because, if the presence of hydrogen causes the molybdenite to reduce directly to the metal instead of to the sesquisulphide, then the hydrogen must dissolve in the solid Mo or MoS_2 or both and thereby change the sulphur potential due to its dissolution. The assumption that this does not happen to a marked degree must be made for gas-equilibria data to be valid for measuring sulphur potentials. The observation that the reduction proceeds from MoS_2 directly to the metal is incorrect, is preferred.

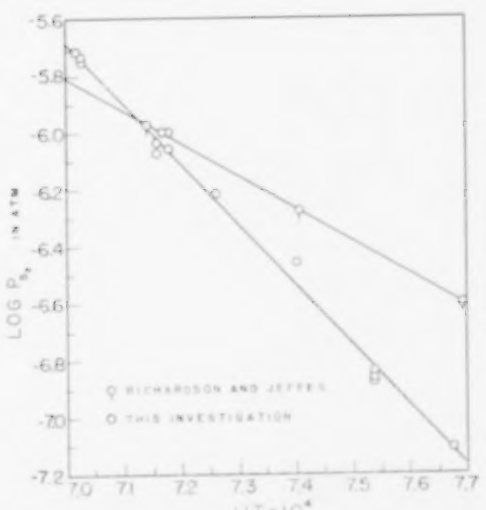

Fig. 2—A comparison of the P_{S_2} calculated from the data reported in the paper for the reaction 4/3 Mo + S_2 ⇄ 2/3 Mo_3S_4 and that reported by Richardson and Jeffes.[4]

It is likely that Parravano and Malquori[2] were studying reaction 2 and not the reduction of molybdenite directly to the metal. On this assumption, the results of this investigation can be compared with their findings. It is seen from Fig. 2 that their data and the data from this study give the same standard free energy in the vicinity of 1400°K. However, the temperature coefficient is vastly different in the two cases. The results reported in this investigation give an entropy which is more consistent with that of reactions of this type. The anomalous nature of the entropy term reported by Parravano and Malquori[2] was pointed out by Richardson and Jeffes.[4]

When better data are available for the energy of dissociation of S_2, the data reported in Table I will have to be recalculated so that the values for the pressure of diatomic sulphur listed in Table II will be more nearly the correct ones. The estimated accuracy also will be much improved.

Summary

1—The S_2 pressure above molybdenum sesquisulphide in equilibrium with molybdenum has been measured, using the Knudsen orifice method coupled with the standard free energy for the dissociation of S_2.

2—By chemical analysis and X-ray determinations, it has been shown that molybdenum sesquisulphide is the sulphide of molybdenum which is in equilibrium with molybdenum metal and sulphur vapor at temperatures around 1100°C.

Acknowledgments

This work was sponsored by the Office of Naval Research under Contract N6ori-47/IV, Project NR 031-014. The author acknowledges the assistance of Messrs. Robert Miller, Donald Beard, and Robert Hudson of the Metals Research Laboratory in carrying out the pressure measurements, in obtaining and interpreting the X-ray measurements, and for performing the calculations, respectively. The cooperation of Mr. Eugene Lucas of Molybdenum Corp. of America in supplying an especially prepared sample of molybdenite and carrying out chemical analyses and Mr. George Timmons of Climax Molybdenum Corp. in supplying a sample of molybdenite is gratefully acknowledged.

References

[1] V. Montoro: *Att. Rendiconti Accademi Lincei.* (1929) **9**, Series 6, p. 331.

[2] N. Parravano and G. Malquori: *Att. Rendiconti Accademi Lincei.* (1928) **7**, Series 6, pp. 109-112, 189-192.

[3] M. Guichard: *Comptes Rendus* (1900) **130**, p. 137; *Annales de Chimie Physique* (1901) **23**, pp. 498, 557.

[4] F. D. Richardson and J. H. E. Jeffes: *Journal* Iron & Steel Institute, London (1952) **171**, p. 165.

[5] C. E. Birchenall and C. L. McCabe: *Trans.* AIME (1953) **197**, p. 707; JOURNAL OF METALS (May 1953).

[6] C. I. Whitman: *Journal of Chemical Physics* (1952) **20**, p. 162.

Martensite Formation in Powders and Lump Specimens of Ti-Fe Alloys

by D. H. Polonis and J. Gordon Parr

IN a recent paper on titanium-rich Ti-Fe alloys,[1] the hardness of quenched powder specimens was given, together with the amounts of martensitic α' they contained. The values disagreed in two respects with previous determinations that Worner[2] made on lump specimens: 1—Some martensitic α' is formed in powder specimens of alloys containing up to 12 atomic pct Fe. On the other hand, Worner reports that, although his results on quenched lumps are not conclusive, alloys containing more than about 4 pct Fe "appear to consist of retained β" although they "may not be strictly unaltered solid solutions." 2—According to Worner, quenched lump specimens show a maximum hardness at a composition about 3.5 pct Fe. Earlier experiments by the authors showed a maximum hardness of martensitic alloys in powder form at 10 pct Fe.

Accordingly, more experiments have been conducted in order to confirm these differences and to determine with more accuracy the minimum composition of quenched lump specimens that consist entirely of retained β.

Lump samples $\frac{1}{8}$ x $\frac{1}{8}$ x 1/20 in. were quenched from 1000°C in helium and, on the whole, showed similar hardness values to the specimens that Worner water-quenched from 950°C. The hardness curve the authors obtained shows a more pronounced peak, but in other respects it is very similar to Worner's curve (Fig. 1).

While it was possible to make fairly reliable measurements of the percentage of martensitic α' in quenched powders (by Geiger spectrometer), the solid samples allowed only approximate estimates to be made from visual observation of line intensities on film. Retained β begins to appear in quenched lumps containing 0.2 pct Fe; at 2.2 pct Fe there are approximately equal quantities of β and α'; in a 4.7 pct Fe alloy only a trace of α' appears. These results are represented as a curve on Fig. 1.

The hardness and constitution of powder samples were verified by repeating both types of quenching experiment described in the earlier paper.[1] Identical results were obtained by the two methods, and they agreed with the figures published previously (Fig. 1).

The appearance of the martensitic structure under the microscope is shown in Figs. 2 and 3. The martensite needles are coarser in the lump; otherwise the structures are similar.

Three conclusions are made at this juncture: 1—The properties of quenched lumps reported by Worner are confirmed, on the whole. The differences between them and the properties of powders are probably due to an effect of specimen size. Differences of behavior in various sizes of specimen have been observed previously in martensite reactions in Fe-Mn alloys[3] and in Cu-Al alloys.[4] 2—The maximum hardness of both quenched lumps and quenched powders appears at a composition where martensite formation has all but ceased. In this respect, powders and lumps behave similarly. 3—Martensitic α' has essentially the same microscopic appearance both in powders and lumps.

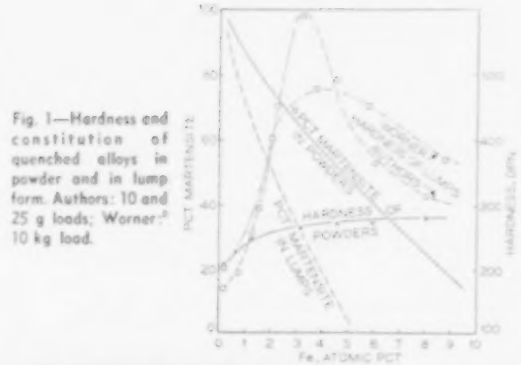

Fig. 1—Hardness and constitution of quenched alloys in powder and in lump form. Authors: 10 and 25 g loads; Worner:[2] 10 kg load.

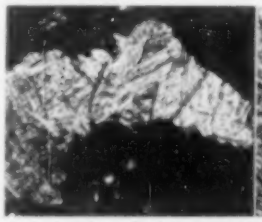

Fig. 2—0.2 pct Fe alloy. Powder quenched from 1000°C. Etched in 1 pct HF, 1 pct H_2O_2, aqueous. X800. Area reduced approximately 45 pct for reproduction.

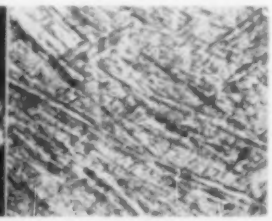

Fig. 3—0.2 pct Fe alloy. Lump specimen quenched from 1000°C. Etched in 1 pct HF, 1 pct H_2O_2, aqueous. X800. Area reduced approximately 45 pct for reproduction.

Acknowledgment

This work is part of a program sponsored by the Defence Research Board of Canada, Project No. 425.

References

[1] D. H. Polonis and J. G. Parr: *Trans.* AIME (1954) **200**, p. 1148; JOURNAL OF METALS (October 1954).
[2] H. W. Worner: *Journal* Institute of Metals (1951) **80**, p. 213.
[3] J. G. Parr: *Research* (1953) **6**, p. 53s.
[4] E. A. Berquist: Unpublished graduate thesis.

D. H. POLONIS and J. G. PARR, Junior Members AIME, are Graduate Student and Research Associate, respectively, Dept. of Mining and Metallurgy, University of British Columbia, Vancouver, B. C., Canada.

TN 243E. Manuscript, Sept. 13, 1954.

AIME OFFICERS:
President—Leo F. Reinartz
Vice-Presidents—T. B. Counselman, L. E. Elkins, Harold Decker, O. B. J. Fraser, A. B. Kinzel, J. B. Morrow
President-Elect—H. DeWitt Smith
Treasurer—G. F. Moulton
AIME STAFF:
Secretary—E. H. Robie
Administrative Ass't. Sec'y.—Ernest Kirkendall
Ass't. Secretaries—J. B. Alford, H. N. Appleton, E. J. Kennedy, Jr., R. E. O'Brien
Ass't. Treasurer—P. J. Apol

aime NEWS

Citations Prepared For Meeting Awards

The following citations have been prepared for those to whom awards will be given at the AIME Annual Meeting in February 1955:

George Herman Deike, Erskine Ramsay Medalist: "As an engineer, manufacturer, and executive, Mr. Deike has served the mining industry with distinction in many ways, particularly in the field of mine safety. His pioneering work in the application of engineering principles in reducing the dangers inherent in mining has earned for him an international reputation. Under his direction as an administrator, inventor, and manufacturer of safety appliances, his company has become preeminent in the manufacture of industrial safety equipment. He has been a leader in the application of scientific research in the promotion of safety and efficiency in industry. His company recently dedicated the world's largest research center devoted exclusively to the development of safety equipment. This laboratory, one of the most modern of its kind, symbolizes his basic philosophy—'keep ahead of safety needs in the mining industry.' Mr. Deike, with all his business responsibilities, has always taken a very active part in civic and community activities, and his genial personality and his humane qualities have endeared him to his host of friends everywhere."

Edwin Letts Oliver, James Douglas Medalist: "Noted for his invention of the Oliver continuous filter—a most outstanding contribution to nonferrous metallurgy and widely applicable to industrial fields throughout the world. A man of far-flung interests, a distinguished engineer and administrator, beloved and respected for assistance given to younger engineers."

Edward W. Davis, Robert H. Richards Award Recipient: "For his inspiring leadership and notable technical contributions in the utilization of taconite as a source of iron ore."

E. D. Gardner, Jackling Award Recipient: "For significant contributions to technical progress in the field of mining, and for his Lecture, *Mining Technology—Outlook for the Future.*

W. G. Pfann, Mathewson Medalist: "For three papers published in the JOURNAL OF METALS: *Principles of Zone Melting, Segregation of Two Solutes, with Particular Reference to Semiconductors,* and *Redistribution of Solutes by Formation and Solidification of a Molten Zone.*

F. W. Boulger and **R. H. Frazier, Robert W. Hunt Medalists:** "For their paper, *The Influence of Carbon and Manganese on the Properties of Semi-killed Hot-Rolled Steel,* published in the Supplement to the JOURNAL OF METALS, May 1954."

Gust Bitsianes, J. E. Johnson Jr. Award Recipient: "For his paper on *The Topochemical Aspects of Iron Ore Reduction* and his other contributions to the literature in the manufacture of pig iron."

Harold Vagtborg Jr., Rossiter W. Raymond Award Recipient: "For his paper, *Equilibrium Vaporization Ratios for a Reservoir Fluid Containing a High Concentration of Hydrogen Sulfide,* published in the JOURNAL OF PETROLEUM TECHNOLOGY."

R. E. Thurmond, W. E. Heinrichs Jr., and **E. D. Spaulding, Robert Peele Award Recipients:** "For their paper, *Geophysical Discovery and Development of the Pima Mine, Pima County, Arizona,* published in MINING ENGINEERING."

In addition to the above, an AIME junior member has been selected to receive the Alfred Noble Prize in 1955, awarded to a junior member of the Founder Societies or the Western Society of Engineers each year for a paper of particular merit. The winner this year was Cornelius S. Roberts for his paper, *Creep Behavior of Magnesium-Cerium Alloys,* published in the May 1954 Supplement to the JOURNAL OF METALS.

Institute Officers Declared Elected

No nominees for AIME Directors and officers for 1955 other than those selected by the Nominating Committee having been named by the membership, the following were declared elected at the November 17 meeting of the Board of Directors: They will take office at the annual business meeting of the Institute in Chicago on February 15: C. E. Reistle Jr., President-elect; W. A. Dean and W. W. Mein Jr., Vice-Presidents; and D. C. Helms, H. C. Pyle, R. W. French, A. J. Herzig, E. H. Rose, and J. W. Vanderwilt, Directors. All serve for three years except Mr. Reistle as President-elect who will successively become President, and Past President.

Names of the Nominating Committee for AIME Officers in 1956 were published in this journal for December. Members of the Committee will welcome suggestions for a President-elect, two Vice-Presidents, and six other Directors, from any member of the Institute.

Final Survey Being Made For New Building

A final survey of what New York, Philadelphia, Pittsburgh, and Chicago have to offer is being made by the Committee of the Five Presidents, named to recommend a site for the proposed new engineering societies building. A meeting is scheduled for Feb. 1, 1955 at which time a definite recommendation to the boards of the Founder Societies and the AIChE is expected to be made.

Blast Furnace Group Nominates Officers

The Nominating Committee of the AIME Blast Furnace, Coke Oven and Raw Materials Committee has nominated the following officers: W. E. Marshall, Chairman, 1 yr; F. M. Hamilton, Vice-Chairman, 2 yr; J. W. Duncan, Secretary, 1 yr; and E. J. Andberg, Member, Executive Board, 4 yr. The nominees will take office after the 1955 annual conference to be held at the Bellevue-Stratford Hotel in Philadelphia, April 18 to 20.

The Jan. 12, 1955 meeting of the AIME Bessemer Committee scheduled to be held in Pittsburgh has been cancelled. The Bessemer Committee will now meet at Hamilton, Ont., Canada on Apr. 4 and 5, 1955. The meeting will feature a visit to the converter plant of the Dominion Foundries & Steel Ltd. on Monday April 4. Headquarters for the meeting will be at the Royal Connaught Hotel in Hamilton.

President and Mrs. Reinartz Guests of Ohio Valley Section

President Reinartz is shown with J. H. Melvin, Ohio Geological Survey, Ohio State University, Columbus, Ohio, and H. P. Gaw, Armco Steel Corp., Middletown, Ohio, at the dinner meeting held by the Ohio Valley Local Section.

Leo F. Reinartz, President of AIME, and his wife were guests of the Ohio Valley Local Section at a dinner meeting held in their honor at the Deshler-Hilton Hotel, Columbus, Ohio. The meeting was attended by 67 members and wives.

Mr. Reinartz, after being introduced to the group by Harold P. Gaw, Section Chairman, discussed some of the problems and policies of AIME. A similar talk, explaining AIME policies, will be given by one of the national officers to each of the local sections of AIME this year.

The growth rate of the society was considered to be very good, approximating 1 pct a month. The quality and number of technical papers published, especially by the Metals Branch, is also satisfactory.

The society still has some financial problems. Local section financing has been improved this year by returning one half of all initiation fees back to the local sections. The Metals Branch continues to show a deficit arising from the publication of technical papers. A special fund of $50,000 is being raised to meet some of this cost.

A big problem remaining is to discover how the society and its members can more effectively encourage young people to enter, and remain in, the engineering profession. The United States is graduating fewer engineers this year than is Russia.

A short discussion period concluded the meeting.

B. Gonser Speaks To Spokane Subsection

Nearly 50 members including visitors from Kellogg, Idaho, Grant's Pass, Ore., Seattle, Wash., and Butte, Mont., attended the first fall meeting of the AIME Spokane Subsection.

The speaker, Dr. Bruce Gonser of Battelle Memorial Institute, discussed the metallurgy of uncommon metals using the recent U. S. Geological Survey charts of availability of metals which use aluminum as 100 pct as a basis. He discussed the sources, unusual methods of production, properties, unsuspected properties obtained by high purity, present uses and possible future uses of some 30 or more metals in the periodic table which up to recently were not available or only in very small amounts. Dr. Gonser pointed out the limitations, ways in which these limitations are being overcome for some metals to be used for high temperature applications, and the possibilities of enlarging the uses of the well-known and common industrial metals by means of these uncommon metals.

The audience made up of geologists, mining engineers, equipment engineers, extractive metallurgists and physical metallurgists followed with keen interest the lecture, the sound exposition and the flights of imagination projecting into the future of some metals. The discussion ranged widely: a brief presentation of the activities of Battelle Memorial Institute and its relations with the mining and metallurgical industries; the opening of new laboratories and offices in several capitals and cities of Europe; research in economics; the recovery of metals from plants and sea weeds; drilling by means of vibration; and the effect of small amounts of impurities on metals such as zinc.

To Support Research Projects

Following endorsement by the AIME, Engineering Foundation has voted support to the following research projects:

Flow of Bulk Solids, by Andrew W. Jenike, Salt Lake City. Dr. Jenike hopes to develop a quantitative method of design for flow of bulk solids in bins, hoppers, chutes, and other material handling equipment. The Minerals Beneficiation Div. of the AIME has given its encouragement to this study. A grant of $5000 by Engineering Foundation has been made contingent on raising an additional $15,000 from other sources.

The other two projects are of interest to the petroleum industry. One, on **Forces Exerted on Oscillatory Fluid Motion on Cylinders,** has to do with the effect of ocean waves on piles, and is of particular interest in connection with equipment and installations used in offshore drilling for oil. A grant of $1500 has been made to D. L. Laird, of the University of California. The other, **Phenomena Underlying Natural Disasters,** is a proposed study which, if successful, would permit the successful forecasting of tidal waves, or sudden unexpected onrushes of water. This, again, would be of value to offshore drilling crews. A grant of $5000 for this study has been given to William L. Donn, of the Lamont Geological Observatory, Columbia University.

Lima, Peru Trip Being Considered

Thought is being given to a trip to Lima, Peru, and the mining districts of that country and Chile, immediately following the Annual Meeting of the AIME in New Orleans in February 1957. The Lima, Peru, Local Section, through its Chairman, Carl Westphal, has invited AIME members to be its guests at that time. Housing accommodations are constantly increasing, and should be adequate two years hence. Travel would presumably be by chartered plane at a cost considerably less than the regular fare. The traditional hospitality of Latin America would be extended to all.

1955 IMD Fall Meeting Sets Attendance Record

A FULL program and several special sessions at the IMD Fall Meeting drew over 800 registrants, setting a new attendance record. The three day meeting in Chicago, November 1 to 3, had some 60 papers on a program consisting of 11 sessions. In many cases, members and guests had a difficult time trying to decide which session to attend.

The Third Annual Symposium on Titanium, again was the largest drawing card, and proved that the interest in this subject has certainly not abated with time. The all-day symposium contained five excellent general papers on titanium in the morning session, under the chairmanship of W. L. Finlay and V. W. Whitmer, and was highlighted by a panel discussion in the afternoon. Speakers at the morning session were: D. J. McPherson, Armour Research Foundation of Illinois Institute of Technology, *Interesting Alloy Systems, Commercial Alloys, Melting and Hot Working of Titanium;* R. I. Jaffee, Battelle Memorial Institute, *General Physical Metallurgy, Including Effects of Interstitials, Heat Treatment and Joining of Titanium;* Harold Kessler, Titanium Metals Corp. of America, *Hydrogen in Titanium;* Gordon Fairbairn, North American Aviation, Inc., *Use of Titanium in Airframes;* and N. E. Promisel, Navy Dept., Bureau of Aeronautics, *Use of Titanium in Aircraft of the Future.* Walter Dean and L. D. Jaffe served as Chairmen for the panel discussion and the panelists were L. A. Best, Douglas Aircraft Co.; L. R. Frazier, General Electric Co.; T. W. Lippert, Titanium Metals Corp. of America; Frank Vandenburgh, Mallory-Sharon Titanium Corp.; Maj. R. J. Kotfila, Wright-Patterson Air Force Base; and J. B. Sutton, E. I. du Pont de Nemours & Co., Inc. A full recording of the papers and panel discussion will appear as a special feature in the February issue of JOURNAL OF METALS.

Another special event was the evening session on Metal Science, led by J. H. Hollomon and Bruce Chalmers, which was outstanding in material, discussion, and attendance. When this session finally was concluded, small discussion groups formed which continued far into the night. Even the refreshments served failed to halt the more important business at hand.

One of the highlights of the IMD program was the Third Annual Symposium on Titanium. The panel consisted of, left to right: Luther A. Best, Loring R. Frazier, Frank H. Vandenburgh, J. Bart Sutton, Ralph J. Kotfila, T. W. Lippert, and Co-chairmen L. D. Jaffe and Walter A. Dean.

In addition to the sessions, various committees got in much paper work and planning for the AIME Annual Meeting and the coming year. Committees active during the meeting were the IMD Program Committee, D. J. Blickwede, Chairman; IMD Publications Committee, W. R. Hibbard, Jr., Chairman; Membership Committee, J. P. Nielsen, Chairman; IMD Executive Committee, J. H. Scaff, Chairman; and the Nuclear Metallurgy Committee, D. W. Lillie, Chairman.

The AIME Chicago Section were hosts at a cocktail party preceding the IMD Annual Dinner on Tuesday evening November 2. Jack Scaff, Chairman of IMD, served as toastmaster at the dinner. He introduced J. W. Halley, Chairman of the Chicago Section, who welcomed the group to Chicago and invited them to return for the Annual Meeting in February. Toastmaster Scaff then introduced the head table guests, and called upon James Austin, ASM President to say a few words. AIME President Leo Reinartz addressed the group, and discussed various Institute activities, and some of his recent travels to AIME meetings and sections. President Reinartz then announced to the group that Ernest Kirkendall was just recently appointed Administrative Assistant Secretary of the AIME, and that there would be a recommendation to the Board of Directors taking office at the Annual Meeting that he be made Secretary of the AIME, upon the retirement of E. H. Robie, with Mr. Robie appointed as Secretary Emeritus. It was necessary for Dr. Kirkendall to make a brief statement to acknowledge the acclaim from his many friends that accompanied this statement.

Speaker for the evening was Dr. W. W. Bauer, Director of Health and Education, Radio and Television, for the American Medical Assn., and Editor of *Todays Health.* He chose as his subject *Thirty Five-Midpoint of Life.* He started by assuming that 35 was the average age of the audience, and traced health conditions back to the time of their birth. By doing this he developed his thesis that conditions and the state of medical knowledge today have shown tremendous advances in the past 35 years, with the virtual disappearance of diphtheria, influenza, and other common diseases of yesteryear. His predictions for the future were that cancer and certain other serious afflictions would be conquered, and the major causes of human death would be those resulting from the uncontrollable breakdown of human tissues associated with old age. Included in his interesting talk were discussions on mental health, and a plea for a planned rather than an abrupt retirement program for both workers and executives.

Usually the heaviest burden of an IMD Fall Meeting falls on the Division Chairman, and this year was no exception. The IMD had a good year under the leadership of Jack Scaff, and the success of the meeting was no small credit to him. Other officers of IMD for the year were Morris Cohen, Past Chairman; J. S. Smart, Jr., Senior Vice Chairman; C. S. Barrett, Vice Chairman; and Ernest Kirkendall, Secretary-Treasurer.

Another feature of the IMD program was the meeting of the Nuclear Metallurgy Committee. Shown left to right are: Frank G. Foote, John H. Frye, Jr., Benjamin Lustman, David H. Gurinsky, J. E. Burke, and Chairman D. W. Lillie.

NOHC Southern Ohio Section Holds Successful Meeting

The 18th Annual Conference of the Southern Ohio Section, NOHC, was held at the Deschler-Hilton Hotel, Columbus, Nov. 4, 1954. Harold P. Gaw Chairman of the Southern Ohio Section opened the Friday meeting.

Robert Sigl of Armco Steel Corp. gave his award winning paper on mixed fuels and their effect on open hearth production. The rest of the morning meeting was given over to the following papers: *Effect of Hot Metal Analysis on Open Hearth* by G. B. Reisenberg, Armco Steel Corp.; *Instrumentation on New Furnaces at Detroit Steel Corp.* by Frank McGough, Detroit Steel Corp.; and *The Taconite Story* by E. W. Davis, University of Minnesota.

During the afternoon session the papers presented were: *Use of Motion Pictures in the Study of Steel Pouring Practices* by A. B. Blockridge, Jr., Jones & Laughlin Steel Corp.; *Refractory of Gun Practice* by David A. Finch, National Malleable & Steel Castings Co.; *Recent Developments in Mold and Stool Design* by George Dornin, Shenango-Penn Mold Co.; and *Measurement of Bath Temperature by Immersion Thermocouple* by Frank Williams, Sr., Armco Steel Corp.

The Executive Board of the National Open Hearth Steel Committee met in Columbus, Ohio, Saturday, Nov. 6, 1954. Plans for their 1955 conference to be held in Philadelphia for the first time were reported. A plant trip through the Fairless Works of U. S. Steel Corp. is included in the program.

Chairmen of the morning operating and combustion session were C. F. Staley, Armco Steel Corp., and R. Thornberry, Newport Steel Corp. The afternoon session on practice and quality was chairmened by Albert Meihack, Empire Steel Corp., and Charles R. Taylor, Armco Steel Corp.

Lee Lambing, Jones & Laughlin Steel Corp., was toastmaster for the annual dinner and the award for the best paper presented at the Southern Ohio Section was given to Mr. Sigl. Speaker of the evening was Rev. Laurence Hall whose topic was *Life With a Capital L.*

Registration was 203. Many of the members who attended the meeting went to the Ohio State-Pittsburgh football game on Saturday.

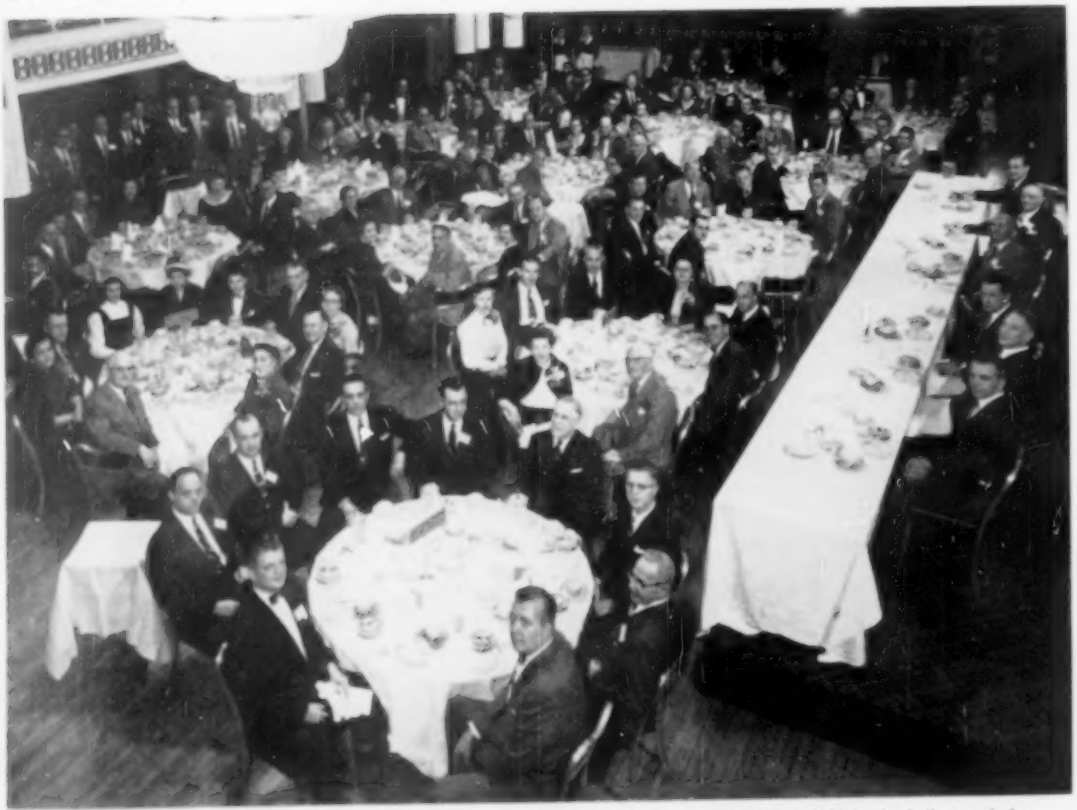

The Fellowship Banquet of the 18th Annual Conference of the Southern Ohio Section, NOHC, was held in the ballroom of the Deshler-Hilton hotel, Columbus, Ohio. H. P. Gaw is Chairman and R. W. Lowry is Secretary-Treasurer of the section.

Chairmen Named For Northwest Conference

Plans for the Pacific Northwest Regional Conference to be held in Spokane, Wash., Apr. 28, 29, and 30, 1955, are going forward according to General Chairman, A. Y. Bethune, Sullivan Mining Co., electrolytic zinc plant, Kellogg, Idaho.

S. E. Maddigan, assistant director, dept. of metallurgical research, Kaiser Aluminum & Chemical Co., Spokane, Wash., is Chairman of the Metals Branch activities. Joseph R. Giegerich, Superintendent, the Sullivan Mine, Consolidated Mining & Smelting Co. of Canada, Ltd., Kimberley, B. C. will head up the Mining Branch activities and John P. Spielman, Dean, School of Mines, State College of Washington, Pullman, will be in charge of the Mineral Industries Education group. A full program of student participation is planned with one evening being set aside for the Educational meeting.

The following division chairmen have accepted commitments and are now working on the various technical programs:

Mining: Joseph C. Kieffer, assistant manager, American Smelting & Refining Co., Wallace, Idaho

Geology: Robert E. Sorenson, chief geologist, Hecla Mining Co., Wallace, Idaho

Minerals Beneficiation: Wm. D. Nesbeitt, manager, the Allis-Chalmers Mfg. Co., Spokane, Wash.

Industrial Minerals: P. Evan Oscarson, mining engineer, 1108 W. 19th Avenue, Spokane, Wash.

Extractive Metallurgy: R. J. Lapee, metallurgist, the Anaconda Copper Mining Co., Great Falls, Mont.

Plans are being made for a special session on *X-Ray Fluorescent Analysis*, Saturday, April 30, with particular reference to its applicability to mining, milling, geology, industrial minerals and ceramic problems. F. R. Morral, X-ray div. chief, dept. of metallurgical research, Kaiser Aluminum & Chemical Corp., Spokane, is in charge.

Philadelphia Section Hears A. B. Cummins

The Philadelphia Section met on Nov. 18, 1954 and enjoyed a cocktail hour and dinner in which both the minerals and metallurgical members participated. Following this, each group retired to its separate lecture.

The speaker for the minerals group was A. B. Cummins, manager of the minerals, magnesia and basic research dept. of the Johns Manville Co. His topic was *Minerals Used by the Johns Manville Co.*

H. H. Ulig, of the Massachusetts Institute of Technology, gave an unusually fine talk on *Metallurgical Factors in Corrosion Reactions.* He showed that in neutral or slightly alkaline waters, the type of ferrous alloy was of minor significance with respect to the corrosion rate. It was then demonstrated that the type of alloy and its heat treatment were very significant factors in corrosion in acid waters. He also showed that the degree of homogeneity of "stainless steels" plays an important part in their corrosion resistance. Dr. Uhlig illustrated his talk with slides which clearly demonstrated various factors influencing corrosion rates.

Connecticut Section Holds Students' Night

The combined second technical session of the Connecticut Section, AIME for the 1954-55 season and Students' Night was held at the Hammond Metallurgical Laboratory at Yale University in New Haven, Conn. Fifty persons attended the session, including 34 members, 9 guests and 7 metallurgical students of the University.

Richard J. Christine, Chairman of the Connecticut Section introduced the students to the assembly as is customarily done on Students' Night. He also announced that the section would sponsor a students' contest for a $25 award to be given to the writer of a metallurgical paper selected by a committee composed of W. R. Hibbard, Sr., W. E. Milligan, and W. D. France. All students enrolled in accredited Engineering Schools in Connecticut will be eligible to participate in this contest.

The guest speaker was Sidney Siegal who is employed by the general plate div. of Metals & Controls Corp. of Attleboro, Mass. Mr. Siegal's informative talk was well received and commenced with a brief chronological development of clad or composite metals. This was followed with a discussion of the theory of metal bonding and various methods for producing the composite metals. Mr. Siegal talked for some length and indicated by slides a new cold bonding technique which was revealed to the public for the first time after being developed by his company. He concluded his talk with the applications for composite metals and disclosed samples indicating the vast number of metal combinations that they had produced.

The meeting was concluded by the awarding of two books as door prizes by Secretary-Treasurer D. E. Trout.

AIME Seeing Double?

This isn't a three dimension slide or do you need glasses. The gentlemen above are the brothers Westerman, new Student Associate members and possibly the first set of twins to join the AIME. Edwin J. is on the left and Richard E. is on the right. Both attend the Montana School of Mines and both expect to receive Bachelors of Science in Metallurgical Engineering. Their signatures are for all purposes identical. Right after the Westerman applications were received at headquarters, another set of twins signed in. They were Norman W. and Ramon G. Bentsen, in the June '55 Class at Oklahoma University. They are majoring in petroleum engineering and were born in Alix, Canada.

Personals

Joseph H. Bach has been appointed assistant to manager, fuel element subdivision, atomic power div., Westinghouse Electric Corp., Pittsburgh. Prior to that he had been section head for Sylvania Electric Products Inc.

R. R. WILLIAMS, JR.

R. R. Williams, Jr., has been appointed manager of mines for the Colorado Fuel & Iron Corp. Mr. Williams had been assistant manager of mines at Pueblo.

George B. McMeans, vice president in charge of operations for the Kaiser Steel Corp., will transfer from Fontana, Calif., to Oakland, Calif.

L. W. Moore was named superintendent of the open hearth dept., Wheeling Steel Corp., Wheeling, W. Va. **G. P. Whitaker, Jr.,** has been promoted to general foreman, succeeding Mr. Moore.

Lewis E. Thelin, formerly with the Scovill Mfg. Co., has accepted a position as assistant chief metallurgist with the Bristol Brass Co., Bristol, Conn.

Albert Krainess is with the J-47 project, jet engine dept., aircraft gas turbine div., General Electric Co., Cincinnati. He had been plant metallurgist for the Burroughs Adding Machine Co., Detroit.

Frank H. Buchella, San Manuel Copper Corp., has been transferred from Tiger to San Manuel, Ariz.

James L. Lane, Kaiser Aluminum & Chemical Corp., has been transferred from Jamaica, B.W.I., to Baton Rouge, La., as civil engineer.

Albert Reilingh has joined the American Metal Co., Ltd., Newcastle, N. B., Canada.

Stuart A. Falconer was named chief metallurgist of the mineral dressing dept., American Cyanamid Co., to fill the vacancy caused by the recent death of S. J. Swainson.

James L. Head, Anaconda Copper Mining Co., New York, was reelected as president of United Engineering Trustees, Inc.

John E. Haig, vice president and secretary was elected president of Ajax Electric Co., Philadelphia. He succeeds the late **William Adam, Jr.**

R. S. Poister, former vice president of operations, and **Walter H. Wiewel,** former vice president of sales, have been named senior vice presidents by Crucible Steel Co. of America, Pittsburgh.

C. E. Amos has been appointed administrative assistant to the vice president, production, Jones & Laughlin Steel Corp., Pittsburgh. Mr. Amos had been assistant to the general manager, ore mines and quarries.

R. K. McKECHNIE

Robert K. McKechnie has been named unit manager, materials application unit, metallurgy dept., General Electric Research Laboratory, Schenectady, N. Y. This is a new unit recently established. Mr. McKechnie has been associated with GE since 1947.

Bennett S. Ellefson was appointed technical director of Sylvania Electric Products Inc., New York.

Carl S. Hallauer was elected president of the Bausch & Lomb Optical Co., Rochester, N. Y. **Joseph F. Taylor** was named chairman of the board and **M. Herbert Eisenhart,** formerly board chairman, was named honorary chairman.

D. T. Wellman, president of the Wellman Bronze & Aluminum Co., Cleveland, Ohio, was elected president of the Magnesium Assn. **James E. Pepall,** president, Magnesium Co. of Canada Ltd., was elected vice president.

F. C. Peterson has been named director of industrial relations for the Dow Chemical Co., Midland, Mich.

Thomas L. Altshuler has accepted a position as design and development engineer at the semiconductor chemical and physical laboratory, Radio Corp. of America, Harrison, N. J.

A. L. Boegehold, former head, metallurgical dept., research laboratories div., General Motors Corp., Detroit, Mich., has been appointed assistant to general manager, research laboratories div.

Maurice J. Day was appointed as director of research and development for Crucible Steel Co. of America. Dr. Day was formerly associated with the Armour Research Foundation of Illinois Institute of Technology as assistant director in charge of program development.

Robert Mahr, Chrysler Corp., **William G. Scholz,** Climax Molybdenum Corp., and **Carl S. Wiedman,** General Electric Co., Carboloy Dept., recently participated as counselors at the 20th Annual Vocational Guidance Meeting held by the Engineering Society of Detroit.

J. E. BURKE

J. E. Burke has been named manager of the newly created ceramics studies section in the metallurgy dept., General Electric Research Laboratory, Schenectady, N. Y. Since 1949 Dr. Burke was manager of metallurgy at the Knolls Atomic Power Laboratory.

Kenneth G. Carroll has joined the staff of the Bayonne research laboratory of the International Nickel Co., Inc., as head of the newly created physics section.

C. L. Kessler has been appointed chief metallurgist at Aluminum Co. of America's Massena, N. Y. works. **A. M. Miller** will replace him as assistant chief metallurgist at the company's Edgewater, N. J. **F. O. Traenkner** has been appointed assistant chief metallurgist at the Massena works.

Nevin K. Hiester has been appointed manager of the chemical and metallurgical engineering section, Stanford Research Institute, Stanford, Calif.

Philip W. Chase was recently appointed assistant vice president—raw materials, U. S. Steel Corp. **August J. Breitenstein** has been appointed director—exploration and planning.

Richard T. Myer has been appointed chief metallurgist of the aluminum fabrication div., Kaiser Aluminum & Chemical Corp., Oakland, Calif. Prior to joining Kaiser, Mr. Myer was chief metallurgist at the Massena Works of the Aluminum Co. of America.

Orrin S. Braden, Jr., formerly assistant superintendent, blast furnaces north, Wheeling Steel Corp., Steubenville, has been appointed supervisor of training. **Edward P. Quick** succeeds Mr. Braden as assistant superintendent. He had been a foreman in the blast furnace dept.

Gordon McMillin has accepted a position with the Canadian Car & Foundry Co., Montreal. He had been associated with the General Steel Castings Corp., Granite City, Ill.

David J. Blythe has been appointed production superintendent, metals manufacturing, National Lead Co.

Frederick H. Schroeder, vice president of Lee Higginson Corp., has been elected a director of Barium Steel Corp.

Cyrus E. Brush has been elected a vice president of American Brake Shoe Co., New York. **Alfred H. Munkenbeck, Jr.**, was named secretary and **William J. Foster, III**, assistant secretary.

Obituaries

An Appreciation of
Swain Joseph Swainson
By Theodore B. Counselman

Swain Joseph Swainson, Member of 1934, died Friday, Oct. 22 at Southold, Long Island after a prolonged illness. He was buried at Westfield, N. J.

He was born in 1901 at Mountain, N. D. and attended the University of North Dakota, from which he received a B.S. degree in 1923, and the University of Utah, from which he graduated with an M.S. degree in 1925. He first did some research work in ore dressing at the University of Utah, and joined the Staff of

S. J. SWAINSON

American Cyanamid as a metallurgist in 1926.

He had much to do with the establishment of that company's mineral dressing laboratories at Stamford, Conn., which are among the largest and most extensive in the world, and for many years was director. His major field of work was in the beneficiation of ores and the extraction of their minerals. He was one of the first to appreciate the importance of the microscope in the solution of mineral dressing problems, and used this technique extensively. He invented many processes related to this field and was the author of numerous papers which were published in technical journals. He was particularly noted for his work in improvements in froth flotation, and in heavy media separations.

For several years Mr. Swainson supervised the operations of the Winchester research laboratory of the Atomic Energy Commission, operated at that time under contract by American Cyanamid. This work was concerned with the technique of extraction of uranium from its ores.

Mr. Swainson was very active in various technical societies, particularly in the American Institute of Mining & Metallurgical Engineers. He was on several committees of the Minerals Beneficiation Div., after helping to form that division, and finally became its Chairman and therefore a member of the very exclusive Molahominem Bellum Distinctionus (Mill Gentlemen of Distinction). He was a member of the Robert H. Richards Award Committee and was Chairman at the time of his death. He was also a member of the Mining and Metallurgical Society of America, and the Chemical, Metallurgical and Mining Society of South Africa. Besides belonging to the Mining Club of New York, he was a member of Sigma Alpha Epsilon and of the honorary Scientific fraternity, Sigma Xi.

Mr. Swainson leaves his wife, Cary Mulford Swainson, his father, Oddur Swainson, a sister, Bertha Swainson, and a host of warm friends throughout the profession.

Memorial Resolution for
C. Augustus Carlow

WHEREAS, with the passing of Dr. Charles Augustus Carlow, at his residence, Kincaple, St. Andrews, Scotland, on 13th August, 1954, after an illness of some months' duration, the American Institute of Mining and Metallurgical Engineers lost one of its most distinguished Honorary Members; and

WHEREAS, Dr. Carlow, was during his active life, one of the great leaders of the coal mining industry in Great Britain; the former Chairman and Managing Director of the Fife Coal Company, located in Fifeshire, Scotland, and his family had been connected with the Scottish coal industry for more than a century; and

WHEREAS, through his great scientific and engineering knowledge, Dr. Carlow gave much to the British Coal Industry and that of the world, serving as President of the Mining Institute of Scotland, 1932-36 and President of the Institution of Mining Engineers of Great Britain, 1936-38. Dr. Carlow was elected a member of the American Institute of Mining and Metallurgical Engineers in 1934, and was made an Honorary Member in 1946; and in 1952, a similar honor was conferred upon him by the British Institution; and

WHEREAS, at the Seventy-fifth Anniversary Meeting of the American Institute of Mining and Metallurgical Engineers, held in New York City in March, 1947, Dr. Carlow presented a brilliant and informative paper, "World Coal Resources", in which he set forth in detail the latest and most accurate estimate of the remaining recoverable coal tonnage in the known world; therefore be it

RESOLVED, That the American Institute of Mining and Metallurgical Engineers records with deep sorrow the loss of this distinguished engineer and friend, and be it further

RESOLVED, That this Resolution be included in the Minutes of the Meeting of the Board of Directors, and a copy be sent to the family of the late Dr. Charles Augustus Carlow.

By: Eugene McAuliffe

EHR

Harold A. Knight, who was an assistant editor of JOURNAL OF METALS in 1948, and recently associate editor of two American Chemical Society publications, died November 2, after a long illness.

Mr. Knight, who would have been 64 years old on November 4, joined the American Chemical Society editorial staff in the society's New York office in 1949. At his death, he was associate editor of the Society's official publication, the weekly *Chemical*

and *Engineering News*, and of the bi-weekly *Journal of Agricultural and Food Chemistry*. He specialized in chemical markets and business news and was in charge of the chemical prices section of *Chemical and Engineering News*.

A native of Cazenovia, N. Y., he received a B.A. from Cornell College (Iowa) in 1913 and the B.Litt. from Columbia University in 1914. He started his journalistic career in Syracuse, N. Y., as a reporter for the *Syracuse Herald* in 1914 and the *Syracuse Journal* in 1915.

After serving as associate editor of the *American Shooter* and a member of the New York staff of *Iron Age*, he joined the *New York Journal of Commerce* in 1922 and remained with that publication for 18 years. He was associate editor of *Steel Magazine* in 1940-41; news editor of *Materials and Methods* from 1941 to 1948.

Necrology

Date Elected	Name	Date of Death
1914	Raymond F. Bacon	Oct. 14, 1954
1918	Ernest C. Bieve	July 9, 1954
1940	Malvern Black	Nov. 7, 1954
1943	Charles M. Brown	Aug. 10, 1954
1917	J. J. Carrigan	Unknown
1921	V. A. Gilles	Nov. 9, 1954
1919	Horace H. Graham	Nov. 8, 1954
1905	George A. Guess	Oct. 21, 1954
1908	William Gunsmore	June 5, 1954
1914	Thomas B. Jones	Apr. 19, 1954
1921	Mark C. Lake	Nov. 9, 1954
1902	J. B. Lamblard	Nov. 22, 1954
1953	Hamner Mandl	Apr. 2, 1954
1942	J. B. Martin	May 19, 1954
1941	Walter L. McCloy, Jr.	July 6, 1954
1921	Alex. M. McDonald	Oct. 27, 1954
1938	Francis J. Oakes, Jr.	Aug. 14, 1954
1942	John W. Owen	Oct. 26, 1954
1953	W. R. Ruff	Apr. 6, 1954
1950	Fourrois Robertson	Nov. 13, 1954
1954	George A. Schrader	Nov. 15, 1954
1941	H. Webb Smith	Nov. 14, 1954
1950	Winston W. Spencer	Sept. 21, 1954
1938	Anders P. Svenningson	Unknown
1919	William Trotter	Unknown
1950	Harold J. Walker	Aug. 7, 1954

Proposed for Membership
— Metals Branch AIME —

Total AIME membership on Nov. 30, 1954 was 21,892; in addition 2941 Student Associates were enrolled.

ADMISSIONS COMMITTEE

O. B. J. Fraser, Chairman; R. B. Caples, Vice-Chairman; F. A. Ayer, A. C. Brinker, R. H. Dickson, Mac Genaemer, Ivan A. Given, Fred W. Hanson, T. D. Jones, Sidney Rolle, J. H. Senf, John T. Sherman, F. T. Sisco, Frank T. Worms, R. L. Ziegfeld.

The Institute desires to extend its privileges to every person to whom it can be of service, but does not desire as members persons who are unqualified. Institute members are urged to review this list as soon as possible and immediately to inform the Secretary's office if names of people are found who are known to be unqualified for AIME membership.

In the following list C/S means change of status; R, reinstatement; M, Member; J, Junior Member; A, Associate Member; S, Student Associate.

California
Concord—Bolder, Carl A. (A)

Connecticut
Bridgeport—Hay, Thomas H. (J)
Darien—Chapman, Charles J. (A)
Noank—Reed-Hill, Robert E. (M)

Illinois
Chicago—Allen, Bunnell H. (M)
Chicago—Crowe, Byron L. (M)
Chicago—d'Heurle, Francois M. (J) (R. C/S—S-J)
Chicago—Jacobs, Frank A. (A)
Chicago—Petit, Jean F. (J)
Chicago—Rajala, Benjamin R. (J)
East Chicago—Matthews, Wm. H. (A)
Elmhurst—Lindgren, James R. (J)
Granite City—Tarris, Marcel (A)
La Grange—Allison, Charles R., Jr. (A)
Urbana—Lieberman, David S. (J)

Indiana
Gary—Hager, Harry A. (A)
Hammond—Harris, Robert D. (A)
Hammond—Craig, George H. (J)
Hammond—Johnson, Roger T. (A)
Hobart—Frame, Charles P. (M)
Kokomo—Lewis, Philip S., Jr. (M)

Maryland
Silver Spring—Fuller, Nathan F. (M)

Massachusetts
Arlington—Davis, Richard S. (J)

Minnesota
Minneapolis—Li, Chuh H. (A)

New Jersey
Paterson—Craig, Alexander J., Jr. (J)

New Mexico
Carlsbad—Taylor, Cyrus O. (M)

New York
Bolton Lake—Rogers, Harry C., Jr. (A)
Bayside—Okuno, Roy N. (A)
Buffalo—Suprinick, Harry (J)
Chappaqua—Spendelow, Howard R., Jr. (M) (R. C/S—S-M)
Long Island City—Simkovich, Edward A. (J)
Poughkeepsie—Hymes, Irwin M. (J) (R. C/S—S-J)
Utica—Pirk, Gustav W. (A)
Yonkers—Wung, Frank (A)

Ohio
Canton—Fedock, Michael F. (A)
Canton—Whitmer, Virgil W. (M)
Cleveland—Harmon, Edward L., Jr. (J)
Columbus—Berger, Lewis W. (A) (R. C/S—S-A)
Columbus—Keeler, John R. (M) (R. C/S—J-M)
Columbus—Lenning, Gilbert A. (A)
Columbus—Rough, Frank A. (A)
Columbus—Spriser, Rudolph (A)
Dayton—Kuttle, Ralph J. (A)
Dayton—Masteller, Richard D. (J)
E. Liverpool—Porter, Sidney C., Jr. (A)
Girard—Kauffmann, Edmund J., Sr. (A)
Parma—Sobey, Edmond J. (A)
Steubenville—Drabers, Charles W. (A)
Steubenville—Hoch, Albert J. (A)
Westerville—Keyser, Naaman H. (M)
Wright-Patterson A. F. B.—Deligrasso, Eugene J. (J)
Youngstown—Heuer, George F. (A)
Youngstown—LaVelle, Thomas P. (J)
Youngstown—Theil, Martin (A)

Oregon
Albany—Hayes, Earl T. (M) (R. C/S—J-M)

Pennsylvania
Aliquippa—Coble, John L. (M)
Aliquippa—Olenchak, Daniel L. (A)
Beaver Falls—Lewis, John D. (A) (R. C/S—S-A)
Bethlehem—Bhat, Gopalkrishna (J)
Bethlehem—Butz, Lynford W. (M)
Bridgeville—Huber, William R. (M)
Butler—McGlincy, Joseph T. (A)
Chester—Tracy, Lawrence L. (A)
East Pittsburgh—Akers, George A. (J)
McKeesport—Howell, J. Albert (A)
Philadelphia—McQuillen, Albert L., Jr. (A)
Pittsburgh—Augustine, Alfred (A)
Pittsburgh—Groat, Martin E. (A)
Pittsburgh—Haus, Jan F. (A)
(Mt. Lebanon) Pittsburgh—McDonnell, John G. (M)
Pittsburgh—Meyer, Philip L. (A)
Pittsburgh—Petrosky, Frank J. (A)
Pittsburgh—Reiber, Paul L., Jr. (A)
Sharpsville—Dornin, George A., Jr. (A)
Torresdale—Bryan, Ralph J. (A)

Tennessee
Chattanooga—Buckle, John W. (M) (R. C/S—J-M)

Utah
American Fork—Motz, Karl W. (A)

Canada
Ancaster, Ont.—Hood, John E. (A)

England
Erdington, Birmingham—Phelps, Leonard A. (J)

Germany
Frankfurt—Petersen, Curd W. (M)

Northern Rhodesia
Kitwe—Harris, Louis B. (J)

Switzerland
Schaffhausen—Werner, Alexander (M)

Advertisers' Index

Air Reduction Co., Inc. *G. M. Basford*	*
Ajax Electrothermic Corp. *Thomas R. Sunheim Adv.*	*
Ajax Engineering Corp. *Eldridge, Inc.*	*
Aluminum Co. of America *Fuller & Smith & Ross Inc.*	*
American Bridge Div., U. S. Steel Corp. *Batten, Barton, Durstine & Osborn, Inc.*	9
Bailey Co., Wm. M. *Walker & Downing*	*
Basic Refractories Inc. *The Griswold-Eshleman Co.*	*
Bell Telephone Labs. *N. W. Ayer & Son, Inc.*	*
Buehler Ltd. *Kreicker & Meloan, Inc.*	*
Carondelet Foundry Co. *Whitehead & Sprague, Inc.*	*
Electro Met. Div., Union Carbide & Carbon Corp. *J. M. Mathes, Inc.*	16
Ferro Engineering Co. *C. A. Reece Ind. Publicity*	*
General Electric Co., X-Ray Dept. *Klau, Van Pietersom-Dunlap Assoc.*	5
General Electric Co. *G. M. Basford Co.*	*
Great Lakes Carbon Corp. *Davis, Parsons & Strohmeier, Inc.*	13
Harbison-Walker Refractories Co. *Walker & Downing*	*
Hevi Duty Electric Co. *Camin, Cuttigan, Inc.*	*
International Nickel Co. *Marschalk & Pratt Co.*	14
Minneapolis-Honeywell Regulator Co. *Aitkin-Kynett Co., The*	*
Molybdenum Corp. of America *Smith, Taylor & Jenkins, Inc.*	*
Morgan Construction Co. *Davis Press, Inc., The*	*
National Carbon Div., Union Carbide & Carbon Corp. *William Esty Co., Inc.*	Second Cover
Pennsylvania Engrg. Corp.	*
Pittsburgh Lectromelt Furnace Corp. *Fuller & Smith & Ross Inc.*	*
Ramtite Co., The *Marsteller, Gebhardt and Reed Inc.*	*
Smooth-Harwood Co. *Allbright Associates Adv.*	*
Stokes Machine Co., F. J. *John Mather Lupton Co., Inc.*	2, 3
Sundell-Dressler Corp. *Walker & Downing*	*
Titanium Alloy Mfg. Div., National Lead Co. *Comstock & Co.*	*
United States Graphite Co., The *Price, Tanner & Willox, Inc.*	Fourth Cover
U. S. Steel Corp. Columbia-Geneva Steel Div. Tennessee Coal & Iron Div. U. S. Steel Supply Div. U. S. Steel Export Co. *Batten, Barton, Durstine & Osborn, Inc.*	*
Vanadium Corp. of America *Hazard Adv.*	*
Whiting Corp. *Waldie & Briggs, Inc.*	*
Wyman-Gordon Co. *John W. Odlin Co., Inc.*	Third Cover

* Previous issue.

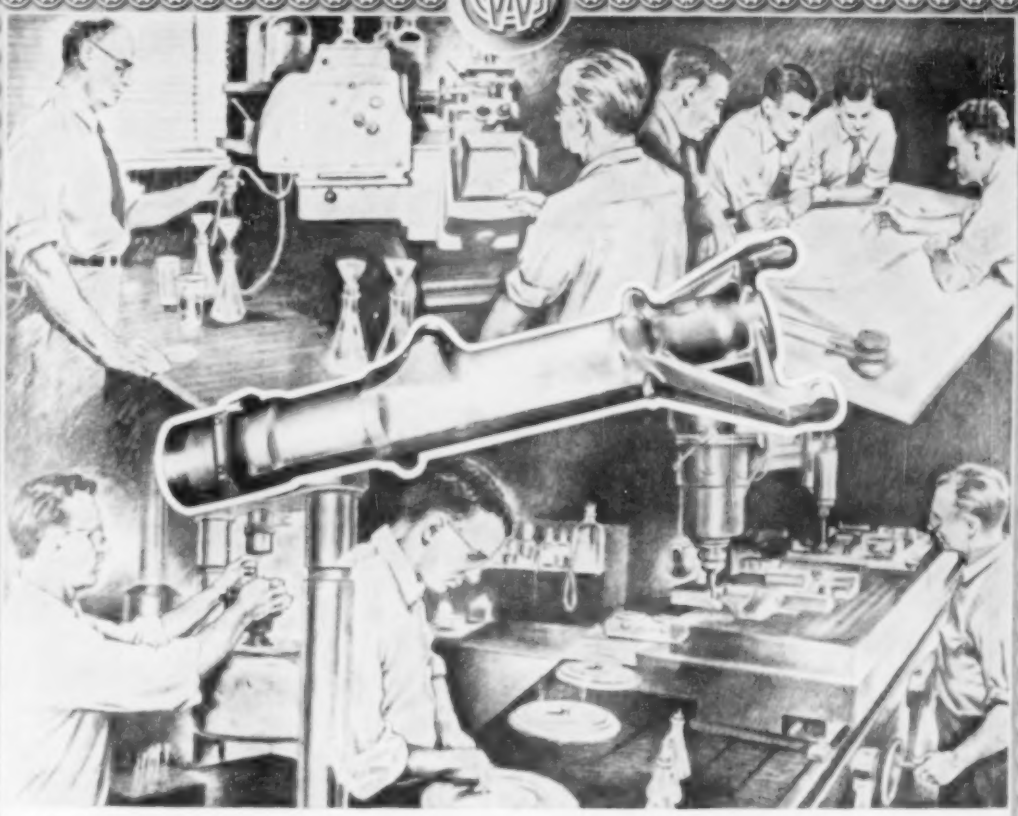

FORGING TECHNICIANS—Yes, that is the compliment paid us by those acquainted with our services. In back of each design is a thorough understanding of engineering and metallurgical needs before production begins . . . assuring forgings of maximum physical properties and uniform quality

THE LANDING GEAR FORGING illustrated, nearly five feet long, is an important component for a modern military fighter . . . another example of Wyman-Gordon's technical contribution to aircraft.

There is no substitute for Wyman-Gordon experience

WYMAN-GORDON

Established 1883

FORGINGS OF ALUMINUM • MAGNESIUM • STEEL • TITANIUM

WORCESTER, MASSACHUSETTS

HARVEY, ILLINOIS DETROIT, MICHIGAN

MAKE EVERY HEAT COUNT!

with RECARB-X. for the ladle

- **FAST CORRECTION FOR OFF-CARBON HEATS** — a convenient 50-pound bag of RECARB-X tossed into the ladle will give two points of carbon pick-up per 100-tons of steel.
- **REDUCED LADLE REACTION** — RECARB-X does not cause churning, boiling or other violent ladle reactions. It avoids oxidation of alloys and temperature losses by dissolving quickly and quietly.
- **IDEAL FOR QUALITY STEEL** — RECARB-X is consistently efficient at all carbon levels . . . effective in maintaining maximum rimming action on all high carbon rimmed heats . . . ideal for close carbon specifications.
- **HELPS THE MELTER** — RECARB-X added to the ladle will insure carbon specifications. RECARB-X gives the melter time to finish all heats to proper S, Mn, P, etc. specifications . . . and to tap at the best temperature.
- **SAFE** — no odor or flames to hurt workmen or damage equipment. Light 50-pound bag is easy to toss into the ladle.
- **ECONOMICAL** — RECARB-X is a profit-making investment. Keep your mill schedule. Put more heats into the soaking pit at exact carbon specifications. Make *every* heat count with RECARB-X.

Write for the RECARB-X bulletin today. Get the full facts and arrange a test . . . we will be happy to cooperate.

OUR 100th YEAR

190

THE UNITED STATES GRAPHITE COMPANY

DIVISION OF THE WICKES CORPORATION • SAGINAW, MICHIGAN

Journal of METALS

JANUARY 1955

VOL. 7, NO. 1, IN THREE SECTIONS—SECTION TWO

TRANSACTIONS SECTION

Structure and Properties of Ti-C Alloys	H. R. Ogden, R. I. Jaffee, F. C. Holden	73
Solution Rate of Solid Aluminum in Molten Al-Si Alloy	C. M. Craighead, E. W. Cowthorne, R. I. Jaffee	81
Mobilities in Diffusion in Alpha Brass	G. T. Horne, R. F. Mehl	88
Energy Stored During Fatigue of Copper	L. M. Clarebrough, M. E. Hargreaves, A. K. Head, G. W. West	99
Titanium-Lead System	P. Forter, H. Margolin	101
Effect of Alpha Solutes on the Heat-Treatment Response of Ti-Mn Alloys	H. R. Ogden, F. C. Holden, R. I. Jaffee	105
Selected Isothermal Sections in the Titanium-Rich Corners of the Systems Ti-Fe-O, Ti-Cr-O, and Ti-Ni-O	W. Rostoker	113
Heat Treatment and Mechanical Properties of Ti-Cu Alloys	F. C. Holden, A. A. Watts, H. R. Ogden, R. I. Jaffee	117
Autoradiography Determination of the Self-Diffusion of Silver	H. Krueger, H. N. Hersh	125
Chromium-Rich Portion of the Chromium-Nickel Phase Diagram	C. Stein, N. J. Grant	127
Stress Analysis of a Single Crystal in Pure Torsion	N. Brown	134
Solubility and Decomposition Pressures of Hydrogen in Alpha-Zirconium	E. A. Gulbransen, K. F. Andrew	136
X-Ray Crystallographic Data on As_2Te_3	J. Singer, C. W. Spencer	144
Metallographic Study of Equilibrium Relationships in 35 Aluminum Alloy	P. R. Sperry	145
Influence of Additives in the Production of High Coercivity Ultra-Fine Iron Powder	E. W. Stewart, George P. Conard, II, J. F. Libsch	152
Resistance Sintering Under Pressure	F. V. Lenel	158

Table of Contents Continued

Physical and Mechanical Properties of Rhenium 168

Effects of Tensile Stress on the Austenite to Ferrite Transformation in Eutectoid Steel 179

Some Characteristics of the Isothermal Martensitic Transformation 183

Melting Point of Germanium and the Constitution of Some Ge-Ga Alloys 187

Contribution of Crystal Structure to the Hardness of Metals 189

Thermal Conductivity of Uranium and Several Uranium Alloys 192

Study of the Effect of Boron on the Decomposition of Austenite 193

Dispersion Hardening of Copper Chromium Alloys 200

Plastic Deformation of Germanium and Silicon by Torsion 203

Purification of Gallium by Zone-Refining 205

Study of a New Mode of Plastic Deformation in Zinc Crystals 206

Isothermal Austenite Grain Growth 215

Structure and Properties of Ti-C Alloys

by H. R. Ogden, R. I. Jaffee, and F. C. Holden

The mechanical properties of Ti-C and Ti-C-O alloys can be altered by heat treatments to dissolve or reject carbon from solid solutions. The maximum strength is obtained by annealing just below the peritectoid temperature. Quenching from the β-carbide field results in softening. Impact behavior is influenced by the extent of solution of interstitials.

CARBON is not as important in titanium alloys as it was in earlier years when graphite induction melting was more prevalent. With induction melting, carbon pickup is about 0.5 to 0.8 pct. Cold-mold arc melting with graphite electrodes, which is among the more current methods, results in carbon pickup of 0.1 to 0.2 pct. The titanium-sponge melting stock itself contains about 0.02 to 0.07 pct C, picked up from the magnesium used in the reduction process. Thus, carbon is still one of the more important contaminants in titanium and needs careful study and evaluation in order to understand titanium and titanium alloys. Moreover, it is equally proper to consider carbon as an alloying addition because, in controlled amounts in titanium alloys, it may serve a most useful function. This is particularly the case where the ultimate in toughness is not required.

The addition of carbon to titanium results in a peritectoid-type system as illustrated in Fig. 1.[1-3] The solubility of carbon is seen to be higher in the α phase than in the β phase in the temperature range of interest. Below the peritectoid temperature, the solubility of carbon in α titanium decreases with decreasing temperature. This type of system permits many microstructural and heat-treatment variations which may influence the properties of the alloys. The study of how the microstructure variations affect mechanical properties is described in this paper.

Experimental Procedures

The experimental techniques and testing methods used in this work were the same as those described in detail in a previous paper.[4] No further descriptions will be given except where changes have been made.

High purity iodide titanium, produced by the New Jersey Zinc Co., was used in all of the alloys. Carbon additions were made using high purity spectrographic carbon electrodes in order to obtain the highest purity carbon available. The alloys were prepared by double arc melting to reduce the possibility of segregation. The alloys were forged at 875°C to ¾ in. round, descaled, vacuum annealed for 5 hr at 900°C to remove the residual hydrogen, and swaged to ¼ in. round at 750°C. All heat treatments were made on material in this initial condition.

H. R. OGDEN, R. I. JAFFEE, and F. C. HOLDEN, Members AIME, are Assistant Chief, Chief, and Principal Metallurgist, respectively, Nonferrous Physical Metallurgy Division, Battelle Memorial Institute, Columbus, Ohio.

Discussion on this paper, TP 3859E, may be sent, 2 copies, to AIME by Mar. 1, 1955. Manuscript, Apr. 15, 1954. Chicago Meeting, November 1954.

Two of the early Ti-C ingots were found to have been contaminated in melting. Vacuum-fusion analyses showed that the two contaminated alloys had picked up oxygen, so the test results on these two alloys permitted an evaluation of ternary Ti-C-O alloys. A list of the alloys and their compositions are given in Table I.

Properties of Ti-C Alloys

In a peritectoid-type system, such as the Ti-C system, the chief microstructural variable which influences the properties is solid-solution strengthening. For a given composition, it is possible to control the disposition of carbon, either in solid solution or as the compound TiC, by suitable heat treatments. When in solid solution, the carbon present in the alloy makes a definite contribution to the strength of the alloy. However, when present as TiC, it has very little effect on the strength. Other microstructural variables considered in this investigation were transformation structures and grain size. As discussed in subsequent sections, these variables have only a minor effect on properties as compared to the solid-solution effect.

Solid-Solution Strengthening: The principal strengthening mechanism for Ti-C alloys has been found to be solid-solution strengthening. Carbon in interstitial solid solution strengthens titanium, but has very little strengthening effect if present as the compound. Since carbon has a higher solubility in

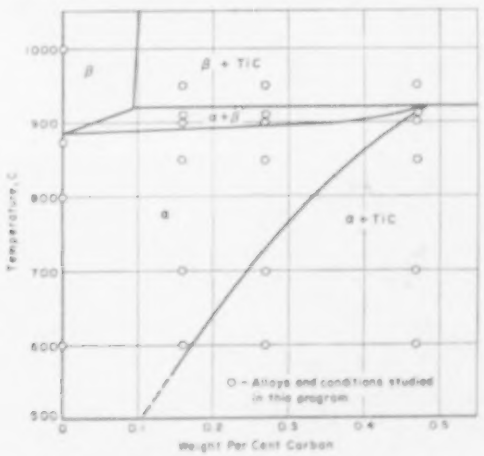

Fig. 1—Transformation diagram of the Ti-C system showing heat treatments used in this study.

The Transactions papers appearing in the Journal of Metals during 1955 will subsequently appear in AIME Transactions Volume 203 and may be permanently referenced to that volume.

Table I. Alloys and Their Composition

Alloy No.	Nominal Composition, Pct C	Analyzed Composition, Pct		
		C	O	H
TM-31	Unalloyed	0.02	0.025	0.0010
TM-5	0.2	0.19	0.12	—
TM-6	0.4	0.38	0.20	—
TM-33	0.2	0.16	0.035	0.0034
TM-34	0.4	0.27	0.028	0.0028
TM-30	0.8	0.47	0.052	0.0027

α titanium than in β titanium in the temperature range of interest, heat treatments in the α field produce the highest strengths.

The properties of the three binary Ti-C alloys, given in Table II, illustrate the solid-solution strengthening effect of carbon. The properties of the hydrogen-free unalloyed titanium base have been presented in another paper.[4]

Ti-0.16 Pct C Alloy. Fig. 2 shows the effect of heat-treating temperatures on the properties of a Ti-0.16 pct C alloy. Microstructures for the corresponding conditions are given in Fig. 3. When this alloy is annealed and quenched from the α field (600° to 850°C), there is little change in properties. The decrease in strength and reduction in area with increasing temperature is probably a result of the increase in α grain size. It should be noted that in the 600°C condition the grains are irregularly shaped (see Fig. 3a). This may be the result of incomplete solution of carbon, restricting grain growth. That this may be the case is indicated by the increase in yield strength from the 600° to the 700°C annealed condition which probably is caused by the solution of carbon. Also, the grains now are completely equiaxed with polyhedral grain boundaries.

When this alloy is annealed and quenched from the β-carbide field, there is a marked decrease in strength and toughness caused by the formation of TiC, and consequent lowering of the carbon in solid solution. Of interest are the high tensile ductilities when this alloy is annealed and quenched from the

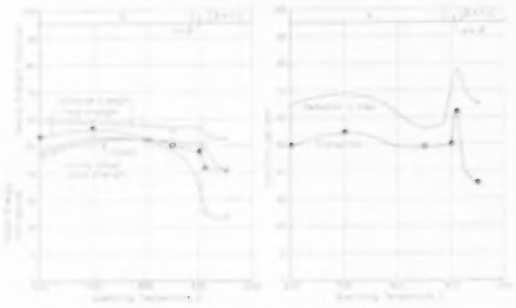

Fig. 2—Properties of a Ti-0.16 pct C alloy.

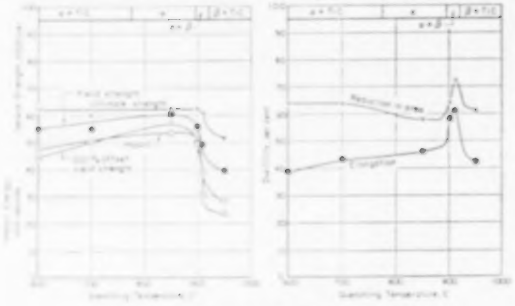

Fig. 4—Properties of a Ti-0.27 pct C alloy.

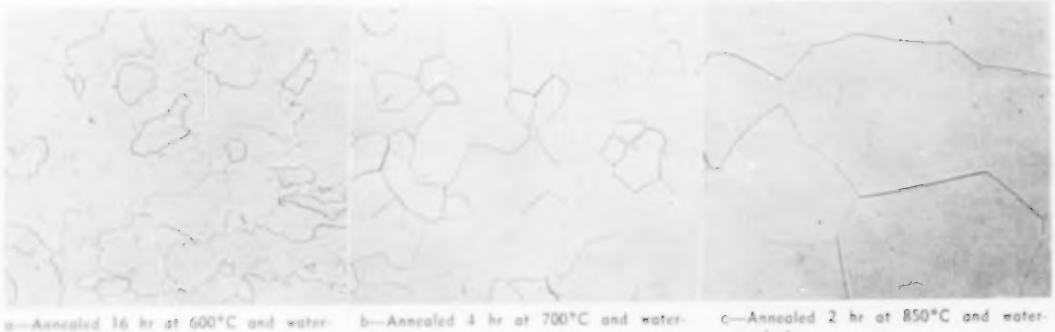

a—Annealed 16 hr at 600°C and water-quenched.

b—Annealed 4 hr at 700°C and water-quenched.

c—Annealed 2 hr at 850°C and water-quenched.

d—Annealed 2 hr at 900°C and water-quenched.

e—Annealed 1 hr at 910°C and water-quenched.

f—Annealed 1 hr at 950°C and water-quenched.

Fig. 3—Microstructures of a Ti-0.16 pct C alloy. X250.

The Transactions papers appearing in the Journal of Metals during 1955 will subsequently appear in AIME Transactions Volume 202 and may be permanently referenced to that volume.

a—Annealed 16 hr at 600°C and water-quenched.

b—Annealed 4 hr at 700°C and water-quenched.

c—Annealed 2 hr at 850°C and water-quenched.

d—Annealed 2 hr at 900°C and water-quenched.

e—Annealed 1 hr at 910°C and water-quenched.

f—Annealed 1 hr at 950°C and water-quenched.

Fig. 5—Microstructures of a Ti-0.27 pct C alloy. X250.

α-β field. The microstructure in this condition is composed of equiaxed grains of α in a matrix of transformed β. The ghost structures seen in Figs. 3d and 3e are believed to be β grain boundaries which completely surround one or more α grains. This is the only system in which the β grain boundaries have been observed in an α-β-annealed condition. The transformed β is α phase, low in carbon content; thus, there is an apparent two-phase structure of hard α (high carbon) in a soft α matrix (low carbon). Because the soft α is the matrix, the tensile ductilities are quite high.

Ti-0.27 Pct C Alloy: Data for the Ti-0.27 pct C alloy are shown in Fig. 4, and corresponding microstructures are shown in Fig. 5. Again in the α-carbide field, the α grain boundaries are irregular and scalloped as a result of grain growth inhibition by carbides. At the level of 0.27 pct C, the strength, particularly the yield strength, is increased by dissolving the TiC particles through the use of a high temperature α anneal. This illustrates the solid-solution strengthening effect of carbon. Comparing this effect with the decrease in strength by increasing the α annealing temperature for the Ti-0.16 pct C alloy shows that, when no carbide is available for solution, the increase in grain size lowers strength. Annealing and quenching from the β-carbide field causes a marked decrease in strength. Again, the

Table II. Tensile Properties of Ti-C Alloys

Specimen No.	Carbon Content, Pct	Annealing Treatment		Microstructure		Average VHN, 5 Kg Load	Elongation, Pct in ½ in.	Reduction in Area, Pct	Ultimate Tensile Strength, Psi	0.01 Pct Offset Yield Strength, Psi	0.1 Pct Offset Yield Strength, Psi	0.2 Pct Offset Yield Strength, Psi
		Temperature, °C	Time, Hr	Phases Present	α Grain Size, Mm							
TM-33-20	0.16	600	16	α	0.02	180	50	65	59,600	48,600	—	53,800†
TM-33-9	0.16	700	4	α	0.06	156	55	70	59,300	53,400	—	56,100†
TM-33-21	0.16	850	2	α	0.10	164	49	56	55,200	48,900	—	49,900†
TM-33-23	0.16	900	2	α + β*	0.06	165	50	71	57,000	35,200	45,100	47,900
TM-33-7	0.16	910	1	α + β*	—	145	62	71	54,400	25,600	38,100	41,700
TM-33-14	0.16	950	1	β* + TiC	—	151	56	65	52,700	23,400	38,000	41,200
TM-34-20	0.27	600	16	α + TiC	0.02	171	39	64	62,100	44,800	53,500	55,200
TM-34-9	0.27	700	4	α	0.06	162	43	64	59,600	50,100	—	54,600†
TM-34-21	0.27	850	2	α	0.15	190	46	58	62,100	56,700	—	60,300†
TM-34-23	0.27	900	2	α + β*	—	184	58	64	62,200	50,600	—	55,500†
TM-34-7	0.27	910	1	α + β*	—	164	61	72	60,500	31,100	44,800	49,100
TM-34-14	0.27	950	1	β* + TiC	—	138	42	61	50,600	23,400	36,700	39,500
TM-30-20	0.47	600	16	α + TiC	0.02	178	37	56	68,400	58,400	—	59,900†
TM-30-9	0.47	700	4	α + TiC	0.02	185	52	61	71,600	67,000	—	67,900†
TM-30-21	0.47	850	2	α + TiC + β*	0.03	225	51	81	80,000	71,800	—	73,200†
TM-30-23	0.47	900	2	α + β*	—	228	50	64	83,000	71,000	—	76,000†
TM-30-7	0.47	910	1	α + β*	—	193	50	69	73,500	47,800	59,500	62,000
TM-30-14	0.47	950	1	β* + TiC	—	164	42	66	63,900	38,600	47,500	49,000

* β transformed to α on quenching.
† Yield point.

high tensile ductilities are found when the Ti-0.27 pct C alloy is quenched from the α-β field.

Ti-0.47 Pct C Alloy: At the level of 0.47 pct C, the strength properties are greatly increased when the carbon is put in solid solution through the use of increasingly higher α annealing temperatures, and they are decreased sharply when the alloy is quenched from the β-carbide field. There is an increase in the reduction in area value when this alloy is quenched from the α-β field, but this increase is not as marked as it is for the lower carbon-content alloys. This is illustrated by the data shown in Fig. 6. Microstructures of this alloy are given in Fig. 7. The α grains in the 600°C annealed condition are irregular in shape as a result of grain-growth inhibition by carbides and become polyhedral after carbon is put in solution by 850°C annealing.

Of significance is the increase in impact value when the Ti-0.47 pct C alloy is quenched from the β-carbide field. The impact values for the Ti-0.16 pct C and Ti-0.27 pct C alloys decreased when quenched from the β-carbide field. The probable explanation for this is that at 0.47 pct C there are numerous TiC particles present in the as-750°C-swaged condition which act as nucleation sites for additional carbide formation. At 0.16 and 0.27 pct C, there are very few TiC particles present in the swaged condition, and, therefore, the carbides formed by heating into the β-carbide field form as networks of small carbides, thus causing low toughness. As will be illustrated in a later section, the difference in impact values noted here occurs at all testing temperatures.

Comparison of Alloys: A further illustration of how heat treatment can affect the properties of Ti-C alloys is given in Fig. 8, where properties are plotted vs carbon content for three different heat treatments. When a low temperature anneal at 600°C is used, carbon additions strengthen titanium up to the solubility limit at that temperature, about 0.15 pct C. When a high temperature α anneal at 850°C is used, the solid-solution strengthening effect of carbon is

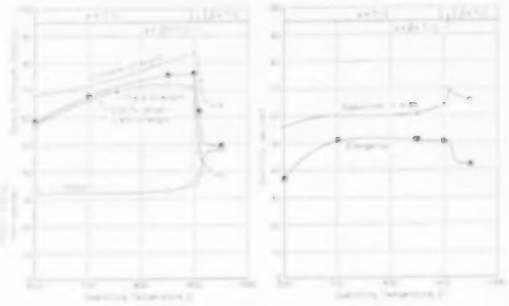

Fig. 6—Properties of a Ti-0.47 pct C alloy.

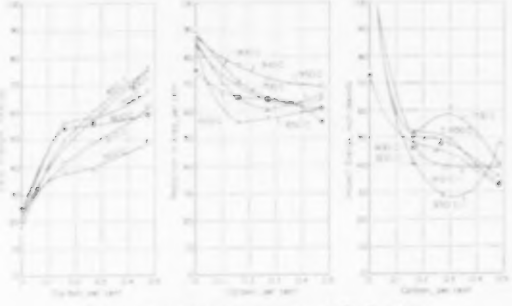

Fig. 8—Mechanical properties of Ti-C alloys.

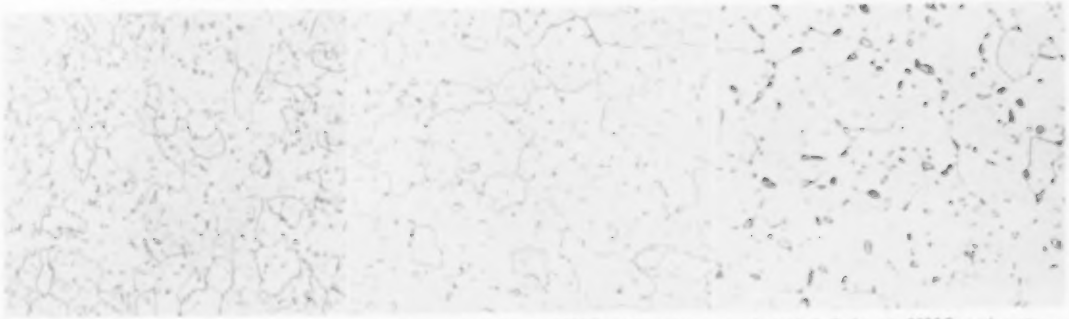

a—Annealed 16 hr at 600°C and water-quenched.

b—Annealed 4 hr at 700°C and water-quenched.

c—Annealed 2 hr at 850°C and water-quenched.

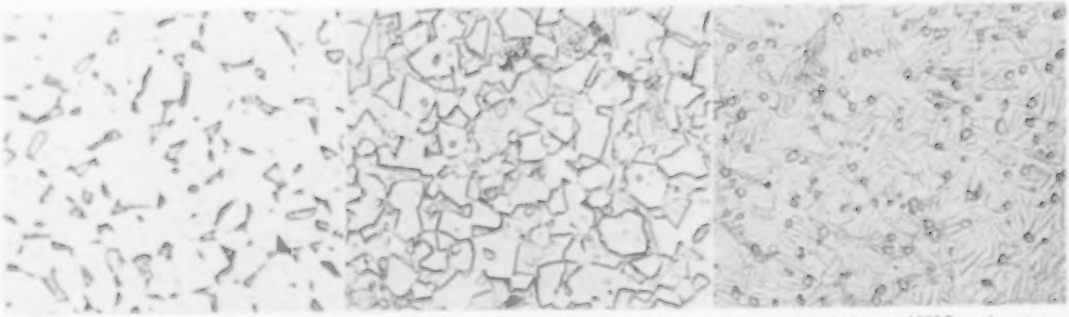

d—Annealed 2 hr at 900°C and water-quenched.

e—Annealed 1 hr at 910°C and water-quenched.

f—Annealed 1 hr at 950°C and water-quenched.

Fig. 7—Microstructures of a Ti-0.47 pct alloy. X250.

obtained up to about 0.45 pct, the solubility limit at that temperature. Quenching from the β-carbide field reduces the amount of carbon in solid solution even below that found at the 600°C anneal and results in the low strength values found. Tensile ductilities and toughness decrease with increasing carbon content, whether in solution or not. Carbon in solid solution appears to decrease tensile ductility and increase toughness slightly.

Effect of Temperature on Impact Resistance

The effects of testing temperature on the impact resistance of titanium-carbon alloys are illustrated in Fig. 9. These data show that, as the quantity of carbon in solid solution is increased, the tendency for a transition from brittle-to-ductile behavior to occur is increased. When these alloys are annealed at 950°C (in the β-carbide field), which results in a very small amount of carbon in solid solution, there is little change in impact value with testing temperature. However, as the annealing treatments are altered so that more carbon is in solid solution, the level of impact value obtained decreases with decreasing temperature. The slope of the impact vs temperature curve increases with increasing carbon content. This is seen by comparing the curves shown in Fig. 9c with those in Fig. 9b. Finally, when sufficient carbon is in solid solution, a definite transition does occur, as shown by the curve for the Ti-0.47 pct C alloy annealed at 850°C (Fig. 9b).

Transformation Structures

Since the solubility of carbon in β titanium is lower than in α titanium, no martensitic type of hardening through supersaturation of the α phase can be expected. Also, as has been pointed out in a previous section, Ti-C alloys are softened by quenching from above the peritectoid temperature. Therefore, transformation hardening as such cannot be considered as a hardening mechanism for these alloys. The β-transformation structure consists of serrated α grains with light subgrain boundaries delineating the α platelets formed from the β. It is also apparent that grain growth in the β-carbide field is inhibited by the presence of carbides.

Grain-Size Effects

Because of the nature of the Ti-C system, it is difficult to separate the effects of grain size from the solid-solution effects except for alloys having low carbon content. Consequently, this discussion will be limited to the Ti-0.16 pct C alloy where it is possible to obtain a variety of α grain sizes without altering the amount of carbon in solid solution. As shown in Fig. 10, increasing the α grain size from 0.02 to 0.10 mm in diam causes a very slight decrease in strength (about the same order of magnitude as found for unalloyed titanium). Reduction in area values are also decreased, although elongation values remain about the same. Impact values are increased with increasing grain size. These results are in general agreement with those reported by the authors for Ti-N and TiAl alloys.[5] The rise in yield strength when going from 0.02 to 0.06 mm grain size is the result of additional solution of carbon on annealing at 700°C as opposed to 600°C.

Effect of Oxygen Additions on Properties of Ti-C Alloys

Oxygen is an α-stabilizing element and has a high solubility in both α and β titanium. Consequently, the effect of oxygen additions on the properties of titanium or titanium-base alloys is to strengthen the

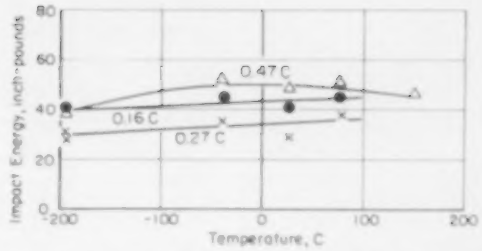

a—Annealed 1 hr at 950°C and quenched. Carbon solubility limit about 0.15 pct.

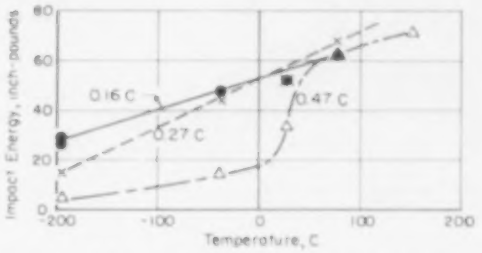

b—Annealed 2 hr at 850°C and quenched. Carbon solubility limit about 0.4 pct.

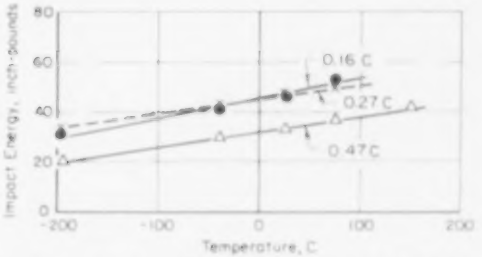

c—Annealed 16 hr at 600°C and quenched. Carbon solubility limit about 0.1 pct.

Fig. 9—Effect of testing temperature on the impact properties of Ti-C alloys.

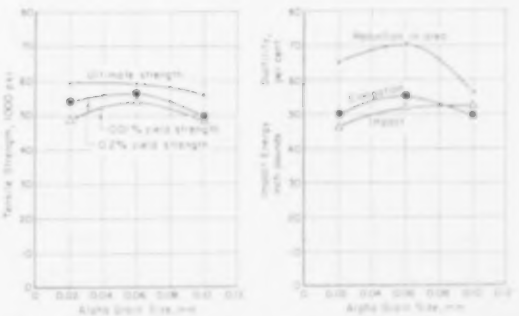

Fig. 10—Effect of α grain size on the properties of a Ti-0.16 pct C alloy.

base metal through solid-solution strengthening, and it would be expected that the combination of oxygen and carbon would be additive in strengthening effect. However, since carbon has a limited solubility in titanium, which does not seem to be affected by the quantities of oxygen present in these alloys, the properties of a ternary Ti-C-O alloy can be altered by heat treatment in the same manner as a

Table III. Tensile Properties of Ti-C-O

Specimen No.	Composition, Pct (Balance Ti)	Annealing Treatment: Temperature, °C	Annealing Treatment: Time, Hr	Microstructure: Phases Present	Microstructure: α Grain Size, Mm	Average VHN, 5 Kg Load	Elongation, Pct in ½ In.	Reduction in Area, Pct	Ultimate Tensile Strength, Psi	0.01 Pct Offset Yield Strength, Psi	0.1 Pct Offset Yield Strength, Psi	0.2 Pct Offset Yield Strength, Psi
TM-5-20	0.19 C-0.12 O	800	16	α	0.05	208	35	50	77,800	60,600	68,400	68,800
TM-5-9	0.19 C-0.12 O	700	4	α	0.07	220	35	59	78,000	70,200	—	74,100†
TM-5-21	0.19 C-0.12 O	850	2	α	0.10	219	41	62	78,000	72,500	—	76,200†
TM-5-19	0.19 C-0.12 O	910	2	α + β*	0.05	202	44	57	70,400	36,400	51,100	67,200
TM-5-14	0.19 C-0.12 O	950	1	α + β* + TiC	—	180	29	46	65,400	30,600	45,600	50,000
TM-5-22	0.19 C-0.12 O	950	2	α + β* + TiC	—	179	34	41	65,200	39,000	50,200	53,800
TM-5-15	0.19 C-0.12 O	1000	1	β* + TiC	—	174	32	42	68,600	36,600	50,800	52,800
TM-6-20	0.38 C-0.2 O	800	16	α + TiC	0.02	220	34	56	84,200	—	—	72,800†
TM-6-9	0.38 C-0.2 O	700	4	α + TiC	0.05	243	37	53	88,600	75,700	—	81,100†
TM-6-21	0.38 C-0.2 O	850	2	α + TiC	0.10	275	38	46	96,300	88,000	—	90,000†
TM-6-19	0.38 C-0.2 O	910	2	α + β*	0.12	264	34	44	97,000	84,600	—	95,200†
TM-6-14	0.38 C-0.2 O	950	1	α + β* + TiC	—	211	30	47	77,700	39,000	54,800	59,500
TM-6-22	0.38 C-0.2 O	950	2	α + β* + TiC	—	187	30	40	78,100	39,500	55,200	60,800
TM-6-15	0.38 C-0.2 O	1000	1	β* + TiC	—	196	27	43	77,200	36,500	55,500	59,400

* Transformed to α on quenching.
† Yield point.

binary Ti-C alloy. The mechanical properties of the Ti-C-O alloys are given in Table III.

By using the same heat treatments used for the binary alloys, it has been found that the strengths of the Ti-C-O alloys are increased as greater amounts of carbon are put into solid solution. This is illustrated by the data shown in Fig. 11 for the Ti-0.19 pct C-0.12 pct O alloy and Fig. 12 for the Ti-0.38 pct C-0.2 pct O alloy. Quenching from the β-carbide field causes a softening effect because of the very low solubility of carbon in the β phase. Tensile-ductility values generally remain high for the heat treatments used, although some loss in ductility, particularly reduction in area, is encountered when the alloys are quenched from the β-carbide field. The increase in ductility values that occurs when the binary Ti-C alloys are quenched from the α-β field does not occur with these alloys. Presumably, this is because the transformed β matrix has been sufficiently hardened with oxygen to preclude high ductilities.

Room-temperature impact values for the Ti-0.19 pct C-0.12 pct O alloy are not altered significantly by heat treatment, although there is a slight decrease when the alloy is quenched from 950° or

Fig. 11—Properties of a Ti-0.19 pct C-0.12 pct O alloy.

Fig. 12—Properties of a Ti-0.38 pct C-0.2 pct O alloy.

Fig. 13—Effect of testing temperature on impact properties of two Ti-C-O alloys quenched from various temperatures.

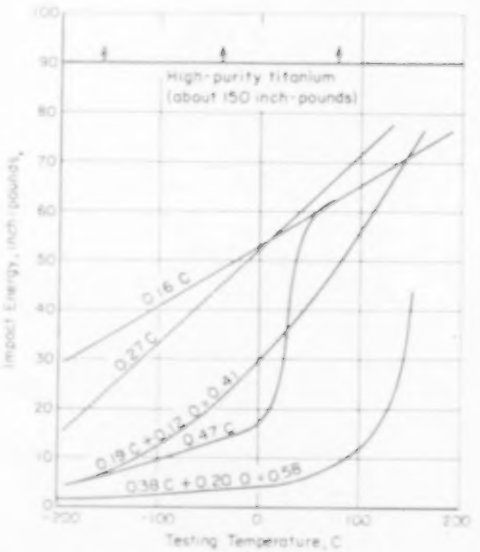

Fig. 14—Effect of testing temperature on the properties of titanium containing various levels of interstitial elements in solid solution. All alloys tested in the 850°C annealed condition.

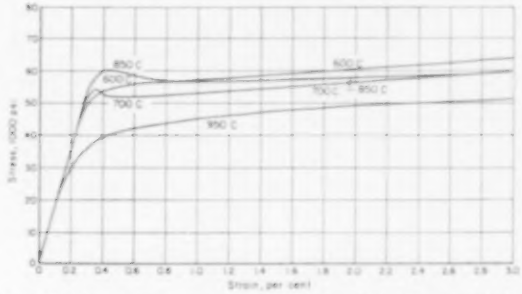

Fig. 15—Stress-strain curves for a Ti-0.27 pct C alloy quenched from several temperatures.

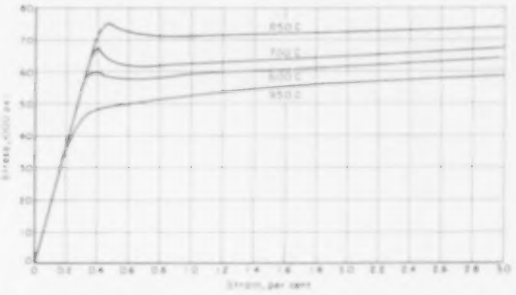

Fig. 16—Stress-strain curves for a Ti-0.47 pct C alloy quenched from several temperatures.

1000°C. The room-temperature impact values for the Ti-0.38 pct C-0.2 pct O alloy are influenced by heat treatment. When this alloy is heat treated so as to put the maximum carbon in solid solution, the room-temperature impact value is the lowest. Impact values decrease as the quantity of carbon in solid solution is increased.

The effect of temperature on the impact properties of the Ti-C-O alloys is illustrated in Fig. 13. For the Ti-0.19 pct C-0.12 pct O alloy no clear-cut transition from ductile-to-brittle behavior is found, but for the Ti-0.38 pct C-0.2 pct O alloy it is readily seen that the transition temperature is a function of heat-treating temperature. In the 850°C quenched condition, where all of the carbon is in solution, the transition occurs at about 125°C. In the 600°C quenched condition, where less carbon is in solution, the transition is about 0°C; and in the 1000°C quenched condition, where there is the least carbon in solution, if a transition does occur it is below —40°C.

It was noted previously for binary Ti-C alloys that the tendency toward transition behavior increases as the quantity of carbon in solid solution is increased. On the basis of the data for Ti-C-O alloys, it appears that the interstitial element, oxygen, also tends to promote a transition behavior. This indicates that interstitial elements, in general, have an adverse effect on the toughness of titanium. Also, it appears that the tendency toward a ductile-to-brittle transition is dependent on the total interstitial content in solid solution in the alloy and not on any particular interstitial element. This is illustrated for alloys containing carbon or carbon and oxygen in Fig. 14. Here it is seen that, as the interstitial content of titanium is increased, there is an increased tendency toward a transition behavior until finally a definite transition occurs. Further additions of interstitial elements raise the transition temperature.

Carbide Precipitation and Solution

The decreasing solubility of carbon in α titanium with decreasing temperature is indicative of a precipitation-hardening system. Indirect evidence indicates that the precipitation of the carbide phase from α titanium proceeds quite rapidly.

Yield Points: When the Ti-C alloys were annealed in the α or α-carbide field, yield points were observed, such as those shown in Figs. 15 and 16. The only cases in 15 such anneals that the yield was not observed was for low temperature 600°C anneals for the Ti-0.27 pct C and Ti-0.19 pct C-0.12 pct O alloys. Annealing so that β is produced, such as in the β-carbide field, resulted in disappearance of the yield point. It appears that carbide precipitation is taking place under conditions of strain, and that the phenomenon observed is strain aging, similar to that observed by Rosi and Perkins[5] in α-annealed commercial titanium (containing 0.05 pct C and 0.08 pct N) at elevated temperatures. The yield point has also been observed by the authors[6] in α-annealed high purity Ti-N alloys containing 0.064 to 0.29 pct N and low carbon from 0.01 to 0.02 pct.

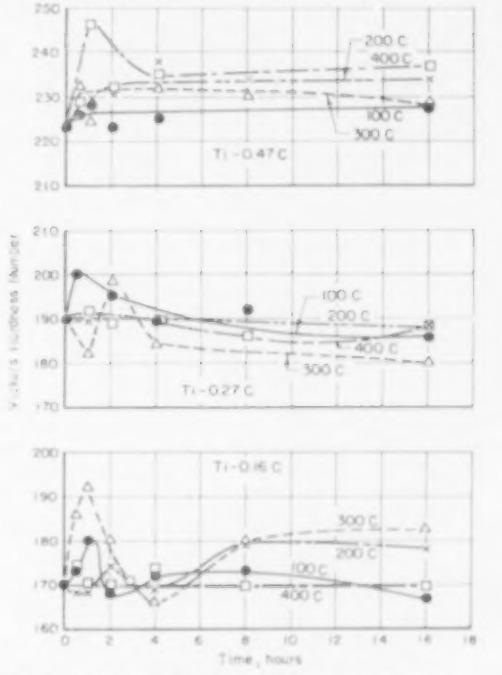

Fig. 17—Effect of aging time at temperatures indicated on the VHN of Ti-C alloys quenched from 850°C.

Precipitation of Carbides: Aging studies carried out on α-quenched Ti-C alloys show that very little hardening response occurs as a result of the precipitation of TiC at temperatures in the range of 100° to 400°C. This is illustrated by the data shown in Fig. 17. In some instances, there is a rise in hardness of about 20 VHN during the first 1 hr of aging. However, within 2 hr the hardness drops to the original hardness level and remains about constant up through 16 hr of aging time. It can be concluded, then, that precipitation hardening as a mechanism for strengthening Ti-C alloys is not practical. Also, it appears that low temperature aging does not cause any significant decrease in hardness from the original as-quenched hardness.

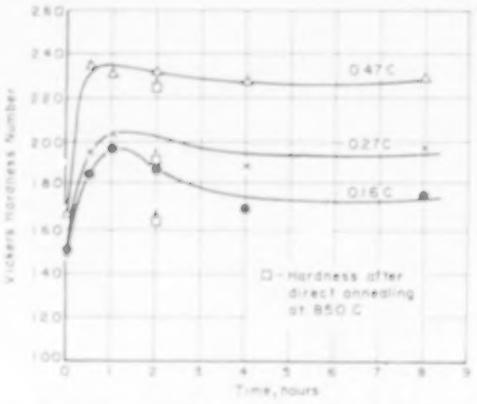

Fig. 18—Effect of reheating time at 850°C on the hardness of Ti-C alloys quenched from the β-carbide field.

Re-Solution of Carbides: The heat treatments performed on the Ti-C alloys illustrate that the carbide phase present in the fabricated condition can be dissolved in the α phase quite readily. The carbide phase formed when alloys are heated into the β-carbide field can also be dissolved in α titanium by reheating below the peritectoid temperature. Since hardness can be directly correlated with soluble carbon content, it is possible to check the time required to dissolve the TiC particles by measuring hardness at different heat-treating times. Fig. 18 shows the effect of time at 850°C on the solution of carbide particles as measured by hardness. It is seen that the hardness increase is greatest in the first half hour, and that after two hours the hardness is greater than it was by direct annealing at 850°C. Actually, a very few carbide particles could be seen in the microstructure after one hour in the Ti-0.16 pct C and Ti-0.27 pct C alloys but not after two hours. In the Ti-0.47 pct C alloy the carbide phase is in equilibrium with α at 850°C, so it is not possible to dissolve all of the particles. However, there appeared to be no change in quantity of carbide present between two and four hours of solution time, indicating that the carbon solubility had been reached in less than two hours. It is believed that the rate of carbide solution is dependent on the size of the carbide particles. Since this variable was not investigated, it is possible that the solution times may vary from those reported here.

Summary

The principal strengthening mechanism found for Ti-C alloys is solid-solution strengthening. Carbon in solid solution in the α phase strengthens titanium; however, at compositions where carbon is present as TiC, increasing the quantity of TiC does not significantly alter the strength. The quantity of carbon in solid solution can be controlled by heat treatments. Quenching from temperatures just below the peritectoid temperature retains the maximum amount of carbon in solid solution. Quenching from the β-carbide field places the alloy in a softer condition than it is in the α-annealed condition because the solubility of carbon in β titanium is quite low. The β phase transforms to α by a martensite reaction on quenching, thus providing a soft α matrix. Tensile ductilities are not changed appreciably by annealing treatments within the α field. Quenching from the β-carbide field lowers the reduction in area and elongation slightly. One interesting change in tensile ductilities occurs when Ti-C alloys are quenched from the α-β field. In this condition, the structure is composed of hard α grains in a matrix of soft α (transformed β); the soft matrix results in high reduction in area values.

The quantity of carbon in solid solution has an effect on toughness. The greater the quantity of carbon in solid solution, the greater is the tendency for the alloy to undergo a transition from brittle-to-ductile behavior. Addition of other interstitial elements, such as oxygen, to a Ti-C alloy increases the tendency for a transition temperature. Carbon present in the alloy as TiC causes a lowering of the magnitude of the impact values but does not appear to cause a transition. The general conclusion from these impact studies is that interstitials in solid solution in titanium cause titanium to undergo a brittle-to-ductile transition and that the higher the interstitial content, the higher is the transition temperature.

The decrease in solubility with decreasing temperature for carbon in α titanium is indicative of an age-hardening system. However, the precipitation of TiC from α titanium at low temperatures (in the range of 300° to 500°C) is so rapid that overaging occurs almost immediately. Therefore, the use of precipitation hardening as a method of improving the strength of Ti-C alloys is not practical.

Acknowledgment

The work described is part of a study of the effect of microstructure in representative titanium alloys prepared with high purity materials. The authors are grateful to Watertown Arsenal and the Army Ordnance Corps for permission to publish this work, which was conducted at Battelle Memorial Institute under Contract No. DA 33-019-ORD 280.

References

[1] R. I. Jaffee, H. R. Ogden, and D. J. Maykuth: Alloys of Titanium with Carbon, Oxygen, and Nitrogen. *Trans.* AIME (1950) **188**, pp. 1261-1266; JOURNAL OF METALS (October 1950).

[2] I. Cadoff and J. P. Nielsen: Titanium-Carbon System. *Trans.* AIME (1953) **197**, pp. 248-252; JOURNAL OF METALS (February 1953).

[3] F. C. Holden, H. R. Ogden, and R. I. Jaffee: Microstructure and Mechanical Properties of Iodide Titanium. *Trans.* AIME (1953) **197**, pp. 238-242; JOURNAL OF METALS (February 1953).

[4] R. I. Jaffee, F. C. Holden, and H. R. Ogden: Mechanical Properties of Alpha Titanium as Affected by Structure and Composition. *Trans.* AIME (1954) **200**, p. 1282; JOURNAL OF METALS (November 1954).

[5] F. D. Rosi and F. C. Perkins: Mechanical Properties and Strain Aging Effects of Titanium. *Trans.* ASM (1953) **45**, pp. 972-991.

Correction

In the November 1954 issue: TP 3858E. *Mechanical Properties of Alpha Titanium as Affected by Structure and Composition* by R. I. Jaffee, F. C. Holden, and H. R. Ogden. On p. 1283, Figs. 1a and 1b have been transposed. Fig. 1a is Fig. 1b and Fig. 1b is Fig. 1a.

Solution Rate of Solid Aluminum in Molten Al-Si Alloy

by C. M. Craighead, E. W. Cawthorne, and R. I. Jaffee

SOLUTION of a solid metal or alloy in a molten metal bath is used daily in melting operations, extractive metallurgical processes, and in brazing. It is generally recognized that temperature, time, agitation, and the composition of the solute metal and the solvent bath all affect solution rate. However, there is little information available in the literature on the kinetics of the process or the relative effect that these variables have on solution rate.

In connection with an aluminum brazing study, data on the solution of aluminum in an Al-Si* bath of approximately eutectic composition were determined. This paper presents quantitative solution-rate data showing the effects that time, temperature, agitation, and composition of the solute metal and solvent bath have on the solution rate of aluminum in Al-Si.

* Al-Si refers to an Al-Si alloy of approximately eutectic (12.5 wt pct Si) composition. Baths containing from 10.5 to 14 wt pct Si were investigated.

Preliminary Work

Composition of the Al-Si Eutectic: Unpublished data, made available by the Hanford Atomic Products Operations of the General Electric Co., indicated that the eutectic in the Al-Si system occurred at 577.2°C and contained 12.5 wt pct Si. This is in contrast to the usually accepted values of 11.6 wt pct Si and 577°C given in the literature.[1,2] In view of the discrepancy between the Hanford data and the literature and the desirability of determining the composition of the Al-Si baths by thermal rather than chemical analysis, the Al-Si system was re-examined in the region of the eutectic.

Six high purity Al-Si alloys, with intended compositions of 5, 8, 11.6, 12.5, 13, and 14 wt pct Si were prepared using 99.91 pct Al and 99.86 pct Si. The high purity silicon powder† was first consolidated by arc-melting in a water-cooled copper crucible using a water-cooled tungsten electrode and an argon atmosphere. This technique is employed extensively for preparing contamination-free titanium alloys and melts of refractory metals.

† Purchased from Electro Metallurgical Co., Lot No. 30008.

The alloys were prepared in a clay-graphite crucible by melting the aluminum and adding the silicon to the melt. The melts were fluxed with chlorine to remove residual sodium.

Chemical and thermal analyses were made on each alloy. The chemical analyses and metallographic examinations were made on 0.250 in. thick chill-cast plates which had been cast in a steel mold to promote rapid solidification. The chemical analyses were made on drillings taken from the cast plates. The results of this work are listed in Table I.

The thermal-analysis data were obtained on 200 gram samples cooled at approximately 1.5° per min. A calibrated chromel-alumel couple was used. The thermal arrests were recorded autographically on a General Electric photoelectric potentiometer recorder. The instrument was calibrated to ±2.5 pct. The thermal emf was bucked with a Leeds and Northrup semiprecision potentiometer so that 1 mv represented the full scale of the GE recorder.

Referring to Table I, it will be noted that the analytical results tend to be lower than the intended compositions by about 0.3 pct Si in the higher ranges. In view of the known difficulties in obtaining accurate silicon determinations by wet analysis when the silicon content is high and in view of the care that was employed in weighing and preparing the alloys, the intended compositions are believed to be more accurate than the analyses. Furthermore, when the thermal-arrest data are plotted against the intended compositions, a smooth curve is obtained, as shown in Fig. 1. This is not the case when the data are plotted against the analytical results.

It will be noted from Table I that the 12.5 pct Si alloy (melt 4) showed a primary arrest at 577.6°C and the eutectic at 576.1°C. The metallographic examination of this chill-cast plate sample showed a small amount of primary silicon. These results, Fig. 1, place the eutectic at slightly less than 12.5 pct Si and are in rather good agreement with the unpublished Hanford data.

In all of the subsequent work, the composition of the Al-Si dipping baths was determined by thermal analysis (spread between the primary arrest and the eutectic temperature) employing 12.5 pct Si and 577.2°C as the composition and temperature of the eutectic.

Material Preparation and Selection of the Techniques: At the beginning of this work, it was anticipated that, owing to oxide film present on the surface of the aluminum, difficulty would be encountered in obtaining rapid uniform wetting of aluminum specimens dipped in the Al-Si bath. The following etchants were investigated as possible methods of providing a thin uniform oxide film on the specimen surface: 1—phosphoric acid (H_3PO_4), 2—fluoboric acid (HBF_4), 3—sodium hydroxide (NaOH), and 4—hydrofluoric acid (HF).

Tests with sheet specimens (2x½x0.06 in.) of 2S aluminum prepared with these etchants indicated that the fast uniform wetting required for this work could not be obtained if any oxide film existed on the specimen surface.

Tests were then conducted by dipping similar specimens etched in 5 pct NaOH and given a thin

C. M. CRAIGHEAD, E. W. CAWTHORNE, and R. I. JAFFEE, Member AIME, are associated with Battelle Memorial Institute, Columbus, Ohio.

Discussion on this paper, TP 3857E, may be sent, 2 copies, to AIME by Mar. 1, 1955. Manuscript, Apr. 15, 1954. Chicago Meeting, November 1954.

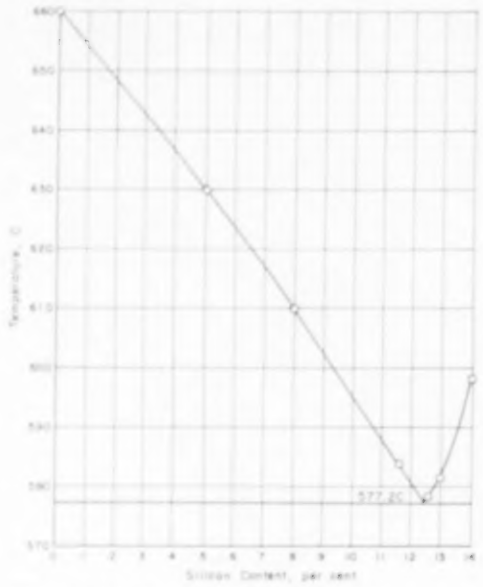

Fig. 1—Composition of the Al-Si eutectic.

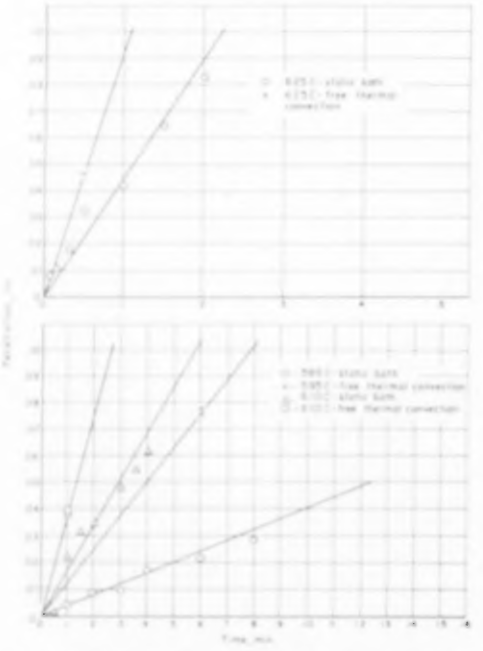

Fig. 2—Effect of thermal convection on the solution of 2S aluminum in the 20 lb Al-Si bath at various temperatures.

brushed coating of Alcoa No. 33* brazing flux. The unpreheated fluxed specimens dipped in Al-10.7 pct Si alloy at 610°C were wet uniformly at dipping times ranging from 2 to 180 sec.

Metallographic examination of the prefluxed sheet specimens showed a clearly defined and continuous aluminum-Al-Si interface. Preliminary measurements of the thickness of these dipped specimens indicated that direct measurement of the specimen before and after dipping would provide greater accuracy than could be attained by using techniques involving specimen weight changes or compositions.

In the preliminary work with sheet specimens it was evident that edge effects would cause an excessive reduction of thickness at the edges of the specimen. Thus it would be impossible to section the dipped specimens to give a truly representative area for measurement. It was decided, therefore, to use cylindrical specimens (7/16 in. diam by 2¼ in. long) in this investigation.

While the furnace equipment for this work was being constructed, several series of fluxed and preheated rod specimens were run in a 5 lb Al-Si bath at 610°C. When these runs were repeated in the 20 lb bath, under otherwise identical conditions, it was immediately evident that there was a marked increase in solution rate in the larger bath. This higher solution rate, attributed to the increased thermal convection currents existing in the larger bath, indicated the necessity for establishing standard static conditions for conducting the investigation. Several tests, made by dipping rod specimens inside a 1⅝ in. ID graphite tube suspended in the 20 lb bath, showed that this technique could be utilized to minimize bath convection currents around the dipped specimen. A comparison of the solution rate of 2S aluminum in the 20 lb bath inside the carbon tube and with the carbon tube removed is shown in Fig. 2.

In preliminary runs to study the effect of agitation on solution rate, a vertical reciprocating motion was imparted to the specimen; however, the flow of molten Al-Si along the specimen resulted in excessive solution at both the top and the bottom of the specimen. The data reported on the effect of agitation were obtained by rotating the dip specimens in the 20 lb Al-Si bath with the graphite tube removed.

Table I. Results of Chemical and Thermal Analyses and Metallographic Examinations of High Purity Al-Si Alloys

Melt	Silicon Content, Wt Pct: Intended	Chemical Analysis	Primary Arrest, °C	Eutectic Arrest, °C	Results of Metallographic Examination
1*	5.0	4.9	629.8	576.7	Primary aluminum
2	8.0	8.0	609.9	577.6	Primary aluminum
3	11.6	11.3	583.7	576.4	Primary aluminum
4	12.5	12.2	577.6	576.1	Primary silicon
5	13.0	12.7	581.3	578.0	Primary silicon
6	14.0	13.7	598.0	578.2	Primary silicon
		Average eutectic arrest		577.2	

* Less than 0.05 pct Fe, 0.05 pct Cu, and 0.03 pct Mn by spectroscopic analysis.

Equipment and Techniques Used in Determining Solution Rate

Furnace and Dipping Equipment: The equipment used in the static dipping of aluminum rod specimens is shown schematically in Fig. 3. The 20 lb Al-Si alloy bath, prepared from 99.75 pct Al and 98 pct Si, was contained in a Dixon No. 20 clay-graphite crucible held in a resistance-heated pot-type furnace. The furnace temperature was controlled with a Foxboro automatic controller and a chromel-alumel thermocouple suspended between the crucible wall and the furnace winding. Bath temperature

* A proprietary mixture of chlorides and fluorides of alkali metals; exact composition not available; melting range of 490° to 600°C.

was determined with a semiprecision potentiometer and a calibrated chromel-alumel thermocouple, in a Sauereisen* cement-coated stainless-steel protection tube, suspended in the molten bath. The maximum deviation in temperature on holding the Al-Si bath for extended periods, up to 32 min in the case of the maximum immersion time, was ±2.0°C.

* Sauereisen Insa-Lute Hi-Temp Cement, No. 7.

The aluminum specimens (7/16 in. diam by 2¼ in. long) were drilled and tapped to a depth of ⅜ in. and suspended on the threaded end of a ¼ in. stainless-steel rod. A metal bracket mounted on the top of the furnace shell served to hold the specimen at a fixed depth in the center of a 1⅝ in. ID by 6 in. graphite tube, held in position by a steel spider resting on the furnace cover. Dilution of the Al-Si inside the tube was minimized by removing the tube and stirring the bath after dipping each specimen.

The rotated specimens, for the determination of the effect of agitation on the solution rate, were mounted on a ¼ in. stainless-steel rod held in the chuck of a Cenco variable-speed stirrer (Type NS1-12). Because of space limitations, dipping was conducted under conditions of free thermal convection with the graphite tube removed from the bath. The specimen velocity was based on the peripheral speed of a rod specimen with an initial nominal diameter of 7/16 in.

Specimen Preparation and Dipping: The aluminum rod specimens used in this work were cut from 7/16 in. diam extruded rod. The 2S aluminum alloy was purchased through commercial sources. The other aluminum alloys were prepared and fabricated at Battelle.

Analyses of the aluminum alloys are listed in Table II.

One end of each 2¼ in. long specimen was drilled and tapped for attachment to the suspension rod. The specimens were then prepared as follows: 1—degrease in acetone, 2—etch 20 sec in 5 pct NaOH at 70° to 80°C, 3—wash in cold running water, 4—dip in 50 pct HNO_3, and 5—wash in cold running water.

After the specimen diameter was measured, the upper ¾ in. of each specimen was coated with Aquadag or Sauereisen No. 7 cement to provide an unattacked bearing surface for clamping in the vise of a metallographic specimen cutter. The remaining surface was given a thin brushed coating of Alcoa No. 33 brazing flux.

The coated specimens were mounted on the stainless-steel suspension rod or on the rod held in the chuck of the variable-speed stirrer and preheated by holding 4½ to 5 min in a resistance-heated tube furnace maintained at bath temperature. The preheated specimens were immersed immediately in the dipping bath, held for the desired time, as measured by a stop watch, then pulled and quenched in cold water. Several series of rod specimens after static dipping at 600°C are shown in Fig. 4.

In dipping rotated specimens at the higher rates of agitation, it was necessary to immerse the specimen in the molten bath alloy before starting rotation in order to prevent "throw-off" of the molten flux, with resultant incomplete wetting at the specimen surface. Specimens dipped at higher rates of agitation were given a 10 sec static dip before starting the timed dipping period. Blanks for determination of initial diameter were given a 10 sec static dip at corresponding temperatures.

Measurement of Solution: With the exception of 16 of the more irregular specimens resulting from dipping at the higher rates of agitation, all solution measurements were determined by direct measurement of specimen diameter before and after dipping.

The initial diameters of the etched specimens were determined to an accuracy of 0.0001 in. by micrometer caliper. After dipping, four transverse sections from the attacked area of each specimen

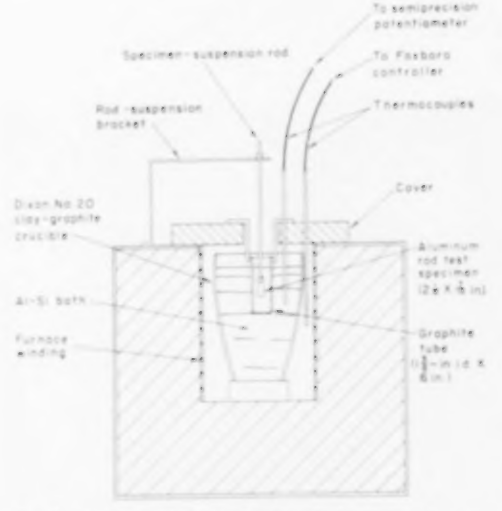

Fig. 3—Equipment for static dipping of aluminum rod specimens.

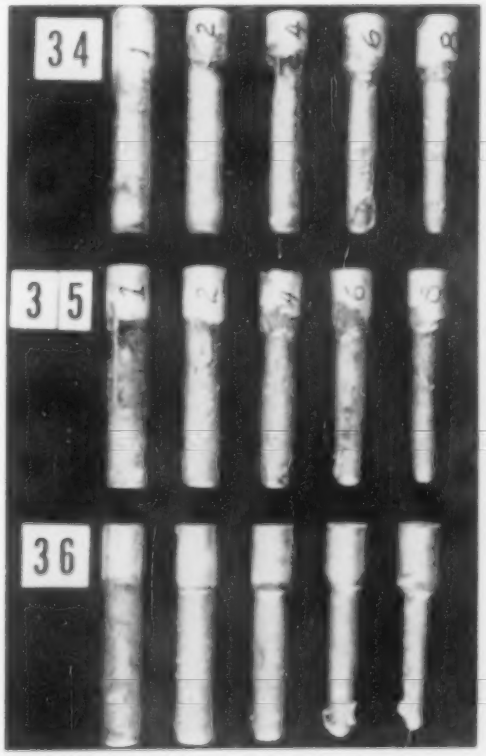

Fig. 4—Typical 7/16 in. diam rod specimens after a static dip at 600°C. Time of dipping, in min, is indicated on each specimen.

Table II. Analyses of the Aluminum Alloys

Lot	Designation	Composition, Wt Pct							
		Si	Fe	Cu	Mn	Mg	Zn	Cr	Ti
1	2S	0.13	0.40	0.12	0.012	<0.001	<0.1	<0.02	<0.008
2	2S	0.11	0.40	0.15	0.008	<0.001	<0.1	<0.02	<0.023
3	2S	0.15	0.54	0.11	0.01	0.03	<0.1	<0.01	<0.01
4	2S	0.15	0.53	0.11	0.01	<0.01	<0.1	<0.01	<0.01
Heat 9480	99.5	0.14	0.28	—	—	—	—	—	—
Heat 9481	99.8	0.06	0.08	—	—	—	—	—	—
Heat 9482	99.8 + 0.35Mg	0.06	0.08	—	—	0.30	—	—	—
Heat 9483	63S	0.46	0.26	—	—	0.71	—	—	—

were mounted, polished, and etched with 0.5 pct HF to delineate the aluminum-Al-Si interface.

Typical microstructures of specimens dipped at 600°C under static conditions and at an agitation rate of 2.5 fps are shown in Fig. 5.

As illustrated, there is a thin precipitated layer of primary aluminum at the interface between the 2S and the Al-Si. The absence of constituents in this zone which are present in the 2S identifies this area as primary aluminum which has precipitated from the adhering molten Al-Si on quenching. These micrographs clearly illustrate that the solution of the 2S has been by uniform dissolution, rather than by intergranular attack. This appearance was characteristic of all of the alloys and baths and aided in delineating the boundary. All measurements were made from the base of this primary aluminum zone.

In Fig. 5, where the grain boundaries of the 2S are made evident by heavy etching, it appears that the primary aluminum dendrites are oriented with respect to the grains in the underlying 2S.

Using a Gaertner traveling microscope, reading to an accuracy of 0.005 mm at X100, four measurements of final diameter were made on each of the four sections by rotating the section 45° between readings. The average value of the 16 measurements was taken as the diameter of the specimen. In a typical case involving 5 tests at 585°C ranging in duration from 4 to 32 min, the maximum standard deviation from the average diameter was ±0.0046 in. The average penetration was calculated as one half the difference between the initial and final diameters. Solution-time curves plotted from these data showed a linear relation between the amount of solution and the time of immersion. Solution-rate data were calculated from these curves. A typical time-penetration curve is shown in Fig. 6.

Where irregularity of the dipped specimen precluded direct measurement of final diameter, as in the case of a number of the specimens dipped at higher rates of agitation, the mounted sections were photographed at X15 or X20. The photographs were cut out along the aluminum-Al-Si interface and the amount of solution was calculated on the basis of the weight of the cut-out photograph of the attacked section and the weight of the printing paper per unit area as determined for each photograph.

The results of this study, covering the effect of bath temperature, silicon content of the bath, agitation, metal purity, and the iron content of the bath, on the solution rate of aluminum in molten Al-Si are given in the following sections of this paper. Because of the large number of measurements, the results are summarized in graphical and tabular form.

Effects of Bath Temperature and Silicon Content of Bath on the Solution Rate of 2S Aluminum in Al-Si

Static solution rates of 2S aluminum were determined at temperatures of 585°, 595°, 600°, 610°, and 625°C for Al-Si baths containing 10.5, 11.8, 12.5, and 14 pct Si. In all cases, the silicon content of the bath was established by thermal analyses. These Al-Si baths were prepared from 99.75 pct Al and 98 pct Si. The iron content did not exceed 0.33 pct and other impurities, copper, manganese, magnesium, etc., were low.

Specimen-immersion times in the Al-Si baths ranged from a minimum of 5 sec at 625°C to a maximum of 32 min at 585°C. The solution rates, as derived from these data, are listed in Table III. In several cases, the solution rates reported in Table III are averages of two determinations. The agree-

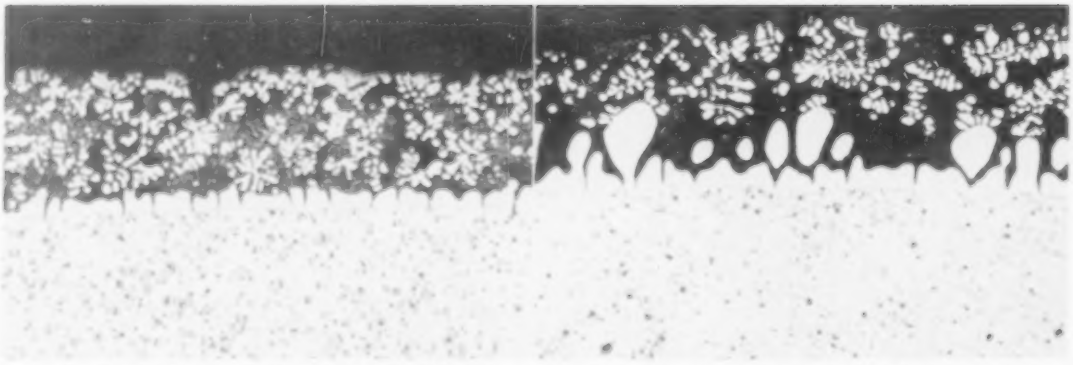

a—Dipped under static conditions for 2 min at 600°C. Heavily etched in 0.5 pct HF. X250. Area reduced approximately 40 pct for reproduction.

b—Dipped 20 sec at 600°C with an agitation rate of 2.5 fps. Heavily etched in 0.5 pct HF. X250. Area reduced approximately 40 pct for reproduction.

Fig. 5—Typical microstructures of 2S aluminum rod specimens dipped under static and nonstatic conditions.

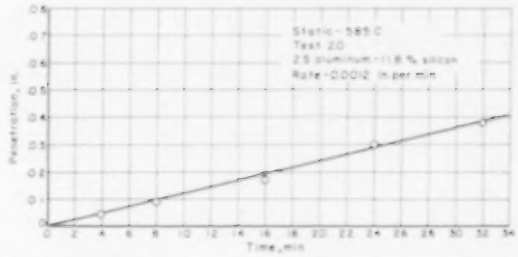

Fig. 6—Typical time-penetration curve for 2S aluminum in Al-Si (11.8 pct Si) at 585°C.

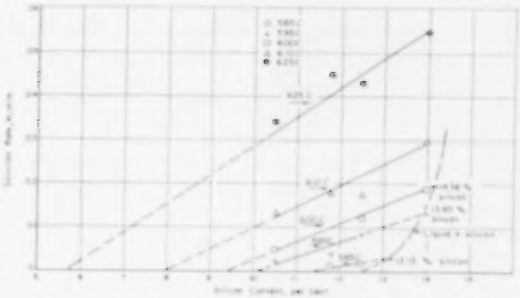

Fig. 7—Effect of silicon content on the solution rate of 2S aluminum in Al-Si at 585°, 595°, 600°, 610°, and 625°C.

ment between individual values was considered excellent and showed a high order of reproducibility.

Fig. 7 is a plot of the solution-rate data vs silicon content of the bath for the five operating temperatures. In this graph, the curves for each of the operating temperatures extrapolate to zero solution rate at the silicon content corresponding to the primary thermal arrest for the given temperature (e.g., the liquidus). Aluminum is in equilibrium with the bath at or below the liquidus, and the solution rate of the aluminum specimen would be zero.

The solution-rate curves also have been extrapolated for each temperature to the silicon content corresponding to the liquidus on the hypereutectic side. This was done to show the limits over which the Al-Si bath would operate in the liquid range. The solution rates of aluminum in hypereutectic baths would continue to be high up to and past the liquidus point. The best curves drawn through the experimentally determined points are straight lines extending from a minimum to a maximum solution rate.

It is evident from foregoing discussion that the temperature difference between the operating temperature of the bath and the liquidus temperature for a bath of a given silicon content is an important variable. Temperatures of only a degree or so above the primary thermal arrest for hypoeutectic silicon alloys should produce a minimum solution rate, as shown in Fig. 7.

Solution-rate curves based on the ΔT existing between the temperature of the primary arrest and the operating temperature of the bath were prepared for each of the compositions investigated (10.5, 11.8, 12.5, and 14 pct Si).

Fig. 8, based on data obtained from these curves, shows the solution rate vs silicon content for constant ΔT's of 5°, 10°, 15°, 20°, and 25°C. This family of curves shows that, for any ΔT, the minimum solution rate is obtained when the bath contains between 11.8 and 12.5 pct Si. Above the eutectic concentration (12.5 pct Si), the solution rate of 2S aluminum in Al-Si increases very rapidly.

Fig. 9 is a plot of solution rate vs 1/T(absolute). The solution rates employed in these graphs have been taken from the straight-line relationship established in Fig. 7, rather than the actually determined experimental values. It will be noted that, for each concentration of silicon, there is a temperature zone wherein the straight-line relationship of log solution rate vs 1/T(absolute) holds. The slopes of the straight-line part of the curves corresponds to a heat of activation for the solution process of about 75,000 cal per mol of aluminum. This heat of activation might be considered as a heat of solution. Actually, not much significance is attached to

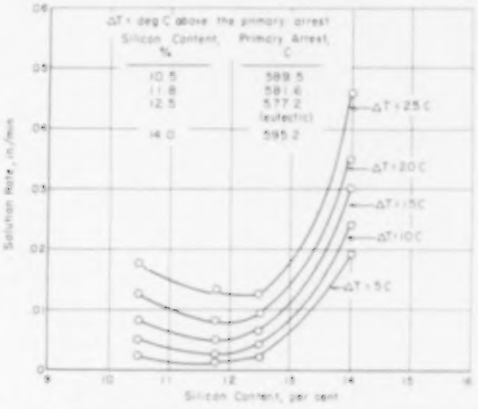

Fig. 8—Curves showing the optimum silicon contents for minimum solution rate at various operating temperatures.

it because the curves are not straight lines as the liquidus temperatures are approached. Practically, the lines could be extrapolated to find solution rates that could be expected at higher temperatures.

Effect of Agitation

Solution rates of 2S aluminum in eutectic Al-Si (12.5 pct Si) were determined at 585° and 600°C for agitation rates ranging from 0.5 to 2.5 fps. The agitation was obtained by rotating the 7/16 in. diam specimen at the appropriate rpm to give the selected

Table III. Effect of Silicon Content of the Al-Si Bath on the Solution Rate* 2S Aluminum at 585°, 595°, 600°, 610°, and 625°C

Series No.	Bath Temperature,** °C	Silicon Content of Bath,† Wt Pct	Solution Rate, In. per Min
56	595	10.5	0.0024
57	600	10.5	0.0051
58	610	10.5	0.0132
59	625	10.5	0.0340
20	585	11.8	0.0012
14 and 19	595	11.8	0.0040
13 and 18	610	11.8	0.0177
16	625	11.8	0.0480
21 and 48	585	12.5	0.0018
22 and 43	590	12.5	0.0084
23 and 49	600	12.5	0.0123
24	610	12.5	0.0175
25	625	12.5	0.0430
42	600	14.0	0.019
61	610	14.0	0.030
60	625	14.0	0.055

* Static conditions: specimen dipped in 1¾ in. ID graphite tube suspended in bath.
** ±2.0°C.
† Determined by thermal analysis.

Fig. 5—Typical microstructures of 2S aluminum rod specimens dipped under static and nonstatic conditions.

Table IV. Effect of Agitation Rate* on the Solution of 2S Aluminum in Al-Si (12.5 pct Si)

Series No.	Bath Temperature,** °C	Silicon Content of Bath,† Wt Pct	Agitation Rate, Fps	Solution Rate, In. per Min
21 and 48	585	12.5	Static††	0.0018
27	585	12.5	0.5	0.0193
28 and 28A	585	12.5	2.5	0.0630
25 and 49	600	12.5	Static††	0.0123
29 and 29B	600	12.5	0.5	0.086
31	600	12.5	1.0	0.119
32	600	12.5	1.5	0.150
33	600	12.5	2.0	0.190
36	600	12.5	2.5	0.210

* Specimens of 3/16 in. diam rotated in bath without graphite tube.
** ±2.0°C.
† Determined by thermal analysis.
†† Specimen dipped in 1¾ in. ID graphite tube suspended in bath.

linear velocity at the periphery. A reciprocating motion, as noted earlier, was found to give excessive solution at the top and bottom of the specimen and therefore could not be employed to establish solution rates. At the higher agitation rates, the coating of brazing flux was removed rapidly from the surface of the specimen and nonreproducible results were obtained. With the higher agitation rates, a 10 sec static immersion, to permit initial uniform attack on the specimen, was employed. In many cases the agitated specimens were too irregular in cross-section for measurements with the traveling microscope. These specimens were sectioned, polished, etched, and photographed at X15 to X20. The average solution was determined as described in the section "Measurement of Solution."

The solution rates, as derived from plots of the data similar to Fig. 6, are listed in Table IV. Fig. 10 is a plot of the solution-rate data vs agitation rate for the two temperatures. It is immediately evident that agitation greatly accelerates the solution of 2S aluminum in eutectic Al-Si at a constant temperature.

The effect of agitation is roughly linear with peripheral velocity; the rates increase about 16 times from static to 2.5 fps at 600°C and about 40 times at 585°C. The slope of the 600°C curve corresponds to an increase in rate of about 0.1 in. per min penetration for each ft per sec increase in peripheral velocity. At 585°C, the rate increases about 0.035 in. per min for each ft per sec increase in velocity.

The potent effect of temperature carries over to the agitated specimens. An increase in temperature of 15°C almost triples the solution rate at agitation rates of 0.5 to 2.5 fps. Of the variables studied in this investigation, agitation rate and temperature were found to be the most significant factors. In work on baths with silicon contents ranging from 10.5 to 14.0 pct Si, silicon contents in excess of the eutectic composition were also found to affect solution rate markedly, as shown in the previous section.

Effect of Metal Purity and Bath Impurities

The effect of the composition of the aluminum alloy used for dipping was investigated using static conditions, temperatures of 585° and 600°C, and a eutectic Al-Si (12.5 pct Si) bath. The metal purity varied from 2S (99 pct Al) to 99.8 pct Al. In addition to the above material, 99.8 pct Al with 0.3 pct added magnesium and alloy 63S were tested. The analyses of the 2S rods and the alloys prepared for these tests are listed in the section on "Furnace and Dipping Equipment."

The solution rates derived from plots of the data similar to Fig. 6 are listed in Table V. At 585°C, there appears to be no trend as the purity of the aluminum is increased from 99 to 99.8 pct. The solution rates of 99.5 and 99.8 pct Al are both higher than the solution rate of the 2S metal. However, the solution rate with high purity 99.8 pct Al is lower than that of the less pure 99.5 pct Al. At this temperature, the 99.8 pct Al with 0.3 pct added mag-

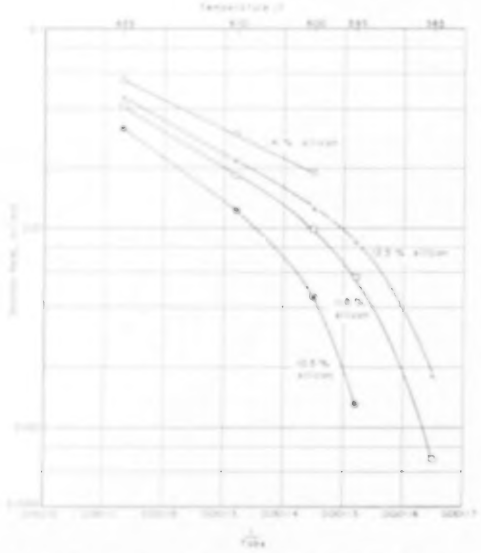

Fig. 9—Relationship between solution rate and absolute temperature. Solution rate data taken from Fig. 7.

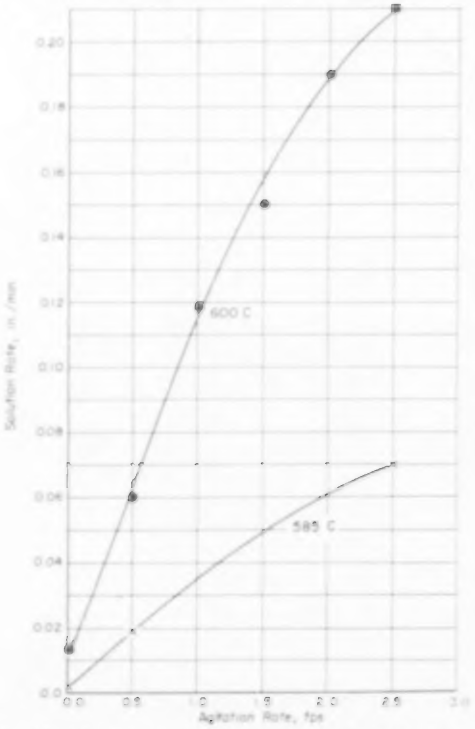

Fig. 10—Effect of agitation on the solution rate of 2S aluminum in Al-Si (12.5 pct Si) at 585° and 600°C.

Table V. Effect of Metal Purity on the Static Solution Rate* of Aluminum in Al-Si (12.5 pct Si) at 585° and 600°C

Series No.	Metal	Bath Temperature,** °C	Silicon Content of Bath,† Wt Pct	Solution Rate, In. per Min.
21 and 48	99 pct Al	585	12.5	0.0018
38	99.5 pct Al	585	12.5	0.0024
39	99.8 pct Al	585	12.5	0.0021
40	99.8 pct Al + 0.3 pct Mg	585	12.5	0.0014
41 and 42	63S	585	12.5	0.0014
23 and 49	99 pct Al	600	12.5	0.0123
34	99.5 pct Al	600	12.5	0.009
35	99.8 pct Al	600	12.5	0.008
36	99.8 pct Al + 0.3 pct Mg	600	12.5	0.011
37	63S	600	12.5	0.010

* Specimen dipped in 1¾ in. ID graphite tube suspended in bath.
** ±2.0°C.
† Determined by thermal analysis.

nesium and alloy 63S had identical solution rates, and their solution rates were lower than that of 2S.

At 600°C, the solution rates of all of the alloys were lower than that of the 2S, with the high purity 99.8 pct Al showing the lowest solution rate.

As a result of this limited investigation of the effects of metal purity on the solution of aluminum in eutectic Al-Si, it is concluded that, although minor differences may exist between the various alloys, metal purity itself is not a major variable.

Iron is the chief impurity present in Al-Si alloys. The effect of the iron content of the Al-Si bath on the solution rate of 2S aluminum was investigated for eutectic alloys using static conditions and two temperatures, 585° and 600°C. Baths with iron contents ranging from 0.20 to 0.74 pct were employed.

The solution rates with four levels of iron are listed in Table VI. Fig. 11 is a plot of the solution rates at 585° and 600°C vs iron content. These data show that, by increasing the iron content of the bath to concentrations in excess of about 0.5 pct, the solution rate of 2S aluminum in the eutectic Al-Si bath is markedly lowered. This finding is considered to be of considerable importance and should be investigated more fully. It is known that iron lowers the corrosion resistance of Al-Si and this may be a limiting factor in application.

Conclusions

Quantitative solution-rate data for the solution of 2S aluminum and some aluminum alloys in molten Al-Si have been obtained for a number of operating

Table VI. Effect of Iron on the Static Solution* of 2S Aluminum in Al-Si (12.5 pct Si) at 585° and 600°C

Series No.	Bath Impurity, Wt Pct	Bath Temperature,** °C	Silicon Content of Bath,† Wt Pct	Solution Rate, In. per Min
21 and 48	††	585	12.5	0.0018
50	0.42 Fe	585	12.5	0.0019
52	0.58 Fe	585	12.5	0.0010
54	0.74 Fe	585	12.5	0.0005
23 and 49	††	600	12.5	0.0123
51	0.42 Fe	600	12.5	0.0119
53	0.58 Fe	600	12.5	0.0110
55	0.74 Fe	600	12.5	0.0094

* Specimen dipped in 1¾ in. ID graphite tube suspended in bath.
** ±2.0°C.
† Determined by thermal analysis.
†† Average of two determinations in normal Al-Si bath containing 0.20 pct Fe and 0.24 pct Fe.

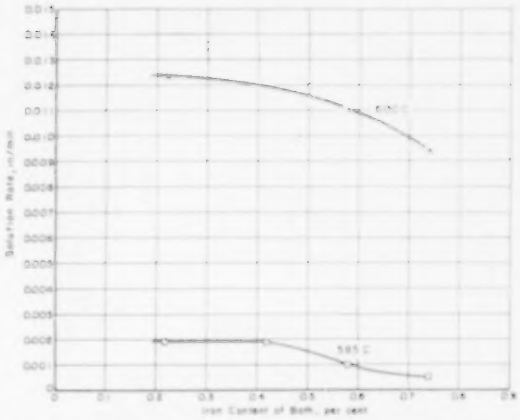

Fig. 11—Effect of iron content of the bath on the solution rate of 2S aluminum in Al-Si (12.5 pct Si) at 585° and 600°C

conditions. Static tests conducted at 585°, 595°, 600°, 610°, and 625°C, for baths containing 10.5, 11.8, 12.5, and 14 pct Si, show a linear relation between the time of immersion at a constant temperature and the depth of penetration. Temperature was found to increase markedly the solution rate. For example, with the 10.5 pct Si bath, the solution rate at 595°C was 0.0024 in. per min. At 625°C, the solution rate was 0.034 in. per min, 14 times the solution rate at 595°C. For a given ΔT (difference between the primary thermal arrest of the Al-Si bath and the operating temperature), the optimum concentration of silicon for minimum penetration lies between 11.8 and 12.5 pct Si. With silicon concentrations in excess of 12.6 pct, the solution rate increases rapidly for any selected ΔT.

The effect of agitation was studied using a eutectic Al-Si bath at two temperatures, 585° and 600°C. Agitation, measured in peripheral speed, at constant temperature greatly increases the solution rate of 2S aluminum, the increase being roughly linear with increasing peripheral speed. With an increase in temperature of 15°C, the solution rate was almost tripled at any fixed agitation rate between 0.5 and 2.5 fps.

The effect of the purity of the aluminum being dipped was investigated using a eutectic Al-Si bath and two temperatures, 585° and 600°C. Although minor differences in the solution rates of the various alloys were obtained, metal purity itself is not a major variable.

Iron in the Al-Si bath in concentrations in excess of about 0.5 pct greatly lowered the solution rate of 2S aluminum at 585° and at 600°C.

Acknowledgments

The authors wish to express their appreciation to Richard D. Bucheit and Robert B. Ashbrook for their invaluable assistance during the course of this investigation. Work was performed under AEC Contract W-7405-eng-92.

References

[1] E. H. Dix, Jr. and A. C. Heath, Jr.: Equilibrium Relations in Aluminum-Silicon and Aluminum-Iron-Silicon Alloys of High Purity. *Proceedings* AIME Institute of Metals Division (1928) **78**, p. 164.

[2] A. G. C. Gwyer and H. W. L. Phillips: Constitution of Alloys of Aluminum with Silicon and Iron. *Journal* Institute of Metals (1927) **38**, p. 29.

Mobilities in Diffusion in Alpha Brass

by G. T. Horne and R. F. Mehl

Diffusion coefficients and mobilities were determined as functions of concentration in the α phase of the Cu-Zn system. Use was made of incremental diffusion couples to determine the Kirkendall effect at various concentrations. Darken's analysis was used to calculate the individual diffusion coefficients and mobilities from these data. The general diffusion coefficient is a single-valued function of the concentration in this system to within the limits of accuracy of the experimental methods used. The form of the various functions (diffusion coefficients and mobilities) of concentration is the same in every case; it is essentially the same as the usual *D* vs c curve.

As Darken[1] has pointed out, the knowledge that the movements of different atoms diffusing in the same lattice need not proceed at the same rate is old. Ionic lattices are the classical examples; application of the generalization to lattices with metallic bonding was much more slowly accepted. It remained for Kirkendall[2] to show clearly that metallic diffusion need not be symmetrical with respect to both species. Several investigators[3-5] have confirmed the initial observation of a "Kirkendall effect:" marker movement accompanying diffusion. They have extended it to other systems and conditions. The theoretical interpretations have been many;[6] one of the first and simplest of these is that of Darken[1] which is essentially mechanism independent. Darken has shown that the Kirkendall experiment permits a calculation of the individual diffusion coefficients and, coupled with activity data, offers a means of measuring the mobilities of the separate atoms in a binary diffusion process.

There is no published information on the effects of concentration and temperature on the individual diffusion coefficients or on the mobility values in binary solid solution; this paper provides such information for zinc and copper in α brass.

For purposes of clarity, the overall *D* value obtained, for example, from the Boltzmann-Matano solution to Fick's law, will be designated as the "general diffusion coefficient," and the diffusion coefficients for the separate diffusing species will be designated as the "individual diffusion coefficients."

G. T. HORNE, Junior Member AIME, and R. F. MEHL, Member AIME, are Assistant Professor and Professor, respectively, Dept. of Metallurgical Engineering, Carnegie Institute of Technology, Pittsburgh.

Discussion on this paper, TP 3864E, may be sent, 2 copies, to AIME by Mar. 1, 1955. Manuscript, Feb. 15, 1954. Chicago Meeting, November 1954.

This paper is based on a portion of a thesis by G. T. Horne submitted in partial fulfillment of the requirements for the degree of Doctor of Philosophy to the Graduate Committee, Carnegie Institute of Technology.

Experimental Procedure

The authors have accepted Darken's[1] analysis and have measured mobilities on this basis. The findings of da Silva and Mehl[7] are accepted: that the Matano interface, defined as the origin of coordinates for the Boltzmann-Matano solution to Fick's law, coincides with the original weld interface; that the "shift" of a marker is the distance between the Matano interface and the marker; that the observed porosity is too small sensibly to affect this result; and that the shift is a linear function of the Matano area, the area defined as the absolute magnitude of the area on either side of the Matano interface.

Alloys: The α-phase of the Cu-Zn system was chosen for investigation. The measurements were made on incremental couples for two separate reasons: 1—it has been questioned whether *D*, the general diffusion coefficient, is a single-valued function of concentration (a comparison of the *D*-values for couples with small concentration range, e.g., 10 vs 20 pct Zn, against those from a wide concentration range, e.g., 0 vs 30 pct Zn, will answer that question); and 2—on the Darken analysis, the mobility can be determined only at the concentration at which the marker is observed to lie (this is but one concentration in a single couple) but choosing a series of incremental couples in the range between 0 and 30 pct Zn provides mobility values at several concentrations, thus giving mobility as a function of concentration. Four alloys were chosen; nominally, pure copper, copper with 10 pct Zn, copper with 20 pct Zn, and copper with 30 pct Zn. This allowed six different types of diffusion couples to be prepared, promising mobility determinations at six different concentrations, but having a minimum range of 10 pct Zn. The copper was an especially prepared pure copper supplied through the courtesy of the Ameri-

Table I. Analyses of Alloys Used in This Investigation

Alloy (Nominal)	Constituent, Wt Pct											Constituent, Atomic Pct	
	Cu	Zn	Pb	Fe	Sn	Sb	Ni	Bi	As	Te	C	Cu	Zn
Cu	—	—	0.0001	0.0001	nil	0.0001	0.0002	0.00001	0.0005	0.0001	Saturated	100	0
Cu-10 pct Zn	90.18	9.80*	0.005	0.01	—	—	—	—	—	—	—	90.4	9.6
Cu-20 pct Zn	80.20	19.75*	0.005	0.01	—	—	—	—	—	—	—	80.6	19.4
Cu-30 pct Zn	70.04	29.90*	0.02	0.05	0.02	—	—	—	—	—	—	70.6	29.4

* Zinc analyses by difference only.

can Smelting and Refining Co.; the 30 pct Zn alloy was a special naval cartridge brass, supplied by the Naval Gun Factory; the 10 pct Zn and the 20 pct Zn alloys were selected commercial alloys supplied by the American Brass Co.; analyses, obtained from the suppliers, are to be found in Table I. Analyses of the brasses, done in concurrence with the analytical work on the diffusion couples, agreed with those supplied.

The brasses were received in the form of rolled and annealed plate approximately ½ in. thick. Grain-size determinations, longitudinal and transverse (both across the plate and through its thickness), showed an equiaxed structure; these determinations are shown in Table II. The copper was received as as-cast 1 in. diam rods; the grain size (shown in Table II) was very large. The grain size after diffusion was large; the average grain diameter was 5 to 10 mm, being larger for couples showing greater diffusion-higher temperature and/or longer time and/or greater gradient. (The grain length, in the direction of diffusion, was not as great; it was limited to the zone of diffusion.)

From the brass plates, disks approximately 1¼ in. in diameter were cut; the copper rods were cut into disks approximately ⅝ in. thick. The disks were turned down slightly and were accurately faced on both sides, the flats were perpendicular to the turned cylindrical surface and parallel to each other. The disks were then given a metallographic polish and cleaned.

The markers used were 3 mil W wire supplied by the Sylvania Electric Products Co. As was mentioned by da Silva and Mehl,[7] this is about the smallest-size wire that can be conveniently distinguished during the machining of the diffused couple. The wire was wound around one of the disks of the prospective diffusion couple (in the case of the triple-disk couples, the one chosen was, of course, the center disk) to give four or five strands marking the interface. The couple was then assembled and pressed to approximately 5000 lb to embed the wires in the alloys.

Pressed couples were placed in a vertical furnace of da Silva's design[7] and welded, under pressure, at a nominal temperature of 50°C below the solidus of the lower-melting alloy. They were held at temperature for ½ hr. Heating times ran in the neighborhood of ½ hr; cooling times were somewhat longer. Welding was done in an atmosphere of flowing dried hydrogen. The amount of diffusion that occurred during welding was considered to be small with respect to that during the diffusion run and was neglected. That this was a reasonable assumption is shown by the fact that duplicate diffusion runs, at short and long times (see the next section), yielded the same diffusion-penetration curves when plotted on a reduced coordinate of $x\sqrt{t}$.

Diffusion Treatments: The diffusion of the welded couples was carried out in bombs of 1½ in. ID black iron pipe, closed on both ends with standard caps. The couples were placed in the bombs "floating" in a mixture of lampblack and chips of brass of the zinc content of the highest brass in any of the couples in that bomb. The machined chips served as a reservoir of zinc vapor to protect the couples from dezincification, and the lampblack kept the couples away from each other, the chips, and the interior of the bomb.

The diffusion runs were carried out in a flowing hydrogen and/or nitrogen atmosphere. A maximum of six diffusion couples, three in each of two bombs, were run at the same time. The long-time characteristics of the controller-furnace arrangement showed a random migration of some 3°C total range. An integration of the time-temperature record (including heating and cooling times) was made by inspection; it is felt that the values reported are within ±2°C and ½ hr elapsed time in all cases except couples 049, 065, and 069; here the time may perhaps be in error by 1 hr.

Table II. Grain Size of Alloys

Alloy (Nominal)	Grain Size, Average Grain Diameter in Mm
Cu	~10
Cu-10 pct Zn	0.065
Cu-20 pct Zn	0.065
Cu-30 pct Zn	0.090

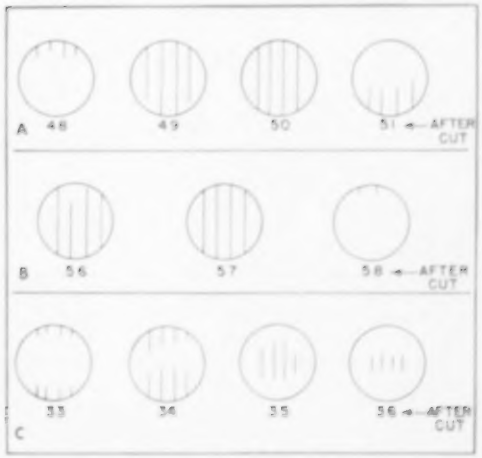

Fig. 1—Examples of appearance of wire interfaces. A, couple 050; interface, center cut 50 +. B, couple 071; interface, end cut 57—. C, couple 066; interface, end cut 35—.

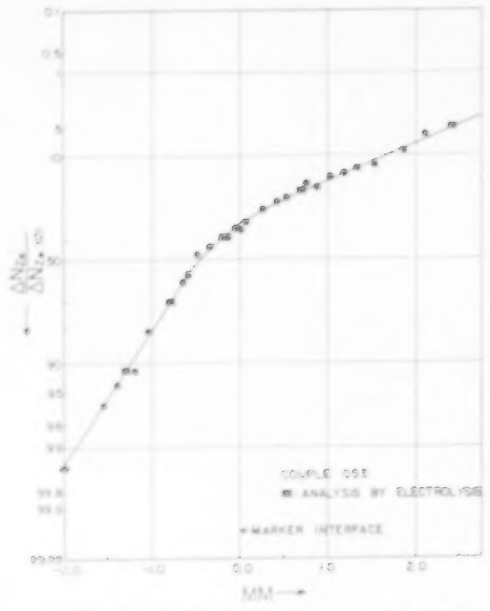

Fig. 2—Probability plot of data from couple 053 (10/30, 144.2 hr at 887°C).

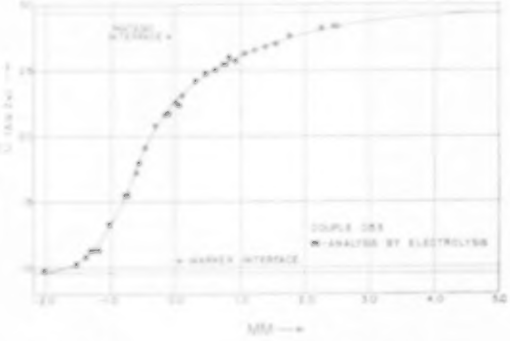

Fig. 3—Rectangular concentration-penetration curve, couple 053 (10/30, 144.2 hr at 887°C).

Two temperatures were selected to be the primary basis for this work, about 780°C and 850°C; runs also were made at two temperatures above these and at one below. Triple-disk couples (double diffusion couples) were used for long-time runs at the base temperatures and duplicate short-time runs were also made in an effort to check the data at these base temperatures. In addition, duplicates of these runs were made to allow for the possibility that couples might part during machining.

Machining: After the diffusion anneal, two parallel flat surfaces, approximately ½ in. wide, were carefully machined parallel to the cylindrical axis of the couple. These surfaces were so oriented as to be as nearly as possible normal to the axes of the wire markers. The surfaces were given a metallographic polish and were etched so that the wires were easily visible under low power magnification.

The couple was mounted in a lathe and, with the aid of a low power telescope and the wire ends, the wire interface was aligned perpendicular to the lathe axis. The specimen was now turned to a diameter of 0.6 to 0.8 in. depending upon the original size of the couple (the copper disks were originally <1.00 in. in diameter; the brasses, about 1.25 in.), the length of the diffusion run and the ambient vapor pressure of zinc during the run. The end of the couple was then machined away and the cutting of specimens for analysis begun at a distance from the interface approximately 50 pct larger than the distance at which the first detectable concentration difference was to be expected.

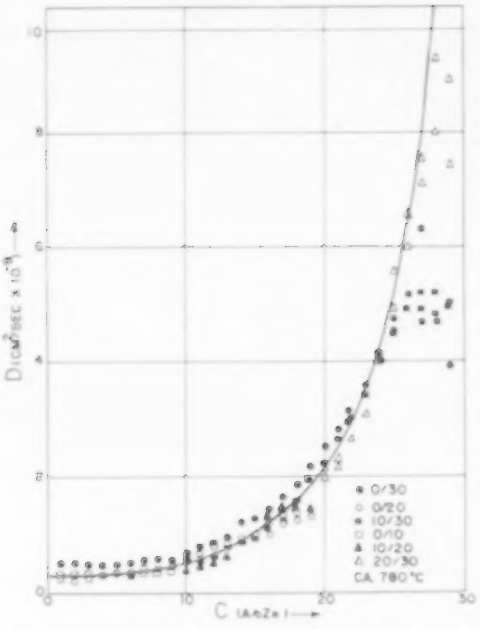

Fig. 4—General diffusion coefficient vs concentration, about 780°C.

In the region where the concentration-penetration curve was expected to be flat, samples of 8 mil thickness were cut; as the interface was approached, this was lowered to 4, then 2 mil. Essentially all of the concentration-penetration curve was cut into samples of 2 mil thickness. All of the cross-section was taken for the sample.

Distances were measured on the feed micrometer on the lathe. After every five cuts, an independent measurement was taken with a portable micrometer. In no case were the two independent measurements in disagreement by more than 1 mil over the total length of the specimens cut.

Upon approaching the wire interface, extra care was taken so as to observe the first appearance of the wires. Sketches were accurately drawn of the appearance of the wires on each interface (between two cuts) at which they could be seen. With 3 mil marker wires, it is possible to have them situated so that they appear at only one interface. Slight displacement from this position will, however, cause the wires to be visible at two succeeding interfaces.

Two separate and distinct factors can cause the wires to appear in more than two interfaces: misalignment of the couple (wire interface not perpendicular to the axis) and a nonplanar wire interface. Welded couples appear to be especially prone to the second fault; an extreme example can be seen in Fig. 1c. And, of course, despite all precautions, the first fault will appear in varying degrees.

However, the sketches made of the appearance of the wires allowed the wire interface plane to be determined within the limits of the procedure in all cases studied here. It is to be noted that this procedure will allow the determination of the interface plane to the closest 1 mil only; it can be said, for example, that the wire interface lies within ½ mil of the interface after cut 68 or within ½ mil of the center of cut 53. This can be improved only to the extent that the true position of the wire interface can be said to be more probably in one direction from this selected position than in the other. The uncertainty in the usual case can be limited to a total of ½ mil rather than ±½ mil. This is the basis for the positioning of the wire interface shown in Fig. 1.

Chemical Analysis: Usually, every third machined sample was sent for chemical analysis. Samples were analyzed for copper by titration with thiosulphate using an outside iodine indicator. These samples which were contaminated with tungsten from the wires were analyzed for both copper and zinc electrolytically, and the percentage of copper was calculated from these analyses. Analysis points that were in doubt were bracketed by two or three "fill-in" samples analyzed subsequently but in the same manner. The expected accuracy of these analyses was ±0.2 pct Cu. Some six to ten samples throughout the diffusion zone were analyzed for copper by electrolysis. The points determined by this inherently more accurate method were treated with some greater confidence in cases of doubt.

Results

The results of the chemical analyses* were plotted first on "probability" paper, as in Fig. 2; this allows the drawing of smooth curves, especially at the ends of the penetration curves, with greater justification than is possible when drawing the penetration

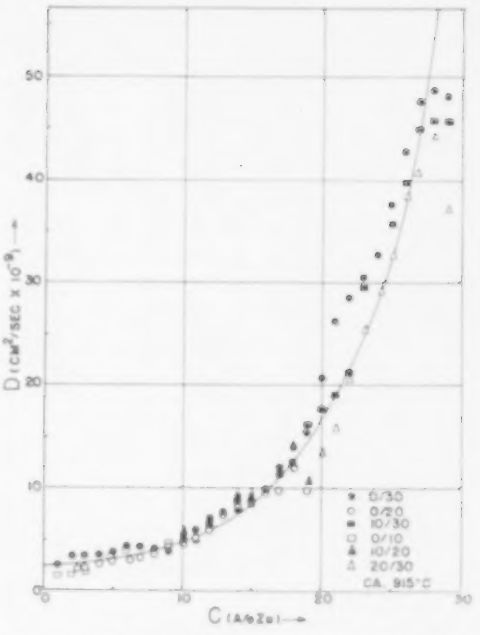

Fig. 6—General diffusion coefficient vs concentration, about 915°C.

* Because of limitations of space, complete results of chemical analysis are not herein reproduced. For these data order Document 4404 from American Documentation Institute, 1719 N St. N.W., Washington 6, D. C., remitting $1.25 for microfilm (images 1 in. high on standard 35 mm motion picture film) or $1.25 for photocopies (6x8 in.) readable without optical aid.

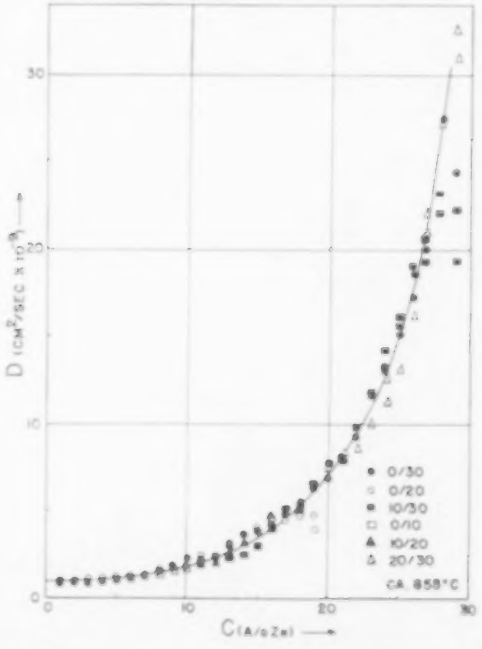

Fig. 5—General diffusion coefficient vs concentration, about 855°C.

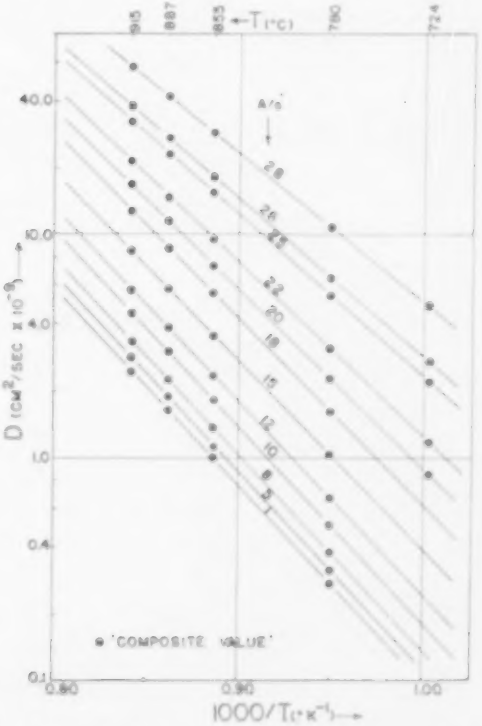

Fig. 7—Activation behavior vs composition for the "composite" general diffusion coefficient.

curves directly. The smooth "probability" curve was then transformed to regular rectangular coordinates and replotted as the usual concentration-penetration curve as in Fig. 3. From these, D as a function of concentration was obtained from the Boltzmann-Matano solution. Some of the values so obtained are plotted in Figs. 4 through 6. At 780° and 855°C, there were a minimum of five and a maximum of eight D-values at a given concentration; at 915°C there were a minimum of three and a maximum of four D-values at a given concentration. Because of overlap, all these points are not plotted in Figs. 4 through 6; in every case, however, the maximum spread is plotted. D-values were obtained also at 724° and 887°C but are not plotted.

Scatter among the individual diffusion-coefficient values is in evidence, especially at the ends of the concentration range of any given sample. The diffusion coefficients vary more toward the high ends than they do at the low concentrations (with the exception of couple 031 and possibly 060). The effect of the 6° temperature difference around 780°C is not discernible. There appears to be no evidence that D is not a single-valued function of the concentration; it appears that D is a single-valued function of the concentration to within the limits of accuracy of the experimental methods used. This is the same result obtained by Wells et al.[5] for the diffusion of carbon in austenite.

On large-scale plots of the type of Figs. 4 through 6, the functions $D(c)$ were drawn by inspection as smooth curves. Values of D were read at various concentrations from these curves and plotted as $\log_e D$ vs $1/T$°K as shown in Fig. 7. The best straight lines were drawn through the points at given concentrations and these smoothed values appear as the "composite" values in Fig. 7 and the smooth curves in Figs. 4 through 6. Calculated values of $Q(c)$ and $D_o(c)$ (from the Arrhenius equation in the form $D = D_o e^{-Q/RT}$) are plotted in Fig. 8.

The $Q(c)$ values are somewhat lower than those of da Silva and Mehl,[7] approaching theirs only at the higher zinc concentrations. The D_o values show an

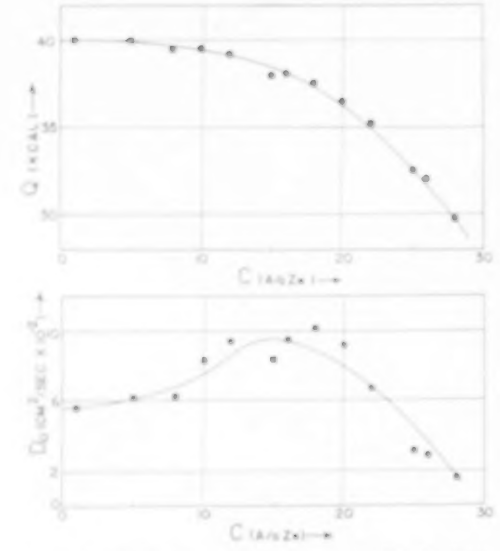

Fig. 8—Constants from the Arrhenius equation ($D = D_o e^{-Q/RT}$) vs concentration.

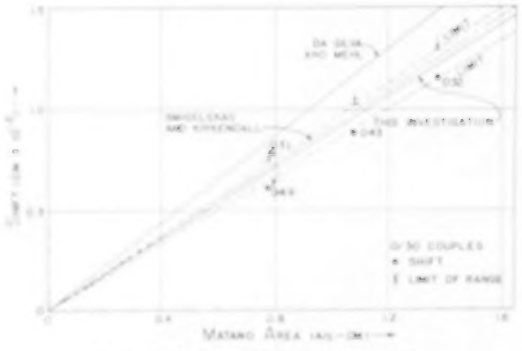

Fig. 9—Shift vs Matano area, 0/30 couples.

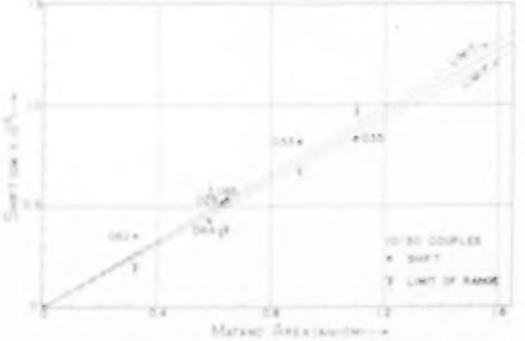

Fig. 10—Shift vs Matano area, 10/30 couples.

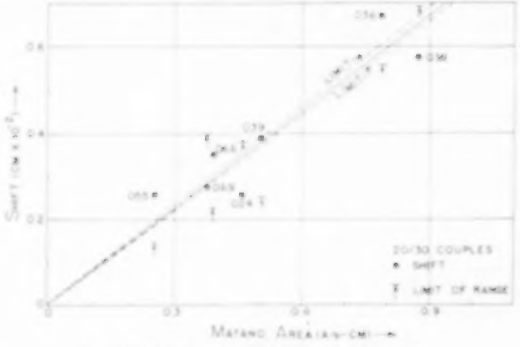

Fig. 11—Shift vs Matano area, 20/30 couples.

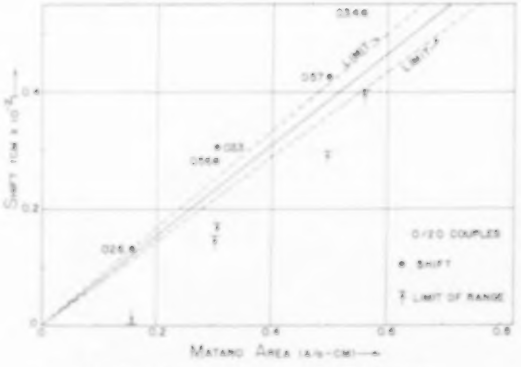

Fig. 12—Shift vs Matano area, 0/20 couples.

Table III. Derived Data (Raw) for All Couples

Couple Type	Couple	T, °C	t, Hr	A_{Matano}, Atomic Pct Cmx10⁻⁴	C_{wire}, Atomic Pct Zn	C_{Matano}, Atomic Pct Zn	Shift, Cm x10⁻⁴	Range
0/10	050	776	477½	1325	5.0	5.0	0.0	12.7
	025	780	361	1065	5.0	5.0	0.0	12.7
	061	854	92	1130	5.2	5.2	1.4	14.1
	037	855	323½	2160	5.2	5.2	0.0	12.7
	060	914	114 1/3	1910	5.6	5.6	1.5	14.2
10/20	028	780	361	1910	15.35	15.3	6.8	19.5
	059	783	94	985	15.35	15.3	1.1	13.8
	073	854	92	1900	15.1	15.1	0.1	12.6
	027	855	323½	3640	15.25	15.2	5.3	18.0
	071	914	114 1/3	3290	15.0	15.0	16.6	3.9
0/20	033	780	361	3050	11.65	11.2	30.2	17.5
	026	783	94	1570	11.65	11.2	13.1	0.4
	006	854	92	3020	12.2	11.75	28.2	15.5
	034	855	323½	5600	12.2	11.7	51.2	40.3
	057	914	114 1/3	4990	12.15	11.7	43.4	29.7
20/30	055	724	431½	2530	25.45	25.3	26.6	13.9
	039	776	477½	5025	25.25	25.2	38.6	25.9
	024	780	361	4600	25.3	25.25	25.5	38.2
	068	854	92	3960	23.4	25.25	35.0	22.3
	036	855	323½	7850	25.4	25.3	67.0	54.3
	038	855	479½	8775	25.4	25.3	56.0	69.7
	069	915	39¾	3720	25.1	25.0	27.6	40.3
10/30	029	780	361	6290	22.3	21.8	51.5	38.8
	062	783	94	3230	22.2	21.8	33.9	21.2
	064	854	92	5880	22.65	22.3	42.3	55.0
	035	855	323½	10950	22.75	22.4	83.3	96.0
	053	887	114½	9025	22.75	22.3	80.4	67.7
	065	915	39¾	6470	22.3	21.8	52.9	40.2
0/30	031	780	361	7900	20.15	19.2	76.6	63.9
	032	855	323½	13650	20.8	19.8	116.8	129.5
	043	887	144½	10790	20.3	19.4	89.0	101.7
	049	915	39¾	7870	20.65	19.9	60.9	73.6

unusual (and perhaps unlikely) passage through a maximum. Again they approach the values of da Silva and Mehl only at the higher zinc concentrations. The values show much less dependence on concentration than do those of the latter authors. But because of the large extrapolation involved, based on values determined over a very short range of temperature, little significance can be attached to these values.

Calculation of the Shift: The shift velocity was calculated on the basis of the finding of da Silva and Mehl that the shift is equal to the distance between the Matano (original) interface and the wire interface. The coordinates of the Matano interface have, of course, been calculated in connection with the calculation of D; the wire interface position has been determined from the machining operation, but is known only to within ½ mil. It is this range of ½ mil which is shown in Table III: the value of "shift" is that corresponding to the measured coordinate of the interface; the "range" is ± ½ mil depending on whether the expected deviation was forward or backward from the wire interface. Included in this table are values of the concentration at the wire interface and the concentration at the Matano (original) interface.

As can be seen from Table III, the measured shifts vary up to 120×10^{-4} cm; many are under 50×10^{-4} cm. Under these conditions, this ½ mil uncertainty must be cut down, since the velocity of marker motion cannot be calculated if the position is in doubt by 50 to 100 pct.

The authors have accepted the finding of da Silva and Mehl that, independent of temperature, the shift is a linear function of the Matano area; they do not know, but may suspect, that this relationship is also independent of composition range in a given system. Plots of this type can be found in Figs. 9 through 15, the first six for a given concentration range, the last for all couples here studied. Within a given concentration range, there is no apparent deviation from the da Silva relationship; there is, however, a trend within the total range so that it appears that the

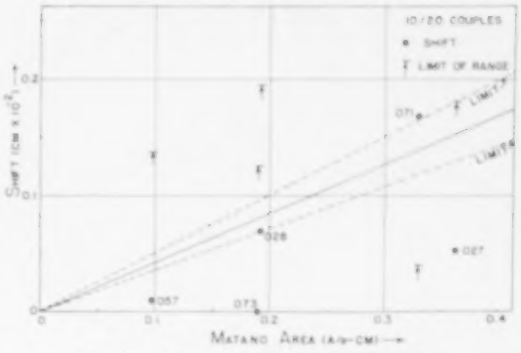

Fig. 13—Shift vs Matano area, 10/20 couples.

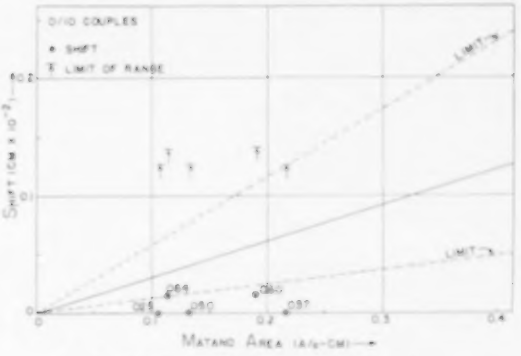

Fig. 14—Shift vs Matano area, 0/10 couples.

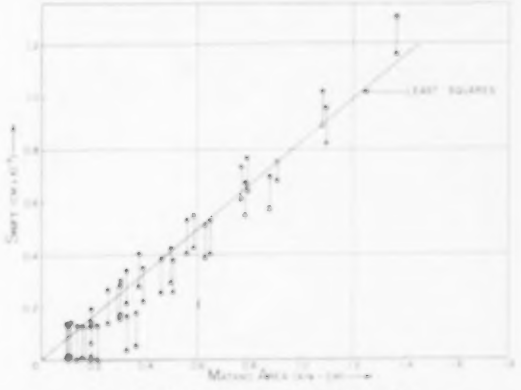

Fig. 15—Shift vs Matano area, all couples.

slopes vary with the range. This will be accepted for the moment, returning to Fig. 15 later.

Figs. 9 through 14 do serve to limit the possible extent of the shift sharply; the remaining uncertainty has been arbitrarily bisected to give the constant relating shift to Matano area.

If the values of shift are selected from these plots, it is assumed implicitly that the measured Matano areas are accurate and correct. But, in view of the scatter in D-values found previously, it would appear that this is not the case; some of this scatter must be due to inaccuracies in measurements of areas and, more important, to inconsistencies among the plotted concentration-penetration curves. This may be checked and some of the uncertainties removed by plotting the logarithm of the measured

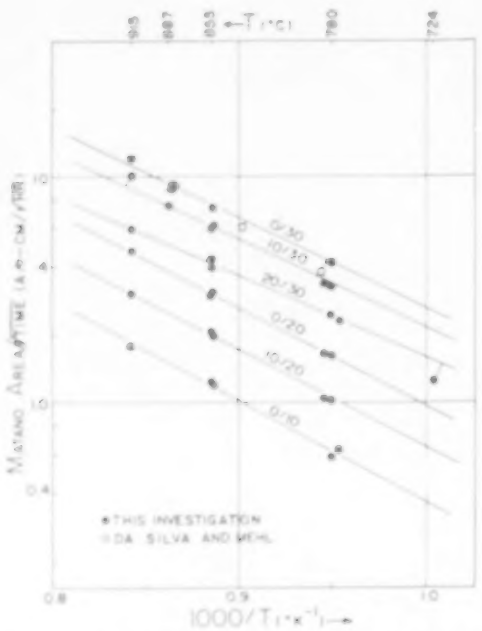

Fig. 16—Activation behavior vs composition for the Matano area divided by (time)$^{1/2}$.

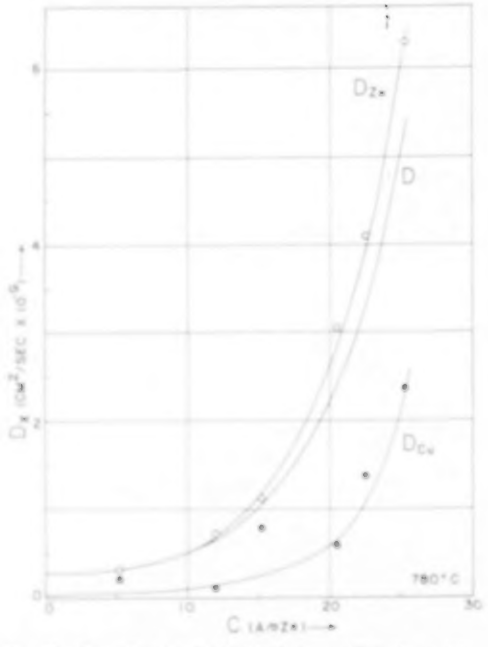

Fig. 17—General and individual diffusion coefficients vs concentration, 780°C.

Matano area divided by (time)$^{1/2}$ (a ratelike constant) against $1/T$ in a given concentration range. This has been done in Fig. 16. It will be seen that, in a few cases, this procedure leads to a much improved approximation to the Matano area.

To be as accurate as possible, the data of Figs. 9 through 15 should now be replotted, utilizing the more accurate Matano-area values. In practice,

Table IV. Derived Data (Smoothed) for All Couples

Couple Type	Couple	A_{Zn+}, Atomic Pct Cmx10^{-4}	C_{Zn+}, Atomic Pct Zn	Shift, Cmx10^{-4}	$\left(\frac{dN_{Zn}}{dx}\right)_-$, Cm^{-1}
0/10	050	1200		5.8	1.26
	020	1140		3.4	1.38
	061	1115	3.2	3.35	1.25
	027	2105		6.3	0.640
10/20	028	1975		8.1	0.964
	059	1040		4.5	1.22
	073	1870	13.2	7.7	0.791
	027	3525		14.5	0.399
	071	3240		13.3	0.434
0/20	033	3020		23.5	1.46
	026	1580		12.2	2.99
	056	2880	11.5	22.3	1.52
	034	5415		42.2	0.866
	057	5066		38.8	1.08
20/30	055	3180		24.0	0.285
	039	5090		38.0	0.281
	024	4555		34.5	0.294
	066	3870	25.2	29.2	0.399
	036	7335		55.0	0.213
	038	8910		67.0	0.1845
	069	3685		27.5	0.391
10/30	029	6455		51.0	0.792
	062	5480		28.0	1.53
	064	5760	22.1	45.5	0.792
	035	10850		86.0	0.4025
	063	9060		71.5	0.524
	065	5670		45.0	0.818
0/30	031	7885		79.5	1.18
	032	13990		122.5	0.911
	043	11280	19.6	101.0	0.836
	049	7180		64.0	1.08

however, the slopes are quite insensitive to the smoothed Matano areas. In the present case, none of the Matano areas which were inconsistent were "critical;" they did not serve as limiting values for the slope. It is sufficient, then, to read from Figs. 9 through 14 the shift corresponding to the smoothed Matano area for this couple. These values are reported in Table IV together with the measured tangents to the concentration-penetration curves at the wire interface which are necessary in calculating the individual diffusion coefficients. The values given for shift in the 0/10 couples and, to some exteht, in the 10/20 couples are quite arbitrary. The possible limits for the shift "rate," as seen in Figs. 13 and 14, are widespread; long-time diffusion runs are needed to limit this range. The concentration at the Matano interface listed in Table IV is an average of the values listed in Table III. There is, apparently, no consistency in the values for either the marker concentration or the Matano interface concentration; this is in agreement with the observations of Thomas and Birchenall.[9]

Calculation of the Individual Diffusion Coefficients, D_{Zn} and D_{Cu}: Darken's equations for the determination of the individual diffusion coefficients, written in terms of the general diffusion coefficient D (the Boltzmann-Matano D), the coordinates of the marker x_m, the fractional concentration N, the tangent to the concentration-penetration curve at the marker $(dN/dx)_m$ and the time t, are

$$D = N_{Zn} D_{Cu} + N_{Cu} D_{Zn}$$

$$\frac{x_m}{2t} = (D_{Zn} - D_{Cu}) \left(\frac{dN_{Zn}}{dx}\right)_m.$$

The D which was used was the composite D previously reported and obtained at an average wire concentration; the tangents were measured at the observed wire interfaces. Computed values of D_{Zn} and D_{Cu}, and the difference $D_{Zn} - D_{Cu}$ are reported in Table V with the appropriate D's and are shown in Figs. 17 through 19. The difference $D_{Zn} - D_{Cu}$ is shown in Fig. 20; activation plots are shown in Figs. 21 and 22.

Several points appear immediately. It can be seen that the values of D_{Zn} behave quite regularly, even in activation plot; the activation energy for D_{Zn} does not differ appreciably from that for D at the same concentration. On the other hand, the D_{Cu} values behave with some abandon. Since each of the individual diffusion coefficients depends on exactly the same four measured quantities: D, dN_{Zn}/dx, $v = x_m/2t$, and N_{Zn}, much of the difference in behavior must be accounted as illusory. Because of the low fractional concentration of zinc, most of the difference $D_{Zn} - D_{Cu}$ appears as a difference between D and D_{Cu}, little between D and D_{Zn}. The difference approaches D, leaving a very small "residual" D_{Cu}; and, between these two factors, a small error in $D_{Zn} - D_{Cu}$ becomes several hundred percent in D_{Cu}. Some smoothing of the data is obviously in order at this point.

The quantity D_{Zn}, being apparently little affected by experimental errors, was read directly from the activation plots as drawn; this is the smoothed D_{Zn}. The difference $D_{Zn} - D_{Cu}$ was next corrected by drawing a smooth function $(D_{Zn} - D_{Cu})$ (c). Since D_{Cu} may be expected to approach D_{Cu}^* (o), the self-diffusion coefficient of copper in pure copper, at low concentrations of zinc (otherwise the function $D_{Cu}(c)$ would be discontinuous), an attempt was made to extrapolate these functions through points representing $(D_{Zn} - D_{Cu}^*)$ (o) from the data of Maier and Nelson[17] as the most recent. The extrapolation succeeded and the curves were drawn this way. This is, of course, the extrapolation attempted by Rhines and Mehl,[18] but in its improved form. The Rhines and Mehl extrapolation simply shows that the individual diffusion coefficients of several solutes in dilute solution in copper approach the same limiting value at zero concentration.

From the $(D_{Zn} - D_{Cu})$ (c) curves, it appears that some of the error is a more or less random error at a given concentration. In view of the scatter in D values obtained, this is to be expected. But there appears to be a systematic error also; it appears that the velocity of shift taken from the plots of shift vs Matano area must be in error in two cases. In the case of the 10/20 couples where the difference is consistently low, the slope, shift vs Matano area, must be too low. Depending as it does in this case on two couples (see Fig. 13; an error in the direction

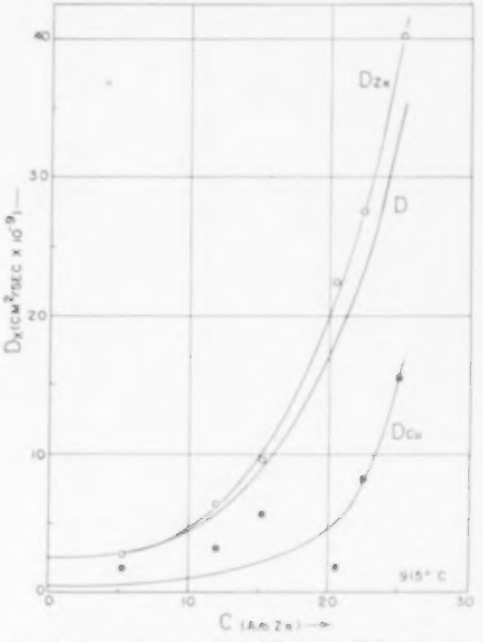

Fig. 19—General and individual diffusion coefficients vs concentration, 915°C.

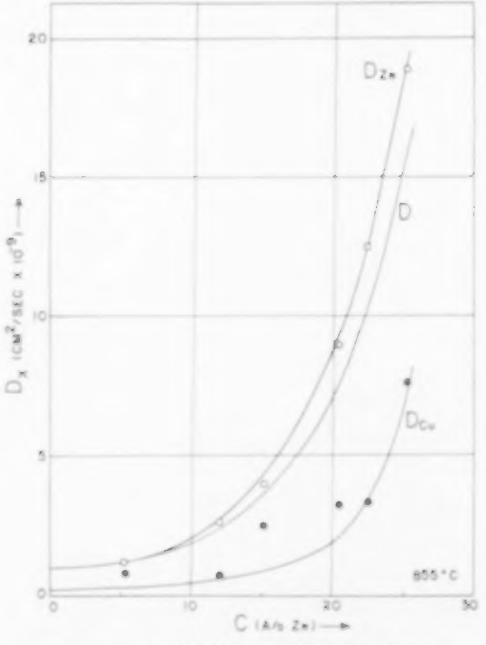

Fig. 18—General and individual diffusion coefficients vs concentration, 855°C.

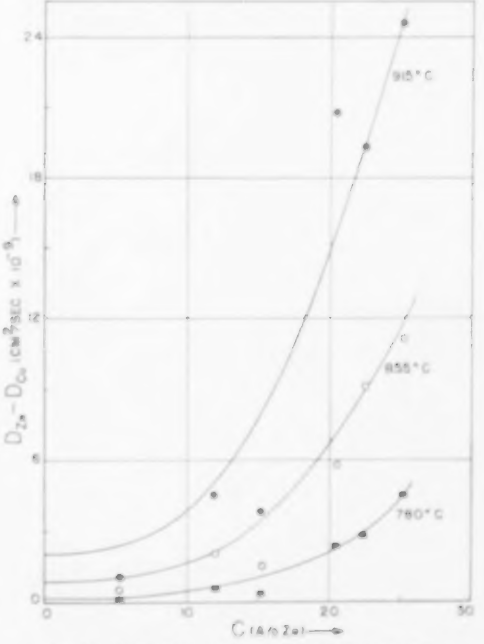

Fig. 20—The difference $D_{Zn} - D_{Cu}$ vs concentration.

Table V. Computed Values of the Individual Diffusion Coefficients

Couple	C_{Zn} Atomic Pct Zn	D Sq Cm per Sec x 10^{-5}	Raw D_{Zn} Sq Cm per Sec x 10^{-5}	Raw D_{Cu} Sq Cm per Sec x 10^{-5}	Raw $D_{Zn} - D_{Cu}$ Sq Cm per Sec x 10^{-5}	Smoothed D_{Zn} Sq Cm per Sec x 10^{-5}	Smoothed D_{Cu} Sq Cm per Sec x 10^{-5}	Smoothed $D_{Zn} - D_{Cu}$ Sq Cm per Sec x 10^{-5}
050		0.29	0.30	0.21	0.09	0.30	0.047	0.25
021		0.31	0.32	0.22	0.09	0.32	0.050	0.27
061	6.2	1.14	1.16	0.75	0.42	1.19	0.200	0.96
037		1.15	1.17	0.75	0.42	1.20	0.203	0.965
036		2.80	2.85	1.83	1.02	2.92	0.550	2.37
028		1.07	1.12	0.78	0.34	1.225	0.210	1.015
059		1.15	1.23	0.70	0.53	1.315	0.225	1.09
073	15.2	3.70	3.90	2.50	1.66	4.225	0.770	3.45
027		3.75	3.98	2.46	1.52	4.28	0.780	3.48
071		8.80	9.27	5.65	3.72	10.03	1.95	8.08
033		0.66	0.735	0.12	0.62	0.750	0.126	0.605
026		0.70	0.77	0.17	0.60	0.777	0.135	0.642
056	13.6	2.35	2.62	0.40	2.22	2.60	0.490	2.11
034		2.40	2.65	0.56	2.09	2.66	0.500	2.16
057		5.75	6.28	1.81	4.36	6.35	1.32	5.03
035		2.90	2.99	0.25	2.72	2.795	0.835	1.96
058		5.30	6.30	2.36	3.94	6.35	2.20	4.15
024		5.80	6.74	2.20	4.52	6.72	2.30	4.42
066	25.3	16.0	16.8	7.6	11.1	19.1	6.90	12.2
038		16.1	16.9	7.7	11.1	19.2	7.00	12.2
018		16.1	16.6	8.1	10.6	19.2	7.00	12.2
069		34.0	40.2	15.4	24.7	40.2	15.7	24.5
039		3.00	3.92	1.20	2.72	3.95	1.05	2.90
054		3.90	4.11	1.40	2.71	4.20	1.10	3.10
062	22.5	10.2	12.3	3.55	8.70	12.1	3.50	8.78
055		10.4	12.5	3.3	9.20	12.4	3.57	8.80
053		16.0	19.0	5.8	13.1	19.0	5.70	13.3
063		23.6	27.4	8.1	19.3	27.3	8.30	19.0
031		2.40	2.87	0.57	2.30	2.87	0.57	2.30
068		7.60	9.89	3.20	6.78	9.30	2.00	7.30
042	20.5	13.4	14.9	3.20	11.6	14.75	3.20	11.55
040		18.6	22.2	1.50	20.7	21.4	4.75	16.65

of the deviation of couple 071 and in the center of couple 027 must be present here), this is somewhat surprising. In the 0/10 couples, where the difference is also low, the slope again must be too low; here the needed correction is less and almost within the remaining band of uncertainty (see Fig. 14).

It is interesting to note that the curves were originally drawn in the manner indicated previously. Later, a check was made to determine the curves which would follow if the "least squares" line of Fig. 15 were used, indicating a constant slope, shift vs Matano area, independent of time, temperature, or composition range within a given system (αCu — Zn). The resulting values, D_{Zn}, D_{Cu}, and

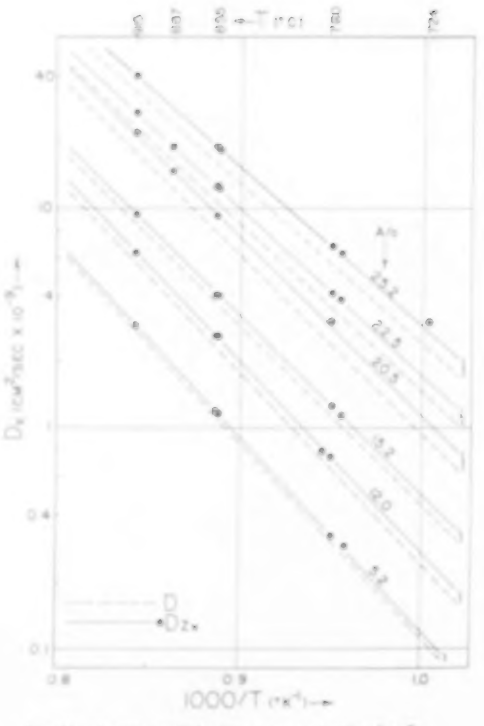

Fig. 21—Activation behavior vs concentration for D_{Zn}.

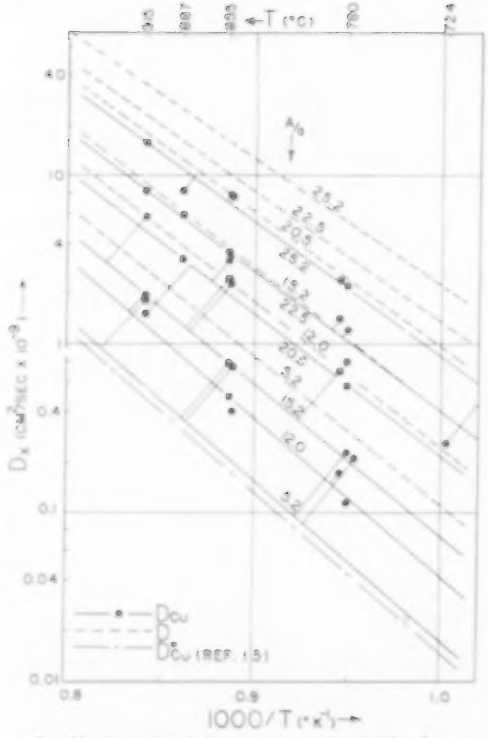

Fig. 22—Activation behavior vs concentration for D_{Cu}.

$D_{Zn} - D_{Cu}$, are practically indistinguishable from the values obtained by the foregoing smoothing process. It is felt that this is good indirect evidence that the da Silva-Mehl relationship: marker shift is a linear function of the Matano area, is independent of time, temperature, or concentration range in a given system. Furthermore, the foregoing smoothing process explicitly assumes that the individual diffusion coefficients, D_{Zn} and D_{Cu}, follow an activation behavior —an assumption, but not an unlikely one. Using the least squares' slope of Fig. 15, however, activation-behavior results and this is further evidence of the validity of the da Silva and Mehl relationship.

Calculation of the Individual Mobilities B_{Zn} and B_{Cu}: Darken's equations, solved for the individual mobilities in terms of the individual diffusion coefficients, D_{Zn} and D_{Cu}, the absolute temperature T, Boltzmann's constant k, the fractional concentration N_{Zn}, N_{Cu}, and the activity coefficients $\gamma = a/n$ are

$$B_{Zn} = D_{Zn}/[kT\{1 + N_{Zn}(d \ln \gamma_{Zn}/d N_{Zn})\}]^*$$

$$B_{Cu} = D_{Cu}/[kT\{1 + N_{Cu}(d \ln \gamma_{Cu}/d N_{Cu})\}]^*.$$

The activity terms were evaluated from the data of Herbenar et al.;[10] these data differ little from those of Hargreaves,[9] used by most investigators, but appear to be more self-consistent.

The resulting mobilities as a function of concentration are plotted in Figs. 23 through 25 and an activation plot as Fig. 26. Activation energies as calculated are shown in Table VI. The difference between the activation energies for the mobilities must be the same as the difference between the activation energies for the individual diffusion coefficients, since the equality, $D_{Zn}/D_{Cu} = B_{Zn}/B_{Cu}$, must be preserved.

* These equations reduce to the Einstein relation, $D = kTB$, in an ideal solution.

Discussion

The General Diffusion Coefficient, D: Experimentally, the general diffusion coefficient D has been determined as a function of concentration and temperature from incremental diffusion couples in the α-brass system. The results depend, except for experimental variables, only upon the Boltzmann-Matano solution to Fick's law.

The Boltzmann-Matano solution to Fick's law appears to yield results which are not in any way as much in error as might be expected. It is a little surprising that the results obtained at the end of the concentration range of a given couple correspond so well to those near the center of another couple. In particular, there appears to be no grounds for assuming, as LeClaire[11] has done, that determinations of D are suspect merely because a couple of large concentration range and the Boltzmann-Matano solution have been used; the results of Rhines and Mehl[12] and da Silva and Mehl[5] are closer to the present results, determined at least partly incrementally, than are those of Seith and Kraus.[13]

Table VI. Observed Activation Energies, Q (Kcal)

Atomic Pct Zn	$Q(D)$	$Q(D_{Zn})$	$Q(D_{Cu})$	$Q(B_{Zn})$	$Q(B_{Cu})$
5.2	40	40	44.3	38	42
12.0	39	39	43	37.4	41.3
15.2	38	38	41	36.5	39.5
20.5	36.5	36.5	39	35.5	37.3
22.5	35.2	35.2	36	34	36.5
25.2	32.5	32.5	33	32.0	33.7

There appears, then, to be no evidence that the function $D(c)$ is not single-valued; the individual variation between couples is more than sufficient to account for previous equivocal results.[9] This variation is also sufficient to overshadow any second-order corrections, such as could be made by a change to weight per unit volume from atomic percent.

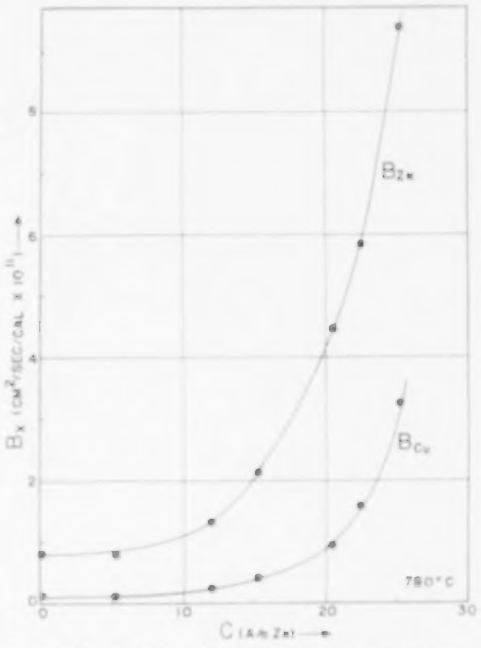

Fig. 23—The mobilities of zinc and copper vs concentration, 780°C.

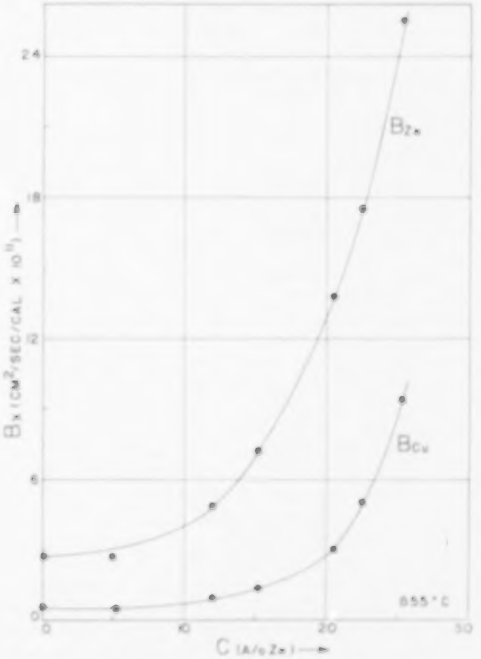

Fig. 24—The mobilities of zinc and copper vs concentration, 855°C.

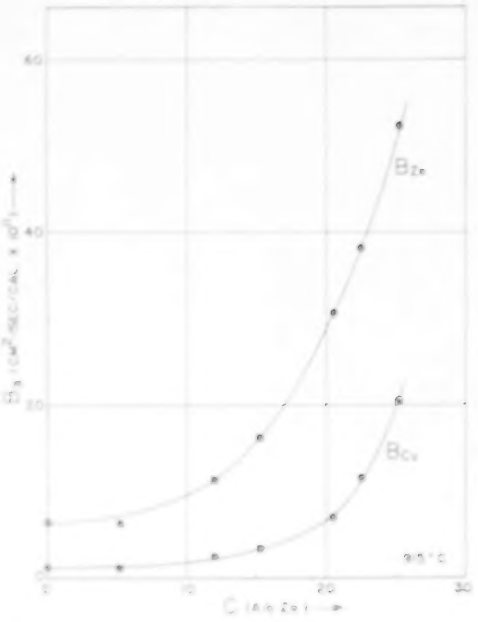

Fig. 25—The mobilities of zinc and copper vs concentration, 915°C.

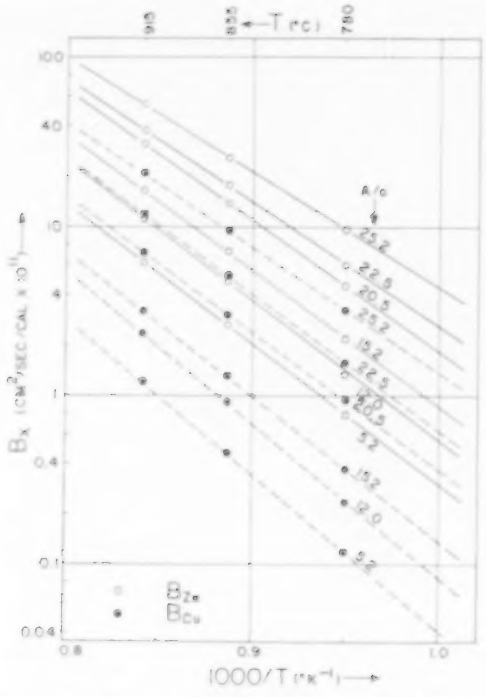

Fig. 26—Activation behavior vs concentration for mobilities of zinc and copper.

No study of porosity in the reported couples was made and there are none in the literature known to the authors for other than 0/30 couples (in the α-brasses). It can be assumed that the porosity would be less in any smaller-range couple (possibly proportional to the Matano area), but the question of how much less is unanswered at the present time. But because of this, and the apparent single-valuedness of D as determined full range and incrementally, there is no discernible effect of porosity on the general diffusion coefficient.

The present values of $D(c, T)$ fall near the center of the range collected by Kuczynski,[3] but differ in that the present investigation found that the activation energy decreases with increasing zinc content; the same result was found, to an even greater degree, by da Silva and Mehl.[7] From investigations of this type, with or without the low temperature determinations based on anelastic phenomena, little reliance can be placed on the D_0 values. Similarly, the absolute accuracy of the values of D is indeterminate depending, as it does, on so many operations, particularly manual.

The Individual Diffusion Coefficients, D_{Zn} and D_{Cu}.— Experimentally, the magnitude of the Kirkendall effect has been determined for six types of diffusion couples within the α-brass range. These results have been used, through Darken's analysis, to yield values of the individual diffusion coefficients D_{Zn} and D_{Cu}. These values depend on experimental variables, on Darken's analysis, and on two experimental relations reported by da Silva and Mehl.

The coincidence of the Matano interface and the original weld interface, experimentally observed by da Silva and Mehl, has been used to position the original interface in the couples studied here. The linear relation between the shift of a marker and the Matano area in a given type of couple, also observed by da Silva and Mehl, has been used to remove experimental uncertainties in the amount of shift. These have been accepted as experimental facts, valid within the limit of accuracy of the techniques. The reader is referred to the original paper[7] for a discussion of these; nothing in the present data appears to be at variance with their findings.

There are unresolved doubts as to the assumptions implicit in Darken's analysis,[6] but, again, there does not appear to be any aspect of the present data which in itself casts doubt on the analysis.

The presence of porosity affects the calculation of the marker shift when the shift is determined in the present fashion. Again, there are no available data to attempt to correct all shifts for this factor; even in 0/30 couples, there is some uncertainty as to the magnitude of the correction and the manner of its proper application and little information on variation with temperature. The expected influence would be to increase the variation of D_{Zn} and B_{Zn} with concentration. But it is felt that the accuracy inherent in the technique does not justify all such corrections even though they were available.

There is one disturbing feature present. Once again scatter was observed in the concentrations at the wire interface; they varied by 0.5 atomic pct Zn in some cases. There is no evidence that this varying concentration at the wire (c_w) is a function of temperature. It is, on occasion, the same at high temperatures as at low but different at intermediate temperatures; the concentration at the Matano interface shows similar behavior. There is no evidence that this varying c_w is a function of time; the variation with time at a given temperature and type of couple appears to be less than the general scatter. Yet, for a 0/30 couple, Smigelskas and Kirkendall[1] found the wires marking about 22.0 atomic pct Zn, da Silva and Mehl[7] found values scattered around

21.3 atomic pct Zn (they thought they detected a variation with temperature; Thomas and Birchenall[22] dispute this in the Cu-Ni system); and the wires were found in the present 0/30 couples scattered around 20.5 atomic pct Zn. In the penetration curves obtained by the present authors, the distance between 20.5 and 22.0 atomic pct Zn at 780°C (Smigelskas and Kirkendall worked at 785°C) and 400 hr elapsed time was about 200×10^{-4} cm, some 200 pct greater than the observed shift, the rate of which agrees with that of Smigelskas and Kirkendall within 12 pct. All that the present authors can say is that there is no apparent reason why the large difference in concentration at the markers is observed.

Summary and Conclusions

1—The general diffusion coefficient D and the individual diffusion coefficients D_{Zn} and D_{Cu} have been measured in α brass as functions of concentration and temperature using Darken's analysis on data from incremental diffusion couples of overlapping range. The basic data were obtained directly from concentration-penetration curves using the Matano interface as the original interface.

2—Experimentally, the coefficient relating marker shift to Matano area is a constant independent of time, temperature, and the concentration range of the diffusion couple in the foregoing system.

3—Using the aforementioned diffusion coefficients and activity data from the literature, mobilities of zinc and copper were determined as functions of concentration and temperature.

4—The diffusion coefficients and mobilities are single-valued functions of the concentration to within the limits of the experimental method.

5—As expected, neither the individual diffusion coefficients nor the mobilities are simple functions of the concentration; they are all of the same form as the usual D vs c curve.

6—The individual diffusion coefficient D_{Zn} approaches the self-diffusion coefficient for copper D^*_{Cu} (o) at low concentrations of zinc.

7—Discrepancies were observed as to the concentration at which a marker is found; no solution was suggested.

Acknowledgments

This work was carried out under sponsorship of the Office of Naval Research, Contract N6 ori-47/IV, Project No. NR 031-184. The authors gratefully acknowledge the sponsorship and permission to publish the results.

The authors would also like to acknowledge the receipt by one of them of a fellowship from the American Brake Shoe Co., Mahwah, N. J., and a fellowship from the Westinghouse Electric Corp., Pittsburgh, without which the work could not have been performed.

References

[1] L. S. Darken: Discussion of ref. 4. *Trans.* AIME (1947) **171**, p. 138.
[2] E. O. Kirkendall, L. Thomassen, and C. Upthegrove: *Trans.* AIME (1939) **133**, p. 186; METALS TECHNOLOGY (October 1938).
[3] E. O. Kirkendall: *Trans.* AIME (1942) **147**, p. 104; METALS TECHNOLOGY (February 1942).
[4] A. D. Smigelskas and E. O. Kirkendall: *Trans.* AIME (1947) **171**, p. 130.
[5] L. C. C. da Silva and R. F. Mehl: *Trans.* AIME (1951) **191**, p. 155; JOURNAL OF METALS (February 1951).
[6] R. S. Barnes: *Proceedings* Physical Society (1952) **B65**, p. 512.
[7] R. W. Balluffi and B. H. Alexander: *Trans.* AIME (1952) **194**, p. 1315; JOURNAL OF METALS (December 1952).
[8] W. Seith and A. Kottman: *Angewandte Chemie* (1952) **64**, p. 379.
[9] J. Bardeen and C. Herring: Most of the theories are discussed and summarized. *Atom Movements*, (1951) Cleveland, ASM.
[10] L. S. Darken: *Trans.* AIME (1948) **175**, p. 184; METALS TECHNOLOGY (January 1948).
[11] C. Wells, W. Batz, and R. F. Mehl: *Trans.* AIME (1950) **188**, p. 553; JOURNAL OF METALS (March 1950).
[12] D. E. Thomas and C. E. Birchenall: *Trans.* AIME (1952) **194**, p. 867; JOURNAL OF METALS (August 1952).
[13] M. S. Maier and H. R. Nelson: *Trans.* AIME (1942) **147**, p. 39.
[14] F. N. Rhines and R. F. Mehl: *Trans.* AIME (1938) **128**, p. 185; METALS TECHNOLOGY (January 1938).
[15] A. W. Herbenar, C. A. Siebert, and O. S. Duffendack: *Trans.* AIME (1950) **188**, p. 323; JOURNAL OF METALS (February 1950).
[16] R. Hargreaves: *Journal* Institute of Metals (1939) **64**, p. 115.
[17] A. D. LeClaire: *Philosophical Magazine* (1951) **62**, p. 673.
[18] W. Seith and W. Kraus: *Ztsch. für Elektrochemie* (1938) **44**, p. 98.
[19] O. Kubaschewski: *Trans.* Faraday Society (1950) **46**, p. 713.
[20] A. D. LeClaire: *Progress in Metal Physics* (1949) **I, IV**, New York, Interscience Publishers.

Technical Note

Energy Stored During Fatigue of Copper

by L. M. Clarebrough, M. E. Hargreaves, A. K. Head, and G. W. West

RECENTLY Welber and Webeler[1] reported that during the annealing of fatigued copper no energy was released, but that energy was absorbed in the range of temperature 250° to 400°C. In view of the fact that strain hardening occurs during the fatigue of copper, this result was surprising and it seemed desirable to check the measurements. This note describes measurements made by a different technique which indicates that energy is stored during the fatigue of copper.

Two test bars with gage length ¾ in. in diameter and 6 in. long were machined from OFHC copper and annealed in vacuum for 1 hr at 600°C. These were fatigued to fracture in an Avery pulsator at a frequency of 2000 cycles per min. The first specimen fractured after 0.25×10^7 cycles under a push-pull

Table I. Stored Energy and Hardness Change in Fatigue and Tension

Deformation	Stored Energy, Cal per G	Dpn, As-Deformed	Dpn, After Annealing
Fatigue, 0.25×10⁶ cycles	0.84±0.91	—	—
Fatigue, 6.0×10⁶ cycles	0.66±0.61	72	49
Tension, 30 pct reduction in area	0.87±0.088	102	41

stress of ±11,200 psi and the second after 6x10⁷ cycles under a stress of ±9,000 psi.

Three specimens 1⅝ in. long, none including the zone of fracture, were machined from each bar for measurement of the stored energy by the differential calorimetric method which has been described previously.[1,2] The method involves heating two identical specimens, one deformed and one annealed, through the range of temperature in which the stored energy is released, under conditions which virtually eliminate any transfer of heat between the specimens or to their surroundings. The specimens are heated at a constant rate (6°C per min) and the difference in the electrical powers required to heat the specimens is observed continuously by means of a differential wattmeter. The curve of power difference, ΔP, as a function of time (or temperature) shows the manner of release of the energy as the temperature is increased. After all the stored energy has been released, the apparatus is allowed to cool and a second heating made to obtain a second curve as a base line. The total stored energy is calculated from the area between the two curves.

A typical curve of power difference, ΔP, for a specimen of fatigued copper is shown in Fig. 1 and a ΔP curve for a specimen of the same material deformed 30 pct in tension is given for comparison. In this diagram, the positive sign of ΔP represents release of energy from the deformed specimen. The average values of total stored energy obtained and the decreases in hardness accompanying the release of energy are shown in Table I.

It is clear from Fig. 1 and Table I that energy is released during the annealing of fatigued copper. The shape of the ΔP curves for the fatigued specimens is markedly different to that for specimens deformed in tension. For the fatigued specimens, the stored energy is released over a range of temperature of 210°C (between 220° and 430°C) while the corresponding range of temperature for specimens deformed in tension is only 60°C (270° to 330°C).

No evidence of recrystallization was found by microscopic examination of the fatigued specimens before and after the release of energy. In contrast to this, the sharp peak observed in the ΔP curve for specimens deformed in tension has been shown to coincide with recrystallization.[3,4,5] For undirectional deformation, irrespective of whether the method is tension, compression, or torsion, this sharp peak is always observed and found to coincide with recrystallization. It appears that some mechanism other than normal recrystallization is responsible for the gradual release of energy from fatigued copper.

The results of the present experiments therefore are contrary to those of Welber and Webeler al-

L. M. CLAREBROUGH, M. E. HARGREAVES, and G. W. WEST are associated with the Div. of Tribophysics, Commonwealth Scientific and Industrial Research Organization, Melbourne, Australia, and A. K. HEAD is on the Staff, Aeronautical Research Laboratories, Dept. of Supply, Melbourne, Australia.

TN 2458. Manuscript, Oct. 13, 1954.

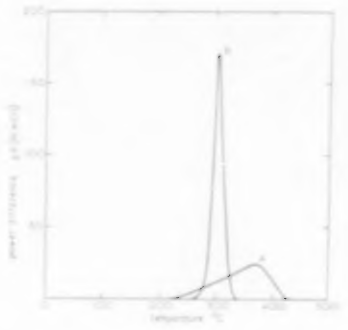

Fig. 1—The energy stored in copper during fatigue (*A*) and tension (*B*).

though the methods of stressing used are probably comparable. The frequencies are the same; further, in the authors' experience,[6] it is likely that an annealed copper specimen would creep under the initial fluctuating tensile stress of 1000 to 20,000 psi used by Welber and Webeler and in a machine of the constant displacement type, as used by them, the mean stress thus would be reduced almost to zero. The resulting range of stress would be approximately ±9500 psi, which lies between the ranges used in the present experiments. Thus, any difference in the results due to the method of stressing would be such that an extra quantity of stored energy due to the deformation in creep would be expected in the results of Welber and Webeler.

Therefore, the marked discrepancy between the present results and those obtained by Welber and Webeler is due probably to differences in the techniques used for the measurement of the stored energy. For example, with a method such as that of Welber and Webeler in which a single specimen is used, serious errors may arise if the thermal resistance between the specimen and the element heating it is not the same at corresponding stages of the first and second heatings. Such errors would be difficult to detect and might escape notice. Changes in thermal resistance of this nature have been detected with the present differential technique but, if they are the same for both specimens, the resulting error is negligible whereas, if they are different, they are always detected and the result is rejected.

The authors' results indicate that energy is stored during fatigue of copper, as would be expected from the fact that strain hardening accompanies fatigue and from current conceptions of the nature of fatigue. The amount of energy stored and the change in hardness during fatigue are of the same order as those observed for specimens deformed by 30 pct in tension.

References

[1] B. Welber and R. Webeler: *Trans.* AIME (1953) **197**, p. 1558; JOURNAL OF METALS (November 1953).

[2] L. M. Clarebrough, M. E. Hargreaves, D. Michell, and G. W. West: *Proceedings* Royal Society (1952) **215A**, p. 507.

[3] L. M. Clarebrough, M. E. Hargreaves, D. Michell, and G. W. West: *Journal* Scientific Institute (1953) **30**, p. 282.

[4] L. M. Clarebrough, M. E. Hargreaves, and G. W. West: *Philosophical Magazine* (1953) **44**, p. 913.

[5] L. M. Clarebrough, M. E. Hargreaves, and G. W. West: To be published.

[6] W. A. Wood and A. K. Head: *Journal* Institute of Metals (1951) **79**, p. 89.

[7] F. P. Bullen, A. K. Head, and W. A. Wood: *Proceedings* Royal Society (1953) **216A**, p. 332.

[8] R. B. Davies: To be published.

Titanium-Lead System

by Paul Farrar and Harold Margolin

The Ti-Pb diagram was investigated in the region 0 to 58 pct Pb and from 500°C to liquidus temperatures. Three reactions were encountered: 1—$\beta \rightarrow \alpha + Ti_3Pb$ at 725 ± 10°C; 2—$\beta + L \rightarrow Ti_3Pb$ at 1305 ± 10°C; and 3—the possible eutectic $L \rightarrow Ti_3Pb$ and γ between 1200° and 1300°C.

LEAD-RICH alloys have been investigated by Nowotny and Pesl,[1] who used sintered compacts and studied the region from 37.5 to 100 pct Pb by X-ray diffraction analysis. The only phase found in addition to titanium and lead was the hexagonal compound Ti_3Pb. Alloy systems of lead with metals of the transition group, such as iron, chromium, tungsten, cobalt, nickel, or manganese, generally show little liquid or solid solubility.[2] Craighead et al.,[3] however, indicated that lead is soluble in α and β titanium to at least 2.1 pct. They also found that approximately 50 pct of the lead added was lost during the arc-melting of Ti-Pb alloys. In the present investigation, arc-melting also was used to prepare Ti-Pb alloys and similarly large lead losses were encountered.

Experimental Procedure

Alloy Preparation: Considerable difficulty was encountered in the melting of the Ti-Pb alloys and a number of experiments were performed before the method described was developed. Alternate layers of lead and titanium were wrapped with titanium sheet and compacted. This "sandwich" was annealed at 300° to 350°C and was melted according to the procedure described by Cadoff and Nielsen.[4] Using a low current, 150 amp, and an argon atmosphere, four to eight 10 to 20 sec melts were made on each alloy, with the button being turned over between each melt to insure homogeneity. In the high lead range, the preliminary sintering was found to be of doubtful value and was eliminated. In the region above the nominal composition of 70 wt pct Pb, the alloys prepared in this manner always consolidated into two phases. The outside appeared to be composed entirely of lead and the inside was a Ti-Pb alloy. In order to determine whether this phenomenon was caused by a miscibility gap, master alloys with a nominal composition of 40 wt pct Pb were machined and mixed with various percentages of lead sheet. This mixture was compacted and melted in the same manner as the other alloys.

Although these alloys were not homogeneous, they did not show the layering that was observed

Table I. Analysis and Melting Point Data for the Ti-Pb System

Nominal Pct Pb	Pct Pb Calculated by Weight Loss	Pct Pb Analyzed	Pct Pb Plotted	Melting Data, °C	
				Solidus	Liquidus
0	—	—	0	1665	
1	0.85	0.87	0.87	—	—
2	1.50	1.70	1.70	—	—
3	1.69	2.90	2.90	—	—
5	2.59	3.93	3.93	—	—
9	4.14	5.04	5.04	—	—
11	5.14	5.29	5.29	1633	1650
13	6.40	6.42	6.42	—	—
21	6.95	8.28	8.28	—	—
25	13.3	13.3	13.3	1662	1595
28	15.2	15.3	15.3	—	—
30	16.0	—	16.0*	—	—
36	17.1	16.8 to 17.5	17.2	—	—
42	22.3	—	22.3*	—	—
44	24.0	24.0	24.0	—	—
46	32.7	30.4 to 34.3	33.0	—	—
50	35.9	36.3	36.3	1490	1465
48	37.8	37.9	37.9	—	—
54	40.5	—	40.5*	—	—
58	40.9	40.7 to 41.9	41.0	—	—
62	**	45.0	45.0	1505	1385
66	**	47.5 to 50.1	48.7	1504	1355
70	**	54.0	54.0	—	—
68	**	50.8 to 61	59.0	—	—

* Where no analysis was available, the point plotted was that indicated by weight loss.

** A lead covering was removed from these alloys; therefore, weight loss data is meaningless.

P. FARRAR, Student Associate AIME, and H. MARGOLIN, Junior Member AIME, are Research Assistant and Research Associate, respectively, Engineering Research Div., New York University, New York.

Discussion on this paper, TP 3835E, may be sent, 2 copies, to AIME by Mar. 1, 1955. Manuscript, Apr. 19, 1954. Chicago Meeting, November 1954.

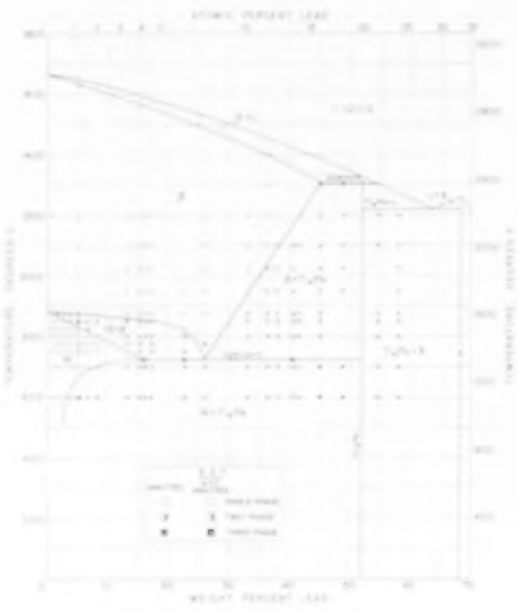

Fig. 1—Iodide titanium-lead phase diagram.

in the sheet compacts. This seemed to indicate that the layering effect was not caused by a miscibility gap, but rather by the method of charge preparation.

A total of 91 alloys were made using the sandwich method, and 23 of the alloys were homogeneous enough to be used in the delineation of the diagram. Iodide titanium and high purity lead were used in the preparation of these alloys. Table I gives the variation of weight loss with nominal and analyzed* composition. In general, the percentage of lead loss decreased at high lead contents, while the spread of lead content in different portions of the button increased.

* The analytical data presented were obtained by Lucius Pitkin, Inc., N. Y.

Heat Treatment: Alloys containing up to 13 wt pct Pb were hot rolled at 750°C prior to heat treatment. The times of heat treatments are given in Table II.

It is believed that equilibrium was attained in all of the alloys annealed above the eutectoid horizontal, but below this temperature equilibrium was not reached in all cases. Although it was approached and probably reached in the low alloy region of the 600° to 725°C treatments, it was not reached in the 500°C treatment.

The method of heat treatment used for temperatures up to and including 1200°C was that described by Cadoff and Nielsen.[3] For heat treatments above 1200°C, the melting-point apparatus described by Cadoff and Nielsen was modified by the insertion of a 1 in. thick bakelite ring between the Vycor plate and the copper container. The lavite radiation shield was not used. Thermocouple leads were passed through the bakelite ring, and the holes around the leads were sealed with De Khotinsky cement. The thermocouple was attached to a single-point controller which selected either a high or low power circuit. The tip of the thermocouple was placed in contact with the specimen, which rested on a molybdenum heater that was modified slightly to give greater areas of contact with the specimen than the heaters used by Cadoff and Nielsen. By this method, the temperature was controlled to within ± 5°C.

There was no apparent loss of lead through vaporization until a temperature just below the melting point of the alloy was reached. Vaporization of lead made it impossible to determine the melting point of the alloys by means of the optical pyrometer. Therefore, the same apparatus which was used for the high temperature heat treatments was used to determine the melting points. The temperature of the specimen was slowly raised until a rounding of the corners of the specimen was observed. This temperature was recorded as the solidus temperature and the temperature at which the alloy flowed freely was taken as the liquidus temperature. By this method, the melting points of the alloy were obtained to within ±10°C. This represents the average of at least two determinations for each point.

Fig. 2—3.93 pct Pb alloy, annealed 24 hr at 875°C, water quenched. α islands (white) + Ti_3Pb precipitate (black) in transformed β matrix. "A" etch. X130. Area reduced approximately 15 pct for reproduction.

Fig. 3—40.5 pct Pb alloy, annealed 1 hr at 1100°C, 1 hr at 700°C, water quenched. Isothermal α matrix + Ti_3Pb. "A" etch for 3 sec, HNO_3 etch for 8 sec. Electrolytically stained, "HG" electrolyte. Oblique light. X750. Area reduced approximately 15 pct for reproduction.

Fig. 4—40.5 pct Pb alloy, annealed for 2 hr at 1100°C, water quenched. β matrix (no transformation visible) + Ti_3Pb. "A" etch for 3 sec, HNO_3 etch for 8 sec. Electrolytically stained, "HG" electrolyte. Oblique light. X750. Area reduced approximately 15 pct for reproduction.

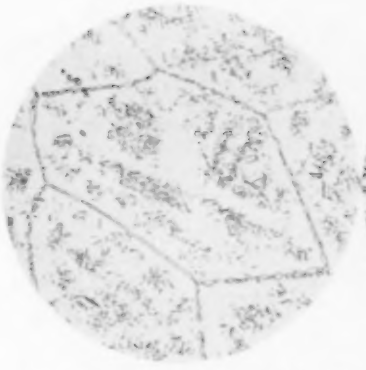

Fig. 5—36.3 pct Pb alloy, annealed for 48 hr at 850°C, water quenched. Ti_2Pb in β matrix. No etch. X130. Area reduced approximately 15 pct for reproduction.

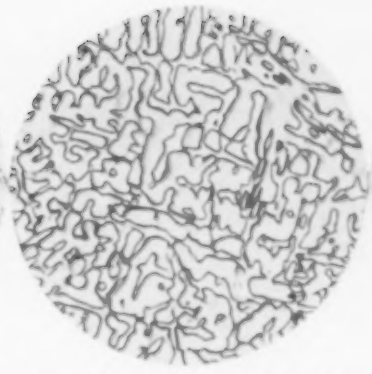

Fig. 6—48.7 pct Pb alloy, annealed for 1 hr at 1200°C, water quenched. β matrix + Ti_2Pb. HNO_3 etch. X300. Area reduced approximately 15 pct for reproduction.

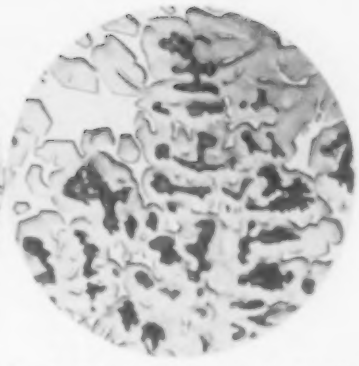

Fig. 7—48.7 pct Pb alloy, annealed for 168 hr at 700°C, water quenched. β (white) + Ti_2Pb (gray) + γ (dark). HNO_3 etch. Electrolytically stained, "HG" electrolyte. X600. Area reduced approximately 15 pct for reproduction.

The average melting points are given in Table I.

Metallography: Specimens were prepared for metallographic examination by electrolytic polishing and were etched with a 25:25:50 HNO_3:HF:glycerine mixture (Remington A-etch) for low lead alloys or with 50:50 HNO_3:H_2O etch for high lead alloys. To increase contrast between Ti_2Pb and other phases, the stain-etching procedure of Ence and Margolin[7] was used also.

The Ti-Pb Diagram

The Ti-Pb diagram is shown in Fig. 1. The portion of the diagram delineated shows three distinct features: 1—the eutectoid reaction by which β decomposes into α and Ti_2Pb; 2—the peritectic reaction $\beta + L \rightarrow Ti_2Pb$; and 3—the possible eutectic decomposition of liquid into Ti_2Pb and γ.

The eutectoid horizontal lies between 700° and 750°C and probably close to 725°±10°C. The microstructures of various alloys between 15 and 25 wt pct Pb were used in an attempt to locate the eutectoid temperature. Microstructures of the 750°C anneal showed α, transformed β, and Ti_2Pb*, similar to Fig. 2. The 700°C treatment of these alloys showed equiaxed α and Ti_2Pb, whereas the 725°C anneal showed structures which could be interpreted as three-phase α, β, and Ti_2Pb. The fact that microstructures produced by annealing at 725°C showed $\alpha + \beta$ indicated that the eutectoid temperature was not above 725°C. It is not certain from the microstructures whether the Ti_2Pb formed at 725°C or during quenching. If the Ti_2Pb formed during the anneal, this would be an indication of oscillation above and below the eutectoid temperature and hence would fix the temperature at 725±10°C.

Additional evidence that the eutectoid temperature was above 700°C was obtained by heat treating specimens at 1100°C for 1 hr, then quenching into a lead bath at 700°C and holding at this temperature for 1 hr before water quenching. The results of this test can be seen by comparing the microstructures of Figs. 3 and 4. Fig. 3 shows a 40.5 pct Pb alloy heat treated in the foregoing manner. Fig. 4 shows a 40.5 pct Pb alloy heat treated at 1100°C for 2 hr and water quenched. In Fig. 4, the matrix shows no transformation structure,** while in Fig. 3 the matrix appears completely transformed. From this, it can be seen that the transformation must have taken place isothermally at 700°C, and therefore this temperature is below the eutectoid horizontal.

The eutectoid composition was placed at 26 pct Pb, although this was not definitely established. From the data available, it would be possible to locate the eutectoid composition in the range 25 to 28 pct Pb. However, the 26 pct Pb alloy heat treated at 775°C was nearly all β; but in separate parts of the specimen, it revealed either α and β or β and Ti_2Pb, the α and Ti_2Pb not being found together. The chemical analysis of two portions of the alloy indicated the same composition, 26 pct Pb. Because large samples were necessary, the local inhomogeneities observed under the microscope were not detectable by chemical analysis. The microstructure of the alloy suggested that the composition of 26 pct Pb lay about midway between the $\alpha + \beta$ and $\beta + Ti_2Pb$ phase fields at 775°C and consequently was the eutectoid composition.

The maximum solubility of lead in α is 16±0.5 wt pct Pb and was determined from the intersection of the α transus with the eutectoid horizontal. The α solvus is not well defined because of the rapid precipitation of small amounts of Ti_2Pb from α on quenching. Since Ti_2Pb is found in all of the α alloys, a marked decrease in solubility of lead is indi-

* The Ti_2Pb probably formed on quenching. This appears likely, since the α phase could not be obtained free of Ti_2Pb regardless of the temperature in the α field from which the alloys were quenched. To see Ti_2Pb in the isothermal α of Fig. 2, a considerably higher magnification would be required.

** Beta containing 38 pct Pb or more is retained on quenching.

Table II. Times of Heat Treatment

Temperature, °C	Time
1500	4 min
1300	20 min
1200	1 hr
1100	2 hr
1025	8 hr
900	16 hr
875	24 hr
850	24 to 68 hr
825	120 hr
800	72 hr
775	168 hr
750	168 hr
725	168 hr
700	168 hr
600	336 hr
500	404 hr

Table III. X-ray Diffraction Pattern of Ti_2Pb.* $a = 5.96_0$ A; $c = 4.81_0$ A; $c/a = 0.807$.

Plane	Estimated Intensity	d, Observed A, This Report	d, Observed A, Nowotny and Pesl	d, Calculated A
100	0.05	5.16	5.211	5.163
101	0.2	4.514	4.550	4.521
110	0.1	2.978	2.976	2.981
200	0.1	2.576	2.582	2.582
002	1	2.394	2.415	2.407
201	1	2.271	2.274	2.275
102	0.1	2.157	2.169	2.161
120	0.01	1.918	1.905	1.922
112	0.2	1.867	1.879	1.872
121	0.15	1.808	1.809	1.808
202	0.2	1.758	1.764	1.761
003	0.01	1.718	1.726	1.721
103	0.05	1.596	1.598	1.592
122	0.05	1.515	1.516	1.515
220	0.1	1.490	1.491	1.491
113	—	—	1.454	1.452
212	0.05	1.398	1.401	1.400
111	0.02	1.372	1.374	1.372
203	0.2	1.307	1.307	1.302
300	0.01	1.295	1.292	1.291
123	0.15	1.265	1.270	1.267
301	0.07	1.246	1.246	1.247
213	0.07	1.239	—	1.238
310	—	—	1.232	1.230
104	0.1	1.199	1.208	1.201
124	0.05	1.164	—	1.172
311	0.05	1.150	1.151	1.150
302	0.02	1.135	1.140	1.137
223	0.05	1.127	1.127	1.127
114	0.1	1.114	1.119	1.116
312	0.1	1.089	1.087	1.086
205	—	—	1.077	1.067
320	0.1	1.068	1.062	1.063
204	0.05	1.021	1.022	1.024
321	} 0.1	1.005	1.009	{ 1.010
400				1.006
313	0.05	1.004	—	1.002
304	0.01	0.9665	0.9666	0.9662
420	0.05	0.9760	0.9733	0.9736
305	0.15	0.8827	—	0.8820
421	—	—	0.8703	0.8705
116	0.01	0.8469	0.8466	0.8465
224	0.2	0.8376	0.8382	0.8383

* Isothermal quenching, 34.6 wt pct Pb, annealed 48 hr at 800°C, water quenched. This alloy also contained γ.

cated. The α solvus, as shown in the diagram of Fig. 1, was determined by the appearance of larger amounts of Ti_2Pb at the grain boundaries than was noticed in alloys quenched from the α field. This procedure can be regarded as yielding only an approximate location of the α transus.

Figs. 5 and 6 are typical $\beta + Ti_2Pb$ microstructures. None of the alloys prepared showed entirely Ti_2Pb. Microstructures of alloys containing within 3 wt pct of either side of Ti_2Pb (31.9 pct Pb) show considerable amounts of β or γ; see, for example, the microstructure of a 48.7 pct Pb alloy of Fig. 6. The solubility range of Ti_2Pb therefore is quite small.

The maximum solubility of lead in β was determined by heat treating an alloy of 45 wt pct Pb at 1300±5°C for 20 min and then quenching. This alloy consisted principally of β with very small amounts of liquid and Ti_2Pb, thus indicating that 45 pct Pb is the limit of solubility in β.

The above heat treatment also located the peritectic horizontal at 1300°C. The average of the melting points of several specimens of the 45 and 48.7 pct Pb alloys placed the peritectic temperature at 1305±10°C.

The solidus and liquidus phase boundaries indicate a very narrow liquid plus β region. This was substantiated by the fact that coring could not be detected in the as-cast alloys. The melting point of iodide titanium was also determined with the apparatus described earlier. The temperature obtained was 1665±10°C, which compares well with the value of 1660±10°C obtained by Schofield and Bacon.[7]

The γ phase may enter into eutectic reaction with Ti_2Pb between 1200° and 1300°C, though the possibility of a peritectic reaction cannot be discarded. Microstructure data obtained from the as-cast alloys tend to support the eutectic. The three phases, β, Ti_2Pb, and γ, are shown in Fig. 7 after a heat treatment at 700°C. The anneal has not eliminated the as-cast structure. The γ phase may either be Ti_3Pb (59 wt pct Pb) or Ti_2Pb (68.3 wt pct Pb), although the latter composition seems more likely.

X-ray Diffraction

Diffraction data for Ti_2Pb was obtained from alloys which contained Ti_2Pb and a second phase, α, β, or γ. The d-values reported for this compound in Table III agree well with the data of Nowotny and Pesl,[5] the c/a value being 0.808 and a = 5.962A. It should be pointed out that, since Ti_2Pb is a type Do_a hexagonal compound belonging to the same space group as α-titanium with a c/a ratio almost ½ that of α-titanium, coincidence of a number of Ti_2Pb lines with those of α take place. Consequently, unless considerable amounts of Ti_2Pb are present, it is not possible to detect the compound in the presence of α.

The γ phase could not be identified as to lattice type because insufficient amounts of this phase were present in the alloys used for X-ray patterns. However, from these patterns it could be seen that γ is not lead.

Summary

The Ti-Pb diagram was investigated in the region from 0 to 58 wt pct Pb. The diagram is characterized by three reactions: 1—the eutectoid decomposition of β into α and Ti_2Pb at 725±10°C; 2—the peritectic reaction $\beta + L \rightarrow Ti_2Pb$ at 1305±10°C; and 3—the possible eutectic decomposition of liquid into Ti_2Pb and γ between 1200° and 1300°C. The eutectoid composition is placed at 26 wt pct Pb and the maximum solubility of lead in α-titanium is 16±0.5 pct at the eutectoid temperature. The maximum solubility of lead in β-titanium at the peritectic temperature is 45 pct. Melting-point data show that the liquid-solid region is quite narrow and that iodide titanium melts at 1665±10°C.

Acknowledgments

The authors wish to express their indebtedness to Mr. A. E. Palty, who carried out much of the early experimentation on the methods of preparing the alloys, and to members of the staff who assisted in carrying out parts of the experimental program. The authors also thank the United States Army Ordnance Corps, Watertown Arsenal, for permission to publish these results. The work was carried out under Watertown Arsenal Contract No. DA-30-069-ORD-208.

References

[5] H. Nowotny and J. Pesl: Investigations in the System Titanium Lead. *Monatschefte fur Chemie* (1951) **82**, p. 344.

[6] M. Hansen: *Aufban der Zweistofflegierungen*. (1936) Berlin. J. Springer.

[7] C. M. Craighead, O. W. Simmons, and L. W. Eastwood: Titanium Binary Alloys. *Trans.* AIME (1950) **188**, p. 465; JOURNAL OF METALS (June 1950).

[8] I. Cadoff and J. P. Nielsen: Titanium-Carbon Phase Diagram. *Trans.* AIME (1953) **197**, p. 248; JOURNAL OF METALS (February 1953).

[9] E. Enve and H. Margolin: Phases in Titanium Alloys Identified by Cumulative Etching. JOURNAL OF METALS (1954) **6**, p. 346.

[7] T. H. Schofield and A. E. Bacon: The Melting Point of Titanium. *Journal* Institute of Metals (1953) **82**, part 4, p. 167.

Effect of Alpha Solutes on the Heat-Treatment Response Of Ti-Mn Alloys

by H. R. Ogden, F. C. Holden, and R. I. Jaffee

Alpha solutes increase the strengths of Ti-Mn alloys through solid-solution strengthening. The substitutional α addition, aluminum, decreases, and the interstitial solutes, carbon and nitrogen, increase the rate of nucleation and growth of α from β. The best combinations of properties of α-β alloys are obtained when there is a sufficient quantity of α phase in the structure to dissolve the α solutes.

OF the many different titanium-base alloy systems, the predominant alloy type is the α-β alloy. The properties of the α-β alloys are dependent on solid-solution strengthening and heat-treatment effects involving the α-β ratio and transformation reactions. Another variable which influences the mechanical properties of α-β alloys is the α-stabilizer content of the alloy. An α solute may be present as an intentional addition, such as aluminum, or as an impurity element, such as carbon, oxygen, or nitrogen. It is known that these α stabilizers, when added to titanium, form single-phase alloys which are not heat treatable but which obtain their strength from solid-solution strengthening.[1-3] Thus, it would be expected that α additions to α-β alloys would increase the strength of the alloys by solid-solution strengthening of the α phase. In addition, they would affect the transformation kinetics of the β-to-α reactions and other processes based on the instability of the β phase.

The effects of heat treatment and structure on the mechanical properties of Ti-Mn alloys have been shown in a previous paper.[4] This system offers a good base to demonstrate the effects of typical α solutes on the properties of α-β alloys. The three α solutes described in this work are aluminum, representative of a substitutional α solute, nitrogen, representative of an interstitial α solute, and carbon, representative of an interstitial compound-forming element. The effects of heat treatment and microstructure on the properties of α alloys containing these three elements are described in concurrent publications.[5-7] Some of these data are used for base-line points in several of the curves used for illustration herein.

Experimental Procedures

Iodide titanium was used as the base for all of the alloys studied in this work. The alloys were prepared as ½ lb ingots by double arc melting in an argon atmosphere. The ingots were forged to ¾ in. rounds, vacuum annealed for 6 hr at 900°C at a pressure of 10^{-4} to 10^{-5} mm of Hg to remove hydrogen, and hot swaged to ¼ in. diam rod. After mechanical descaling, test specimens were prepared for heat treatment. The alloys used in this study together with the fabrication temperatures are given in Table I.

Table I. Compositions and Fabrication Temperatures of Alloys Used in this Investigation

Composition, Pct								Forging Temperature, °C	Swaging Temperature, °C
Intended				Analyzed					
Mn	N	C	Al	Mn	N	C	Al		
3	0.1	—	—	2.68	0.072	—	—	875	750
6	0.1	—	—	5.63	0.11	—	—	875	750
9	0.1	—	—	7.92	0.073	—	—	875	750
3	—	0.1	—	2.87	0.004	0.06	—	875	750
6	—	0.1	—	5.34	0.004	0.09	—	875	750
9	—	0.1	—	8.73	0.005	0.11	—	875	750
3	—	—	2.5	2.73	0.007	—	2.42	875	750
6	—	—	2.5	5.91	0.004	—	2.45	875	750
9	—	—	2.5	8.88	0.005	—	2.46	980	750

Heat treatments were done in argon. For the most part, the specimens were sealed in Vycor capsules under a partial pressure of argon. Quenching was accomplished by breaking the capsule under water. Other cooling methods used included oil quench, argon cool (simulated air cool in an argon atmosphere), and furnace cool. The times for the various heat-treating temperatures are given in Table II.

The tests performed on the alloys consisted of tensile tests on ⅛ in. diam specimens, hardness tests, and microimpact tests. Specimen sizes have been adequately described in a previous publication.[4]

The micrographs presented in this paper were taken from specimens cut from the shoulders of broken tensile specimens. Final polishing was done with Linde B on a slow-speed wheel, and the specimens were etched with a 1½ HF — 3½ HNO_3 solution.

Ti-N-Mn Alloys

The transformation diagram and microstructures of the Ti-0.1 pct N-Mn alloys used in this investigation are given in Fig. 1. The effect of small nitrogen additions on the binary Ti-Mn diagram is to raise the β-transus temperature with little effect on the α solubility of manganese. Also, as has been noted previously,[7] high manganese-content alloys containing nitrogen, when quenched from temperatures high in the β field, contain a subgrain boundary phase which appears to be nitrogen-rich α. Martensite is formed when alloys containing less than about

H. R. OGDEN, F. C. HOLDEN, and R. I. JAFFEE, Members AIME, are Assistant Chief, Principal Metallurgist, and Chief, respectively, Nonferrous Physical Metallurgy Div., Battelle Memorial Institute, Columbus, Ohio.

Discussion on this paper, TP 3860E, may be sent, 2 copies, to AIME by Mar. 1, 1955. Manuscript, Apr. 15, 1954. Chicago Meeting, November 1954.

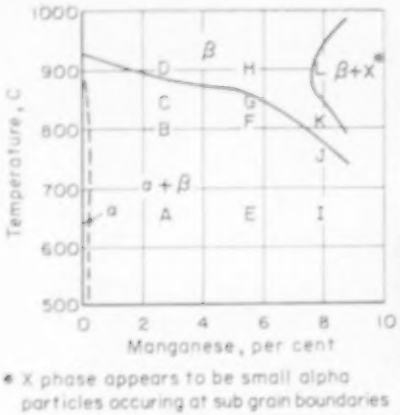

* X phase appears to be small alpha particles occuring at sub grain boundaries

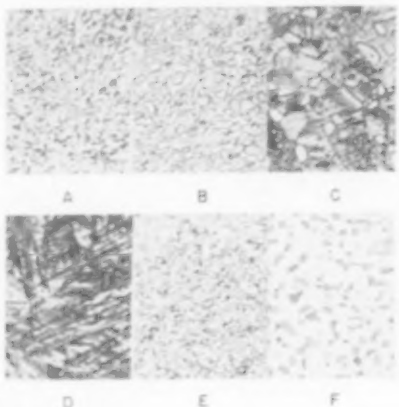

Fig. 1—Transus diagram showing quenching temperatures studied and microstructures of Ti-0.1 pct N-Mn alloys. X250. Area reduced approximately 25 pct for reproduction.

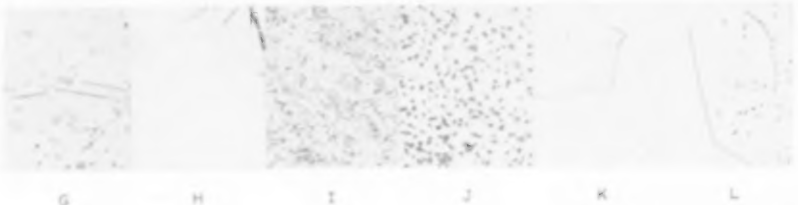

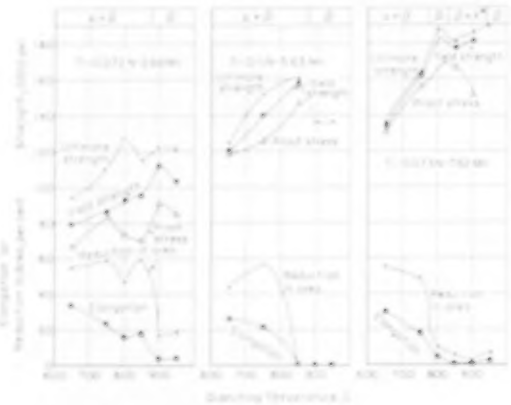

Fig. 2—Mechanical properties of Ti-N-Mn alloys quenched from the annealing temperature. "In graph, right, structure consists of equiaxed β plus veining of α.

Table II. Times and Temperatures Used for Heat Treatment of Alloys

Time, Hr	Temperature, °C
30	850
70	750
5	800 to 810
4	800 to 860
2	800
1	850

5.8 pct Mn are quenched from above about 800°C. The Ti-0.11 pct N-5.63 pct Mn alloy is close to the minimum manganese content at which β can be completely retained by quenching. Only a few martensite needles are seen in the structure of this alloy. Annealing these alloys below the β transus and above 800°C produces structures containing α plus martensite plus β. Annealing below 800°C and below the β transus after fabrication in the α-β field produces equiaxed α-β structures having an α-β ratio dependent on the heat-treating temperature.

As was found for the binary Ti-Mn alloys, the properties of the Ti-N-Mn alloys are influenced by the quantities and compositions of the two phases present in the structure when quenched from the α-β field. This is illustrated by the data in Fig. 2, where it is shown that the strength of a given alloy increases with increasing quenching temperature. Two discontinuities are apparent, however. One is the Ti-0.072 pct N-2.68 pct Mn alloy quenched from 800°C, and the other is the Ti-0.073 pct N-7.92 pct Mn alloy quenched from 800°C. The Ti-0.072 pct N-2.68 pct Mn alloy quenched from 800°C has an α-β structure as compared to an α-martensite or martensite structure when quenched from above 800°C. The β phase in the 800°C quenched sample is of a composition where coherency hardening takes place on quenching, causing formation of β'. The highest strengths obtained for the Ti-0.073 pct N-7.92 pct Mn alloy occurred when the structure was all β phase. This occurs when the quenching temperature is about 800° or 950°C. The presence of the subgrain α that is found in this alloy quenched from 850° or 900°C causes a reduction in strength probably as a result of reduction of the interstitial content of the β phase. The best ductilities are found when these alloys are annealed in the α-β field. The β phase in the Ti-0.11 pct N-5.63 pct Mn alloy quenched from the β field is hard and brittle, indicating β' formation.

The toughness of Ti-N-Mn alloys generally decreases as the quantity of β in the structure is increased, as shown in Fig. 3. The transition temperatures for the Ti-0.11 pct N-5.63 pct Mn and Ti-0.073 pct N-7.92 pct Mn alloys increase with increasing quenching temperature except that the Ti-0.073 pct N-7.92 pct Mn alloy quenched from 850°C has a lower transition temperature than the same alloy quenched from 800°C. This again indicates that the formation of the subgrain boundary phase reduces

the brittleness of the β phase. The formation of martensite in the Ti-0.072 pct N-2.68 pct Mn alloy decreases the transition temperature from that found for the 800°C quenched condition.

Ti-C-Mn Alloys

The transformation diagram and microstructures of the Ti-0.1 pct C-Mn alloys used in this investigation are given in Fig. 4. Carbon, in addition to raising the β-transus temperature, also introduces β-carbide and α-β-carbide fields in the ternary Ti-C-Mn system. Alloys containing less than about 5.4 pct Mn transform, at least partially, to martensite on quenching from above 800°C. The alloy containing 5.34 pct Mn contains a small quantity of martensite when quenched from the β field.

The effect of heat treatment and structure on the properties of Ti-0.1 pct C-Mn alloys, as shown in Fig. 5, is similar to that for the Ti-0.1 pct N-Mn alloys. Increasing the quantity of β phase in the structure causes marked increases in strength with little loss in ductility until the structure is composed of β phase, martensite, or β plus martensite. The high strength of the Ti-0.06 pct C-2.87 pct Mn alloy quenched from 810°C can be attributed to the alloy content of the β phase in that condition. The β phase is of such a composition that, even though some martensite is formed on quenching, the remaining β probably goes to coherency-hardened β'. This is the same effect noted in the Ti-0.1 pct N-2.68 pct Mn alloy. The β phase obtained by quenching the Ti-0.09 pct C-5.34 pct Mn alloy from the β-carbide field is hard and brittle. High strengths with some ductility are obtained in the Ti-0.11 pct C-8.73 pct Mn alloy quenched from the β-carbide field. However, the presence of α obtained by annealing in the α-β-carbide field reduces the strength considerably with a corresponding increase in ductility.

The toughness of these alloys can be directly related to the quantity of α phase in the microstructure. The toughness increases as the quenching temperature is decreased, as shown in Fig. 6. Quenching from the β-carbide field results in very low impact resistance.

Ti-Al-Mn Alloys

The transformation diagram and microstructures of the Ti-2.5 pct Al-Mn alloys used in this investigation are given in Fig. 7. Aluminum, like nitrogen, raises the β-transus temperature with little effect on the α solubility of manganese. No subgrain-boundary phase has been noted in this system. The equilibrium β phase transforms, at least partially, to martensite when alloys containing up through 5.91 pct Mn are quenched from about 800°C.

The properties of the Ti-2.5 pct Al-Mn alloys can be altered by heat treatment, but they are not as dependent on the α-β ratio as are the binary Ti-Mn

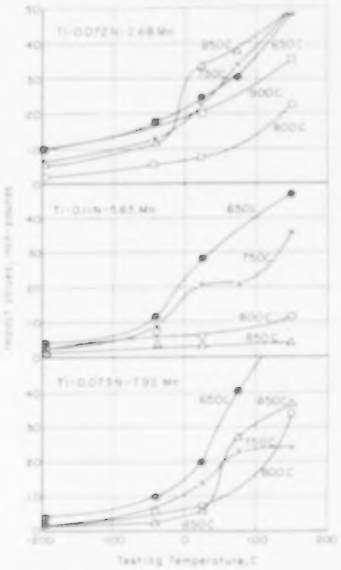

Fig. 3—Impact curves for Ti-0.1 pct N-Mn alloys quenched from various temperatures.

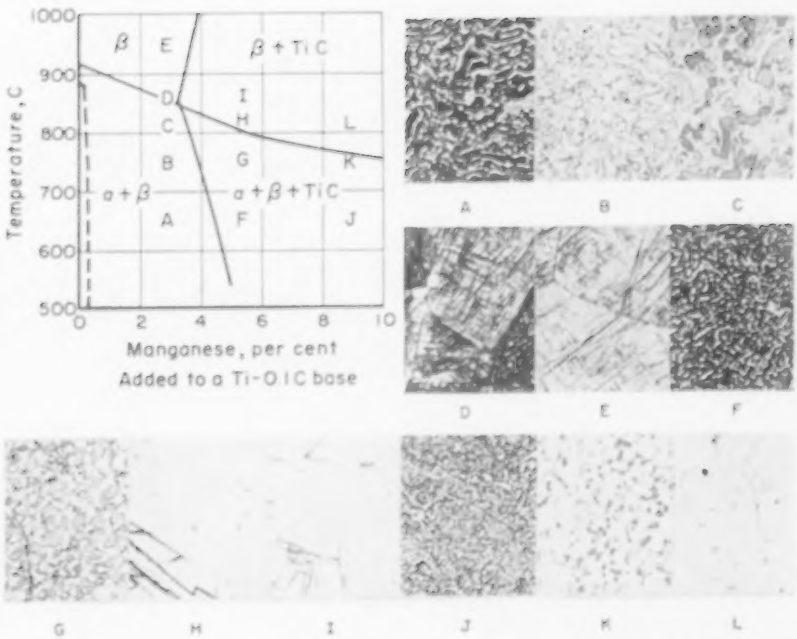

Fig. 4—Transus diagram showing quenching temperatures studied and microstructures of Ti-0.1 pct C-Mn alloys. X250. Area reduced approximately 25 pct for reproduction.

and ternary Ti-N-Mn alloys. Rather, the formation of martensite has a much more potent effect on the properties. This is shown by the data in Fig. 8. Some increase in strength is obtained with little change in ductility when the Ti-2.42 pct Al-2.75 Mn and Ti-2.43 pct Al-5.91 pct Mn alloys are quenched from 800°C, as compared to 650° or 750°C. However, quenching from the β field or from above about 800°C causes a marked increase in strength with a corresponding loss in tensile ductility. Quenching the Ti-2.43 pct Al-5.91 pct Mn alloy from the β field produces a structure consisting of martensite and retained β. As discussed later, the β phase of this composition is mechanically unstable and transforms to martensite during straining, which gives rise to the large spread between the yield strength and the ultimate strength. The same mechanical instability of the β phase occurs in the Ti-2.42 pct Al-2.75 pct Mn alloy quenched from 850°C, but to a much less pronounced degree because of the smaller quantity of β phase present. The composition of the β phase in this alloy quenched from 850°C probably has a manganese content of about 6 pct.

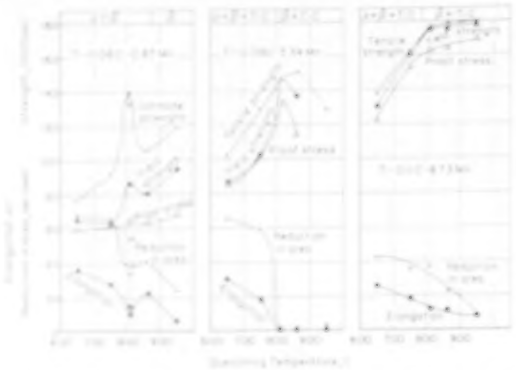

Fig. 5—Mechanical properties of Ti-C-Mn alloys quenched from the annealing temperature.

The strength of the Ti-2.46 pct Al-8.88 pct Mn alloy is relatively unaffected by altering the annealing temperature from 650° to 800°C. The tensile ductilities, however, are markedly affected by annealing temperature and microstructure. The presence of massive α formed by annealing at 750°C results in high ductilities, while the presence of a very small amount of α formed by annealing at 800°C results in low ductilities. The relatively fine α that forms by annealing at 650°C results in low reduction in area, but good elongation values.

The toughness of the low manganese-content Ti-2.5 pct Al-Mn alloys, as shown in Fig. 9, is not so dependent on the α-β ratio as is the case with Ti-N-Mn alloys, although, as a general tendency, toughness increases as the quantity of α in the structure of

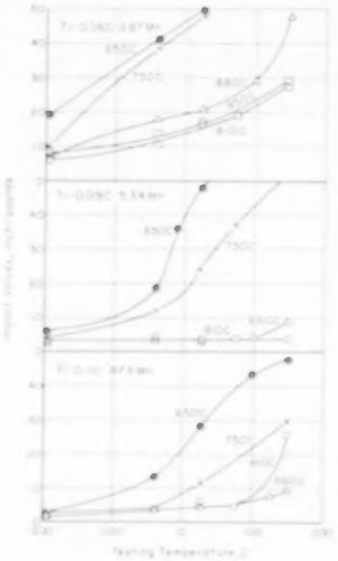

Fig. 6—Impact curves for Ti-0.1 pct C-Mn alloys quenched from various temperatures.

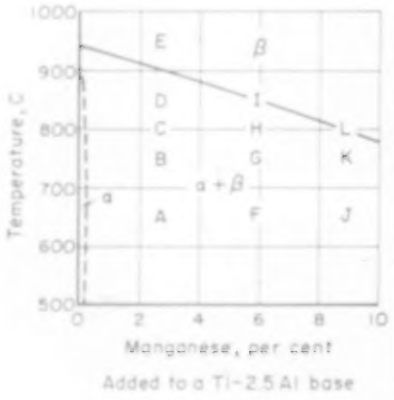

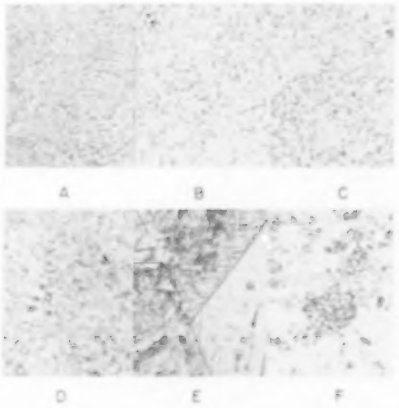

Fig. 7—Transus diagram showing quenching treatments studied and microstructures of Ti-2.5 pct Al-Mn alloys. X250. Area reduced approximately 25 pct for reproduction.

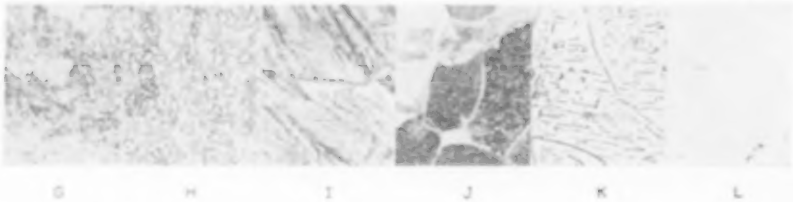

the alloy is increased. Unlike the Ti-0.1 pct N-2.68 pct Mn alloy, the Ti-2.42 pct Al-2.75 pct Mn alloy has the lowest impact resistance when the structure is all martensite. Transition behavior occurs in the Ti-2.46 pct Al-8.88 pct Mn alloy because of the high percentage of β phase in this alloy. The lowest transition temperature occurs for the 750°C quenched condition, which is also the condition which had the highest reduction in area in tension.

Solid-Solution Effects

In a system containing a β stabilizer and an α stabilizer, it would be expected that the α stabilizer would partition to and strengthen the α phase, and the β stabilizer would partition to and strengthen the β phase. Thus, by control of the quantities and compositions of the two phases, either by alloy content or heat treatment, the strength of the alloy can be altered. The β phase, being the stronger of the two phases, will have the dominant effect on the properties, and the strength will increase as the quantity of β phase increases. This is the same effect as was found for binary Ti-Mn alloys,[7] and is illustrated by the data shown in Fig. 10.

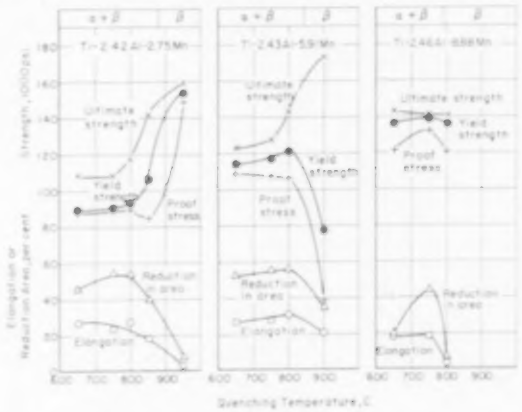

Fig. 8—Effect of quenching temperature on the tensile properties of Ti-2.5 pct Al-Mn alloys.

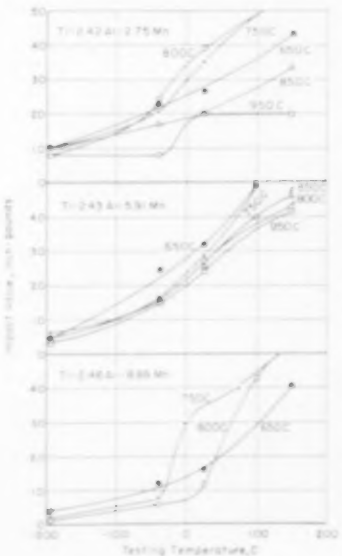

Fig. 9—Impact curves for Ti-2.5 pct Al-Mn alloys quenched from various temperatures.

In the temperature range where transformation effects are not operative, the strengths of α-β alloys increase as the manganese content is increased (that is, an increase in the quantity of β phase in the structure) for a given annealing treatment. Also, for a given composition, an increase in the annealing temperature, which also increases the quantity of β phase in the structure, increases the strength. If it is assumed that the α stabilizer partitions to the α phase, then, as the quantity of α is decreased by higher annealing temperature or higher manganese content, the α phase becomes enriched and stronger. This adds to the strengthening effect gained by the increase in quantity of the β phase. Therefore, the strength of an α-β alloy would be greater than the sum of the strengths of the two terminal phases. In the case of an α solute with restricted solubility, such as carbon, when the α phase is enriched to the limit of its solubility, additivity would be expected to be approached. This is the case for the Ti-C-Mn alloys, as can be seen in Fig. 10. The deviation from additivity in the binary Ti-Mn alloys may also be caused, at least partially, by the partitioning of the interstitial impurities to the α phase.

The ductilities of the ternary Ti-Mn alloys containing α additions are very good as long as transformation effects are avoided and sufficient α phase is present to dissolve the α solutes. When conditions are such that transformation reactions take place or when the alloys are in the all-β condition, the ductilities are very low.

Effect of α Stabilizers on the β to α Reactions

The two reactions that can be affected by the addition of α stabilizers to α-β alloys are the martensite and nucleation-and-growth reactions. In this work no direct attempt was made to determine the effects of α stabilizers on the martensite reaction.

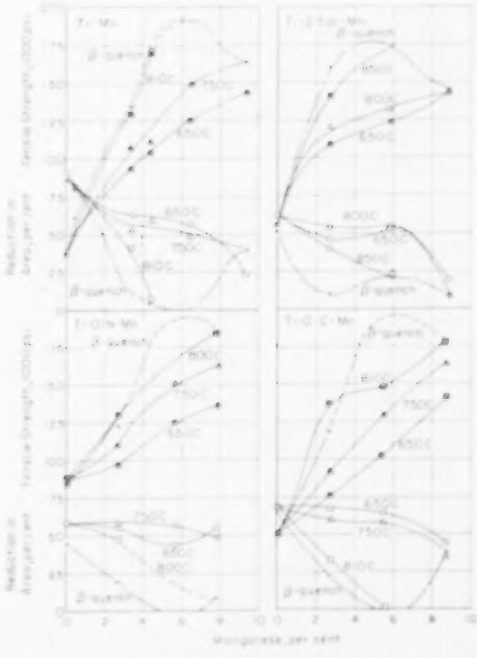

Fig. 10—The effect of manganese content on the properties of Ti-Mn alloys containing aluminum, nitrogen, or carbon in various quenched conditions.

The effect of α stabilizers on the nucleation-and-growth reaction was found to depend on the type of α stabilizer added. The interstitial α stabilizers increase the rate at which α precipitates from β, while the substitutional α stabilizer, aluminum, decreases the rate at which α precipitates from β. This has a direct effect on the transformation kinetics of α-β alloys, particularly in the composition range where β' is formed. It is known that β' is formed when binary Ti-Mn alloys containing about 6 pct Mn are quenched from the β field, resulting in a hard brittle condition. The effect of α stabilizers on the hardness of β-quenched Ti-Mn alloys containing about 6 pct Mn is shown in Table III.

Although there are differences in manganese content in the alloys, the hardness differences can be associated with the rate of formation of α from β which is dependent on the α-stabilizer content. This is shown more clearly by the aging curves for the Ti-6 pct Mn alloys in Fig. 11. The peak hardness obtained on aging does not vary much from alloy to alloy; but, rather, the greatest variation occurs in the as-quenched hardness and in the time required for overaging. This indicates that the reaction rates are so fast in the Ti-Mn alloys containing interstitials that aging actually occurs during the quench. With aluminum present, however, the rate of precipitation of α from β is much slower and a longer time is required for overaging to occur.

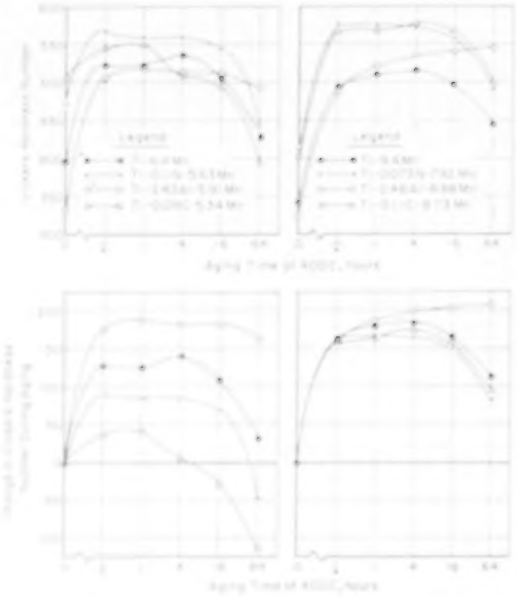

Fig. 11—Effect of ternary α additions on the aging characteristics of β-quenched Ti-Mn alloys.

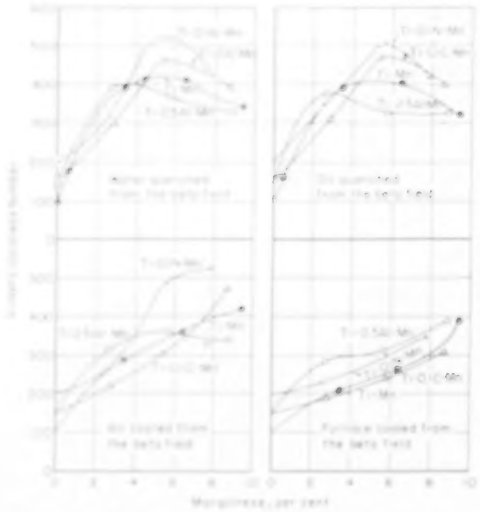

Fig. 12—Effect of cooling rate on the VHN of Ti-Mn alloys annealed in the β field.

The rapidity of the β-to-α precipitation reaction may mask the martensite reaction in many titanium α-β alloys. The formation of β' at temperatures above the M_s temperature may enrich the β phase sufficiently so that no martensite is formed during the quench. This is the case for the Ti-0.09 pct C-5.34 pct Mn alloy where only a few martensite needles are found in this alloy quenched from the β field, while a considerable portion of a binary Ti-5.5 pct Mn alloy is martensite as-quenched. Aluminum by decreasing the rate of α precipitation from β, permits the martensite reaction to occur in the Ti-2.43 pct Al-5.91 pct Mn alloy such that the as-quenched structure is martensite plus β.

At higher manganese contents, 8 to 9 pct, the addition of aluminum still causes a hardness decrease. This may mean that even at these high manganese contents some coherency-hardened β' is formed on quenching which is retarded by the presence of aluminum. However, the hardness increase obtained by the presence of carbon or nitrogen is equivalent to the hardening effect of the same quantity of carbon or nitrogen in solid solution in unalloyed titanium. Furthermore, as shown in Fig. 11 for the 9 pct Mn alloys, the aged hardnesses of the Ti-C-Mn and Ti-N-Mn alloys maintain the hardness differences, indicating that solid-solution hardening of the β phase is accomplished by the presence of the interstitials. Again overaging occurs much more rapidly for the aluminum-free alloys than for the alloys containing aluminum.

Cooling-rate studies also show the effect of the α stabilizers on the β-to-α reaction rates. As shown in

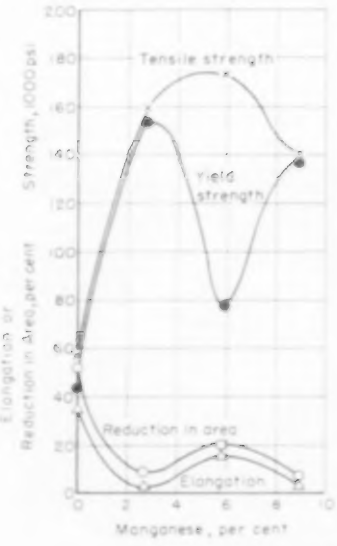

Fig. 13—Tensile properties of β-quenched Ti-2.5 pct Al-Mn alloys.

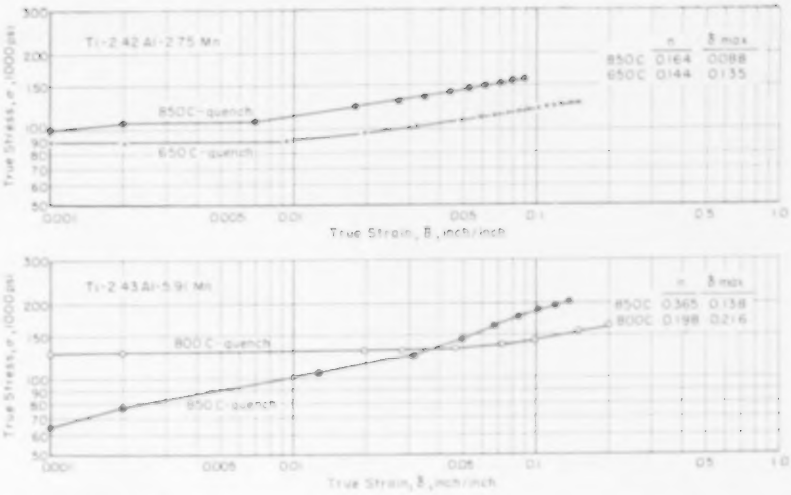

Fig. 14—Flow curves for Ti-Al-Mn alloys.

Fig. 12, when the cooling rate is decreased, the hardness peak moves to higher manganese contents. This shift in hardness peak is more rapid for the alloys containing interstitial α additions and slower for the alloys containing aluminum than for the binary Ti-Mn alloys. In the composition range where the martensite reaction is dominant (up to 4 pct Mn), the hardness of the β-quenched alloys appears dependent on the α stabilizer present in the alloy. The alloys containing interstitial additions are softer, and the alloys containing aluminum are harder than the binary Ti-Mn alloys. This would indicate that the presence of interstitials, which at higher manganese contents increase the rate of the β-to-α nucleation-and-growth reaction, may also cause the nucleation and growth of α in this composition range.

Mechanical Instability of the β Phase

It has been shown that the β phase in the Ti-Al-Mn alloys containing about 6 pct Mn is not subject to β′ formation. Rather, the β-quenched structure consists of martensite plus retained β. The β phase in this condition is not mechanically stable. It will transform to martensite during straining, with the result that the tensile properties exhibit a large spread between flow stresses and the tensile strength. This is illustrated by the data shown in Fig. 13, where it can be seen that there is a sharp drop in yield strength at a manganese content of around 6 pct. The flow curves given in Fig. 14 for the Ti-Al-Mn alloys also show this effect. In the α-β-quenched condition, the Ti-2.43 pct Al-5.91 pct Mn alloy has a flow curve similar to those found for other titanium alloys. However, in the β-quenched condition, the slope of the flow curve is much greater although the uniform elongation is less than that for the α-β condition. This is the result of the transformation occurring during straining. Similarly, the flow curve for the Ti-2.42 pct Al-2.75 pct Mn alloy in the 850°C

Table III. Effect of α Stabilizers on Hardness of β-Quenched Ti-Mn Alloys (6 Pct Mn)

Alloy Composition, Pct (Balance Ti)	VHN, As-Quenched From β Field
6.4 pct Mn	395
5.62 pct Mn–0.11 pct N	474
5.24 pct Mn–0.09 pct C	508
5.91 pct Mn–2.43 pct Al	331

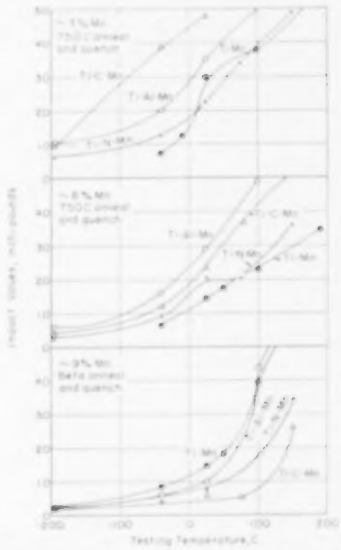

Fig. 15— Effect of α stabilizers on the toughness of Ti-Mn alloys.

quenched condition has a higher slope than in the 650°C quenched condition, indicating some martensite formation during strain.

The mechanical instability of the β phase is not found in the binary Ti-Mn and ternary Ti-Mn-interstitial systems probably because of the rapid β-to-α reaction and formation of β′ in alloys containing about 6 pct Mn. The formation of β′ would enrich the β phase such that the M_s temperature would be below room temperature.

Effect of α Solutes on Toughness of α-β Alloys

As has been pointed out previously, the toughness of an α-β alloy can be improved by increasing the quantity of α phase present in the microstructure. The body-centered-cubic β phase tends to undergo a transition from ductile to brittle behavior; and as the quantity of β phase is decreased, the tendency for the transition to occur is decreased. The effects of the α solutes on the toughness of Ti-Mn alloys are shown in Fig. 15. At a low manganese content (about 3 pct) where the α-β ratio is high, no definite transition can be seen. The alloy containing carbon has the highest impact resistance followed by the Ti-Al-Mn,

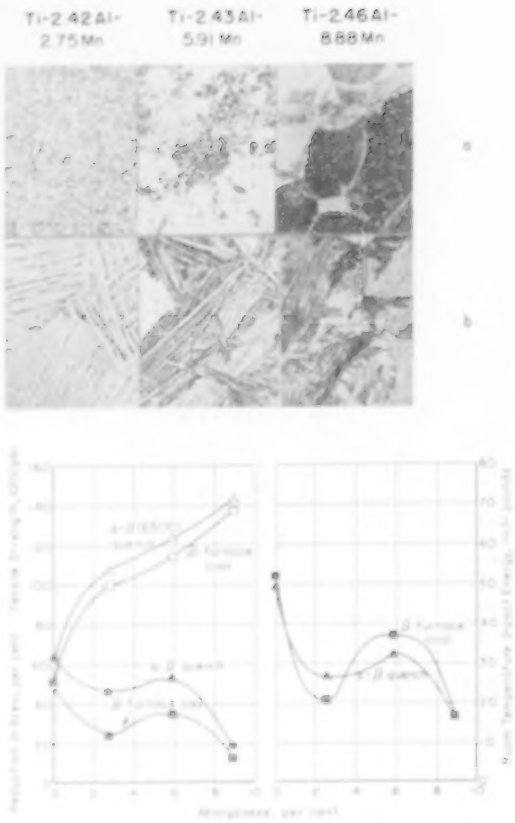

Fig. 16—Effect of grain shape on the properties of Ti-2.5 pct Al-Mn alloys. a—Equiaxed α-β; 650°C quench. b—Acicular α-β; β-furnace cool. X250. Area reduced approximately 25 pct for reproduction.

Ti-Mn, and Ti-N-Mn alloys. At the level of 6 pct Mn, the order is shifted and the Ti-Al-Mn alloy has the highest impact resistance. At about 9 pct Mn, where the alloys are all β phase, the effects of the interstitial elements are most apparent. Nitrogen and carbon raise the transition temperature over those of the Ti-Mn and Ti-Al-Mn alloys. This shows that the interstitial elements, even in the small quantities present in these alloys, have a very detrimental effect on toughness. At lower manganese content, and when massive α phase is present in the structure, aluminum and carbon additions appear to improve toughness, while nitrogen has little effect over that of the binary Ti-Mn alloys.

Effect of Grain Shape on Properties

In work with binary Ti-Mn α-β alloys, it has been shown that grain shape has little effect on strength, but rather strength is governed by the quantities and compositions of the two phases present.[5] Tensile ductility, however, is affected by grain shape, being much higher for equiaxed structures than for acicular structures of the same strength level. The same general trends have been found to hold true for the ternary alloys, as illustrated in Fig. 16 for the Ti-Al-Mn alloys. The strengths of the alloys in the β-furnace-cooled condition (acicular α-β) are lower than in the 650°C quenched condition (equiaxed α-β), and the ductilities are also lower. Impact values appear to be less dependent on structure than are ductility values, although at 6 pct Mn the acicular structure has the highest room-temperature impact value.

Summary

The addition of α stabilizers to an α-β alloy increases the strength of the alloy through solid-solution strengthening. Quenching heat treatments at temperatures below which the β-to-α reactions are operative can alter the strength of the alloy by altering quantities of α and β phases present in the structure. Increasing the quantity of β phase, the stronger of the two phases, increases the strength of the alloy. Also, as the quantity of β phase is increased, the α-stabilizer content of the α phase increases because of the partition of the α solutes to the α phase, which adds to the strength of the alloy.

Interstitial α solutes increase the rate of α formation from β by nucleation and growth while the substitutional α solute, aluminum, decreases the rate of nucleation and growth of α. Consequently, the α-β alloys containing interstitial solutes are more subject to β' formation than binary Ti-Mn alloys on quenching from the β field. The alloys containing 2.5 pct Al are not subject to β' formation; but the β phase that is retained is mechanically unstable, that is, it transforms to martensite during straining.

The best combinations of properties of α-β alloys are obtained when there is a sufficient quantity of α phase in the structure to dissolve the α solutes. Strengths are lower in this condition than when transformation effects are involved, but ductility and toughness characteristics are generally very good.

Acknowledgment

The work described is part of a study of the effect of microstructures on representative titanium alloys prepared with high purity materials. The authors are grateful to Watertown Arsenal and the Ordnance Corps for permission to publish this information. The data presented in this paper were obtained on work done at Battelle Memorial Institute under Ordnance Contract No. DA-33-019-ORD-280.

References

[1] R. I. Jaffee, H. R. Ogden, and D. J. Maykuth: Alloys of Titanium with Carbon, Oxygen and Nitrogen. *Trans.* AIME (1950) **188**, pp. 1261-1266; JOURNAL OF METALS (October 1950).

[2] H. R. Ogden, D. J. Maykuth, W. L. Finlay, and R. I. Jaffee: Mechanical Properties of High Purity Ti-Al Alloys. *Trans.* AIME (1953) **197**, pp. 267-272; JOURNAL OF METALS (February 1953).

[3] R. I. Jaffee, F. C. Holden, and H. R. Ogden: Mechanical Properties of Alpha Titanium as Affected by Structure and Composition. *Trans.* AIME (1954) **200**, pp. 1282-1290; JOURNAL OF METALS (November 1954).

[4] H. R. Ogden, R. I. Jaffee, and F. C. Holden: Structure and Properties of Ti-C Alloys. *Trans.* AIME (1955) **203**, pp. 73-80; JOURNAL OF METALS (January 1955).

[5] F. C. Holden, H. R. Ogden, and R. I. Jaffee: Heat Treatment, Structure, and Mechanical Properties of Ti-Mn Alloys. *Trans.* AIME (1954) **200**, pp. 169-184; JOURNAL OF METALS (February 1954).

[6] F. C. Holden, H. R. Ogden, and R. I. Jaffee: Microstructure and Mechanical Properties of Iodide Titanium. *Trans.* AIME (1953) **197**, pp. 238-242; JOURNAL OF METALS (February 1953).

[7] D. J. Maykuth, H. R. Ogden, R. I. Jaffee, J. W. Holladay, J. G. Kura, and J. H. Jackson: *The Titanium-Manganese, Titanium-Tungsten and Titanium-Tantalum Phase Diagrams.* Final Report on Contract AF 33(038)-8544 to Wright Air Development Center from Battelle Memorial Institute (January 12, 1953).

Selected Isothermal Sections in the Titanium-Rich Corners of the Systems Ti-Fe-O, Ti-Cr-O, and Ti-Ni-O

by W. Rostoker

Single isothermal sections were constructed for the titanium-rich corners of the systems Ti-Fe-O, Ti-Cr-O, and Ti-Ni-O with a view to locating the shape and disposition of the ternary intermediate-phase fields for the compounds isomorphous with Fe_3W_3C.

IN a previous note,[1] it was reported that a group of ternary intermediate phases existed which occurred in the general composition range Ti_2X_2O-Ti_4X_2O where X was one of the following elements: copper, nickel, cobalt, iron, or manganese. In two instances, binary intermediate phases occurred (Ti_2Cu and Ti_2Ni) which appeared to be isomorphous. The X-ray diffraction patterns of the phases could be indexed on a cubic lattice whose cell edge was of the order of 11 kX. Karlsson[2] stated that the line extinctions and line intensities indicated that these phases were isomorphous with Fe_3W_3C and therefore belonged to the space group O_h^7. This author also noted that no unique phase of this type occurred at the composition Ti_2Cr_2O. This latter statement was accepted as true at the time the previous technical note was written.[1] However, work continued along these lines and that reported here has shown that a phase isomorphous with Fe_3W_3C does exist in the vicinity of the composition Ti_2Cr_2O but not at or near Ti_2Cr_2O. The lattice parameter of this phase was found to be 13.01 kX.

Metallographic examination of both as-cast and annealed specimens of these supposed ternary oxide phases disclosed structures which were far from single phase in many instances. It was considered a point of some interest to locate more positively the composition coordinates of the single-phase fields. To this end, single isothermal sections for the systems Ti-Fe-O (1000°C), Ti-Cr-O (1000°C), and Ti-Ni-O (900°C) were constructed.

Phase relationships were studied by both X-ray diffraction and metallographic methods. Alloys were prepared as 10 g buttons by melting in a nonconsumable electrode, water-cooled copper crucible arc-melting furnace using a helium atmosphere. Oxygen was introduced quantitatively by the use of weighed amounts of TiO_2 or TiO. Iodide titanium and the purest available alloying metals were used. All results are discussed in terms of the nominal composition of the melts. Previous experience with making oxygen-rich alloys had shown that oxygen losses were not significant if a homogeneous melt was produced. Weight-loss measurements were used to check loss in metallics during melting. Anneals were conducted in evacuated Vycor bulbs, and annealing times ranged from 24 hr at 1000°C to 48 hr at 900°C. To achieve equilibrium in certain sluggish alloys, seven-day anneals were used. Debye-Scherrer powder patterns were taken in a 14 cm diam camera using filtered CuK radiation (K_{α_1} = 1.541232 kX; K_{α_2} = 1.53739 kX). Specimens were prepared by crushing and screening previously annealed buttons. In general, the X-ray diffraction results were used to identify the major phases, while the metallographic examinations were more useful in indicating the number of phases present. By the use of the combined results and general fundamental rules governing ternary equilibrium, it was possible to construct isothermal sections in good detail. In some instances where auxiliary lattice-parameter data were available, it was possible to lay down tie lines and to locate more positively corners of three-phase fields.

Isothermal Section of the System Ti-Fe-O at 1000°C

The binary systems Ti-O[3] and Ti-Fe[4] have been published. Binary phases, TiO, TiFe, and $TiFe_2$, are likely to be encountered in the titanium-rich corner of the system. The structures are NaCl (B1), CsCl (B2), and MgZn$_2$ (C14) types, respectively. Although preliminary X-ray diffraction studies indicated the presence of a ternary phase in the composition range Ti_2Fe_2O-Ti_4Fe_2O, metallographic examination of two specimens at these compositions revealed the presence of other phases.

Thirty-eight alloys were used to delineate the phase boundaries of the isothermal section illustrated in Fig. 1. The five almost single-phase ter-

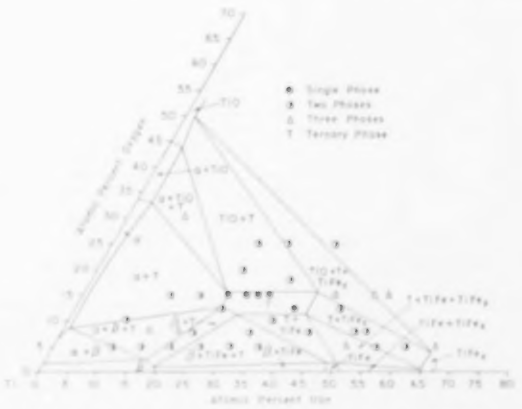

Fig. 1—System Ti-Fe-O. Isothermal section at 1000°C.

W. ROSTOKER is Senior Metallurgist, Metals Research Dept., Armour Research Foundation of Illinois Institute of Technology, Chicago.

Discussion on this paper, TP 3863E, may be sent, 2 copies, to AIME by Mar. 1, 1955. Manuscript, Nov. 27, 1953. Chicago Meeting, November 1954.

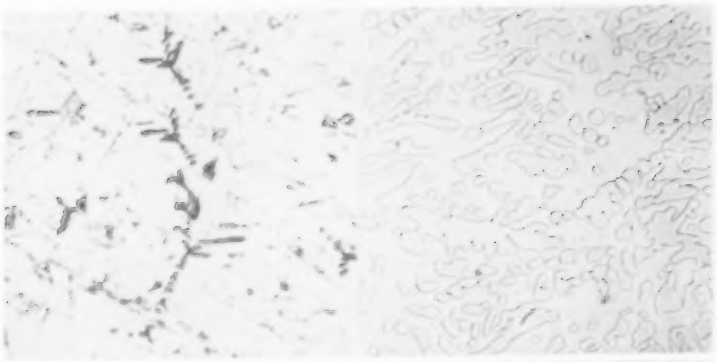

Fig. 2—15 pct O-30 pct Fe-55 pct Ti annealed for 24 hr at 1000°C. Structure almost pure ternary phase with trace dendrites of TiO. X500. Area reduced approximately 25 pct for reproduction.

Fig. 3—15 pct O-20 pct Fe-65 pct Ti annealed for 24 hr at 1000°C. Structure, primary dendrites of α in a matrix of ternary phase. Etched in 2 pct HF, 3 pct HNO_3 in water. X500. Area reduced approximately 25 pct for reproduction.

Fig. 4—15 pct O-50 pct Fe-35 pct Ti annealed for 24 hr at 1000°C. Structure, predominantly TiFe + TiO and a trace of ternary phase. Globules of TiO indicate a region of liquid immiscibility. X750. Area reduced approximately 25 pct for reproduction.

Fig. 5—8 pct O-42 pct Fe-50 pct Ti annealed for 24 hr at 1000°C. Structure, TiFe (primary dendrites) + ternary phase. Etched in 2 pct HF, 3 pct HNO_3 in water. X500. Area reduced approximately 25 pct for reproduction.

nary compound alloys showed a continuous trend in lattice parameters. This trend was useful in locating the directions of tie lines in the adjoining two-phase fields. A knowledge of the variation in lattice parameters of the α and TiO phases with oxygen contents[4] also assisted in this respect. Appropriate microstructures were encountered for each of the phase fields except for the field (β + TiFe + ternary phase). It can only be assumed that equilibrium in this portion of the diagram proceeds extremely sluggishly, as certain alloys were subjected to seven-day anneals. There can be no doubt that this three-phase field must exist because of the positive identification of the (β + ternary phase) and (TiFe + ternary phase) fields. The fan-shaped (TiFe + ternary phase) field was dictated by the lattice parameter of the ternary phase in the 32 pct Fe, 8 pct O alloy.*

* All compositions refer to atomic concentrations.

The directions of the phase-field boundaries and five nearly single-phase specimens whose lattice parameters varied continuously locate the ternary-phase field symmetrically about a direction of constant oxygen content of approximately 15 pct and limited by iron concentrations of 25 and 40 pct. From the general disposition of the ternary phase in as-cast microstructures, it seems likely that it generates by a peritectic reaction with the liquid. This is probably the reason for difficulty in obtaining completely single-phase alloys, since incomplete peritectic reactions in titanium-base systems are notably sluggish in approaching equilibrium. A selection of microstructures in Figs. 2 to 5 illustrate structures in important phase fields.

Isothermal Section of the System Ti-Cr-O at 1000°C

The binary system Ti-Cr has been investigated thoroughly.[5,6] A single intermediate phase $TiCr_2$ exists. Levinger[6] has shown the phase to have two allotropic modifications, $MgCu_2$ (C15) type below 1100°C and $MgZn_2$ type above. As mentioned earlier, X-ray diffraction patterns indicated that a ternary phase, apparently identical with Ti_3Fe_2O, occurred at about the composition Ti_3Cr_2O. Metallographic examination of an alloy at that composition disclosed more than one phase.

A paper on the Ti-Cr-O system has recently appeared under the authorship of Wang and Grant.[7] The work described in that paper was in progress at the same time as that being reported in this paper. Certain differences in phase relationships are noted.

Twenty-three alloys were used to identify the phase fields. Several specimens were annealed for seven days to develop a closer approach to equilibrium in sluggish alloys. The metallographic and X-ray diffraction have been used to construct the isothermal section shown in Fig. 6.

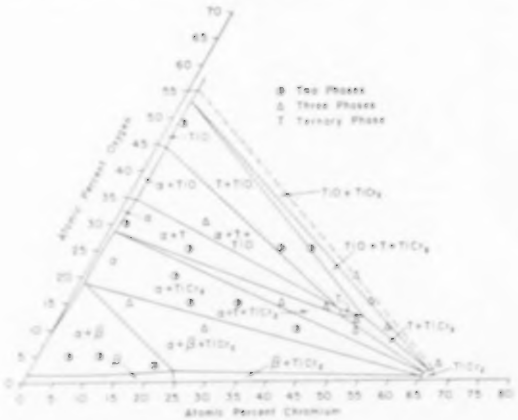

Fig. 6—System Ti-Cr-O. Isothermal section at 1000°C.

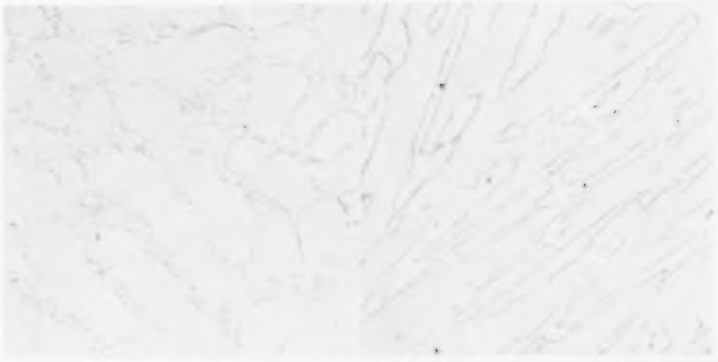

Fig. 7—15 pct O-20 pct Cr-65 pct Ti annealed for 24 hr at 1000°C. Structure, primary dendrites of α in a matrix of (α + $TiCr_2$). X750. Area reduced approximately 25 pct for reproduction.

Fig. 8—25 pct O-15 pct Cr-60 pct Ti annealed for 24 hr at 1000°C. Structure, α (darker etching) + ternary phase (lighter etching). Etched in 2 pct HF, 3 pct HNO_3 in water. X750. Area reduced approximately 25 pct for reproduction.

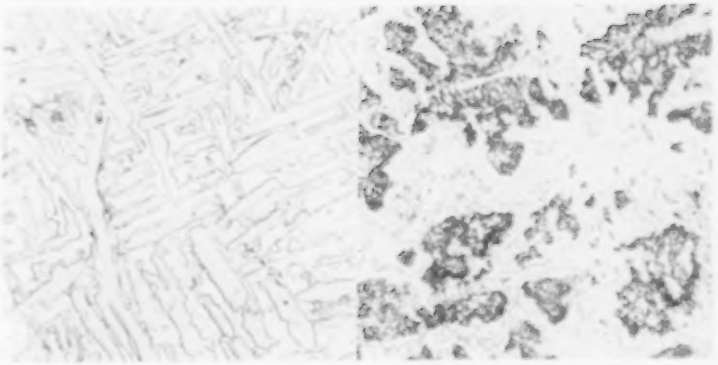

Fig. 9—15 pct O-35 pct Cr-50 pct Ti annealed for 24 hr at 1000°C. Structure, α (dendrites) + mixture of $TiCr_2$ and ternary phase. X750. Area reduced approximately 25 pct for reproduction.

Fig. 10—10 pct O-55 pct Cr-35 pct Ti annealed for 24 hr at 1000°C. Structure, $TiCr_2$ (dendrites) + ternary phase (light matrix) + TiO (dark dispersion). Etched in 2 pct HF, 3 pct HNO_3 in water. X750. Area reduced approximately 25 pct for reproduction.

The lines of a cubic phase isomorphous with other members of the ternary oxide group were noted consistently as the predominant diffraction pattern in high chromium-content alloys. It was not found possible to develop a completely single-phase structure in alloys which, from the directions of phase boundaries, must occur in or adjacent to the single-phase field. This difficulty was also reported by Wang and Grant. The narrow region of occurrence of this phase was inferred from the directions of phase boundaries and tie lines. Its location must be considered approximate. The miscibility range does not include the ideal composition Ti_2Cr_2O. A selection of microstructures in Figs. 7 to 10 illustrate structures in important phase fields.

Wang and Grant presented an isothermal section at 1200°C which is comparable in composition range to Fig. 6. Unfortunately, the two sections describe temperature levels 200°C apart. Certain points of comparison should be made, however. The disposition of the (α + β), (β + γ), and (α + β + γ) phase fields are essentially similar. The major point of difference is the question of existence of a second ternary intermediate phase called eta (η) by Wang and Grant. It must be stated that the set of interplanar spacings for the ϵ phase of Wang and Grant is sufficiently in agreement with the set for that which is termed ternary phase (T) in this paper to consider them identical. However, the η-phase diffraction lines of Wang and Grant were not encountered in patterns of any of the alloys herein reported. For instance, all of the diffraction lines of an alloy containing 15 pct O and 35 pct Cr could be indexed in terms of α, $TiCr_2$, and T (or ϵ) phase. In an alloy containing 20 pct O and 15 pct Cr, only α and $TiCr_2$ could be identified. The three-phase field (TiO + T + $TiCr_2$) was not encountered by Wang and Grant, although it could very well exist even in their diagram if a hypothetical phase field ($T(\epsilon)$ + β-Cr) were removed.

It is not possible to reconcile these differences, although it must be reiterated that comparison is being made with isothermal sections at different temperatures. In both instances, the positive identification of ternary phases were by X-ray diffraction analysis only. The possibility does exist that the η phase occurs at 1200°C but decomposes eutectoidally between 1200° and 1000°C. The two isothermal sections would then be compatible. There is no evidence in Wang and Grant's paper that η exists below 1200°C.

Isothermal Section of the System Ti-Ni-O at 900°C

The Ti-Ni system[7] has been published. The Ti_2Ni phase is known to have a cubic structure isomorphous with the ternary phases under study. Two other intermediate phases, TiNi and $TiNi_3$, occur. These phases are of B_2 and DO_{19} types, respectively.

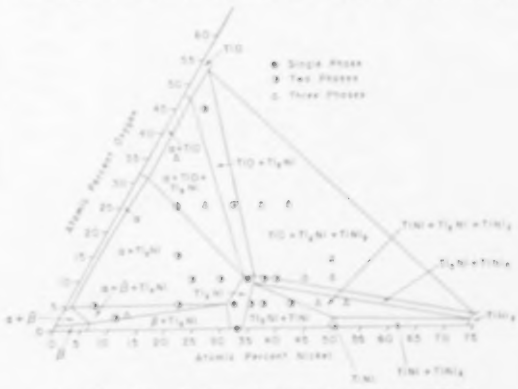

Fig. 11—System Ti-Ni-O. Isothermal section at 900°C.

Fig. 12—5 pct O-30 pct Ni-65 pct Ti annealed for 48 hr at 900°C. Structure almost completely Ti_2Ni with traces of β. X500. Area reduced approximately 25 pct for reproduction.

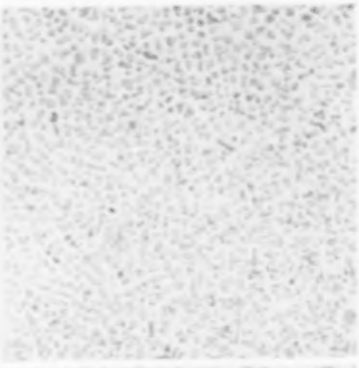

Fig. 13—25 pct O-20 pct Ni-55 pct Ti annealed for 48 hr at 900°C. Structure, TiO + Ti_2Ni (matrix). Etched in 2 pct HF, 3 pct HNO_3 in water. X750. Area reduced approximately 25 pct for reproduction.

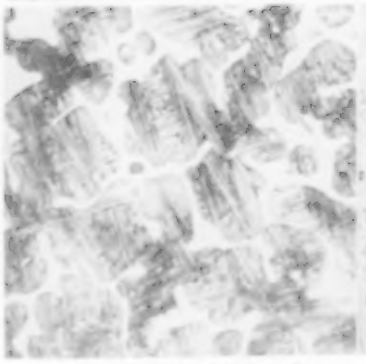

Fig. 14—35 pct O-5 pct Ni-60 pct Ti annealed for 48 hr at 900°C. Structure, α + TiO + Ti_2Ni. Dendrites are α, the banding is TiO, and the matrix is Ti_2Ni. X750. Area reduced approximately 25 pct for reproduction.

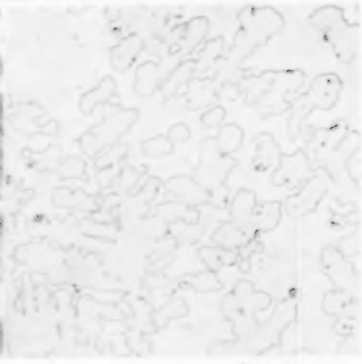

Fig. 15—25 pct O-30 pct Ni-45 pct Ti annealed for 48 hr at 900°C. Structure, $TiNi_3$ (dendrites) + Ti_2Ni (light etching matrix) + TiO (darker etching matrix). Etched in 2 pct HF, 3 pct HNO_3 in water. X750. Area reduced approximately 25 pct for reproduction.

Fig. 16—5 pct O-50 pct Ni-45 pct Ti annealed for 48 hr at 900°C. Structure, TiNi (dendrites) + Ti_2Ni (lighter etching matrix) + $TiNi_3$ (darker etching matrix). Etched in 2 pct HF, 3 pct HNO_3 in water. X750. Area reduced approximately 25 pct for reproduction.

The Ti-Ni-O system is of particular interest as a case where the ternary-phase lattice can tolerate a complete evacuation of the interstitial atoms. The approximate location of the single-phase field was made from studies on 27 alloys. The isothermal section at 900°C was chosen to avoid the occurrence of liquid-phase fields associated with the low binary eutectic temperature (995°C) in the Ti-Ni system. Based on recognition of number and identification of phases in each of the annealed alloys, the isothermal section illustrated in Fig. 11 has been constructed.

Judging from those alloys which were single-phase or nearly so and from the directions of phase boundaries, it is concluded that the Ti_2Ni phase has a narrow miscibility field extending into the ternary system in the direction of a constant ratio of Ti:Ni. The interpretation is that the structure is permitting the occupation of vacant interstitial sites approximately up to the saturation which the other isomorphous ternary phases permit. Figs. 12 to 16 offer microstructures representative of a number of the phase fields encountered.

Summary

The approximate size and location of the ternary-phase fields of the compounds isomorphous with Fe_3W_3C have been determined for three titanium-rich ternary systems. The transition element associated with titanium in the species of intermediate phase appears to exercise considerable influence on its location and range of miscibility. Judging from the disposition of the phase fields at 1000°C, it appears unlikely that these phases will be encountered in normal forgeable titanium alloys based on the Ti-Fe and Ti-Cr systems.

Acknowledgment

The contents of this paper represent a portion of work conducted at the Armour Research Foundation for the Materials Laboratory of the Wright Air Development Center, Wright-Patterson Air Force Base, Ohio, Contract AF 33(038)-8708. The author is grateful to this latter organization for permission to publish. The X-ray analyses were done with the assistance of Mrs. Anne Humphreys. The metallographic work was done under the supervision of Mr. Cornelius A. Johnson.

References

[1] W. Rostoker: *Trans.* AIME (1952) **194**, p. 209; JOURNAL OF METALS (February 1952).
[2] N. Karlsson: *Nature* (1951) **168**, p. 558.
[3] E. S. Bumps, H. D. Kessler, and M. Hansen: *Trans.* ASM (1953) **45**, p. 1008.
[4] R. J. Van Thyne, H. D. Kessler, and M. Hansen: *Trans.* ASM (1952) **44**, p. 974.
[5] F. B. Cuff, N. J. Grant, and C. F. Floe: *Trans.* AIME (1952) **194**, p. 848; JOURNAL OF METALS (August 1952).
[6] B. W. Levinger: *Trans.* AIME (1953) **197**, p. 196; JOURNAL OF METALS (February 1953).
[7] C. C. Wang and N. J. Grant: *Trans.* AIME (1954) **200**, p. 200; JOURNAL OF METALS (February 1954).
[8] H. Margolin, E. Ence, and J. P. Nielsen: *Trans.* AIME (1953) **197**, p. 243; JOURNAL OF METALS (February 1953).

Heat Treatment and Mechanical Properties of Ti-Cu Alloys

by F. C. Holden, A. A. Watts, H. R. Ogden, and R. I. Jaffee

Hypoeutectoid Ti-Cu alloys are responsive to heat treatment, and considerable variation of mechanical properties may be produced by transformation of the β phase. Control of cooling rate, isothermal transformation, or quench tempering determine the transformation structure and properties. The transformation products are similar to those of carbon steel.

THE equilibrium diagram for the Ti-Cu system has been studied by various investigators, and the most recent diagram is that determined by Joukainen, Grant, and Floe.[1] The titanium-rich portion of this diagram is reproduced in Fig. 1. The alloy compositions and annealing temperatures used in this work are shown.

The Ti-Cu alloys containing up to 17 wt pct Cu are representative of an active eutectoid alloy system. Joukainen et al.[1] have stated that β phase cannot be retained on quenching and this has been confirmed in the present work. The similarity between the Ti-Cu system and the Fe-C system is evident and, as will be shown later, many of the transformation products appear to have similar microstructures.

Heat treatments in this program were designed to produce the structures of primary interest for study and determination of mechanical properties.

Experimental Procedures

Preparation of Alloys: Five ½ lb ingots, ranging in composition from 0.8 to 6.83 pct Cu, were prepared by double arc melting in an atmosphere of high purity argon. Titanium melting stock was obtained from high purity iodide titanium, and copper additions were made from copper wire clippings. Segregation was reduced by inversion melting, in which the once-melted ingots were inverted in the crucible and remelted. The double-melted ingots were forged at 1600°F to ¾ in. diam rods, with both heating and forging operations being carried out in air. Surface scale was removed by grit blasting and grinding, after which the forgings were vacuum annealed at 900°C. The alloys then were swaged to ¼ in. diam rod at 750°C and test specimens were cut from this material.

The vacuum annealing operation was to remove dissolved hydrogen, which is commonly present in the iodide titanium as-received. Although vacuum fusion analyses were not obtained for all these alloys, past experience indicates that the 6 hr treatment with a limiting pressure of 10^{-5} to 10^{-6} mm of Hg is sufficient to reduce the hydrogen level to 10 to 30 ppm. Vacuum fusion analysis of the 0.8 pct Cu alloy showed 19 ppm of hydrogen.

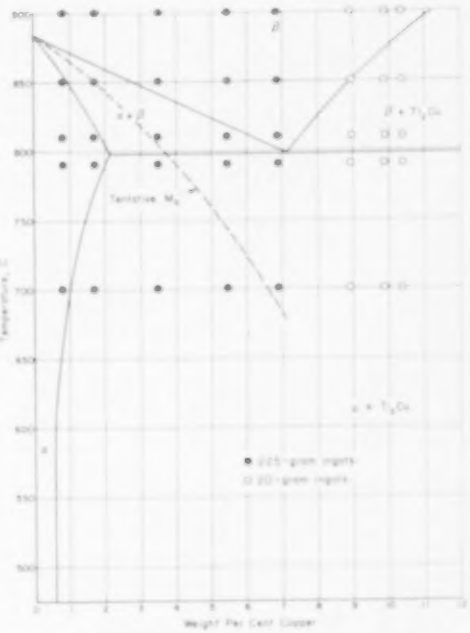

Fig. 1—Titanium-rich portion of Ti-Cu system, after Joukainen, Grant, and Floe.[1]

In addition to the five hypoeutectoid alloys, three 15 g ingots were prepared with nominal copper additions of 9, 10, and 11 pct. Fabrication procedures were similar, except that these alloys were rolled to 0.040 in. sheet. Microstructure specimens only were obtained. Table I shows analyzed compositions and fabrication temperatures for these alloys.

Heat Treatments: All heat treatments were made in potentiometer-controlled, resistance-wound tube

F. C. HOLDEN, Member AIME, A. A. WATTS, H. R. OGDEN, Member AIME, and R. I. JAFFEE, Member AIME, are Principal Metallurgists, Assistant Chief, and Chief, respectively, Nonferrous Physical Metallurgy Div., Battelle Memorial Institute, Columbus, Ohio.

Discussion on this paper, TP 3861E, may be sent, 2 copies, to AIME by Mar. 1, 1955. Manuscript, Apr. 15, 1954. Chicago Meeting, November 1954.

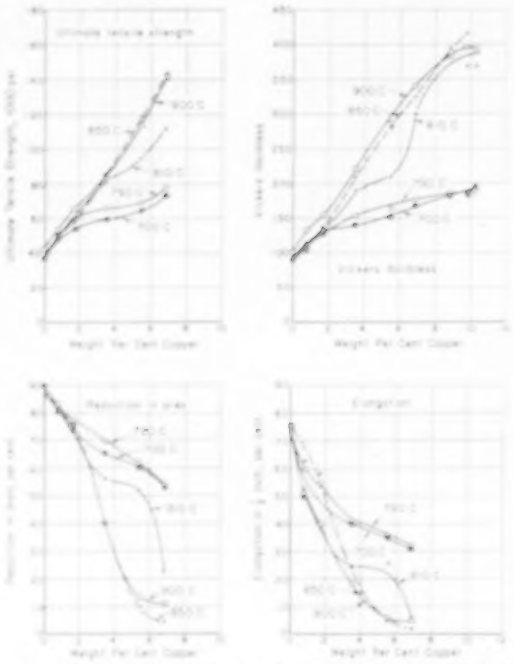

Fig. 2—Mechanical properties of Ti-Cu alloys annealed at indicated temperatures and water quenched.

furnaces under an inert atmosphere. Specimens were either encapsulated in Vycor under a partial pressure of argon or suspended in a flowing atmosphere of argon. Various cooling rates were obtained by water and oil quenches, by argon cooling (air-cooling rate under an inert atmosphere), and by furnace cooling. Attempts to obtain cooling rates more rapid than a water quench by use of NaCl and NaOH solutions showed no evidence of improvement, and these were discontinued. Typical cooling curves for the argon and furnace cooling rates have been presented in earlier work.[5]

Isothermal-transformation studies were made by quenching from an argon atmosphere into a bath of molten tin maintained at the transformation temperature by a potentiometer controller. After the desired holding time, the specimens were removed from the tin bath and water quenched.

Mechanical Testing. Tensile properties were obtained from $\frac{1}{8}$ in. diam tensile specimens with a $\frac{1}{2}$ in. gage length. Tests were made on Baldwin-Southwark universal testing machines at a uniform strain rate of 0.005 in. per min; the 2000 or 2400 lb scale was used. Strain readings were taken from Type A-7 SR-4 resistance strain gages to about 2 pct elongation and from a lever-type extensometer to the limit of uniform elongation.

Impact tests were made on micro impact test specimens by using a Tinius-Olsen testing machine with a 200 in.-lb capacity and an impact velocity of 11.37 fps. Details of test specimens and methods of testing have been described previously.[6]

Water-Quenched Alloys

An important feature of the Ti-Cu alloy system is the fact that β phase is not retained at room temperature. This is distinct from the alloys of titanium with chromium, iron, and manganese in which the eutectoid reaction is sluggish. The transformation which occurs is governed by the alloy composition and by the method of cooling, and considerable variations in mechanical properties may be obtained as a result of this transformation. The types of microstructures obtained by water quenching from the single-phase α and β fields may be listed as 1—equiaxed α, and 2—martensitic transformed β. The serrated transformation structures associated with unalloyed titanium and with the low copper-content alloys on quenching from above the β transus are considered as martensitic transformed β in this classification.

Alloys water quenched from the two-phase fields contain microstructures which may be classified as 1—α + Ti_2Cu, 2—α + transformed β, and 3—Ti_2Cu + transformed β. The β transformation product of the latter two structures does not appear to be martensitic but has a nodular appearance. These nonmartensitic β-transformation products are of considerable interest and are discussed in later sections of this paper.

Mechanical properties of the quenched alloys are presented in Fig. 2 and typical microstructures are shown in Figs. 3 and 4.

Solid-solution strengthening of the α phase is effective up to the solubility limit at the annealing temperature. Separation of the structural and solid-solution effects is possible in the composition range of 0 to 1.7 pct Cu because both equiaxed α and transformed β structures can be produced. Transformed β structures in this composition range are 5000 to 6000 psi stronger than corresponding equiaxed α structures. The effects of α grain size on mechanical properties are minor. For the 0.8 pct Cu alloy, an increase in grain size from 0.05 to 0.02 mm results in no change in tensile properties except for a slight decrease in yield strength. It may be concluded that grain-size effects in the single-phase α structure are negligible.

Specimens annealed and quenched from below the eutectoid temperature contain increasing quantities of Ti_2Cu in an α matrix as the copper content is increased above the solubility limit. The effect on mechanical properties is a slight increase in strength accompanied by a decrease in ductility. For a given alloy composition, highest ductilities are obtained in this condition.

The strengths of specimens quenched from the $\alpha + \beta$ field are increased considerably above those of the same alloys quenched from below the eutectoid temperature. This strength difference increases with copper content. Examination of microstructures

Table I. Compositions and Fabrication Temperatures of the Alloys Tested

Alloy	Composition (Balance Titanium), Pct				Fabrication		
		Analyzed					
	Nominal Copper	Copper	Nitrogen	Hydrogen, Ppm	Forging Temperature, °C	Vacuum Annealing Temperature, °C	Swaging Temperature, °C
TM 40	1.0	0.8	—	10	875	900	750
TM 41	2.0	1.7	—	—	875	900	750
TM 42	3.75	3.48	0.002	—	875	900	750
TM 44	5.5	5.44	—	—	875	900	750
TM 43	7.1	6.83	—	—	875	900	750
9 Cu	8.0	8.80	0.002	—	875	900	750*
10 Cu	10.0	9.94	0.002	—	875	900	750*
11 Cu	11.0	10.33	0.003	—	875	900	750*

* These alloys were rolled to 0.040 in. strip.

shows equiaxed α grains in a matrix of transformed β which appears to be nodular rather than martensitic. It may be that the presence of α promotes the nucleation and growth decomposition of the β phase, preventing the formation of martensite.

Highest strengths are obtained by water quenching from the β field to produce a martensite structure. The ultimate tensile strengths and Vickers hardness values in this condition increase almost directly with copper content, which indicates that strength of β-quenched specimens is determined by the quantity of copper in solid solution at the quenching temperature. The microstructures show a uniform increase in fineness of the martensite as the copper content is increased. The differences in properties and microstructures obtained by quenching from different temperatures in the β field are minor and are probably caused by cooling-rate effects. Ductilities of the β-quenched specimens decrease rapidly as the copper content is increased. The presence of proeutectoid α in the microstructures of specimens quenched from the α-β field reduces their strength, but ductilities are considerably improved over those of the β-quenched specimens.

Micro impact tests were run at room temperature on specimens representing all the quenched conditions. In addition, the effect of testing temperature on impact resistance was determined for selected microstructural conditions. Fig. 5 shows the variation of room temperature impact-energy values with copper content for a number of annealing temperatures. The effects of testing temperature are shown in the curves of Fig. 6. Specimens annealed and quenched from below the eutectoid temperature have the highest impact-energy values. Copper in solid solution decreases the impact resistance rapidly until the limit of solubility is reached. Further additions of copper cause only a small decrease in impact-energy values as the quantity of Ti_2Cu phase in the microstructure is increased. The impact be-

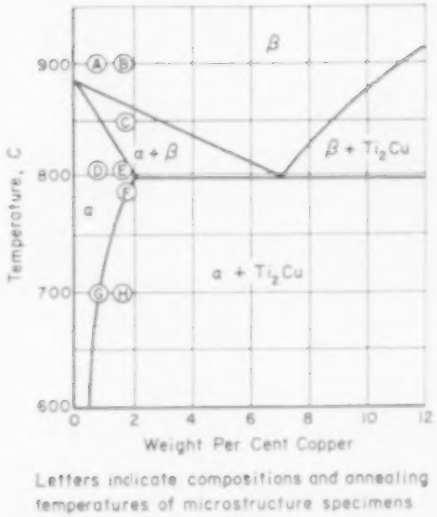

Letters indicate compositions and annealing temperatures of microstructure specimens

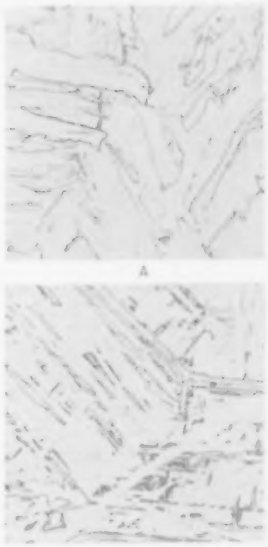

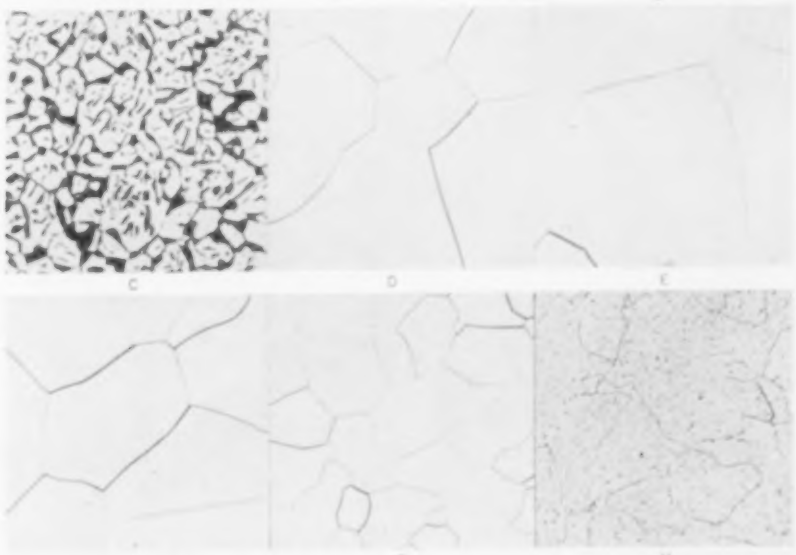

Fig. 3—Microstructures of quenched alloys. X250. Area reduced approximately 20 pct for reproduction.

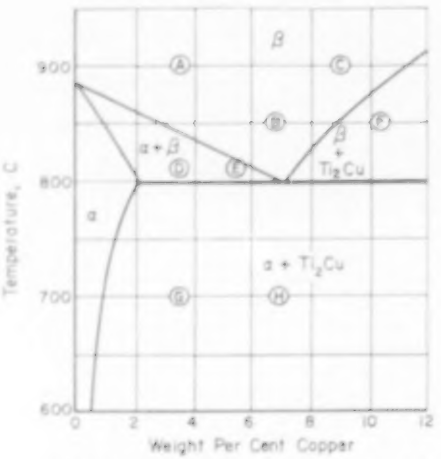

Letters indicate compositions and annealing temperatures of microstructure specimens

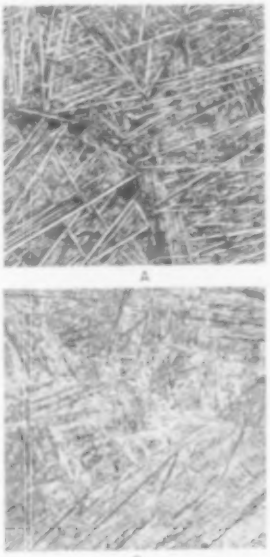

Fig. 4—Microstructures of quenched Ti-Cu alloys. X250. Area reduced approximately 20 pct for reproduction.

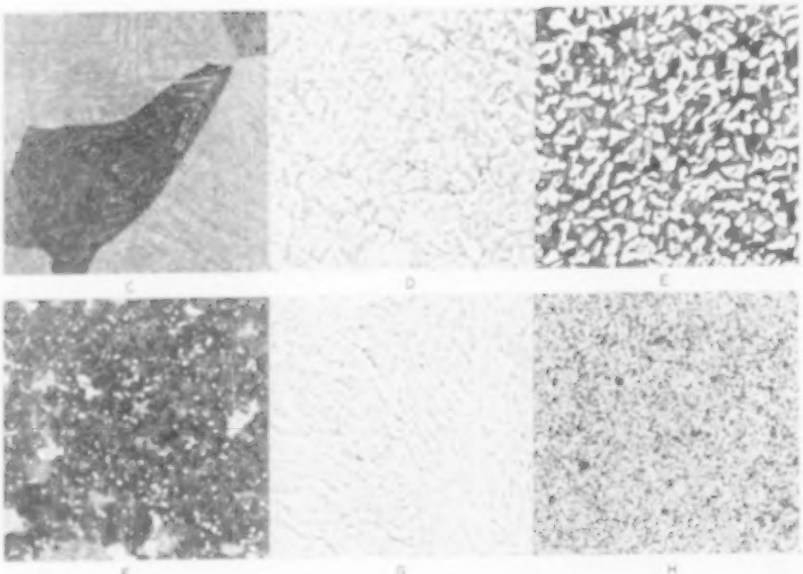

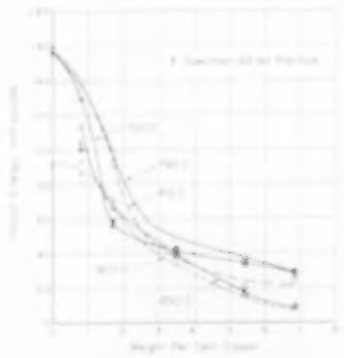

Fig. 5—Effect of copper content on room temperature impact-energy values for Ti-Cu alloys annealed and quenched from various temperatures.

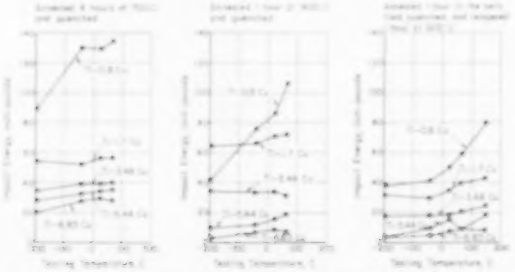

Fig. 6—Effect of testing temperature on the impact-energy values of Ti-Cu alloys in various microstructural conditions.

havior may be considered as ductile up through at least 6.82 pct Cu for specimens in this condition. Specimens annealed at higher temperatures in the α-compound field exhibit a similar decrease in impact energy as the copper content is increased.

Impact energies of the β-quenched specimens are about 20 in.-lb lower than the the impact energies of

specimens annealed below the eutectoid temperature and above 5 pct Cu are below 20 in.-lb. With the exception of the Ti-0.8 pct Cu alloy, little change in impact energy occurs with changes in testing temperature from −196° to 150°C. The Ti-0.8 pct Cu alloy specimens, particularly those in the β-quenched condition, show a considerable increase in impact-energy values as the testing temperature is increased.

Cooling-Rate Studies

For an alloy system in which a high temperature phase transforms on cooling, a study of the effects of different cooling rates on microstructures and mechanical properties is often of considerable value. In this work, specimens were cooled from the β field at three cooling rates, in addition to the cooling rate obtained by a water quench. The microstructures were observed, hardness measurements were obtained in all cases, and tensile and impact specimens that had been argon cooled were tested. The cooling rates studied included those obtained by 1—water quenching, 2—oil quenching, 3—cooling in argon (simulated air cooling rate under an argon atmosphere), and 4—cooling in the furnace. Attempts to obtain a cooling rate more rapid than a water quench were made by using iced NaCl and NaOH solutions. The results showed, however, that no increase in cooling rate was obtained. These tests were discontinued.

The effects of cooling rate on microstructures are shown in the micrographs of Fig. 7. At the lower copper contents (up to 1.7 pct Cu), the effect of decreasing cooling rate is to increase the coarseness of the already coarse transformed β. At 3.42 pct Cu, the cooling-rate effect is similar, although the fineness of the martensite structure in the water-quenched condition is much greater than that of the two alloys that contain less copper. Specimens containing from 5.44 to 10.33 pct Cu show considerable variations in microstructure resulting from changes in cooling rate. At the lower cooling rates, a eutectoid decomposition product is formed as nodules progressing from prior β-grain boundaries. At very low cooling rates, particularly at the higher copper contents, the eutectoid decomposition product appears lamellar and similar to the fine pearlite structures of carbon steels. In most instances, however, the structures are too fine to be resolved under the microscope. The eutectoid decomposition product forms rapidly and the cooling rate in argon is usually low enough to permit complete transformation. In specimens oil quenched from the β field, about 20 pct of the struc-

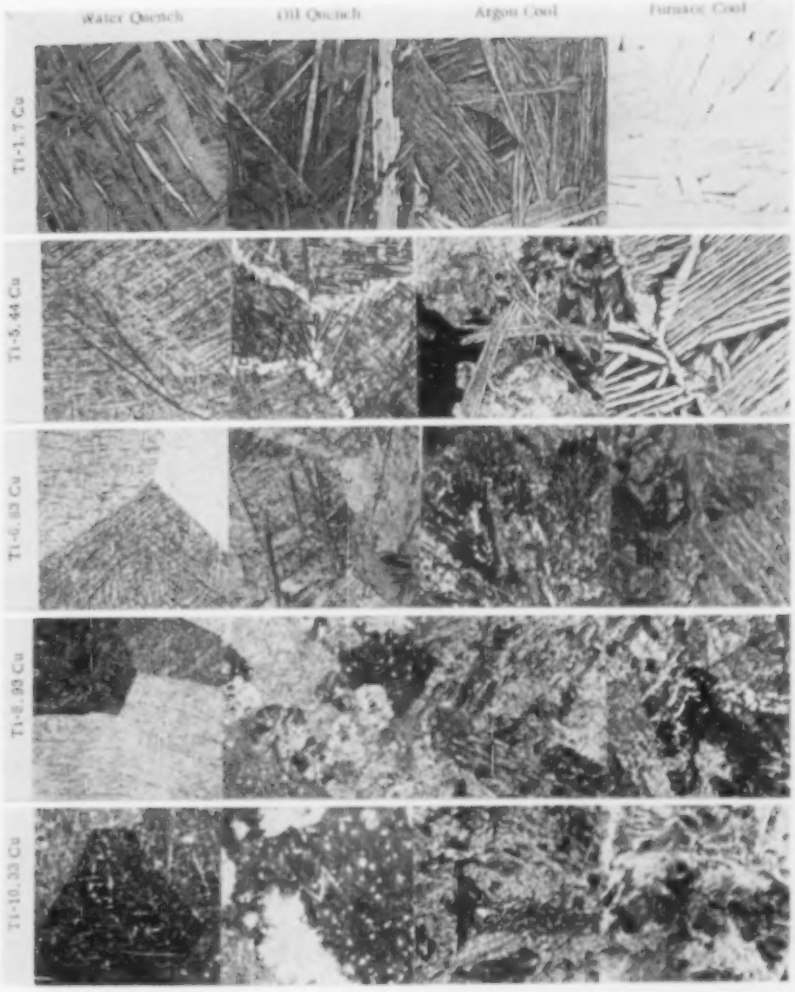

Fig. 7—Effect of cooling rate on the microstructures of Ti-Cu alloys annealed in the β field. X250. Area reduced approximately 20 pct for reproduction.

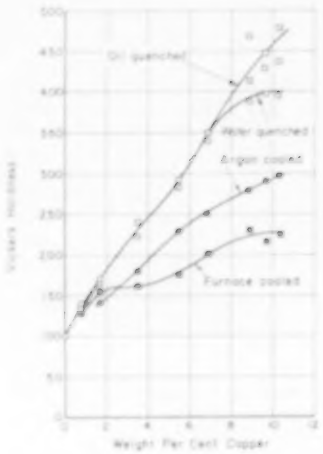

Fig. 8—Effect of cooling rate on VHN of Ti-Cu alloys annealed in the β field.

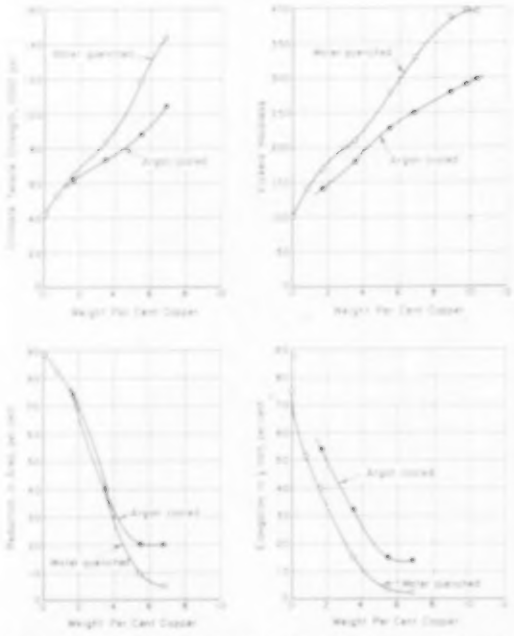

Fig. 9—Mechanical properties of Ti-Cu alloys argon cooled and water quenched from the β field.

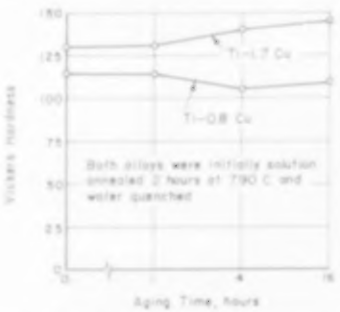

Fig. 10—Effect of 400°C aging on hardness of Ti-Cu alloys solution annealed in the α field.

ture is nodular product and is formed near the prior β-grain boundaries, with the balance of the structure transformed to martensite.

The effect of cooling rate on hardness is shown in

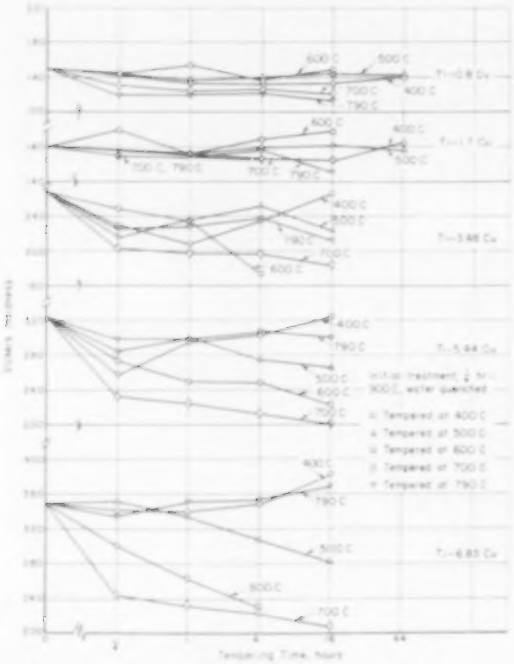

Fig. 11—Effect of tempering on the hardness of Ti-Cu alloys.

the curves of Fig. 8. No significant change in hardness occurs between the water quench and oil quench for alloys containing up through about 7 pct Cu. The hypereutectoid alloys are harder in the oil-quenched condition, where considerable nodular product is formed, than in the water-quenched condition, in which the microstructure appears to be all martensite. The possibility that some β was retained by water quenching was checked by X-ray diffraction of the Ti-10.33 pct Cu alloy, and only diffuse α lines were observed. In the oil-quenched sample, two very faint Ti_2Cu lines were observed in addition to diffuse α lines. No β lines were observed. It appears, then, that the combination of the nodular product and martensite produced by oil quenching the hypereutectoid alloys is a harder structure than the martensite structure produced by water quenching. In the hypoeutectoid alloys, the small amount of nodular product that is formed during oil quenching does not influence the hardness. Eutectoid structures of pearlitic type, produced by lower cooling rates, are softer than structures containing martensite.

The variations in hardness caused by differences in cooling rate increase with copper content, and considerable control of strength may be obtained at the higher copper contents by control of the cooling rate from the annealing temperature.

Because complete transformation to the eutectoid decomposition product takes place during cooling in argon, tensile and impact tests were made in this condition. Results of these tests are presented in the curves of Fig. 9. The results of tests of the β-quenched specimens are included for comparison. The strength properties of specimens cooled in argon are lower, and ductility and impact resistance are considerably improved over these properties of the β-quenched specimens.

Aging Studies

The increase in the solubility of copper in α

titanium with increasing temperature suggests the possibility of strengthening these alloys by precipitating Ti_2Cu particles in a low temperature aging process. Aging studies were undertaken with specimens containing 0.8 and 1.7 pct Cu solution annealed in the α field, quenched to room temperature, and aged at 400°C for 1, 4 , and 16 hr. Hardness data are presented in Fig. 10, and show that no appreciable change occurs during this aging process.

Tempering Studies

Many of the characteristics of the Fe-C alloy system appear in the Ti-Cu system. This similarity suggests that the improvements in mechanical properties obtained in steels by tempering a quenched structure may be obtained in the Ti-Cu alloys. Hardness and microstructure studies have been made on specimens quenched from the β field and tempered at temperatures from 500° to 790°C for various times. In addition, tensile and impact specimens were tested in a selected quenched-and-tempered condition.

The effects of tempering on hardness are shown graphically in Fig. 11, and representative microstructures are shown in Fig. 12. The curves show that as the tempering temperature is increased from 400° to 700°C a decrease in hardness occurs as the tempering time is increased. Hardness is maintained by tempering at 790°C, but microstructural evidence shows that these treatments were actually above the eutectoid temperature. The alloys containing 0.8 and 1.7 pct Cu show only minor changes in hardness as a result of the tempering treatment, while the degree of response in the other specimens increases with copper content. The decomposition of the martensite resulting from tempering a β-quenched specimen is shown in the micrographs of Fig. 12. It can be observed here that the acicularity of the microstructures is not destroyed, and structures comparable to the spheroidized structures of tempered steels were not obtained. The presence of the nodular eutectoid structure was observed in a number of these specimens, but its quantity does not appear to be determined by either a tempering temperature or time. Its formation probably is caused by an insufficiently rapid quench from solution-annealing temperature.

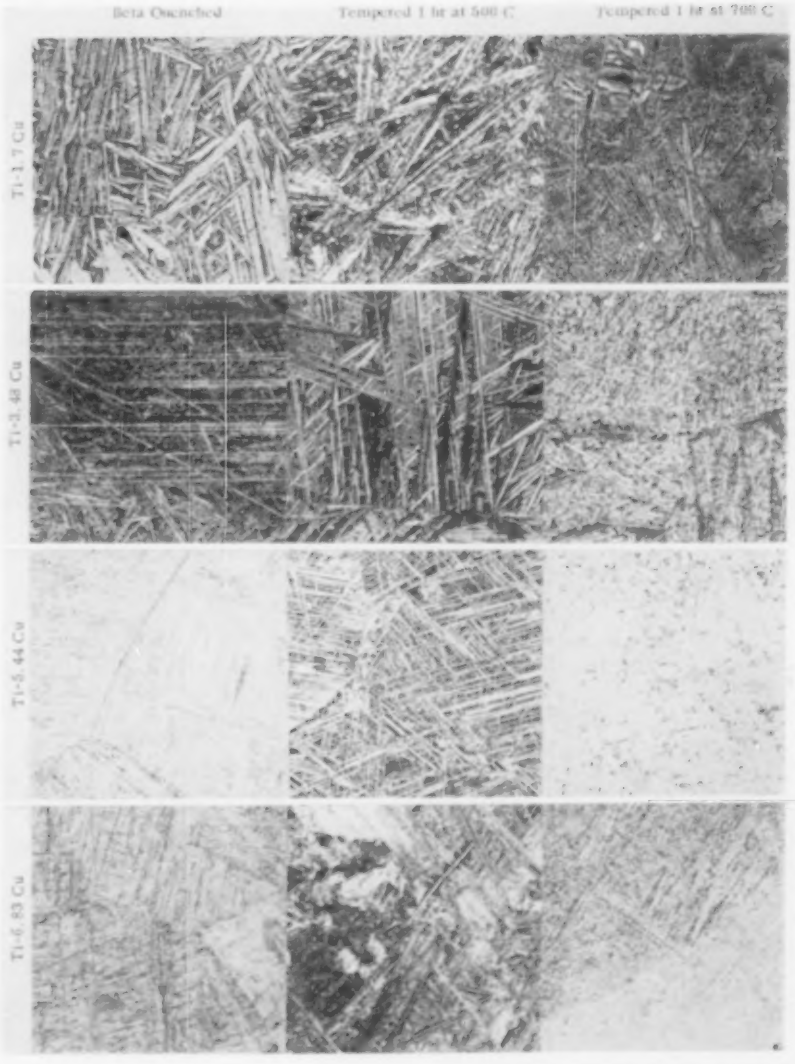

Fig. 12—Effect of 1 hr temper on microstructure of Ti-Cu alloys quenched from the β field. X250. Area reduced approximately 20 pct for reproduction.

A tempering treatment of 1 hr at 600°C was selected for tempering specimens used in the determination of tensile and impact properties. This treatment was chosen on the basis of hardness measurements to produce the same strength levels as those of the argon-cooled specimens. Tensile properties are shown in Fig. 13. The tensile properties of the β-quenched specimens are included for comparison. Impact-temperature curves are presented in Fig. 6.

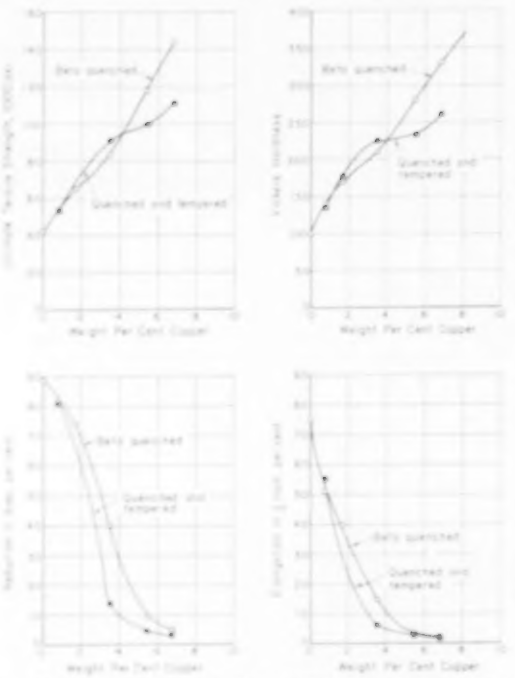

Fig. 13—Effect of tempering 1 hr at 600°C on the mechanical properties of β-quenched Ti-Cu alloys.

Strength properties are increased slightly by the tempering treatment for alloys containing 1.7 and 3.48 pct Cu and are decreased for the 5.44 and 6.83 pct Cu alloys. Ductility and impact resistance also are decreased below those of the β-quenched specimens. The argon-cooled specimens at the same strength level possess better ductility and impact properties than do the quenched and tempered specimens. Impact values, particularly at the lower copper contents, are lower than those for the other conditions (see Fig. 6). With the exception of the increase in impact resistance with testing temperature noted for specimens containing 0.8 pct Cu, no significant effect of temperature on impact-energy values was observed. The lowering of ductility and impact-energy values for the tempered specimens may be associated with the rejection of copper as Ti_2Cu from the martensite during the tempering process.

Unlike the effect of tempering on carbon steels, tempering of β-quenched Ti-Cu copper alloys does not improve ductility and toughness, but, rather, is definitely detrimental to these properties.

Isothermal-Transformation Studies

The variations in microstructure and mechanical properties which are observed when alloys containing over 3.48 pct Cu undergo transformation make

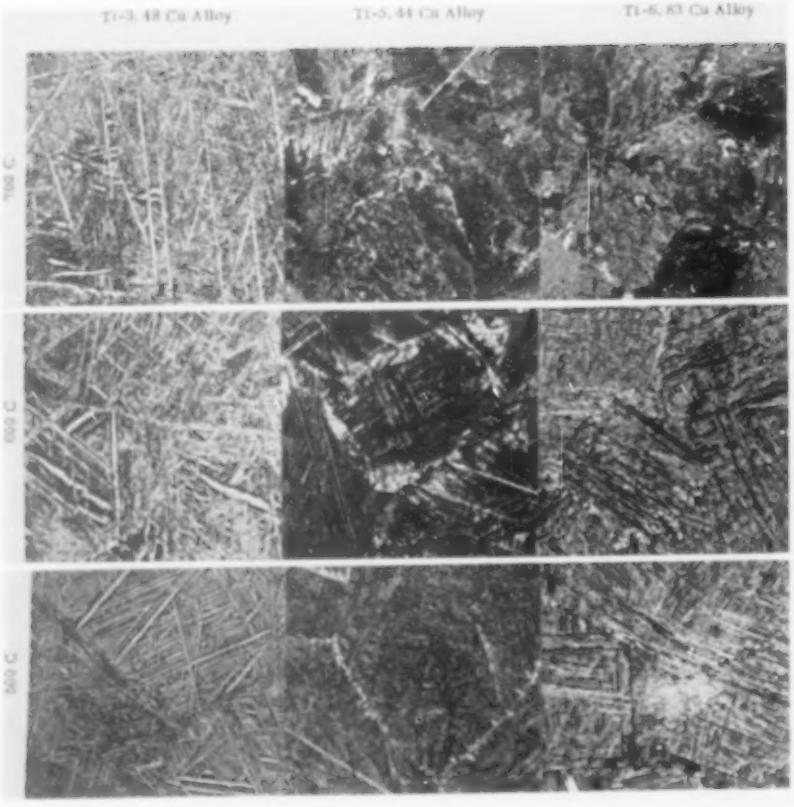

Fig. 14—Microstructures of Ti-Cu alloys. Specimens annealed ¼ hr in β field. Isothermally transformed for 60 min and quenched to room temperature. X250. Area reduced approximately 20 pct for reproduction.

an understanding of the transformation processes desirable. One method of studying these transformations is to quench directly to the transformation temperature for various periods of time so that the temperature at which the transformation occurs is known. Isothermal-transformation studies were made on the Ti-Cu alloys containing up to 6.83 pct Cu. The alloys were isothermally transformed at 500°, 600°, and 700°C for times of 1, 15, and 60 min. Representative microstructures are shown in Fig. 14.

From study of the microstructures, an approximate M_s curve may be constructed, as shown by the dotted curve in Fig. 1. Although the number of tests performed was not sufficient to determine *TTT* curves, some general observations on the transformation kinetics were made.

1—The M_s and M_f temperatures decrease with increasing copper content. The M_s temperature is above 700°C at 3.48 pct Cu and below 700°C at 6.83 pct Cu.

2—The nodular eutectoid decomposition product is formed by a nucleation and growth process and proceeds rapidly to completion at temperatures above the M_s. Complete transformation in 1 min is observed for the 6.83 pct Cu alloy isothermally transformed at 700°C.

3—A lamellar eutectoid decomposition product is observed for the higher copper content alloys in the furnace-cooled condition. This structure is typical of the transformation product obtained by isothermal transformation at high temperatures (just under the eutectoid temperature), analogous to the coarse pearlite structures in steels.

Summary

The transformations of greatest interest in the Ti-Cu alloys in the composition range studied are those which involve the decomposition of the β phase. Low temperature aging of the α phase by precipitation of Ti_2Cu shows little promise of increasing strength by this process. Solid-solution strengthening of the α phase is effective but is limited to alloys containing less than 2.1 pct Cu. Strengths are increased at a rather slow rate by an increase in the quantity of Ti_2Cu in a saturated α matrix produced by annealing below the eutectoid temperature. The maximum strengths which have been obtained in the hypoeutectoid alloys have been obtained by quenching from the β field. Strengths of these martensitic structures increase almost directly with copper content at a rate of about 14,000 psi for each percentage of copper added. Hardness data indicate that slightly higher strengths, particularly in hypereutectoid alloys, can be produced by use of an oil quench in place of the water quench. The similarities in phase relationships which exist for the Ti-Cu alloys and Fe-C alloys are apparent in their microstructures. Eutectoid decomposition products produced by slow cooling or by isothermal transformation appear very similar to the nodular pearlite structures found in steels. The desirable combinations of properties obtained in tempered martensite steels have not been produced in Ti-Cu alloys.

Acknowledgment

This work is part of a study of the effect of microstructure on the properties of representative titanium alloys.

The authors are grateful to Watertown Arsenal and the Ordnance Corps for permission to publish this information. The data presented in this paper were obtained on work done at Battelle Memorial Institute under Ordnance Contract No. DA-33-019-ORD-280.

References

[1] A. Joukainen, N. J. Grant, and C. F. Floe: Titanium-Copper Binary Phase Diagram. *Trans.* AIME (1952) **194**, pp. 766-770; JOURNAL OF METALS (July 1952).

[2] F. C. Holden, H. R. Ogden, and R. I. Jaffee: Heat Treatment, Structure, and Mechanical Properties of Ti-Mn Alloys. *Trans.* AIME (1954) **200**, pp. 169-184; JOURNAL OF METALS (February 1954).

[3] F. C. Holden, H. R. Ogden, and R. I. Jaffee: Microstructure and Mechanical Properties of Iodide Titanium. *Trans.* AIME (1953) **197**, pp. 238-242; JOURNAL OF METALS (February 1953).

Technical Note

Autoradiography Determination of the Self-Diffusion of Silver

by Helmut Krueger and Herbert N. Hersh

USE of autoradiography in diffusion studies offers the advantage that no repeated sectioning is necessary and that the analyses are performed in a simple manner over the continuous range of penetration depths. As part of a program of solid-state physics, it was desired to develop the autoradiographic method[1] quantitatively for use in diffusion studies. Results are reported here for the self-diffusion of silver. Silver was chosen because the existing data are good enough to evaluate the technique.[2]

The silver used in this investigation was obtained in the form of ¼ in. diam rods of polycrystalline material, 99.99 pct purity. The radioactive silver, Ag^{105} (β, γ), was obtained as the nitrate and converted to the chloride for use in a standard cyanide plating bath. The diffusion specimens were ½ in. lengths of the rod. They were mounted in bakelite and the exposed circular face carefully ground and polished. Prior to electrodepositing radioactive

H. KRUEGER, formerly associated with Lewis Flight Propulsion Laboratory, National Advisory Committee for Aeronautics, Cleveland, is now associated with Brush Laboratories Co., Cleveland, and H. N. HERSH, formerly associated with Lewis Flight Propulsion Laboratory, National Advisory Committee for Aeronautics, Cleveland, is now associated with the Research Dept., Zenith Radio Corp., Chicago.

TN 249E. Manuscript, Apr. 13, 1954.

silver on the polished face, it was given a light potassium-cyanide etch and then a reverse-current etch in the plating bath. Approximately one out of every 10^7 Ag ions in the solution was radioactive Ag^{105}. The bakelite was removed subsequently from the specimens for the diffusion anneal.

A tube furnace 40 in. long with a controlled temperature gradient was used for the diffusion anneal. Helium was passed through the furnace at a constant rate and protected the silver from oxidation. Careful measurements of the temperature profile by movable thermocouples made it possible to carry out the diffusion anneal of several specimens simultaneously even though they were at different temperatures. Specimens were placed in alundum boats at different positions in the furnace and removed at different times and allowed to air cool. The temperatures at each position were recorded at regular intervals. Average temperatures were obtained by a method of exponential averaging,[6] using the equation, $\int_0^t e^{+\frac{E}{RT}}\,dt = t\exp(-E/RT,\ldots)$, and an approximate value of E, 45,000 cal per mol. Possible errors in specimen position and thermocouples are estimated to cause an uncertainty of ±3°C in the specimen temperatures. There is a possible variation from furnace fluctuations of ±1°C. The probable errors due to temperature uncertainties would cause deviations in the activation energy of less than 1 pct. The method of exponential averaging eliminates any uncertainty in the time of diffusion, t, giving the effective time at temperature.

In order to make the autoradiographs, the specimens were first cut perpendicular to the plated surface (parallel to the diffusion direction) in the central plane of the rod. This procedure yielded a specimen which was a half cylinder. The exposed cross-section (the central plane) was ground and polished metallographically. Careful preparation of the surface is necessary because of the possibility of smearing from relatively active portions of the specimen. The final polishing was done therefore in a direction normal to the direction of diffusion. Then the resulting smooth surface was exposed directly to the photographic film in a simple autoradiographic camera for periods up to several weeks. The sensitive films from ordinary DuPont film-badge refills, which are sensitive to β-rays and also to γ-rays, were used. In order to detect errors due to sectioning and polishing, further autoradiographs were prepared from the same samples after resectioning.

The developed film, containing the photographic density-penetration profile, was scanned backwards and forwards parallel to the diffusion direction with a Leeds and Northrup recording microphotometer

Fig. 1—Profile of photographic density. The β-radiation intensity values were obtained by subtraction of the extrapolated background curve which is due mainly to γ-radiation from the whole volume of the diffusion zone.

Table I. Summary of Available Data

Investigators	D_o, Sq Cm per Sec	E, Cal per Gram-Atom	$D_{1000°K}$, Sq Cm per Sec
Johnson[4] and Hoffman and Turnbull[3]	0.895	45,900	7.94×10^{-5}
Slifkin, Lazarus, and Tomizuka[2]	0.351	43,680	9.64×10^{-5}
This investigation	0.835	44,900	1.22×10^{-4}
Kuczynski[5]	0.6	42,000	3.86×10^{-5}
Kuczynski[5]	0.9	45,700	8.71×10^{-5}

which had a resolution width of 0.0083 cm. On the microphotometer chart, 2 in. correspond to 0.1 cm of film. By means of a previously measured linear relation between photographic density and β-radiation intensity and the microphotometer conversion factor, the microphotometer trace was converted into a radioactivity vs (penetration distance)^2 curve (a vs x^2), Fig. 1.

The darkening of the film is caused by both β and γ-radiation. The β-radiation comes from only a thin layer because of the high self-absorption of the silver for β-rays. On the other hand, the self-absorption for γ-rays is quite small, so that γ-radiation from the whole specimen is effective in darkening the film. The correction for the γ contribution to the darkening was made by extrapolation of the long linear region of the curve which is quite removed from the diffusion zone and subtraction from the total activity. A semiquantitative estimate based on the relative yields of γ and β-radiation from Ag^{105} and their efficiency in darkening photographic film indicated that the correction was of the proper order of magnitude. The slope of the straight line which results is inversely proportional to the diffusion coefficient. All distances were corrected for thermal expansion of the silver at the diffusion temperature and the shrinkage of the photographic film upon development.

For the experimental configuration employed in the present study, the theory of volume diffusion requires that the activity of diffusing substance vary exponentially as the square of the distance. Values of D were calculated from the measured slope of the log a vs x^2 plot by means of the equation $D = -4t(\text{slope})^{-1}$. Least-squares treatment of the straight line resulting from a plot of log D vs $1/T$ over the range 980° to 1150°K yielded the relation $D = 0.834\exp(-44{,}900/RT)$.

For the purpose of comparison, values of D_o and E obtained by least-squares treatment of all the available previous data, are given in Table I, together with computed values for D at 1000°K. It may be seen that the method used in this investigation gives values in a reasonable agreement with other methods.

References

[1] H. C. Gatos and A. Azzam: *Trans.* AIME (1952) **194**, p. 407; JOURNAL OF METALS (April 1952).

[2] L. Slifkin, D. Lazarus, and T. Tomizuka: *Journal of Applied Physics* (1952) **23**, p. 1032.

[3] R. E. Hoffman and D. Turnbull: *Journal of Applied Physics* (1951) **22**, p. 634.

[4] W. A. Johnson: *Trans.* AIME (1941) **143**, p. 107; METALS TECHNOLOGY (January 1941).

[5] G. C. Kuczynski: *Journal of Applied Physics* (1950) **21**, p. 632.

[6] G. C. Kuczynski: *Trans.* AIME (1949) **185**, p. 169; JOURNAL OF METALS (February 1949).

[7] H. N. Hersh: *Journal* American Chemical Society (1953) **75**, p. 1529.

Chromium-Rich Portion of the Chromium-Nickel Phase Diagram

by Charles Stein and Nicholas J. Grant

A more complete determination of the chromium-rich portion of the Cr-Ni phase diagram was made, based in part on resistivity measurements. The existence of a eutectoid reaction at 1215°C, in addition to the previously reported eutectic reaction at 1343°C, was confirmed. Metallographic studies, lineal analysis, and diffusion-couple evidence were utilized to support and extend the findings of the resistivity measurements. Delineation of the α chromium solvus line shows that the maximum solubility of nickel in α chromium decreases rapidly from 25 wt pct Ni at the eutectoid temperature to 16 wt pct Ni at 950°C.

IN recent years alloys of high chromium and nickel content have become of more interest as better performance of metals at higher temperatures is sought. It has become increasingly important, therefore, that the Cr-Ni binary diagram, which is composed of two of the elements commonly found in many high temperature alloys, be known more accurately. In particular, the chromium-rich portion of this diagram has for a long time remained incompletely determined and has been reported in the literature with a great deal of conflicting evidence.

In general, electrolytic chromium of nominal purity was used by most of the earlier workers, who, except for Jenkins et al.,[1] made no further attempt to purify the metal.

In the present redetermination of the chromium-rich portion of the Cr-Ni phase diagram, every effort was made to use the purest component metals available and to retain this purity throughout the preparation of the alloys and their subsequent handling.

Early work by Voss,[2] Bain,[3] and Phebus and Elake[4] indicated that the Ni-Cr binary diagram was a simple eutectic system with rather extensive terminal solid solutions. Later, Nishigori and Hamasumi,[5] Tasaki,[6] Weaver and Jellinghaus,[7] Matsunaga,[8] and Jette, Nordstrom, Queneau, and Foote[9] attempted to determine the limits of the phase fields. Except for Jette and coworkers, the other investigators agreed that the temperature of the eutectic reaction occurred between 1320° and 1340°C and at a composition of 50 or 51 pct Cr. There was, however, considerable disagreement as to the melting point of the chromium-rich alloys and the limits of the solid-solution fields.

As a result of the studies of Jenkins et al.,[1] the liquidus and solidus curves up to 80 and 90 pct Cr, respectively, were outlined. In addition, the solid-solution phase fields at higher temperatures had been investigated and showed only two phases.

The boundary of the chromium-rich α phase was not determined precisely according to these authors, but indications were that it tended to confirm the earlier work of Nishigori and Hamasumi.

A more recent investigation by Taylor and Floyd,[10] using X-ray methods, essentially corroborated the diagrams proposed by Jenkins et al., and by Wise and Eash[11] (see Fig. 1). Again, no indication of a third phase in the chromium-rich portion of the diagram appeared.

The earlier observations, however, are not substantiated by the modifications to the Ni-Cr binary diagram proposed by Bloom and Grant.[12] In the investigation carried out by Bloom and Grant, X-ray methods showed that an eutectoid reaction existed at approximately 1180°C, in addition to the eutectic reaction at 1343°C (see Fig. 1). Their determination of the melting point of pure chromium was 1930°C (later revised to 1903°C).[13]

Experimental Procedure and Results

The chromium used for this study was electrolytic chromium, made available by the United States

Fig. 1—Cr-Ni phase diagram showing the simple eutectic and the eutectic-eutectoid versions.

C. STEIN and N. J. GRANT, Member AIME, are former Research Assistant, Dept. of Metallurgy, and Associate Professor of Metallurgy, respectively, Massachusetts Institute of Technology, Cambridge, Mass.

Discussion on this paper, TP 3882E, may be sent, 2 copies, to AIME by Mar. 1, 1955. Manuscript, Apr. 1, 1954. Chicago Meeting, November 1954.

This paper is based on a thesis by C. Stein submitted, in partial fulfillment of the requirements for the degree of Master of Science, to the Dept. of Metallurgy, Massachusetts Institute of Technology.

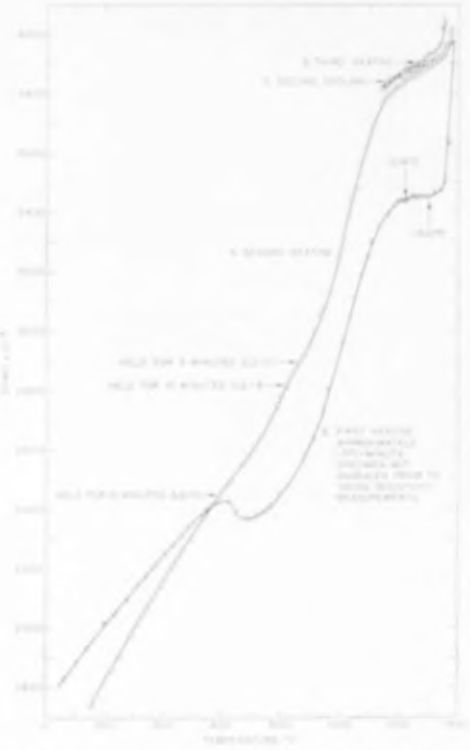

Fig. 2—Resistivity curves for alloy 65, 65.64 pct Cr-34.25 pct Ni.

Bureau of Mines, the nominal composition of which was 99.5 pct Cr and the major impurity being oxygen. This chromium was crushed to a particle size of 20 to 60 mesh and was purified by annealing at 1375°C for approximately 48 hr in a stream of dry hydrogen. The average oxygen content of the chromium was reduced thereby to approximately 0.02 pct.* The nickel used for the alloys was Mond nickel of 99.87 pct nominal purity.

* A typical chemical analysis made on the chromium after annealing in dry hydrogen at 1300°C for 3 hr was reported by Pollock[7] to be 0.022 pct O, 0.006 pct N, and 0.006 pct N.

The alloys were made from these purified component metals by charging them into a water-cooled, copper crucible, tungsten arc furnace. All melting was done under an atmosphere of helium which was purified by passing the gas through tubes of anhydrous calcium sulphate, anhydrous magnesium perchlorate, and phosphorous pentoxide, then over hot platinized asbestos, and finally over titanium sponge heated to approximately 950°C.

Before melting the charge, the arc furnace was alternately evacuated to the limit of a rotary oil pump and then flushed with the purified helium. This operation was repeated several times. The charge was melted; then the button was turned over and remelted several times, without breaking the seal on the furnace. Finally, a portion of each melt was sucked up into a 7 mm Vycor tube by the use of an aspirator bulb attached to the end of Vycor tubing and entering through the top of the furnace. This method was selected in view of the impossibility of producing small diameter bars suitable for resistivity measurements by such methods as casting or hot forging.

The average length of specimen thus produced, from a 150 g charge, was approximately 10 cm. Five centimeters of this length were used for resistivity measurements, the remainder being used for metallographic studies and chemical analysis.

Chemical analyses are listed in Table I.

Resistivity Measurements: Eleven specimens, approximately 5 cm long by 7 mm in diameter and ranging in composition from 50 pct Cr-50 pct Ni to 90 pct Cr-10 pct Ni, were prepared by the method outlined previously for resistivity measurements.

Four wires were spot welded onto the resistivity specimens to act as current and potential leads. At first, pure nickel was used for these lead wires in order to decrease the contamination of the specimens, especially at elevated temperatures. However, this limited the temperature of investigation to that of 1343°C, the reported eutectic temperature. Later, pure molybdenum leads were used to delineate the phase diagram at the higher temperatures.

The specimens were supported between alumina disks, which were used as heat shields. A Pt—Pt-10 pct Rh thermocouple was used for temperature measurements. The entire apparatus was sealed in a double-wound platinum furnace, and all resistivity measurements were made while the samples were in a purified helium atmosphere. Each specimen was annealed in the furnace, under helium, and allowed to furnace cool before resistivity measurements were made.

The temperature over the test specimen length did not vary by more than ±1° at 1300°C. The variation in resistance thus produced was within the accuracy of the double Kelvin bridge[8] on which the resistivity measurements were made. As stated by the manufacturer, the accuracy of this bridge is ±0.1 pct between 0.002 Ω and 1 Ω, and proportionately less below 0.002 Ω. This permits a reading accurate to $\pm 2 \times 10^{-6}$ Ω in the range employed for this study.

In order to approach as close to equilibrium conditions as possible, the samples were heated and cooled at rates not exceeding 2°C per min. In addition, to further ensure the attainment of equilibrium at each point, the temperature was held constant for approximately 3 min before a resistivity measurement was taken. For some specimens, there was a critical temperature range between 800° and 1100°C where

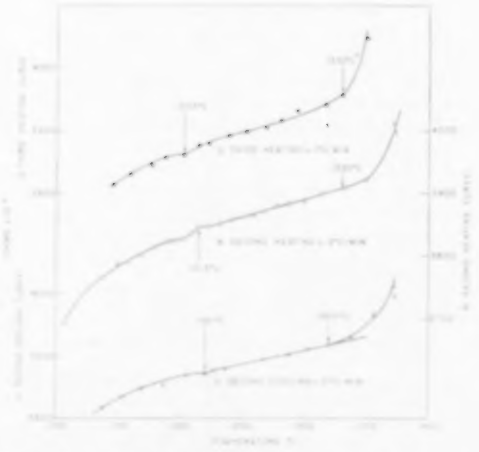

Fig. 3—Resistivity curves for alloy 65 (note expanded resistivity scale), 65.64 pct Cr-34.25 pct Ni.

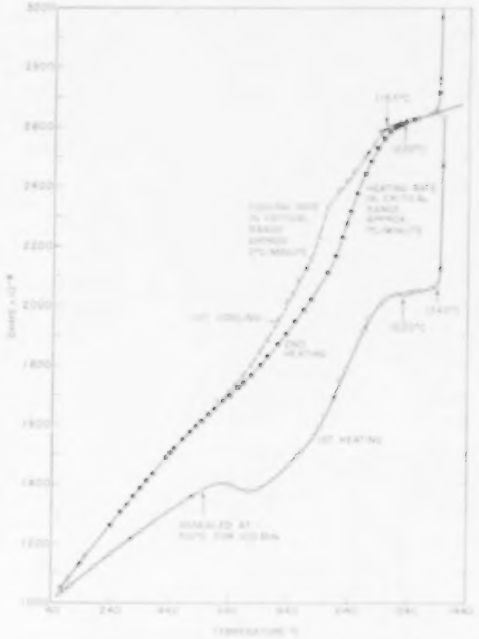

Fig. 4—Resistivity curves for alloy 68, 68.03 pct Cr-31.77 pct Ni. Pure nickel leads.

heating rates in excess of 1.0°C per min no longer resulted in equilibrium. Consequently, these specimens were held at temperature in this critical range until there no longer was any change in resistance with time.

Figs. 2 to 6 show typical temperature vs resistance curves for four of the alloys.

If resistivity measurements are taken during the annealing treatment, as was done on alloy 65, the results would be similar to that shown in curve *A*, Fig. 2. Between 550° and 800°C, there is a sharp dip in the curve, then the curve rises steeply, breaks at 1218° and 1300°C, and then rises sharply again. After this specimen had been furnace cooled and heated a second time, the sharp dip between 550° and 800°C failed to reappear in spite of the fact that the alloy had been held at temperature, several times, to ensure the attainment of equilibrium. Since the break in the curve is nonreproducible on subsequent cooling or heating, it is unlikely to be due to a phase change. This nonreproducible dip in the annealing curve appeared in every alloy so treated (see, for example, Figs. 4 and 6). When a high temperature X-ray camera was used on alloy 85, the γ nickel lines grew in intensity as the temperature was increased through the 550° to 800°C temperature range. This suggests that the rapid quench from the melt has supersaturated the chromium matrix with nickel. The precipitation of this excess nickel phase between 550° and 800°C results in an increase in the γ nickel X-ray lines and a decrease in the resistance of the alloy.

Other heating cycles of alloy 65 reproduced the two breaks in the curve occurring at the higher temperatures. An enlargement of the upper portion of this curve is shown in Fig. 3 where the reproducibility of these two breaks is demonstrated by a second cooling and two reheating cycles. The average

Table I. Chemical Analysis of Alloys Prepared in Arc Furnace by Aspirator Method*

Alloy No.	Pct Ni	Pct O_2	Pct N_2	Pct C	Pct Si	Pct Cr†
100	—	—	—	0.22	0.255	99.53
90	9.60	0.212	0.612	0.01	0.600	88.97
85	15.36	0.035	0.193	0.02	0.142	84.25
82	17.73	—	—	—	—	82.27
80	18.08	0.053	0.0001	—	0.144	81.72
75	25.12	0.073	0.0067	—	0.08	74.72
72	27.40	0.056	0.0014	—	0.245	72.30
68	31.77	0.151	0.0011	0.02	0.025	68.03
66	34.32	—	—	0.02	0.032	65.63
65	34.25	—	—	0.05	0.065	65.64
64	35.4	—	—	—	—	64.6
50	49.48	0.119	0.02	—	0.06	50.32
0	99.6	0.0045	0.0007	0.09	0.01	—

* Oxygen and nitrogen content determined by vacuum fusion method.

† Analysis made for nickel, oxygen, nitrogen, carbon, and silicon. Chromium content given as the balance.

temperatures of these breaks in the curves are taken as 1213° and 1326°C.

The wires used on alloy 68 (Fig. 4), the proposed eutectoid composition, were pure nickel. This specimen had been annealed at 510°C for over 1 hr before resistivity measurements were started. It is evident that the rate of precipitation of nickel from the supersaturated chromium phase is extremely slow below 800°C and that annealing at 510°C for 100 min did not permit equilibrium to be achieved. Therefore, on reheating this alloy after the annealing treatment, the resistivity curve shows the dip between 600° and 800°C. While some nickel had precipitated on annealing at 510°C, the supersaturated chromium did not reject the balance of the excess nickel phase until a temperature in excess of approximately 600°C had been reached. Above 1340°C, the curve rises sharply, indicating that melting at the junction of the lead wires with the specimen had taken place. Between 1220° and 1340°C no break occurs in the curve, indicating that phase boundaries between these two temperatures were not crossed. The cooling curve and second heating curve corroborate this finding. This alloy therefore was chosen as the eutectoid composition; the choice was substantiated later by lineal analysis results.

After 1340°C had been reached on the first heating cycle, the specimen was cooled and resistivity measurements were taken from 1340° to approxi-

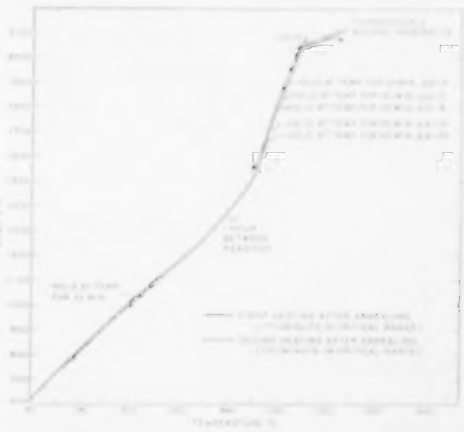

Fig. 5—Resistivity curves for alloy 80, 81.72 pct Cr-18.08 pct Ni.

Table II. Transition Temperature From Resistivity Measurements

Alloy No.	Chemical Analysis		Transition Temperature, °C	Phase Boundaries Crossed	Remarks: Annealing Temperatures, Heating and Cooling Rates
	Pct Cr	Pct Ni			
[illegible]	50.32	49.46	1220	$\alpha + \gamma \mid \beta + \gamma$	Annealed, 1300°C; cooling rate 1.5°C per min
64	64.6	35.4	1220	$\alpha + \gamma \mid \beta + \gamma$	Annealed, 1275°C for 1.5 hr
66	65.63	34.32	1213	$\alpha + \gamma \mid \beta + \gamma$	Second heating: 2°C per min; second cooling: 2°C per min; third heating: 1°C per min
			1327	$\beta + \gamma \mid \beta$	
67	67.64	34.25	1215	$\alpha + \gamma \mid \beta + \gamma$	First heating rate: 2°C per min; second heating rate: 1°C per min
			1326	$\beta + \gamma \mid \beta$	
68	68.03	31.77	1230	$\alpha + \gamma \mid \beta$	Annealed 310°C, 100 min.; second heating rate: 1°C per min; first cooling: 2°C per min
72	72.2	27.4	1212	$\alpha + \gamma \mid \alpha + \beta$	Annealed 1100°C, 1 hr; first and second heating rates: 1°C per min
			1246	$\alpha + \beta \mid \beta$	
73	74.72	25.12	1215	$\alpha + \gamma \mid \alpha + \beta$	Annealed 1100°C; first heating: 1°C per min; first cooling: 2°C per min
			1279	$\alpha + \beta \mid \beta$	
80	81.72	18.68	1130	$\alpha + \gamma \mid \alpha$	Annealed; first and second heating rates: 1°C per min
82	82.27	17.73	1120	$\alpha + \gamma \mid \alpha$	Annealed 900°C, 5 hr; first, second, and third heating rates: 1.5°C per min
			1272	$\alpha \mid \alpha + \beta$	
			1363	$\alpha + \beta \mid \beta$	
83	84.23	15.28	800	$\alpha + \gamma \mid \beta$	Annealed 1100°C, 1 hr; first heating rate: 1°C per min
			1325	$\alpha \mid \alpha + \beta$	
85	86.97	9.89	543	$\alpha + \gamma \mid \alpha$	Annealed 1100°C, 1 hr; first heating rate: 2°C per min; first cooling and second heating: 1°C per min

mately 500°C. The rate of cooling in the critical range near the transition temperature was approximately 2°C per min. This was fast enough to suppress the eutectoid reaction by 55°. In the lower temperature ranges, however, where the rates of cooling and heating are not quite as critical, the points on cooling at 2°C per min coincide with those of a second heating curve made at approximately 1°C per min. With the slower heating rate, the eutectoid reaction is again found to take place at 1220°C.

Attainment of equilibrium in the range below the transition temperature is illustrated in Fig. 5 for alloy 80. On the first heating cycle after annealing the specimen, the alloy was held at five different temperatures for various times until there no longer was any change of resistance with time. It therefore was assumed that, at temperatures above the last point of holding, the alloy would continue to be in equilibrium. The substantiation of this assumption is shown by the exact reproduction of the break in the curve occurring at 1130°C when heating this specimen a second time at the same rate in the critical range.

Fig. 6—Resistivity curves for alloy 80, 82.27 pct Cr-17.73 pct Ni

Fig. 6 for alloy 82 shows three heating curves in which three breaks in the curve are reproduced. In curve *A* the breaks occur at 1125°, 1265°, and 1350°C. When the specimen had been furnace cooled and reheated at approximately the same rate, the breaks in the curve occurred at 1115° and 1275°C. The last transition temperature was not indicated, since one of the molybdenum lead wires broke. The specimen therefore was furnace cooled, new molybdenum lead wires were welded on, and the specimen was reheated for a third time. These results are shown in curve C of this figure where breaks in the curve are noted at 1120°, 1275°, and 1375°C. The average values for these transition temperatures therefore are taken as 1120°, 1272°, and 1363°C.

Table II is a summary of the test results of resistivity vs temperature for the 11 different alloys. The resulting equilibrium diagram, drawn from the transition points appearing in the resistivity vs temperature curves, is shown in Fig. 19 and will be discussed subsequently.

Metallographic Studies: From the original 10 cm length of sample sucked up from each melt, small pieces were cut off for metallographic studies. Eleven compositions, ranging from 90 pct Cr-10 pct Ni to 50 pct Cr-50 pct Ni, were quenched from three different temperatures, 1300°, 1250°, and 1180°C, into different quenching media. The annealing times at temperature were 5, 23, and 26 hr, respectively. Specimens quenched from the lower two temperatures were annealed in a horizontal globar furnace under a flow of purified helium. Quenching was achieved by quickly sliding a porcelain boat containing the specimens out of the furnace and into the quenching medium. In order to retain the phases existing at the elevated temperatures, a faster method of quenching was required. This was accomplished by building a special apparatus in which the specimens were treated in a pure helium atmosphere and were quenched in a timed interval of less than 0.5 sec.

The results of the heat treatments are seen in some typical micrographs, Figs. 7 through 15. For

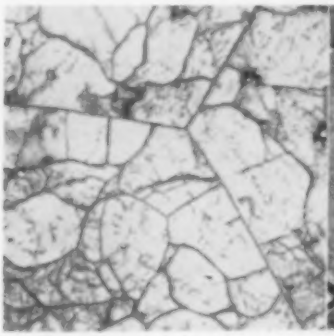

Fig. 7—68.03 pct Cr-31.77 pct Ni, annealed 5 hr at 1300°C, brine quench. α' chromium. X500.

Fig. 8—64.6 pct Cr-35.4 pct Ni, annealed 5 hr at 1300°C, brine quench. α' chromium (dark phase) and γ nickel (light phase). X500.

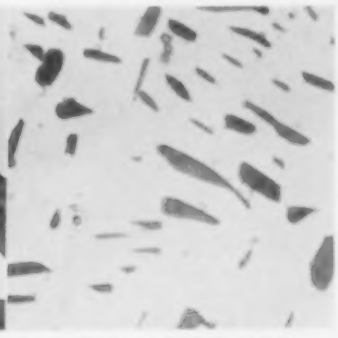

Fig. 9—50.32 pct Cr-49.48 pct Ni, annealed 5 hr at 1300°C, brine quench. α' chromium (dark phase) and γ nickel (light phase). X500.

Fig. 10—81.72 pct Cr-18.08 pct Ni, annealed 23 hr at 1250°C, liquid N_2 quench. α chromium. X500.

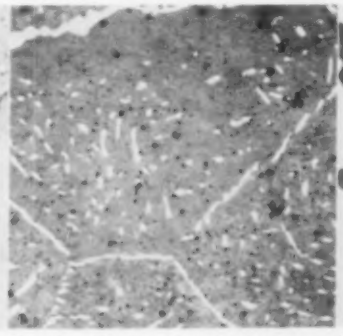

Fig. 11—65.63 pct Cr-34.32 pct Ni, annealed 23 hr at 1250°C, liquid N_2 quench. α' chromium (dark phase) and γ nickel (light phase). X500.

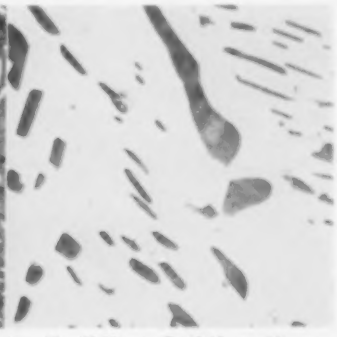

Fig. 12—50.32 pct Cr-49.48 pct Ni, annealed 23 hr at 1250°C, liquid N_2 quench. α' chromium (dark phase) and γ nickel (light phase). X500.

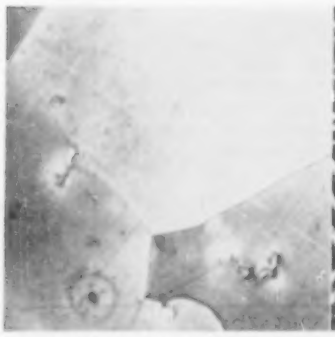

Fig. 13—81.72 pct Cr-18.08 pct Ni, annealed 26 hr at 1180°C, brine quench. α chromium. X500.

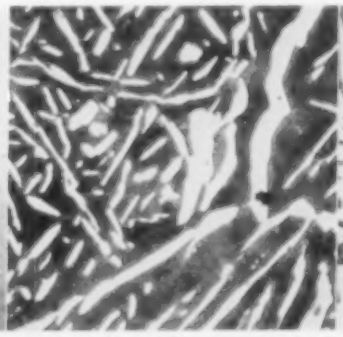

Fig. 14—68.03 pct Cr-31.77 pct Ni, annealed 26 hr at 1180°C, brine quench. α chromium (dark phase) and γ nickel (light phase). X500.

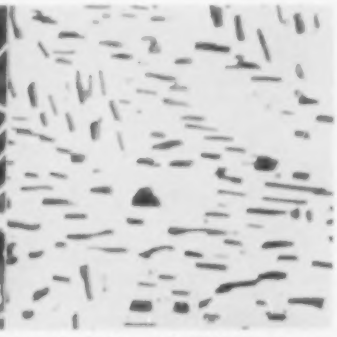

Fig. 15—50.32 pct Cr-49.48 pct Ni, annealed 26 hr at 1180°C, brine quench. α chromium (dark phase) and γ nickel (light phase). X500.

convenience, Table III gives a summary of the alloys treated, the annealing temperature, time at temperature, quenching media, and the phases present. The specimens were prepared for micrographs by mechanically polishing and etching with hot concentrated hydrochloric acid.

In a few of the micrographs presented, carbide, nitride, or oxide particles appear and may be identified as white grain-boundary particles, long needles, and dark angular particles, respectively.

The metallographic study clearly delineated the boundary between the β and the $\beta + \gamma$ fields, the boundary between the α and the $\alpha + \gamma$ fields, and the eutectoid reaction.

The delineation of the $\alpha + \beta$ boundaries was not clear from metallographic evidence. For example, alloy 82 quenched from 1300°C, and alloy 75 quenched from 1250°C, appear to be single phases, while supposedly in a two-phase field.

This apparent anomaly may be explained by these two facts 1—The β chromium which formed during annealing in the two-phase field $\alpha + \beta$ probably transformed to the α chromium phase on quenching from the elevated temperature. 2—The $\alpha + \beta$ phase

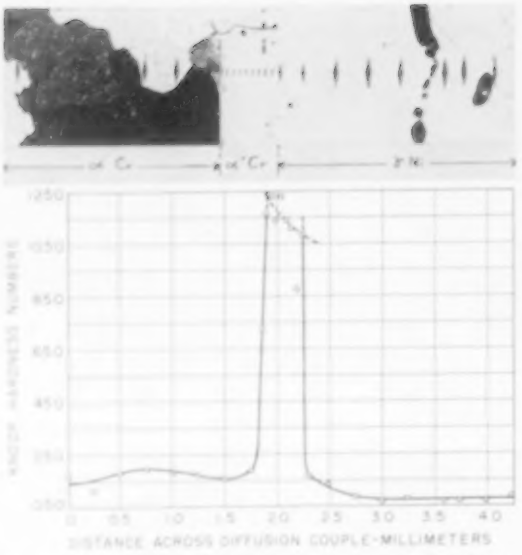

Fig. 16—Microstructure and Knoop hardness across a diffusion couple annealed for 1 week at 1300°C in helium, ice brine quench. Micrograph at X35. Area reduced approximately 35 pct for reproduction.

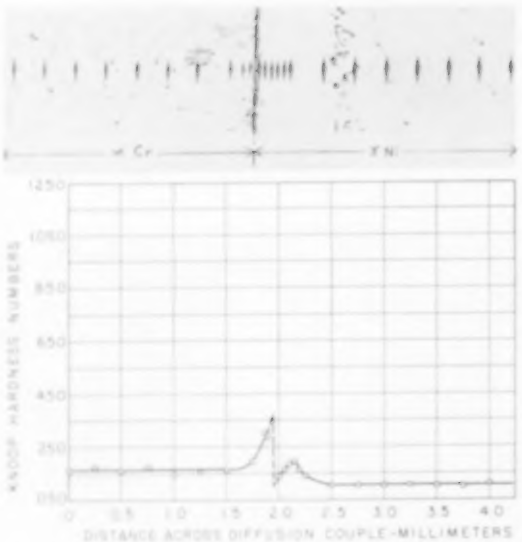

Fig. 17—Microstructure and Knoop hardness across a diffusion couple annealed for 2 weeks at 1180°C in helium, ice brine quench. Micrograph at X35. Area reduced approximately 35 pct for reproduction.

field may be even narrower than that shown by resistivity measurements, making it difficult to anneal a specimen at the correct temperature to show the two-phase structure.

Cr-Ni Diffusion Couples: In order to demonstrate that a third phase exists at elevated temperatures in the Cr-Ni binary system, a diffusion couple was made using pure chromium and pure nickel as component parts (for chemical analysis, see Table I). The two metals were carefully ground flat, tied together with pure nickel wire, and annealed for 169 hr (approximately one week) at 1300°C, in purified helium. The couple was quenched into ice brine and then mechanically polished and etched with hot concentrated hydrochloric acid. Knoop hardness readings were then taken across the diffusion zone. Fig. 16 shows a micrograph taken across the diffusion zone and the corresponding hardness curve across the field. The micrograph shows quite clearly that three different phases exist at elevated temperatures in the Cr-Ni binary system. Indeed, the Knoop hardness readings taken across the α' chromium phase field show that this intermediate phase has vastly different properties than either the α chromium or the γ nickel phases into which it decomposes. The Rc hardness values converted from the Knoop values show the maximum hardness of the α' chromium to be approximately Rc 79, and the average about Rc 77, suggesting that the α' phase may be a martensitic phase.

A second diffusion couple was made to demonstrate that the eutectoid temperature lies above 1180°C. This couple was made by reacting pure chromium and Mond nickel under purified helium for 368 hr (approximately two weeks) at 1180°C and quenching into ice brine. After mechanically polishing and etching with hot concentrated hydrochloric acid, Knoop hardness readings were taken across the diffusion zone. Fig. 17 shows a micrograph of this diffusion zone and the corresponding hardness values. The existence of only two phases is clearly shown.

Lineal Analysis: Verification of the limits of the $\alpha + \gamma$ and $\beta + \gamma$ phase fields found by resistivity measurements was achieved by lineal analysis taken on five specimens quenched from 1180°C and on four specimens quenched from 1250°C.

Table IV lists the alloys used in the lineal analysis, the quenching temperature, the volume percentage of γ nickel found for each alloy, and the limits of the two phase fields. These data are plotted in Fig. 18. According to the lever law, the weight fraction of the chromium phase is linearly proportional to the composition. The volume fraction is not linearly related to the composition nor to the weight fraction, but this would be a good first approximation if the densities of the chromium and nickel phases were about the same. Making this approximation, straight lines were drawn through the points of Fig. 18 and extrapolated to meet the 100 and 0 pct γ nickel horizontals. The intersection of these straight lines give the limits of the $\alpha + \gamma$ and $\beta + \gamma$ phase fields at 1180° and 1250°C, respectively.

Putman,[9] from lineal analysis work on Ni-Cr alloys, showed that the difference between the

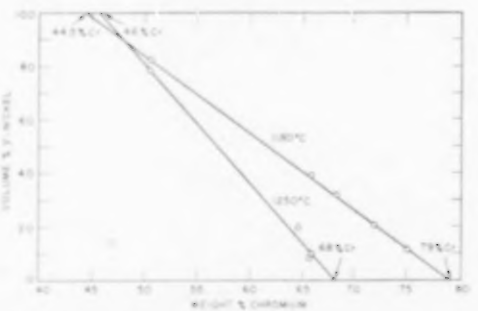

Fig. 18—Lever law relationships from lineal analysis data to establish chromium solubility limits for the $\alpha + \gamma$ field at 1180°C and for the $\beta + \gamma$ field at 1250°C.

Table III. Description of Micrographs*

Alloy No.	Chemical Analysis		Annealing Temperature, °C	Time at Temperature, Hr	Quenching Medium	Magnification	Number of Phases	Description of Phases
	Pct Cr	Pct Ni						
90	88.97	9.6	1300	5	Liquid N_2	X100	1	α — chromium
85	84.25	15.36	1300	5	Liquid N_2	X500	1	α — chromium
82	82.27	17.73	1300	5	Liquid N_2	X500	—	—
80	81.72	18.08	1300	5	Liquid N_2	X500	—	—
75	74.72	25.12	1300	5	Liquid N_2	X500	1	α' — chromium
72	72.30	27.40	1300	5	Liquid N_2	X500	1	α' — chromium
68	68.03	31.77	1300	5	Brine	X500	1	α' — chromium
66	65.63	34.32	1300	5	Brine	X500	1	α' — chromium
64	64.6	35.4	1300	5	Brine	X500	2	α' — chromium + γ — nickel
50	50.32	49.48	1300	5	Brine	X500	2	α' — chromium + γ — nickel
84	84.25	15.36	1250	23	Liquid N_2	X100	1	α — chromium
82	82.27	17.73	1250	23	Liquid N_2	X500	1	α — chromium
80	81.72	18.08	1250	23	Liquid N_2	X500	1	α — chromium
75	74.72	25.12	1250	23	Liquid N_2	X500	—	—
72	72.30	27.40	1250	23	Liquid N_2	X500	—	—
68	68.03	31.77	1250	23	Liquid N_2	X500	1	α' — chromium
66	65.63	34.32	1250	23	Liquid N_2	X500	2	α' — chromium + γ — nickel
64	64.6	35.4	1250	23	Liquid N_2	X500	2	α' — chromium + γ — nickel
50	50.32	49.48	1250	23	Liquid N_2	X500	2	α' — chromium + γ — nickel
84	84.25	15.36	1180	26	Brine	X500	1	α — chromium
82	82.27	17.73	1180	26	Brine	X500	1	α — chromium
80	81.72	18.08	1180	26	Brine	X500	1	α — chromium
72	72.30	27.40	1180	26	Brine	X500	2	α — chromium + γ — nickel
68	68.03	31.77	1180	26	Brine	X500	2	α — chromium + γ — nickel
65	65.64	34.25	1180	26	Brine	X500	2	α — chromium + γ — nickel
50	50.32	49.48	1180	26	Brine	X500	2	α — chromium + γ — nickel

* All specimens were mechanically polished and etched with concentrated hydrochloric acid.

densities of the α chromium and the γ nickel is reasonably small, especially at the higher temperatures where the solid solutions are closer in composition. Because no more than three traverses were made on each alloy listed in Table IV, further correction for the difference in densities of the solid-solution phases was not thought necessary, since the approximation was within the limits of experimental error.

The limits of the $\alpha + \gamma$ phase field at 1180°C and of the $\beta + \gamma$ phase field at 1250°C, found by lineal analysis, are 79 and 44.5 pct Cr, and 68 and 46 pct Cr, respectively. These limits are superimposed on the phase diagram appearing in Fig. 19 where a comparison with the limits of the phase fields found by resistivity measurements can be made.

Summary and Conclusions

The experimental evidence obtained through resistivity measurements, substantiated in part by metallographic work and more fully by lineal analysis and work with diffusion couples, has delineated the chromium-rich portion of the Cr-Ni equilibrium diagram (see Fig. 19).

A comparison of this diagram with the Cr-Ni diagram determined by Wise and Eash[5] (see Fig. 1) shows several important differences. In addition to the eutectic reaction determined by Wise and Eash at 1343°C, the present work indicates that a eutectoid reaction occurs at 1215°C, between a high temperature chromium phase, β, and two solid solutions, α chromium and γ nickel.

The solvus lines of the chromium-rich alloys determined in both of these investigations have similar shapes; however, resistivity measurements and lineal analysis from the present work show that, in general, the solubility of nickel in chromium is higher than that reported in the earlier work.

The transition in pure chromium, from the α to the β phase, was determined by Bloom and Grant to be 1840°C (see Fig. 1). A comparison of the phase diagram proposed by these authors and that of the present work shows that the two are very similar. However, the eutectoid composition of 65 pct Cr

Table IV. Lineal Analysis

Chemical Analysis		Total Number of Counts	Volume Pct γ Nickel
Pct Cr	Pct Ni		
Specimens Quenched From 1250°C			
Limits of the $\beta + \gamma$ Phase Fields: 68 Pct Cr and 46 Pct Cr			
50.32	49.48	10,267	78.27
64.6	35.4	10,427	19.54
65.64	34.25	16,295	8.01
65.63	34.32	10,259	16.05
Specimens Quenched From 1180°C			
Limits of the $\alpha + \gamma$ Phase Fields: 79.0 Pct Cr and 44.5 Pct Cr			
50.32	49.48	9,073	82.05
65.64	34.25	10,471	39.64
68.03	31.77	10,175	32.53
72.30	27.40	11,366	20.85
74.72	25.12	11,193	11.56

Fig. 19—Proposed Cr-Ni phase diagram based on the current work and on two recent versions.

reported from the X-ray diffraction work of Bloom and Grant has been adjusted to 68 wt pct Cr based on resistivity measurements and on lineal analysis.

The maximum solubility of nickel in chromium, as determined in the present work, decreases rapidly between 1215° and 1100°C, where it is 25 and 18 pct Ni, respectively. Below 1100°C, the solubility of nickel in α chromium changes but little.

The thermal analysis work of Jenkins, Bucknall, Austin, and Mellor[1] on alloys rich in chromium showed anomalous breaks in the curves at 950°C on cooling and at 1100°C on heating. This temperature range is approximately the one determined by resistivity measurements to be the critical range wherein heating or cooling rates in excess of 1.5°C per min no longer results in the attainment of equilibrium conditions. This critical heating and cooling rate probably occurs due to the very sharp change in the solubility of nickel in α chromium in this temperature range, as just discussed.

In addition to the boundaries determined in this work, selected values from the work of Bloom and Grant and Wise and Eash were taken to form a proposed Cr-Ni phase diagram, as shown in Fig. 19.

Acknowledgments

The authors wish to express their sincere thanks to Mr. Albert G. Bucklin, Mrs. Gloria Johnson, and Mr. Ralph Kimble for extensive assistance throughout the program. The sponsorship of the Bureau of Aeronautics is gratefully acknowledged.

References

[1] C. H. M. Jenkins, E. H. Bucknall, C. R. Austin, and G. A. Mellor: *Journal* Iron and Steel Institute (1937) **136**, No. 2, p. 193.

[2] G. Voss: *Ztsch. für Anorg. Allgem. Chemie* (1908) **57**, p. 34.

[3] C. H. Bain: *Trans.* AIME (1923) **68**, p. 625.

[4] W. C. Phebus and F. C. Blake: *Physical Review* (1925) **25**, p. 107.

[5] S. Nishigori and M. Hamasumi: *Science Reports* Tohoku Imperial University (1929) **8**, p. 491.

[6] M. Taski: *Proceedings* World Engineering Congress (1929) **36**, p. 231.

[7] F. Weaver and W. Jellinghaus: *Mitteilungen* Kaiser-Wilhelm-Institut für Eisenforschung (1931) **13**, p. 93.

[8] B. Matsunaga: *Japan Nickel Review* (1933) **1**, p. 347.

[9] E. R. Jette, V. H. Nordstrom, B. Queneau, and F. Foote: *Trans.* AIME (1934) **111**, p. 361.

[10] A. Taylor and R. W. Floyd: *Journal* Institute of Metals (1953) **81**, p. 451.

[11] E. M. Wise and J. T. Eash: *Metals Handbook* (1948) p. 1195. Cleveland, ASM.

[12] D. S. Bloom and N. J. Grant: *Trans.* AIME (1951) **191**, p. 1009; JOURNAL OF METALS (November 1951).

[13] D. S. Bloom, J. W. Putman, and N. J. Grant: *Trans.* AIME (1952) **194**, p. 626; JOURNAL OF METALS (June 1952).

[14] J. W. Putman: Doctor of Science Thesis, Dept. of Metallurgy, Massachusetts Institute of Technology (1953).

[15] *Notes on the Kelvin Bridge, Note Book E-53 (1)* Leeds and Northrup Co. (1951).

Technical Note

Stress Analysis of a Single Crystal in Pure Torsion

by Norman Brown

IT has been observed that a hexagonal-close-packed crystal will undergo the same macroscopic displacements as an isotropic material if the basal plane is perpendicular to the axis of twist.[1] Other orientations may produce both bending and twisting, but this analysis will be confined to pure torsion of a right circular cylinder. The z axis, the axis of twist, and the specimen axis are coincident. The displacements are given by

$$U_z = \phi rz, \; U_r = U_\theta = 0 \qquad [1]$$

where ϕ is the angle of twist per unit length. This requires rotational slip, as discussed by Frank[2] and Wilman,[3] which may be observed readily. The relative rotation of adjoining slip planes is simply produced by a movement of a planar grid of screw dislocations.[4,5] The screw dislocations are of the same sign and they move radially inward. For hexagonal-close-packed metals, the grid is hexagonal and the screw dislocations lie in the $\langle 2\bar{1}\bar{1}0 \rangle$ directions.

The displacement of a point is the resultant of two displacements produced by intersecting screws sweeping over the point. The dislocations must pass over the point (r, θ) in such a manner that its resultant displacement corresponds to the observed macroscopic displacement. If θ is measured from the $[10\bar{1}0]$ direction, then for $0 < \theta < \pi/3$, only the $[1\bar{2}10]$ and $[\bar{2}110]$ type screw dislocations are needed to produce the required displacement. If n_1 screws of type $[1\bar{2}10]$ and n_2 of type $[\bar{2}110]$ pass over a point, then, in order that $U_r = 0$

$$n_1 \sin \theta - n_2 \sin (\pi/3 - \theta) = 0 \qquad [2]$$

If the tangential displacement is to be independent of θ, then

$$n_1 \cos \theta + n_2 \cos (\pi/3 - \theta) = N \qquad [3]$$

where N is independent of θ and thus depends only on r. Nb is the tangential displacement where b is the Burgers vector. Since U_r is a linear function of r, then N must be a linear function of r. If a_1 is the outer radius and a_2 is the inner radius to which the plastic deformation has extended, then

$$N = N_{a_1} \frac{(r - a_2)}{(a_1 - a_2)} \qquad [4]$$

This function meets the conditions that at

N. BROWN, Junior Member AIME, is Assistant Professor of Metallurgy, School of Metallurgical Engineering, University of Pennsylvania, Philadelphia.

TN 237E. Manuscript, Apr. 2, 1954.

$$r = a_o; N = N_o$$

$$r = a_i; N = 0.$$

For $r < a_i$, the deformation is still elastic.

The stress to produce plastic deformation will be calculated from energy considerations. The external work in the plastic range equals the work to move the dislocations plus the increase in elastic strain energy of the inner core. The elastic contribution may be neglected by considering that part of the torque, T_p, necessary to twist the outer plastic shell. Let the external plastic work be given by

$$\int_0^{\chi_p} T_p d\chi$$

where χ_p is the angle of plastic twist per unit length.

In terms of the stress, the external work is

$$\int_0^{\chi_p} T_p d\chi = \int_{r_i}^{r_o} \int_0^{\chi_p} \tau_{xy} 2\pi r^2 dr d\chi. \quad [5]$$

It is noted that

$$\chi_p = \frac{Nb}{r} = \frac{N_o b}{(a_o - a_i)} \frac{(r - a_i)}{r}. \quad [6]$$

The work to move a single dislocation is given by the theorem that the work is equal to the force per unit length acting on the dislocation time the area swept out by the dislocation.[5] The incremental work for $(n_i + n_i)$ dislocations to sweep out an increment of area is given by

$$F_s (n_i + n_i)\, r dr d\theta$$

where F_s is the force per unit length. This force depends on the state of the metal. The total work in moving dislocations is given by

$$\int_0^{\pi} \int_{a_i}^{r_o} F_s (n_i + n_i)\, r dr d\theta \quad [7]$$

$(n_i + n_i)$ is obtained from solving Eqs. 2 and 3 and bringing in Eq. 4.

$$n_i = \frac{N \sin (\pi/3 - \theta)}{\sin \pi/3} = \frac{N_o (r - a_i) \sin (\pi/3 - \theta)}{(a_o - a_i) \sin \pi/3}. \quad [8]$$

$$n_i = \frac{N \sin \theta}{\sin \pi/3} = \frac{N_o (r - a_i) \sin \theta}{(a_o - a_i) \sin \pi/3}. \quad [9]$$

Entering Eqs. 8 and 9, Eq. 7 becomes

$$\frac{6}{\sin \pi/3} \int_0^{\pi/3} \int_{a_i}^{r_o} \frac{F_s N_o}{(a_o - a_i)} [\sin (\pi/3 - \theta) + \sin \theta] (r - a_i)\, r dr d\theta. \quad [10]$$

Symmetry permits the change in the limits of integration of θ. Since the external plastic work is equal to work in moving the dislocations, Eq. 10 is joined to Eqs. 5 and 6 by

$$\int_{a_i}^{r_o} \int_0^{\frac{\tau_{xy} b}{G} \frac{r - a_i}{r}} \tau_{xy}\, 2\pi r^2 dr d\chi = \frac{6}{\sin \pi/3} \int_0^{r_o} \int_0^{\pi/3} F_s \frac{N_o}{(a_o - a_i)} [\sin (\pi/3 - \theta) + \sin \theta] (r - a_i)\, r dr d\theta. \quad [11]$$

Table I. Dependence of Yield Stress in Torsion on Crystal Lattice

Type of Crystal	Slip System		τ_{xy}/c
Hexagonal-close-packed	$\langle 2\bar{1}\bar{1}0 \rangle$	(0001)	$2\sqrt{3}\,\pi$
Face-centered-cubic	$\langle 1\bar{1}0 \rangle$	(111)	$2\sqrt{3}\,\pi$
Body-centered-cubic 110	$\langle 1\bar{1}1 \rangle$	(110)	$2\sqrt{3}\,\pi$

τ_{xy} is to be evaluated in terms of F_s. Considering only incipient yielding in a very thin shell, work hardening may be neglected. Therefore, F_s may be taken outside the integral sign and τ_{xy} is independent of χ. Therefore

$$2\pi\tau_{xy} \frac{N_o b}{(a_o - a_i)} \int_{a_i}^{r_o} r (r - a_i)\, dr = \frac{F_s N_o}{(a_o - a_i)} \frac{6}{\sin \pi/3} \int_0^{\pi/3} [\sin (\pi/3 - \theta) + \sin \theta]\, d\theta \int_{a_i}^{r_o} (r - a_i)\, r dr. \quad [12]$$

The integral

$$\int_0^{\pi/3} [\sin (\pi/3 - \theta) + \sin \theta]\, d\theta = 1. \quad [13]$$

Thus, the term $6/(\sin \pi/3)$ is related to the geometry of the dislocation grid, which in turn, depends on the crystal structure. Eq. 12 becomes

$$2\pi\tau_{xy} b = \frac{6F_s}{\sin \pi/3} \quad [14]$$

or

$$\tau_{xy} = \frac{2\sqrt{3}}{\pi} \frac{F_s}{b}.$$

But F_s/b is equal to τ_s, the resolved shear stress.[5] Therefore, a hexagonal-close-packed crystal with basal plane perpendicular to the twist axis yields when

$$\frac{\tau_{xy}}{\tau_s} = \frac{2\sqrt{3}}{\pi} = 1.1.$$

It is interesting to calculate how the result varies with crystal structure. The only change comes in the crystal structure factor (Eq. 13), which depends on the geometry of the dislocation grid. The results for the common crystal structures are given in Table I where the slip plane is perpendicular to axis of twist.

For an isotropic medium $\frac{\tau_{xy}}{\tau_s} = 1$.

Acknowledgment

This work was supported by the Office of Ordnance Research, United States Army on Contract DA 36-034-ORD 491RD.

References

[1] S. S. Hsu and B. D. Cullity: On the Torsional Deformation and Recovery of Single Crystals. *Trans.* AIME (1954) **200**, p. 305; JOURNAL OF METALS (February 1954).

[2] F. C. Frank: Report of a Conference on the Strength of Solids, University of Bristol, England. Physical Society (1948).

[3] H. Wilman: *Nature* (1950) **165**, p. 321.

[4] A. H. Cottrell: *Dislocations and Plastic Flow in Crystals*. (1953) New York, Oxford.

[5] W. T. Read, Jr.: *Dislocations in Crystals*. (1953) pp. 60, 178. New York, McGraw-Hill Book Co. Inc.

Solubility and Decomposition Pressures of Hydrogen in Alpha-Zirconium

by Earl A. Gulbransen and Kenneth F. Andrew

Thermodynamic information on the solubility of hydrogen in exothermic metals is limited. Thus, the overall solubility decreased as the temperature rose, which suggests the heat of solution of hydrogen in the metal is negative; yet the terminal solubility in the metal phase increased, which suggests an endothermic reaction. A thermodynamic analysis, therefore, was made of the several equilibria involved when hydrogen dissolved in the metal. Equations were derived expressing the solubility, terminal solubility, and decomposition pressures of hydrogen in terms of the heat, entropy, and free energy of solution of hydrogen in the given phase. The relations between the thermodynamic functions for the α-zirconium and δ-hydride phase were developed.

The thermodynamic quantities were determined experimentally by the measurement of the decomposition pressures over a broad composition and temperature range. Two new methods of analyzing the experimental data were developed for determination of the terminal solubility.

STUDIES[1,2] of the impact strength of zirconium at room temperature indicated that small quantities of hydrogen, of the order of 10 parts per million, embrittles the metal. Micrographic[1] and X-ray diffraction[2] studies showed this embrittlement to result from the precipitation of a second phase upon slow cooling. These studies suggested that the terminal solubility of hydrogen in the metal phase increased with increase of temperature. This behavior appeared to contradict the effect of temperature on exothermic hydrogen occluders such as zirconium. For these metals, the solubility of hydrogen should decrease with increase of temperature. Before these facts could be understood, a thorough analysis of the several equilibria was essential.

It was the purpose of this paper to consider the several equilibria involved when hydrogen was reacted with zirconium from both the theoretical and experimental points of view. Since the overall solubility of hydrogen in the metal has been considered by a number of workers,[3-7] it was proposed to study the composition range 0 to 6 atomic pct H in detail.

Literature

Schwartz and Mallett[3] determined the terminal solubilities of hydrogen in the metallic phase from diffusion studies. They extrapolated concentration-penetration curves to the boundary between the solid solution phase and the hydride phase at the surface. Their results showed values of 2.6 atomic pct at 400°C and 5.2 atomic pct at 500°C. Extrapolations of the data to room temperature suggested very low values for the terminal solubilities. This study confirmed the hydrogen embrittlement results and indicated that the terminal solubilities increased as the temperature was raised.

The solution of hydrogen in zirconium over the complete concentration range was studied by Hall, Martin, and Rees[4] and by others.[5-7] The results showed that hydrogen was absorbed up to a maximum composition of 66 atomic pct or $ZrH_{1.9}$. This composition represented the ε-hydride phase. The maximum amount of hydrogen absorbed increased with pressure and decreased with temperature. Due to this temperature behavior, zirconium was classed as an exothermic occluder.[7]

In 1930 Hägg[8] studied the crystal structures of the Zr-H alloys over a broad composition range. Four hydride phases were found. However, the range of homogeneity of the several phases was not studied. Gulbransen and Andrew[9] recently studied the phase diagram of this system by X-ray diffraction methods and by a thermodynamic method based on decomposition pressure measurements. The results showed that only two hydride phases existed for low temperatures, the δ and the ε-phases of Hägg.[8] Both phases had broad regions of homogeneity. The lower limit of the two-phase region of α and δ-phases suggested a terminal solubility of 4 atomic pct at 500°C. This value was in agreement with the results of Schwartz and Mallett.[3]

To avoid hydrogen embrittlement at low temperatures, it was necessary to heat the metal in high vacuum at elevated temperatures. To choose the conditions of temperature and high vacuum, it was

E. A. GULBRANSEN, Member AIME, and K. F. ANDREW are associated with Chemical Dept., Research Laboratories, Westinghouse Electric Corp., East Pittsburgh, Pa.

Discussion on this paper, TP 3888E, may be sent, 2 copies, to AIME by Mar. 1, 1955. Manuscript, Apr. 14, 1954. Chicago Meeting, November 1954.

essential to know the equilibrium decomposition pressures as a function of temperature and concentration. Schwartz and Mallett[3] have obtained preliminary values of the decomposition pressures by extrapolation of the absorption measurements of Hall, Martin, and Rees.[4] However, a comparison of these estimated values with the experimental observations of Gulbransen and Andrew[5] at 500°C for a 4.3 atomic pct alloy showed the extrapolated values to differ from the experimental values by a factor of 100 to 1000. It appeared that the present understanding of the behavior of hydrogen in metals was not adequate as a basis for extrapolation.

Theory

The solubility of hydrogen in metals was treated briefly by Fowler and Guggenheim[6] from the point of view of the contribution of the hydrogen atoms in the metal lattice to the grand partition function. Semiquantitative agreement was obtained for the overall solubility at high pressures and high temperatures. Since the crystal structure factor was neglected, no predictions were possible for the composition range of interest here.

Recently a paper has appeared by Rees[7] on the statistical mechanics of two-component interstitial solid solution. These equations have been applied by Martin and Rees[8] to an interpretation of the overall solubility of hydrogen in zirconium.

In this section the general application of thermodynamic principles to the several equilibria will be considered. The object of such a treatment was to express (in terms of fundamental thermodynamic quantities) the normal solubility, decomposition pressure, and the terminal solubilities of hydrogen in the metal phase. These thermodynamic quantities could be determined experimentally or from statistical thermodynamic considerations.

Preliminary: The dissolution of hydrogen in the α and δ-hydride phases of zirconium was given by the equations[9]

$$\tfrac{1}{2}\,H_2(\text{gas}) = H\ (\text{dissolved in } \alpha\text{-Zr}) \qquad [1]$$

and

$$\tfrac{1}{2}\,H_2(\text{gas}) = H\ (\text{dissolved in } \delta\text{-phase}). \qquad [2]$$

The equilibrium condition was given by

$$\tfrac{1}{2}\,F_{H_2(\text{gas})} = \overline{F}_{H(\alpha)} \qquad [3]$$

and

$$\tfrac{1}{2}\,F_{H_2(\text{gas})} = \overline{F}_{H(\delta)}. \qquad [4]$$

Here, $F_{H_2(\text{gas})}$ refers to the free energy of hydrogen in the gas phase and $\overline{F}_{H(\alpha)}$ and $\overline{F}_{H(\delta)}$ refer to the partial molar free energy in the α and δ-phases. Although the hydrogen atoms could be dissociated in the metal in the form of ions and electrons, it was assumed for the authors' purpose that hydrogen existed as atoms in the lattices.

Since the gas phase was ideal for these conditions, the authors set[10]

$$\tfrac{1}{2}\,F_{H_2(\text{gas})} = \tfrac{1}{2}\,F^\circ_{H_2(\text{gas})} + \tfrac{1}{2}\,RT \ln p_{H_2}. \qquad [5]$$

Here, $F^\circ_{H_2(\text{gas})}$ refers to the molar free energy of hydrogen at unit pressure and p_{H_2} was the pressure of hydrogen.

The effect of concentration of hydrogen in the metal or hydride on the partial molar free energy was then considered. To do this, the authors set

$$\overline{F}_H = \overline{F}^\circ_H - T\overline{S}_p. \qquad [6]$$

Here, $\overline{S}_p$ was the partial molar entropy of number and position. $\overline{F}^\circ_H$ was the standard partial molar free energy and was the value of $\overline{F}_H$ when $\overline{S}_p = 0$.

$\overline{H}_H$ was assumed to be invariant with composition for a given phase and the change in $\overline{S}_H$ with composition was due solely to the entropy of number and position.

$\overline{S}_p$ was derived from statistical considerations, provided that the number and location of the hydrogen atom sites were known. For both the α-phase and the two hydride phases, the hydrogen atoms occupy tetrahedral interstices of which there were two for each zirconium atom.[11]

The problem was to express the entropy of number and position of N_H hydrogen atoms arranged in N_s sites. If a random distribution was assumed, the entropy expression was

$$S_p = R \ln \frac{N_s!}{N_H!\,(N_s - N_H)!}. \qquad [7]$$

The corresponding partial molar entropy term was

$$\overline{S}_p = \frac{\partial S_p}{\partial N_H} = -R \ln \frac{N_H}{N_s - N_H}. \qquad [8]$$

Substituting in Eq. 6 gives the expression

$$\overline{F}_H = \overline{F}^\circ_H + RT \ln \frac{N_H}{N_s - N_H}. \qquad [9]$$

If $\overline{F}^\circ_H = \overline{H}^\circ_H - T\overline{S}^\circ_H$ is now substituted, the following is obtained

$$\overline{F}_H = \overline{H}^\circ_H - T\overline{S}^\circ_H + RT \ln \frac{N_H}{N_s - N_H}. \qquad [10]$$

Here, $\overline{H}^\circ_H$ was the standard partial molar heat of formation and $\overline{S}^\circ_H$ was the standard partial molar entropy of formation. This equation corresponded to the more familiar free energy equation if the term $N_H/(N_s - N_H)$ was replaced by the mol fraction or concentration. It follows from Eqs. 6 and 8 through 10 that the standard reference state for hydrogen was defined for each phase separately but would correspond to the state in which half of the tetrahedral interstices were filled, or a Zr/H ratio of unity.

Effect of Temperature and Pressure on Solubility of Hydrogen in α-Zirconium: Eqs. 4, 5, and 10 were combined to express the solubility as a function of pressure and of temperature. Thus

$$\tfrac{1}{2}\,F^\circ_{H_2(\text{gas})} + \tfrac{1}{2}\,RT \ln p_{H_2} = \overline{H}^\circ_H - T\overline{S}^\circ_H + RT \ln \left(\frac{N_H}{N_s - N_H}\right). \qquad [11]$$

Rearranging and applying to the α-phase gives

$$\frac{N_{H(\alpha)}}{N_s - N_{H(\alpha)}} = (p_{H_2})^{1/2} \exp \left[\frac{\tfrac{1}{2}\,F^\circ_{H_2(\text{gas})} - (\overline{H}^\circ_{H(\alpha)} - T\overline{S}^\circ_{H(\alpha)})}{RT}\right]. \qquad [12]$$

Since $\tfrac{1}{2}\,F^\circ_{H_2(\text{gas})} = \tfrac{1}{2}\,H^\circ_{H_2(\text{gas})} - \tfrac{1}{2}\,T\overline{S}^\circ_{H_2(\text{gas})}$ then

$$\frac{N_{H(\alpha)}}{N_s - N_{H(\alpha)}} = (p_{H_2})^{1/2} \exp - \left[\frac{(\overline{H}^\circ_{H(\alpha)} - \tfrac{1}{2}\,H^\circ_{H_2(\text{gas})}) - T(\overline{S}^\circ_{H(\alpha)} - \tfrac{1}{2}\,S^\circ_{H_2(\text{gas})})}{RT}\right]. \qquad [13]$$

This expression included Sieverts' law which states that the solubility of hydrogen was proportional to the square root of the pressure. Since a large amount of entropy was lost on condensing the gas into the metal, the term $(\bar{S}^{\circ}_{H_{(\alpha)}} - \frac{1}{2} S^{\circ}_{H_2(gas)})$ was negative and when multiplied by $-T$ gave a positive contribution in the exponential term. Thus, if the solubility was to decrease with increase of temperature, $(\bar{H}^{\circ}_{H_{(\alpha)}} - \frac{1}{2} H^{\circ}_{H_2(gas)})$ must be negative and larger than $T(\bar{S}^{\circ}_{H_{(\alpha)}} - \frac{1}{2} S^{\circ}_{H_2(gas)})$. If $(\bar{H}^{\circ}_{H_{(\alpha)}} - \frac{1}{2} H^{\circ}_{H_2(gas)})$ was positive, the solubility increased with temperature, since the entropy contribution was positive.

A similar equation was derived for the δ-phase, $ZrH_{1.5}$. However, it was not expected that this equation would hold for the high hydrogen concentrations observed for the δ-phase.

Terminal Solubilities of Hydrogen in α-Zirconium in Equilibrium with the δ-Phase: The condition of equilibrium was

$$\bar{F}_{H_{(\alpha)}} = \bar{F}_{H_{(\delta)}} \qquad [14]$$

Substituting Eq. 10 for each phase

$$\bar{H}^{\circ}_{H_{(\alpha)}} - T\bar{S}^{\circ}_{H_{(\alpha)}} + RT \ln\left(\frac{N_{H_{(\alpha)}}}{N_{\circ} - N_{H_{(\alpha)}}}\right) = \bar{H}^{\circ}_{H_{(\delta)}} - T\bar{S}^{\circ}_{H_{(\delta)}} + RT \ln\left(\frac{N_{H_{(\delta)}}}{N_{\circ} - N_{H_{(\delta)}}}\right). \qquad [15]$$

Rearranging and collecting terms

$$\frac{N_{H_{(\alpha)}}}{N_{\circ} - N_{H_{(\alpha)}}} \Big/ \frac{N_{H_{(\delta)}}}{N_{\circ} - N_{H_{(\delta)}}} = \exp\left[\frac{(\bar{H}^{\circ}_{H_{(\alpha)}} - \bar{H}^{\circ}_{H_{(\delta)}}) - T(\bar{S}^{\circ}_{H_{(\alpha)}} - \bar{S}^{\circ}_{H_{(\delta)}})}{RT}\right]. \qquad [16]$$

Eq. 16 could be used in two ways. First, if the solubilities of hydrogen in the two phases were known, the term

$$\left[(\bar{H}^{\circ}_{H_{(\alpha)}} - \bar{H}^{\circ}_{H_{(\delta)}}) - T(\bar{S}^{\circ}_{H_{(\alpha)}} - \bar{S}^{\circ}_{H_{(\delta)}})\right]$$

could be evaluated. Second, if the partial molar heats and entropies of formation of a hydrogen atom in the α and δ-phases were known, the ratio of the solubilities could be calculated.

The values of $(\bar{H}^{\circ}_{H_{(\alpha)}} - \frac{1}{2} H^{\circ}_{H_2(gas)})$ and $(\bar{H}^{\circ}_{H_{(\delta)}} - \frac{1}{2} H^{\circ}_{H_2(gas)})$ could be determined experimentally from the slope of logarithmic plots of the decomposition

a—Log P vs $1/T$ plot. 1-*A-C*, α + δ phases; 2-*B-C*, α + δ phases; *A-B*, α phase; *B*, solubility limit.

b—Sieverts' law plot. 1-*A-B*, α phase. 2-*A-B*, α phase; *B-C*, α + δ phases; *B*, solubility limit.

Fig. 1—Methods for determination of terminal solubilities in α-zirconium.

Table I. Analyses of Zirconium Samples, Wt Pct

	Foote Zr, Typical
Si	0.01
Fe	0.04
Al	0.01
Cu	<0.01
Ti	0.03
Mn	<0.001
Ca	0.01
Mg	<0.003
Pb	<0.001
Mo	<0.001
Ni	0.01
Cr	0.001
Sn	0.001
W	<0.001
N	<0.01
O	<0.01
H	<0.02
C	<0.001
Hf	2.40

pressures of hydrogen versus $1/T$. The values of $\bar{S}^{\circ}_{H_{(\alpha)}}$ and $\bar{S}^{\circ}_{H_{(\delta)}}$ could be determined from Eq. 13 and from knowing the values of the solubility at a given temperature and the values of $\bar{H}^{\circ}_{H_{(\alpha)}} - \frac{1}{2} H^{\circ}_{H_2(gas)}$ and $\bar{H}^{\circ}_{H_{(\delta)}} - \frac{1}{2} H^{\circ}_{H_2(gas)}$.

Eq. 16 could be used to predict the temperature behavior of the terminal solubility of $N_{H_{(\alpha)}}$. To do this, it was necessary to assume $N_{H_{(\delta)}}$ at the two-phase boundary to be invariant with temperature. This has been shown to be approximately true from previous studies.[4] Eq. 16 suggests that if $\bar{H}^{\circ}_{H_{(\alpha)}} > \bar{H}^{\circ}_{H_{(\delta)}}$ and negative, then the ratio on the left decreases or $N_{H_{(\alpha)}}$ increases with temperature, while if $\bar{H}^{\circ}_{H_{(\alpha)}} > \bar{H}^{\circ}_{H_{(\delta)}}$ and negative then the ratio increases and $N_{H_{(\alpha)}}$ decreases with temperature. These equations show that the terminal solubility $N_{H_{(\alpha)}}$ could show an endothermic behavior while the overall solubility was exothermic in nature.

Decomposition Pressures and the Removal of Hydrogen From the Metal: Eq. 13 was rearranged to give

$$p_{H_2} = \left(\frac{N_{H_{(\alpha)}}}{N_{\circ} - N_{H_{(\alpha)}}}\right)^2 \exp\left[\frac{2(\bar{H}^{\circ}_{H_{(\alpha)}} - \frac{1}{2} H^{\circ}_{H_2(gas)}) - 2T(\bar{S}^{\circ}_{H_{(\alpha)}} - \frac{1}{2} S^{\circ}_{H_2(gas)})}{RT}\right]. \qquad [17]$$

The terms in the exponential expression were evaluated experimentally and thus the equilibrium pressure could be calculated for a given temperature and concentration.

Method

Decomposition Pressures of Hydrogen in α-Zirconium: Eqs. 4 and 5 showed that the partial molar free energy of hydrogen atoms in α-zirconium were related to the decomposition or equilibrium pressures p of hydrogen. In addition, thermodynamics gave the following equation

$$\tfrac{1}{2} \frac{d \ln P}{d\, 1/T} = \frac{\bar{H}^{\circ}_{H_{(\alpha)}} - \frac{1}{2} H^{\circ}_{H_2(gas)}}{R}. \qquad [18]$$

Thus, a series of measurements of the decomposition pressures as a function of temperatures gave both the partial molar free energy and the partial molar heat of formation of the given hydrogen alloy from the gas and metal. Since these quantities differ for the several phases, a study over a broad concentration and temperature range enabled all of the neces-

sary thermodynamic quantities to describe the Zr-H alloy system to be determined.

A static method was chosen to measure the decomposition pressures. The temperature range was selected so that the pressures were in the range of $1x10^{-4}$ to $1x10^{-1}$ mm of Hg. For the volume of the system and the size of the specimens used, appreciable composition changes were observed only for pressures above 10^{-1} mm of Hg.

The hydrogen alloys were in the composition range of $ZrH_{0.02}$ to $ZrH_{1.99}$. They were prepared by direct reaction with hydrogen and the weight increase determined by a sensitive vacuum microbalance. Without removing the specimen from the apparatus, the equilibrium decomposition pressures were measured in the temperature range of 425° to 600°C using a calibrated McLeod gage. To determine equilibrium pressures in the range of $1x10^{-4}$ mm of Hg, it was essential to use an all-glass vacuum system which had been carefully degassed or evacuated for a period of 16 hr or longer. A description of the system has been given.[15, 16]

Solubility: The normal solubility in the α-zirconium phase was determined by direct measurement of the weight gain for a given temperature and pressure. The terminal solubilities of hydrogen in α-zirconium in equilibrium with the δ-hydride phase were evaluated in two ways, as shown in Fig. 1. Fig. 1a shows the log P vs $1/T$ method. Fig. 1a, 1, shows a typical plot for a mixture of α and δ-phases when both phases were present for all temperatures. Fig. 1a, 2, shows a typical plot when the two-phase region BC goes over into a single-phase region AB. The temperature at which the two phases were in equilibrium was that given by the point B. The slopes of the two parts of the plot gave the values of

$$(\overline{H}^{\circ}_{H_2(g)} - \tfrac{1}{2} H^{\circ}_{H_2(g)}) \text{ and } (\overline{H}^{\circ}_{H(\delta)} - \tfrac{1}{2} H^{\circ}_{H_2(g)}).$$

The intersection of CB with BA gave the temperature at which the given hydrogen alloy composition represented the terminal solubility.

The second method shown in Fig. 1b was based on Sieverts' law. Here, the decomposition pressures at a given temperature were plotted as a function of the square of the concentration. A straight-line relationship was found which confirms Sieverts' law. Fig. 1b, 1, shows a typical plot for compositions within the α-zirconium solid solution phase. Fig. 1b, 2, shows a similar plot for the case where the solubility limit was reached at point B. The line B-C indicated that the decomposition pressure was constant over the two-phase region. The intercept of AB and BC gave the terminal solubility.

Experimental

A vacuum microbalance and associated apparatus was used for the preparation of all of the specimens. The construction, sensitivity, and use of this type of microbalance has been described.[15, 16]

The specimens were small strips of 5 mil thick, high purity zirconium containing 2.40 pct Hf. Table I shows spectrographic and chemical analyses of the zirconium. The preparation of the specimens has been described.[7] High purity hydrogen was prepared by diffusion of purified hydrogen through palladium.

A calibrated McLeod gage of high sensitivity was used to measure the decomposition pressures. To assure that the equilibrium pressures were actually determined, measurements were made on both the decomposition (heating cycle) and absorption (cooling) cycle.

Results

Decomposition Pressures: Figs. 2, 3, and 4 show typical log pressure vs $1/T$ graphs obtained for the compositions $ZrH_{0.075}$, $ZrH_{1.99}$, and $ZrH_{1.665}$. Table II summarized the experimental data for 11 compositions, 8 of which were in the range of $ZrH_{0.02}$ to $ZrH_{1.99}$. The data for the composition $ZrH_{0.075}$, $ZrH_{0.99}$, and $ZrH_{1.99}$ were typical for the two-phase region. The compositions were given in units of H/Zr and also in parts per million by weight, while the decomposition pressures were given in mm of Hg. The data were tabulated over the temperature range of 425° to 600°C.

For a composition $ZrH_{0.075}$, Fig. 2 showed the α-zirconium phase to be the stable phase over the temperature range studied. An analysis of the slope of the plot (see Eq. 18) gave a value of −28,900 cal per mol for the standard partial molar heat of formation of hydrogen in the metal.

For a composition $ZrH_{1.99}$, Fig. 3 showed the α-zirconium phase to be the stable phase over the section AB of the graph, while a mixture of the α-zirconium phase and the δ-hydride phase were stable over the section BC. Point B gave the temperature at which the composition $ZrH_{1.99}$ represented the terminal solubility. The slope of AB gave a standard partial molar heat of formation of −28,700 cal per mol for the α-zirconium phase while the slope of BC gave a value for the standard partial molar heat of formation of −45,800 cal per mol for the δ-phase. This calculation assumes that the composition of the δ-phase was invariant with temperature. The validity of this assumption was supported by X-ray diffraction and decomposition pressure studies on the Zr-H phase diagram.[8]

Table II. Decomposition Pressures of Zr-H Alloys

Composition		P, Mm of Hg at Temperature, °C							
H/Zr	Ppm	425	450	475	500	525	550	575	600
0.015	165	—	3.2×10^{-4}	6.5×10^{-4}	1.3×10^{-3}	2.1×10^{-3}	3.8×10^{-3}	6.4×10^{-3}	1.06×10^{-2}
0.020	220	3.0×10^{-4}	7.0×10^{-4}	1.33×10^{-3}	2.4×10^{-3}	4.2×10^{-3}	6.0×10^{-3}	—	—
0.025	274	4.0×10^{-4}	1.0×10^{-3}	1.85×10^{-3}	3.35×10^{-3}	5.8×10^{-3}	9.5×10^{-3}	—	—
0.029	318	4.0×10^{-4}	1.3×10^{-3}	3.0×10^{-3}	5.4×10^{-3}	9.3×10^{-3}	—	—	—
0.034	372	5.0×10^{-4}	1.6×10^{-3}	3.8×10^{-3}	7.6×10^{-3}	1.4×10^{-2}	—	—	—
0.048	525	5.4×10^{-4}	1.65×10^{-3}	5.0×10^{-3}	1.3×10^{-2}	—	—	—	—
0.068	745	4.0×10^{-4}	1.3×10^{-3}	4.2×10^{-3}	1.2×10^{-2}	3.2×10^{-2}	7.8×10^{-2}*	1.0×10^{-1}*	1.6×10^{-1}*
0.079	866	4.0×10^{-4}	1.4×10^{-3}	4.3×10^{-3}	1.3×10^{-2}	3.6×10^{-2}	7.2×10^{-2}*	1.25×10^{-1}*	1.9×10^{-1}*
0.103	1130	6.0×10^{-4}	1.7×10^{-3}	5.2×10^{-3}	1.25×10^{-2}	—	—	—	—
0.54	5920	5.4×10^{-4}	1.7×10^{-3}	5.0×10^{-3}	1.35×10^{-2}	—	—	—	—
0.99	10850	6.3×10^{-4}	1.8×10^{-3}	5.4×10^{-3}	1.4×10^{-2}	3.4×10^{-2}	7.8×10^{-2}*	—	—

* Composition changes occur

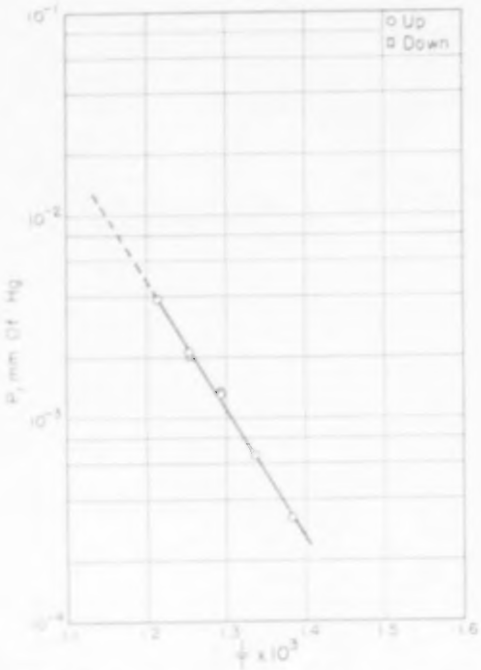

Fig. 2—Decomposition pressure vs $1/T$. $ZrH_{2.000}$, α-zirconium; $\Delta H = -28{,}900$ cal per mol.

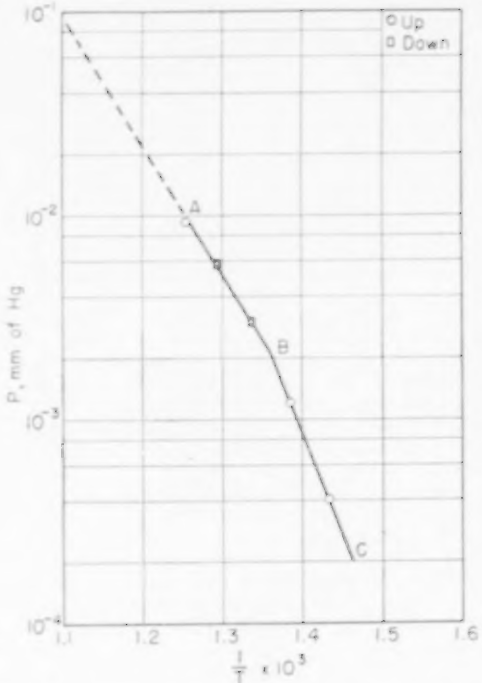

Fig. 3—Decomposition pressure vs $1/T$. $ZrH_{1.750}$; *A-B*, α-zirconium; $\Delta H = -28{,}700$ cal per mol. *B-C*, $\alpha + \delta$ phases; $\Delta H = -45{,}800$ cal per mol.

Fig. 4 showed a log P vs $1/T$ graph for the composition $ZrH_{1.750}$. It was of similar shape to that described in Fig. 3. Because the composition changed above a pressure of 10^{-1} mm of Hg, the AB portion of the curve cannot be used directly for calculation of the $(2\bar{H}^{\circ}_{H(\alpha)} - H^{\circ}_{H_2(gas)})$ value.

An average value of $-28{,}500$ cal per mol was calculated for $(2\bar{H}^{\circ}_{H(\alpha)} - H^{\circ}_{H_2(gas)})$ for the α-phase, while an average value of $-45{,}750$ cal per mol was calculated for $(2\bar{H}^{\circ}_{H(\delta)} - H^{\circ}_{H_2(gas)})$ for the δ-phase.

Terminal Solubilities—Log P vs 1/T Method: Fig. 5 showed a plot of the decomposition pressure data for the determination of the terminal solubilities. The line AB on the figure represented the average data for the $ZrH_{2.000}$ (7.32 atomic pct) and the $ZrH_{1.750}$ (6.37 atomic pct) compositions in the two-phase region. These curves differ slightly from the log P vs $1/T$ plots of the two-phase region for compositions $ZrH_{1.9}$ and $ZrH_{1.8}$. The intersection of the decomposition pressure curve for the α-zirconium phase with the line AB gave the temperature at which the given composition represented the terminal solubility. These values were tabulated in Table III.

Terminal Solubilities—Sieverts' Law Plots: Figs. 6 and 7 showed plots of the decomposition pressure as a function of the square of the concentration of hydrogen for 450° and 500°C. The terminal solubilities determined from these plots were tabulated also in Table III.

Fig. 8 showed the terminal solubilities plotted on a logarithm scale vs $1/T$. The data of Schwartz and Mallett[5] were also included. At 500°C the terminal solubility in the α-zirconium phase was $ZrH_{2.000}$, while the value in the δ-phase is $ZrH_{1.750}$. These correspond to 4.32 and 58.33 atomic pct, respectively.

Table III. Terminal Solubilities of Hydrogen in α-Zirconium

Temperature, °C	Method	Atomic Pct	Terminal Solubilities H/Zr x 100	Ppm
450	Sieverts' law plot	2.86	2.94	322
475	Sieverts' law plot	3.48	3.61	396
500	Sieverts' law plot	4.32	4.32	496
525	Sieverts' law plot	5.23	5.34	607
550	Sieverts' law plot	6.1	6.5	715
378	Log P vs 1/T	1.48	1.50	165
410	Log P vs 1/T	1.96	2.00	220
450	Log P vs 1/T	2.82	2.90	318
471	Log P vs 1/T	3.3	3.40	372

Calculations and Discussion

Standard Partial Molar Heats of Formation: For the slopes of the log P vs $1/T$ plots, the authors have calculated the following quantities

$$(\bar{H}^{\circ}_{H(\alpha)} - \tfrac{1}{2} H^{\circ}_{H_2(gas)}) = -\tfrac{1}{2}(28{,}500) = -14{,}250 \text{ cal per gram-atom} \quad [19]$$

and

$$(\bar{H}^{\circ}_{H(\delta)} - \tfrac{1}{2} H^{\circ}_{H_2(gas)}) = -\tfrac{1}{2}(45{,}750) = -22{,}875 \text{ cal per gram-atom.} \quad [20]$$

The value of $\bar{H}^{\circ}_{H(\alpha)} - \tfrac{1}{2} H^{\circ}_{H_2(gas)}$ could be independently evaluated by the use of Eq. 13. Thus, if $\left(\frac{N_{H(\alpha)}}{2 - N_{H(\alpha)}}\right)$ was plotted against $1/T$ for a given pressure, the slope of the plot was the standard partial molar heat of solution of hydrogen. Fig. 9 showed the plot and gave a value of $-13{,}800$ cal per gram-

atom of hydrogen. Considering the errors involved, the two values were in reasonable agreement. It was noted that, under constant pressure conditions, the solubility decreases with increase of temperature. In this sense, zirconium was an exothermic occluder.

The difference in

$$\overline{H}^{\circ}_{H(\alpha)} - \overline{H}^{\circ}_{H(\delta)} = 8{,}625 \text{ cal per gram-atom.} \quad [21]$$

The errors in these calculations were of the order of ±300 cal per gram-atom.

Standard Partial Molar Entropies of Formation: Eq. 13 was used to calculate the standard partial molar entropy of solution of the particular hydrogen alloy. For 500°C, $N_{H(\alpha)} = 0.0452$, p = 1.71×10^{-5} atm, $\overline{H}^{\circ}_{H(\alpha)} - \frac{1}{2} H^{\circ}_{H_2(gas)} = -14{,}250$ cal per gram-atom and $N_s = 2$.

Substituting and solving, the authors had

$$2\overline{S}^{\circ}_{H(\alpha)} - S^{\circ}_{H_2(gas)} = -30 \text{ cal per mol per °C (E.U.).}$$

Since $S^{\circ}_{H_2(gas)} = 37.8$ at 500°C[6]

$$\overline{S}^{\circ}_{H(\alpha)} = 3.9 \text{ E.U. per gram-atom.} \quad [22]$$

In a similar manner, a value of 1.83 E.U. per gram-atom was calculated for the δ-phase. The difference in the standard partial atomic entropies of hydrogen in the α-zirconium and δ-hydride phase was

$$\overline{S}^{\circ}_{H(\alpha)} - \overline{S}^{\circ}_{H(\delta)} = 3.9 - 1.85 = 2.05 \text{ E.U. per gram-atom.} \quad [23]$$

Standard Partial Molar Free Energies of Solution: This quantity was calculated for each phase by the use of the equation

$$\overline{F}^{\circ}_{H(\alpha)} - \tfrac{1}{2} F^{\circ}_{H_2(gas)} = (\overline{H}^{\circ}_{H(\alpha)} - \tfrac{1}{2} H^{\circ}_{H_2(gas)}) - T(\overline{S}^{\circ}_{H(\alpha)} - \tfrac{1}{2} S^{\circ}_{H_2(gas)}). \quad [24]$$

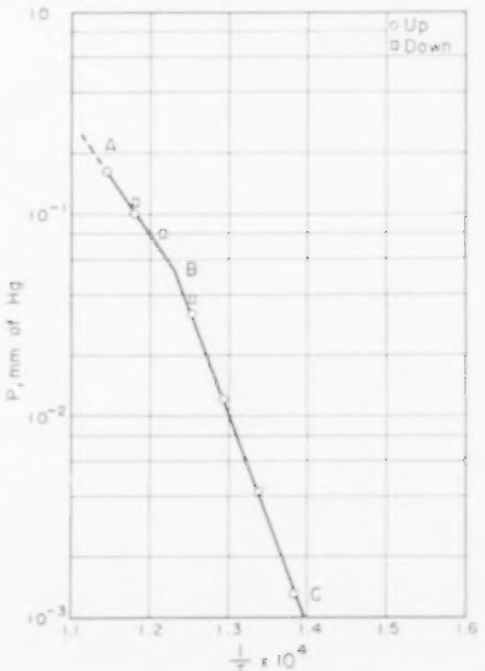

Fig. 4—Decomposition pressure vs $1/T$. $ZrH_{1.96}$. A-B, α-zirconium; B-C, α + δ phases; ΔH = −47,100 cal per mol.

At 500°C for the α-zirconium, the authors obtained

$$\overline{F}^{\circ}_{H(\alpha)} - \tfrac{1}{2} F^{\circ}_{H_2(gas)} = -2{,}605 \text{ cal per gram-atom} \quad [25]$$

and for the δ-hydride phase

$$\overline{F}^{\circ}_{H(\delta)} - \tfrac{1}{2} F^{\circ}_{H_2(gas)} = -9{,}734 \text{ cal per gram-atom.} \quad [26]$$

Partial Molar Free Energies of Solution: To calculate the partial molar free energy, the following equation was used

$$\overline{F}_H = \overline{F}^{\circ}_H + RT \ln \left(\frac{N_H}{2 - N_H} \right) \quad [27]$$

Using the value of $N_{H(\alpha)}$ of 1.4 and a temperature of 500°C, a value obtained was

$$\overline{F}_{H(\alpha)} \text{ at } 500^{\circ}\text{C} = -8{,}428 \text{ cal per gram-atom.} \quad [28]$$

This value was compared to the results given in a previous paper[6] for the free energy of formation of the δ-phase in contact with α-zirconium. A value of −12,560 was tabulated, or for one hydrogen atom a value of −8,433 cal. This result was in agreement with the result shown in Eq. 28.

The partial molar free energy of hydrogen in the α-zirconium phase in equilibrium with the δ-phase was calculated also. Using the result of Eqs. 25 and 27, for a terminal solubility, $N_{H(\alpha)}$ of 0.0452, and at 500°C, the value of $\overline{F}_{H(\alpha)} = -8{,}390$ cal per atom was

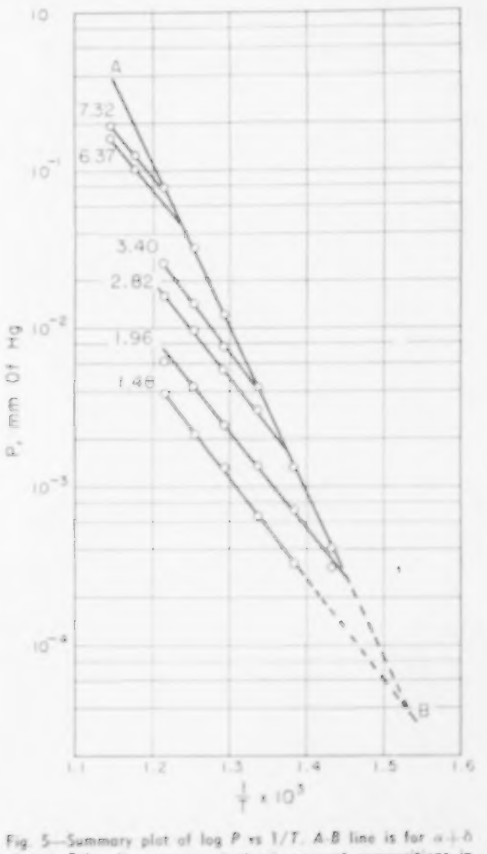

Fig. 5—Summary plot of log P vs $1/T$. A-B line is for α + δ phases. Other lines represent atomic percent compositions in α phase.

obtained. This value was in agreement with the value for the δ-phase.

Difference in Partial Molar Free Energies at 500°C: For solubility calculations, the difference in the standard partial molar free energies for the α-zirconium and δ-hydride phases was important. Thus, from Eqs. 25 and 26

$$\bar{F}^{\circ}_{H_2\alpha} - \bar{F}^{\circ}_{H_2\delta} = 7{,}129 \text{ cal per gram-atom.} \quad [29]$$

This quantity could be calculated in a somewhat independent manner from the theory and data. Thus, Eq. 16 expressed the ratio of the solubility of hydrogen in the α-zirconium and δ-phases in terms of this free energy function. If $N_{H\alpha} = 0.0452$ and $N_{H\delta} = 1.4$ are substituted, the following value at 500°C is obtained

$$\bar{F}^{\circ}_{H_2\alpha} - \bar{F}^{\circ}_{H_2\delta} = 7{,}092 \text{ cal per gram-atom.} \quad [30]$$

The agreement was good. The errors in the calculation were of the order of ±200 cal.

Temperature Dependence of the Entropy Term: The entropy of hydrogen atoms in the α-zirconium and δ-hydride phases was assumed to be vibrational. The relation between the frequency of vibration ν, the temperature T, and the entropy S, was given by the equation[9]

$$S = R\left[(h\nu/kT)\,(e^{h\nu/kT})^{-1} - \ln\left(1 - e^{-h\nu/kT}\right)\right]. \quad [31]$$

Here, h was Planck's constant and k was Boltzman's constant.

In the δ-phase, the hydrogen atom sites were in a symmetrical fluorite arrangement with an H-H spacing of 2.39A. The $\bar{S}^{\circ}_{H_2\delta}$ of this phase could be considered as divided among the three modes of vibration or 1.9/3 = 0.63 E.U. per gram-atom per mode of vibration. Calculations using Eq. 31 gave a value of ν of 3.98×10^{13} vibrations per sec. This frequency was in agreement with some independent calculations by Zener[10] on hydrogen in metals.

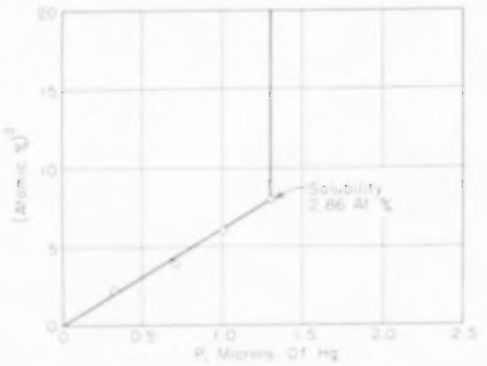

Fig. 6—Sieverts' law plot at 450°C.

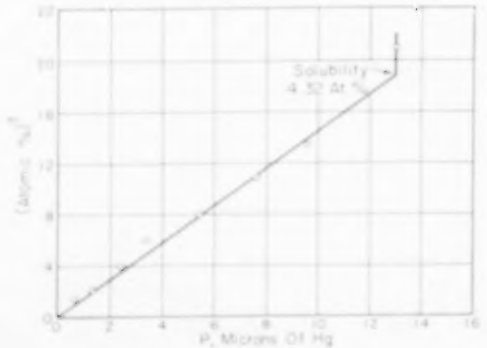

Fig. 7—Sieverts' law plot at 500°C.

Table IV. Comparison of α-Zirconium and δ-Hydride Phase

	α-Zirconium	δ-Hydride
Structure	Hexagonal-close-packed	Face-centered-cubic (fluorite)
Location of hydrogen	Tetrahedral interstices	Tetrahedral interstices
a parameter, A	3.228	4.78
c parameter, A	5.140	4.78
Zr-Zr distance, A	3.228	3.38
Zr-H distance, A	1.928	2.069
H-H distance, A (minimum)	1.285	2.39

The hydrogen atoms occupying the tetrahedral interstices in α-zirconium had a different arrangement than the symmetrical arrangement in the δ-phase. Table IV summarized the structural elements and the interatomic distances. The tetrahedral interstices in α-zirconium occurred in pairs with a spacing of 1.29A in the c direction. For low concentrations of hydrogen, only one of these sites of a given pair could be occupied. In analyzing the modes of vibration of hydrogen atoms in this structure, it was necessary to assume two nearly normal modes of vibration similar to those found for the δ-hydride phase and one exceptional mode of vibration in which the hydrogen atom essentially oscillated between the two adjacent sites. The shape of the potential curves would suggest a much lower frequency of vibration for this mode.

The authors have estimated the entropy associated with this vibration as follows: The value of $\bar{S}^{\circ}_{H_2\alpha}$ was 3.9 E.U. per gram-atom. The entropy of two normal vibrations was subtracted and the following was had at 500°C

$$S_{vib} = 3.9 - 1.3 = 2.6 \text{ E.U. per gram-atom.} \quad [32]$$

This corresponds to a vibration frequency of 1.21×10^{13}.

Then the values of the normal entropy of one vibration S_{vib} and the value of the exceptional entropy of one vibration S_{vib} were calculated as a function of temperature based on Eq. 31.

Table V summarized the results.

Since the authors had evaluated both $\bar{H}^{\circ}_{H_2\alpha} - \bar{H}^{\circ}_{H_2\delta}$ and $T\,(\bar{S}^{\circ}_{H_2\alpha} - \bar{S}^{\circ}_{H_2\delta})$, they calculated $\bar{F}^{\circ}_{H_2\alpha} - \bar{F}^{\circ}_{H_2\delta}$ over a series of temperatures.

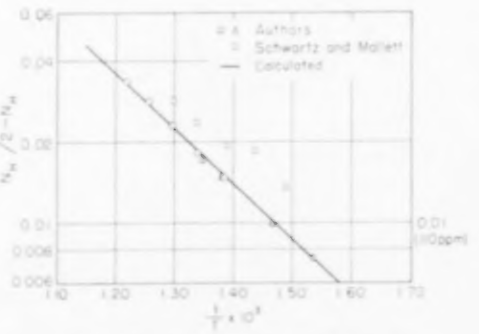

Fig. 8—Terminal solubility of H in α-zirconium.

Calculation of Terminal Solubilities as a Function of Temperature: Since the solubility $N_{H(\alpha)}$ was approximately independent of temperature[5] between 25° and 500°C, the authors simplified Eq. 16 to give

$$N_{H(\alpha)} = \frac{4.68}{\exp\left[\frac{(\bar{F}^{\circ}_{H(\alpha)} - \bar{F}^{\circ}_{H(\alpha)})}{RT}\right] + 2.24} \quad [33]$$

Table V showed the results of the calculations for $N_{H(\alpha)}$ using Eq. 33, while Fig. 8 showed the agreement of the calculated values with experiment. The agreement was good. Eq. 33 could be used to estimate the solubility at low temperatures. However, due to the low values for the terminal solubilities, it was impossible to check the predictions.

Temperature Dependence of Decomposition Pressure: Eq. 13 could be rearranged to calculate the decomposition pressure at any temperature and concentration in the α-phase. Thus

$$p_{H_2} = \left(\frac{N_{H(\alpha)}}{N_s - N_{H(\alpha)}}\right)^2 \exp 2 \left[\frac{(\bar{H}^{\circ}_{H(\alpha)} - \tfrac{1}{2} H^{\circ}_{H_2(gas)}) - T(\bar{S}^{\circ}_{H(\alpha)} - \tfrac{1}{2} S^{\circ}_{H_2(gas)})}{RT}\right]. \quad [34]$$

To use this equation, the authors substituted the value of $(\bar{H}^{\circ}_{H(\alpha)} - \tfrac{1}{2} H^{\circ}_{H_2(gas)}) = -14{,}250$ cal per gram-atom for the α-zirconium phase. To determine $(\bar{S}^{\circ}_{H(\alpha)} - \tfrac{1}{2} S^{\circ}_{H_2(gas)})$, the values of the normal and exceptional vibration entropy terms were calculated to give $\bar{S}^{\circ}_{H(\alpha)}$ while the term $S^{\circ}_{H_2(gas)}$ was obtained from tables.[10] Table VI summarized the calculations on the thermodynamic functions of hydrogen in the α-zirconium phase based on the assumed model. Using Eq. 34 and the values for $(\bar{F}^{\circ}_{H(\alpha)} - \tfrac{1}{2} F^{\circ}_{H_2(gas)})$, the decomposition pressure of any given alloy within the α-zirconium phase could be calculated to an accuracy of ±20 pct. However, no check on the equation at low temperatures could be given and, therefore, the authors could not set a limit to its application. Since the equation was based on a reasonable model, the calculated values at low temperature were perhaps nearer the true values than the results of empirical extrapolation.

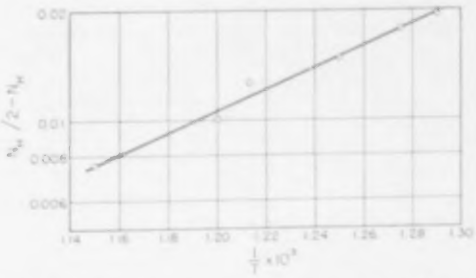

Fig. 9—Solubility of H in α-zirconium vs 1/T. $P = 0.01$ mm of Hg, slope $= (H^{\circ}_{H(\alpha)} - \tfrac{1}{2} H^{\circ}_{H_2(gas)}) = -13{,}800$ cal per mol.

Then the practical problem of removing hydrogen to reach a given concentration for temperatures of 500° to 700°C was calculated. Table VII showed the results. The results indicated a vacuum of 1.2×10^{-7} mm of Hg was necessary at 700°C to remove hydrogen down to a concentration of one part per million by weight. This value was approximately 20 times the equilibrium pressures given by Schwartz and Mallett.[3]

Summary

1—A thermodynamic analysis was made of the behavior of hydrogen in exothermic occluders. Equations were derived for the solubility, terminal solubility, and decomposition pressures as a function of temperature.

2—The decomposition pressure method was used to determine the solubility and terminal solubility experimentally. The decomposition pressure data were presented in the form of tables and graphs.

3—The several thermodynamic quantities were evaluated from the data at 500°C. A value of −14,250 cal per gram-atom was found for the stand-

Table V. Summary of Calculations of Terminal Solubilities of Hydrogen in α-Zirconium Phase

Temperature, °C	Normal S_{vib}/R	S_{vib} E.U.	Exceptional S_{ex}/R	S_{ex} E.U.	$S_{vib} - S_{ex}$ E.U.	$T\Delta S$ Cal per Gram-Atom	$\bar{H}^{\circ}_{H(\alpha)} - \bar{H}^{\circ}_{H(\alpha)}$ Cal per Gram-Atom	$\bar{F}^{\circ}_{H(\alpha)} - \bar{F}^{\circ}_{H(\alpha)}$ Cal per Gram-Atom	N_H or H/Zr	$\frac{N_H}{2 - N_H}$
700	1.96	0.94	0.60	3.04	2.10	2049		6570	0.1453	0.0783
600	2.19	0.79	0.67	2.83	2.04	1786		6830	0.0873	0.0456
500	2.47	0.63	0.75	2.60	1.97	1524	8616	7092	0.0446	0.0228
400	2.84	0.47	0.86	2.34	1.87	1250		7360	0.0159	0.0095
300	3.33	0.32	1.01	2.04	1.72	988		7628	0.005574	0.002879
200	4.04	0.18	1.23	1.70	1.52	719		7897	0.00105	5.26×10^{-4}
100	5.12	0.072	1.56	1.30	1.22	456		8160	6.87×10^{-5}	3.43×10^{-5}
0	7.00	0.031	2.13	0.82	0.79	216		8400	8.68×10^{-6}	4.34×10^{-6}

Table VI. Thermodynamic Functions α-Zirconium Phase

Temperature, °C	S_{vib}/R E.U.	$T S_{vib}/R$ E.U.	S_{ex}/R E.U.	$\bar{S}^{\circ}_{H(\alpha)}$ E.U.	$\frac{1}{2}S^{\circ}_{H_2(gas)}$ E.U.	$\frac{\bar{S}^{\circ}_{H(\alpha)} - \frac{1}{2}S^{\circ}_{H_2}}{2}$ E.U.	$T\frac{(\bar{S}^{\circ}_{H(\alpha)} - \frac{1}{2}S^{\circ}_{H_2})}{2}$ Cal per Gram-Atom	$\frac{\bar{H}^{\circ}_{H(\alpha)} - \frac{1}{2}H^{\circ}_{H_2}}{2}$ Cal per Gram-Atom	$\frac{\bar{F}^{\circ}_{H(\alpha)} - \frac{1}{2}F^{\circ}_{H_2}}{2}$ Cal per Gram-Atom
700	0.94	1.88	3.04	4.92	19.3	−14.9	14,497	−14,250	+247
600	0.79	1.58	2.83	4.41	19.4	−15.0	13,995		−1135
500	0.63	1.26	2.60	3.86	18.9	−15.0	11,600		−2650
400	0.47	0.94	2.34	3.28	18.5	−15.2	10,230		−4020
300	0.32	0.64	2.04	2.68	17.9	−15.2	8,710		−5540
200	0.18	0.36	1.70	2.06	17.2	−15.1	7,142		−7108
100	0.072	0.146	1.30	1.45	16.4	−14.9	5,558		−8692
0	0.031	0.062	0.82	0.882	15.4	−14.5	3,959		−10291

Table VII. Equilibrium Pressures at Two Concentrations for Several Temperatures

Temperature, °C	Equilibrium Pressure (Mm of Hg)	
	100 Ppm	1 Ppm
500	5.1×10^{-4}	5.1×10^{-6}
600	4.2×10^{-3}	4.2×10^{-5}
700	1.2×10^{-2}	1.2×10^{-4}

ard partial molar heat of solution of hydrogen for the α-zirconium phase, while a value of −22,875 cal per gram-atom was found for the δ-hydride phase. A value of −15.0 E.U. per gram-atom was found for the standard partial molar entropy of solution of hydrogen in the α-zirconium phase, while a value of −17.0 E.U. per gram-atom was found for the δ-hydride phase. The standard partial molar free energy of hydrogen atoms in the α-phase was −2,605 cal per gram-atom and in the δ-phase was −9,734 cal per gram-atom.

4—To obtain the temperature dependence of these thermodynamic quantities, a statistical thermodynamic analysis was made of the vibration modes of the hydrogen atoms in the two structures as a function of temperature. The thermodynamic quantities involved in the expressions for the solubility, terminal solubilities, and decomposition pressures were calculated for the temperature range of 0° to 700°C. Good agreement was found with the experimental results.

5—The standard partial molar free energies of solution of hydrogen in the α and δ-phases were used to explain the exothermic nature of the overall solubilities and the endothermic nature of the terminal solubilities.

6—The practical problem of removal of hydrogen from the metal at high temperatures and at high vacuum was discussed, using the decomposition pressure equation.

Acknowledgment

The authors are indebted to Dr. C. Zener and other members of the Laboratories for their helpful suggestions and criticisms of this work.

References

[1] W. L. Mudge, Jr.: *Zirconium and Zirconium Alloys.* (1953) p. 730. Cleveland. ASM.

[2] C. M. Schwartz and M. W. Mallett: *Trans.* ASM (1954) **46**, pp. 640-654.

[3] M. N. A. Hall, S. L. H. Martin, and A. L. G. Rees: *Trans.* Faraday Society (1945) **41**, p. 306.

[4] E. A. Gulbransen: Review article to be published. *Zirconium and Zirconium Alloys.* Sponsored by United States Atomic Energy Commission.

[5] D. P. Smith: *Hydrogen in Metals.* (1948) Chicago. The University of Chicago Press.

[6] E. A. Gulbransen and K. F. Andrew: *Journal* Electrochemical Society (1954) **101**, p. 474.

[7] G. Hägg: *Ztsch. für Physikalische Chemie* (1930) **11**, p. 439.

[8] R. W. Fowler and E. A. Guggenheim: *Statistical Thermodynamics.* (1952) Cambridge, England. University Press.

[9] A. L. G. Rees: *Trans.* Faraday Society (1954) **50**, p. 335.

[10] S. L. H. Martin and A. L. G. Rees: *Trans.* Faraday Society (1954) **50**, p. 343.

[11] C. Wagner: *Thermodynamics of Alloys.* (1952) Cambridge. Addison-Wesley Press.

[12] E. A. Gulbransen: *Trans.* Electrochemical Society (1942) **81**, p. 187.

[13] E. A. Gulbransen: *Advances in Catalysis.* (1953) **5**, p. 133. New York. Academic Press.

[14] E. A. Gulbransen: *Review of Scientific Instruments* (1944) **15**, p. 201.

[15] *Selected Values of Chemical Thermodynamic Properties.* National Bureau of Standards (March 31, 1947) Series III.

[16] J. R. Partington: *An Advanced Treatise on Physical Chemistry.* (1949) **1**, p. 325. New York. Longmans, Green and Co. Inc.

[17] C. Zener: Private communication.

Technical Note

X-Ray Crystallographic Data on As_2Te_3

by Joseph Singer and Chester W. Spencer

A PARTIAL phase diagram for the As-Te system is given in Hansen.[1] The only compound reported is As_2Te_3, melting at 362°C. Stoichiometric quantities of reagent-grade elements were reacted in evacuated quartz and directionally cooled. The resulting ingot consisted of very thin threadlike crystals from which only very small single-crystal fragments were isolated. A powder diffraction diagram disclosed nonisomorphism with the analogous V-VI compounds insofar as these have been reported: Sb_2S_3, As_2S_3, Bi_2S_3, and Bi_2Te_3 data in the ASTM index of powder patterns, together with the single-crystal data on Sb_2Se_3[2] were used for the comparison with the observed spacings. Single-crystal data confirmed the uniqueness of the As_2Te_3 structure.

Single-crystal Weissenberg diagrams have so far yielded the following data: As_2Te_3 is monoclinic, space group C-m ($0k0$ data still lacking), $a = 14.4$A, $b = 4.05$A, $C = 9.92$A, $\beta = 97°$. The cell volume is about 580A³. The set of isomorphous orthorhombic cells of Sb_2Se_3, Sb_2S_3, and Bi_2S_3 are apparently related to As_2Te_3 in having one lattice constant close to 4.0 and with cell volumes as large as 540A³. Assuming $Z = 4$ for As_2Te_3 also, the density is calculated as 6.1 which agrees well with a roughly determined value of 6.0.

A complete structure analysis is under way.

J. SINGER and C. W. SPENCER, Junior Member AIME, formerly associated with Sylvania Electric Products, Inc., Bayside, N. Y., are associated with Bridgeport Brass Co., Bridgeport, Conn., and Carnegie Institute of Technology, Pittsburgh, respectively.

TN 236E. Manuscript, Aug. 20, 1954.

[1] M. Hansen: *Der Aufbau der Zweistofflegierungen.* (1936) Berlin. Julius Springer.

[2] R. W. G. Wyckoff: *Crystal Structures.* New York. Interscience Publishers Inc.

Metallographic Study of Equilibrium Relationships In 3S Aluminum Alloy

by Philip R. Sperry

Aluminum alloy 3S was examined to determine the relationship between the applicable phase diagram and the microstructures produced under conditions tending toward non-equilibrium as well as equilibrium. The only phases present in the alloy were aluminum, (Mn,Fe)Al_6, αAl_{12}(Mn,Fe)$_3Si_2$, and silicon. It was found that the alloy behaved essentially as though it belonged to the Al-Mn-Si system. The effects of various solidification rates and of various homogenization treatments were studied. Particular attention was given to a nonuniform precipitate distribution which reflected the solute distribution in the cast aluminum solid solution. Some possible explanations for the solute distribution based on characteristics of the Al-Mn-Si or Al-Mn systems were discussed.

ALUMINUM alloy 3S (aluminum plus 1.25 pct Mn) is one of the oldest and the most widely used of the wrought aluminum alloys. In spite of this fact, there are some aspects of the metallography of 3S which have not been revealed or which have not been brought to the attention of the metallurgist working with the alloy. The purpose of this investigation was to demonstrate in general how some of the fundamentals of equilibrium phase diagrams may be applied to the study of an alloy and to show specifically the origin of certain metallographic features of aluminum alloy 3S. It is hoped that this information can serve as a basis for solving specific problems relating microstructure to such things as mechanical properties, recrystallization, grain growth, and surface finish.

Literature Survey

Considering that alloy 3S contains only one alloying addition, manganese, it seems reasonable that it would have characteristics pertaining to the Al-Mn system. However, those characteristics might well be altered by the impurities in the commercial alloy, especially iron and silicon. Therefore, not only the simple binary but also more complex systems had to be reviewed.

One characteristic of the Al-Mn system worthy of mention is its sluggishness, which leads to conflicting solubility data[1-3] and makes it relatively easy to supersaturate the solid solution and shift the eutectic composition during rapid solidification.[3,4] Another characteristic is the strong influence which small amounts of impurities, especially iron, exert in lowering the solid solubility of manganese.[2,3,5] Undissolved manganese is ordinarily present in an intermetallic phase, $MnAl_6$, having an orthorhombic crystal structure.[6,7,8] A metastable precipitating phase designated as "G" has been reported but small amounts of iron and silicon suppress this phase entirely.[9]

Raynor has established that $MnAl_6$ can dissolve a considerable amount of iron by a substitution of iron for manganese atoms up to 50 atomic pct.[10] Consequently, in the Al-Mn-Fe liquidus diagram, the eutectic valley separating the primary aluminum and (Mn,Fe)Al_6 fields is fairly close to a constant Mn + Fe content.[11] This is an important consideration in regulating the composition of 3S and also other aluminum alloys with high manganese additions.[12]

P. R. SPERRY is Research Metallurgist, Dept. of Metallurgical Research, Kaiser Aluminum and Chemical Corp., Spokane.

Discussion on this paper, TP 3886E, may be sent, 2 copies, to AIME by Mar. 1, 1955. Manuscript, Apr. 9, 1954. Pacific Northwest Metals and Minerals Conference, May 1954. Chicago Meeting, November 1954.

The constitution of the Al-Mn-Fe-Si system under nonequilibrium conditions has been worked out by Phillips and Varley.[9] In the present investigation, it was confirmed that this system is applicable for aluminum alloy 3S. A phase, αAl(Mn,Fe)Si, is found which is part of a series of solid solutions running from the ternary phases, αAlMnSi to αAlFeSi.[10-14] This phase has a cubic crystal structure. It will be shown further on that, for illustrative purposes, the Al-Mn-Si system diagrams can be used, thereby simplifying the graphic presentation.

An excellent reference for diagrams and typical microstructures from some of the applicable ternary systems is Hanemann and Schrader's *Atlas Metallographicus*.[15]

Experimental Procedure

The material used for the experiments described herein was obtained from 3S sheet ingot selected at random from Kaiser Aluminum and Chemical Corp. Trentwood Rolling Mill. The analysis was as follows: 1.08 pct Mn, 0.60 pct Fe, 0.23 pct Si, 0.16 pct Cu, 0.04 pct Mg, and 0.02 pct Ti.

Although this was the only composition which was used for formal experimentation, the observations made here were found to be applicable to other lots of 3S examined in the author's laboratory.

Melts weighing about 100 g were made in alumina-lined crucibles. Stirring and skimming were done with pure graphite rods. Lime-coated chromel-alumel thermocouples were inserted into each melt and the cooling rate was recorded with a Foxboro recording potentiometer. Various solidification rates were obtained by cooling in the furnace and in still air and by pouring into molds. Each sample was quenched when it had cooled to 454°C (850°F). The average cooling rates from 675° (1250°) to 620°C (1150°F), bracketing the solidification range of 3S, were as follows for various melts: melt *A*, 0.5°C (1°F) per min; melt *B*, 2°C (4°F) per min; melt *C*, 11°C (20°F) per min; and melt *D*, 70°C (125°F) per min.

Samples cut from each melt were given various heat treatments which will be described with the results.

Identification of phases was accomplished metallographically, using the etching characteristics and optical properties of the phases. An etchant which was found most satisfactory for distinguishing among the phases was a solution of 1 part H_3PO_4 (85 pct) to 9 parts water. Etching was carried out by immersion for 1½ min with the etchant held at 50°C (120°F). The effect of this etch on the various constituents appearing in the micrographs, Figs. 2 through 8 and Fig. 10, is as follows (the effect of rotating the sample when viewed between crossed polarizers is also included):

1—(Mn,Fe)Al_6 is unattacked, retains its light gray color, and is outlined very slightly or not at all; changes from light to dark in polarized light.

2—αAl(Mn,Fe)Si is attacked, outlined, darkened somewhat, and small particles sometimes are dissolved out; does not change in polarized light.

3—Silicon is unattacked and darker gray than (Mn,Fe)Al_6; does not change in polarized light.

Phase identities were confirmed by X-ray diffraction. For this purpose, the aluminum matrix was dissolved away in a solution of methanol and iodine, leaving the intermetallic phases in the form of a fine residue. The residue was used as the powder sample for obtaining a Debye-Scherrer diffraction pattern.

Some additional melts were made of Al-Mn binary alloys of moderate and high purity. The former was made from 99.8 pct Al and electrolytic manganese. The latter was made from 99.99 pct Al and a master alloy made with the same grade of aluminum and pure anhydrous manganous chloride. Contents of these melts are given in Table I.

These binary alloys were chill-cast in copper molds or remelted and cooled at the same rate as 3S melt *D* and were given various heat treatments.

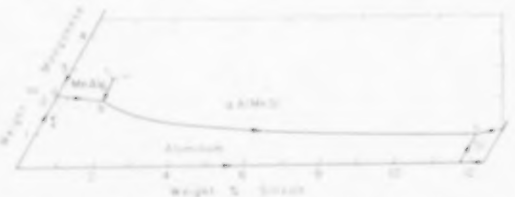

Fig. 1—Portion of the liquidus surface of the Al-Mn-Si constitution diagram (from data of Phillips[9]). The arrowheads indicate decreasing temperature. The points and lines are given in tabular form below.

Line or Point	Reaction	Temperature °C (°F)
a	——	658 (1216)
ab	Eutectic E_1: liquid ⇌ Al + $MnAl_6$	——
b	Peritectic *P*: liquid + $MnAl_6$ ⇌ Al + αAlMnSi	649 (1200)
bc	Eutectic E_2: liquid ⇌ Al + αAlMnSi	——
c	Eutectic E_3: liquid ⇌ Al + αAlMnSi + Si	573 (1063)

Table I. Content of Melts in Weight Percent

Mn	Fe	Si	Cu	Al
1.81	0.13	0.10	0.01	Balance
1.97	0.003	0.02	0.005	Balance
1.25	Not analyzed but made from same materials as 1.97 pct Mn alloy			

Results and Discussion

Phase Identification: No more than four phases were found in any of the samples examined. One of these phases was, of course, the aluminum solid solution. The others were as follows:

1—(Mn,Fe)Al_6. This phase is distinguished in slowly solidified structures by its habit of forming long hollow prisms with cross-sections in the form of parallelograms. In rapidly cooled alloys, the habit is not well defined and cannot be used as a distinguishing feature.

2—αAl(Mn,Fe)Si. This phase is characterized by its scriptlike appearance when in eutectic form. When an alloy containing αAl(Mn,Fe)Si has been heated near its solidus temperature, the constituent particles sometimes assume the shape of cubic dodecahedra ({110} faces) so that in cross-section they have a polygonal shape, generally six-sided.

3—Silicon. Silicon is usually easy to recognize by its bluish-gray color. In 3S it is found only in a very fine aggregate structure.

Some investigators[16-18] have attributed the difference in appearance and etching characteristics between the two phases (Mn,Fe)Al_6 and αAl(Mn,Fe)Si to varying amounts of iron in solution in $MnAl_6$ rather than to the presence of two entirely different phases. The present identification by X-ray diffraction and by optical properties definitely establishes that there are two separate manganese-containing phases in 3S alloy.

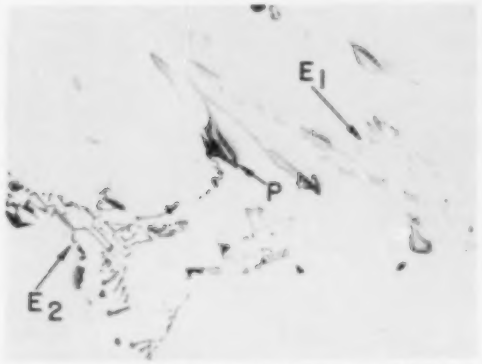

Fig. 2—Microstructure of 3S aluminum alloy solidified at 0.5°C (1°F) per min (melt *A*). The structures due to the eutectic and peritectic reactions of Fig. 1 are indicated. $(Mn,Fe)Al_6$ is light grey; αAl(Mn,Fe)Si is darkened. Etched with 10 pct H_3PO_4. X100. Area reduced approximately 33 pct for reproduction.

Although the composition of the alloy and of the individual phases demonstrates that 3S must be considered as a four-component alloy, it was noted that all the phases present were common to the Al-Mn-Si system. With due regard to phase rule considerations, it was found feasible to simplify this study by representing 3S as an Al-Mn-Si alloy. In this way, some of the complexities of three-dimensional space models could be avoided, while at the same time some of the complications of multicomponent systems could be illustrated.

Process of Solidification: The process of solidification could be studied best by relating the microstructures of melts solidified at different rates to the probable change in composition of the liquid metal during solidification. The liquidus surface of the ternary Al-Mn-Si diagram (Fig. 1) served as the simplest means of depicting liquid composition changes. It must be remembered that the compositions and temperatures of nonvariant points in the Al-Mn-Si system will no longer strictly apply because of the iron which is present.

The microstructure of the most slowly cooled melt (0.5°C per min) is shown in Fig. 2. Three features are indicated in this micrograph, each feature being related to the Al-Mn-Si diagram, Fig 1. First there is the binary eutectic E_1 which results from the reaction

$$\text{liquid} \rightarrow \text{Al} + \text{MnAl}_6$$

Then a peritectic P is indicated, resulting from

$$\text{liquid} + \text{MnAl}_6 \rightarrow \text{Al} + \alpha\text{AlMnSi}.$$

This peritectic is revealed in more detail in Fig. 3. Finally there is shown the eutectic E_2, resulting from

$$\text{liquid} \rightarrow \text{Al} + \alpha\text{AlMnSi}.$$

In Fig. 1, alloy x corresponds to a typical 3S composition. Since the alloy lies in the primary aluminum field, the first solid to precipitate from the cooling melt will be primary aluminum. As solidification progresses, the liquid composition changes, following some such path as indicated by the dashed line in Fig. 1 until line ab is intercepted. Along the eutectic valley indicated by line ab, the eutectic E_1 separates out. When the liquid reaches composition b, the peritectic reaction P begins. As is usual under nonequilibrium conditions, the peritectic does not go to completion and the liquid composition continues to change along line bc, precipitating another eutectic, E_2, until solidification is complete.

At a higher rate of solidification, 2°C per min, the microstructure was similar but much finer and there was introduced a rosette type of structure. At the high magnification of Fig. 4, these rosettes could be resolved into aluminum, αAlMnSi, and silicon, showing that the liquid composition had so changed that the last to solidify had comprised the ternary eutectic E_3

$$\text{liquid} \rightarrow \text{Al} + \alpha\text{AlMnSi} + \text{Si}.$$

This is in accord with the observations of Phillips[9,10] and of Hanemann and Schrader.[11] It is interesting to note that, although the eutectic E_2 contains about 11.5 pct Si, it was found in an alloy with only 0.23 pct Si. Of course, it was found only in very small amount.

Solidification at rates of 11° and 70°C per min produced further refinement of the cast structure. Simultaneously, there was an increase in the proportion of $MnAl_6$ to αAlMnSi. There was very little evidence of the peritectic reaction, and the quantity of eutectic αAlMnSi had decreased substantially, as shown in Fig. 5a and b. Occasional very fine rosettes, presumably composed of the ternary eutectic E_3, could still be found. The inference to be gathered from the greater proportion of $MnAl_6$ is that silicon

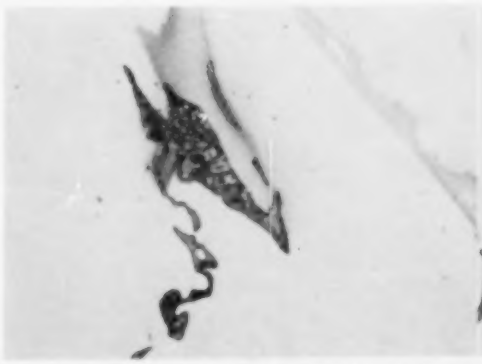

Fig. 3—Enlarged view of peritectic structure shown in Fig. 2. An aggregate structure of aluminum and αAl(Mn,Fe)Si (outlined) results from reaction of the liquid melt with $(Mn,Fe)Al_6$. Etched with 10 pct H_3PO_4. X500. Area reduced approximately 33 pct for reproduction.

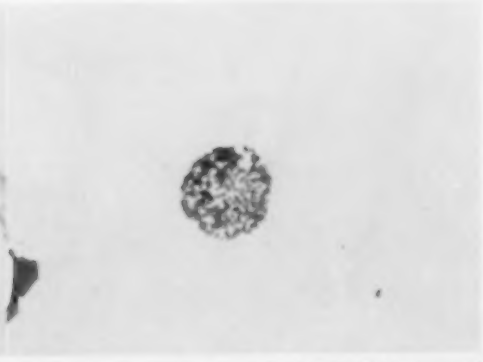

Fig. 4—Rosette structure found in 3S solidified at rates of 2°C (4°F) per min and greater. The rosette is composed of the ternary eutectic, structure, E_3, aluminum + αAl(Mn,Fe)Si (darkened) + Si (grey, unetched). Etched with 10 pct H_3PO_4. X1000. Area reduced approximately 33 pct for reproduction.

was not being concentrated in the liquid metal to the extent that it had been at slower cooling rates so that the αAlMnSi eutectic was less likely to form. The peritectic reaction was almost completely suppressed by the most rapid solidification rate.

The microstructure of the most rapidly solidified sample (70°C per min) resembled that of ordinary 3S direct-chill ingots with respect to type of constituents, constituent size, and grain size. Coarser structures such as that of the 11°C per min sample are encountered in a narrow zone close to the surface of commercial ingots. The two slower cooling rates have no practical significance.

Heating the Cast Structure: It was obvious from the discussion of the solidification of 3S that increasing solidification rate brought about greater departure from the equilibrium structure. Subsequent heating would be expected to restore equilibrium, with the degree of restoration dependent on temperature and time. The first studies on homogenization were made at 640°C (1180°F), since this was about the highest temperature which could be used without the danger of serious melting. All samples were water quenched.

When the most slowly solidified specimen was heated at 640°C (1180°F), it was found that the $MnAl_6$ was gradually replaced by αAlMnSi as Fig. 6 shows. The reaction began at the interface of the aluminum solid solution and the $MnAl_6$ phase. An aggregate structure composed of aluminum and αAlMnSi formed first. Then the aluminum in the aggregate spheroidized and finally the individual αAlMnSi crystals divorced themselves from the aggregate and assumed the characteristic polygonal shape shown in Fig. 6. It is clear that the peritectic reaction *P* had not gone to completion during solidification and that heating caused it to proceed in the solid state.

Similar transformation of $MnAl_6$ to αAlMnSi occurred in the samples solidified more rapidly. Fig. 7 shows the structure of melt *C* after heating for 25 hr. The smaller particle size and the finer dendritic structure of the more rapidly solidified castings permitted more rapid coalescence of individual αAlMnSi particles. The effect of time of heating is shown by melt *D* samples heated at 640°C (1180°F) for 1 and 25 hr, Figs. 8a and b. The quantity of $MnAl_6$ transformed did not increase appreciably after heating 1 hr and agglomeration proceeded at a greater rate than in the coarser cast structures.

It is noteworthy that, after homogenization heat treatment, the quantity of αAlMnSi exceeded that

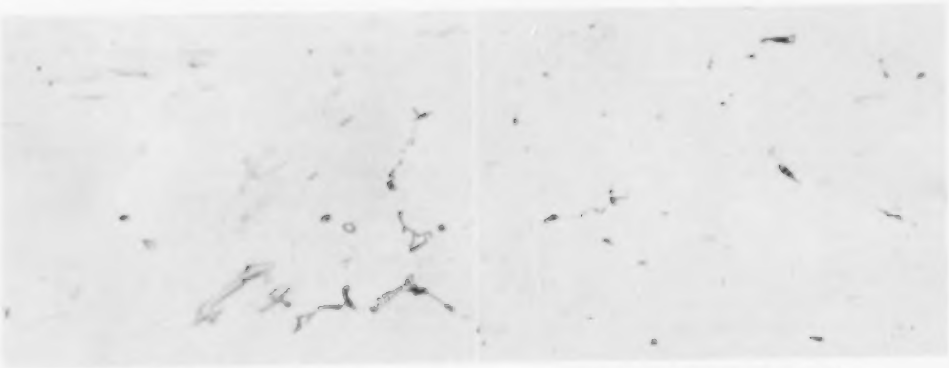

a—11°C (20°F) per min, melt *C*. b—70°C (125°F) per min, melt *D*.

Fig. 5—3S aluminum alloy solidified at 11°C (20°F) and 70°C (125°F) per min. Note the increasing proportion of (Mn,Fe)Al$_6$ as the cooling rate increases. Etched with 10 pct H_3PO_4. X250. Area reduced approximately 33 pct for reproduction.

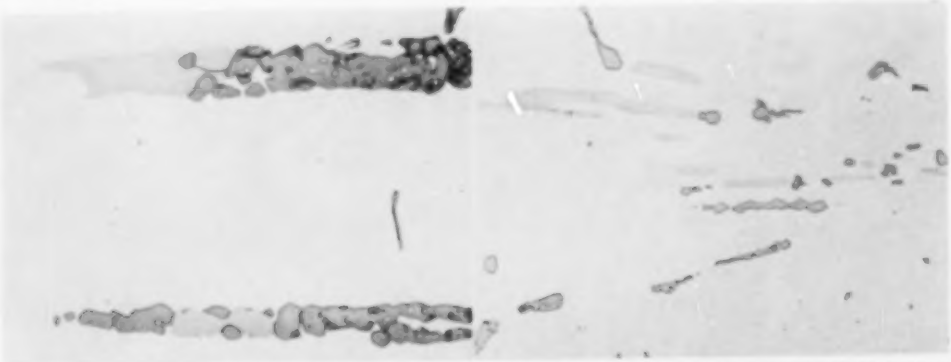

Fig. 6—Melt *A* heated at 640°C (1180°F) for 97 hr. The (Mn,Fe)Al$_6$ has been largely replaced by the aggregate of aluminum and αAl(Mn,Fe)Si. The latter phase eventually coalesces into a characteristic polyhedral shape. Etched with 10 pct H_3PO_4. X500. Area reduced approximately 33 pct for reproduction.

Fig. 7—Melt *C* heated at 640°C (1180°F) for 25 hr. Same phases as in Fig. 6. Etched with 10 pct H_3PO_4. X500. Area reduced approximately 33 pct for reproduction.

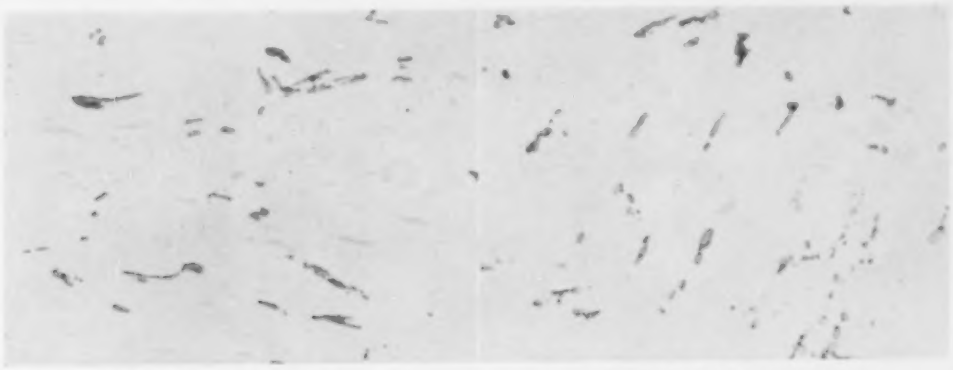

a—Melt *D* heated at 640°C (1180°F) for 1 hr. b—Melt *D* heated at 640°C (1180°F) for 25 hr.

Fig. 8—Melt *D* heated at 640°C (1180°F) for 1 and 25 hr. Same phases as in Fig. 6. Etched with 10 pct H_3PO_4. X500. Area reduced approximately 33 pct for reproduction.

of $MnAl_6$, reversing the situation in the cast structure. To see how this fits the equilibrium picture, reference again can be made to the Al-Mn-Si diagram. The distribution of phases in the solid state is shown schematically in Fig. 9 where the range of compositions for 3S is indicated by the shaded area. The two-phase field, Al+$MnAl_6$, is very narrow and hence is confined to extremely low silicon alloys which are not likely to be found commercially. The 3S composition range lies within the three-phase field, Al+$MnAl_6$+αAlMnSi, where the proportion of $MnAl_6$ to αAlMnSi is very sensitive to silicon content. Some 3S alloys with silicon near the upper specification limit of 0.60 pct have been found to contain only αAlMnSi as the second phase.

It was noted that, in those cast structures containing the ternary eutectic rosettes, heating caused the rosettes to disappear very quickly. The silicon phase in the rosettes in these alloys would be quite unstable, as Fig. 9 shows. It is to be expected that remelting during heating occurred in these silicon-rich areas but that the liquid disappeared as silicon diffused outward.

When a lower homogenization temperature, 595°C (1100°F), was used, the alteration of the microstructure was similar to that which occurred at 640°C (1180°F) except that agglomeration of the αAlMnSi was not as rapid. In contrast to the very light and well coalesced precipitate at 640°C, a moderately heavy precipitate was formed within the dendrites. At high magnification, this precipitate could be identified as αAlMnSi (see Fig. 10). Of special interest was the distribution of this precipitate. Fig. 11 shows the same sample as was shown in the previous figure but it has been re-etched with 0.5 pct hydrofluoric acid in order to reveal the fine precipitate particles. This pattern of precipitation will be the subject of the next section of this discussion.

The transformation of $MnAl_6$ to αAlMnSi was found to proceed fairly rapidly even at temperatures as low as 425°C (800°F). The continuation of this reaction is strongly dependent upon diffusion of silicon.

Relation of Precipitation Pattern to Cast Structure: The nonuniform distribution of precipitate in 3S aluminum alloy pictured in Fig. 11 has been an object of concern in the production of 3S sheet where good surface quality for subsequent anodizing is required. The relation between this microstructure and nonuniformities in the appearance of anodic coatings was described by Röhrig and Käpernick.[17] The combination of a coarse cast grain structure and heterogeneous precipitation can cause streaking which is visible to the naked eye in the anodic coating on sheet rolled from such material. Therefore, the origin of such a nonuniform precipitate is of practical interest.

Close examination of the precipitate distribution shows that it cannot be explained solely on the basis of solid-solution coring, although coring is undoubtedly a factor. Actually the distribution is found to be related to the dendritic structure in the manner shown schematically in Fig. 12. In the dendrite core, there are relatively few generally coarse precipitate particles. As the outer rim of the dendrite is approached, the particles grow smaller but much more numerous. Up to this point, the concentration of precipitate can be said to be based upon normal dendritic segregation or coring. However, in the volume of metal separating one dendrite arm from another, and incidentally containing the eutectic structures, the precipitate suddenly drops off to nothing. Heating of cast 3S at 540°C (1000°F) or

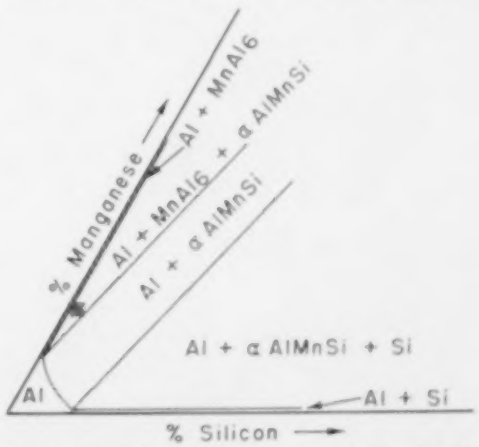

Fig. 9—Typical isothermal section through the Al-Mn-Si phase diagram showing distribution of phases in the solid state (from ref. 17). The shaded area indicates the composition range of 3S aluminum alloy.

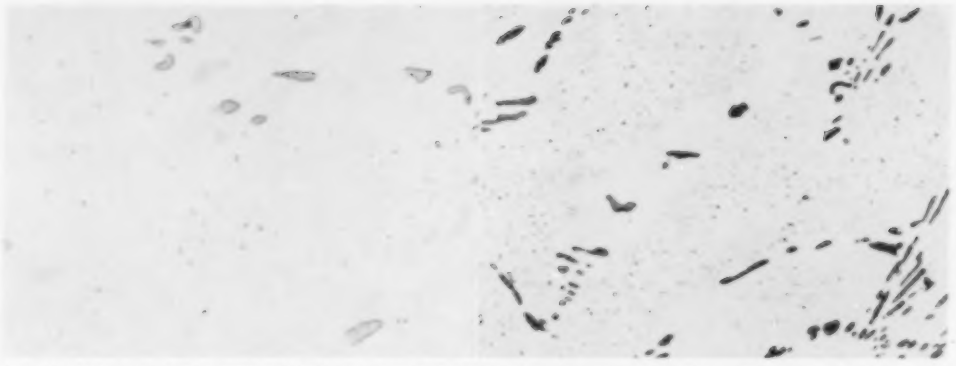

Fig. 10—Melt *D* heated at 595°C (1100°F) for 25 hr. The larger precipitate particles can be identified as αAl(Mn,Fe)Si by their etching characteristics. Etched with 10 pct H_3PO_4. X1000. Area reduced approximately 33 pct for reproduction.

Fig. 11—Same sample as Fig. 10 but re-etched with ½ pct HF to reveal fine precipitate. X500. Area reduced approximately 33 pct for reproduction.

lower does bring out a fine precipitate within these eutectic areas but it still remains very light compared to that in the dendrites.

The pattern of precipitation just described is not confined to 3S aluminum alloy alone. It has been noted by the writer in many different alloys containing manganese or chromium as alloy additions. Some references to this type of precipitate have been made by Seeman et al.,[5,6] and by Chadwick, Muir, and Grainger.[4] In no case has a satisfactory explanation been given.

Before the nature of the precipitate distribution could be decided, it was necessary to establish whether the distribution was a direct reflection of the solute distribution in the cast solid solution or whether diffusion during the heating used to bring about precipitation caused the heterogeneity. This was accomplished by etching the as-cast structure of 3S to reveal inhomogeneities in the solid solution. Fig. 13 shows the result. Using oblique illumination, it can be seen that there is a sudden change in the rate of etching between the dendritic aluminum and the aluminum near the eutectic phases. The dendrites are depressed, indicating more rapid etching. The lines of demarcation between rapid etching and slow etching aluminum are found to resemble the lines of demarcation between heavy concentrations of precipitate and light concentrations, as in Fig. 11.

Having concluded that the precipitation pattern reflects the concentrations of solute in the solid solution, it can be logically assumed that the aluminum having the lowest concentration of some solute element (assumed to be manganese), always found in the dendrite interstices, is the aluminum which formed during crystallization of the binary eutectics comprising Al+(Mn,Fe)Al$_6$ and Al+αAl(Mn,Fe)Si. These eutectics are of a type designated as "entartetes Eutektium" (degenerate eutectic) by the Germans and as "divorced eutectic" in this country. Because they solidify over a range of temperatures, there is a continuous orientation relationship between primary aluminum and the eutectic aluminum (demonstrated in the case of 3S by methods of anodic film etching and examination in polarized light). The intermetallic phase of the eutectic appears to bear no relation to the aluminum.

The explanation of why the eutectic aluminum is so depleted in manganese could be based on the normal process of solidification of the binary eutectics (three-phase equilibria) to be expected in the ternary Al-Mn-Si system. Fig. 14 presents a series of isothermal sections within the solidification range

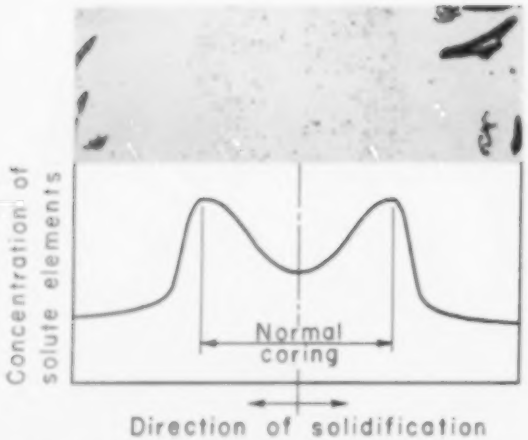

Fig. 12—The micrograph shows a typical section through a dendrite arm. X500. Area reduced approximately 20 pct for reproduction. The distribution of the solute in the original cast structure, as suggested by the precipitation pattern, is shown schematically.

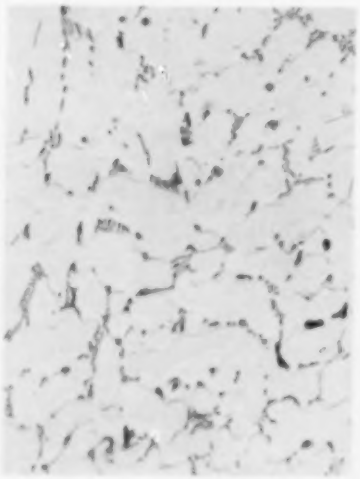

Fig. 13—Melt *D* cast structure etched with ½ pct HF for 1 min and photographed with oblique illumination. The dendritic aluminum has etched more rapidly than the eutectic aluminum.

with two typical three-phase equilibrium triangles. Each triangle connects a particular liquid composition (locus of points = line *abc*) with an aluminum solid-solution composition (locus of points = line *def*) and with the applicable second solid phase, $MnAl_6$ or αAlMnSi. The composition change of the aluminum solid solution during the crystallization of the binary eutectics was taken from Hanemann and Schrader.[17] At temperature t_2 where the four-phase equilibrium peritectic reaction occurs, there is a plane surface connecting all four phases. It is seen that for both binary eutectics the manganese content of the aluminum solid solution drops off rapidly as the liquid composition moves along the lines indicating the eutectic valleys. It is quite conceivable that this equilibrium depletion of the manganese in the eutectic aluminum is sufficient to account for solute distribution in cast 3S structures.

An additional factor to be considered is the tendency of manganese to supersaturate the solid solution as reported by Hofmann.[3] For this reason some binary Al-Mn alloys were studied. First, an impure alloy, made with 99.8 pct Al and electrolytic manganese and containing 1.81 pct Mn, was chill cast and then heated to bring out the precipitate. It contained only $MnAl_6$ as the second phase and yet it showed a very marked precipitate pattern of the same type which appeared in 3S. However, the 0.13 pct Fe and 0.10 pct Si in this alloy still left doubt as to whether its behavior was typical of a pure binary Al-Mn alloy. Hence the higher purity alloys with 1.25 and 1.97 pct Mn were made up and examined metallographically. The 1.25 and 1.97 pct Mn alloys displayed relatively slight concentration gradients when compared with 3S or with the less pure 1.81 pct Mn alloy. The chill-cast 1.97 pct Mn sample contained practically no eutectic structure, even though it represented the equilibrium eutectic composition. This demonstrates the capacity for supersaturation of aluminum with manganese already mentioned. Both alloys contained a small amount of eutectic when solidified at a slower rate, the same as that used for 3S melt *D*. The primary aluminum, however, exhibited extremely little coring and the concentration gradients in the eutectic areas were very slight. It seems most likely that the solute distribution in the aluminum solid solution of 3S cast samples is not a characteristic of the Al-Mn binary system. Rather, it could be explained more readily on the basis of normal solid solution coring followed by solidification of a binary divorced eutectic in a ternary alloy system.

Conclusions

The microstructures of 3S aluminum alloy have their origin in the Al-Mn-Fe-Si system but they can be most simply described by reference to the Al-Mn-Si phase diagram. The phases which can be found in the alloy are aluminum, $(Mn,Fe)Al_6$, $\alpha Al(Mn,Fe)Si$, and silicon. A precipitation pattern commonly found in 3S cast microstructures after heating could also be explained on the basis of normal solidification processes in the Al-Mn-Si system.

Acknowledgments

The author wishes to thank the numerous members of the staff of the Kaiser Dept. of Metallurgical Research for their assistance with experimental work and their helpful criticism in preparing this paper and to express his appreciation to Mr. Paul P. Zeigler, Director, for permission to publish it.

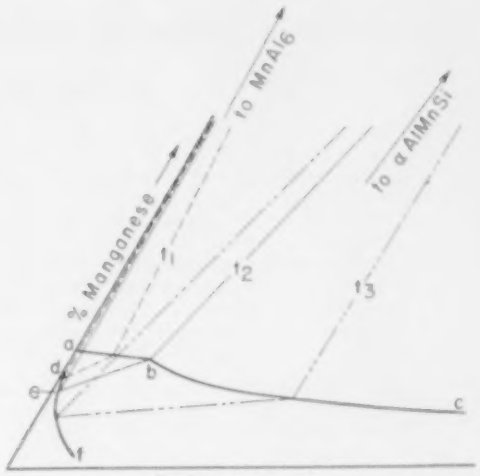

Fig. 14—Schematic representation of liquid-solid equilibria during solidification of an Al-Mn-Si alloy. Temperature $t_1 > t_2 > t_3$. Line *abc*, the eutectic valley, gives the locus of liquid compositions in equilibrium with aluminum solid solutions whose locus is *def* and with either $MnAl_6$ or αAlMnSi. The peritectic reaction at t_2 represents four phases in equilibrium.

References

[1] E. Butchers and W. Hume-Rothery: *Journal* Institute of Metals (1945) **71**, pp. 87-91.
[2] E. H. Dix, Jr., W. L. Fink, and L. A. Willey: *Trans.* AIME (1933) **104**, pp. 335-352.
[3] W. Hofmann: *Abhandlungen der Braunschweigischen Wissenschaftlichen Gesellschaft* (1949) **1**, pp. 83-88.
[4] E. Butchers, G. V. Raynor, and W. Hume-Rothery: *Journal* Institute of Metals (1943) **69**, pp. 209-228.
[5] H. Wolf and H. Neunzig: *Aluminium* (April 1952) pp. 131-140.
[6] G. Marchand: *Canadian Journal of Technology* (1953) **31**, pp. 15-28.
[7] G. V. Raynor and W. Hume-Rothery: *Journal* Institute of Metals (1943) **69**, pp. 415-421.
[8] W. Hofmann: *Aluminium* (Dec. 1938) pp. 865-872.
[9] A. D. I. Nicol: *Acta Crystallographica* (1953) **6**, pp. 285-293.
[10] G. V. Raynor: *Journal* Institute of Metals (1944) **70**, pp. 531-542.
[11] K. Little and W. Hume-Rothery: *Journal* Institute of Metals (1948) **74**, pp. 521-524.
[12] H. W. L. Phillips: *Journal* Institute of Metals (1943) **69**, pp. 291-316.
[13] H. W. L. Phillips and P. C. Varley: *Journal* Institute of Metals (1943) **69**, pp. 324-350.
[14] M. Monticelli-Papania: *Alluminio* (1951) **20**, pp. 136-146.
[15] J. N. Pratt and G. V. Raynor: *Journal* Institute of Metals (1951) **79**, pp. 211-232.
[16] G. Phragmén: *Journal* Institute of Metals (1950) **77**, pp. 489-552.
[17] H. Hanemann and A. Schrader: *Atlas Metallographicus Band III, Teil 2.* (1952) Dusseldorf. Stahleisen M.B.H.
[18] L. J. Barker: *Iron Age* (May 26, 1949) **163**, No. 21, pp. 74-78.
[19] H. Röhrig and E. Käpernick: *Ztsch. für Metallkunde* (1943) **35**, pp. 117-120.
[20] M. Dudek, H. Mahl, and H. J. Seemann: *Metall* (March 1948) pp. 75-80.
[21] H. J. Seeman and M. Dudek: *Ztsch. für Metallkunde* (1948) **39**, pp. 319-320.
[22] R. Chadwick, N. B. Muir, and H. B. Grainger: *Journal* Institute of Metals (1953-54) **82**, pp. 75-80.

Influence of Additives in the Production of High Coercivity Ultra-Fine Iron Powder

by Edward W. Stewart, George P. Conard, II, and Joseph F. Libsch

The effects of several additives upon the reduction characteristics of hydrogen-reduced ferrous formate are described. The various additives inhibit sintering of the reduced iron particles by apparently different mechanisms. The magnetic properties of the low density compacts produced from the resulting ultra-fine iron powders were improved markedly.

THE permanent magnetic characteristics of ultra-fine iron powder prepared by various means have been a subject of considerable interest and experimentation in the past few years. When such particles are small enough to show single domain behavior, they possess 1—permanent saturation magnetization, and 2—high coercive force. In the absence of domain boundaries, the only magnetization changes in a particle occur through spin rotation which is opposed by relatively large anisotropy forces. With decreasing particle size, the coercive force tends to increase to a maximum and then decrease because of the instability in magnetization associated with thermal fluctuations.

Kittel[1] has calculated the critical diameter at which a spherical particle of iron can no longer sustain domain boundaries or walls to be approximately 1.5×10^{-5} cm.

Stoner and Wohlfarth[2, 3] in England and Neel[4, 5] in France have shown from purely theoretical calculations that the high coercive force expected from single domain particles is dependent upon crystal anisotropy, shape anisotropy, or strain anisotropy contributions.

Further work by Weil,[6] Bertaut,[7] and many others has contributed much to the understanding of fine particle theory.

Neel[8] and Meikeljohn[9] have demonstrated that a decrease in particle size below a critical value of approximately 160A leads to a quite rapid decrease in coercive force because of the prevention of stable magnetization by thermal agitation.

Lihl,[10] working with powders prepared by the reduction of formate and oxalate salts of iron, has shown the marked influence of powder purity upon magnetic properties. Maximum coercive force was obtained in powders of approximately 65 pct metallic iron content while the maximum energy product, $(BxH)_{max}$, occurred in powders of 85 pct metallic iron content.

Careful consideration of the preceding theoretical considerations and experimental results has led to the manufacture of permanent magnets from ultra-fine ferromagnetic powders by powder metallurgy techniques. Such work has been done by Dean and Davis,[11] the Ugine Co. of France,[12, 13] and Kopelman.[14]

The aforementioned work of Kopelman and the Ugine Co. was concerned somewhat with the effect of various additives upon the properties of hydrogen-reduced ferrous formate. Virtually no work, however, has been published on the effects of additives on the reduction rates of metal formates, although unpublished work by Ananthanarayanan[15] showed promise of improved energy product in ultra-fine iron compacts prepared by the hydrogen reduction of a coprecipitated mixture of magnesium and ferrous formate.

After consideration of the preceding information, it was hoped that a better balance between the metallic iron content and particle size of the reduced iron powder could be accomplished by a prevention of the attendant sintering of the partially reduced iron powder during the reduction reaction. It appeared possible that magnesium oxide might interpose a mechanical barrier between adjacent iron particles and prevent their sintering together, while metallic cadmium and metallic tin would interpose a liquid barrier which might accomplish the same purpose. The degree to which these materials were effective in accomplishing the foregoing objective and the experimental details associated with the work are reported in the following sections of this paper.

Experimental Procedure

Preparation of Formate and Oxide Mixtures: To obtain ferrous formate of reproducible reduction characteristics, a slight modification was made in the technique of Fraioli and Rhoda.[16] A supersaturated solution of ferrous formate was mixed with an equal volume of 95 pct ethyl alcohol and the formate crystals precipitated by stirring and screened to —325 mesh. These crystals were in the shape of elongated hexagons, approximately 4x10 micron in dimension. Various preparations of such ferrous formate, designated as lot III, were reduced for 2 hr, yielding ultra-fine iron particles of exceedingly reproducible size, metallic iron content, and magnetic properties. The magnesium and cadmium formates were prepared by the reaction of dilute formic acid with their respective carbonates, while the tin formate was prepared by the reaction of dilute formic acid with stannous hydroxide.

To evaluate the effect of metallic formate additives in intimate mixture with the ferrous formate, varying amounts of magnesium, cadmium, and tin formates were coprecipitated with the latter. The designations of these materials and their chemical compositions are given in Table I. Due to the differing solubilities of the various formates in aqueous media,

E. W. STEWART, formerly Graduate Research Assistant, Dept. of Metallurgy, Lehigh University, is associated with the Titanium Development Section, du Pont de Nemours Inc., Newport, Del., G. P. CONARD, II, and J. F. LIBSCH, Members AIME, are Assistant Professor and Professor of Metallurgy, respectively, Lehigh University, Bethlehem.

Discussion on this paper, TP 3846E, may be sent, 2 copies, to AIME by Mar. 1, 1955. Manuscript, Apr. 7, 1954. Chicago Meeting, November 1954.

Table I. Designation of Coprecipitated Formates and Their Approximate Chemical Composition

Designation	Composition
Lot III, M 10 F	10 pct Mg per unit contained iron in the formate
Lot III, M 2 F	2 pct Mg per unit contained iron in the formate
Lot III, M 0.4 F	0.4 pct Mg per unit contained iron in the formate
Lot III, C 6 F	6 pct Cd per unit contained iron in the formate
Lot III, C 4 F	4 pct Cd per unit contained iron in the formate
Lot III, C 2.5 F	2.5 pct Cd per unit contained iron in the formate
Lot III, S 5 F	5 pct Sn per unit contained iron in the formate

actual composition may vary widely from the nominal. However, the compositions given in Table I were verified either by spectrographic means or quantitative chemical analysis and found to be accurate to within ±5 pct.

In order to evaluate the effect of mixtures of metallic oxides and ferrous formate and to correlate the effect of these mixtures with the effect of coprecipitated material of the same composition, varying amounts of cadmium oxide and stannous oxide were mixed with ferrous formate on rolls under an argon atmosphere. The designations of these materials and their approximate chemical compositions are given in Table II.

Powder Reduction: The mixed or coprecipitated formate powders were reduced in 10 g lots in a stream of dry purified hydrogen, flowing at the rate of 20 cu cm per sec. The reduction equipment used was that of Ananthanarayanan,[9] consisting of a small resistance wound furnace accurate to ±5°F and a quartz tube into which the formate powder was inserted in a stainless steel boat. After reduction, the ultra-fine iron powder, which is pyrophoric, was placed under a Kjeldahl joint in the quartz tube and covered with benzene to protect the material from atmospheric oxygen.

Determination of Ultra-Fine Powder Properties: The reduced powder, while wet with benzene, was compacted at 60 tsi into bars approximately 3.2x0.3x0.3 cm in dimension. These bars were stored under benzene until their magnetic properties were measured on a Sanford-Bennett-type high H permeameter[10] at a field strength of 4000 oersteds.

Since data by Franklin[11] and Ananthanarayanan[9] indicate excellent correlation between electron microscopy, X-ray line broadening, and nitrogen adsorption methods in the determination of particle size, the method of X-ray line broadening was chosen for reasons of convenience in this work.

Lastly, the metallic iron content, as measured by the hydrogen evolution method, was chosen as a parameter for the determination of the degree of reduction of the material under a given set of conditions of formate composition and reduction temperature.

Experimental Results and Analysis of Data

The magnetic properties, intrinsic coercive force ($_iH_c$), saturation induction (B-H), and remanence (B_r), the X-ray particle size (Å), and the metallic iron content are plotted against the reduction temperature in °F for formates of given compositions in Figs. 1 through 12.

Reduction of Ferrous Formate: The properties of ultra-fine iron produced from lot III ferrous formate without an additive material are shown as dashed curves on each figure for comparison purposes (Figs. 1 through 12). Maximum intrinsic coercive force obtained from the lot III ferrous formate occurs at a reduction temperature of 475°F (Fig. 1), a metallic iron content of 65 pct as predicted by Lihl[10] (Fig. 4), and a particle size of 290Å (Fig. 3). Above 500°F, the lot III ferrous formate is almost completely reduced, possessing an extremely low intrinsic coercive force, together with a high metallic iron content of 93 to 95 pct. In this temperature range, the saturation induction and remanence values (Fig. 2) increase quite rapidly with increasing temperature until at 800°F the reduced iron powder possesses essentially soft magnetic characteristics.

The maximum energy product $(BxH)_{max}$ obtained from lot III ferrous formate was $0.3x10^6$ gauss-oersteds and occurred in powders reduced at 500°F for 120 min, showing a metallic iron content of 85 pct and a compact density of 4.3 g per cu cm.

Influence of Magnesium Formate Additions: Increasing percentage additions of magnesium formate result in a gradual increase in the temperature at which maximum $_iH_c$ is obtained (475° to 575°F) and a 50 pct increase in $_iH_c$ (330 to 504 oersteds). The reduction characteristics of lot III ferrous formate are so altered that the ultra-fine iron powder retains its permanent magnetic characteristics over the entire reduction temperature range studied (Fig. 1). Conversely, saturation induction and remanence values exhibit a marked decrease from their original values as the percentage addition of magnesium formate is increased (Fig. 2). This behavior appears associated with the influence of the magnesium formate addition upon particle size.

Table II. Designation of Mixed Lot III, Ferrous Formate and Metallic Oxides and Their Chemical Composition

Designation	Composition
Lot III, C 6 (O)	6 pct Cd per unit contained iron in the formate
Lot III, S 5 (O)	5 pct Sn per unit contained iron in the formate
Lot III, S 2 (O)	2 pct Sn per unit contained iron in the formate
Lot III, S 0.2 (O)	0.2 pct Sn per unit contained iron in the formate

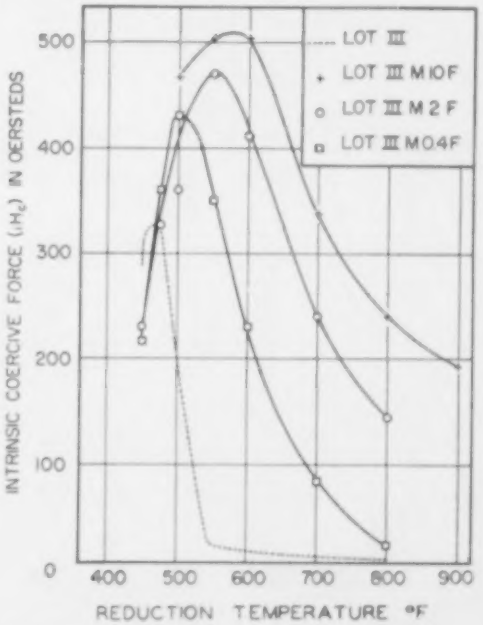

Fig. 1—Variation of intrinsic coercive force with temperature of reduction for compacted powders produced from lot III, ferrous formate plus magnesium formate.

As the contained magnesium increases, the particle size for a specific reduction temperature decreases until, with lot M10F, the values are virtually constant to 800°F, indicating that greater magnesium formate additions are unlikely to further improve $_iH_c$ values (Fig. 3).

The increase in maximum $_iH_c$ and the lateral shift in the coercive force vs temperature curve may be attributed to prevention of sintering of the reduced iron by the mechanical interference of the magne-

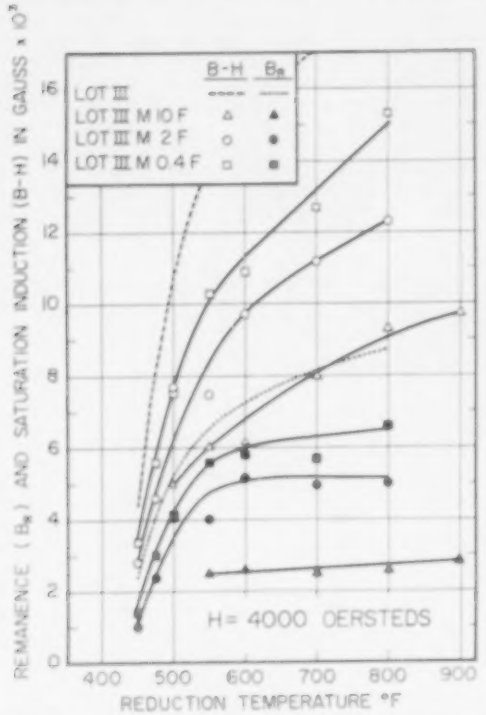
REMANENCE (B_R) AND SATURATION INDUCTION (B-H) IN GAUSS x 10^3
B-H
B_R
LOT III
LOT III M 10 F
LOT III M 2 F
LOT III M 0.4 F
H= 4000 OERSTEDS
REDUCTION TEMPERATURE °F

Fig. 2—Variation of saturation induction and remanence with temperature of reduction for compacted powders produced from lot III, ferrous formate plus magnesium formate.

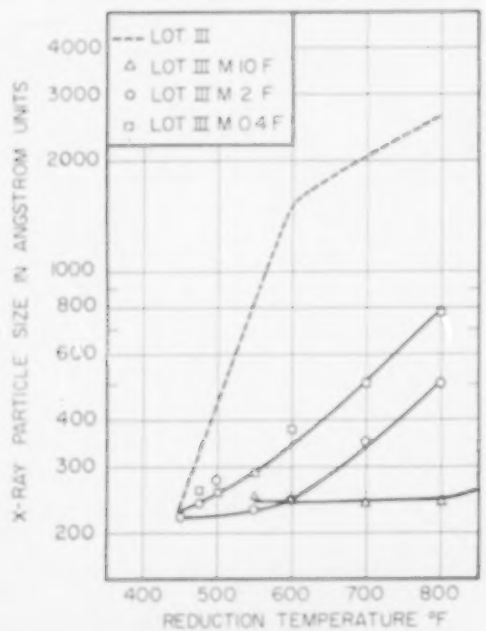

Fig. 3—Variation of particle size with temperature of reduction for powders produced from lot III, ferrous formate plus magnesium formate.

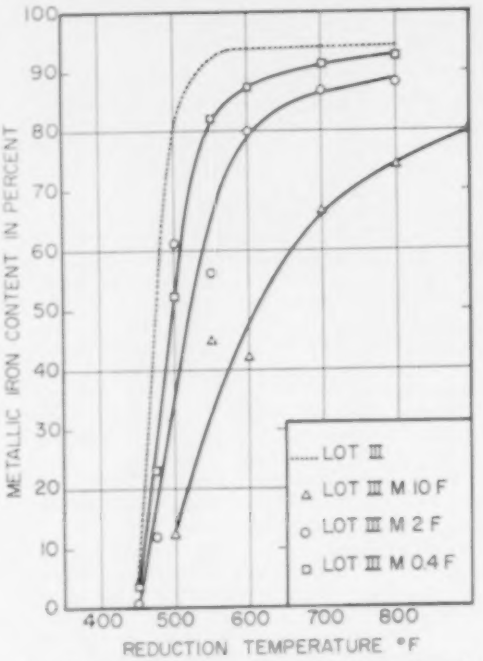

Fig. 4—Variation of metallic iron content with temperature of reduction for powders produced from lot III, ferrous formate plus magnesium formate.

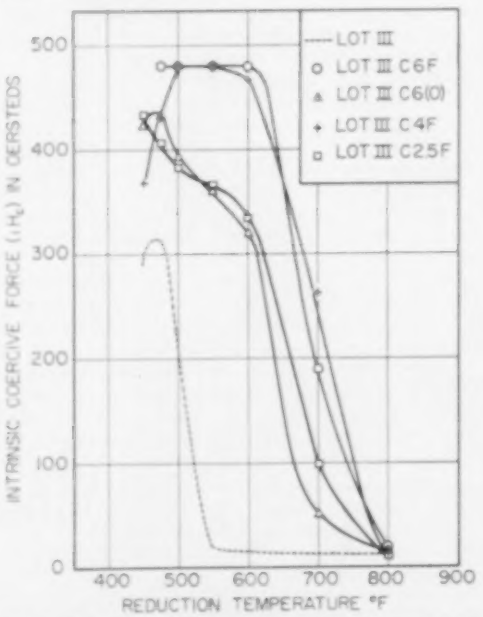

Fig. 5—Variation of intrinsic coercive force with temperature of reduction for compacted powders produced from lot III, ferrous formate plus cadmium formate or cadmium oxide.

sium oxide formed upon decomposition of the magnesium formate, together with an inhibiting action of that oxide upon the normal course of the reduction reaction (Fig. 4). This inhibiting action, probably caused by an interference with the diffusion of the reaction products from the partially reduced iron particles, would explain the marked decrease observed in the saturation induction and remanence values.

The maximum energy product $(BxH)_{max}$ obtained from lot III ferrous formate plus magnesium formate was 0.75×10^6 gauss-oersteds, an improvement of 150 pct over the original lot III, and occurred in lot III M2F powders containing approximately 3.2 pct MgO which were reduced at 600°F for 120 min with a metallic iron content of 84 pct and a density of 4.4 g per cu cm.

Influence of Cadmium Formate or Oxide Additions: Increasing percentage additions of cadmium formate do not result in a shift in the temperature at which maximum $_iH_c$ is obtained, but rather result in a broadened temperature range for maximum $_iH_c$ (475° to 600°F) and a 45 pct increase in $_iH_c$ (330 to 480 oersteds), Fig. 5. Saturation induction and remanence values in the lower temperature range (450° to 600°F) undergo a considerable decrease with increasing cadmium content, although the values obtained between 500° to 600°F remain approximately constant, Fig. 6. The sharp decrease in $_iH_c$, together with an equally steep increase in saturation induction and remanence values at reduction temperatures above 600°F, result from a minimization of the effect of the cadmium additive due to its increase in vapor pressure and subsequent rapid evolution above its melting point of 609.6°F.

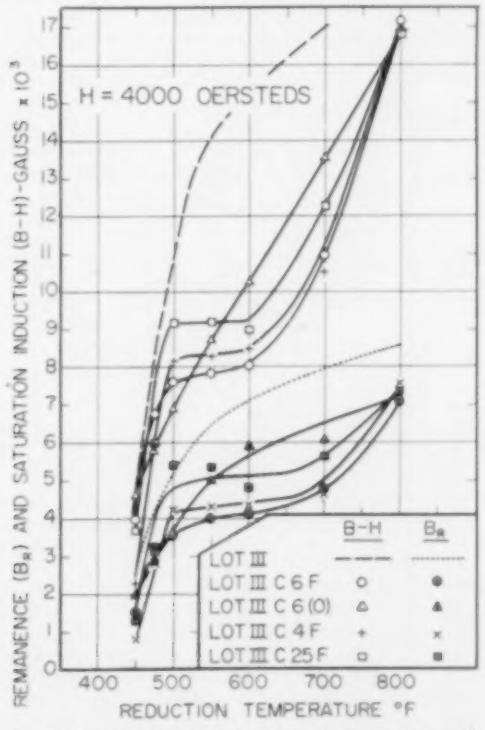

Fig. 6—Variation of saturation induction and remanence with temperature of reduction for compacted powders produced from lot III, ferrous formate plus cadmium formate or cadmium oxide.

Increasing cadmium formate additions effectively inhibit growth of the reduced iron particles to 600°F. However, above 600°F the particle size increases quite rapidly for all compositions and approaches a value of 1800A as the cadmium is volatilized (Fig. 7).

The observed increase in $_iH_c$ and decrease in saturation induction and remanence values would appear to result from a decreased particle size obtained by a prevention of the sintering of the reduced iron powder and, at the same time, an inhibition of the normal course of reduction (Fig. 8). The mechanism proposed to explain the plateau effect in magnetic properties occurring between 500° to 600°F is one associated with the rate of reduction of the cadmium formate, the appearance of metallic cadmium at approximately 500°F, and the rate of its subsequent vaporization. This vapor appears to act as an insulating blanket which effectively halts particle growth and retards reduction at a given point as long as it is present.

That this plateau effect is absent in the cadmium-oxide-ferrous formate mixture, lot III C 6 (0), may be attributed to the more ready reduction of cadmium oxide, which would lead to the appearance and volatilization of the metallic cadmium early in the reduction. However, it may be argued that the absence of the plateau is related to the distribution of the cadmium.

The maximum energy product $(BxH)_{max}$ obtained from lot III ferrous formate plus cadmium formate was 0.82×10^6 gauss-oersteds, an improvement of 160 pct over the original lot III, and occurred in lot III C 2.5F powders containing approximately 2.5 pct Cd which were reduced at 500°F for 120 min with a metallic iron content of 68 pct and a density of 4.3 g per cu cm.

Influence of Tin Formate and Oxide Additions: Increasing percentage additions of stannous oxide

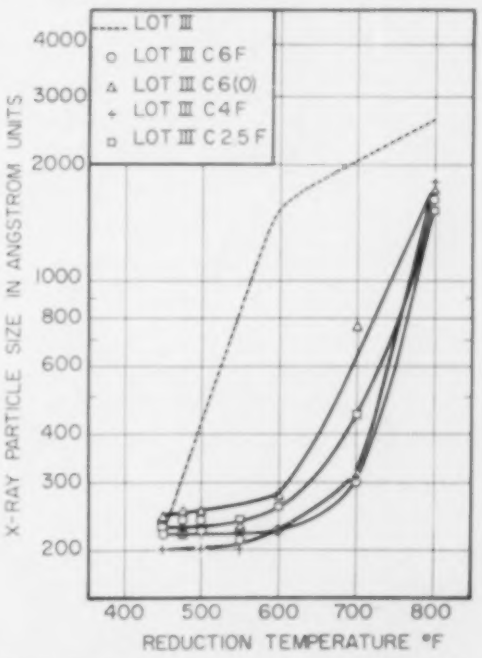

Fig. 7—Variation of particle size with temperature of reduction for powders produced from lot III, ferrous formate plus cadmium formate or cadmium oxide.

result in an upward displacement of the entire $_iH_c$ vs reduction temperature curve and a 50 pct increase in $_iH_c$ (330 to 504 oersteds), Fig. 9. Saturation induction and remanence values approach a maximum at approximately 600°F and then remain relatively constant or decrease slightly with increasing reduction temperature (Fig. 10).

As before, the particle size for a given reduction temperature decreases with increasing tin content until the curve remains virtually horizontal. Even very small amounts of tin exhibit a marked effect upon the diameter of the ultra-fine iron particles produced (Fig. 11).

The upward displacement of the $_iH_c$ curve would appear to be simply a result of a smaller particle size for a given reduction temperature. The sudden decrease in $_iH_c$ at approximately 500°F may be associated with formation of a liquid tin barrier at that temperature which would be expected to coat the partially reduced iron particles. This barrier, by its interference with sintering and diffusion, would account for the lack of further increase in the degree of reduction observed above 600°F (Fig. 12) which in turn accounts for the approximately constant saturation induction and remanence values for a given composition observed above that temperature.

As might be expected, values obtained by the addition of the tin as the oxide, lot III S 5(0), and as the coprecipitated formate, lot III S5F, were in excellent agreement, but are displaced toward the lower temperatures in the case of the oxide due to its higher reducibility in hydrogen.

The maximum energy product $(BxH)_{max}$ obtained from lot III ferrous formate plus tin formate was 0.75×10^6 gauss-oersteds, an increase of 150 pct over lot III and occurred in lot III S5F powder with approximately 5 pct contained Sn, reduced at 550°F

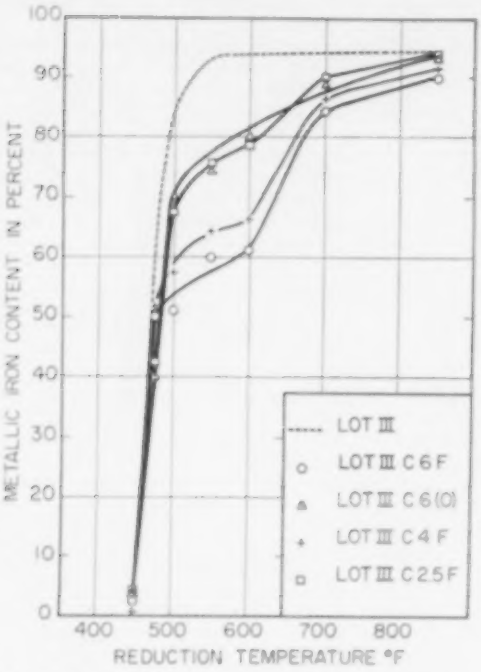

Fig. 8—Variation of metallic iron content with temperature of reduction for powders produced from lot III, ferrous formate plus cadmium formate or cadmium oxide.

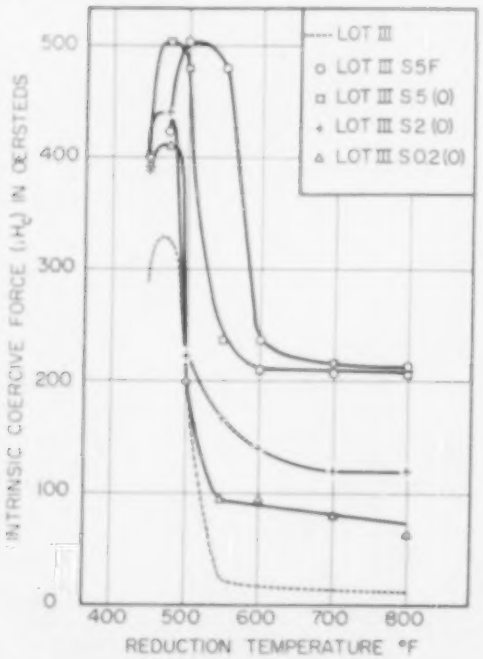

Fig. 9—Variation of intrinsic coercive force with temperature of reduction for compacted powders produced from lot III, ferrous formate plus tin formate or stannous oxide.

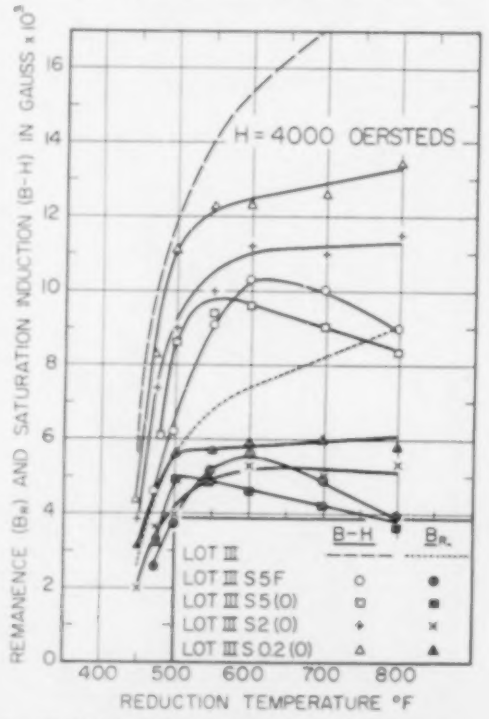

Fig. 10—Variation of saturation induction and remanence with temperature of reduction for compacted powders produced from lot III, ferrous formate plus tin formate or stannous oxide.

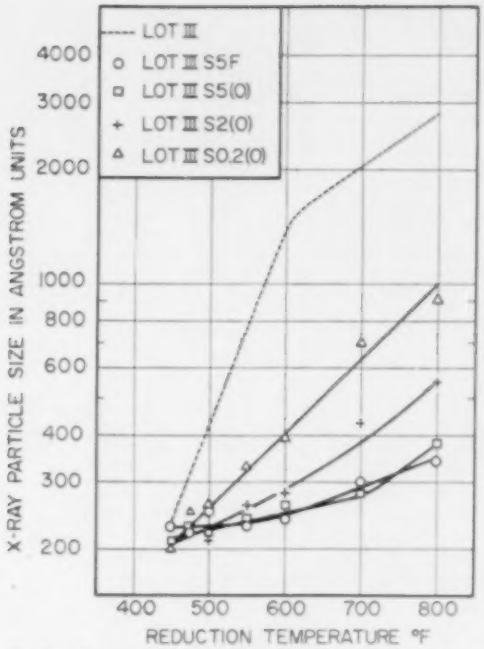

Fig. 11—Variation of particle size with temperature of reduction for powders produced from lot III, ferrous formate plus tin formate or stannous oxide.

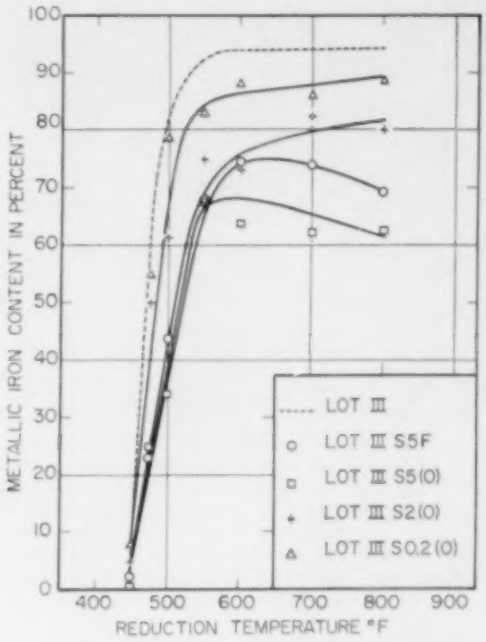

Fig. 12—Variation of metallic iron content with temperature of reduction for powders produced from lot III, ferrous formate plus tin formate or stannous oxide.

for 120 min with a metallic iron content of 69 pct and a density of 4.3 g per cu cm.

Conclusions

A significant improvement in the permanent magnetic properties of ultra-fine iron powder obtained from hydrogen-reduced ferrous formate has been produced by the addition of various metallic compounds prior to reduction. The more important findings of this investigation may be summarized briefly as follows:

1—Magnesium formate, cadmium formate, cadmium oxide, stannous oxide, and tin formate, when added to ferrous formate prior to its reduction, produce effects which differ in detail, but which in general indicate a retardation both in the degree of sintering and the degree of reduction of the ultra-fine iron powder produced at a given reduction temperature.

2—The effect of these additives upon the magnetic properties of the ultra-fine iron compacts are such that the energy product, $(BxH)_{max}$, of these compacts is increased approximately 150 pct over that obtained from the original ferrous formate under comparable reduction and testing conditions.

3—Fine powder permanent magnets possessing energy products of 0.82×10^6 gauss-oersteds, coupled with densities of 4.3 g per cu cm, have been prepared.

4—It appears practical to control effectively both the particle size and metallic iron content of ultra-fine iron powder by use of the correct amount of a given additive to the ferrous formate prior to its reduction.

5—The use of additives facilitates the production of fine iron powder with critical particle size by broadening the range of temperature for successful reduction.

Acknowledgments

The authors would like to thank Dr. Ananthanarayanan whose research provided a background for this work, the Franklin Institute of Research, Philadelphia, for allowing the use of their equipment for magnetic measurements, and the Office of Naval Research for sponsoring the research program which led to these results.

References

[1] C. Kittel: *Physical Review* (1946) **70**, p. 965.
[2] E. C. Stoner and E. P. Wohlfarth: *Nature* (1947) **160**, p. 650.
[3] E. C. Stoner and E. P. Wohlfarth: *Trans.* Royal Society (1948) **A240**, p. 599.
[4] L. Neel: *Comptes Rendus* (1947) **224**, p. 1488.
[5] L. Neel: *Comptes Rendus* (1947) **224**, p. 1550.
[6] L. Weil: International Powder Metallurgy Day, Graz. *No. 17* (July 1948). See also *Metallurgy Powder Report* (1948) **2**, p. 190.
[7] F. Bertaut: *Comptes Rendus* (1949) **229**, p. 417.
[8] L. Neel: *Comptes Rendus* (1949) **228**, p. 664.
[9] W. H. Meikeljohn: *Review of Modern Physics* (1953) **25**, I, p. 302.
[10] F. Lihl: *Acta Physica Austriaca* (1951) **4**, Bd. 4, p. 360.
[11] R. S. Dean and C. W. Davis: United States Patent No. 2,239,144 (applied, July 11, 1938; patented, Apr. 22, 1941).
[12] British Patent 590,392 (Convention date, Apr. 7, 1942).
[13] British Patent 594,681 (Convention date, July 26, 1944).
[14] British Patent 596,875 (Convention date, Aug. 21, 1943).
[15] B. Kopelman: *Electrical Engineering* (1952) **71**, p. 447.
[16] N. I. Ananthanarayanan: Doctora Dissertation, Lehigh University (1953).
[17] A. V. Fraioli and R. N. Rhoda: *Inorganic Synthesis* (1953) **IV**, New York, McGraw-Hill Book Co.
[18] R. L. Sanford and E. G. Bennett: *Journal of Research* National Bureau of Standards (1934) **23**, p. 415.
[19] R. D. Franklin, R. Campbell, and J. Weinman: *Journal of Applied Physics* (1953) **24**, No. 8, p. 1040.

Resistance Sintering Under Pressure

by F. V. Lenel

Resistance sintering under pressure is a method of hot pressing in which a powder compact is subjected to pressure and simultaneously heated by passing a low voltage high amperage current through it. Equipment for this process is described. Its basic characteristics such as resistance requirements for powders and compacts, temperature distribution in compacts, and gas reactions during resistance sintering are discussed. Examples of the sintering process in compacts made of a single metal or an alloy powder and in compacts made of mixtures of powders are presented. Potential commercial applications of the process are evaluated.

THE usual sequence of operations in commercial powder metallurgy is to compact metal powders in a die at room temperature and sinter the compact subsequently without applying pressure while the compact is in the sintering furnaces. In hot pressing, on the other hand, the compacting and the sintering are combined. The loose powder, or in many cases a cold formed compact, is inserted into the die which is held at the hot pressing temperature, the compact is left in the die until it attains its temperature, and then pressure is applied and maintained for a given length of time. The die may be heated by surrounding it with a suitable furnace, by high frequency induction heating, or by passing current through the die. In hot pressing, compacts of high density and good mechanical properties can be produced in a relatively short time.

One of the principal difficulties in hot pressing is the lack of suitable die materials which will have adequate strength at the hot pressing temperature. This difficulty can be overcome at least partially by heating only the material to be hot pressed without heating the die directly. This can be done by passing a low voltage high amperage current through the material and simultaneously subjecting it to pressure. Either loose powders or compacts can be hot pressed by this method in which the desired temperature is produced by the power dissipated in the metal powder. This method of hot pressing has been termed "electrical resistance sintering under pressure." The most significant differences between this operation and conventional hot pressing are: 1—The sintering times are very short, usually a fraction of a second and at most a few seconds. 2—The powder and die are initially cold. 3—Heat is generated within the powder itself and not conducted in from the die. 4—The pressure used is high. 5—Cooling following sintering is rapid, amounting to a quench.

Resistance sintering of metal powders under pressure has been suggested repeatedly. In 1933, G. F. Taylor[1] proposed an apparatus which consisted of an insulating tube made of glass, or a ceramic filled with the powder to be pressed, and plungers above and below the powder. The powder was to be heated by passing an electric current through it and pressure was then applied. The apparatus was intended principally for hot pressing cemented carbides. Although the principle of resistance sintering under pressure is clearly shown in this patent, few details are given. A sintering period of a second or a fraction of a second, which is terminated by the operation of an inertia switch, is mentioned but no values for current density are mentioned. Low pressures, such as atmospheric pressure or a somewhat higher pressure exerted through a lever, are suggested. W. D. Jones[2] discussed electrical resistance sintering under pressure and proposed using resistance welding apparatus for this purpose. In a patent issued in 1944, G. D. Cremer[3] described a method of electrical resistance sintering under pressure using resistance welding apparatus which was to be applied mostly to nonferrous metals such as copper, brass, bronze, and aluminum. Current densities of 400,000 amp per sq in., sintering times of 1 and 2 cycles of 60 cycle current, and pressures of 5 to 10 tsi are proposed. Cremer suggested using an

F. V. LENEL, Member AIME, is Professor of Metallurgical Engineering, Rensselaer Polytechnic Institute, Troy, N. Y.

Discussion on this paper, TP 3883E, may be sent, 2 copies, to AIME by Mar. 1, 1955. Manuscript, Jan. 18, 1954. New York Meeting, February 1954.

electrically conducting die which was to be insulated from the metal powder by coating it with a mixture of aluminum flakes and stearic acid or some other insulating flake coating. W. F. Ross[4] received a patent in 1945 in which the method of resistance sintering under pressure was modified by introducing a gradually increasing pressure and varying current.

Resistance sintering under pressure was studied intensively at Rensselaer Polytechnic Institute during the past few years on the basis of several Navy research contracts. In these studies, it was attempted to gain an understanding of the basic characteristics of the process and to learn in what respect resistance sintering under pressure differs from other powder metallurgy processes. At the same time, the application of resistance sintering to a number of different materials was investigated, such as nickel and cobalt-base high temperature alloys, the refractory metals, molybdenum, titanium, zirconium and some of their alloys, cemented carbides, and other cermets.

This paper will be limited to a discussion of the equipment used and of certain basic characteristics of the process. Specific applications will be used only as examples to illustrate these basic characteristics, but will not be discussed in detail as such. In a final section, potential applications of the sintering process are treated.

Equipment

Machines used in resistance sintering are very similar to spot welding machines. A machine especially adapted to the technique was built by the Precision Welding Machine Co. and is shown in Fig. 1. It consists essentially of two pressure cylinders, one above and one below the work to which two electrodes are attached. Each electrode can be moved separately and independently. The pressure applied to each electrode can be varied by changing the gage pressure of the compressed air admitted to the cylinder up to a maximum load of 17,000 lb. The rate of head travel is also variable up to a very rapid rate. Pressure and rate of head travel are so adjusted that compacts of maximum density are produced. Too low a pressure or too low a rate of head travel will result in incompletely densified compacts. Pressure above a certain minimum, which depends upon the material to be sintered and the other sintering conditions, are of no help in improving the properties of the compact and may distort other components of the sintering assembly.

The electrodes carry the low voltage high current power which is supplied by a welding transformer to the work. The welding transformer in turn is connected to an autotransformer which is also housed inside the body of the machine. The autotransformer is supplied with 600 v single-phase current through a motor-generator set.

Two General Electric thyratron control panels provide control of the sintering sequence and the sintering current. One of the panels is seen in the foreground, the other panel is partially covered by the first one. The sequence timer permits the automatic timing of the following sequence: 1—close electrodes, 2—apply pressure, 3—first pulse of current, 4—maintain pressure with no current flow, 5—second pulse of current, 6—maintain pressure with no current flow, and 7—open electrodes. The current is switched on and off for each of the two current pulses by two sets of ignitron tubes. The sintering time and the interval during which no current flows, usually called "chill time," are expressed in cycles of 60 cycle current, each cycle corresponding to 1/60 sec.

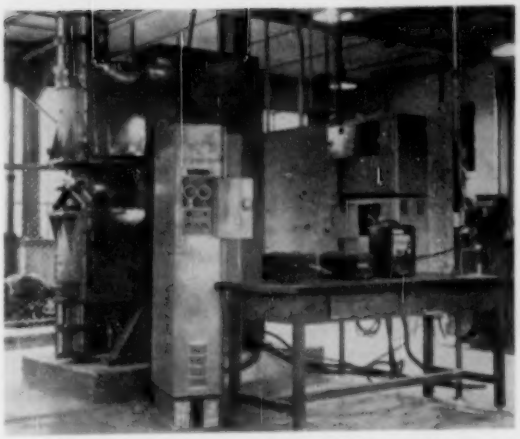

Fig. 1—Photograph of resistance sintering machine.

The amount of current flowing during each pulse can be controlled by phase shifting of thryatron tubes; it is expressed as percentage of full-phase current. The voltage applied during each pulse can be set by proper connection of the ignitron tubes with the taps of the autotransformer, which make it possible to vary the nominal voltage for each pulse from a minimum of 10 to a maximum of 40 v. These tap controls can be seen on the body of the machine. Because of the change in resistance of the compacts during sintering, the current during the sintering pulses generally will vary considerably. If a series of samples is to be sintered and the total heat generated in each of these samples is to be the same, it is not only necessary that the setting controlling the phase shifting of the thyratrons be the same in each case, but also that the initial resistance and the rate of change in resistance in all the samples in the series be the same.

It is sometimes easier to insure constant heat input from sample to sample by using current regulators, which automatically control the firing of the thyratron tubes in such a way that the current remains constant throughout a sintering pulse, provided the changes in resistance are not too great or too rapid. Two current regulators, one for each of the sintering pulses, which can be put into or taken out of the circuit at the option of the operator, can be seen on the right of Fig. 1.

When the current regulators are used, the current to be passed through the sample can be controlled. Current is first passed for at least 30 cycles through a dummy load, its magnitude is read on an Esterline Angus recording ammeter connected to the primary of the transformer, and the current regulator set so that the desired current is passed. This current is then passed through the sample to be sintered. If no current regulator is used and the current therefore varies, an indication of the total heat input may be obtained by means of an ampere squared second meter which reads the product of the time and the integrated square of the current passed through the sample.

A visual record of the current passing through the sample during each cycle of the sintering pulses is provided by a Brush direct-inking magnetic oscillograph connected to the primary of the transformer.

Determination of the total heat input during re-

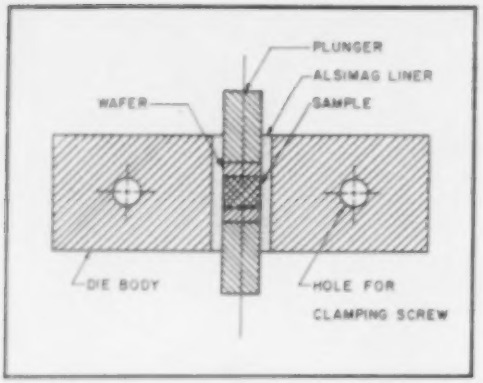

Fig. 2—Schematic sketch of resistance sintering die assembly.

sistance sintering would require measuring the instantaneous values of resistance during current pulses. Such resistance measurements are difficult, since they should include only the actual resistance of the sample but no contact resistances.

A schematic cross-section of the setup for resistance sintering is shown in Fig. 2. The die body made of brass is split for easy opening and inserting of the ceramic liner. Most of the work was done on ½ in. diam cylindrical compacts for which a ¾ in. OD, ½ in. ID ceramic liner of suitable length made of a steatite composition with the trade name "Alsimag 35" is used. The green compact, or in some cases the loose powder, is placed between two so-called wafers which consist of Monel, steel, molybdenum, or tungsten, depending on the material to be sintered. The plungers are made from a high conductivity, high strength copper alloy such as Mallory No. 3 metal. The entire assembly is placed between the electrodes of the spot welder. Pressure is applied and the proper sintering current is passed. The purpose of wafers, which have a higher thermal and electrical resistivity and a higher melting point than the plungers, is to equalize as much as possible the heat distribution within the sample. Without the wafers, the heat would be conducted off too rapidly through the plungers and the ends of the samples would be insufficiently sintered. The sample is removed by unbolting the split die and by cracking open the liner.

This arrangement, which requires a new liner for each sample to be sintered, is satisfactory only for research investigations or in those cases where the cost of the sintered compact is sufficiently high to warrant the use of expendable liners. Experiments have indicated that steatite-type ceramic liner may be satisfactory for repeated use in sintering certain materials if the liners are adequately backed up, for instance, by shrinking them into steel dies. In other cases, the final answer to the liner problem appears to lie in metallic liners having a thin ceramic coating. Considerable additional development work will be necessary to find a solution to the liner problem for each practical application of resistance sintering under pressure.

Resistance of Powder and Compacts

A basic requirement for satisfactory resistance sintering under pressure is a sufficiently low resistance of the material to be sintered, be it the loose powder, the unsintered ("green") compact, or in some cases even a presintered compact.

An essential auxiliary apparatus for resistance sintering therefore is a device for measuring the room-temperature resistance of powders, green compacts, or presintered compacts. Such a device is shown in Fig. 3. It consists of a small laboratory press, a dc current source, 2 electrodes, an ammeter, and a millivoltmeter. Green or presintered compacts can be inserted directly between the electrodes. Loose powders are confined within a nonconducting die during the test. In comparing different lots of a given powder, it is only necessary to determine relative values for the resistance of the powder or compacts under a given pressure, which was chosen at 2500 psi for green compacts and 10,000 psi for loose powder.

The resistance of powder compacts depends upon the bulk resistivity of the material from which it is made and the contact resistances between individual particles. The former cannot be changed, but the latter often can be manipulated. The pressure with which the green compacts are pressed will affect the contact area and therefore the contact resistance between the particles. Particle size and particle-size distribution will have its effect upon contact resistances. Even more important are surface films on many powder particles which may greatly increase the contact resistance. Particularly in powders which are difficult to deform plastically, it is important to remove, if possible, these surface films before attempting to resistance sinter the powders under pressure. Many metal powders therefore are subjected to a reducing treatment in hydrogen before being compacted. Such a treatment has been found very satisfactory for iron, molybdenum, cobalt, nickel, chromium, stainless steel, and other powders. No such treatment is possible in the case of metals such as titanium or zirconium, nor of electrically conducting ceramic powders such as the carbides, nitrides, borides, and silicides of the transition elements. Difficulties were encountered with certain of the ceramic powders which had high resistance in powder form even though the compounds in compact form have low resistivity. This applies to very fine zirconium boride and molybdenum disilicide powders with particle sizes of a few microns. Apparently in the preparation of these powders, a certain amount of oxidation takes place so that surface films of high electrical resistance are formed which make it impossible to resistance sinter the powders even though they can be satisfactorily sintered in conventional hot pressing. When mixtures of ceramics and metals

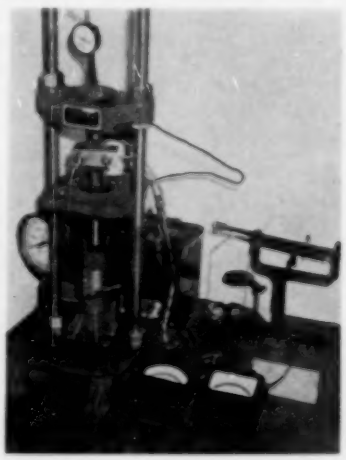

Fig. 3—Apparatus for measuring resistance of powders.

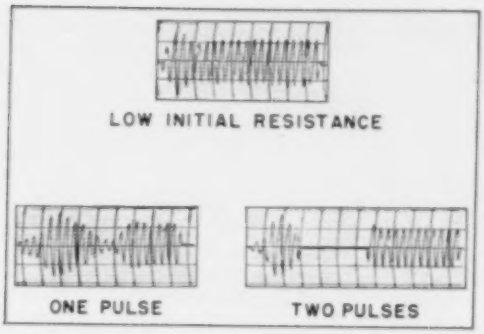

Fig. 4—Brush oscillograph current traces for one and two-pulse resistance sintering. Bottom two traces are for high initial resistance.

are to be sintered in which the ceramic constituent is an insulator, the percentage of the metal constituent has to be high enough so that a continuous path for the electric current through the compact is provided.

Compacts whose resistance in the direction of current passage is of the order of 0.1 ohm or higher (i.e., a resistivity of 0.1 ohm-cm for the material in a ½ in. high, ½ in. diam powder compact) will not pass sufficient current for sintering. If the resistance is somewhat lower down to a range of 0.01 ohm, sintering will still be unsatisfactory because the current will not pass uniformly through the cross-section of the compact. A very small current will pass first through the path of least resistance in the compact. This path will be heated sufficiently to cause a breakdown of resistance. More current will then flow through the path of breakdown which is soon greatly overheated and expelled, while the rest of the compact through which hardly any current passes stays relatively cold.

Compacts whose initial resistance is in the range of several milliohms often will exhibit very large and rapid changes in resistance during sintering. The sintering of these compacts can be controlled better by using two sintering pulses rather than one. Voltage and current for the first pulse are so adjusted that the resistance of the compact breaks down and the time must be just long enough to accomplish this purpose without overheating the compact. The second pulse does the actual sintering.

The advantages of two pulse sintering in compacts having a relatively high initial resistance is illustrated in Fig. 4. This figure shows the current traces of the Brush magnetic oscillograph during the sintering of three iron compacts. The low initial resistance of the first compact is only one fifth as large as the high initial resistance of the second and third which had about the same resistance. All three compacts were sintered using the current regulators. When the low resistance compact was sintered with a single pulse of 20 cycles, the current was essentially constant after the first 3 cycles; in other words, the current regulator effectively compensated for the changes in resistance during sintering. When the second compact was sintered with a single pulse, the changes in resistance were so large and so rapid that the current regulator was unable to follow these changes. Hunting occurred and the current did not become constant until 14 cycles had passed. In sintering a high resistance compact with two pulses of 6 and 12 cycles and a 10 cycle interval in between, the current control was considerably more satisfactory, as the current was essentially constant during the entire second pulse. Sintering with two pulses has also been found very advantageous when no current regulators were used. The setting of the phase-shifting controls for each of the pulses, and if desired also, the voltage setting for each of the pulses must be so adjusted that the desired resistance breakdown occurs during the first pulse and the actual sintering during the second pulse. These adjustments as well as the adjustment of the number of cycles for each pulse and the interval between pulses are generally made by trial and error.

Temperature and Temperature Distribution

Because the sintering times during resistance sintering under pressure are of the order of a fraction of a second, the conventional methods of measuring the temperature and temperature distribution in the compacts, such as thermocouples or optical pyrometers, cannot be used. Whether a compact is satisfactorily sintered or not is generally determined by measuring its density and other physical and mechanical properties and by observing its microstructure. In certain cases the microstructure may give a direct clue to the temperature reached during sintering. If, for instance, two metals such as nickel and chromium which form a eutectic are mixed and sintered and if the eutectic structure can be observed in the microstructure, the temperature must have been at least as high as the eutectic temperature. Where it is desired to have exact knowledge of the temperature distribution within a compact, small metal wires of suitable melting point may be placed in the compact. After sintering, the compact is examined to see whether the wires have melted or not. By using a number of wires with different melting points and placing them at a number of different positions in the compact, a satisfactory picture of temperature distribution can be obtained, although the method is certainly laborious.

Fig. 5 shows the temperature distribution in a sintered iron compact determined in this manner. The maximum temperature in this compact is in the center and a temperature gradient runs from the center to the outside of the compact. The temperature at compact-wafer interface is, to a large extent, a function of the size of the wafer and the electrical and thermal resistivity of the material of which it is made. The lower temperature at the compact-liner interface is to be expected, since the liner is not heated by the current and therefore conducts heat away. As long as the properties at the circumference of the sintered compact are not impaired, this lower temperature is desirable because it keeps the compact from reacting with the liner material at the sintering temperature. In critical cases, it is even possible to grind incompletely sintered material from the outside of the compact.

In metal and alloy powder compacts, particularly when their length is not much larger than their diameter, it is found that the compacts are satisfactory from the point of view of density, micro-

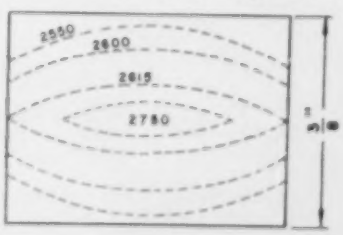

Fig. 5—Temperature distribution in a sintered iron compact. Plast iron, 15 ka, 20 cycles.

Table I. Comparison of Properties of Resistance Sintered, Conventionally Sintered, and Arc-Cast Titanium

Raw Material	Treatment	Tensile Strength, Psi	Elongation, Pct	Reduction in Area, Pct
Titanium sponge	Arc-cast, rolled, and annealed	80,000	25	55
Bureau of Mines titanium powder	Conventionally sintered in vacuum, rolled, and annealed	82,000	28	—
du Pont titanium sponge	As-resistance sintered under pressure	62,200	25.6	39.5
Bureau of Mines titanium powder	As-resistance sintered under pressure	91,000	5.2	—

structure, and mechanical properties even if a certain temperature gradient exists during sintering. Sintering experiments with certain cermets showed that in these materials an even temperature distribution is very critical, apparently because the temperature range within which these materials can be sintered is relatively narrow. The resistance sintering experiments on a titanium carbide cermet illustrate this point. The mixture to be sintered consisted of 80 pct of titanium carbide containing a minor proportion of columbium and tantalum carbide and 20 pct nickel corresponding to the grade K 151 A of Kennametal Inc. The powder was mixed with 1 pct of stearic acid in order to facilitate the handling of the green compacts. The mixture was cold pressed into a 5 g ½ in. diam compact at 25 tsi, heated very slowly in a graphite container to 1000°F in order to drive off the stearic acid, and then presintered for 1 hr at 2300°F in hydrogen. This presintering treatment reduced the resistance of the compact and therefore made it easier to resistance sinter. It also facilitated handling the compact. It was shown previously that a compact sintered between flat wafers is hotter in the center of the compact than on its outside. In order to equalize more nearly the temperature within the cemented titanium carbide compact, it was sintered between one flat wafer and one concave wafer. This arrangement, in effect, causes an uneven distribution of the current over the circular cross-section of the sample. More current will flow near the edge where the path of the electrical current is shorter than will flow through the center where the path is longer. Therefore, more heat will be developed near the edge, but the excess amount of heat is conducted off through the wall of the liner and the overall temperature distribution is more even. Considerable work was necessary to find the best curvature for resistance sintering the 5 g ½ in. diam titanium carbide cermet compacts. Whether a given wafer shape gave satisfactory compacts or not was evaluated by determining the hardness distribution throughout the compact. For this purpose, the compacts were ground flat on either side and hardness traverses were run across their diameter. Then additional grinding cuts were taken and new traverses were run. The result for the best titanium carbide cermet compacts is shown in Fig. 6.

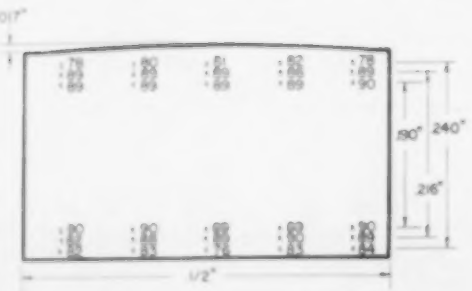

Fig. 6—Hardness distribution in a resistance sintered titanium carbide cermet compact. R A hardness readings.

It will be seen that near the surface there are still numerous soft spots which correspond to porous or insufficiently sintered areas, but that further inside the compact the hardness was quite uniform and of the same magnitude as for conventionally sintered compacts of this same composition. The thermal shock resistance and the oxidation resistance of the powder compacts were also equal to that of conventionally sintered material. In order to make strength tests, rectangular compacts ⅛x⅛x1 in. were resistance sintered. These compacts however were not as uniform in hardness as the cylindrical compacts. Therefore it is not surprising that they also were not equivalent in modulus of rupture.

Gas Reactions During Resistance Sintering

One of the most striking consequences of the very short resistance sintering times is the possibility of sintering, without atmosphere protection, metals which react readily with gases. This is illustrated by experiments on resistance sintering titanium and zirconium metal powders, both of which react very rapidly at elevated temperatures with hydrogen, nitrogen, and oxygen. The conventional sintering of cold-pressed titanium and zirconium metal powder compacts is performed therefore in high vacuum.[1, 2] Resistance sintering experiments on titanium were performed on titanium metal powder and titanium sponge. The powder was obtained from the United States Bureau of Mines and had been prepared by acid leaching of the reaction product between titanium tetrachloride and magnesium metal. The titanium sponge samples had been prepared by E. I. du Pont de Nemours and the National Lead Co. by purification through vacuum distillation of the reaction product between titanium tetrachloride and magnesium metal.

A typical treatment for both sponge and powder compacts yielding compacts of 4.50 to 4.54 g per cc density, 99 to 100 pct of theoretical, was as follows: the powder or sponge was cold-pressed at 35 tsi into green compacts weighing 7 g each. Three of these compacts were resistance sintered in tandem with a sintering pressure between 7½ and 10 tsi, 11 ka current, and a sintering sequence of 10 cycles on, 10 cycles off, 10 cycles on using the current regulator. The sintered compacts were ½ in. in diam and approximately 1¼ in. long. For determining the tensile properties, the compacts were machined into subsize specimens with a gage length of ¾ in. and a gage diameter of 0.160 in. The properties of specimens even when they were resistance sintered from the same lot of titanium powder or sponge exhibited a fairly wide variation. Some typical results of tensile tests are compared with those on conventionally sintered and on arc-cast titanium in Table I. It will be seen that the resistance sintered Bureau of Mines powder compacts were much less ductile than the resistance sintered sponge titanium compacts. These latter compacts were as ductile although not quite as strong as commercial arc-cast titanium or conventionally sintered, cold rolled, and annealed Bureau of Mines powder compacts. Differences in impurity content of the raw materials, the sponge being purer than the powder, may have contributed to the

Fig. 7—Inclusion in resistance sintered compact from Stellite 30 alloy powder. X500. Area reduced approximately 35 pct for reproduction.

Fig. 8—Resistance sintered compact from Bureau of Mines titanium powder. X200. Area reduced approximately 35 pct for reproduction.

Fig. 9—Resistance sintered compact from du Pont titanium sponge. X250. Area reduced approximately 35 pct for reproduction.

difference in ductility between the resistance sintered sponge and powder compacts. The principal reason for the ductility difference and also for the variation from lot to lot is, however, the difference in the amount of impurities picked up from adsorbed or occluded gases during resistance sintering. More of the gases are contained in compacts made from powders which have a relatively high specific surface than in compacts from sponge with a low specific surface.

This explanation was confirmed by experiments on resistance sintering zirconium metal powder. The zirconium powder used was obtained from Sylvania Electric Products Inc. and had been prepared by converting zirconium "crystal bars" (zirconium from the thermal decomposition of zirconium iodide) into zirconium hydride and decomposing this hydride into zirconium metal powder. This powder had not come into contact with air, but was shipped under argon. From this powder, compacts were prepared by cold compacting in air followed by resistance sintering in air on the one hand and, on the other hand, by cold compacting in a dry box in an atmosphere of argon without letting the powder get in contact with air until just before the green compact was resistance sintered, and then resistance sintering in air.

The cold compacting and resistance sintering conditions were otherwise identical: 10 g samples of powder were cold compacted into ½ in. diam cyclindrical specimens under a pressure of 35 tsi and resistance sintered with a pressure of 8 tsi, 11 ka current, and a sintering sequence of 6 cycles on, 5 cycles off, 11 cycles on using the current regulator. The ductility of the compacts was tested by grinding them into rectangular bars with a ⅜ in. square cross-section, cold rolling them between flat rolls with reductions of 1 and 2 pct per pass, and noting at what percentage of reduction in thickness the first cracks appeared. The results in Table II are compared with those of Hausner[5] on zirconium hydride compacts conventionally sintered in a vacuum into sintered zirconium. It is obvious that the compacts cold pressed in air were much less ductile than the ones pressed in argon. Evidently, the air adsorbed and occluded during cold pressing reacted with the metal during resistance sintering, causing it to become brittle. If air was excluded during compacting, the compacts could be cold rolled 30 to 40 pct before edge cracking, which is only slightly less than Hausner's compacts.

The absence of a protective atmosphere, or more particularly a reducing atmosphere, in resistance sintering under pressure means, of course, that any oxides present in the compact will not be reduced and thus will be present in the sintered part. This indicates again how necessary it is to treat carefully before resistance sintering those metal powders whose oxides can be reduced. Fig. 7 clearly demonstrates this point. It shows oxide inclusions in a specimen sintered from an alloy powder having the composition of alloy 422-19, Stellite 30, which contains nominally 25 pct Cr, 16 pct Ni, 6 pct Mo, 0.4 pct C, and the balance cobalt. It is interesting to note that a certain amount of spheroidization of the inclusions seems to have taken place in spite of the short sintering time. Nevertheless, such oxide networks constitute a path of weakness in the compact and are one of the reasons for the inferior properties sometimes observed in compacts resistance sintered under pressure.

Rapid Cooling of Resistance Sintered Compacts

Rapid cooling after sintering is one of the basic characteristics of resistance sintering under pressure. It may be illustrated by micrographs of titanium and zirconium compacts in the "as-sintered" condition, which means that they were effectively quenched from above the transformation temperature. Figs. 8, 9, and 10 show the structure of compacts from Bureau of Mines titanium powder, du Pont titanium sponge, and Sylvania zirconium powder. All samples exhibit the typical Widmanstaetten structure of quenched titanium and zirconium. It is particularly pronounced in the Bureau of Mines titanium powder which has reacted with adsorbed and occluded atmospheric impurities during resistance sintering.

Sintering Process in Single Metal or Alloy Powder Compacts

When cold pressed compacts of a single metal powder or an alloy powder are sintered without the application of pressure, the initial interparticle bonds formed during pressing at points of contact grow laterally, and the total volume of void space is decreased by the rapid movement of metal into

Table II. Comparison of Properties of Conventionally and Resistance Sintered Zirconium

Treatment	Density	Hardness, R_A	Pct Reduction in Thickness Upon Cold Rolling When First Edge Cracks Appeared
Zirconium hydride powder conventionally sintered in vacuum	6.50	—	53 to 72
Zirconium powder compacted in air and resistance sintered under pressure in air	6.48 to 6.52	60	0½ to 3
Zirconium powder compacted in argon and resistance sintered under pressure in air	6.54 to 6.60	56½ to 57	32 to 42

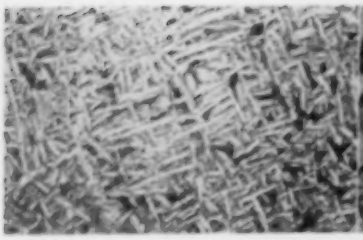

Fig. 10—Resistance sintered zirconium powder compacts. X600. Area reduced approximately 35 pct for reproduction.

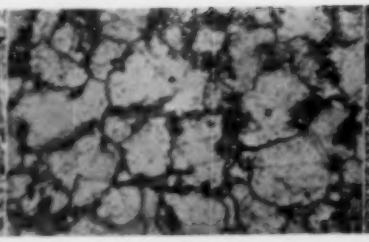

Fig. 11—Typical grain size of resistance sintered compact from Stellite 30 alloy powder. X1000. Area reduced approximately 35 pct for reproduction.

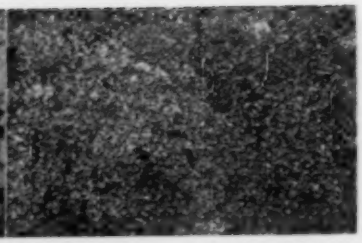

Fig. 12—Resistance sintered molybdenum powder compact with fine grain size. X100. Area reduced approximately 35 pct for reproduction.

Fig. 13—Resistance sintered molybdenum powder compact with medium grain size. X100. Area reduced approximately 35 pct for reproduction.

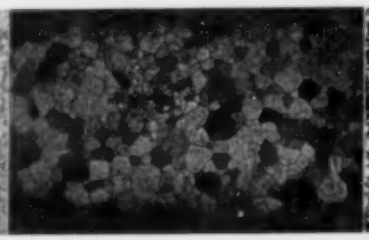

Fig. 14—Resistance sintered molybdenum powder compact with coarse grain size. X100. Area reduced approximately 35 pct for reproduction.

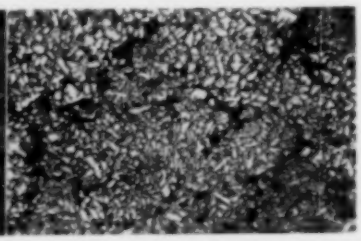

Fig. 15—Dendritic structure in atomized brass powder. X500. Area reduced approximately 35 pct for reproduction.

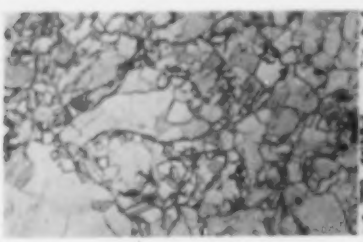

Fig. 16—Resistance sintered brass powder compact. X500. Area reduced approximately 35 pct for reproduction.

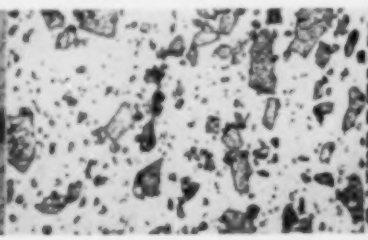

Fig. 17—Resistance sintered compact of 80 pct Ni, 20 pct Cr. Lowest energy input. X100. Area reduced approximately 35 pct for reproduction.

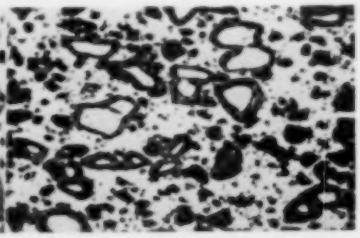

Fig. 18—Resistance sintered compact of 80 pct Ni, 20 pct Cr. Next to lowest energy input. X100. Area reduced approximately 35 pct for reproduction.

regions of sharp curvature next to the bonds. Because surface tension, the driving force, is greatest where the curvature is greatest, the pores spheroidize and the smaller ones disappear as sintering progresses. Recrystallization and grain growth begin at the bonds between particles where the deformation has been most severe. Grain growth is first confined within individual particles until the continuity of the metal has been increased by spheroidization and disappearance of voids, at which time considerable grain growth occurs. Any unreduced oxides or other nonmetallic inclusions usually spheroidize during sintering. During ordinary sintering, therefore, a powder compact changes from a group of particles held together by bonds at the points of contact and surrounded by a nearly continuous network of voids to a dense continuous metal with equiaxed grains, spheroidized, evenly distributed pores, and spheroidized inclusions.

In hot pressing, it is the applied stress rather than surface-tension forces which promotes densification of the compact. If temperature and pressure are high enough, complete densification may be expected in a very short time. In electrical resistance sintering under pressure, compacts of high density could be prepared if a suitable current, which means a sufficiently high sintering temperature, was chosen. This is illustrated in Table III which shows how the density of molybdenum compacts, which are resistance sintered under pressure, increases with increasing current inputs. For purpose of comparison, the density of molybdenum bars prepared by the classical method of resistance sintering refractory metals without pressure is also given.

When cylindrical compacts, which have a ratio of length to diameter of not more than 1, were resistance sintered under pressure, it was always found possible to obtain densities of 98 pct of theoretical and higher even in the case of refractory metals like molybdenum or refractory alloy powders like Stellite 30. If the ratio of length to diameter was larger than 1, difficulties were encountered with the refractory alloy powder Stellite 30. In order to produce a specimen long enough for stress-rupture testing, three green compacts ½ in. diam and ½ in. long were sintered in tandem choosing a power input just short of melting the specimen. The resulting compacts had densities of 8.33 to 8.34 g per cc which are 99.2 to 99.3 pct of theoretical and would appear quite satisfactory. However, when these compacts

were machined into test specimens, the density decreased to 8.12 to 8.15 g per cc which indicated that the porosity in the compacts was concentrated in its center and therefore impaired their strength properties.

When recrystallization and grain growth during conventional sintering and during hot pressing are compared, both favorable and unfavorable factors are evident. Since, during hot pressing, extensive contact between powder particles is more rapidly established, grain growth becomes possible at an earlier stage than in sintering without pressure. On the other hand, the shorter sintering times in hot pressing, and particularly in resistance sintering under pressure, will be unfavorable to grain growth. The grain size of compacts resistance sintered under pressure is therefore generally small. As an example, the microstructure of a Stellite 30 alloy powder compact with a grain size of $\frac{1}{2}\times10^{-4}$ mm is shown in Fig. 11. In this case a larger grain size would have been desirable, since Grant[7] found that precision cast cobalt-base high temperature alloys have increasing high temperature strength with increasing grain size up to a grain size of 12 to 14 grains per specimen cross-section.

Occasionally, grain growth was observed even though the sintering times were very short. For the case of molybdenum powder, this is shown in Figs. 12, 13, and 14. These are microstructures of sections of three compacts from the same powder resistance sintered under pressure, 10 cycles at 20 ka, 20 cycles at 20 ka, and 20 cycles at 28 ka, respectively. The grain size of the specimen, Fig. 12, is about the same as the particle size of the molybdenum powder, but increasing amounts of grain growth have occurred in the other two specimens. To produce grain growth such as in the specimen Fig. 14, the sintering temperature must have been very near but yet below the melting point of molybdenum. Temperature control close enough to produce such large grain sizes reproducibly throughout an entire compact and from compact to compact generally is not feasible.

Sintering Process in Compacts Made of Mixtures of Powders

If a homogeneous alloy is produced by sintering a compact made from a mixture of elemental metal powders, homogenization takes place through diffusion in the solid state. In powder compacts with the usual particle-size distribution from a few microns to about 150 microns, the diffusion taking place during the very short sintering times of resistance sintering under pressure is insufficient to accomplish homogenization even at temperatures just below the appearance of a liquid phase. In order to achieve a considerable degree of alloying between the metal powders in the mixture, the compact has to be heated high enough so that a liquid phase is formed. Experiments which illustrate this point were conducted on compacts consisting of iron powder plus graphite. Copper wires which melt about 85°F below the eutectic temperature for the Fe-C system were imbedded in the compact to serve as temperature indicators. Only in compacts where the compact had melted was there any appreciable quantity of pearlite formed, indicating that diffusion of carbon into the iron took place only near or above the eutectic temperature.

Table III. Density Comparison of Molybdenum Compacts Resistance Sintered With and Without Pressure

Treatment	Relative Density, Pct
Resistance sintered under 5 tsi pressure, 20 ka current, 20 cycles	92.5
Resistance sintered under 5 tsi pressure, 22 ka current, 20 cycles	94.6
Resistance sintered under 5 tsi pressure, 24 ka current, 20 cycles	97.6
Resistance sintered without pressure	90 to 92

This does not mean that no solid-state diffusion at all takes place during resistance sintering under pressure, but only that distances over which diffusion can be observed are very short and that the degree of homogenization is limited. An example for such short-range diffusion during resistance sintering is shown in Figs. 15 and 16. In Fig. 15 the microstructure of an as-pressed but unsintered 70 pct Cu-30 pct Zn brass alloy powder compact is shown which clearly shows the cored dendritic structure of the atomized powder. In Fig. 16, which represents a resistance sintered compact of the same brass powder, the homogeneous equiaxed structure of annealed brass is apparent. The dendrite cell size in the atomized brass powder particles is only 2 to 5 microns and the variation in composition would probably be only 10 to 15 pct. The diffusion therefore is indeed quite short range.

When the sintering temperature is raised sufficiently so that a liquid phase is formed, structures can be produced by resistance sintering which combine high density with any desired degree of inhomogeneity. This is illustrated by the microstructures in Figs. 17 to 20 for compacts from a mixture of 80 pct Ni and 20 pct Cr, which were resistance sintered under a series of increasing energy inputs, ranging from 16 ka at 10 cycles to 25 ka at 10 cycles for ½ in. diam, ½ in. long samples. In the microstructure of Fig. 17, no reaction has yet taken place between the chromium which is attacked by the elec-

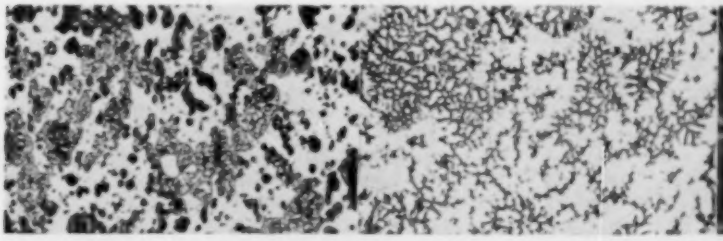

Fig. 19—Resistance sintered compact of 80 pct Ni, 20 pct Cr. Next to highest energy input. X100. Area reduced approximately 35 pct for reproduction.

Fig. 20—Resistance sintered compact of 80 pct Ni, 20 pct Cr. Highest energy input. X100. Area reduced approximately 35 pct for reproduction.

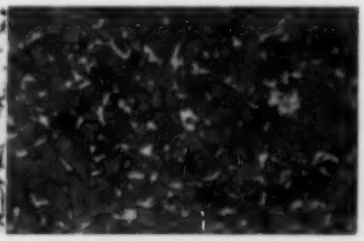

Fig. 21—Compact of 90 pct WC-10 pct Co with 50 pct —20 micron, 50 pct —3 micron WC. Conventionally sintered. X1500. Area reduced approximately 35 pct for reproduction.

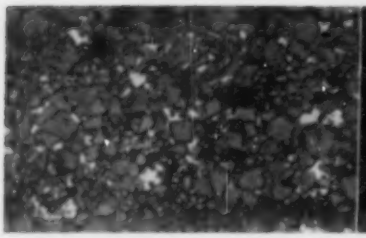

Fig. 22—Compact of 90 pct WC-10 pct Co with 50 pct —20 micron, 50 pct —3 micron WC. Resistance sintered. X1500. Area reduced approximately 35 pct for reproduction.

Fig. 23—Resistance sintered compact of 92 pct WC-8 pct Co. Low energy input. X1500. Area reduced approximately 35 pct for reproduction.

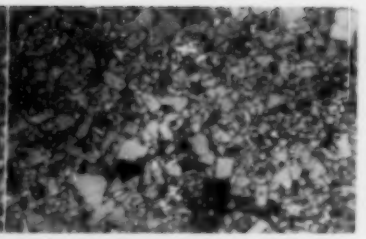

Fig. 24—Resistance sintered compact of 92 pct WC-8 pct Co. Excessively high energy input. X1500. Area reduced approximately 35 pct for reproduction.

trolytic chromic-acid etch and the nickel which is unattacked. In the compact represented by Fig. 18, the temperature has been raised above the Ni-Cr eutectic temperature and a liquid has been formed at the Ni-Cr interface which solidifies as the dark-etching eutectic surrounding the chromium particles. In the microstructure Fig. 19, all but the largest chromium particles have been dissolved in the liquid phase and the constituents are a matrix of nickel which remained solid during sintering and the dendrites representing the liquid phase during sintering. In Fig. 20, the entire structure was liquid during sintering and solidified in the typical cored dendritic structure of a cast solid-solution alloy.

It may be well to emphasize that it is generally not practical to resistance sinter compacts which become entirely liquid during sintering. A higher percentage of liquid phase can be tolerated in resistance sintering under pressure than in conventional hot pressing because a rather viscous, partly liquid, partly solid compact will not readily squeeze out or expel between punch and die lining during the very short sintering time. However, when the entire compact is liquid, expulsion generally can not be prevented.

Resistance sintering under pressure can also be applied to systems, which are conventionally sintered at a temperature between the solidus and the liquidus, such as the cemented tungsten carbides. During conventional sintering, the final densification of these alloys is accomplished by a process of solution and reprecipitation of the carbide phase in the binder. In resistance sintering, the densification is due to the applied pressure and the solution and reprecipitation during the very short sintering time can be minimized. This is illustrated in Figs. 21 and 22. Both figures represent microstructures of compacts having a composition of 90 pct WC and 10 pct Co, the WC powder being a mixture of 50 pct material with a maximum particle size of 3 microns and 50 pct material with a maximum particle size of 20 microns. The structure in Fig. 21 was obtained by conventionally sintering a 7 g ½ in. diam compact for 90 min at 2640°F, while the structure in Fig. 22 was obtained by resistance sintering a compact of the same size without the current regulator under a pressure of 9 tsi and with a sintering sequence of 5 cycles on with 45 pct of full-phase heat, 30 cycles off, and 7 cycles on with 45 pct full-phase heat. Both compacts have a density of 14.5 g per cc and a hardness of Ra 88. It is apparent that much less growth of the fine carbide particles has taken place in the resistance sintered than in the conventionally sintered sample. On the other hand, if the current input is such that high sintering temperatures are reached during resistance sintering, it is possible to make the carbide particles grow even though the sintering time is very short. This is illustrated in Figs. 23 and 24, which show the microstructure of two compacts pressed from the same carbide-powder mixture of 92 pct WC and 8 pct Co. The compact in Fig. 23 was resistance sintered 10 cycles at 13 ka, while the one in Fig. 24 was resistance sintered 20 cycles at 16 ka. This latter treatment overheats the cemented carbide compact and results in lower density and the formation of graphite by decomposition of WC.

Potential Applications of Resistance Sintering Under Pressure

The basic characteristics of resistance sintering under pressure have been discussed in the preceding sections. It may be well to point out those features of the process which distinguish it from other powder metallurgical processes. They may eventually lead to commercial applications, but they also involve obstacles which may prevent exploitation.

Resistance sintering under pressure demands precise electronic controls in order to regulate the time of each of several current pulses and the amount of current flowing during each pulse. Even when these controls are available, extensive experimentation is usually necessary to work out the optimum conditions for sintering.

The size of parts sintered by this method is limited. Most of the ½ in. diam specimens sintered at Rensselaer Polytechnic Institute required currents of 5000 to 25,000 amp or current densities of 25,000 to 125,000 amp per sq in. for sintering them in 10 to 30 cycles. It has been shown that larger parts up to 3 in. in diameter can be resistance sintered under pressure when the sintering times are lengthened to several seconds and a sufficiently large power source is available; nevertheless, this size limitation must be considered.

Most of the specimens sintered were either cylinders or rectangular shapes. Even in these simple parts which have uniform thickness in the direction of pressing and of current passage, problems are encountered in obtaining uniform temperature distribution. It is therefore probable that the new method of sintering will always be confined to relatively simple shapes.

The most outstanding feature of resistance sintering under pressure is the very short sintering time necessary to produce dense compacts. This short sintering time may be used directly to speed up the production of sintered compacts. A rotating table with positions for cold compacting, for loading the die, for resistance sintering, and for unloading may be visualized. The plungers and wafers used in sintering would be made integral with the electrodes,

so that the entire process could be made automatic. The process thus may be applied to a more rapid production of inserts for cemented carbide cutting tools. The most serious problem still to be solved for this as for any other application would be a suitable liner material.

The short sintering time in resistance sintering under pressure may be used to arrest certain undesirable reactions, as for instance that between the reactive metal powders, titanium and zirconium, and atmospheric gases so that compacts of these metals can be sintered in air. Also included in this group of arrested reactions would be sintering into dense compacts of a combination of materials one of which is unstable at high temperature. It may be possible to make the time at temperature so short that decomposition or sublimation of the unstable material is suppressed. Combinations of diamonds and nickel powder sintered at temperatures near the melting point of nickel without decomposition of the diamonds might be considered or combinations of molybdenum and chromium sintered near the solidus of the alloy without excessive sublimation of the chromium.

One of the greatest problems in hot pressing is to find a die material which will stand up at high temperatures and will not react with the hot pressed compact. Because of the short sintering time in resistance sintering, the demands on high temperature strength and chemical inertness of the refractory liners which serve as dies and are only heated by conduction from the compacts may be more easily met, although the additional problem of thermal shock may be introduced. The resistance sintering method therefore should be particularly applicable to producing solid bodies from powders having high melting points which have to be sintered at high temperatures. One standard method of sintering the refractory metals is by resistance sintering but without the application of pressure. As outlined previously, molybdenum can be resistance sintered to considerably higher densities under pressure than without. Whether this possibility will become of commercial interest depends on the question whether there is a demand for the relatively small dense parts of simple shape which are suitable for the method.

Other powders which have to be sintered at high temperatures are the electrically conducting refractory carbides, nitrides, borides, and silicides and their mixtures with metal powders. In resistance sintering these materials, the problems of adequate electrical conductance of the powders and of achieving even temperature distribution are particularly acute, as have been outlined heretofore. Where these problems can be solved, parts may be resistance sintered if they have suitable sizes and shapes.

One of the most interesting characteristics of resistance sintering is the possibility of producing high density compacts in which the process of alloy formation is arrested at a desired stage as was illustrated for Ni-Cr alloys. There is a good chance that such dense compacts having a particular degree of inhomogeneity may have unexpected properties which cannot be achieved by more conventional processing methods. Only very few of the innumerable combinations of incompletely alloyed materials were investigated at Rensselaer Polytechnic Institute. Partially alloyed compacts having the composition of Stellite 30 alloy were produced from elemental powders. Their stress-rupture strength was, however, poorer than that of more homogeneous compacts made from alloy powder. Another attempt to make use of arrested alloy formation was made in the preparation of cemented tungsten carbides with iron and nickel as binders on the basis of the following reasoning: The combination of strength, toughness, and cutting ability in carbides with cobalt as a binder is due to the fact that the carbides which are dissolved in the cobalt matrix during sintering are completely reprecipitated during cooling so that the finished product consists of carbide particles in a matrix of pure cobalt. Iron and nickel are unsatisfactory as binders in conventional sintering because, after dissolving the carbides, they do not precipitate them completely upon cooling, leaving a hard and brittle rather than a soft and ductile matrix in the finished product. If the solution of the carbides in the iron or nickel binder phase could be effectively prevented during the short resistance sintering time, a structure of carbides in a matrix of pure iron or nickel should result, similar to that of carbides with cobalt as a binder.

This reasoning assigns the unsatisfactory behavior of nickel and iron as binders entirely to the fact that the binder metals are soluble in and form complex carbides with tungsten carbide and does not take into account the matter of interfacial tension forces between carbide and binders. The attempt to produce satisfactory cemented carbides with iron and nickel as binders was unsuccessful judging from the comparative properties of the cemented carbides, but the reasons for this lack of success have not yet been ascertained. In these two cases, it was not possible to produce materials with superior properties by making use of arrested alloy formation. Nevertheless, it is entirely possible that the most successful applications of resistance sintering under pressure may yet be found in this field.

Acknowledgments

This work was conducted under Navy Bureau of Ships Contract NObs 31493. Some of the results obtained in work under Navy Bureau of Aeronautics Contract NObs 51005 and Navy Bureau of Ships Contract NObs 55219 are also included in this paper. Permission to publish this work is appreciated.

The author wishes to acknowledge the contributions of the following men who as graduate students assisted in this work: W. D. Doty, W. F. Moore, J. H. Westbrook, M. H. Binstock, W. E. Seymour, D. A. Vermilyea, M. Hill, A. Lesnewich, N. F. Hopson, A. B. Backensto, Jr., O. W. Reen, R. R. Turk, F. H. Domina, M. Weissmann, and M. F. Hoffman.

References

[1] G. F. Taylor: Apparatus for Making Hard Metal Compositions. United States Patent No. 1,896,854 (February 7, 1933).

[2] W. D. Jones: *The Metal Industry* (January 1940) p. 69; (March 1940) p. 225.

[3] G. D. Cremer: Powder Metallurgy. United States Patent No. 2,355,954 (August 15, 1944).

[4] W. F. Ross: Method and Apparatus for Making Solid Objects from Metal Powders. United States Patent No. 2,372,605 (March 27, 1945).

[5] R. S. Dean, J. R. Long, F. S. Wartman, and E. L. Anderson: Preparation and Properties of Ductile Titanium. *Trans.* AIME (1946) **166**, p. 369; METALS TECHNOLOGY (February 1946).

[6] H. H. Hausner, H. S. Kalish, and R. P. Angier: Powder Metallurgy of Zirconium. *Trans.* AIME (1951) **191**, p. 625; JOURNAL OF METALS (August 1951).

[7] N. J. Grant: *Trans.* ASM (1947) **39**, p. 335.

Physical and Mechanical Properties of Rhenium

by Chester T. Sims, Charles M. Craighead, and Robert I. Jaffee

The fabrication of rhenium metal by powder metallurgy techniques is discussed. The following physical and mechanical properties have been measured and are reported: lattice constants, melting point, electrical resistivity, thermal expansion, spectral emissivity, modulus of elasticity, tensile properties and ductility at room and elevated temperatures, work hardening, recrystallization, grain growth, and oxidation resistance.

IT is only occasionally that a metal reaches present-day technology with as little known about its properties as element No. 75, rhenium. Relatively scarce to date, it has been studied only infrequently and used less. Previous work on rhenium has been carried out primarily by European scientists. However, realization that rhenium occurs in commercial quantities in the United States recently has focused attention on this metal.

Rhenium is a very dense high melting hexagonal-close-packed metal. Like tungsten and molybdenum, its highest oxide is volatile. However, when protected by reducing or inert atmospheres, its strength at high temperatures is greater than that of tungsten. Rhenium work hardens more than any other known pure metal, but, on annealing, becomes quite soft and ductile. Its vapor pressure is approximately that of tantalum, but it does not enter into the so-called "water cycle" nearly as readily as does tungsten. (The water cycle is a deleterious phenomenon causing blackening of lamp bulbs and vacuum tubes with subsequent failure of the filaments.)

These and other properties, some already known and some found as a result of the current researches, have indicated that rhenium has many potential uses, primarily of an electrical or electronic nature. Rhenium or its alloys soon may be found in service as electron-tube filaments, cathodic emitters, or as electrical contact materials. In addition, rhenium or its alloys have potential use in such devices as high temperature thermocouples, and high wear-resistant parts such as precision instrument points.

C. T. SIMS, C. M. CRAIGHEAD, and R. I. JAFFE, Member AIME, are associated with Nonferrous Physical Metallurgy Div., Battelle Memorial Institute, Columbus, Ohio.

Discussion on this paper, TP 3847E, may be sent, 2 copies, to AIME by Mar. 1, 1955. Manuscript, Apr. 26, 1954. Chicago Meeting, November 1954.

Table I. Spectrochemical Analyses of Ammonium Perrhenate and Rhenium

Element*	Pct Present	
	Ammonium Perrhenate, As-Purified	Rhenium Reduced from Ball-Milled Ammonium Perrhenate
Aluminum	0.004	0.094
Calcium	Not found	0.017
Copper	0.0003	0.0021
Iron	0.0030	0.024
Magnesium	0.005	0.038
Manganese	Not found	0.002
Silicon	0.005	0.028
Total analyzed impurities	0.017	0.205

* Elements checked but not found: antimony, arsenic, barium, beryllium, bismuth, boron, cadmium, chromium, cobalt, columbium, gallium, germanium, gold, lead, molybdenum, nickel, platinum, potassium, sodium, strontium, tellurium, titanium, tungsten, vanadium, zinc, zirconium, and silver.

Preparation and Fabrication

Rhenium, in the form of potassium perrhenate, was made available for this study by the Kennecott Copper Corp. The potassium perrhenate was reduced to rhenium metal in two stages, accompanied by leaching to remove potassium in the form of hydroxide. This impure metal was then oxidized to rhenium heptoxide and dissolved in water. The solution was neutralized with ammonium hydroxide to produce highly purified ammonium perrhenate, a typical analysis of which is shown in Table I. The ammonium perrhenate was ground to −325 mesh in a rubber-lined ball mill with Burundum balls. This operation caused a certain amount of impurity pick-up, as reflected in the rhenium analysis shown in Table I. The fine ammonium perrhenate was reduced to metal with hydrogen. Particle size of the powder ranged from 1 to 25 microns, as illustrated by Fig. 1.

Table II. Vacuum Fusion Analyses of Three Types of Rhenium

Type of Rhenium	Pct Present		
	Hydrogen	Oxygen	Nitrogen
Vapor deposited*	0.00014	0.0009	<0.0008
Arc melted†	0.00010	0.0010	<0.0002
Fabricated from sintered bar††	0.00006	0.0006	<0.0005

* Rhenium deposited on a tungsten wire by decomposition of a rhenium halide at elevated temperatures.
† Vapor-deposited rhenium bar, cut and arc melted.
†† Rhenium metal powder of the type reported in Table I.

Rhenium in the form of vapor-deposited wire, formed by the decomposition of a rhenium halide on a hot tungsten wire, was used for experimental purposes in some instances. Arc-melted rhenium buttons, formed by fusion under argon of pieces cut from either pressed powder bars or vapor-deposited rod, also were used occasionally. The gas analyses of the three types of rhenium are recorded in Table II.

Pressing and Sintering—*Pressing:* Preliminary experimentation had shown that fabrication of massive rhenium prepared by arc casting or hot wire deposition from the hexachloride was very difficult. The underlying reason for this situation was the large grain size, which caused serious secondary tensile cracks on cold or hot working. Therefore, powder metallurgy techniques were employed for consolidation.

Rhenium metal powder, of the type previously described, was pressed into ¼x¼x6 in. bar stock in a hardened steel die; an ether solution of stearic acid was used to lubricate the die walls. The die pressure necessary to secure maximum compacting was 30 tsi. This produced densities of 35 to 40 pct of "theoretical" (21 g per cc). The bars were very fragile, but increasing or decreasing the die pressure did not improve the as-pressed density. Further densification probably cannot be achieved easily by pressing alone because of rhenium's exceedingly high work-hardening capacity.

Presintering and Sintering: Sintering was divided into two steps: presintering to improve the strength for handling, and sintering for densification to a massive workable structure of low porosity. Presintering was done in vacuum. This treatment consists of heating the pressed rhenium bar for 2 hr at 1200°C in a vacuum of about 0.01 micron pressure. Very little densification occurs (40 to 45 pct of theoretical), but the bar is strengthened sufficiently to be handled for sintering.

The final sintering is conducted under flowing tank hydrogen in a "bottle" of the type commonly used for sintering molybdenum and tungsten bars in industry. The resistance-heated bars are held vertically between water-cooled electrodes. The lower electrode extends into a pool of mercury providing a flexible contact to allow for shrinkage. Sufficient current (about 1200 amp at 6 to 8 v) is passed through the bars to raise their temperature to 2700°C after emissivity corrections are applied. The temperature is read with an optical pyrometer and is close to 90 pct of that required to cause fusion. A brief summation of the pressing and sintering procedures is given in Table III.

Approximately 30 rhenium bars, 60 to 65 g, have been sintered in this manner, and in almost all cases the resulting density fell between 85 and 93 pct of the theoretical.

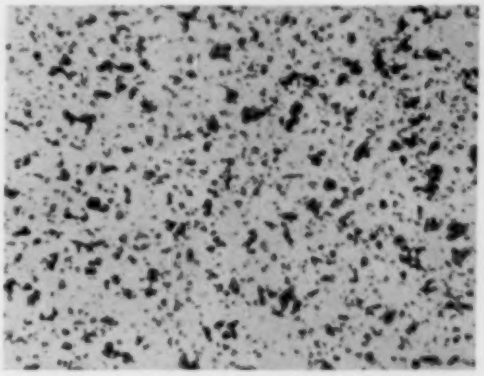

Fig. 1—Rhenium metal powder reduced from ammonium perrhenate. Particle size, 1 to 25 microns. X100. Area reduced approximately 25 pct for reproduction.

Hot working: Rhenium appears to be characterized by hot shortness, and, despite claims by Agte et al.[1] that rhenium is both hot and cold workable, no fully satisfactory method for hot working has yet been developed in the present study. The hot shortness is caused by a low melting (297°C) oxide, Re_2O_7, which readily forms at grain boundaries when rhenium is hot worked in air.

No success was obtained in attempts to hot work either arc-cast, hot wire-deposited, or sintered powder metallurgy-type rhenium by forging, swaging, or rolling at temperatures ranging from 800° to 1750°C. In fact, a most graphic picture of rhenium's hot shortness may be seen in Fig. 2 which shows a very pure 50 g arc-cast button before and after two blows by a forging hammer at 1500°C. The metal has virtually exfoliated at the grain boundaries.

An experiment indicating that oxygen was the cause of hot shortness was conducted at this time. Three arc-melted buttons from the same piece of crystal-bar rhenium were used. The first specimen was retained as a blank for study in the as-cast condition. The second was heated in hydrogen at 1500°C for 30 min, then cooled in the hydrogen atmosphere without exposure to air. The third specimen was heated in hydrogen to 1500°C for 10 cycles of 3 min each, being air quenched between each heating period to simulate the conditions under which it normally would have been hot worked. The metallographic structure of the three specimens is shown in Fig. 3 and their gas content recorded in Table IV.

The first button showed a low oxygen, hydrogen, and nitrogen content and a clean structure. The second button showed a slight decrease in gas content, particularly oxygen and hydrogen, but also exhibited some precipitation of foreign phases at

Table III. Procedure for the Preparation of Sintered Rhenium Bar from Rhenium Powder

Operation	Time, Hr	Temperature, °C	Percentage of Theoretical Density Achieved	Remarks
Pressing	—	—	40	30 tsi; lubricate die with stearic acid
Presintering	2	1200	45	Pressure of 0.01 micron
Sintering	1	2700	90	Hydrogen atmosphere

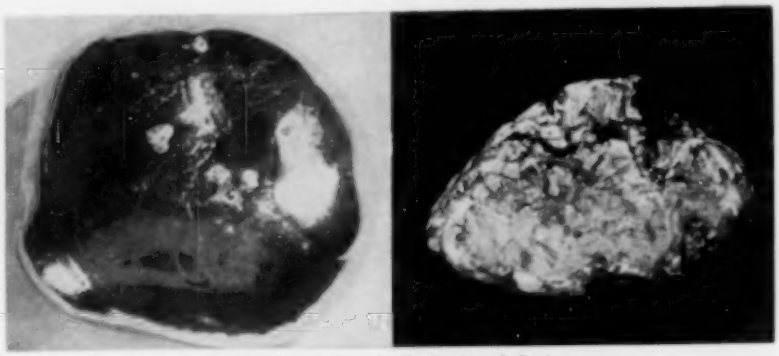

a—Arc-melted rhenium button. X2.

b—Button of *a* after two blows with forging hammer at 1500°C.

Fig. 2—Hot shortness in the forging of rhenium.

the grain boundaries, possibly as a result of diffusion within the metal at the elevated temperature. The gas content of the third specimen increased greatly because of the 10 air quenches, and precipitation of foreign phases at the grain boundaries was heavy. This was probably due to inward diffusion of ambient gases, principally oxygen, during the exposure to air. It is highly probable that much of the grain-boundary precipitate is the low melting oxide, Re_2O_7, which liquefies at hot working temperatures and sufficiently weakens the grain interfaces to cause hot shortness.

Subsequent attempts to hot swage arc-melted, hot wire-deposited, and sintered rhenium, encapsulated in steel and evacuated, were also unsuccessful. Deoxidation additions of 1 pct thorium, aluminum, zirconium, titanium, and uranium were ineffective.

Only one instance of successful hot working has been noted. Sintered metal, cold rolled to about 75 pct reduction by a procedure to be described, was hot rolled at 1475°C with moderate success. A total reduction of 60 pct was obtained; the metal was reduced about 15 pct per pass. Little or no cracking occurred other than some previously present as a result of imperfect cold working. Surface condition was fair. The partial success of this one hot-rolling experiment indicates that, with care and by using a judicious amount of prior cold working, powder metallurgy-type rhenium may be hot worked. Success with the cold working of rhenium led to abandonment of the studies of hot working. However, further investigation of this method is planned.

Cold Working: Cold working of arc-cast rhenium has been somewhat successful but hot wire-deposited metal has not been cold worked successfully as yet. With sintered-type rhenium, satisfactory cold-working procedures have been developed. These procedures have been adequate for the preparation of wire, rod, and sheet in laboratory quantities.

Early experiments, principally with arc-cast rhenium, established two salient points: 1—Rhenium appears to be extremely hot short, as already emphasized. 2—Rhenium work hardens tremendously.

The extreme resistance to deformation (rhenium work hardens from 250 to over 800 VHN when reduced 30 pct in cross-sectional area by swaging) caused serious secondary tensile cracking of arc-cast metal when cold reductions of 10 pct or more were attempted.

Accordingly, it was thought that, if a fine grained surface structure could be obtained by repeated light deformation and recrystallization, cracking would be eliminated and heavier reductions then might be possible. This general procedure was successful, as illustrated by the fabricated forms shown in Fig. 4, and has evolved into the cold-working methods to be described.

Swaging: A sintered billet, often not quite square, is cold rolled by light reductions to a square, as shown in Fig. 5a. Following the squaring, it is necessary to anneal for ½ hr at 1700° to 1750°C to maintain a low hardness. Next, the bar is cold peened or hand forged on the corners. This is done in several steps and gives a cross-section as shown in Fig. 5b. This operation usually causes a mild creping of the original square faces, which is eliminated by very mild rolling.

The final preparation step is to cold roll the bar on the flats formed by the hammering operation to an octagon, as shown in Fig. 5c. Intermediate anneals maintain the hardness at a low level.

Swaging is then started, reductions being possible at either 10 or 20 pct in cross-sectional area per pass (Fig. 5d). Annealing accompanies each swaging

a—As-received arc-melted button.

b—Heated in hydrogen at 1500°C for 30 min, hydrogen muffle cooled.

c—Heated in hydrogen at 1500°C for 10 periods of 3 min each, air quenched between cycles.

Fig. 3—Micrographs of three heat-treated rhenium buttons. X 500. Area reduced approximately 50 pct for reproduction.

Table IV. History and Gas Content of Three Rhenium Buttons

Button	Condition	Vacuum Fusion Analysis, Ppm: Oxygen	Hydrogen	Nitrogen	Reference, Fig. 4
Ia	As arc melted	10	1.0	<2	a
Ib	Heated in hydrogen at 1500°C for 30 min; hydrogen muffle cooled	3	0.2	<4	b
Ic	Heated in hydrogen at 1500°C for 10 periods of 3 min each; air quenched between cycles	76	12.0	13	c

pass and is of the order of 1 to 2 hr at 1700° to 1750°C. Each anneal must reduce the surface hardness below 300 VHN before the next swaging operation is permitted or the post-annealing hardness will creep upward, the bar eventually becoming so work hardened that surface cracking appears. A hardness reading should be taken after every other cycle to provide proper control.

Wire Drawing: At 60 to 65 mil diam, swaging ceases; wire drawing is the next logical fabrication step, but rhenium possesses such great resistance to deformation that reduction to wire has been accomplished so far only with considerable difficulty. The 60 to 65 mil rod is first scalped with a fine aluminum oxide wheel to remove surface imperfections. The surface is then polished with 600 grit paper. Drawing commences at reductions of 10 pct with anneals between each pass. The best lubricant for drawing, among many tested, has a lithium stearate base. Even with this lubricant, rhenium tends to develop longitudinal pitted or scarred areas after a few passes.

Wire drawing has produced sound 40 to 50 mil wire with a good surface. While rhenium has been drawn to a 12 mil diam, the surface was not satisfactory. Small cracks and fissures were present. The same condition exists, to a lesser degree, in 20 to 30 mil drawn wire.

From the results experienced in wire drawing, a rolling or hammering type of reduction would appear to be preferable. Rhenium should respond to such treatment, as its excellent ductility is obvious from data reported in this paper. In preliminary work, rhenium has been reduced to fine square wire with a good surface by using a Turk's Head draw plate.

Cold Rolling: The technique of cold reductions and intermediate anneals was used in the fabrication of rhenium sheet. The sintered bar was first cold rolled a total of about 5 pct by a number of small reductions to reduce edge cracking. Following this preliminary fabrication, reductions of 10 pct per pass, with intermediate anneals between each step, were employed to fabricate 10 mil strip. In all cases, the final surface finish was excellent. Occasionally, some edge cracking occurred early in fabrication, but this was removed by grinding and did not propagate.

Rhenium sheet, for use in such devices as electron tubes, crucibles, etc., can be fabricated by cold rolling. When annealed, it can be bent readily; sharp bends, however, should be accompanied by one or two intermediate anneals.

Cold rolling in form rolls has been successful, also, but has not been utilized as extensively as other types of fabrication.

Physical Properties

Some of the physical and mechanical properties of rhenium have not been determined, and others have been measured by only one investigator. Thus, it was felt that a general reappraisal of the physical and mechanical properties of rhenium was desirable. A discussion of the important physical properties determined in this investigation follows.

Lattice Constants: Considerable disagreement is found in the literature with respect to the lattice constants of rhenium, a hexagonal-close-packed metal. The most accurate work with the purest materials appears to have been done by Stenzel and Weertz,[5] who obtained the results recorded in Table V. Other values have been determined by Agte et al.,[3] Goldschmidt,[4] and Moeller.[6]

Three sets of values have been obtained in the present work: one for purified powder reduced from ammonium perrhenate and two for crystal-bar rhenium, one a major and the other a minor pattern. All work was done by X-ray diffraction.

As can be seen in Table V, the constants determined from powder and from crystal bar (minor phase) agree well with the work of Stenzel and Weertz. The crystal-bar major phase does not agree closely, however, which could be a result of impurities present in the crystal bar and not in the other materials studied. Interstitial impurities tend only to expand the lattice, while substitutional impurities may cause either expansion or contraction. Since the major crystal-bar pattern is indicative of a contracted lattice, the conclusion may be drawn that part of the crystal bar exposed in test contained substitutional impurities.

Since the minor crystal-bar pattern, the powder pattern, and the work of Stenzel and Weertz agree quite closely, the powder pattern value from the present work is preferred. In general, these values are all slightly lower than those found by previous

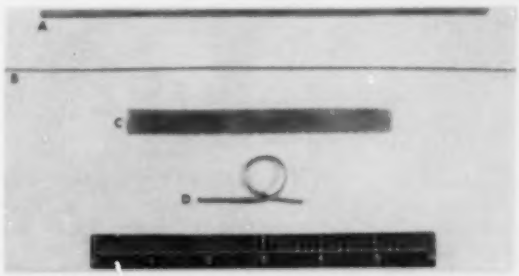

Fig. 4—Rhenium fabricated from sintered bar. *A* is 0.160 in. diam swaged rhenium wire; *B*, 0.060 in. diam swaged rhenium wire; *C*, 0.026 in. thick rolled rhenium sheet; and *D*, 0.080 in. diam annealed rhenium wire illustrating its ductility.

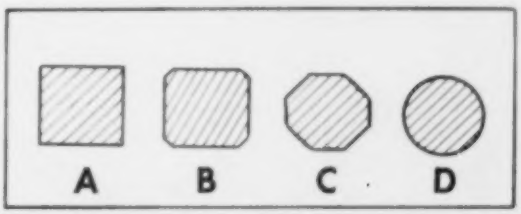

Fig. 5—Steps in the preparation of rhenium rod. *A* is as-sintered rhenium cross-section; *B*, as-edge-forged rhenium cross-section; *C*, as-octagonized rhenium cross-section; and *D*, as-swaged rhenium cross-section.

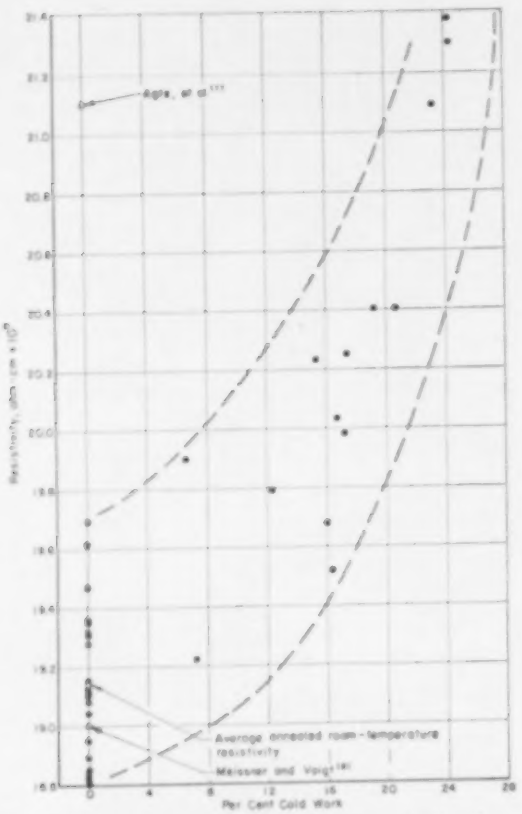

Fig. 6—Room temperature resistivity and the effect of cold work on the resistivity of rhenium.

investigators, and tend to emphasize the high density of rhenium reported subsequently.

Melting Point: Agte et al.[1] determined the melting point of rhenium to be 3440±60°K (3167±60°C) by the bored-hole method. Pressed and sintered rhenium was used, containing 0.01 pct impurity according to their paper. Jaeger and Rosenbohm[7] reported 3160°C (3453°K) a few years later, in excellent agreement with Agte's work.

Recently, in the present investigation, highly purified ammonium perrhenate was reduced to rhenium powder and the melting point of rhenium redetermined. The spectrographic analysis of this material is not available as yet. Two measurements were made by the bored-hole method; the hole depth was about seven times the diameter, assuring black-body conditions, and the bar was heated by self-resistance. The measurements were made with a calibrated Leeds and Northrup optical pyrometer containing a calibrated filter to cover the range of

Table V. Lattice Constants of Rhenium

a_o, A	c_o, A	c/a	Investigator	Remarks
2.760*	4.458*	1.615	Present work	Purified powder
2.753*	4.445*	1.615	Present work	Crystal bar (major)
2.760†	4.460†	1.616	Present work	Crystal bar (minor)
2.760‡	4.458‡	1.615	Stenzel and Weerts[9]	

* Accurate to ± 0.001A.
† Accurate to ± 0.005A.
‡ Converted from the literature to true angstrom units.

Table VI. Melting Point of Rhenium

Temperature, °C	Temperature, °F	Investigator
3170±60	5740±110	Agte et al.[1]
3160	5720	Jaeger and Rosenbohm[7]
3180±20	5760±40	Present work

temperature measured. The values obtained were 3175° and 3184°C; the average value is reported in Table VI. These values also check closely the two values found in the literature and conclusively establish the melting point of rhenium as occurring in the 3160° to 3180°C temperature range. Thus, rhenium has the second highest melting point of the metals, being exceeded only by tungsten (3380°C). One additional measurement was of interest, as it was obtained by the bored-hole method in crystal-bar rhenium vapor deposited on a fine tungsten wire. Since the hole for melting-point determination passed through the tungsten wire, the lowest melting eutectic of tungsten and rhenium should have been the melting point measured. Melting actually occurred at 2810°C, agreeing very closely with the value of 2800°C found by Becker and Moers[6] for the lowest melting eutectic in the W-Re system.

Density: The density value most commonly accepted in the literature for rhenium is that of 20.53 g per cc, calculated by Agte et al.[1] from the presently accepted atomic weight of 186.31 and the lattice constants they determined. In the same work, they obtained an experimental density of 20.9 g per cc, indicating that their lattice constants were somewhat in error. One other value has been reported in the literature, that of Goldschmidt,[5] who calculated 21.40±0.06 g per cc. This, however, was based on an atomic weight now known to be incorrect.

In the current investigation, several density measurements (see Table VII) were made on a fabricated rod approximately 0.150 in. in diameter and 6.6 in. long. This rod had been swaged from over 0.20 in. diam and was completely sound, as verified by metallographic inspection.

Density values obtained by water displacement measurements with this bar were 21.02 and 21.03 g per cc. These are the highest measured densities recorded for rhenium and since most impurities could only lower the density, they are probably the most correct. In addition, calculation of the theoretical density from the lattice constants, as determined above, gave the last value in Table VII, 21.04 g per cc, in excellent agreement with the experimental value of 21.02±0.01 g per cc.

The values obtained in this work establish rhenium as the fourth most dense element, following osmium (22.6), iridium (22.5), and platinum (21.5).

Electrical Resistivity: The resistivity of rhenium at 20°C has previously been determined by Agte et al.[1] and the resistivity at 0.16°C was measured by Meissner and Voigt.[8] These values are reported in Table VIII where the value of Meissner and Voigt has been corrected at 20°C by the use of Agte's temperature coefficient of resistivity (3.11×10^{-4} per °C in the range from 0 to 100°C).

In the current work, determination of the resistivity at room temperature and the effect of cold work on resistivity were combined. Several rhenium wires, ranging in initial size from 50 to 60 mil diam and usually about 8 in. long, were annealed to hardnesses well below the 300 VHN threshold. The resistance of these wires was then measured by a nul method on a Kelvin bridge. With the diameters

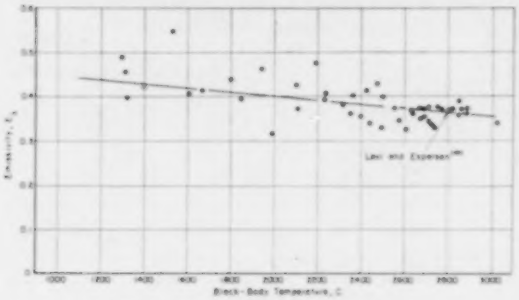

Fig. 7—Spectral emissivity of rhenium.

known from micrometer measurements, the test length standard, and resistances taken from the Kelvin bridge, the resistivity was then calculated.

Following the recording of a few annealed rhenium measurements in the foregoing manner, the wires were reduced cold by wire drawing in amounts ranging from 6.5 to 24.2 pct reduction in cross-sectional area. The resistance was then measured and the resistivity calculated for the as-worked wires. The wires were then annealed and the resistivities were calculated at the lower diameters. This cycle continued until 24 annealed readings and 14 as-cold-worked readings were recorded. The data are presented in graphical form in Fig. 6.

Considerable spread is noticeable among the annealed readings, but the average value agrees quite closely with the findings of Meissner and Voigt, about 2 microhm-centimeters below the more commonly accepted value of Agte. The cold-worked resistivities also show some spread, but conclusively establish that cold-working increases the resistivity of rhenium about 2 microhm-centimeters with 25 pct reduction. Possibly Agte's rhenium was not sufficiently well annealed.

Thermal Expansion: The linear thermal expansion of rhenium was determined by Agte et al.[3] at room temperature and 1917°C by X-ray methods. Their constants were: $\beta\,[001] = 12.45 \times 10^{-6}$ per °C ± 8 pct, and $\beta\,[100] = 4.67 \times 10^{-6}$ per °C ± 8 pct. Thus the *c*-axis expansion was 2.6 times the *a*-axis; they claimed no variation with temperature.

In the present work, the linear thermal expansion coefficients for a 150 mil annealed rhenium rod 3 in. long have been determined in a recording dilatometer over a temperature range from 20° to 1000°C. The measurements, as reported in Table IX, show a slight increase in expansivity with increasing temperature. The mean expansion coefficient between 20° and 500°C is 6.7×10^{-6}, slightly higher than tungsten which is 4.45×10^{-6} for the same range.[5]

Spectral Emissivity: The first value of spectral emissivity reported in the literature was that of Becker and Moers,[4] coworkers of Agte, who calculated a value of $E_\lambda = 0.42$. The specific temperature for this value was not mentioned. More recently, Levi and Espersen[10] reported a value of $E_\lambda = 0.366$ at about 2800°C.

During current determinations of the melting point of rhenium by the bored-hole method, the spectral emissivity was also determined over a rather wide range of elevated temperatures. Black-body temperatures at the base of a hole, over six times as deep as its diameter, were measured by an optical pyrometer and compared to the surface reading of the bar adjacent to the hole. All necessary corrections for the absorption of sight glasses, etc., were introduced. After several melting-point determinations on different rhenium bars, approximately 45 sets of readings were available at temperatures ranging from 1300° to 3000°C. These were related by the well known equation

$$\frac{1}{T} - \frac{1}{T'} = \frac{\lambda}{C_2} \ln E_\lambda$$

where T is the black-body temperature, °K; T' is the brightness temperature, °K (surface temperature); λ is 0.655, the wave length; C_2 is 14.362, a constant; and E_λ is the thermal emissivity.

The emissivity, E_λ, was solved for each set of individual points and plotted as a function of the black-body temperature (see Fig. 7). The data show a very definite approximately linear decrease of E_λ as the temperature increases. At 2800°C black-body temperature, the present data checks extremely well with that of Levi and Espersen; at about 1400°C, it checks with the value found by Agte and coworkers.

For more common usage, a plot of the data presented as black-body vs brightness temperature, calculated from Fig. 7, is presented in Fig. 8.

Table VII. Density Determinations on Rhenium

Density, G per Cc	Type of Rhenium	Determination Method	Investigator
21.40±0.08	Unknown	From lattice constants	Goldschmidt[9]
20.53	Probably crystal bar	From lattice constants	Agte et al.[3]
20.9	Probably crystal bar	Probably water displacement	Agte et al.[3]
21.02±0.01	Swaged, sintered bar	Water displacement	Present work
21.03±0.01			
21.04±0.01	Crystal bar	From lattice constants	Present work

Table VIII. Resistivities of Annealed Rhenium at or Corrected to 20°C

Resistivity, ρ, Ohm-Cm x 10^6	Investigator
21.1±15 pct	Agte et al.[3]
19.0*	Meissner and Voigt[8]
19.14±0.25†	Present work, average

* Corrected from 0.16°C.
† Corrected from an average temperature of 25°C.

Mechanical Properties

Mechanical data for rhenium has been virtually undetermined as evidenced by the literature, despite hints from time to time that this metal might show rather high properties. The present work shows that rhenium is an amazingly strong metal and, unlike tungsten, it is ductile at room temperature. Furthermore, it is not made brittle by recrystallization.

Table IX. Linear Thermal Expansion Coefficients for Pure Rhenium

Temperature Range, °C	Coefficient, λ per °C x 10^{-6}
20 to 100	6.6
20 to 200	6.6
20 to 300	6.6
20 to 400	6.6
20 to 500	6.7
20 to 600	6.7
20 to 700	6.7
20 to 800	6.8
20 to 900	6.8
20 to 1000	6.8

Modulus of Elasticity: No attempt had ever been made to determine Young's modulus of elasticity for rhenium. However, Köster,[15] in a basic study of Poisson's ratio in the periodic system, estimated the modulus of rhenium to be about 73x10⁶ psi.

Three annealed rhenium rods have been used in present measurements of this modulus. In each case, the material was swaged to 150 mil diam, then a ⅛ in. standard tensile section was ground at the center of the rod. After grinding, the specimens were annealed, and two type A-7 strain gages applied. Load vs elongation curves were plotted from the average reading of the two strain gages as the specimen was loaded and unloaded. A total of six determinations were made because four successive determinations were recorded on one of the three test specimens.

The resulting modulus values are reported in Table X, all having been calculated from the return, or unloading, curve. By using this technique, any adjustment of the specimens in the grips would have occurred prior to unloading and any error could only have made the modulus value lower. The average of the six determinations, 66.7(±2.9)x10⁶ psi, is somewhat lower than Köster's estimated value but is also one of the highest moduli ever measured. It places rhenium third among all metals in this respect and falls between tungsten and osmium, as would be expected from the periodic arrangement.

Table X. Moduli of Elasticity for Annealed Rhenium

Specimen	Modulus of Elasticity, Psi
25	72.6x10⁶
28	65.8x10⁶
27, determination 1	64.9x10⁶
27, determination 2	66.4x10⁶
27, determination 3	64.6x10⁶
27, determination 4	67.1x10⁶

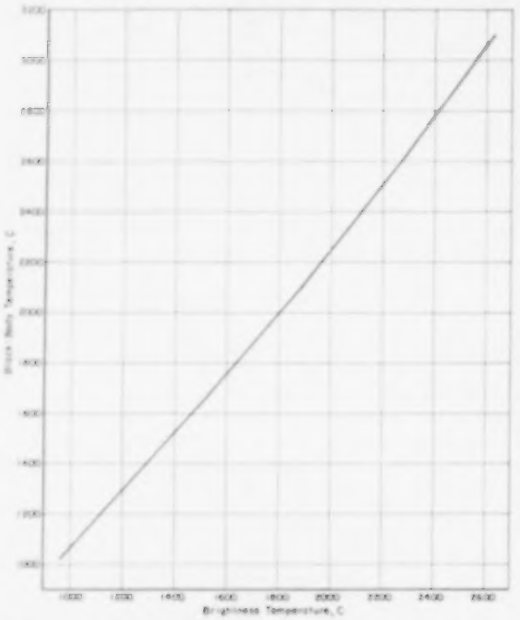

Fig. 8—Black-body vs brightness temperature for sintered rhenium bars.

Tensile Strength and Ductility: In Agte's[4] paper on rhenium, the ultimate tensile strength and the ductility of an 0.25 mm diam halide process vapor-deposited rhenium wire (with 0.03 mm W core) were reported as about 70,000 psi and 24 pct, respectively. Early in the current work, this type of test was repeated with a ⅛ in. reduced section ground into an 0.20 in. diam crystal bar (also vapor-deposited by the halide process). The ultimate tensile strength, 75,000 psi, checked very closely with Agte's results but the elongation was only 3 pct. Subsequent metallographic work showed that the crystal bar tested represented a conglomeration of large loosely coherent rhenium grains hanging on a tungsten wire, rather than a sound structure. This also may have been true of Agte's metal. More recent tensile tests on sound fine-grained rhenium prepared by powder metallurgy procedures, give far higher strengths and ductility.

Room Temperature Tensile Tests: Three tensile tests have been conducted on pure annealed rhenium. All were on round swaged rod of approximately 50 mil diam and all were fabricated from sintered bar. Into each was ground a standard ⅛ in. diam round tensile specimen. Special grips were built to hold the ends of the 150 mil rods. Two SR-4 type A-7 strain gages were applied and the elasticity modulus measured as reported previously. One A-7 strain gage was then removed, and a specially constructed extensometer for use with specimens of this size was attached to the specimen. Strain then

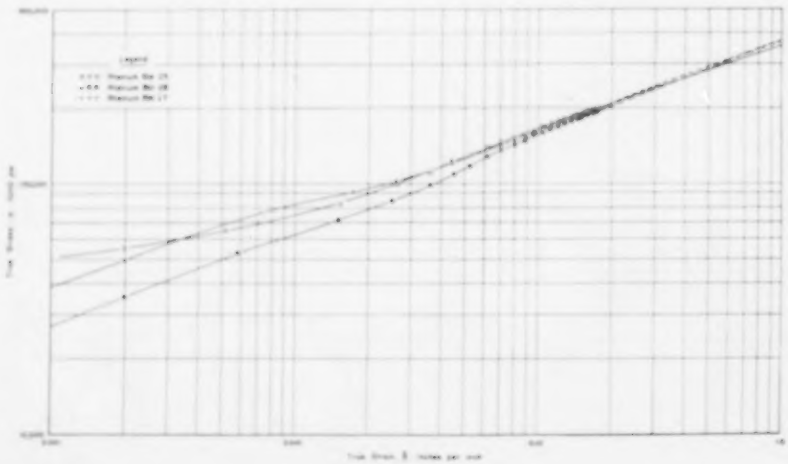

Fig. 9—True stress-strain diagram for three pure rhenium specimens.

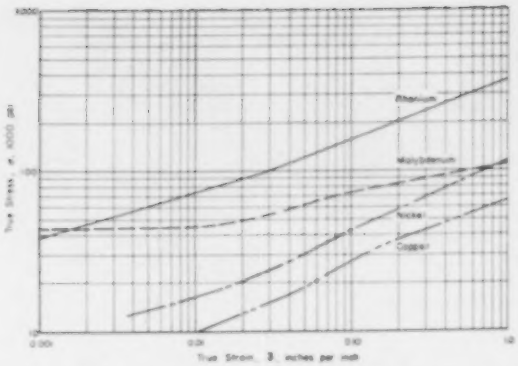

Fig. 10—Average true stress-strain diagram for rhenium and other metals.[15, 28]

was recorded by the remaining A-7 strain gage and the extensometer.

Load vs elongation curves within the range of the strain gages were plotted for each tensile test, and from these were obtained the proportional limits and 0.1 and 0.2 pct offset yield strengths recorded in Table XI. In addition, Table XI contains the measured values of ultmate tensile strength, elongation, and reduction of area.

Annealed rhenium rod possesses an average ultimate tensile strength of about 165,000 psi combined with excellent ductility. This is more than double the tensile strength found by Agte and the present authors for crystal-bar rhenium, indicating the mechanical unsoundness of the as-deposited metal used in tensile tests in both instances. The tensile strength of annealed rhenium is much higher than that of annealed molybdenum (about 70,000 psi)[28] and annealed tungsten wire 20 to 40 mil diam (about 110,000 psi).[14] The large spread between the relatively low yield strength and high ultimate strength reflects the high work hardening of rhenium. In addition, rhenium has an elongation of 25 pct at room temperature, roughly equivalent to the elongation of molybdenum;[28] tungsten has no ductility under these conditions.

The true stress, σ, and true strains, δ, were calculated for a number of points as determined by extensometer readings; the plot of their relationship for each specimen is shown in Fig. 9. The true stress and true strain can be related by the flow equation

$$\sigma = B\,\delta^n$$

where B is the strain coefficient, the true stress at unit strain; and n is the strain-hardening exponent.

These constants are listed in Table XI also and were obtained from Fig. 9. B was read directly from the intercepts of the true stress-strain curves at $\delta = 1.0$, while n was obtained from the limiting slope of the curves.

Fig. 10 compares true stress-strain curves for molybdenum,[28] nickel,[28] and copper[28] with the average of the three rhenium curves. Rhenium possesses a strain-hardening exponent similar to that of nickel and copper, but since the initial strength is as high or higher than molybdenum, the combination of the high strain-hardening rate and the high initial strength produce values for B equalling nearly 400,000 psi. Probably no other metal has such a high combination of work-strengthening properties, tensile strength, and ductility as is found in rhenium.

Elevated Temperature Tensile Tests: The tensile properties of rhenium at elevated temperatures are

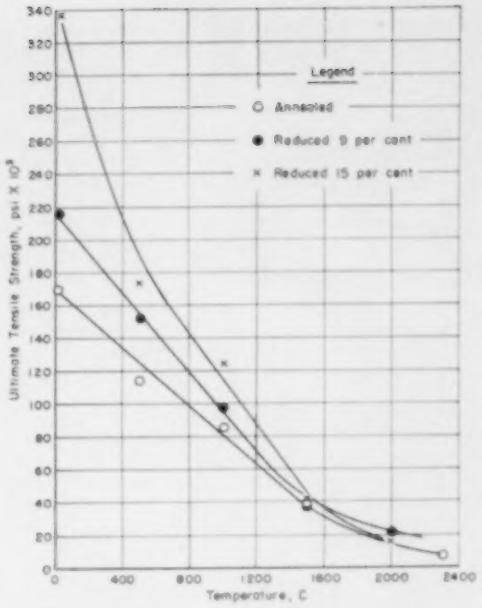

Fig. 11—Ultimate tensile strength of annealed and cold-worked 0.050 to 0.065 in. diam rhenium wire at elevated temperatures.

of importance from the standpoint of its use as an electrical filament material.

Rhenium wire, in sizes ranging from 50 to 65 mil diam, has been tested for tensile strength and ductility from room temperature to around 2000°C. Results have been obtained on annealed wire, wire reduced about 9 pct in cross-sectional area by drawing, and wire reduced about 15 pct in cross-sectional area by swaging and drawing.

For test purposes, wire lengths of 4 to 5 in. were inserted between screw-tightened grips mounted on steel rods, the free ends of which were grasped in an Amsler universal testing machine. Because of the tendency of rhenium to oxidize, the wire and grips were enclosed in a pyrex tube and one end fitted with a freely moving gasket so as not to affect load readings when the wire was stressed. Dry helium was passed through the tube and the rhenium heated by self-resistance. Temperature was read by an optical pyrometer, sighted through a hole in an asbestos shield surrounding the pyrex tube.

Table XI. Tensile and Elongation Data for Pure Annealed Rhenium*

	Specimen 26	Specimen 27	Specimen 28	Average Value for Specimens 25, 27, and 28
Proportional limit, psi	38,100	30,800	18,100	28,300
0.1 pct offset yield strength, psi	50,000	44,000	31,800	42,000
0.2 pct offset yield strength, psi	55,200	49,500	35,000	46,000
Ultimate tensile strength, psi	168,000	164,000	161,000	164,000
Elongation in ½ in., pct	24.6	23.0	25.+†	24
Reduction of area, pct	34.1	30.1	31.1	31.7
True stress at unit strain, B, psi	390,000	370,000	370,000	387,000
Strain-hardening exponent, n	0.333	0.360	0.373	0.353

* Standard ASTM ¼ in. diam reduced section, ½ in. gage length.
† Broke outside punch marks.

Table XII. High Temperature Strength and Ductility of Annealed and Cold Worked 0.05 to 0.065 In. Diam Rhenium Wire

Black-Body Temperature, °C	Annealed			Reduced 9 Pct in Area			Reduced 15 Pct in Area		
	Ultimate Tensile Strength, Psi x 10^3	Elongation in 3.65 In., Pct	Reduction of Area, Pct	Ultimate Tensile Strength, Psi x 10^3	Elongation in 3.15 In., Pct	Reduction of Area, Pct	Ultimate Tensile Strength, Psi x 10^3	Elongation in 3.15 In., Pct	Reduction of Area, Pct
Room temperature	170	10	16	216	8	6	337	—*	2
500	114	9	19	152	7	9	174	1	1
1000	85	1 to 2	2 to 3	98	2 to 3	1	124	1	3
1500	38	1 to 2	2	37	2	1	40	1	10
2000	—	—	—	22	2 to 3	1	15	1	4
2300	7.7	1 to 2	2	—	—	—	—	—	—

* Specimen slipped in grips; value not available.

The results are recorded in Table XII and shown graphically in Fig. 11. The tensile strength drops off rapidly with increased temperature, as it does for all metals. Increasing amounts of cold work increase both the room and elevated temperature strengths below 1500°C. Above 1500°C, recrystallization proceeds sufficiently to reduce the wrought strength to approximately that of annealed rhenium. Rhenium's high temperature ductility, however, is not as high as expected. While more ductile at room temperature than other refractory metals, rhenium is less ductile at elevated temperatures. For annealed and 9 pct reduced rhenium, the elongation falls to a constant value of 1 to 2 pct between 500° and 1000°C; for 15 pct reduced rhenium, the low elongations are found below 500°C.

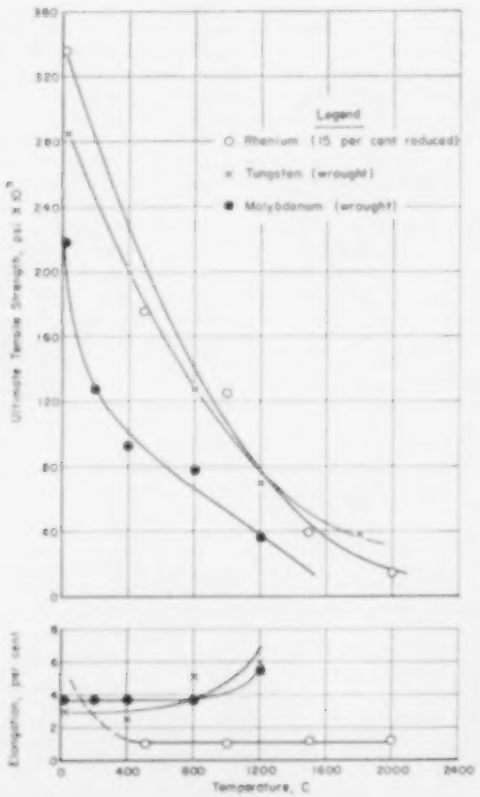

Fig. 12—Elevated temperature tensile properties of wrought rhenium (15 pct reduced), molybdenum,[14] and tungsten.[15]

An appraisal of rhenium's high temperature behavior compared to other refractory metals, tungsten and molybdenum, is given in Fig. 12. It must be borne in mind that the rhenium data is from metal reduced only 15 pct in cross-sectional area, whereas the comparative data for the other metals is from fully wrought stock. Reduction of 15 pct in rhenium is not sufficient to give a fully wrought structure but, even so, makes the rhenium slightly stronger than wrought tungsten below 1200°C. Accordingly, if data from fully wrought rhenium were available, its tensile strength would probably be considerably greater than shown. Another interesting point is the very high tensile strength of 15 pct reduced rhenium at room temperature, about 335,000 psi. These data were secured from 64 mil diam wire. Fine rhenium wire, or the fully wrought rhenium, may have even higher strength than the 600,000 to 700,000 psi strength values found for 0.5 mil drawn tungsten.[9]

Work Hardening and Recrystallization: The literature yields no information as to the work hardening or recrystallizing behavior of rhenium, except for Winkler's[17] statement that annealed rhenium work hardens from 247 to 637 VHN when cold worked; this shows that rhenium work hardened rather extensively, results that have been verified by the current work.

A specimen of pure swaged rhenium rod was annealed to a surface hardness of 270 VHN, the structure of which is shown in Fig. 14c. Note the extremely fine grain size. After annealing, the rod was reduced 10 pct in cross-sectional area by swaging, and a group of small specimens removed for recrystallization studies. Extensive transverse and longitudinal hardness measurements were taken. Next,

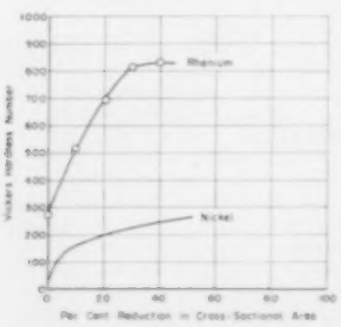

Fig. 13—Cold work hardening characteristics of rhenium and nickel.[18]

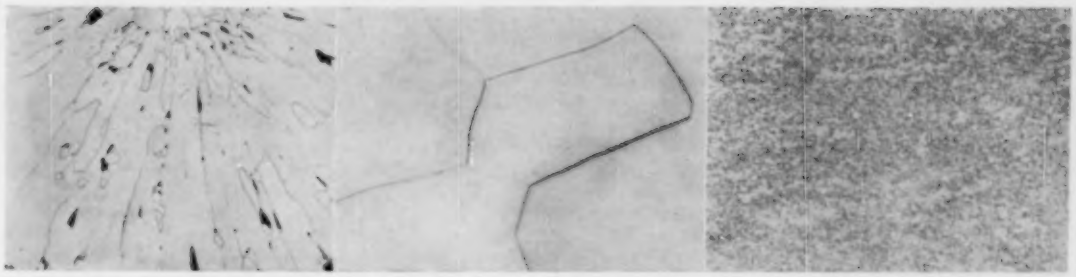

a—Hot wire-deposited rhenium, near center of bar, VHN is 166. Average grain size is 0.06 mm.

b—Rhenium arc melted from cut crystal bar, VHN is 135. Average grain size is 3 mm.

c—Annealed rhenium from compacted, sintered, and swaged metal powder; VHN is 270. Average grain size is 0.004 mm.

Fig. 14—Hardness and grain structures of hot wire-deposited, arc-melted, and powder metallurgy types of rhenium. All in the annealed condition. X100. Area reduced approximately 55 pct for reproduction.

the bar was reduced an additional 10 to 20 pct total reduction in cross-sectional area, hardness readings taken, and specimens removed. This cycle was repeated until 40 pct reduction was recorded, at which point some cracking of the swaged bar from the repeated cold working was apparent. The metallographic structure was almost completely wrought at 40 pct reduction.

Fig. 13 shows the work-hardening curve secured from the hardness data compared to corresponding data for nickel[11] a metal which work hardens appreciably. Rhenium work hardens to over 800 VHN with 30 pct reduction in cross-sectional area by swaging. No other pure metal is known to work harden as much. These results emphasize the need for proper control of preworking hardnesses during fabrication.

In addition to the foregoing results on powder metallurgy-type rhenium, a few hardness determinations were completed on arc-cast and hot wire-deposited rhenium. Fig. 14 shows the typical unworked structures obtained when rhenium is consolidated by these two methods, compared with a structure of annealed rhenium prepared by powder metallurgy methods. The annealed hardnesses obtained from all three of these methods are included in the figure.

The largest grained metal, that prepared by arc melting, has the lowest hardness. The crystal bar (hot wire-deposited metal) also has a low hardness and it should be noted that its structure is primarily composed of large grains, also. The large grain size present in crystal bar and arc-melted metal causes these types of metal to be much more difficult to work than powder metallurgy rhenium.

After establishment of the work-hardening characteristics of rhenium, the recrystallization behavior was determined. Specimens from each group of 10, 20, 30, and 40 pct reduced metal were annealed for 1 hr at temperatures ranging from 700° to 1700°C, generally at 100°C temperature intervals. Hardnesses were measured after each annealing treatment. The hardness values vs annealing temperature curves are plotted in Fig. 15, which also includes a series of grain size curves discussed subsequently.

As shown by the data, little, if any, softening occurred below the 800°C annealing temperature. Subsequently higher annealing temperatures involved a rapid drop in hardness for the 20, 30, and 40 pct reduced metal. Around 1300°C, metallographic examination showed a nearly completely recrystallized structure of the type illustrated in Fig. 14c. The hardness had dropped to about 350 VHN at

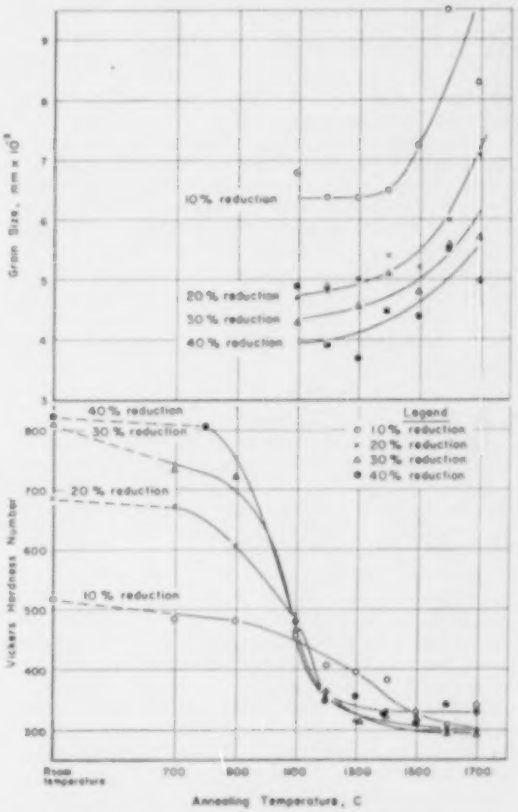

Fig. 15—The effect of 1 hr annealing treatments on the hardness and grain size of cold-worked rhenium.

this point. Higher annealing temperatures caused a further, but less abrupt, drop in hardness.

The 10 pct reduced metal, containing less cold work and thus less available energy to trigger recrystallization, softened and recrystallized more slowly, not being recrystallized completely until about 1500°C.

Thus, it may be concluded that for pure rhenium reduced 10 pct in cross-sectional area by cold work, the recrystallization temperature is 1500°C. For rhenium possessing greater amounts of cold reduction, up to 40 pct in cross-sectional area, 1300°C is the recrystallization temperature. It must be noted,

however, that for the purpose of cold fabrication of rhenium, 1 hr anneals at, or slightly above, these recrystallization temperatures are insufficient. The hardness must, in general, be depressed below 300 VHN and 2 hr at 1700° to 1750°C are usually necessary to accomplish this; the additional time and temperature will bring the recrystallized grain size back up to the value it possessed before cold working.

Grain Size and Grain Growth: Following the recrystallization study reported above, grain counts were made on material annealed in the temperature range 1100° to 1700°C for all degrees of reduction. The Jeffries method of grain size estimation was used. The results are represented by the series of grain growth curves in Fig. 15. Despite some scatter of the plotted points, the graph clearly shows that increasing amounts of cold work produce successively finer grain sizes upon recrystallization, as would be expected. In addition, reductions up to 20 pct cause the highest rate of work hardening and the greatest rate of grain size decrease. Further reduction increases these effects but at a lower rate.

Grain growth generally commences in the temperature range 1300° to 1400°C, at which temperatures the hardness curves show that recrystallization is about complete; this allows grain growth to start. As expected, the 10 pct reduced metal lags in both softening and the initiation of grain growth; grain growth in it commences in the temperature range 1400° to 1500°C at the completion of recrystallization. Under all circumstances, the grain size remained very small, varying from about 0.004 to 0.010 mm average grain diameter. This is much finer than the relatively large grain size exhibited by crystal bar and arc-melted rhenium, as exemplified by Fig. 14.

Oxidation Resistance

Rhenium would be expected to possess a volatile oxide commensurate with its position in the periodic table adjacent to neighboring osmium, which has this characteristic. Agte and coworkers[1] verified this and stated that rhenium oxidized at the same rate as tungsten at 1000°C; above 1600°C, it oxidized one third as fast as tungsten.

No oxidation tests have been run with powder metallurgy-type rhenium in the current work but cut sections of arc-melted buttons have been exposed to air over a wide range of temperature. Despite the possibility of some variance in results because of the coarse grain size of arc-melted rhenium, it is probable that the following test results are broadly correct for any type of rhenium, whether it be sintered, arc-melted, hot wire-deposited, or electroplated:

Quarter buttons of arc-cast rhenium, each weighing about 3 g, were exposed to slowly moving air in a muffle furnace at 300°, 600°, 900°, 1200°, and 1500°C. The results are recorded in Table XIII. As can be seen, a catastrophic oxidation rate commenced above 600°C, at which time white fumes were given off; this is also the case with molybdenum. This white or yellowish oxide is Re_2O_7, rhenium heptoxide, which melts at 297°C and boils at 363°C; it is the highest oxide of rhenium.

Table XIII. Oxidation of Rhenium in Air*

Exposure Temperature, °C	Exposure Time, Hr	Specimen Weight, G	Specimen Area, Sq Cm	Weight Change, G	Rate of Attack, G per Sq Cm per Hr
300	1	2.3983	1.39	+0.0007	−0.0005
600	1	2.3833	1.47	−0.0172	0.0117
900	1	2.1973	1.29	−1.5015	1.17
1200	0.5	2.5961	1.78	−2.2734	2.56
1500	0.25	3.0609	1.74	−2.2694	5.24

* Note: Specimens prepared by quartering arc-melted buttons weighing about 15 g.

Metallographic examination showed that the attack on the specimens exposed to the higher temperatures was of a general nature, the grain oxidizing at about the same rate as the grain boundaries. That the oxide travels rapidly into the grain boundaries when rhenium is heated in air, however, is well verified by the exfoliation occurring when rhenium is hot forged in air, as in Fig. 2.

Rhenium in general, except for electroplated metal, does not tarnish readily in air at room temperature. All forms of rhenium, prepared by many different methods, have been stored in the open in this laboratory for about two years and no surface oxidation of any sort has been observed. Electroplated metal, however, must be fired in hydrogen to prevent tarnishing.

Summary and Conclusions

1—Sintered massive rhenium bars can be prepared by pressing minus 325 mesh rhenium powder at 30 tsi,* presintering in vacuum at 1200°C, and sintering in hydrogen at 2700°C.

2—Sintered rhenium bars can be fabricated to rod, wire, sheet, and foil by a series of cold-working and annealing operations.

3—Rhenium metal appears to be hot short; this inhibits hot working.

4—The lattice constants of rhenium are: $a_o = 2.760 \pm 0.001$A, $c_o = 4.458 \pm 0.001$A, and $c/a = 1.615$.

5—The melting point of rhenium is 3180±20°C.

6—The theoretical density of rhenium is 21.04± 0.01 g per cc, which compares to a measured value of 21.02±0.01 g per cc.

7—The electrical resistivity of annealed rhenium is 19.14±0.02 microhm-cm at 20°C; this increases with increasing amounts of cold work.

8—The mean thermal expansion coefficient for rhenium over the temperature range 20° to 1000°C is 6.8×10^{-6} per °C.

9—The spectral emissivity of rhenium has been established as a straight-line function with temperature, decreasing from 0.42 at 1400°C to 0.36 at 2800°C.

10—The tension modulus of elasticity for rhenium is $66.7(\pm 2.9) \times 10^6$ psi.

11—Annealed rhenium at room temperature has an ultimate tensile strength of about 164,000 psi, a 0.1 offset yield strength of 42,000 psi, and a 0.2 offset yield strength of 46,000 psi. Under these conditions, it is ductile and has about 24 pct elongation with 20 pct reduction in area.

12—Rhenium work hardens more than any other known metal.

13—Rhenium recrystallizes and grain growth commences in the temperature range 1300° to 1500°C. The annealed grain size of sintered and worked rhenium is very fine, averaging about 0.004 mm.

14—Rhenium oxidizes when heated in air, very rapid oxidation occurring when rhenium is heated in air at temperatures above 600°C, but does not tarnish at room temperature.

Acknowledgments

The authors wish to express their appreciation to J. B. Johnson and the Air Research and Development Command, United States Air Force, Wright-Patterson Air Force Base, for permission to publish the results of work obtained at Battelle Memorial Institute under Contract No. AF 33(616)-232. They also are indebted to the Kennecott Copper Corp. for supplying sufficient potassium perrhenate to conduct this work and to D. M. Rosenbaum who prepared rhenium metal powder from the perrhenate. The authors wish to express their gratitude to Robert Ashbrook, Cecil Criner, and Bruce Ross, who performed much of the experimental work and to R. D. Buchheit and George Wheeler for preparation of the metallographic specimens.

References

[1] C. Agte, H. Alterthum, K. Becker, G. Heyne, and K. Moers: Physical and Chemical Properties of Rhenium. *Ztsch. Anorg. Allgem. Chemie* (1931) **196**, pp. 129-159.

[2] W. Stenzel and J. Weertz: Precision Determination of Lattice Constants of Non-Cubic Substances. *Ztsch. Kristallographie* (1933) **84**, pp. 20-44.

[3] V. Goldschmidt: The Crystal Structure, Lattice Constants, and Density of Rhenium. *Ztsch. für Physik. Chemie* (1929) **2**, abstract B, pp. 244-252.

[4] K. Moeller: The Lattice Constants of Rhenium. *Naturwissinschaften* (1931) **19**, p. 575.

[5] F. Jaeger and E. Rosenbohm: Exact Measurements of the Specific Heats of Metals at Higher Temperatures: XII. Specific Heat of Metallic Rhenium. *Proceedings* Academy of Science, Amsterdam (1933) **36**, pp. 786-788.

[6] K. Becker and K. Moers: On the Melting Point of the System Tungsten-Rhenium. *Metallwirtschaft* (1930) **9**, p. 1063.

[7] E. Wood: *Physical Review* (1947) **72**, p. 437.

[8] W. Meissner and B. Voigt: Measurements with the Aid of Volatile Helium: XI. Resistance of Rhine Metal at Low Temperatures. *Annalen der Physik* (1930) **7**, p. 916.

[9] C. Smithells: *Tungsten*. (1952) pp. 197, 161. London. Chapman and Hall.

[10] R. Levi and G. Espersen: Preparation of Rhenium Emitters and Measurements of Their Thermionic Properties. *Physical Review* (1950) **78**, pp. 231-234.

[11] W. Köster: Poisson's Ratio in the Periodic System. *Trans.* Electrochemical Society (1943) **49**, p. 233.

[12] *Metals Handbook*. (1948) pp. 21, 1051, 1131. Cleveland. ASM.

[13] M. H. LaChance, W. L. Bruckart, C. M. Craighead, and R. I. Jaffee: Recrystallization of Wrought Hydrogen-Sintered Molybdenum and its Alloys. *Trans.* ASM (1953) **45**, p. 321.

[14] R. Kiefer and W. Hotop: *Pulvermetallurgie and Sinterwerkstoffe*. (1943) Berlin. Springer-Verlag.

[15] W. L. Bruckart: Battelle Memorial Institute, unpublished data supplied.

[16] G. Geil and N. Carwile: Tensile Properties of Copper, Nickel, and Some Copper-Nickel Alloys at Low Temperatures. *Circular 520* National Bureau of Standards (1952) pp. 67-96.

[17] O. Winkler: The Frictional Strength of Noble Metals and of Base Metals Having High Melting Points. *Ztsch. für Elektrochemie* (1943) **49**, pp. 221-228.

Effects of Tensile Stress on the Austenite to Ferrite Transformation in Eutectoid Steel

by L. S. Birks and E. F. Bailey

The effect of stress on the austenite to ferrite transformation in carbon steel was studied by X-ray diffraction techniques. Tensile stress was found to cause reorientation of austenite above the transformation temperature, to accelerate equilibrium conditions at the transformation temperature, and to cause precipitation of large carbides at a critical value of stress.

IN the past, a number of papers[1] have discussed the effect of stress on the austenite to martensite transformation at relatively low temperatures. In general, it has been shown that tensile stress induces some transformation at a given temperature, while compressive stress retards the transformation. Very little work has been reported on the effect of stress on the transformation from austenite to ferrite plus carbide near the A_1 point in steel. One of the few papers in the literature[2] reports an increase in A_1 of about 1°C in pearlitic steel upon the application of tensile stress.

In this paper, the effect of tensile stress on eutectoid steel at, and above, the A_1 point was studied in

L. S. BIRKS is associated with the United States Naval Research Laboratory, Washington, and E. F. BAILEY, formerly with the United States Naval Research Laboratory, is associated with Engineering Products Dept., RCA Victor Div., Radio Corp. of America, Camden, N. J.

Discussion on this paper, TP 3754E, may be sent, 2 copies, to AIME by Mar. 1, 1955. Manuscript, Apr. 15, 1953. New York Meeting, February 1954.

an especially designed X-ray diffraction spectrometer. The X-ray results were substantiated and extended by high temperature tensile tests, microstructure, and dilatometer measurements.

Experimental Procedure

The material used was AISI 1090 steel in both flat strips and round bars. It was austenitized at 1650°F (900°C) and air cooled prior to testing.

X-Ray Diffraction Tests: The specimens were flat strips 0.012 in. thick, 3⅛ in. long, and 9/16 in. wide, notched at the center as shown in Fig. 1. They were mounted vertically in a specially constructed vacuum furnace and heated by electrical conduction. Because of the thermal conduction of the copper electrodes near the ends of the specimen and, even more important, the reduced cross-section at the curved notch, the temperature is not constant along the specimen. It reaches a peak value at the center of the notch and drops off toward the ends. The size of the X-ray beam was limited, however, so that diffraction was observed for only a small region of the notch and the specimen could be adjusted in mounting so that any desired portion of the notch could be observed. Temperature was measured by a Pt—Pt-10 pct Rh thermocouple spot welded to the face of the specimen away from the X-ray beam. Unless otherwise specified, the temperatures listed refer to the temperature at the center of the notch. The specimen mounting allowed for tensile loading through a lever arrangement from outside the vacuum without interrupting the X-ray measurements. The whole vacuum furnace and loading mechanism was mounted on a focusing Geiger-counter X-ray spectrometer so that the diffraction pattern could be recorded continuously during the test. The X-ray beam is constrained to the horizontal plane. The peak intensities of the X-ray diffraction lines from the austenite, γ phase (111) and/or (200) planes, and from the ferrite, α phase (110), were used as measures of the amounts of the two phases present. Specimens were heated to 1650°F (900°C) for 15 min, then cooled to the testing temperature, and either held there or cooled gradually through the transformation region under constant load.

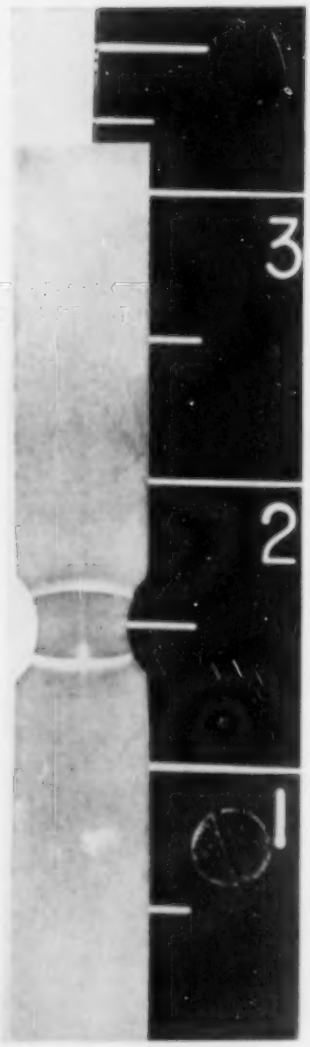

Fig. 1—X-ray specimen after loading to 12,200 psi. The light bands are the regions of severe plastic deformation which occur just above the A_1 temperature. Scale is in inches.

Tensile Tests: Standard tensile bars of 0.505 in. diam were heated by a concentric electric heater while mounted on a conventional testing machine. Fiducial circles 0.100 in. apart were inscribed along the gage length. Specimens were held at 1650°F (900°C) for 30 min, then cooled to the testing temperature. Bars were pulled to fracture at temperatures of 1300° (704°C), 1320° (716°C), and 1340°F (727°C) (these temperatures were based on the X-ray and dilatometer results), and immediately quenched by an air blast.

Microstructural Examination: After testing, the tensile bars and X-ray specimens were mechanically polished and etched in 1 pct nital or alkaline sodium picrate. Quantitative determinations of carbides in the strained regions were made by lineal analysis. Both light and electron micrographs were prepared to illustrate the reaction under stress.

Dilatometry: Dilatometer measurements were made in a clear fused-quartz dilatometer at various cooling rates from 60° to 1°F per min.

Results

There were several effects of stress observed depending on the temperature during stress and whether or not the temperature was held constant or

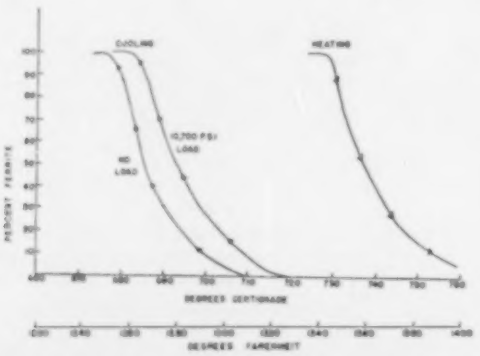

Fig. 2—Calculated percentage of ferrite vs temperature, showing the effect of stress on the austenite to ferrite transformation for a cooling rate of about 50°F per min. A slower cooling at about 4°F per min causes the curve for no load to coincide with the 10,700 psi curve.

a—Center of specimen where temperature was well above A_1.

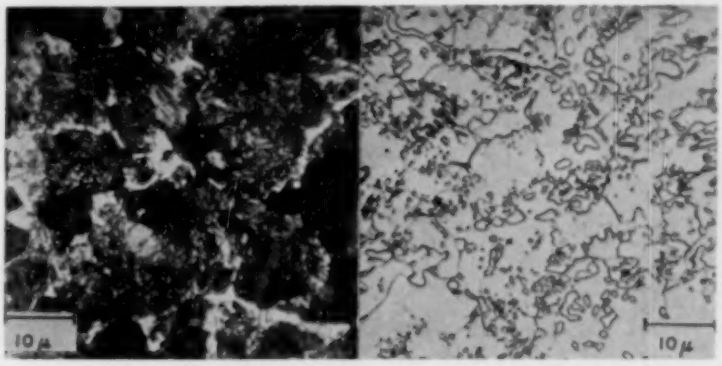

b—Region of plastic deformation where temperature was within about 5°F of A_1.

Fig. 3—Micrographs of X-ray specimen stressed at 12,200 psi.

varied during stress. In each case, the effects were repeated on several specimens, some 30 in all being tested.

Reorientation of Austenite Well Above the A_1 (1325°F) Temperature: In the X-ray apparatus a specimen was held at 1365°F (740°C) after austenitizing at 1650°F (900°C). Before loading, the γ phase (111) diffraction line had a peak intensity (on an arbitrary scale) of 80, while the (200) line had a peak intensity of 53. When a tensile load of 7000 psi was applied, the peak intensity of the (111) line decreased from 80 to 42 and the peak intensity of the (200) line increased from 53 to 76. When the specimen was recycled through the heating and loading operations, the same results were observed each time. The experimental conditions did not allow a determination of whether the austenite lattice was rotating during slip or whether there was rapid recrystallization with a preferred orientation resulting. This change in the relative intensity of the X-ray diffraction lines is similar to the change corresponding to the development of "cube texture" in metals such as copper on annealing after severe reduction by rolling.

Acceleration of Equilibrium Conditions at Ar°: An X-ray specimen was cooled at about 50°F per min from 1340° (730°C) to 1240°F (670°C) with the Geiger-counter spectrometer set at a position to record the changing peak intensity of the ferrite, α phase (110) diffraction line as the temperature was lowered. At 1240°F, the α phase (110) line had reached its maximum intensity corresponding to 100 pct ferrite. The curve of percentage of ferrite vs temperature during cooling is plotted in Fig. 2 in which the percentage of ferrite was obtained by scaling the measured peak intensity at each temperature to the peak intensity at 1240°F as 100 pct ferrite. From Fig. 2, the *Ar* temperature appears to be approximately 1305°F (708°C) which temperature was substantiated by dilatometer measurements. The experiment was repeated with the same cooling rate but with the specimen loaded to 10,700 psi and the results plotted in Fig. 2. Loading the specimen to 10,700 psi raised *Ar* by about 18° (10°C) for the 50°F per min cooling. As the cooling rate was reduced, *Ar* approached A_1 and the curve for an unstressed specimen cooled at only 4°F per min (not shown in Fig. 2) very nearly coincides with the curve for 10,700 psi load.

Other Effects at Ar: The stress necessary to cause plastic deformation (yielding) has a minimum value just above A_1 temperature, and stress appears to raise A_1 slightly. The experiment described herein was based on the observation of bands of severe plastic yielding such as are shown in Fig. 1 when specimens were loaded with more than 12,000 psi at temperatures well above A_1. The higher the temperature at the center of the notch, the further from the center the bands appeared. As described in the experimental procedure, the X-ray beam can be set to yield information about any desired portion of the notched region. For this experiment, the thermocouple was mounted near the end of the notch rather than at the center and the X-ray beam diffracted from the same region. With the end of the notch adjusted to just above the A_1 temperature, the center of the notch obviously will be well above A_1 (optical pyrometer measurements indicated it was about 25°F above A_1) while outside the notch the temperature will be below A_1. For a specimen held in this condition, the X-ray pattern before loading showed both γ phase and α phase diffraction lines. Upon loading to 12,000 psi or over, there was sudden yielding, not at the center of the specimen but at the two bands which are visible in Fig. 1. The X-ray record during this time showed an increase in the intensity of the α phase (110) line and decrease in

Fig. 4—Electron micrograph of region b in Fig. 3.

* *Ar* is the temperature at which transformation commences during cooling.

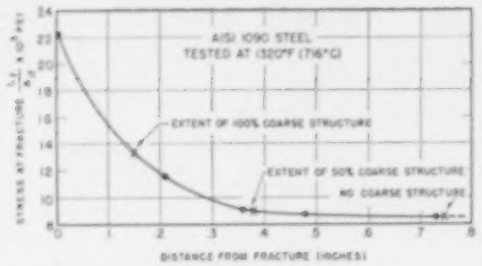
AISI 1090 STEEL
TESTED AT 1320°F (716°C)
EXTENT OF 100% COARSE STRUCTURE
EXTENT OF 50% COARSE STRUCTURE
NO COARSE STRUCTURE
DISTANCE FROM FRACTURE (INCHES)

Fig. 5—Stress in tensile bar at time of fracture. If L_i is the load at fracture in psi and A_i is the cross-sectional area of the specimen at the distance i in. from fracture, then the calculated stress L_i at A_i is L_i/A_i. This is the ordinant on the graph. The coarse structure is spheroidized carbides as in Fig. 3b or very coarse pearlite.

the γ phase (111) line, indicating that some transformation from austenite to ferrite had occurred simultaneously with yielding. The amount of increase in α phase was judged from curves, such as those in Fig. 2, to correspond to an increase in A_1 temperature of about 5°F. The micrograph shown in Fig. 3a is typical of the region at the center of the notch where the temperature was about 25°F above A_1 (the micrograph was taken after cooling, of course), and Fig. 3b is at the region of severe plastic deformation. The extreme coarseness of the pearlite and spheriodal carbides in the stress affected region should be noted. Ordinarily, to obtain such coarse carbide structure would require a very slow cooling rate (approximately 1°F per min) or a spheroidizing treatment. Fig. 4 is an electron micrograph of the stress affected region and shows that there are no small carbides present. Lineal analysis indicates 13 pct carbide which is the equilibrium composition.

Tensile tests corroberated the minimum stress necessary for yielding at A_1. Bars pulled at 1340° (730°C) and 1300°F (705°C) showed a small uniform reduction in area along the bar. A bar pulled at 1320°F (715°C) showed the same severe necking and very coarse carbides as the corresponding region of the X-ray specimen. Fig. 5 depicts the stress at each point along the longitudinal axis of the tensile bar at time of fracture for the 1320°F test. When the fractured bar was examined metallographically, it was found that the same coarse microstructure of Fig. 3b extended outward from the fracture to a point corresponding to about 13,000 psi. Thus, 13,000 psi seemed to be the minimum stress required for the development of the same plastic yielding and coarse carbides which were observed in the X-ray specimen at about 12,000 psi. The figures of 13,000 psi for the tensile tests and 12,000 psi for the X-ray tests are felt to be in reasonably good agreement.

Controlled compressive stress could not be applied at elevated temperatures with the equipment available. However, forging and rolling at temperatures from 1280° (620°C) to 1650°F (900°C) in 20°F steps did not cause a similar coarsening of the microstructure.

Discussion and Conclusions

The results given above appear to be related parts of the same phenomenon. The effects which occur depend on the particular temperature and stress values as would be expected. The strain rate undoubtedly enters also, but no equipment was available for controlling the rate; the tensile loading employed was essentially static loading for both the X-ray specimens and the standard tensile bars. In each instance, it is presumed that slip takes place in the γ phase along the (111) planes. When the temperature is well above A_1, this slip leads to reorientation of the lattice which is not surprising, since it is well known that working will often cause recrystallization and preferred orientation in metals. The high temperature X-ray method offers a very convenient way of observing such effects, inasmuch as the reorientation can be examined continuously during the experiment rather than after the effects have taken place.

The acceleration of equilibrium conditions by stress during cooling can be explained by the stress supplying necessary energy for nucleation and growth of the ferrite phase. As was described previously, small stress does not raise Ar above A_1 but merely hastens the occurrence of the transformation at a temperature where it normally occurs if cooled at a sufficiently slow rate.

When a critical load is applied just above A_1, sudden plastic deformation takes place, A_1 is raised by approximately 5°F, and large carbides are precipitated. Two possible mechanisms for such reactions are suggested. The sudden yielding may lead to a large number of dislocations in the γ phase. From work reported by Buffington and Cohen,[3] it is known that the self-diffusion rate of iron increases rapidly with increasing strain rate; thus the diffusion rate of carbon might be expected to increase also. The rapid diffusion of carbon to dislocations would deplete the remaining austenite of carbon and lead to instability of the γ phase with ensuing transformation to the α phase.

The other mechanism is based on a reaction similar to the known shear transformation from austenite to martensite in suitable alloys. After slip of the γ phase along (111) planes, some of the atoms are approximately in the proper positions for the α phase. Such an atomic arrangement would not favor the carbon atoms remaining in the interstices. This, coupled with the rapid diffusion rate of carbon during yielding, could very well lead to the precipitation of large carbides and stabilization of the atoms in the α-phase positions. The increase of A_1 by only 5°F and the critical value of stress fit in with this explanation better than with the previous one. For instance, when the temperature is too far above A_1, the carbon will not tend to precipitate and the lattice will revert to the γ phase. Also, the stress required to cause the proper slip of the γ-phase lattice to make the atomic arrangement similar to that of the α phase would be expected to have a critical value. However, the authors are not attempting at this time to choose one or the other of these explanations but merely to present them as possibilities.

Acknowledgment

The authors wish to thank R. T. Seal, G. L. Gregg, and T. C. Lupton for their parts in obtaining the data.

References

[1] B. L. Averbach, S. A. Kulin, and M. Cohen: *Trans.* AIME (1952) **194**, p. 661; JOURNAL OF METALS (June 1952). An extensive bibliography is contained in this article.

[2] F. Sauervald and Th. Sperling: *Ztsch. für Physik* (1929) **56**, p. 544.

[3] F. S. Buffington and M. Cohen: *Trans.* AIME (1952) **194**, p. 859; JOURNAL OF METALS (August 1952).

Some Characteristics of the Isothermal Martensitic Transformation

by C. H. Shih, B. L. Averbach, and Morris Cohen

The isothermal formation of martensite is studied in Fe-Ni-Mn and Fe-Mn-C alloys under conditions where the athermal transformation is completely avoided, there being no martensite present at the beginning of the isothermal reaction. The initial rate of martensite formation is extremely low under these conditions, but it increases greatly as soon as some martensite is formed. It appears that true initial characteristics of the isothermal reaction can be studied only in samples wherein the formation of martensite on cooling is completely eliminated.

THE phenomenon of isothermal martensite formation is well established[1-6] but the observations have been made in the presence of varying quantities of athermal martensite. Complete avoidance of athermal martensite and the formation of martensite under pure isothermal conditions have been reported by Kurdjumov and Maksimova[2] in an Fe-Ni-Mn alloy (23 pct Ni, 3.4 pct Mn, and the balance Fe) and have been confirmed by recent experiments of Cech and Hollomon[5] in a similar alloy. In each case, the isothermal transformation rate was a maximum at the beginning of the transformation and decreased as the reaction proceeded. These initial transformation rates were used by Fisher[7] for the confirmation of calculated nucleation rates based on classical nucleation theory extended to include the effect of elastic strain energy. Cech and Hollomon have admitted, however, that up to 3 pct martensite formed on cooling in their samples and thus was present at the initiation of their isothermal runs.

In this paper, experiments on similar alloys are described, except that care was taken to remove the incidental martensite developed at the surface prior to the isothermal reaction. It is shown here that the reaction rate at the beginning of the strictly isothermal reaction is very low. As soon as some detectable amount of martensite is produced, the transformation rate increases rapidly but ultimately decreases as the reaction proceeds. When martensite is allowed to form isothermally in the presence of about 2 pct of prior martensite, the *apparent* initial reaction rate is a maximum and corresponds to the observations of Kurdjumov and Maksimova and Cech and Hollomon. It is evident that the cooperative nature of the martensitic reaction results in a significant stimulating or autocatalytic effect on the isothermal reaction rate.

C. H. SHIH, B. L. AVERBACH, Member AIME, and M. COHEN, Member AIME, are associated with Dept. of Metallurgy, Massachusetts Institute of Technology, Cambridge, Mass.

Discussion on this paper, TP 3848E, may be sent, 2 copies, to AIME by Mar. 1, 1955. Manuscript, Apr. 12, 1954. Chicago Meeting, November 1954.

Table I. Chemical Composition of Alloys, Pct

Alloy	Mn	Ni	C	Si	N	O
A	3.62	23.2	0.016	0.04	0.001	0.015
B	4.33	22.95	—	—	—	—
C	5.24	—	1.10	—	—	—

Experimental Procedure

The chemical compositions of the alloys used in this investigation are listed in Table I. The Fe-Ni-Mn alloys *A* and *B* were melted in an induction furnace, cast into ingots 2 in. diam by 4 in. long, and forged into $\frac{3}{8}$ in. diam rods. The manganese steel (alloy C) was melted in an arc furnace and cast into ceramic molds $\frac{1}{4}$ in. diam by 5 in. long. The rods were sealed in evacuated Vycor tubes and homogenized at 1175° to 1200°C for 50 hr. The long homogenization resulted in some manganese loss from the surface, producing a thin layer of transformed material. This surface layer was removed by grinding and the specimens were then swaged to 0.050 in. diam wire.

Measurements of electrical resistance were made with a Kelvin double bridge to follow the course of the martensitic transformation. A small permanent magnet was also useful in scanning an entire specimen for small localized quantities of martensite. This test is almost as sensitive as the electrical resistance method in detecting the presence of martensite (which is ferromagnetic in these alloys) and it was especially useful in deciding whether a specimen was completely free of martensite. The wire specimens (0.050 in. diam by 2.5 in. long) were sealed in evacuated tubes and austenitized for 5 min at 1150°C. The specimens were quenched into water and, unless otherwise stated, stress-relieved for 1 hr at 650°C in order to induce greater uniformity in the subsequent martensitic transformation. As dem-

onstrated later, quenching stresses were found to result in nonuniform transformation across the section of the specimens. Electrical resistance measurements were conducted as a function of time at −196° to −90°C and the resistance changes were calibrated in terms of martensite formation by means of metallographic lineal analyses of the transformed samples. It is estimated that the sensitivity of the resistance method was about 0.2 pct martensite.

There was sufficient manganese loss during the austenitizing treatment, even though it was carried out in sealed-off tubes, to cause the initiation of some martensite near the surface on cooling below room temperature. If the wire specimens were electrolytically polished (removing 0.002 to 0.003 in.) prior to the subzero cooling treatment, it was possible to quench into liquid nitrogen (−196°C) and to return quickly to room temperature without any formation of martensite.* This was checked by electrical resistance measurements, metallographic examination, and qualitative tests with a permanent magnet over the entire length of the specimen, both at −196°C and at room temperatures, in order to ascertain that no martensite had formed in localized areas. Most of the work is reported in detail for the Fe-Ni-Mn alloy *A*. Supplementary runs were made on alloys *B* and *C*.

* Thus the M_s temperatures for the athermal martensitic transformation in these alloys were below −196°C.

Experimental Results

Fig. 1 shows the progress of the martensitic transformation in alloy *A* reacted isothermally at a series of temperatures. Each specimen was quenched into liquid nitrogen for about 30 sec to insure temperature equalization, quenched upward to the indicated temperature, and observed for a period of time. A few specimens also were cooled directly to the reaction temperature but these behaved quite similarly to those first quenched into liquid nitrogen, provided that the direct quenching was sufficiently rapid to avoid any transformation during cooling. Thus it was possible to follow the progress of the isothermal transformation without the complication of prior martensite introduced on cooling.

No martensite was detected by the electrical resistance method at −196°C for holding times up to about 30 min, and then the transformation proceeded very slowly at this temperature. At −152°C the reaction was considerably faster, but even here (Fig. 1, insert) the initial reaction rate was small. The reaction rate was a maximum, and the incubation a minimum at −140°C; at higher temperatures, the reaction rate decreased. In each case, however, there was an apparent induction period in which no martensite was detected. Induction periods in the isothermal transformation were also reported by Kulin and Speich[4] for an Fe-Cr-Ni alloy, but they felt that their experimental observations were uncertain in this respect.

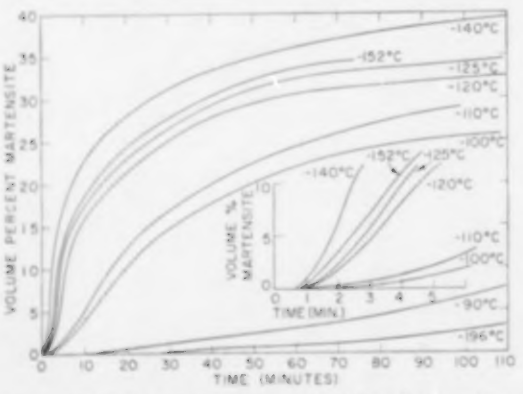

Fig. 1—Isothermal transformation curves at indicated temperatures for samples containing no initial martensite. (Insert figure shows the incubation period and the early transformation.)

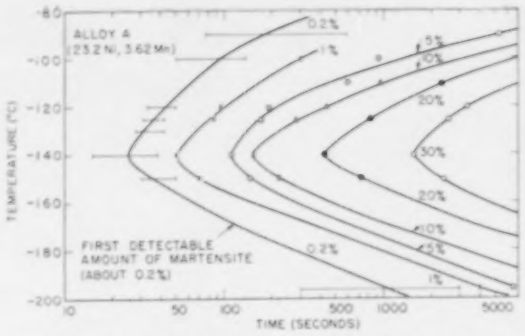

Fig. 2—Transformation-temperature-time curves showing progress of isothermal martensite formation in samples containing no initial martensite.

The time required to detect the first trace of martensite (0.2 pct transformation in the present work) is shown in Fig. 2. The horizontal line at each temperature level indicates the range of values obtained for the incubation period in 3 to 5 different specimens. The time to reach temperature, about 10 sec, was subtracted in each instance. The variation of the incubation period from piece to piece is probably caused by small differences in chemical composition, inasmuch as the transformation is critically dependent on the alloy content. The general C-shape of the transformation-temperature-time curves in Fig. 2 is similar in form to findings of Cech and Hollomon.[5]

The effect of martensite formed prior to the isothermal transformation is indicated by the following experiment: Specimens were quenched into liquid nitrogen and held long enough to develop 1.5 to 2.0 pct martensite. Each specimen was then upquenched to higher temperatures and the isothermal martensitic transformation observed. Fig. 3 demonstrates that the induction periods previously observed have disappeared and that the initial rates of martensite formation have become much more rapid than at the equivalent temperatures in Fig. 1. These data check reasonably well with those presented by Kurdjumov and Maksimova and Cech and Hollomon. It should be noted that the final amounts of transformation product are about the same for each of the corresponding temperatures in Figs. 1 and 3; the initial rates of transformation are, however, quite different.

It was recognized that the stress-relieving heat treatment at 650°C might introduce a stabilization phenomenon which could affect the transformation. In order to investigate this point, two specimens were austenitized at 1150°C and quenched. One (specimen 1) was stress relieved at 650°C, electropolished, and then reacted at −196°C. The other (specimen 2) had an identical treatment except that the stress relieving was omitted. The transformation curves are shown in Fig. 4. The stress-relieved

and the nonstress-relieved samples have induction periods of 28 and 18 min, respectively, and the latter react somewhat more rapidly than the others on subsequent holding. This difference is due primarily to the tensile stresses in the central region of the as-quenched specimen. It is known that tensile stresses tend to promote the martensitic transformation,[8] and this phenomenon is operative in the present alloys to a marked degree, unless stress relieving is introduced. Fig. 5 shows the entire cross-section of a specimen isothermally transformed without stress relief; the preponderance of martensite in the center is evident. Stress-relieved specimens display a more uniform reaction over the cross-section and the measured rates are more self-consistent. It is considered, therefore, that the transformation curves in Fig. 1 represent the true isothermal reaction in specimens which are initially free of martensite and substantially free of quenching stresses. It is clear also that the incubation in the isothermal reaction is not caused by stabilization during the stress relieving because the incubation is observed when the stress relieving is omitted.

Alloy *B* did not transform above or at the temperature of liquid nitrogen, but it did form martensite when stressed at the latter temperature. Since alloys *A*, *B*, and those used by Kurdjumov and Maksimova and Cech and Hollomon have almost identical nickel contents, the temperature (T_m) at which the maximum rate of isothermal transformation occurs was plotted as a function of manganese content in Fig. 6. The compositions were adjusted to 23.0 pct Ni by assuming that 1 pct Mn is twice as effective as 1 pct Ni.[9] It is evident that T_m is strongly dependent on the manganese content, and the discrepancies in the literature on Fe-Ni-Mn alloys[6,9] thus are explainable on the basis of slight variations in composition. The classical nucleation theory[7,10] for substitutional iron-base alloys predicts that the maximum rate of transformation should decrease with increasing alloy content, but that the temperature corresponding to the maximum rate should remain virtually unchanged. The latter prediction is contrary to the marked variation in T_m as a function of manganese content indicated in Fig. 6.

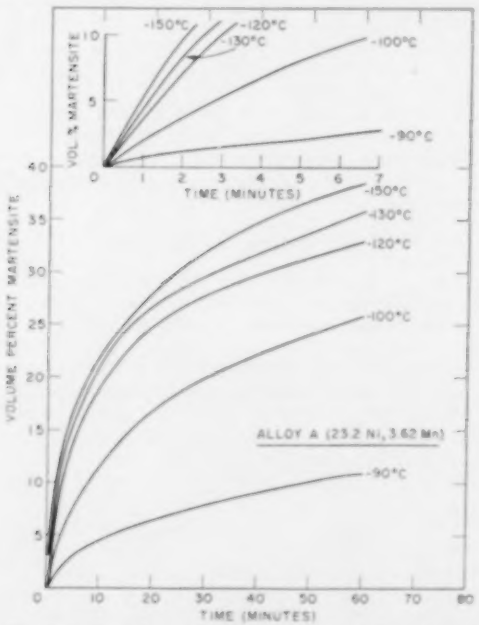

Fig. 3—Isothermal transformation curves at indicated temperatures for samples with 1.5 to 2 pct initial martensite. (Insert figure shows the absence of an incubation period in the early transformation.)

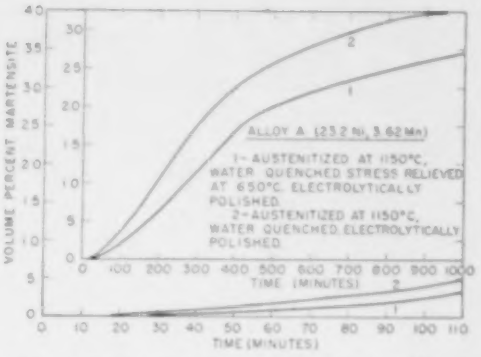
VOLUME PERCENT MARTENSITE
TIME (MINUTES)
ALLOY A (23.2 Ni, 3.62 Mn)
1- AUSTENITIZED AT 1150°C, WATER QUENCHED STRESS RELIEVED AT 650°C, ELECTROLYTICALLY POLISHED.
2- AUSTENITIZED AT 1150°C, WATER QUENCHED, ELECTROLYTICALLY POLISHED.

Fig. 4—Effect of stress relief on martensite formation at −196°C.

It is also possible to avoid martensite formation on subcooling in an alloy containing 5.24 pct Mn and 1.10 pct C (alloy C). Fig. 7 shows that this material exhibits a substantial incubation period (about 20 min at −196°C) and then transforms isothermally like alloy *A*. The reaction is extremely sensitive to composition, different pieces of the same bar displaying large variations in transformation behavior. A small increase in carbon content is sufficient to inhibit the transformation completely, while a small decrease in carbon brings the M_s into the temperature range of interest here and it becomes impossible to avoid the athermal reaction prior to the isothermal transformation.

Discussion of Results

These data indicate that in certain alloys martensite can form by a completely isothermal process. In the absence of initial martensite produced on cooling, there is an induction period in the isothermal transformation wherein no martensite (within a sensitivity of 0.2 pct tranformation) is observed. On the other hand, in the presence of 1 to 2 pct prior martensite, the reaction rate is a maximum at the beginning of the isothermal transformation.

Fig. 5—Distribution of martensite formed isothermally (100 min at −196°C) in a quenched specimen without stress relief. Alloy *A* (23.2 pct Ni, 3.62 pct Mn), longitudinal section, etched with Vilella's reagent. X75. Area reduced approximately 25 pct for reproduction.

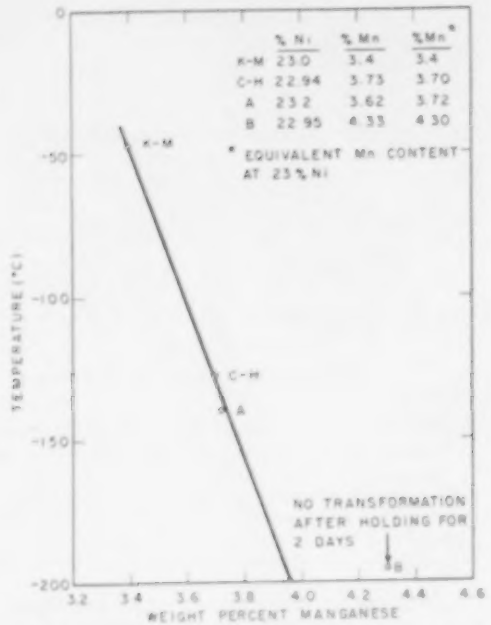

Fig. 6—Temperature (T_m) of maximum rate of isothermal martensite formation in Fe-Ni-Mn alloys.

It would thus appear that Fisher's calculations[1] which predict a maximum initial rate and which are fitted to the Cech and Hollomon data are not representative of the true isothermal reaction. The equations of Kurdjumov and Maksimova also fail in this respect. The free energies of nucleation based on Fisher's treatment of the Cech and Hollomon data are approximately 10,000 to 27,000 cal per mol in the temperature range of −196° to −90°C. If the initial transformation rates (unstimulated by prior martensite) are used in the same calculations, the free energy of nucleation required to form a nucleus 11,000 to 29,000 cal per mol.

One factor that leads to these rather large values for the free energy of nucleation is the assumption of random nucleation due to thermal fluctuations. Alternatively, if the strain embryo concept is adopted,[2] the nucleation is regarded as occurring only at preferred sites, but still under the impetus of thermal fluctuations. The preferred sites are pictured as regions of local strain or imperfections in the lattice, having a distribution of free energies above that of the unstrained matrix. If F_c is the free energy of nucleation required to form a nucleus from the perfect lattice, then a strain embryo of free energy F could be activated by the increment of free energy $\Delta F_c = F_c - F$. This would be a more probable event than nucleation from the perfect lattice and the most potent embryos would be nucleated first. If F is larger than F_c, nucleation can take place without benefit of thermal fluctuations; this is the athermal mode of the martensitic transformation. However, when F is smaller than F_c, the embryo must wait for a thermal fluctuation to provide the increment of free energy necessary for nucleation; this is the isothermal mode of the martensitic transformation. In order to find only the isothermal transformation, as in the present investigation, ΔF_c must be larger than RT to avoid athermal and immediate isothermal transformation, but ΔF_c should not be too

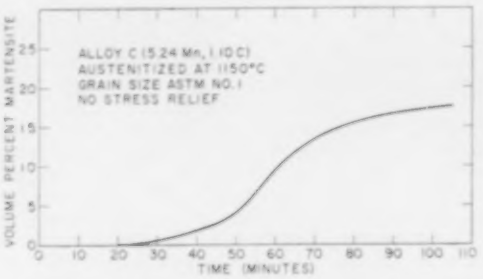

Fig. 7—Isothermal formation of martensite in a manganese steel at −196°C in a sample containing no initial martensite.

large if appreciable transformation is to occur within convenient periods of time at these subzero temperatures. Such requirements seem to be met in relatively few alloys.

The magnitude of ΔF_c for the alloy A studied here may be estimated from the initial rates of isothermal transformation. It is assumed that, at each reaction temperature, the rate of nucleation ($\dot{N}$) is constant during the incubation period at least up to the time (t_i) of the first detectable amount of martensite (0.2 pct). Then

$$0.002 = \dot{N}\, v\, t_i \qquad [1]$$

where $\dot{N}$ is nuclei per cu cm per sec, v is the volume of each initial martensitic plate $= \pi r^2\delta/2$ for a lenticular shape of radius r and thickness δ, and t_i is the time in seconds required to detect the first 0.2 pct martensite. According to metallographic measurements, $r = 1.6\times10^{-4}$ cm and $\delta = 8\times10^{-6}$ cm for the first plate formed in each austenitic grain. Plates of this size correspond to 3 pct by volume of the austenitic grain, and this is the same for each reaction temperature. This is in good agreement with the value of 5 pct adopted by Fisher[1] although his analysis of the Cech and Hollomon data results in an unexpected range from 1.4 to 6.9 pct, depending on the reaction temperature.

The rates of nucleation derived from Eq. 1 are listed in Table II. These values are smaller by a factor of about 10^7 than the Cech and Hollomon rates employed in Fisher's calculations. $\dot{N}$ is related to ΔF_c through the relation

$$\dot{N} = n_s\, \nu \exp\left[-\Delta F_c/kT\right] \qquad [2]$$

where n_s is the number of preferred sites per cu cm at which the initial martensitic plates are nucleated; ν is the lattice vibration frequency, taken as 10^{12}

Table II. Initial Nucleation Rates and Activation Energies for Isothermal Martensite Formation. Alloy A: 23.2 pct Ni, 3.62 pct Mn

Temperature, °C	t_i, Sec	$\dot{N}$, Nuclei per Cu Cm per Sec	$\Delta F_c/RT$	ΔF_c, Cal per Mol
−90	200	33	38.0	13,900
−100	100	67	37.3	12,900
−110	60	110	36.8	12,000
−120	40	167	36.3	11,100
−130	30	180	36.0	10,300
−140	25	270	35.7	9,500
−150	35	190	36.2	8,900
−160	65	103	36.7	8,300
−170	120	57	37.0	7,700
−180	300	23	38.4	7,150
−190	650	10	39.1	6,500
−196	1000	7	39.9	6,150

sec^{-1}; ΔF_v is the increment of free energy required to activate the most potent embryos; k is Boltzmann's constant; and T is absolute temperature.

If it is assumed that there is one most potent embryo per grain of austenite, n_v can be taken as the number of grains per cu cm, or 10^3 for the observed grain size of ASTM Nos. 1 and 2.

The values of ΔF_v calculated from Eq. 2 are listed in Table II. The temperature dependence of ΔF_v is closely similar to that found for Fe-Ni alloys by Machlin and Cohen.[8]

The concept of preferred sites for the nucleation of martensite, even in the absence of prior martensite, leads to reasonable values for ΔF_v. Random nucleation seems unlikely in that it would require considerably higher energies of nucleation (by a factor of ~2) to account for the low rates of nucleation during the early stages of the isothermal martensitic transformation.

Summary

1—Isothermal formation of martensite has been studied in Fe-Ni-Mn and Fe-Mn-C alloys in the absence of athermal or prior martensite.

2—Contrary to the findings of other investigators, the reaction rate at each temperature is quite small initially and increases to a maximum because of autocatalytic effects only after some martensite is present.

3—Unless the autocatalytic phenomenon is taken into account, the classical nucleation theory should not be applied to the maximum transformation rates but to the much lower initial rates. Also, the assumption of random nucleation leads to relatively high energies of nucleation.

4—More reasonable values for the energies of nucleation are derived on the basis of preferred nucleation sites in the virgin austenite. This is consistent with the strain embryo concept of martensite nucleation.

Acknowledgments

This work stems from an investigation on austenitic manganese steels conducted under a grant-in-aid received from the Climax Molybdenum Co. The authors also wish to thank Mr. Edward Sudenfield for his assistance in various phases of the experimentation.

References

[1] G. V. Kurdjumov and O. P. Maksimova: Kinetics of Austenite to Martensite Transformation at Low Temperatures. *Doklady Akademii Nauk SSSR* (1948) **61**, No. 1, p. 83; H. Brutcher Translation No. 2187.

[2] G. V. Kurdjumov and O. P. Maksimova: On the Energy of Formation of Martensite Nuclei. *Doklady Akademii Nauk SSSR* (1950) **73**, p. 95; H. Brutcher Translation No. 2565.

[3] S. C. Das Gupta and B. S. Lement: Isothermal Formation of Martensite at Subzero Temperatures in a High Chromium Steel. *Trans.* AIME (1951) **191**, p. 727; JOURNAL OF METALS (September 1951).

[4] S. A. Kulin and G. R. Speich: Isothermal Martensite Formation in an Iron-Chromium-Nickel Alloy. *Trans.* AIME (1952) **194**, p. 258; JOURNAL OF METALS (March 1952).

[5] E. S. Machlin and Morris Cohen: Isothermal Mode of the Martensitic Transformation. *Trans.* AIME (1952) **194**, p. 489; JOURNAL OF METALS (May 1952).

[6] R. E. Cech and J. H. Hollomon: Rate of Formation of Isothermal Martensite in Fe-Ni-Mn. *Trans.* AIME (1953) **197**, p. 685; JOURNAL OF METALS (May 1953).

[7] J. C. Fisher: Application of Nucleation Theory to Isothermal Martensite. *Acta Metallurgica* (1953) **1**, No. 1, p. 32.

[8] S. A. Kulin, M. Cohen, and B. L. Averbach: Effect of Applied Stress on the Martensitic Transformation. *Trans.* AIME (1952) **192**, p. 661; JOURNAL OF METALS (June 1952).

[9] Morris Cohen: The Martensite Transformation. *Phase Transformations in Solids.* (1951) p. 599. New York. John Wiley and Sons, Inc.

[10] J. C. Fisher: Martensite Nucleation in Substitutional Iron Alloys. *Trans.* AIME (1953) **197**, p. 918; JOURNAL OF METALS (July 1953).

Technical Note

Melting Point of Germanium and the Constitution of Some Ge-Ga Alloys

by E. S. Greiner and P. Breidt, Jr.

THIS note reports a determination of the melting point of germanium, and the liquidus of the Ge-Ga alloys; lattice constants of the α phase are given.

The alloys were prepared by melting germanium (>20 ohm-cm resistivity) and gallium (99.6 pct) in evacuated silica tubes. The materials (50 to 70 g) were heated at 1000°C, held in the liquid state for about ¾ hr, and then cooled rapidly in the tubes. Points on the liquidus were obtained by thermal analysis which consisted of obtaining time-temperature data during heating and cooling the materials in high purity graphite crucibles and a helium atmosphere. Temperatures were determined with a Pt—Pt-Rh thermocouple protected by a silica sheath. The couple was calibrated against a National Bureau of Standards calibrated couple and also against the freezing points of copper, silver, aluminum, and the 28.1 wt pct Cu, 71.9 wt pct Ag alloy eutectic.

The samples for X-ray analysis were prepared by heating small pieces of the ingots in evacuated glass or quartz tubes at temperatures between 600° and 900°C for periods ranging from 2 hr to 22 days, periods deemed sufficient for equilibrium to be attained, followed by quenching in water. The heat-treated samples were ground to powder for X-ray analysis. The lattice constants of the germanium-rich phase (α) were determined with a back-reflection focusing camera. The X-ray reflections (331 and 422 Cr Kα, 422 and 333 Cr Kβ) were corrected

E. S. GREINER, Member AIME, and P. BREIDT, JR. are associated with Bell Telephone Laboratories Inc., Murray Hill, N. J.

TN 2515. Manuscript, Sept. 22, 1954.

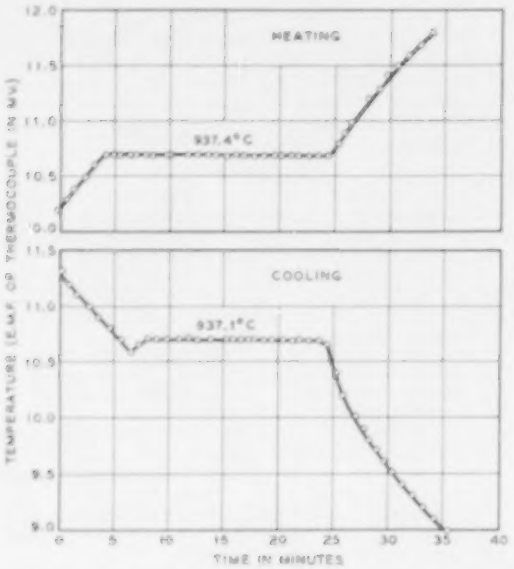

Fig. 1—Thermal analysis of germanium. Time-temperature plots for heating and cooling. Pt—Pt-Rh thermocouple, reference junction at 0°C.

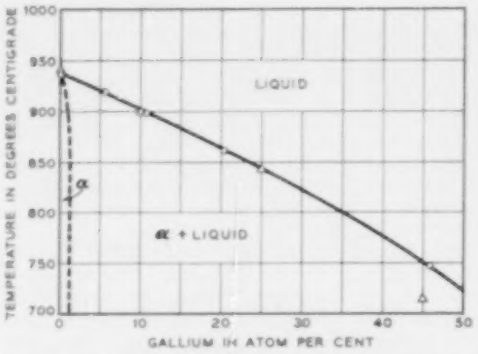

Fig. 2—Constitution of germanium-rich Ge-Ga alloys. Circles represent present investigation; triangles, Klemm et al.[6]

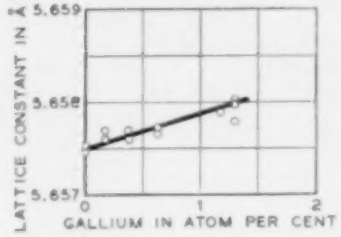

Fig. 3—Lattice constants of α phase Ge-Ga alloys at 25°C.

for refraction.[1] The precision of the lattice constant determinations, calculated by Cohen's method,[2] was one part in 50,000.

The duration of the constant temperature arrests while melting or freezing, for the five tests on germanium, was from 7 to 20 min depending upon the rate of heating or cooling; one set of data is plotted in Fig. 1. The temperatures of the arrests for the two samples of germanium are given in Table I. The precision of the thermocouple calibration was ±0.5°C. Hence, the melting or freezing point of these samples of germanium is 937.2 ±0.5°C. Early investigators reported the melting point of germanium as high as 958°C,[3,4] others obtained 949°C;[5] more recently, 940°C has been reported.[6,7]

Thermal analyses of germanium alloys containing up to 45.91 atomic pct Ga showed that discontinuities associated with the liquidus occurred at the temperatures given in Table I, designated by circles in Fig. 2. These data are in good agreement with earlier results[6] for the alloys containing up to 25 atomic pct Ga. At 45 atomic pct Ga, however, the present investigation showed the liquidus is approximately 30°C higher than the point at this composition reported previously. The higher value is consistent with a smooth curve for the liquidus in this system.

Table I. Thermal Analysis Data

Sample No.	Gallium, Wt Pct	Gallium, Atomic Pct	Thermal Arrest, Heating, °C	Thermal Arrest, Cooling, °C	Thermal Arrest, Average, °C
Germanium (A)	—	—	937.2	937.0	
Germanium (A)	—	—	937.4	937.1	
Germanium (A)	—	—	937.5	937.1	
Germanium (A)	—	—	937.4	937.4	
Germanium (B)	—	—	937.3	937.0	937.2
Ge-Ga, No. 1	5.37	5.58	918	918	
Ge-Ga, No. 2	10.26	10.64	900	898	
Ge-Ga, No. 3	19.76	20.40	—	862	
Ge-Ga, No. 4	45.09	45.91	—	747	

The lattice constants of a series of Ge-Ga alloys containing up to 1.30 atomic pct Ga, heated to temperatures between 600° and 900°C for various periods and quenched, are plotted in Fig. 3. The addition of gallium increases the lattice constants of the alloys in the α phase approximately 0.0004A per atomic pct Ga. This enlargement of the lattice is qualitative evidence that gallium dissolves in solid germanium. The trend of the values suggests a solid solubility of approximately 1 atomic pct Ga at these temperatures.

Burton, Kolb, Slichter, and Struthers,[8] from freezing experiments, obtained a value of approximately 0.1 for the distribution coefficient C_s/C_l of germanium-rich alloys. C_s and C_l are the atom concentrations of gallium in the solid and liquid at specific temperatures. If a value of 0.1 at 900°C and the liquidus concentration from Fig. 2 are used, the solubility of gallium at this temperature is 1 atomic pct. This value is consistent with the X-ray diffraction data.

References

[1] E. R. Jette and F. Foote: *Journal of Chemical Physics* (1935) **3**, p. 605.

[2] M. U. Cohen: *Review of Scientific Instruments* (1935) **6**, p. 68.

[3] L. M. Dennis, K. M. Tressler, and F. E. Hance: *Journal* American Chemical Society (1923) **45**, p. 2033.

[4] W. Biltz: *Ztsch. Anorg. Allgem. Chemie* (1911) **72**, p. 313. J. L. Crenshaw: Reference quoted. *Chemical Abstracts* (1912) **6**, p. 176.

[5] T. R. Briggs, R. O. McDuffie, and L. H. Willisford: *Journal of Physical Chemistry* (1929) **33**, p. 1080.

[6] R. Schwarz and G. Elstner: *Ztsch. Anorg. Allgem. Chemie* (1934) **217**, p. 289.

[7] H. Stöhr and W. Klemm: *Ztsch. Anorg. Allgem. Chemie* (1939) **241**, p. 305.

[8] W. Klemm, L. Klemm, E. Hohmann, H. Volk, E. Orlamünder, and H. A. Klein: *Ztsch. Anorg. Allgem. Chemie* (1948) **256**, p. 239.

[9] J. A. Burton, E. D. Kolb, W. P. Slichter, and J. D. Struthers: *Journal of Chemical Physics* (1953) **21**, p. 1991.

Contribution of Crystal Structure to the Hardness of Metals

by W. Chubb

By measuring the hardness of metals at temperatures just above and just below their allotropic change point, it has been established that crystal structure has a real effect upon the strength of metals. The DPH of cobalt, iron, titanium, uranium, and zirconium have been measured at temperatures up to 1000°C. It was found that the body-centered-cubic crystal structure is always the softer structure when it is involved in an allotropic transformation. The close-packed and more complex structures are inherently harder, and may be expected, therefore, to be better base materials for high strength alloys.

IT has been observed that for metals with nearly the same melting point (i.e., tin and lead, magnesium and aluminum) the metal with the more complex crystal structure has a higher tensile strength and hardness. It might be asked whether this effect is really caused by the difference in crystal structure; and, if so, just what is the contribution of crystal structure to the strength of these metals. A qualitative answer to these questions can be obtained by measuring the change in hardness produced by the change in structure in metals exhibiting allotropic forms.

The evidence for changes in mechanical properties during allotropic transformations is rather meager. In 1909, Rosenhain and Humfrey[1] observed that "β" iron showed much less deformation at the transformation temperature than α iron. By means of a torsion test, Lee[2] found that iron bars were "critically plastic" at the α-γ transformation temperature. Sauerwald and Knehans[3] have shown that the dynamic hardness of iron increases between 900° and 1000°C. In 1930, Albert Sauveur[4] presented data on the hardness, tensile strength, and torsional strength of pure iron up to 1000°C. He concluded, "At 900°C, the α iron transforms into γ iron, and this is accompanied by increased strength and stiffness and decreased ductility."

The same year, Schischokin[5] obtained data on the hardness of thallium at temperatures above and below its transformation temperature. His data are replotted on semilogarithmic coordinates as Fig. 1. The fact that his data fall on straight lines in this type of plot is believed to attest to the purity of his metal and the accuracy of his results. In 1941, Nadai and Manjoine[6] obtained tensile data on pure iron with an indicated increase in strength at about 900°C. These experiments make it quite evident that changes in mechanical properties occur when a metal transforms from one crystal structure to another; but, except for Schischokin's data on thallium, none of the measurements seem accurate enough to determine the relative magnitude of the mechanical property change.

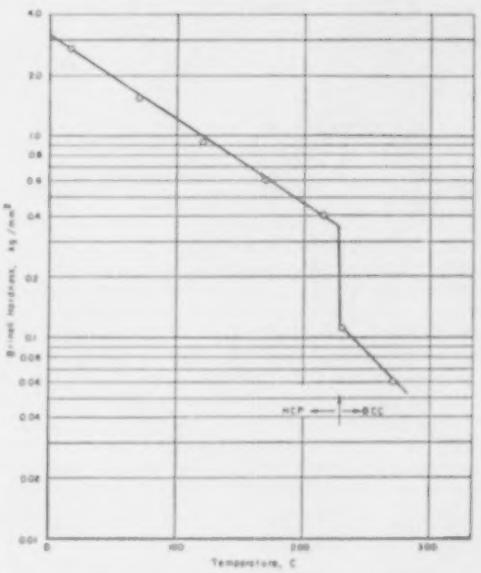

Fig. 1—Hardness of pure thallium at elevated temperatures. After Schischokin.[5]

Materials

The metals that have been examined for changes in hardness during transformation include 1—as-deposited commercial electrolytic cobalt about 99.7 pct pure, 2—Armco ingot iron, 3—arc-melted iodide titanium of a purity in excess of 99.8 pct, 4—uranium of a purity in excess of 99.5 pct, 5—arc-melted iodide zirconium of a purity in excess of 99.8 pct, 6—annealed, 0.08 pct C, rimmed steel, and 7—commercially pure RC55 titanium. While the purity of the first five of these materials leaves something to be desired, it will be noted that the observed hardness discontinuities occurred at the accepted transformation temperatures. (These temperatures are indicated by vertical arrows in Figs. 1 and 3 through 7.) The last two materials are commercial alloys introduced to show the effect of minor alloying elements upon the hot hardness curve.

Apparatus

Hardnesses at elevated temperatures were determined by means of a vacuum hot hardness machine. A diagram showing the basic features of this machine appears as Fig. 2. This machine is essentially a deadweight hardness machine in a furnace within a vacuum chamber. The sapphire-tipped indentor

W. CHUBB, Junior Member AIME, is associated with Battelle Memorial Institute, Columbus, Ohio.

Discussion on this paper, TP 3906E, may be sent, 2 copies, to AIME by Apr. 1, 1955. Manuscript, Mar. 10, 1954. Chicago Meeting, February 1955.

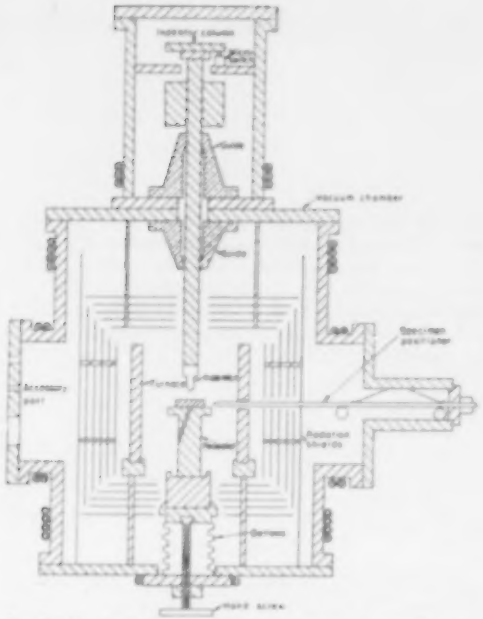

Fig. 2—Hot hardness machine. Area reduced approximately 80 pct for reproduction.

has a 136° pyramid tip and is heated to approximately the same temperature as the specimen. This arrangement allows a direct comparison between hardness measurements made at elevated temperatures and measurements made at room temperature with standard equipment. In fact, all room temperature data reported in Figs. 3 through 7 were determined by using a Vickers machine with a 10 kg load.

The absolute accuracy of the hot hardness machine has been checked by comparing readings taken at room temperature using this machine with those taken using a Vickers machine. The hardness numbers obtained agree within 5 pct. The reproducibility of results obtained with this equipment is illustrated by the results for an 0.08 pct C rimmed steel (Fig. 4). This curve is a composite of two hot hardness runs on the same specimen, one from 300° to 800°C and the other from 750° to 950°C. Temperature measurements were accurate to ±10°C, and the heating rate was equivalent to 2° or 3°C per min.

In a typical hot hardness run, the vacuum chamber is evacuated to an absolute pressure of less than 5 microns Hg. The specimen and indentor are heated to temperature by means of radiant energy from a commercial resistance heating unit. The specimen temperature is measured and the voltage input to the furnace is controlled by means of a thermocouple in the pedestal. When the specimen temperature is stabilized at the desired temperature, the pedestal is raised until the specimen contacts the indentor and raises the indentor column off a microswitch. The indentor and indentor column weigh 870 g and are allowed to remain in contact with the specimen for approximately 10 sec. After 10 sec, the pedestal is lowered, the specimen is moved to a new position, and the process is repeated. In this manner, a series of hardness measurements can be made at temperatures up to 1000°C.

Results of Experiments

The hardness data obtained show that for cobalt there is practically no change in DPH during transformation from hexagonal-close-packed to face-centered-cubic (Fig. 3); for Armco iron the transformation from body-centered-cubic to face-centered-cubic is accompanied by a threefold increase in hardness (Fig. 4); for thallium, titanium, and zirconium, the transformation from hexagonal-close-packed to body-centered-cubic is accompanied by a threefold decrease in hardness (Figs. 1, 5, and 7); for uranium, the transformation from complex tetragonal to body-centered-cubic is accompanied by a decrease in hardness of about 25 times (Fig. 6).

Data for the commercial alloys, low carbon mild steel, and RC55 titanium, are included in Figs. 4 and 5 to show the effects of impurities and minor alloying additions upon the hot hardness curve. In general, alloying elements tend to raise the level of the whole hot hardness curve and tend to obscure the

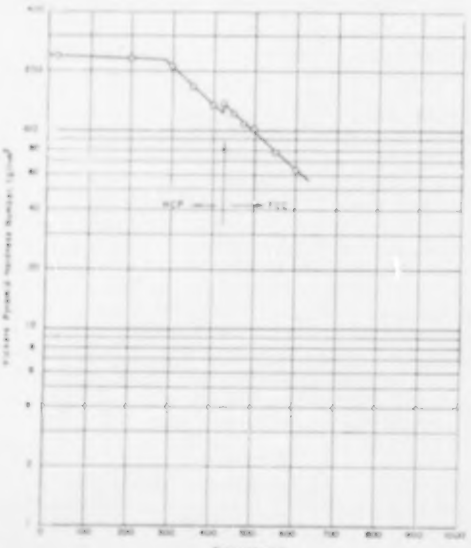

Fig. 3—Hardness of electrolytic cobalt at elevated temperatures.

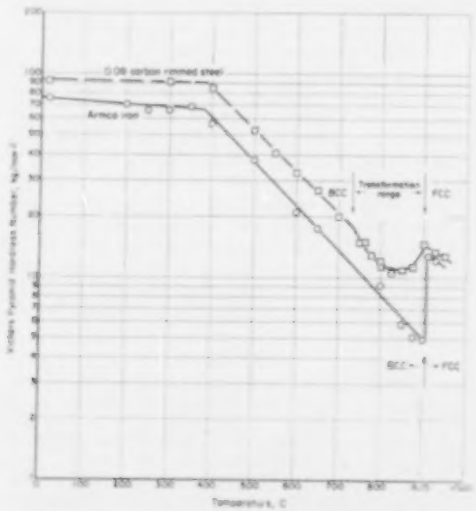

Fig. 4—Hardness of iron at elevated temperatures.

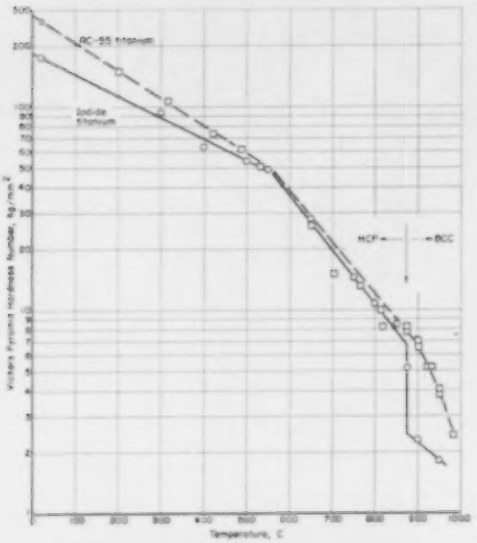

Fig. 5—Hardness of titanium at elevated temperatures.

mechanical property changes at the transformation temperature.

In each case, the data are plotted on semilogarithmic coordinates. This method of presentation has the advantage that much of the data seem to fall on straight lines. While no explanation for this straight-line relationship has been established, one of the breaks[5] occurs at 0.55 of the melting point (which temperature is known as the equicohesive temperature) and another coincides with allotropic transformations. For alloys, deviations from linearity also occur as a result of precipitation phenomena.[6-10] From this coincidence, it might be supposed that the straight-line portions of the curves correspond to temperature ranges in which there is no significant change in modes of crystal deformation.

An analysis of Fig. 4 will disclose that α iron, as represented by Armco iron, continues to soften between 730° and 900°C and that at 900°C γ iron is harder than α iron at 730°C. In a 0.08 pct C steel under equilibrium conditions, somewhat less than 20 pct γ iron will coexist with α iron at 825°C. Since a few hard particles in a soft matrix do not contribute much to the hardness of the whole, the hardness curve below 825°C is essentially the hardness curve for α iron. It may be concluded from this that the weakness of low carbon steels in their transformation range is caused to a great extent by the softness of α iron at these temperatures.

As illustrated in the introduction, there is good correlation between these hardness data and other mechanical properties; however, the correlation with other physical properties is poor. Many of the physical properties of metals change during an allotropic transformation, but there seems to be little correlation with mechanical properties. For example, the density of titanium and zirconium increases as the hardness decreases in transformation; the density of iron increases as the hardness increases in transformation.

These experiments show that the hardness changes caused by allotropic transformation are related to the type of transformation; the relative magnitude of the property change appears to be a characteristic of the crystal structure change. The body-centered-cubic crystal structure is always the softer structure when it is involved in a transformation. The face-centered-cubic and hexagonal-close-packed lattices have approximately the same structural strength and contribute more to the hardness of metals than the body-centered-cubic lattice. Highly complex lattices, although less dense, contribute even more to the strength of a metal. Each crystal structure contributes characteristically to the strength of an alloy. However, several other factors, such as the melting point, are involved in the strength of a metal, so that it does not follow

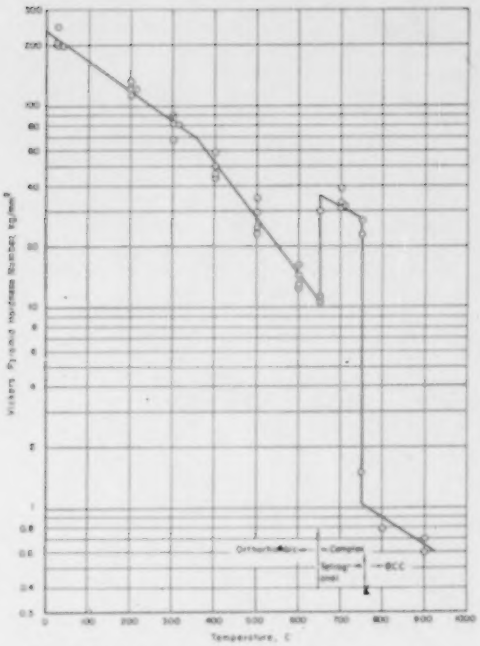

Fig. 6—Hardness of uranium at elevated temperatures.

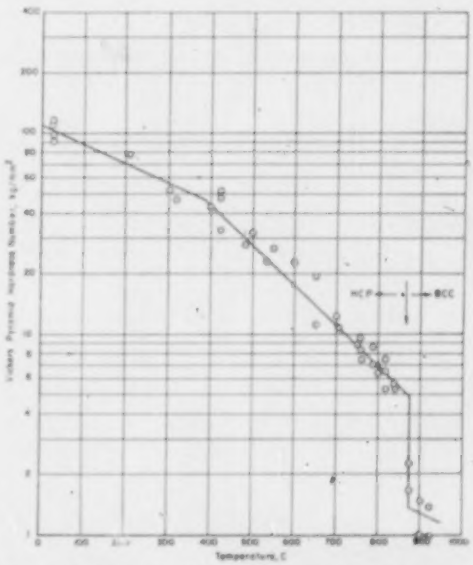

Fig. 7—Hardness of iodide zirconium at elevated temperatures.

that a face-centered-cubic metal must always be stronger than a body-centered-cubic metal. It is suggested, however, that for those metals that exhibit allotropic forms, alloys based on the stronger lattice will have an initial advantage over those based on the weaker lattice. This factor may explain why face-centered-cubic "austenitic" alloys of iron tend to have better high temperature strength than body-centered-cubic "ferritic" alloys of iron.

These experiments show that the symmetry of the lattice is an important factor in the strength of metals at elevated temperatures. Conversely, symmetry is related to the ease of deformation of the lattice. These observations tend to support the theory that one mechanism of deformation at elevated temperatures involves glide or slip along crystallographic planes.

Acknowledgments

The author is indebted to C. A. Anderson for aid in the design and construction of the hot hardness machine used in these experiments. The work was performed under AEC Contract W-7405-eng-92.

References

[1] W. Rosenhain and J. C. W. Humfrey: The Crystalline Structure of Iron at High Temperatures. *Proceedings* Royal Society, London (1909) **83**, p. 200.

[2] A. Sauveur: *The Metallography and Heat Treatment of Iron and Steel*. (1935) p. 123, Fig. 94. The University Press.

[3] F. Sauerwald and K. Knehans: The Temperature Dependence of the Hardness of Metals with Relation to Hot Working. *Ztsch. für Anorg. Allgem. Chemie* (1924) **140**, p. 227.

[4] A. Sauveur: Steel at Elevated Temperatures. *Trans.* American Society for Steel Treating (1930) **17**, p. 410.

[5] W. Schischokin: The Hardness and Extrusion Pressure of Metals at Various Temperatures. *Ztsch. für Anorg. Allgem. Chemie* (1930) **189**, p. 263.

[6] A. Nadai and M. J. Manjoine: High Speed Tension Tests at Elevated Temperatures. *Trans.* ASME (1941) **63**; *Journal of Applied Mechanics* (1941) p. A-77.

[7] J. H. Westbrook: Temperature Dependence of the Hardness of Pure Metals. *Trans.* ASM (1953) **45**, p. 221.

[8] E. Fetz: Dynamic Hardness Testing of Metals and Alloys at Elevated Temperatures. *Trans.* ASM (1942) **30**, p. 1419.

[9] E. Fetz: Dynamic Hardness Testing at Elevated Temperatures. *Iron Age* (Dec. 23, 1943) **152**, No. 27, p. 42; (Dec. 30, 1943) p. 40.

[10] H. Cornelius and W. Trossen: Dynamic Hardness Testing. *Stahl und Eisen* (1940) **60**, p. 293.

[11] T. Matsuda: On the Dynamic Hardness of Bronze and Brass at Elevated Temperatures. *Science Reports* Tohoku Imperial University, Japan (1925) **13**, p. 401.

[12] G. M. Enos, G. T. Peer, and J. C. Holzwarth: Dynamic Hot Hardness Testing with Special Reference to Isothermal Transformations. *Metal Progress* ASM (1948) **54**, p. 51.

Technical Note

Thermal Conductivity of Uranium and Several Uranium Alloys

by James L. Weeks

THERMAL conductivities of several samples of uranium and uranium alloys were determined using an apparatus previously described.[1] The value previously reported for uranium,[2] 0.035 cal per sec per cm per °C at 70°C, is in error due to the failure of a thermocouple during the determination on uranium. The defective thermocouple was detected after a reanalysis of the data obtained during the run and since has been replaced. Subsequently, runs on several samples of uranium show the thermal conductivity of uranium to be 0.069 cal per sec per cm per °C at 70°C.

The accuracy of the determinations was checked by measuring a sample of synthetic sapphire whose thermal conductivity was previously reported[1,2] and found to be in agreement with other values.[3-5]

The values given in Table I are believed correct to ± 3 pct or 0.003 cal per sec per cm per °C, whichever is larger. The samples were provided by J. H. Kittel of the Argonne National Laboratory, Metallurgy Div.

Table I. Thermal Conductivity of Uranium and Several Uranium Alloys

Specimen	Alloying Element, (Pct)*	Remarks	Thermal Conductivity at 70°C, Cal per Sec per Cm per °C
1B2	0.03 C	As-rolled rod	0.070$_2$
2B3	0.08 C	As-rolled rod	0.070$_2$
3B1	1.1 Zr	As-rolled rod	0.059$_5$
4B4	2.2 Zr	As-rolled rod	0.057$_1$
5A3	0.1 Cr	As-rolled rod	0.064$_5$
7B1	0.5 Cr	As-rolled rod	0.066$_8$
A-6	none	High purity, quenched from 1000°C	0.071$_6$
A-8	none	High purity, quenched from 800°C	0.071$_6$
35	none	Prepared from hot-pressed UH_3	0.064$_6$

* Balance uranium.

References

[1] J. L. Weeks and R. L. Seifert: Apparatus for the Measurement of the Thermal Conductivity of Solids. *Review of Scientific Instruments* (1953) **24**, pp. 1054-1057.

[2] J. L. Weeks and R. L. Seifert: Note Regarding the Thermal Conductivity of Synthetic Sapphire. *Journal* American Ceramic Society (1952) **35**, p. 15.

[3] J. Francl and W. D. Kingery: Thermal Conductivity: IV, Apparatus for Determining Thermal Conductivity by a Comparative Method; Data for Pb, Al_2O_3, BeO, and MgO. *Journal* American Ceramic Society (1954) **37**, No. 2, Part II, pp. 80-84. (Part II: special issue on thermal conductivity.)

[4] W. D. Kingery, J. Francl, R. L. Coble, and T. Vasilos: Thermal Conductivity: X, Data for Several Pure Oxide Materials Corrected to Zero Porosity. *Journal* American Ceramic Society (1954) **37**, No. 2, Part II, pp. 107-110. (Part II: special issue on thermal conductivity.)

[5] Edwin Ruh: New Jersey Ceramic Research Station, Rutgers University. Private communication.

J. L. WEEKS is associated with the Chemistry Div., Argonne National Laboratory, Lemont, Ill.

TN 240E. Manuscript, Aug. 5, 1954.

Study of the Effect of Boron on The Decomposition of Austenite

by C. R. Simcoe, A. R. Elsea, and G. K. Manning

Boron increases the hardenability of hypoeutectoid steels by decreasing the nucleation rate of ferrite and bainite. It is postulated that concentrations of lattice imperfections, such as exist at the grain boundaries, furnish the necessary energy for nucleus formation. Boron, because of its atomic diameter, will concentrate at lattice imperfections where sites of suitable size are present. Boron will decrease the energy of these local areas by occupying these sites. This mechanism accounts for the large increase in hardenability observed with small amounts of boron. The loss of the boron hardenability effect and the boron precipitate formation are explained on the basis of increased concentration of boron at the grain boundaries either with increasing boron content of the material or with increasing temperature.

COMMON alloying elements affect both the nucleation and growth rates of the austenite decomposition reactions.[1] This effect is largely a result of the slow diffusion rates of these elements. Although a small addition of boron markedly increases the hardenability of steel, the diffusion rate of boron, which is of the same order of magnitude as that of carbon, can hardly account for this effect. An addition of boron in the range of 0.001 to 0.003 pct is about as effective as an addition of 0.30 pct Mo, 0.40 pct Cr, or 1.25 pct Ni in increasing the hardenability of a 0.40 pct C steel;[2] however, increasing the carbon content of the steel decreases the effectiveness of the boron addition.[3, 4]

The difficulty in understanding why so small an addition of boron can replace much larger quantities of the more strategic alloys, together with the erratic behavior sometimes encountered in boron-treated steels, has interfered with their general acceptance by industry. In the belief that an understanding of the mechanism by which boron increases the hardenability of steel should lead to a more general acceptance of boron-treated steels, a research investigation to determine this mechanism was undertaken at Battelle Memorial Institute under sponsorship of Wright Air Development Center.

Experimental Work

In order to study the effect of boron on the transformation of austenite to ferrite and bainite, a group of steels was made with a basic composition similar to that of the SAE 8600 series. This base composition was chosen because it has sufficient hardenability to permit accurate measurement of the times required for transformation to start at various temperatures. The chemical analyses of the steels used in the first part of this investigation are listed in Table I.

These steels were made as 200 lb heats in an induction furnace. The furnace charge was Armco ingot iron with the alloying elements added as ferroalloys. After the alloy additions were made, the heat was deoxidized with 0.125 pct Al. A 100 lb ingot was cast and an addition of 0.003 pct B, as ferroboron, was made to the metal remaining in the furnace. This metal was cast into a second 100 lb ingot.

Table I. Chemical Analyses of Experimental Steels

Steel Type, SAE No.	Analysis, Pct								
	B	C	Mn	Si	Ni	Cr	Mo	P	S
8620	—	0.22	0.85	0.29	0.51	0.41	0.14	0.012	0.026
86B20	0.001	0.22	0.85	0.25	0.51	0.40	0.15	0.012	0.023
8635	—	0.38	0.79	0.25	0.50	0.54	0.15	0.015	0.027
86B35	0.002	0.37	0.83	0.27	0.50	0.55	0.14	0.016	0.025

The ingots were forged to 1¼ in. diam bar stock from which end-quench hardenability specimens were obtained. Part of this material was further reduced by hot rolling to 1x¼ in. bar stock from which specimens were obtained for isothermal transformation studies.

Studies of Nucleation and Growth: End-quench hardenability tests were performed on these steels, using an austenitizing temperature of 1600°F. The hardenability curves, shown in Fig. 1, indicate that boron treatment resulted in considerable increase in hardenability of the steels. Any such change in hardenability must result from a change in the transformation rate of the austenite, and these rate changes can be established readily by isothermal transformation studies.

Isothermal transformation studies were conducted on these steels as follows: specimens were austenitized at 1600°F for 15 min, transferred to a lead bath operating at a constant subcritical or intercritical temperature, held for various lengths of time, and water quenched. The specimens were sectioned for metallographic examination to determine the amount and the type of transformation products present.

In order to determine the effect of boron on the formation rate of ferrite, isothermal transformation tests were made on the 0.20 pct C steel in both the boron-treated and boron-free condition at an intercritical temperature of 1375°F where ferrite is the only decomposition product of this low carbon austenite. The results of these tests are shown in Fig. 2, where the percentage of ferrite formed is plotted as a function of time at temperature. It is apparent that boron markedly decreased the transformation rate of austenite to ferrite at this temperature.

C. R. SIMCOE, A. R. ELSEA, Member AIME, and G. K. MANNING, Member AIME, are associated with Battelle Memorial Institute, Columbus, Ohio.

Discussion on this paper, TP 3923E, may be sent, 2 copies, to AIME by Apr. 1, 1955. Manuscript, Apr. 6, 1954. Chicago Meeting, February 1955.

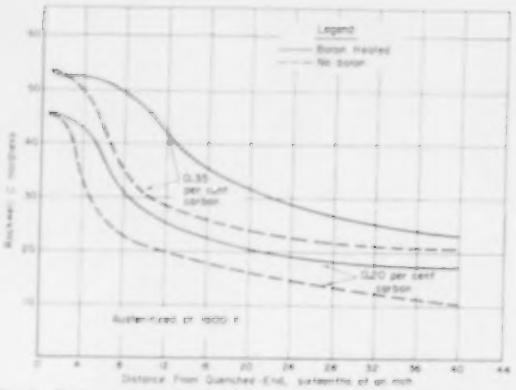

Fig. 1—End-quench hardenability curves for SAE 8600 series steels with the indicated carbon contents.

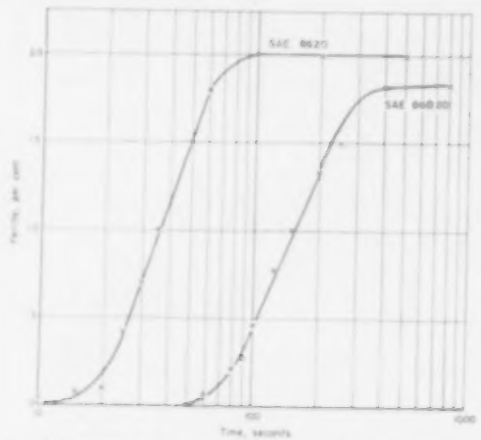

Fig. 2—Percentage of austenite transformed to ferrite as a function of time at 1375°F for SAE 8620 and 86B20 steels.

It is generally agreed that the formation of ferrite is by a nucleation and growth process,[1-3] and the curves shown in Fig. 2 are of the sigmoid type which is common for these nucleation and growth reactions.[4] Consequently, the reactions may be analyzed using the mathematical methods developed for this purpose.

The influence of boron on the growth rate of ferrite was determined by measuring cross-sectional areas of the largest ferrite particles observed in samples of both a boron-treated and a boron-free steel which were held for progressively longer times at the isothermal transformation temperature. Assuming these areas to be circular, radii were calculated and were plotted as a function of transformation time in Fig. 3. The slopes of the initial straight-line portions of the curves represent the growth rates of the ferrite particles. Since these slopes are about the same for both the boron-treated and boron-free steels, apparently boron had little effect on the growth rate of the ferrite.

To determine the effect of boron on the nucleation of ferrite, the number of ferrite particles visible in three or four typical fields was averaged, and the number of particles per unit area of specimen surface was calculated from this value. In Fig. 4 the number of ferrite particles per unit area of specimen surface is shown as a function of time at 1375°F for the 0.20 pct C steels. These data show that boron

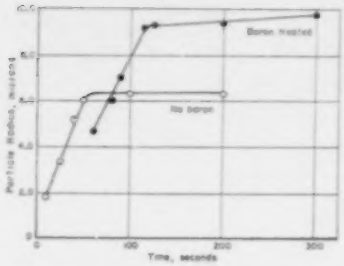

Fig. 3—Radius of largest ferrite particles present as a function of time at 1375°F for SAE 8620 and 86B20 steels.

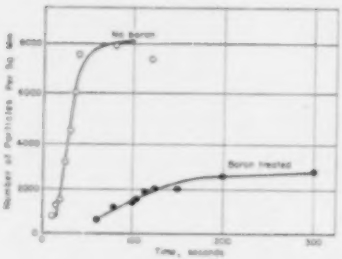

Fig. 4—Number of ferrite particles per unit area of specimen surface as a function of time at 1375°F for SAE 8620 and 86B20 steels.

treatment greatly reduced the rate at which new particles formed. That boron might affect the transformation rate by decreasing the nucleation rate has been suggested by other investigators,[4,7] but no quantitative data have been presented to verify this conclusion.

Similar studies were made on the 0.35 pct C steel, both at 1250°F and in the bainite formation temperature range at 850°F. The reaction rates of austenite to ferrite for these steels at 1250°F is shown in Fig. 5. The particle radii and the particle count have been plotted as a function of the reaction time in Figs. 6 and 7. These data, like those for the 0.20 pct C steel at 1375°F, show that boron had little effect on the growth rate but had a considerable effect on the rate at which new ferrite particles formed.

The reaction rate of austenite to bainite at 850°F for the 0.35 pct C steel is shown in Fig. 8. Accurate measurements of the particle areas and counts could not be made for bainite because of the acicular nature of the product. Nevertheless, after a given amount of austenite had transformed to bainite, there were fewer but larger particles of bainite in the boron-treated steel than there were in the boron-free steel. This effect is similar to that which boron had on the transformation of austenite to ferrite at higher temperatures; it indicates that boron decreased the nucleation rate of bainite also.

The effect of boron on the nucleation rate of ferrite can be placed on a semiquantitative basis, using the mathematical analyses that have been developed for the nucleation and growth processes.[4,8] It is assumed that treating the ferrite particles as spheres will not invalidate the calculations. Actually, they form as irregular-shaped polygons, at least at the higher temperatures. Furthermore, it is assumed that the formation of a small amount of ferrite will have only a small effect on the composition of the remaining austenite. Because of these assumptions, the mathematical analysis of the ferrite reaction will not yield absolute values for nucleation and growth rates, but the values obtained should furnish a basis for comparing the reaction rates in a boron-treated and a boron-free steel.

The master reaction curve by Johnson and Mehl[4] for general nucleation can be used to determine the

rate of nucleation if the growth rate and the fraction of transformed ferrite are known. These values have been determined for the 0.20 and the 0.35 pct C steels, both in the boron-treated and untreated conditions; they are shown in column 3 of Table II.

A method for calculating the rate of nucleation based on grain-boundary nucleation has been developed by Dorn et al.[5] The rate of nucleation can be calculated in this manner from a knowledge of the fraction transformed and the number of transformed particles per austenite grain observed on the polished surface of the specimen. The rate of nucleation calculated on this basis is shown in column 4 of Table II. A calculated rate of growth also can be obtained from the master curves of Dorn. These values are shown in column 5 of Table II. The values for the experimentally determined rate of growth are shown in column 6. Calculation by either method shows that boron has considerable effect on the nucleation rate of ferrite. It must be emphasized, however, that these values obtained by calculation are only relative values for the boron-treated and a boron-free steel. Accurate methods for analyzing the ferrite reaction have not been developed.

Loss of Boron Hardenability Effect and Formation of Boron Precipitate: As the austenitizing temperature increases, the structure of steel generally becomes more homogeneous and the grain boundary area decreases, resulting in increased hardenability. However, boron steels generally exhibit less hardenability when quenched from temperatures of approximately 2000°F, or higher, than when quenched from 1600°F.[4] Figs. 9 and 10 illustrate the reaction rates of ferrite formed at 1250°F from both the boron-treated and the untreated steels and from austenitizing temperatures of 1600° and 2100°F. If, after austenitizing at 2000°F or above, the specimens are lowered to 1600°F, the boron hardenability effect will return as a function of time. This effect of time at 1600°F on the bainite reaction is shown in Fig. 11.

It has been shown by other investigators[6,7] that a precipitate forms at the grain boundaries in specimens of boron steels that have been austenitized at 2000°F, quenched to 1200°F, and held for a short time. However, if the specimens are held at 1600°F for various times before the 1200°F treatment, the amount of boron precipitate which forms decreases as the time at 1600°F increases. Fig. 12 shows the microstructure of two samples, one quenched directly from 2100° to 1250°F and the other lowered to 1600°F for 10,000 sec before quenching to 1250°F.

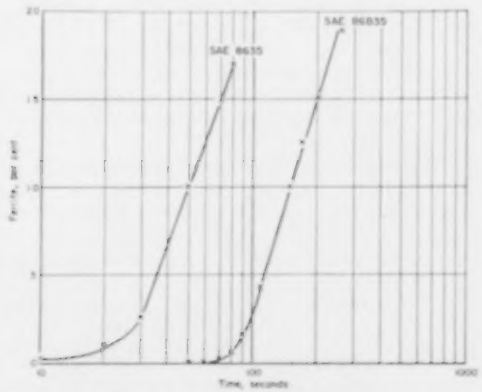

Fig. 5—Percentage of austenite transformed to ferrite as a function of time at 1250°F for SAE 8635 and 86B35 steels.

Table II. Values for the Nucleation and Growth of Ferrite Calculated from Isothermal Transformation Data

Steel Type, SAE No.	Isothermal Transformation Temperature, °F	Calc N_v Johnson and Mehl[3] Nuclei per Cu Mm per Sec	Calc N_v Dorn[5] Nuclei per Sq Mm per Sec	Calc G Dorn[5] Mm per Sec x 10^{-4}	Experimental G, Mm per Sec x 10^{-4}
8620	1375	21,500	281	1.27	1.4
86B20	1375	78.5	29	0.55	1.32
8635	1250	6,550	180	0.96	1.3
86B35	1250	596	10	0.58	0.67

This behavior of boron steel indicates that the loss of the boron effect and the grain boundary concentration of boron, which must precede the precipitate, occur concurrently.

To study the effect of the boron content of the steel on the hardenability and the loss of hardenability at high austenitizing temperatures, a series of five ingots was made from a single 500 lb heat. After the heat was deoxidized with 0.125 pct Al, additions of 0, 0.0008, 0.004, 0.007, and 0.010 pct B as ferroboron were added to the furnace prior to pouring the ingots. The chemical analyses of these materials are listed in Table III.

After the ingots were forged and rolled to 1 in. diam bar stock, they were subjected to hardenability tests from various austenitizing temperatures, Fig. 13. This basis for judging hardenability was chosen because of the difficulty in determining accurately the point of inflection in the hardenability curves for these steels, and Rc 40 hardness occurs very close to the point of inflection in those instances where it can be determined.

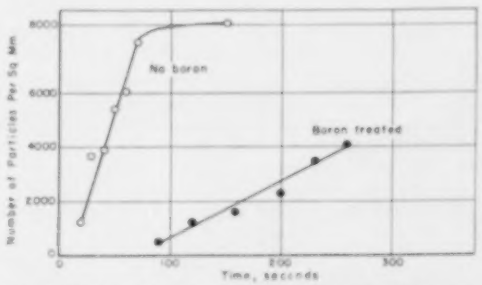

Fig. 6—Number of ferrite particles per unit area of specimen surface as a function of time at 1250°F for SAE 8635 and 86B35 steels.

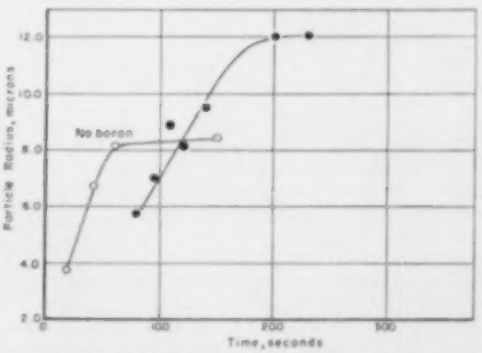

Fig. 7—Radius of largest particles present as a function of time at 1250°F for SAE 8635 and 86B35 steels.

Table III. Chemical Analyses of Single Heat of Steel with Five Boron Contents

Ingot No.	Chemical Analyses, Pct									
	B	C	Mn	Si	Ni	Cr	Mo	P	S	Al
1	0.0000	0.35	0.87	0.24	0.52	0.43	0.14	0.030	0.019	0.10
2	0.0005	0.34	0.86	0.31	0.51	0.43	0.15	0.031	0.019	0.10
3	0.003	0.36	0.87	0.23	0.51	0.42	0.14	0.032	0.018	0.09
4	0.006	0.33	0.85	0.27	0.50	0.42	0.14	0.028	0.018	0.09
5	0.01	0.36	0.88	0.23	0.51	0.43	0.13	0.031	0.017	0.08

As shown in Fig. 13, all the boron steels had higher hardenability than did the boron-free steel. However, the steel with the smallest boron addition, 0.0005 pct, had the highest hardenability and this steel did not decrease in hardenability until the austenitizing temperature was increased to above 1800°F. The hardenability of the 0.003 pct B steel was only slightly less than that of the 0.0005 pct B steel at 1500°F, but the decrease resulting from increasing temperature was evident at 1600°F. The 0.006 pct B steel had significantly less hardenability at all austenitizing temperatures than did the steels with the two lower boron contents. The 0.01 pct B steel had approximately the same hardenability at all austenitizing temperatures.

The increase in hardenability with austenitizing temperature in the boron-free steel is presumably caused by the increasing grain size. The boron steels exhibited a similar increase in grain size, as shown in Table IV, but the hardenability decreased. This decrease in hardenability with increasing grain size (austenitizing temperature) is typical of most boron steels.[6,7]

Small specimens of these steels were subjected to the special treatment to develop the boron constituent at the grain boundaries. This treatment, developed by Grange and Garvey,[5] consisted of austenitizing the specimens at 2300°F for 10 min, lowering the temperature to 1200°F for 10 sec, and then quenching in water. Metallographic examination of these specimens showed that the boron constituent was visible in the specimen which contained only 0.0005 pct B and that the amount of the boron constituent increased as the boron content of the steel increased. Fig. 14 shows the boron constituent developed in steels containing 0.0005, 0.003, 0.006, and 0.01 pct B. The lightly etched area in the 0.003 pct B steel is a ferrite particle. This behavior indicates that the boron hardenability effect is inversely proportional to the amount of boron constituent which will precipitate, not proportional as has been reported in the literature.[4]

Additional experiments were conducted on another group of steels which had received very small additions of boron in the range of 0.0001 to 0.0005 pct. The actual boron contents of these steels could

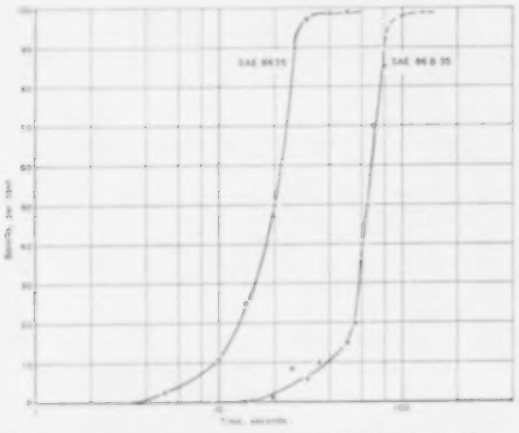

Fig. 8—Percentage of austenite transformed to bainite as a function of time at 850°F for steels SAE 8635 and 86B35.

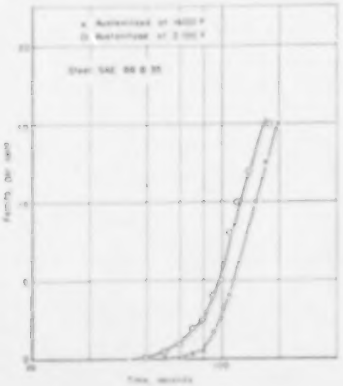

Fig. 9—Percentage of austenite transformed to ferrite in boron steel as a function of time at 1250°F from austenitizing temperatures of 1600° and 2100°F.

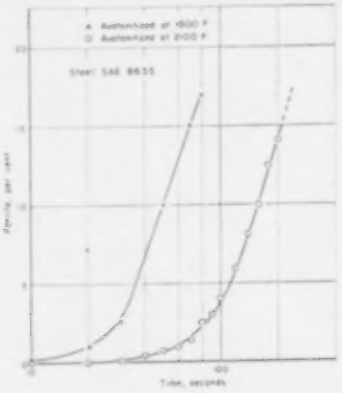

Fig. 10—Percentage of austenite transformed to ferrite in nonboron steel as a function of time at 1250°F from austenitizing temperatures of 1600° and 2100°F.

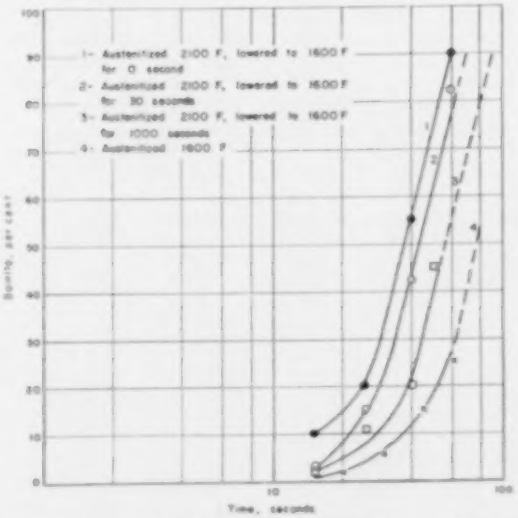
1- Austenitized 2100 F, lowered to 1600 F for 0 second
2- Austenitized 2100 F, lowered to 1600 F for 30 seconds
3- Austenitized 2100 F, lowered to 1600 F for 1000 seconds
4- Austenitized 1600 F
Time, seconds

Fig. 11—Percentage of transformation as a function of time at 850°F after various austenitizing treatments.

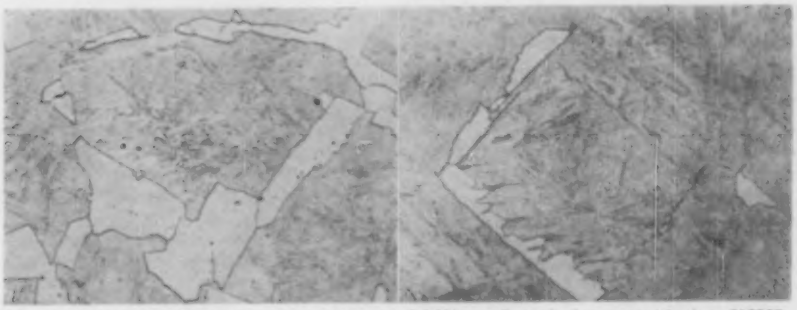

a—0 sec at 1600°F.

b—10,000 sec at 1600°F.

Fig. 12—Micrographs showing structure of 0.35 pct C-0.003 pct B steel when austenitized at 2100°F, lowered to 1600°F for the indicated times, and quenched into lead bath at 1250°F for 250 sec. Picral etch. X1000. Area reduced approximately 30 pct for reproduction.

not be determined by quantitative analyses because the boron content of the steels was below the precision of the analytical method used.

End-quench hardenability tests on these steels at an austenitizing temperature of 1600°F showed that the full boron hardenability effect was obtained for those steels which had received additions of 0.0003 and 0.0005 pct B. When the austenitizing temperature was increased to 2000°F, the steel with the nominal boron content of 0.0003 pct showed practically no loss in hardenability, as shown in Fig. 15, whereas the steel with the nominal boron content of 0.0005 pct showed an appreciable loss of the boron effect. The steel with a nominal boron content of 0.0001 pct showed only a slight increase in hardenability over that obtained for the base composition at all austenitizing temperatures.

Proposed Mechanism for the Boron Effect

The data presented in this paper show conclusively that boron increases the hardenability of the hypoeutectoid steels by decreasing the nucleation rate of ferrite and bainite. Consequently, any attempt to formulate a mechanism for the boron effect must be based on nucleus formation.

Nucleus Formation: Nucleus formation during a phase change is largely a matter of concentration, configuration, and energy fluctuations.[9, 10] The Volmer-Becker theory[11-13] of nucleation states that these fluctuations in a stable phase are such that frequently local areas acquire the concentration and configuration of a lower temperature phase; these areas are termed "germ nuclei" or "embryos." For an embryo to become a stable nucleus at some lower temperature, it must exceed a certain critical size for that particular temperature. A smaller embryo may either redissolve or, through some mechanism, increase in size to become a stable nucleus.

Concentration fluctuations in austenite result from random diffusion of carbon and other elements; the configuration fluctuations are caused by the thermal vibrations of the lattice. However, before an embryo can become a stable nucleus, in addition to the proper concentration and configuration, energy must

Table IV. ASTM Grain Size Numbers for SAE 8635 Steel with Various Boron Contents (0.5 Hr at Temperature)

Boron Content, Pct	Austenitizing Temperature, °F		
	1600	1800	2000
0.0000	9	7	6
0.0005	8	7	6
0.003	9	6	5
0.006	9	6	5
0.01	8	4	3

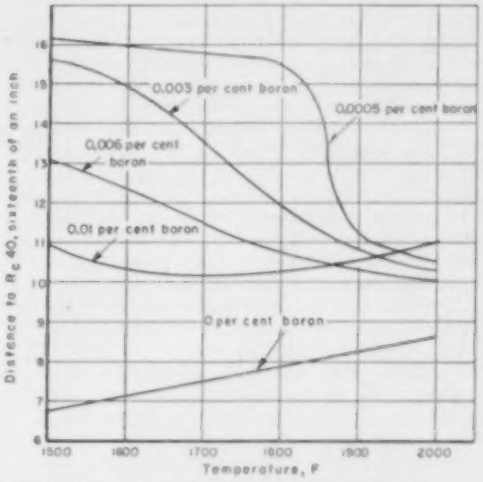

Fig. 13—Hardenability as a function of austenitizing temperature for steel containing various amounts of boron.

be provided for the formation of a new surface, for the volume expansion of the new phase, and for overcoming the strain energy of the nucleus and the parent phase. Areas of high energy exist at the grain boundaries, at the lattice sites occupied by solute atoms, and at other lattice imperfections. The greatest concentration of imperfections is at the grain boundaries and it is here that transformation generally starts.

Effect of Boron on Nucleus Formation: The ratio of the diameter of the boron atom to the iron atom is approximately 0.75,[14] which is large for interstitial atoms where the ratio is usually 0.60 or less and small for a substitutional atom where the ratio should be 0.85 or greater.[15] Thus, the boron atom is not well suited for either interstitial or substitutional solution.

It is postulated that the first boron atoms that are introduced will tend to occupy sites near lattice imperfections, where the atomic spacing is about 0.75 that of the perfect iron lattice. It is further postulated that these favorable sites are found primarily at grain boundaries and that the presence of boron atoms in these sites will lower the energy peaks of these local areas. Further additions of boron continue to lower the energy at the grain boundaries and at the sites of other lattice imperfections until those sites which can readily accommodate the boron atoms are filled. After this boron content has been reached, any additional boron atoms will be forced into less desirable sites, with the result that the

strain energy at the grain boundaries will be increased. According to the postulate, the grain boundary energy available for nucleation at the subcritical transformation temperature is a function of boron concentration, shown schematically in Fig. 16.

Since it is probably the energy at the grain boundaries and other lattice imperfections that enables the embryos to become stable nuclei, boron by lowering the energy of these lattice imperfections would decrease the nucleation rate of ferrite and bainite. However, should the boron content exceed that which can be accommodated at the imperfections, the excess may increase the strain energy or may precipitate as a boron phase at the grain boundaries which in turn will furnish new surfaces and new high energy sites, thereby increasing the nucleation rate of ferrite and bainite.

Boron Precipitate and Hardenability Loss: Since it is postulated that boron concentrates at lattice imperfections and since these lattice imperfections are concentrated at the grain boundaries, it would be expected that the boron distribution in the vicinity of the grain boundary would be similar to that indicated schematically by one of the curves in Fig. 17. Results of the hardenability tests shown in Fig. 13 indicate that increasing the boron content in the steel above approximately 0.0005 pct results in a decrease in hardenability, even at normal austenitizing temperatures. This relationship suggests that, with increasing boron content in the steel, there is a further increase in boron concentration at the grain boundary, as shown schematically in Fig. 17.

Also, from the data in Fig. 13, it may be seen that increasing the austenitizing temperature results in a decrease in hardenability and that the lower the boron content of the steel, the higher the austenitizing temperature must be before the loss of hardenability is encountered. Furthermore, it has been observed that the temperature to which the steel must be heated before the boron constituent can be developed at the grain boundaries decreases as the boron content of the steel is increased. This behavior, together with the fact that any boron steel must be heated to a relatively high temperature before the boron constituent can be developed at the grain boundaries, strongly suggests that boron concentrates at the grain boundaries with increasing austenitizing temperature. This increase in boron concentration at the grain boundaries with increasing austenitizing temperature is shown schematically in Fig. 18.

On direct quenching, the boron distribution which is established at a high austenitizing temperature will be retained to the transformation temperature. If this boron concentration at the grain boundaries exceeds that amount which results in the minimum grain boundary energy, there will be a loss in the boron effect. However, if after austenitizing at a high temperature, the temperature is lowered to a normal austenitizing temperature and held for a period of time to permit redistribution of the boron, an accompanying recovery of the hardenability effect will result as shown by data in Figs. 11 and 12.

The postulated mechanism for the boron harden-

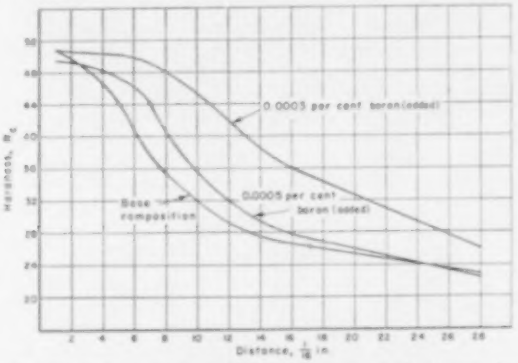

Fig. 15—End-quench hardenability curves on steels of very low boron contents when austenitized and quenched from 2000°F.

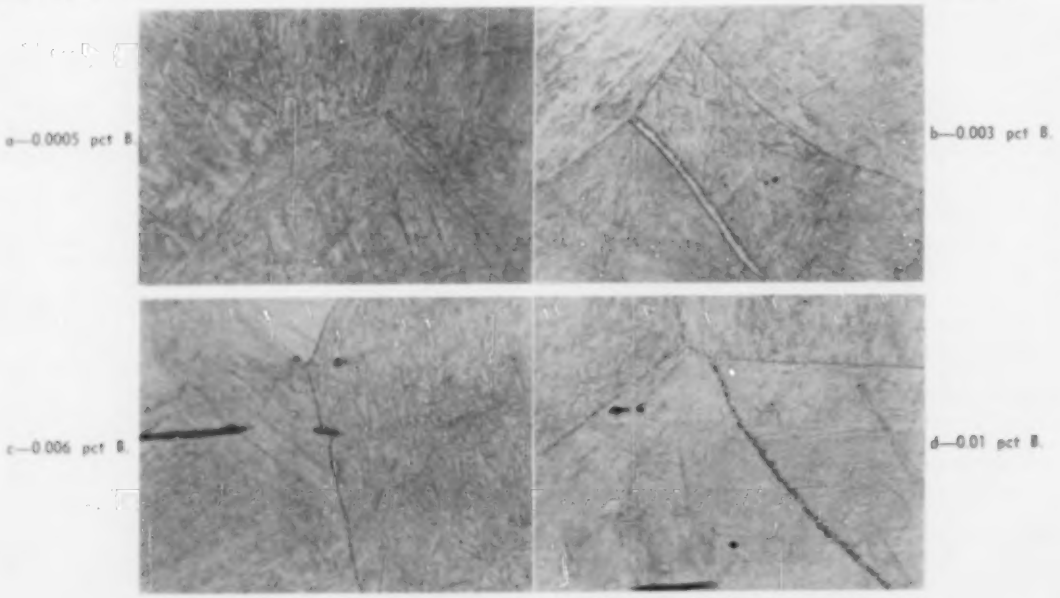

Fig. 14—Micrographs showing boron constituent developed in steels of various boron contents. Isothermal specimens, austenitized at 2300°F for 10 min, lowered to 1200°F for 10 sec. Picral etch. X1000. Area reduced approximately 30 pct for reproduction.

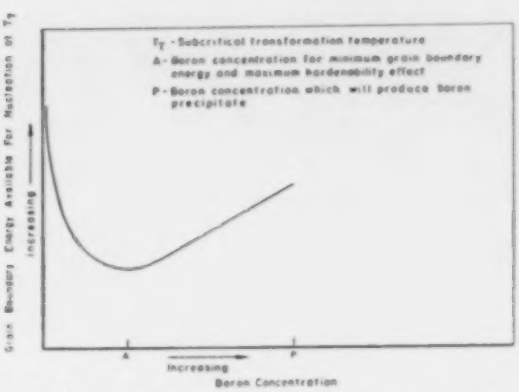
T_T - Subcritical transformation temperature
A - Boron concentration for minimum grain boundary energy and maximum hardenability effect
P - Boron concentration which will produce boron precipitate
Grain Boundary Energy Available For Nucleation at T_T Increasing
A
P
Increasing
Boron Concentration

Fig. 16—Schematic representation of grain boundary energy available for nucleation as a function of boron concentration at a subcritical transformation temperature.

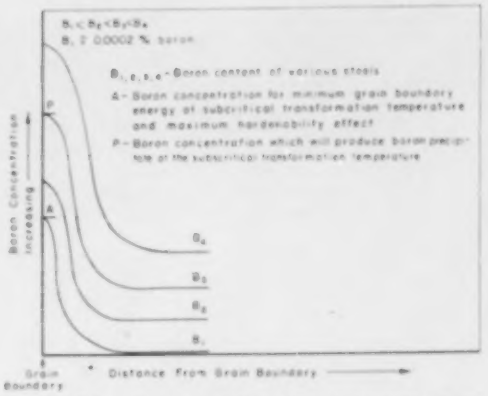
$B_a < B_b < B_c < B_d$
B_a = 0.0002 % boron
$B_{a,b,c,d}$ - Boron content of various steels
A - Boron concentration for minimum grain boundary energy at subcritical transformation temperature and maximum hardenability effect
P - Boron concentration which will produce boron precipitate at the subcritical transformation temperature
Boron Concentration Increasing
P
A
B_d
B_c
B_b
B_a
Grain Boundary
Distance From Grain Boundary

Fig. 17—Schematic representation of boron concentration at the grain boundary as a function of boron content of the steel.

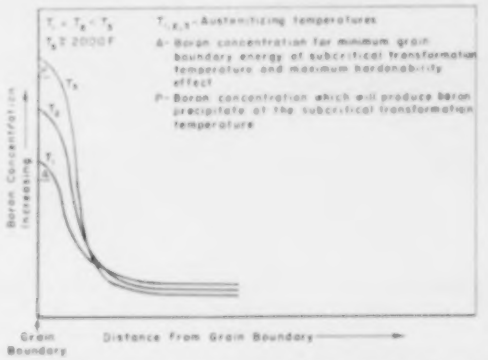
$T_1 < T_2 < T_3$
T_3 = 2000 F
$T_{1,2,3}$ - Austenitizing temperatures
A - Boron concentration for minimum grain boundary energy at subcritical transformation temperature and maximum hardenability effect
P - Boron concentration which will produce boron precipitate at the subcritical transformation temperature
Boron Concentration Increasing
T_3
T_2
T_1
Grain Boundary
Distance From Grain Boundary

Fig. 18—Schematic representation of boron concentration at the grain boundary as a function of austenitizing temperature.

ability effect suggests that a steel containing a certain small but critical amount of boron (that amount which would result in the minimum grain boundary energy available for nucleation at the transformation temperature) would show the maximum boron hardenability effect and that this hardenability effect could be retained to fairly high austenitizing temperatures. This behavior was exhibited by a steel which had received an addition of 0.0003 pct B; and since it is unusual in actual steelmaking practice to obtain full recovery of the boron, it is probable that the actual boron content of this steel was less than 0.0003 pct. With this small critical boron content, the number of boron atoms is of the same order of magnitude as the number of lattice imperfections that are estimated to be present in austenite. Thus, the amount of boron required to achieve the maximum hardenability effect seems to be consistent with the postulate that the effective boron is located largely at lattice imperfections.

Conclusions

The principal conclusions of this investigation are as follows:

1—Experimental evidence shows that boron increases the hardenability of hypoeutectoid steels by decreasing the nucleation rate of ferrite and bainite with little or no effect on the growth rate.

2—The boron effect which is lost at high austenitizing temperatures is recovered as a function of time by lowering the temperature to the normal austenitizing temperature range before quenching.

3—The boron precipitate, which forms at approximately 1250°F after austenitizing at 2000°F or higher, does not appear if the temperature is first lowered to the normal austenitizing temperature range for a short time before isothermal treatment at 1200°F.

4—If the boron content does not exceed a critical value (approximately 0.0001 to 0.0003 pct), the steel can be austenitized at 2000°F with little loss in hardenability and without forming the boron precipitate.

5—A mechanism has been proposed to explain the effect of boron on the nucleation of ferrite and bainite. This mechanism assumes that lattice imperfections furnish the energy required for nucleation. It is further proposed that boron, because of its size, concentrates at lattice imperfections. Because the energy level of these imperfections is lowered by the presence of boron, they are less likely sites for nucleation. These imperfections occur in the greatest abundance at grain boundaries. The loss in hardenability and the boron precipitate which occur when austenitizing at approximately 2000°F are explained on the basis of increased boron concentration at the grain boundaries with increasing boron content of the steel or with increasing austenitizing temperature. When the concentration of boron at the imperfections is raised above a critical value, the energy peak at the imperfection begins to increase and the imperfection again becomes a more favorable site for nucleation.

Acknowledgments

The authors wish to express their appreciation of the sponsorship of this research by the Aeronautical Research Laboratory, Wright-Patterson Air Force Base, Ohio, and for their permission to publish this paper. The micrographs included in this paper were prepared by Mr. R. D. Buchheit of Battelle Memorial Institute.

The research on the mechanism by which boron increases the hardenability of steel was sponsored by the Aeronautical Research Laboratory, Wright Air Development Center, under Contract No. AF 18(600)-155.

References

[1] R. F. Mehl: The Decomposition of Austenite by Nucleation and Growth Process. *Journal* Iron and Steel Institute (1948) **159**, p. 113.

[2] *Metals Handbook*. (1948) Cleveland. ASM.

[3] G. D. Rahrer and C. D. Armstrong: The Effect of

Carbon Content on the Hardenability of Boron Steels. *Trans.* ASM (1948) **40**, p. 1099.

[6] R. A. Grange and T. M. Garvey: Factors Affecting the Hardenability of Boron-Treated Steels. *Trans.* ASM (1946) **37**, p. 136.

[7] R. F. Mehl and A. Dube: The Eutectoid Reaction. *Phase Transformations in Solids.* New York. John Wiley & Sons Inc.

[8] W. A. Johnson and R. F. Mehl: Reaction Kinetics in Processes of Nucleation and Growth. *Trans.* AIME (1939) **135**, p. 416.

[9] T. G. Digges, C. R. Irish, and N. W. Carwile: Effect of Boron on the Hardenability of High-Purity Alloys and Commercial Steels. *Journal of Research* National Bureau of Standards (R. P. 1938) p. 41; (1948) p. 545.

[10] J. E. Dorn, E. P. De Garmo, and A. E. Flanegan: Nucleation and Growth Rates of Pearlite. *Trans.* ASM (1941) **29**, p. 1022.

[11] R. Smoluchowski: Nucleation Theory. *Phase Transformations in Solids.* (1951) p. 149. New York. John Wiley & Sons Inc.

[12] A. H. Cottrell: *Theoretical Structural Metallurgy.* (1948) London. Arnold.

[13] M. Volmer: *Kenetik det Phasenbildung.* (1939) Dresden. Steinkopff.

[14] R. Becker: *Annalen der Physik* Leipzig (1938) **32**, p. 128.

[15] R. Becker: *Proceedings* Physical Society (1940) **52**, p. 71.

[16] C. S. Barrett: *Structure of Metals* (1952) New York. McGraw-Hill Book Co. Inc.

[17] W. Hume-Rothery: *The Structure of Metals and Alloys.* (1945) London. Institute of Metals.

Dispersion Hardening of Copper-Chromium Alloys

by W. R. Hibbard, Jr. and E. W. Hart

The room temperature flow characteristics of a series of Cu-Cr alloys are found to be related to the amount and characteristics of the chromium-rich precipitate. The results are consistent with the theory of Fisher, Hart, and Pry, which considers the trapping to dislocation loops around precipitate particles.

THE use of dispersed phases for hardening metals, particularly high temperature alloys, has been practiced for several years. Current theories describing the effects of dispersions on the basis of dislocation theory have been proposed by Mott and Nabarro,[1,2] Orowan,[3] and Fisher, Hart, and Pry.[4] These theories recently have been discussed by Hart,[5] who pointed out that the experimental data available for comparison with theoretical calculations for overaged alloys are confined to studies by Gensamer, Pearsall, Pellini, and Low,[6] Shaw, Sherby, Starr, and Dorn,[7] and some hitherto unpublished data on Cu-Cr alloys which will be described herein.

Certain difficulties were associated with the interpretation of the first two studies. Gensamer, Pearsall, Pellini, and Low[6] were concerned principally with interparticle spacing and did not document particle sizes. Shaw, Sherby, Starr, and Dorn[7] included all the data in their report which was necessary for the theoretical evaluation, but their study is subject to some question[10] due to difference in prior history of various specimens and due to systematic differences in particle characteristics[10] which appeared to be associated with differences in the magnification of their microscopic examination.

The current study was undertaken to obtain critical data in a manner which avoids some of these limitations.

Specimens of eight Cu-Cr alloys remaining from a previous investigation[10] were available in the form of 100 mil sheet of the compositions shown in Table I. At 200 mil this material had been previously annealed ½ hr at 1000°C, water quenched, and cold rolled 50 pct. Samples were further cold rolled to a thickness of 20 mil for a total reduction of 90 pct.

Table I. Composition and Treatment of Alloys

Alloy, Wt Pct Cr	Si	Fe	Cu	Final Anneal	Average Diameter Grain Size, Mm
0.00	0.01	0.01	99.97	½ hr 400°C	0.016
0.19	0.01	0.03	99.82	½ hr 800°C	0.022
0.34	0.01	0.02	99.64	½ hr 800°C	0.016
0.48	0.01	0.02	99.52	8 hr 800°C	0.015
0.61	0.01	0.03	99.39	8 hr 800°C	0.018
0.75	0.01	0.03	99.16	8 hr 800°C	0.017
0.95	0.01	0.03	99.01	24 hr 800°C	0.016
1.15	0.01	0.03	98.77	24 hr 800°C	0.018

Sheet tensile specimens of standard geometry with a gage length 2½ in. long and 0.20 in. wide were machined from this sheet. These specimens were then annealed in a dried N_2-H_2 atmosphere for the times and temperatures indicated in Table I. This anneal served two purposes: 1—to obtain a fairly uniform and nearly constant grain size of 0.015 to 0.022 mm average diameter, and 2—to precipitate a fairly uniform, nearly spherical overaged dispersion of essentially pure chromium. A typical microstructure illustrating the grain size and the uniformity of the dispersion is shown in Fig. 1. A typical dispersion illustrating the range of sizes and shapes of the particles is shown in Fig. 2.

The tensile specimens were tested in the Instron equipment described in ref. 11 at room temperature at a strain rate of 0.04 in. per in. per min. Three tests were run on each alloy with sufficient reproducibility that a single true stress-true plastic strain curve could be drawn through the three sets of data for each alloy. Typical curves are shown in Fig. 3.

W. R. HIBBARD, JR., Member AIME, and E. W. HART are associated with Metallurgy Research Dept., Research Laboratory, General Electric Co., Schenectady.

Discussion on this paper, TP 3885E, may be sent, 2 copies, to AIME by Apr. 1, 1955. Manuscript, June 14, 1954. Chicago Meeting, February 1955.

Fig. 1—1.15 pct Cr-Cu alloy annealed 24 hr at 800°C. $K_2Cr_2O_7$ etch. X250.

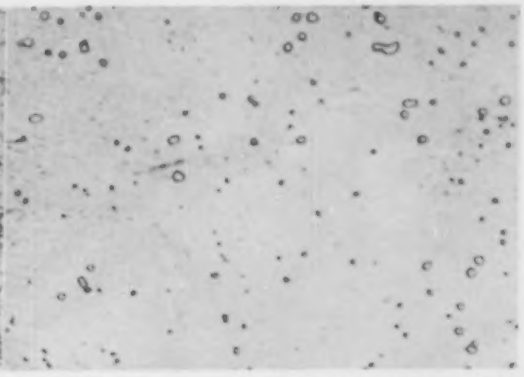

Fig. 2—0.61 pct Cr-Cu alloy annealed 8 hr at 800°C. $K_2Cr_2O_7$ etch. X2000.

The volume fraction of chromium present as precipitate was calculated from the composition, assuming equilibrium at 800°C. The results are indicated in Table II under the symbol f. The number of particles per square centimeter of area was counted from random micrographs at X6000. For each alloy four counts were made totaling at least 400 particles in each case. The accuracy of this count is considered to be from 3 to 5 pct. The results are indicated in Table II under the symbol n. The equivalent mean planar radius of particles in microns was calculated from the particle count, assuming a uniform particle size, and is indicated in Table II under the symbol r. The particle radius in this case is, of course, derived data and assumes that the variation in the apparent particle size such as is shown in Fig. 2 is a result of differences in the plane of observation.

Results and Discussion

There appeared to be no significant difference between the yield strengths of the various alloys. Therefore, it was easily possible to evaluate the effect of the dispersions on the basis of the flow stress at a strain of 25 pct. 25 pct was chosen because it is within the range of strain where the difference between the flow curves of the various alloys is essentially constant. These values are indicated in Table II and are plotted as a function of composition in Fig. 4. The solubility of chromium in copper at 800°C is 0.15 wt pct; and based on the interpolation in Fig. 4, the value of the flow stress for the saturated solid solution matrix was determined as 41,300 psi. This value is considered to be accurate within 300 psi.

The strengthening increment due to the dispersed precipitate at a strain of 25 pct is listed in Table II under the symbol σ_s, and is plotted as a function of the volume fraction of precipitated chromium in Fig. 5.

Fig. 6 shows the relationship between the number of particles and the volume fraction of precipitated particles which suggests that, with the exception of the 0.34 pct Cr alloy, the number of particles was maintained fairly uniformly within about 10 pct. This plot suggests that the effect of additional chromium was to increase the size of the particles and to decrease slightly the number of particles.

Hart[7] has pointed out that, if as in this case there is no change in yield stress as a result of the dispersed phase, the difference between the stress-strain curve of a solid solution matrix and the

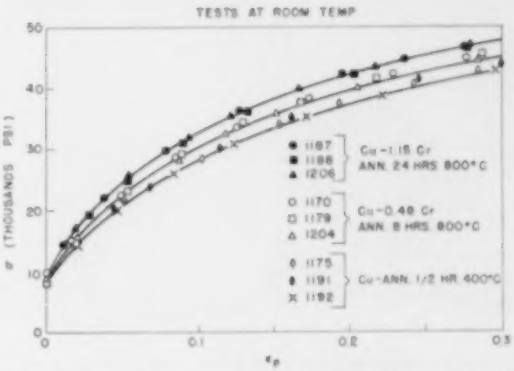

Fig. 3—Stress-strain curve for copper, 0.48 pct Cr-Cu, and 1.15 pct Cr-Cu.

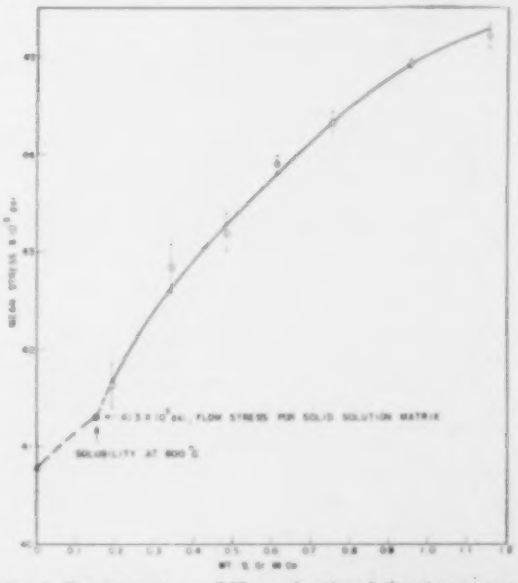

Fig. 4—Flow stress at $\epsilon = 0.25$ as a function of chromium content in copper. Mean stress at 25 pct strain vs composition showing probable error of mean.

stress-strain curve of the matrix with the dispersed precipitate should be essentially constant beyond the strain of about 10 pct. This prediction is based

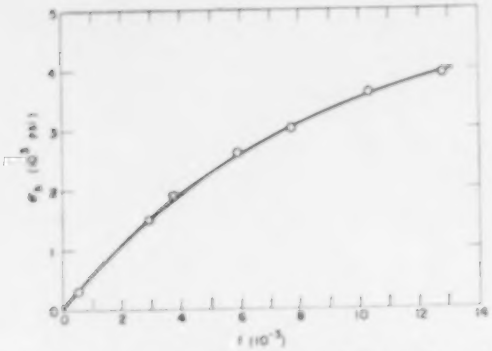

Fig. 5—Strengthening increment at $\epsilon = 0.25$ due to dispersed phase as a function of volume fraction of the dispersed phase.

Table II. Flow Stress and Precipitate Characteristics of Alloys

Alloy, Wt Pct Cr	σ at $\epsilon = 0.25$ Psi	σ_p,* Psi	f†	n‡	r,** Microns
0.00	41.3×10^6	—	—	—	—
0.19	41.6×10^6	0.3×10^6	0.516×10^{-4}	9.246×10^6	0.042
0.34	42.8×10^6	1.5×10^6	2.45×10^{-4}	12.04×10^6	0.080
0.48	43.2×10^6	1.9×10^6	3.74×10^{-4}	8.83×10^6	0.116
0.61	43.9×10^6	2.6×10^6	5.93×10^{-4}	8.58×10^6	0.148
0.75	44.3×10^6	3.0×10^6	7.73×10^{-4}	8.43×10^6	0.171
0.93	44.9×10^6	3.6×10^6	10.30×10^{-4}	7.69×10^6	0.207
1.15	45.2×10^6	3.9×10^6	12.87×10^{-4}	6.76×10^6	0.246

* Hardening stress at $\epsilon = 0.25$ [σ at $\epsilon = 0.25$] $-$ 41.3×10^6].
† Volume fraction of chromium as precipitate calculated from composition, assuming equilibrium at 800°C.
‡ No. particles per square centimeter counted from random micrographs, X6000.
** Radius of equivalent sphere which would have the same root mean square planar radius as the particles calculated from $\sqrt{3/2}\,r$.

upon the theory of Fisher, Hart, and Pry,[5] which considers the strain hardening increment due to stresses from dislocation loops trapped around precipitate particles.

Fig. 7 shows a plot of a difference in the true stress between the alloys with a precipitate (0.48 and 1.15 pct Cr) and the solid solution matrix alloy* as a function of the true plastic strain. This difference in flow stress is essentially constant beyond 15 pct strain and is a function of the amount of precipitate, as indicated in Fig. 5.

* 0.19 pct Cr alloy contains a small amount of precipitate but is the closest measured alloy to the saturated solid solution alloy. Based on Fig. 5, the error involved in using this alloy as the base value is less than 300 psi.

Summary

The flow characteristics of a series of Cu-Cr alloys have been investigated as a function of the amount and characteristic of the precipitate. Above about 15 pct strain, the increment in the flow stress due to the precipitate is essentially constant and a function of the amount of precipitate. The results are entirely consistent with the theory of Fisher, Hart, and Pry[5] as discussed by Hart.[7]

Acknowledgment

The tensile tests were conducted by E. A. Smith and the calculations were made by Mrs. M. V. Doyle.

References

[1] N. F. Mott and F. R. N. Nabarro: *Proceedings* Physical Society, London (1940) **52**, p. 86.
[2] N. F. Mott: *Journal* Institute of Metals (1948) **62**, p. 307.

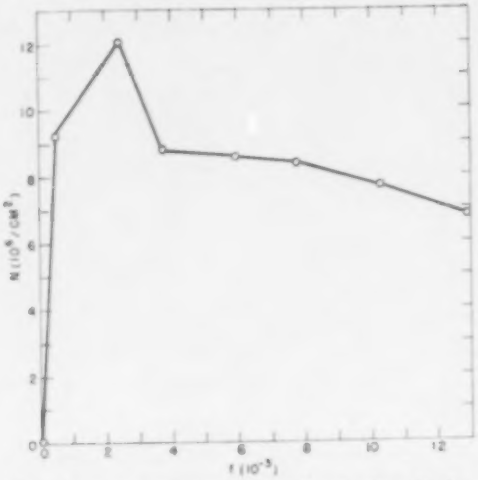

Fig. 6—Number of particles as a function of volume fraction of the dispersed phase.

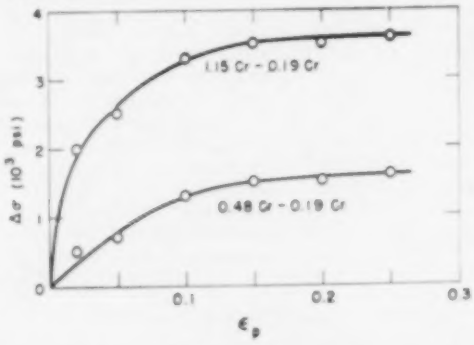

Fig. 7—Difference in flow stress between alloys indicated as a function of strain.

[3] N. F. Mott and F. R. N. Nabarro: *Report of a Conference on Strength of Solids.* (1948) p. 1. London. Physical Society.
[4] N. F. Mott: *Imperfections in Nearly Perfect Crystals.* (1952) Ed. by Shockley et al., p. 173. New York. John Wiley & Sons.
[5] R. Orowan: *Symposium on Internal Stresses in Metals and Alloys.* (1948) p. 451. London. Institute of Metals.
[6] J. C. Fisher, E. W. Hart, and R. H. Pry: *Acta Metallurgica* (1953) **1**, p. 336.
[7] E. W. Hart: Theories of Dispersion-Hardening. *Trans.* ASM (1954) **46A**, p. 95.
[8] M. Gensamer, E. B. Pearsall, W. S. Pellini, and J. R. Low, Jr.: *Trans.* ASM (1942) **30**, p. 983.
[9] R. B. Shaw, L. A. Sheppard, C. D. Starr, and J. E. Dorn: *Trans.* ASM (1953) **45**, p. 249.
[10] W. R. Hibbard, Jr., F. D. Rosi, H. T. Clark, Jr., and R. I. O'Herron: The Constitution and Properties of Copper-rich Copper-chromium and Copper-nickel-chromium Alloys. *Trans.* AIME (1948) **175**, p. 283; METALS TECHNOLOGY (February 1948).
[11] R. P. Carreker, Jr. and W. R. Hibbard, Jr.: Tensile Deformation of High-purity Copper as a Function of Temperature, Strain Rate, and Grain Size. *Acta Metallurgica* (1953) **1**, p. 654.
[12] W. R. Hibbard, Jr. and R. W. Guard: Discussion of paper by C. D. Starr, R. B. Shaw, and J. E. Dorn. *Trans.* ASM (1954) **46**, p. 1087.
[13] R. W. Guard and W. R. Hibbard, Jr.: Discussion of paper by W. H. Giedt, O. D. Sherby, and J. E. Dorn. *Paper 53-A-78* ASME.

Plastic Deformation of Germanium and Silicon by Torsion

by Earl S. Greiner

Germanium and silicon have been plastically deformed in torsion at elevated temperatures. Slip took place on the four {111} planes. Dislocations, revealed by etch pits on a {111} face, occurred in rows that were traces of operative slip planes.

THE plastic deformation of germanium and silicon by bending and tension at elevated temperatures has been reported by Gallagher.[1] Translational slip during plastic flow in these materials, according to Gallagher[1] and Treuting,[2] occurs on {111} planes. Recent work by Treuting[3] indicates the direction of slip to be <110>. The present paper describes the plastic flow characteristics of germanium and silicon deformed by torsion.

Torsional deformation was accomplished by twisting ¼x¼x2 in. specimens held in molybdenum grips and contained in an atmosphere of helium in a transparent quartz tube and heated by an external resistance furnace. The angular displacements were measured on a graduated circle with a pointer attached to the movable grip. Temperatures were measured with a chromel-alumel couple; the hot junction was within the quartz tube and in close proximity to the specimen.

Photographs of samples of germanium and silicon twisted at 850° and 1180°C, respectively, are shown in Fig. 1. The germanium was twisted 230° per in. and the silicon 80° per in. These deformations are larger than those used in experiments to be described later and are presented only to emphasize the extensive plasticity of these materials.

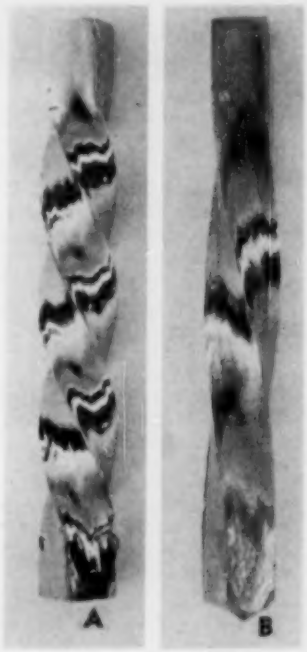

Fig. 1—Germanium and silicon plastically deformed in torsion. a—Germanium, 850°C. b—Silicon, 1180°C.

Germanium

A single crystal specimen of germanium (*n*-type, 7 ohm-cm resistivity) with a $(11\bar{1})$ plane normal within 3° of the torsion axis, Fig. 2, was chemically polished with CP-4 solution* and then twisted 9° per in. at 600°C. After the deformation, the surfaces of the square specimen contained straight-line markings as shown schematically in Fig. 2. The slip lines in the $(\bar{1}10)$ face are illustrated by the micrograph in Fig. 3. Stereographic analysis showed that the slip lines 1 and 2 in the $(\bar{1}10)$ face are traces of $(11\bar{1})$ and (111) planes, while slip lines 3 and 4 in the $(\bar{1}\bar{1}2)$ face are traces of $(\bar{1}11)$ and $(\bar{1}\bar{1}1)$ planes. Thus, slip occurred on all four octahedral planes, but predominately on the one almost normal to the torsion axis.

The slip lines from the (111) plane were observed only in the {110} faces. This suggests that plastic flow in the $(11\bar{1})$ plane consisted of slip in the $[\bar{1}10]$ direction. Several investigators[4-6] have reported experimental evidence of rotational slip about a normal to the slip plane. If rotational slip had occurred during the twisting of these specimens of germanium, the slip lines from the $(11\bar{1})$ plane should have appeared in the four lateral faces instead of in only two. Perhaps the absence of rotational slip is brought about by the square cross-section. A cylindrical specimen would have a more uniform stress distribution in torsion than one with a square cross-section, and may deform by rotational slip.

A specimen of germanium (*n*-type, 5 ohm-cm resistivity) twisted less than 8° per in. at 550°C, was cut to expose the (111) face 19° 28′ from the torsion axis, Fig. 4a. This face, after metallographic

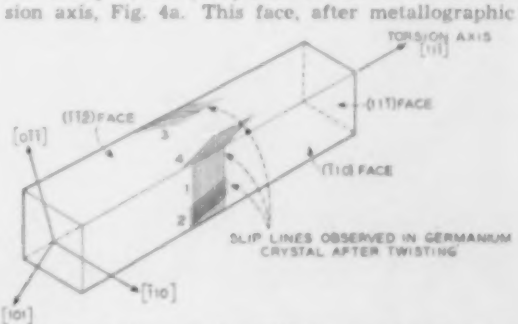

Fig. 2—Sketch of crystal with a (111) plane normal to the torsion axis.

* 15 cc HF, 25 cc HNO_3, 15 cc $HC_2H_3O_2$, and 3 to 4 drops of Br_2.

E. S. GREINER, Member AIME, is Member of Technical Staff, Bell Telephone Laboratories Inc., Murray Hill, N. J.

Discussion on this paper, TP 3884E, may be sent, 2 copies, to AIME by Apr. 1, 1955. Manuscript, May 24, 1954. Chicago Meeting February 1955.

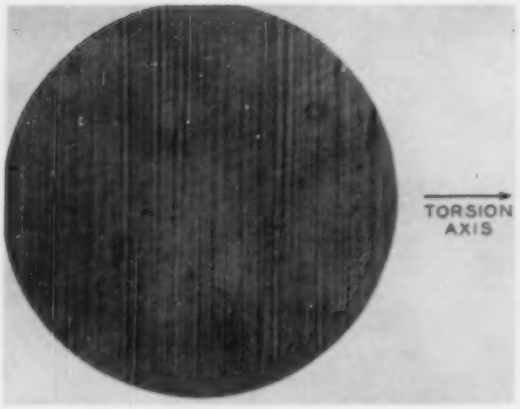

Fig. 3—Slip lines in a (1̄10) face of germanium crystal twisted 9° per in. at 600°C. X150. Area reduced approximately 75 pct for reproduction.

polishing and etching with CP-4 solution, showed an array of etch pits largely located in rows having [11̄0] and [101̄] directions, Figs. 4b and c. The rows are on traces of the (11̄1) and (1̄11) slip planes in the plane of observation. Vogel, Pfann, Corey, and Thomas' have shown that pits like these are formed when dislocation lines intersect such faces. Similar etch pits have been reported in germanium deformed by bending.[5, 6]

The density of pits varied; the maximum occurred near the surface at "*a*," Fig. 4a. Fig. 4b is representative of this area and has a measured density of about 12×10^7 per sq cm. Fig. 4c shows the pits at "*b*," Fig. 4a; here the density is about 8×10^7 per sq cm. The portion of the germanium within the grips during the deformation was nearly free of pits, as would be expected, since this part of the specimen was not deformed.

Silicon

A single crystal of silicon (p-type, 6 ohm-cm resistivity), with the long axis nearly in a <001> direction and the sides nearly parallel to {110} planes, was polished with a solution of HNO_3 and HF.* The

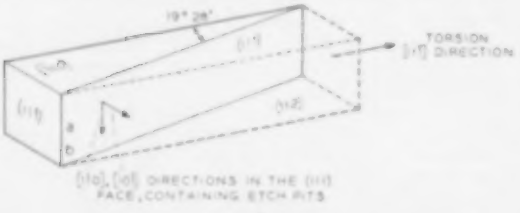

a

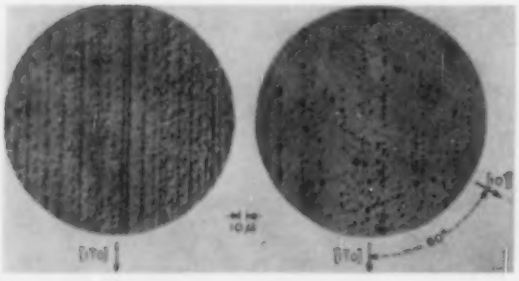

b c

Fig. 4—Dislocations revealed in the (111) face of germanium crystal plastically deformed in torsion.

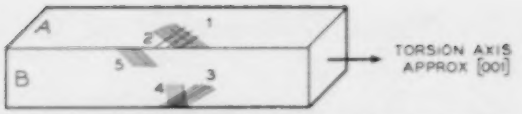

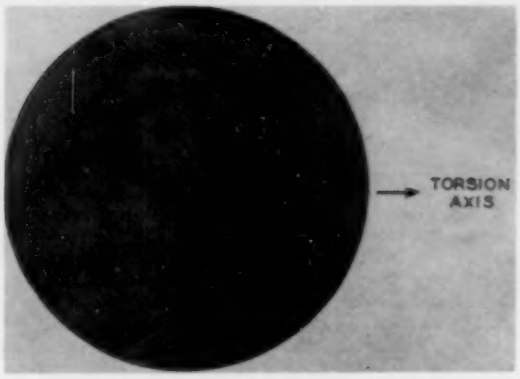

Fig. 5—Slip lines in two faces (nearly parallel to {110} planes) of silicon crystal twisted 8° per in. at 1000°C. Micrograph shows slip lines in face *A*. X100. Area reduced approximately 75 pct for reproduction.

* 20 cc HNO_3 and 5 cc HF.

specimen was then twisted 8° per in. at 1000°C. Slip lines in two of the faces are shown schematically in Fig. 5, where a micrograph of the slip lines in face *A* is also included. Stereographic analysis showed that lines 1 and 4 are traces of the (11̄1) plane, lines 2 and 4 are of the (111) plane, and line 3 is of the (1̄11) plane. The direction of slip lines 5 could be determined only approximately, but stereographic analysis indicates these lines are traces of the (1̄11) plane. Thus, both in this specimen of silicon with the torsion axis nearly in a <001> direction and in the previous specimen of germanium with the torsion axis in a <111> direction, slip occurred on all four octahedral planes.

Summary

1—Germanium and silicon have been plastically deformed in torsion at elevated temperatures; the slip plane is {111}.

2—If a {111} plane of a germanium crystal (having a square cross-section with {110} and {112} lateral faces) is almost normal to the torsion axis, slip appears to occur on this plane in a <110> direction. Slip also occurred on the three other {111} planes.

3—Dislocations, revealed by etch pits on a {111} face, were observed in a specimen of germanium deformed by torsion. The pits occurred in rows that were traces of operative {111} slip planes. The density of dislocations increased with the amount of deformation. In one of the more severely deformed areas, the dislocation density was about 10^7 per sq cm.

Acknowledgments

The author is pleased to thank W. C. Ellis and E. E. Schumacher for counsel and encouragement, and J. N. Hobstetter and R. G. Treuting for helpful discussions.

References

[5] C. J. Gallagher: *Physical Review* (1952) **88**, p. 721.
[6] R. G. Treuting: JOURNAL OF METALS (1952) **4**, p. 1044.

[3] R. G. Treuting: Private communication.
[4] R. D. Heidenreich and W. Shockley: *Report on Strength of Solids.* (1948) p. 57. London. Physical Society.
[5] D. M. Evans, D. N. Layton, and H. Wilman: *Proceedings* Royal Society (1951) **A205**, p. 17.
[6] D. C. Jillson: *Trans.* AIME (1950) **188**, p. 1009; JOURNAL OF METALS (August 1950).
[7] F. L. Vogel, W. G. Pfann, H. F. Corey, and E. E. Thomas: *Physical Review* (1953) **90**, p. 489.
[8] C. J. Gallagher: *Bulletin* American Physical Society (1953) **28**, No. 4, p. 10.
[9] G. L. Pearson, W. T. Read, Jr., and F. J. Morin: *Physical Review* (1954) **93**, p. 666.

Technical Note

Purification of Gallium by Zone-Refining

by D. P. Detwiler and W. M. Fox

IN the course of research on semiconducting intermetallic compounds, it became necessary to obtain gallium metal of greater purity that that available commercially. Several methods were considered for further purification, including acid leaching,[1] fractional crystallization,[2] and zone-refining.[3-4] The method of fractional crystallization was discarded as being equivalent to zone-refining in purification but inefficient in material and time. Both acid leaching and zone-refining were tried, and the method finally adopted is a combination of the two.

The acid leaching technique has been reported[1] to produce gallium in which no impurities are detectable spectroscopically. Although this method is very effective in removing oxides and surface contaminants, semiconducting material made of gallium subjected only to leaching indicated little reduction in the concentration of metallic impurities. Zone-refining, however, appears very effective in removing trace metallic impurities, but comparatively ineffective in removing the surface oxide film. Consequently, the method evolved consists of acid leaching to thoroughly clean the surface, followed by zone-refining to remove metallic impurities.

The low melting point and relatively high thermal conductivity of gallium introduce some difficulty in maintaining frozen and molten zones in zone-refining. To accomplish this, it is found necessary to reduce the effective ambient temperature by circulating ice water in coils about the regions that are to be kept frozen, while heat is supplied to the molten regions by resistance coils. The power supplied to the heating coils is regulated by a constant-voltage transformer and a variable autotransformer. Both heating and cooling coils are mounted on a transite base. The gallium ingot is held in a closed pyrex tube sliding inside the heating and cooling coils, the reciprocating method of Tanenbaum et al.[4] being employed to move the molten zones through the ingot at a rate of 2 in. per hr. This apparatus is shown in Fig. 1.

Fig. 1—Gallium zone-refiner. The cooling coils are covered with asbestos.

Table I. Spectrographic Analysis

Gallium Treatment	Pb, Pct
As-received	0.00X
Acid leached	0.00X
Purified end of zone melt	0.000
16 cm from pure end of zone melt	0.000
24 cm from pure end of zone melt	0.00X
32 cm from pure end of zone melt	0.00X

The results of a spectroscopic analysis[5] of a zone-refined ingot, as well as of the material as-received and after acid leaching, are shown in Table I. The ingot was 32 cm in length, and received 37 molten-zone passes, the molten zone being about 4 cm long. The only impurity found was lead, the following elements being reported also as checked but not found in the pure material: Al, Sb, As, Ba, Be, Bi, B, Cd, Ca, Cr, Co, Cb, Cu, Ge, Au, Fe, Mg, Mn, Mo, Ni, Pt, Si, Ag, Na, Sr, Sn, Te, Ti, W, V, Zn, and Zr. There thus appears no indication of pickup of Al, Mg, or Si from the pyrex boat as reported by Zimmerman[2] in his fractional crystallization.

Thus it appears that definite removal of lead from gallium occurs during the zone-refining process. It also may be concluded that a more sensitive analytical procedure than spectroscopy is required to evaluate quantitatively the purity of zone-refined metals. One such procedure which is proposed for use in the near future is the measurement of very low temperature resistivity. Although this will not identify the impurities present, it offers a very sensitive check of total impurity.

Acknowledgment

This work was supported by the Air Research and Development Command, United States Air Force.

References

[1] F. Sebba and W. Pugh: *Journal of the Chemical Society* (1937) p. 1373.
[2] W. Zimmerman, III: *Science* (1954) **119**, p. 411.
[3] W. G. Pfann: *Trans.* AIME (1952) **194**, pp. 747, 861; JOURNAL OF METALS (July, August 1952).
[4] M. Tanenbaum, A. J. Goss, and W. G. Pfann: *Trans.* AIME (1954) **200**, p. 762; JOURNAL OF METALS (June 1954).
[5] F. Montariol, R. Reich, P. Albert, and G. Chaudron: *Comptes Rendus* (1954) **238**, p. 815.
[6] Spectroscopic analysis performed by the W. B. Coleman Co., Philadelphia.

D. P. DETWILER, formerly associated with The Franklin Institute Laboratories, Philadelphia, is now associated with the New York State College of Ceramics, Alfred, N. Y., and W. M. FOX is associated with The Franklin Institute Laboratories, Philadelphia.

TN 250E. Manuscript, Sept. 3, 1954.

Study of a New Mode of Plastic Deformation in Zinc Crystals

by J. J. Gilman

Zinc monocrystals, when compressed nearly parallel to their basal planes (within 2°), deform in a new way; and certain deformation markings, called "μ-bands," are typical of this new mode. Characteristics of these μ-bands are described. Mechanical behavior of low angle zinc monocrystals was investigated in some detail. Recrystallization did not occur upon annealing of μ-banded specimens that were free of deformation twins. μ-Bands do not seem to be the result of nonbasal slip, but rather, a result of a microbuckling mechanism. μ-Bands differ qualitatively and quantitatively from ortho kink bands. A dislocation model, consistent with some of the features of μ-bands, is described.

THE plastic deformation of zinc monocrystals with slip planes (0001) nearly parallel to the stress axis was studied in this investigation. In a previous investigation, it was shown that some low angle zinc crystals (those with slip planes making angles of more than about $2.5\pm1°$ with the compression axis), deform by ortho kinking while others (those with slip planes making angles of less than $2.5\pm1°$ with the compression axis) deform in a new way.[1] This new mode of deformation will be described in some detail here. Some of its striking features are: 1—it operates only for compressive stresses, 2—its temperature dependence is anomalous, and 3—it exhibits a new type of "yield-point" behavior.

The mode of deformation to be discussed is not new in the sense that no previous evidence of its existence had been reported. The markings that it creates on the cleavage surfaces of zinc crystals have been described by several investigators.[2-6] However, this is the first time that it has been made to operate under controlled conditions so that its response to mechanical variables, temperature, and aging treatments could be investigated and its geometry completely described.

Apparently, Jillson[2] as well as Holden[3] and Pratt[4] believed that the small bands they observed were simply small versions of ortho kink bands. In fact, two of these authors[3, 4] called the markings "micro kink bands." In spite of the precedence, it is felt that this term is not entirely suitable because these bands do not have the same genesis as kink bands, and they are qualitatively different in structure. As will be indicated by later discussion, the bands seem to be related to the tensile deformation bands observed in aluminum. The present author has chosen to call the bands "micro deformation bands," or simply "μ-bands," and the deformation process, "μ-banding."

J. J. GILMAN, Member AIME, is associated with Metallurgy Research Dept., Research Laboratory, General Electric Co., Schenectady.

Discussion on this paper, TP 3868E, may be sent, 2 copies, to AIME by Apr. 1, 1955. Manuscript, Jan. 7, 1954. Chicago Meeting, February 1955.

Experimental Methods

Crystals were grown from 99.999+ pct Zn obtained from the New Jersey Zinc Co. The details of the technique are given elsewhere.[6] It should suffice to say that the crystals were seeded for orientation control, and precision pyrex tubes were used for molding them. About 40 crystals were used, yielding some 130 specimens.

Fig. 1 illustrates the typical form of the specimens and shows how the orientation angles are defined. The crystal specimens were usually 1⅝ in. long and about 150 mil in diameter. The angle between the slip or cleavage plane (0001) and the specimen axis is designated by χ_0, while α is the angle between the maximum slope of the (0001) plane and the nearest close-packed direction $[1\bar{2}10]$, varying from 0° to 30°.

The crystals were cut into specimens with a jeweler's saw and the ends were squared by filing (specimens held in V-block). Crystals of this orientation are stiff toward bending, so this procedure introduced only deformation localized at the ends. Then the specimens were polished either chemically in 50 pct HNO_3 or electrolytically in 20 pct chromic acid.

The mechanical tests were made with an Instron testing machine. This machine weighs by means of electric strain gages on elastic bars and is quite stiff, since the full-load deflection of its load cells is at most 0.002 in. Most of the testing was done at a

crosshead speed of 0.002 in. per min and a recording chart speed of 1 in. per min, giving a strain magnification of X500.

Two compression jigs were used (shown schematically in Fig. 2). Jig *a* was used for room temperature testing. It has high precision bronze bearings which result in rigid axial motion of its crosshead. Jig *b* was used for the high and low temperature tests. Its bearings are rather loose because they had to operate freely without lubrication. It was found by experience that this did not appreciably affect the results.

High temperatures (to 200°C) were obtained by immersing jig *b* in hot silicone oil and low temperatures by means of baths of ice water, dry ice-acetone, liquid nitrogen, and Freon 12. No attempt was made to control the temperature more closely than ±2.5°C.

Standard microscopic and X-ray methods were used for examining the crystals. The orientations of the crystals were found by the Greninger back-reflection technique with an accuracy of ±½°.

Results

Mechanical Tests—*Introduction:* For borderline orientations (χ_o near 2.5°), one specimen of a given crystal sometimes formed an ortho kink while another did not. This presented an opportunity for comparing the stress-strain curves characteristic of the two modes of deformation, ortho kinking and μ-banding. Fig. 3 contains a typical comparison.

The initial parts of the two curves of Fig. 3 are the same. Both specimens yielded at about the same load, 0.28 kg per sq mm, but immediately thereafter the load rose most rapidly for the specimen that did not kink (curve *A*). The load continued to rise for the unkinked specimen to a much higher maximum value than the maximum load for the specimen that kinked.

Curve *A* in Fig. 3 is typical for specimens that deformed by μ-banding. It was found that the yield points of the curves were not reproducible under the present test conditions. However, the curves were linear at small strains and the slopes of the linear portions of the curves were found to be reproducible. Therefore, this characteristic, Δ, or the plastic modulus, was chosen as the strength parameter. The plastic modulus was determined with the aid of immediate reload curves that were run after each test. These curves indicated the elastic strain in the specimens plus the strain in the machine up to the last plastic load. This nonplastic strain was subtracted from the original curves, and the slopes of the derived curves gave the plastic moduli. For curves without yield points, the plastic moduli were taken at stresses of about 2 kg per sq mm to further insure comparative conditions.

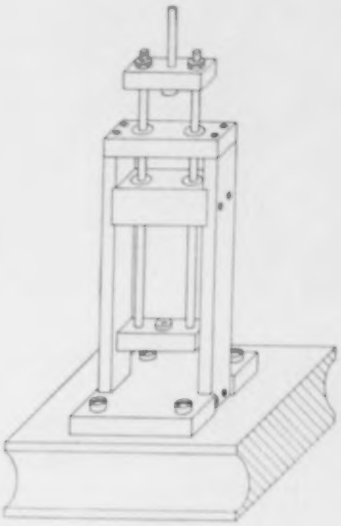

Fig. 2a—Compression jig for room temperature tests.

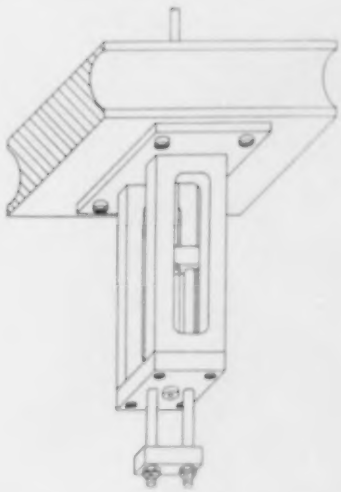

Fig. 2b—Compression jig immersible for low and high temperature test.

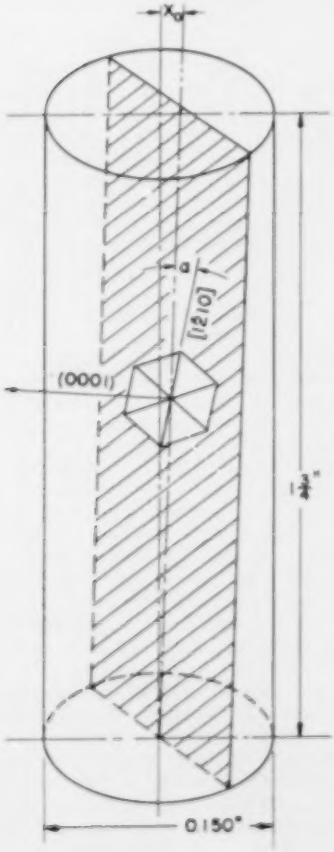

Fig. 1—Geometry of zinc monocrystalline specimens.

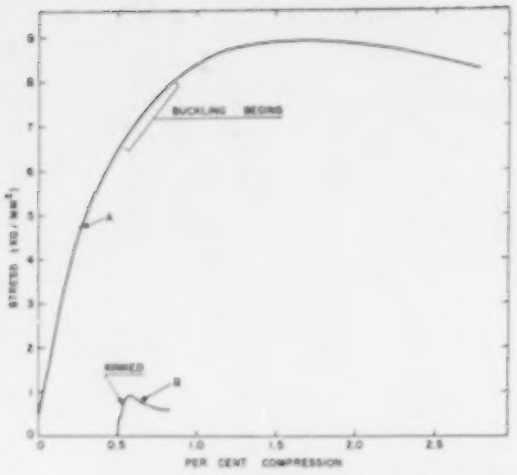

Fig. 3—Comparison of the load-compression curves for the two modes of deformation that are exhibited by low angle zinc crystals $\chi_0 = 2°$ and $\alpha = 7°$. Curve *A* is μ-banding; *B*, ortho kinking.

Fig. 4—Typical plastically buckled crystal.

Another important characteristic of the load-compression curves is the maximum load supported by a specimen. The maximum in the stress-strain curves is a consequence of plastic buckling (illustrated by Fig. 4). It is inversely proportional to the specimen length and depends on the crystal orientation angle α and on the testing temperature. The plane of buckling also depended on α. In crystals with $\alpha = 0$, it contained the specimen axis and the hexagonal axis. The maximum or buckling stresses are reported here for the sake of completeness although the buckling behavior of the crystals will not be discussed in detail.

Orientation Effects: The stress-strain curves for low angle zinc crystals depended markedly on the orientation angle α. (Little effect was noted for χ_0 as long as it was less than 2°.) When $\alpha = 0$ so that a close-packed direction in the crystal was nominally parallel to the compression axis, the crystals were considerably softer than when $\alpha = 30°$ (so that two close-packed directions make equal angles with the compression axis). Fig. 5 shows the variation of the plastic modulus, Δ, and the buckling stress with α. It may be seen that the plastic modulus varied by a factor of almost 4*X* as α changed from 0° to 30°.

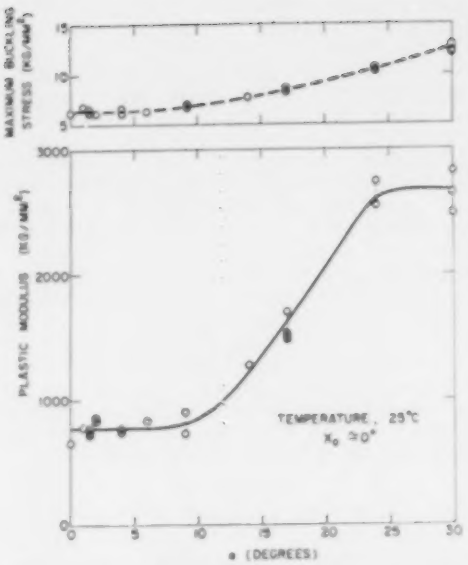

Fig. 5—Effect of orientation angle, α, on the plastic modulus at *RT*. ($\chi_0 \sim 0°$ for all crystals.)

The extremely high strain-hardening rate becomes evident when it is recalled that the elastic modulus for zinc is about 12×10^4 kg per sq mm.

Effect of Temperature: Typical stress-strain curves for crystals compressed at various temperatures are presented in Fig. 6, and the characteristics of the curves are plotted in Fig. 7. The two figures (6 and 7) clearly indicate the rather complex temperature dependence of the deformation process. First, the plastic modulus decreased considerably with decreasing temperature (below −80°C, the slope of the curve after the yield point was taken as the plastic modulus). This softening with *decreasing* temperature seems anomalous in comparison with the temperature dependence of slip in zinc.[10] Second, the yield stress rose rapidly with decreasing temperature in the range −80° to −196°C, and at about −150°C a definite yield point with a drop in load appeared. Finally, at both ends of the temperature range, ortho kinking was observed. It occurred in all of the crystals tested at −196°C and erratically when the temperature was raised to 165° to 185°C. The dotted curves show the probable course of the solid curves if kinking had not intervened.

Prestrain and Strain-Aging Tests: It was believed that the observed increase of strength with increasing temperature might have been caused by a strain-aging mechanism analogous to the one that operates in the blue brittle range of steel. Several sequences of aging and testing were performed in order to test this possibility. The results of these tests were partly negative, inasmuch as they showed no evidence of conventional strain aging, but they did lead to an interesting new result.

It was found that prestrain at 25°C produced a yield-point phenomenon at a lower temperature (−80°C) and that the yield-point elongation depended on the amount of high temperature prestrain. This is illustrated by Figs. 8 and 9. A clear yield point was produced at −80°C by prestraining a virgin crystal at 25°C; see curves *a*, *b*, and *c*. Curves *d* and *e* show that aging at 25°C either after some

strain at −80°C or some strain at 25°C caused no unusual behavior. The shapes of the curves differed somewhat; that is all. Note that the yield stress at 25°C was appreciably higher than the highest prior stress at −80°C. This confirmed the shape of the plastic modulus curve in Fig. 7. The loadings indicated by curves *f* and *h* were performed in order to investigate further the influence of the amount of high temperature strain on the low temperature yield-point elongation. Curve *f* represents a strain of about 0.055 pct, whereas curve *h* shows a strain of 0.006 pct. Curve *g* (following *f*) shows greater yielding than curve i (following *h*), but the respective yield-point elongations are not directly proportional to the amounts of prestrain.

After tests had established that no aging treatments but only prior prestrain at 25°C would produce a yield point at −80°C, some tests were performed in order to see what was happening during the "yield-point elongation" portions of the curves. Fig. 9 presents typical results. The technique was to partially unload a crystal during the course of a test. Curves *a* and *b* of Fig. 9 show that this had little effect at either 25° or −80°C when the yield point was absent. At 25°C there was an increase in the yield stress after partial unloading, but this was small. On the other hand, curve *c* shows a distinct effect when the crystal was partially unloaded during yielding. The effect was to create a new yield point. It was shown that the effect was caused by unloading alone and not by the amount of unloading. This was done by stopping the tensile machine's crosshead for the same length of time as that required for the unloading treatment. For both cases, the effect was the same (curve *c*). It can be seen from curve *c* that partial unloading while the specimen was deforming at constant stress only produced another yield point. As the stress rose above the yield-point value, the effect of partial unloading became small although the yield stress, after partial unloading, was always slightly higher than before.

Finally, a test was run to see whether the prestrain effect would disappear upon 25°C aging. To do this, the specimen was strained at 25°C (curve *d*), held for 16 hr at 25°C, and then cooled and reloaded at −80°C (curve *e*). The aging treatment did not eliminate the low temperature yield point. It did have a striking effect on the value of the yield stress, however. At about the same stress level, the difference between the final stress at 25°C and the yield stress at −80°C was about 6 pct, when the aging time at 25°C was as small as possible, compared with 44 pct change in stress for an aging time of 16 hr.

Effect of Strain Rate: In order to determine the effect of increasing the strain rate 10*X* at 25°C, a test was run at a crosshead speed of 0.02 in. per min and compared with a test on a piece of the same crystal run at the usual speed of 0.002 in. per min. The chart speed was increased to 10 in. per min to keep the magnification constant. The effect was a small decrease in the plastic modulus. This provides further evidence of the absence of appreciable strain aging.

Effect of Annealing: Annealing treatments were given to some of the crystals for three reasons: 1—to determine the effect on the stress-strain curves, 2—to see whether there was a marked change in length during annealing, and 3—to find out whether the crystals would recrystallize.

The effect of annealing on the stress-strain curve was to cause complete recovery to the initial state. Specimens were loaded up to 4 and 8 kg per sq mm at room temperature, unloaded, and then heated at 350°C for 30 min. After they had been repolished to remove the oxide film, they were reloaded at room temperature. The stress-strain curves obtained after annealing were essentially the same as the initial stress-strain curves. Thus, the crystals seemed to have completely recovered to the initial state during the anneal.

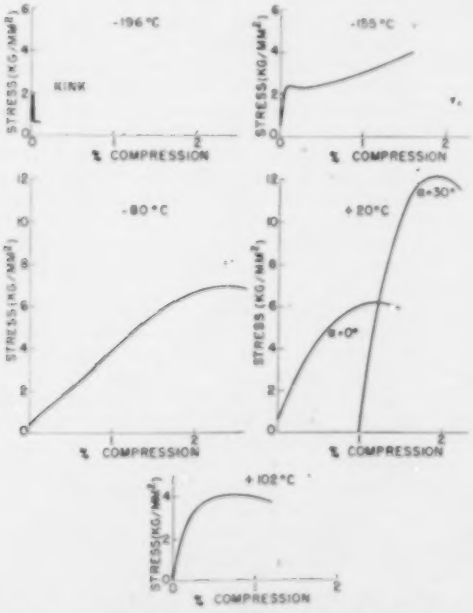

Fig. 6—Compressive stress-strain curves for crystals tested at various temperatures (nominal orientation was $\chi_0 = 0°$ and $\alpha = 0°$ for all crystals.)

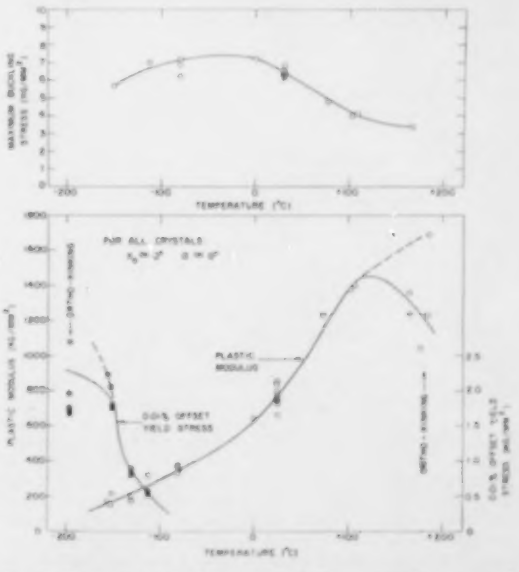

Fig. 7—Characteristics of the stress-strain curves of compressed zinc crystals as a function of temperature (nominal orientation was $\chi_0 = 0°$ and $\alpha = 0°$ for all crystals).

Annealed crystals were examined microscopically before and after etching for signs of recrystallization. None were found.

The length change produced by annealing was small. In a crystal compressed 0.25 pct at room temperature, the length increased less than 0.01 pct during 30 min at 350°C.

Effect of μ-banding on Ortho Kinking: It was pointed out under "Effect of Temperature" that the present crystals deformed by forming μ-bands at room temperature, but at −196°C they formed ortho kink bands. All of the more than two dozen specimens that were tested at −196°C exhibited ortho kinking. No evidence of μ-bands was found for such specimens. Thus, μ-banding seems to be suppressed by lowering the temperature to −196°C. This was investigated further by preloading two crystals at room temperature to 3 kg per sq mm and then reloading them at −196°C. Whereas ortho kinking would ordinarily have occurred with a maximum load of about 1.7 kg per sq mm at −196°C, kinking occurred at 7.0 to 7.7 kg per sq mm after the room temperature preloading. Thus, the maximum kinking load changed by 4.5X and was 4.7 kg per sq mm higher than the preload.

The above results are summarized graphically in Fig. 10. Note that very little deformation, in addition to the prestrain, occurred in specimen *C* prior to kinking. This indicates that little μ-banding occurred at −196°C.

Two conclusions result from these experiments: 1—μ-banding is suppressed by lowering the temperature to −196°C, apparently because the yield stress rises sufficiently that ortho kinking occurs instead; and 2—the formation of μ-bands suppresses ortho kinking.

Tensile Tests: It was stated in "Introduction" that one of the peculiarities of the new mode of deformation is that it operates only in compression. This was demonstrated by tensile tests made on specimens taken from the same crystals that were used for compression tests. The tensile tests showed only elastic deformation up to loads that produced twinning, that is, up to 3.7 kg per sq mm. Bell and Cahn[7]

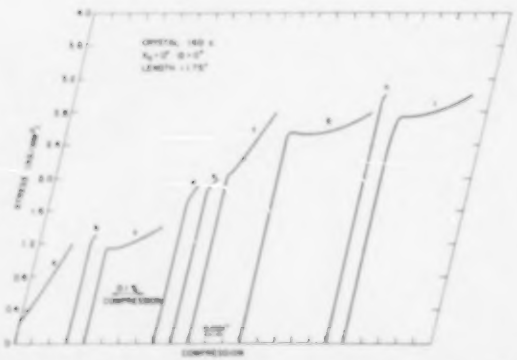

Fig. 8—Effect of prestrain at 25°C on yielding at −80°C in crystal 140a. $\chi_0 = 0°$ and $\alpha = 0°$. Curve *a* is first loading at 25°C of virgin crystal; curve *b*, immediate reload at 25°C; curve *c*, specimen immediately cooled to −80°C and reloaded; curve *d*, specimen heated to 25°C, held 1 hr, reloaded at 25°C; curve *e*, specimen held 1 hr more at 25°C and reloaded at 25°C; curve *f*, specimen immediately reloaded at 25°C; curve *g*, specimen immediately cooled to −80°C and reloaded; curve *h*, specimen heated to 25°C, held ½ hr, and reloaded at 25°C; and curve *i*, specimen immediately cooled to −80°C and retested at −80°C.

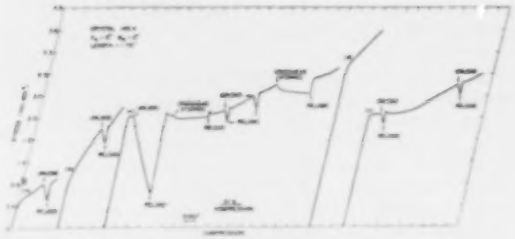

Fig. 9—Yielding phenomena: effect of test interruptions and effect of aging after room temperature prestrain. Crystal 140d. $\chi_0 = 0°$ and $\alpha = 0°$. Curve *a* is first test at −80°C; curve *b*, specimen heated to 25°C, held ½ hr, reloaded at 25°C; curve *c*, specimen immediately cooled to −80°C and reloaded; curve *d*, specimen heated to 25°C, held ½ hr, and reloaded at 25°C; and curve *e*, specimen held 16 hr at *RT*, cooled to and reloaded at −80°C.

have observed tensile twinning stresses in zinc as high as 5.7 kg per sq mm without prior plastic deformation. These stresses are considerably higher than the 0.2 to 0.3 kg per sq mm required to start plastic deformation in compression.

Further evidence that μ-bands form only in compression was found in bend tests on polished specimens or cleavage flakes. Microscopic examination readily showed μ-bands on the compression surfaces of bent crystals, but none on the tension surfaces. (See also ref. 5.)

Compression Followed by Tension: Special grips were attached to several specimens so that they could be compressed and subsequently pulled in tension. The grips, which enabled this to be done with a minimum of handling between the tests, are illustrated in Fig. 11. These tests had two purposes: The primary purpose was to obtain further information about the mode of deformation. There was also some interest in seeing what effect, if any, μ-banding might have on the stress required for twinning.

Fig. 11 indicates typical results. The first tensile test, curve *a*, was made in order to show the absence of tensile deformation in a virgin crystal. Curve *b* shows the plastic deformation produced in compression of the same crystal. Curve *c* shows that pulling the previously compressed crystal caused it to deform plastically up to a stress of roughly half the highest compressive stress. Then the crystal stopped deforming until it finally twinned at a tensile stress of about 5.7 kg per sq mm. The amount of strain that was recovered in the tensile test was approximately equal to the strain produced by the previous compression test.

None of the tests indicated any marked effect of prior compression on the tensile twinning stress. Certainly it was not lowered by prior compression, and it may have been raised somewhat.

Yield-Point Tests: The possibility existed that the yield point at −150°C and the yield point produced by prestrain were somehow related to the conventional impurity yield point that is observed in zinc.[8] Therefore, tests were made on crystals with $\chi_0 = 35°$ that had been grown in the same manner as the low angle crystals. The tests were made in tension and slip was the deformation mode. Wain and Cottrell[9] showed that a minimum strain-aging treatment of 9 hr at room temperature could result in a yield point in impure zinc crystals. Room temperature strain-aging treatments up to 48 hr were tried in this investigation. No yield points resulted. Then a

more severe test was tried. A crystal was strained at room temperature, aged in the testing machine for about 64 hr at room temperature, and tested at −196°C. No yield point was observed.

It was concluded that no conventional impurity yield point could be found for the present crystals, and the yield that appeared at about −150°C must be accounted for in some other way.

End-Effects: In order to check on the importance of the method of loading at the ends of the crystals, specimens that had their ends soldered into brass cups were compressed. The load was applied to the ends of the cups. The plastic moduli for such specimens were the same as for specimens with free ends. It was concluded that the details of the loading method were not essential in obtaining the results described in this report.

Surface Markings—*External Surfaces:* During compression of the low angle zinc crystals, markings appeared on their polished surfaces. Examples of these markings, called μ-bands, are shown in Fig. 12. Many experiments were performed in an attempt to identify these markings.

At best, the μ-bands were difficult to see. They could be seen under the microscope only at relatively low magnifications such as X100. At X400 they began to fade away, and at X1000 they could not be seen at all. The lowest stress at which they could be detected was about 2 kg per sq mm. They could be seen somewhat more easily in specimens deformed at low temperatures than in those deformed at higher temperatures.

The topography of the bands was investigated by means of microinterferometry. This confirmed the wavy contour of the surface indicated by ordinary microscopy, but it gave little additional information.

The geometry of the bands was investigated by holding crystals in a goniometer under a microscope equipped with a graduated rotating eyepiece. The angles that the μ-bands made with the cross-sectional planes were plotted as a function of position on the crystal surface. It was found, for crystals with $\alpha = 0$, that: 1—The bands were elliptical. 2—The bands made an angle of 0° with the cross-sectional plane where the hexagonal axis intersected the surface. 3—Where the diametric basal plane (0001) intersected the surface, the bands disappeared. Adjacent to these points, the angles with the

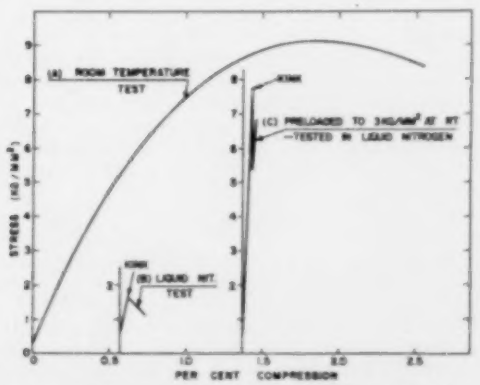

Fig. 10—Load-compression curves showing the effect of temperature on kinking and μ-band formation. $\chi_0 = 2°$, $\lambda_0 = 6°$, and $\alpha = 6°$. Curve *A* is room temperature test; curve *B*, liquid nitrogen test; and curve *C*, preloaded to 3 kg per sq mm at RT, then tested in liquid nitrogen.

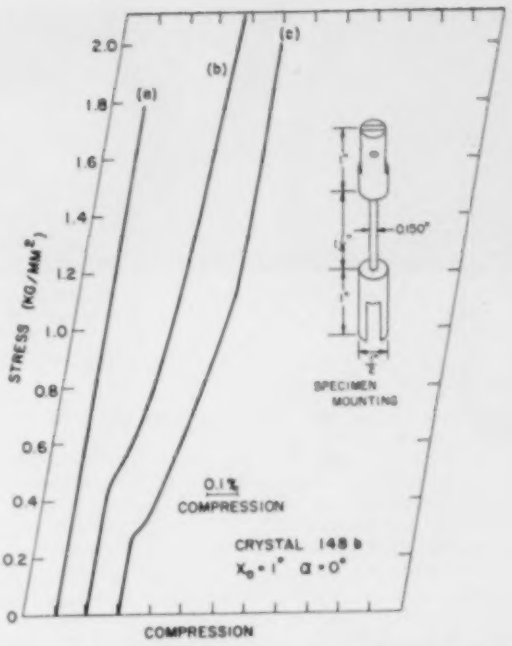

Fig. 11—Effect of compression on a subsequent tensile test of crystal 148b. $\chi_0 = 1°$ and $\alpha = 0°$. Curve *a* is tensile test of virgin crystal; curve *b*, compression test immediately after test of curve *a*; and curve *c*, second tensile test immediately after test of curve *b*.

cross-sectional planes were a maximum. 4—The maximum angles that the μ-bands made with the cross-sectional planes varied from 28° to 32°. 5—The spacing of the bands was about 3×10^{-4} cm. The geometry of the μ-bands that may be readily deduced from foregoing observations is indicated in Fig. 13. Here β is defined as the angle between the hexagonal axis and the plane of the μ-bands.

It was found that one set of bands was present only for small strains (less than about 0.4 pct). For larger strains, two sets of μ-bands usually were observed in crystals with $\alpha = 0$. When $\alpha = 30°$, as many as four sets of markings were observed with a more complex geometrical arrangement than that described previously.

Many attempts were made to detect rotation or movement of the μ-bands as deformation progressed. These failed. This was somewhat disappointing but not surprising, since the strains were always less than 1 pct and β could not be measured more accurately than ±1°. Furthermore, β was measured after deformation at various temperatures. No variations with temperature were detected.

It should be pointed out that markings indicative of basal slip were sometimes observed at low strains. As the strain was increased, these bands tended to disappear, so that only μ-bands could be seen at strains of about 0.7 pct.

Cleavage Surfaces: Markings also were observed on cleavage surfaces (Fig. 12). In one experiment, a crystal was cut into several pieces and the pieces were loaded to 0, 1, 2, 4, 6, 8, and 10 kg per sq mm. After their outer surfaces had been examined microscopically, the specimens were cleaved in liquid nitrogen and their cleavage surfaces were examined.

In another experiment, a small piece was cleaved off one end of a specimen. The small area of exposed

a—Crossed bands on surface of buckled crystal.

b—Crossed bands on surface of crystal deformed at —80°C.

c—Bands on cleavage surface (cleaved after compression); μ-bands very faint.

Fig. 12—Example of μ-bands on the surface of zinc crystals. X100. Area reduced approximately 25 pct for reproduction.

cleavage surface was examined after the specimen had been loaded.

In the first experiment (cleavage after deformation), two things were noted: The specimens became increasingly difficult to cleave as the load was increased, and bands could be seen on the cleavage surfaces which corresponded in size and orientation (90° to $[1\bar{2}10]$ direction) to the bands on the outer surface (see Fig. 12.). However, the bands on the outer surfaces could be seen after much lower loads than those on the cleavage surfaces, and they were more uniform. In the second experiment (cleavage before deformation), the cleavage surface bands had the same orientations as before, but they could be seen more readily.

X-ray Studies—In one of the X-ray experiments, a specimen was loaded repeatedly to higher loads starting at 1 and progressing through 2, 3, 4, 5, 7, and 8 kg per sq mm. After each loading, a back-reflection Laue photograph was taken at the same spot on the surface of the specimen. The spot was chosen so that a reflection from the (0001) plane was obtained. Although the Laue spots became internally subdivided as the load was raised, no asterism was observed until the load became 7 kg per sq mm and the specimen began to buckle (giving macroscopic curvature).

The Laue patterns were also examined for changes in the positions of the spots because these would be expected if the specimen had deformed by slip. No significant shifts could be found.

Oscillating crystal photographs were also made for $CuK\alpha$ reflections from the (0002) planes. These photographs differed only slightly between the undeformed and the deformed crystals.

In short, ordinary X-ray methods showed the existence of a fine structure in the deformed crystals, but they were incapable of resolving it clearly.

Discussion

It is believed that μ-band formation is an important deformation mode in zinc and probably in other crystals. The bands may be seen readily in deformed polycrystals and hence are not peculiar to monocrystals. They inhibit ortho kinking, which indicates that they inhibit slip. There is some evidence that they also increase cleavage strength, and this may be one of the mechanisms by which prestrain affects cleavage fracture.[6]

At first it was thought that the present mode of deformation might simply consist of slip on nonbasal planes. However, this interpretation now seems to be untenable. Instead, it is believed that μ-banding is a form of microscopic buckling. The reasons for this interpretation are as follows:

Geometry: The only slip system that is consistent with the observed surface markings (Fig. 13) is the $(10\bar{1}1)$ plane and the $[10\bar{1}2]$ direction. This seems a highly unlikely system. On the other hand, the bands intersect the (0001) slip plane along the $[10\bar{1}0]$ direction that is 90° to the $[\bar{1}2\bar{1}0]$ slip direction. They make angles with the hexagonal axis of 28° to 32°. Thus, their geometry resembles that of tensile deformation bands (see Cahn,[12] for example), except that their angle with the hexagonal axis about 10° greater than the corresponding angle for tensile bands. They also differ from tensile deformation bands in their size; μ-bands are about 3×10^{-4} cm in width, which is about ten times less than the width of tensile deformation bands in aluminum.

Absence of μ-Banding in Tension: This is a very strong argument against the nonbasal slip interpretation. There is no reason for expecting slip to depend on the sense of the normal stress across the slip planes. Again, however, the absence of μ-bands in tensile deformation is just what would be expected if microbuckling were the deformation mode.

Strain Recovered in Tension: Fig. 11 shows that strain can be recovered from a μ-banded specimen by pulling it in tension. The recovery begins at tensile stresses that are small compared with the highest previous compressive stress. This cannot be explained as a Bauschinger effect or by thermal relaxation. However, it is consistent with the straightening out of buckled regions of a crystal, but it would not be expected for a slip process.

It is believed that the present μ-bands are the same thing as the "micro kink bands" observed by Holden[3] and by Pratt.[5] They have the same general appearance and their sizes are comparable. Holden states his bands were about 3.8×10^{-4} cm wide and 0.09×10^{-4} cm high. He says the kink angle was about 1.4°.

Although the rotations in the μ-bands were not measured in the present work, the maximum rotation angle given by a simple calculation was about 6.5° and the heights were calculated to be about 0.3×10^{-4} cm. These figures, which are not greatly different from Holden's measured values, were obtained by considering the deformed specimens to be buckled into a sine-wave shape on a fine scale. Then it was assumed that the length of the sine wave must be equal to the undeformed length of the specimen.

Pratt[5] presented a small amount of evidence showing that the "micro kink bands" that he observed on

cleavage flakes lay in planes parallel to the hexagonal axis (that is, $\beta = 0$). This may be true for very thin specimens, but β was never equal to zero for the present specimens.

The term "micro kink bands" seems to be inept to this author because there is a qualitative as well as a quantitative difference between μ-bands and ortho kink bands. This is indicated by the differences in the geometry of the two types of band, by the fact that ortho kink bands and μ-bands are sometimes competitive deformation modes, and by the very large size difference—a factor of 10^2 to 10^4.

Although the detailed structure of the μ-bands is unknown, the dislocation model that Hart[10] proposed for tensile deformation bands represents some of their features. In Fig. 14 this model is compared schematically with the model for ortho kink bands that Hess and Barrett proposed.[11] In the model for ortho kink bands (Fig. 14), the dislocations are closely spaced in walls that are widely separated; but in the model for μ-bands (Fig. 14b), the dislocations appear in closely spaced pairs that are separated in walls. Depending on the types of pairs, the bands have one of two inclinations with respect to the slip plane. These correspond to the two observed orientations of μ-bands. The density of excess dislocations in a specimen compressed 1 pct is estimated (from the average lattice curvature) to be 10^{11} lines per sq cm. Although it is not clear how the dislocations might have become arranged as in Fig. 14b, the model seems to warrant some consideration for two reasons: First, the model is consistent with the experimental observations. Second, the experimental conditions (blocked ends of the specimens, no macrobending) require excess dislocations of both signs to exist within the crystals after compression; and of the few possible arrangements that these might assume, the one of Fig. 14b is the only one that fits the present observations.

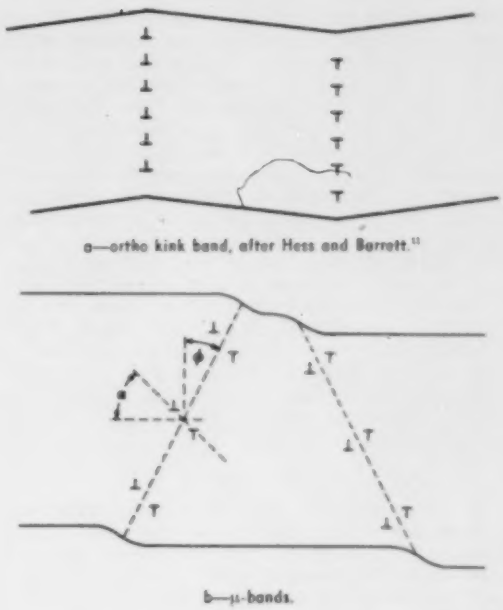

a—ortho kink band, after Hess and Barrett.[11]

b—μ-bands.

Fig. 14—Schematic dislocation models.

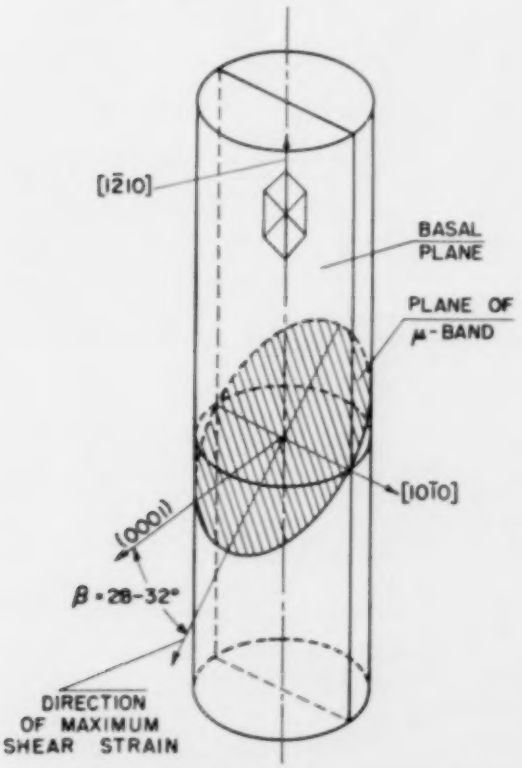

Fig. 13—Schematic geometry of μ-bands in zinc monocrystals with $\chi_0 = 0°$ and $\alpha = 0°$.

Since the details of the deformation mechanism can only be guessed, not much can be done to interpret the orientation and temperature dependence of the plastic modulus. The shape of the curve for the plastic modulus vs α (Fig. 5) cannot be reduced simply by resolving the stress along an appropriate direction. The curve indicates rather that an interaction effect causes much of the strengthening as $\alpha \rightarrow 30°$.

It has been shown that the temperature dependence of the plastic modulus (Fig. 7) seems not to be caused by a strain-aging effect. The next interpretation that comes to mind is that the plastic modulus might decrease with decreasing temperature because of a change in the anisotropy of the elastic constants of zinc with temperature. However, the author does not know how the elastic constants of zinc monocrystals vary with temperature.

The increase of the yield stress for μ-banding as the temperature decreased below −80°C remains completely unaccounted for. Nevertheless, the fact that the yield stress does increase explains why kinking was observed for the specimens tested at −196°C. μ-Banding inhibited kinking at the higher temperatures (Fig. 11), but the yield stress for μ-banding became so high at −196°C that kinking occurred instead.

Apparently, an acute competition between kinking and μ-banding exists in zinc crystals. This is indicated by the sharp change in the deformation mode as χ_0 varies by 1° or less in the range, 2° to 3°.

A partial interpretation can be made of the yield point that was observed at −80°C for specimens prestrained at 25°C. It is believed that a configura-

tional complex was created by the high temperature deformation (partial local buckling, perhaps), which could proceed to deform more easily at the low temperature than if the temperature had remained high. This interpretation contrasts this yield-point phenomenon with the usual type which involves a "locking mechanism." The evidence is: first, the yield-point elongation depended on the *amount* of prestrain as well as on its existence; and, more important, aging 16 hr at 25°C after prestraining caused no essential change in the yield-point elongation at −80°C, even though the yield-point stress was markedly decreased (Fig. 9, curves *d* and *e*).

The secondary yield points that were observed after partial unloading during yielding at −80°C (Fig. 9) indicate the nonhomogeneous nature of the process. The interfaces between yielded and unyielded material must have stopped moving upon partial unloading, and a small over-stress was required to restart them.

Summary

It has been shown that zinc monocrystals, when compressed nearly parallel to their basal planes (within 2°), deform in a new way. Certain deformation markings, called μ-bands, are characteristic of the new mode of deformation. These μ-bands have the following characteristics:

1—They are first observable at compressive stresses of about 2 kg per sq mm.

2—In crystals with the orientation $\chi_c = 0°$, $\alpha = 0°$, they lie in a plane of the $[10\bar{1}0]$ zone which is 90° to the compression axis and they make an angle β of 28° to 32° with the normal to the (0001) plane.

3—In a crystal that is compressed about 1 pct, they are spaced about 3×10^{-4} cm apart.

4—For crystals with $\alpha = 0$, two sets of bands disposed symmetrically about the compression axis are observed. When $\alpha = 30°$, as many as four sets of bands may be seen.

5—The bands do not move perceptibly during deformation, and their geometry is independent of the deformation temperature.

6—The bands may also be observed on cleavage surfaces where they lie 90° to the compression axis.

7—The fine structure indicated by the bands could not be resolved by means of ordinary X-ray techniques.

The mechanical behavior of low angle zinc monocrystals was investigated in some detail. The following points were established:

1—The plastic modulus (slope of the stress-compression curve) depends markedly on the orientation angle α. It goes from ~780 to 2650 kg per sq mm as α goes from 0° to 30°.

2—The plastic modulus (at $\alpha = 0°$) varies strongly with temperature, going from ~270 to 1370 kg per sq mm as the temperature increases from −100° to +100°C. This increase in strength with increasing temperature seems anomalous.

3—The yield stress in compression is small for these crystals at temperatures above −80°C. It rises very rapidly with decreasing temperature below −80°C.

4—At −196°C, as well as at temperatures above about +150°C, μ-bands do not form when zinc crystals are compressed; rather, they deform by kinking.

5—At temperatures near −150°C, a definite yield point is observed for the compression of low angle zinc crystals. No yield point is observed in crystals of the same composition but deformed by basal slip. Thus, the present yield point does not seem to be caused by dissolved gases.

6—Prestrain at 25°C induces a yield point for subsequent deformation at −80°C. Aging alone has no effect. The magnitude of the yield-point elongation at −80°C depends on the amount of prestrain. Aging at 25°C after prestraining does not remove the yield point at −80°C.

7—Prestrain at room temperature inhibits kinking at −196°C.

8—μ-Bands do not form when crystals with $\chi_c = 0$ and $\alpha = 0$ are pulled in tension. Such specimens deform elastically until the stress becomes high enough for twinning. The twinning stresses are 5 to 10*X* higher than the stress required for μ-bands to form in compression.

9—If a specimen is pulled in tension after it has been stressed in compression, it begins to elongate at a low stress and the compressive strain can be largely recovered. The compressive prestrain does not lower the stress for twinning and may raise it slightly.

10—Annealing at 350°C for 30 min causes substantially complete mechanical recovery.

Recrystallization did not occur upon annealing of μ-banded specimens that were free of deformation twins.

It is believed that μ-bands are not the result of nonbasal slip. They seem to be a result of a microbuckling mechanism. They are qualitatively as well as quantitatively different from ortho kink bands. A dislocation model that is consistent with some of the features of the μ-bands is described.

Acknowledgments

The author was ably assisted in this work by V. J. DeCarlo, who grew most of the monocrystals. He was also aided by discussions with J. C. Fisher, E. W. Hart, and G. W. Ardley in the course of the work. R. H. Pry kindly reviewed the manuscript.

References

[1] J. J. Gilman: Mechanism of Ortho Kink Band Formation in Compressed Zinc Monocrystals. *Trans.* AIME (1954) **200**, p. 621; JOURNAL OF METALS (May 1954).

[2] D. C. Jillson: An Experimental Survey of Deformation and Annealing Processes in Zinc. *Trans.* AIME (1950) **188**, p. 1009; JOURNAL OF METALS (August 1950).

[3] J. Holden: Plastic Deformation Features on the Cleavage Surfaces of Metal Crystals. *Philosophical Magazine* (1952) **43**, p. 976.

[4] C. A. Zappfe, C. O. Worden, and F. K. Langraf: *La Met. Italiana* (1951) **3-4**, p. 1.

[5] P. L. Pratt: Cleavage Deformation in Zinc and Sodium Chloride. *Acta Metallurgica* (1953) **1**, p. 692.

[6] J. J. Gilman and V. J. DeCarlo: *Growth of Square and Round Zinc Monocrystals with Controlled Orientations.* To be published.

[7] R. L. Bell and R. W. Cahn: The Nucleation Problem in Deformation Twinning. *Acta Metallurgica* (1953) **1**, p. 752.

[8] H. L. Wain and A. H. Cottrell: Yield Points in Zinc Crystals. *Proceedings* Physical Society (1950) **63B**, p. 339.

[9] E. Ripling and W. Baldwin: Rheotrophic Brittleness: General Behaviors. *Proceedings* ASTM (1951) **51**, p. 1023.

[10] E. Hart: The Structure of Deformation Bands. *Physical Review* (1953) **89**, p. 521.

[11] J. B. Hess and C. S. Barrett: Structure and Nature of Kink-Bands in Zinc. *Trans.* AIME (1949) **185**, p. 599; JOURNAL OF METALS (September 1949).

[12] R. W. Cahn: Slip and Polygonization in Aluminum. *Journal* Institute of Metals (1951) **79**, p. 129.

[13] E. Schmid and W. Boas: *Plasticity of Crystals.* (1950) p. 152. London. F. A. Hughes and Co. Ltd.

Technical Note

Isothermal Austenite Grain Growth

by H. B. Probst and M. J. Sinnott

AN extensive survey of the factors which affect austenite grain growth has already been made.[1] These factors are temperature, time at temperature, rate of heating, initial grain size, hot-working, alloy content, and rate of cooling from the liquidus-solidus temperature. In the present work, a vacuum-melted electrolytic iron was used and the variables studies were temperature, time at temperature, and prior ferrite grain size. Other factors were maintained constant.

The iron used in this study was vacuum-melted electrolytic iron of nominal composition of impurities of 0.07 wt pct. It was supplied as a ½ in. round cold-drawn bar. This iron was tested in three conditions: as-received, annealed 6 hr at 1200°F, and annealed 6 hr at 1600°F. Samples were ⅛ in. disks cut from the bar. The prior anneals were carried out in vacuum and the isothermal treatments were carried out in vacuum-sealed Vycor tubing.

The thermal etch technique was employed to determine the austenite grain size. Prior to sealing the test specimens, one surface of the sample was polished metallographically. This surface, after heating, was examined to determine the austenite grain size, since the austenite boundaries are revealed by thermal etching. This is essentially the only technique available for measuring the austenite grain size of low carbon steels or pure irons without altering the composition. It has been shown to yield results that are in agreement with other methods used for determining austenite grain sizes.[2] The specimen size was quite large compared to the grain size measured, so inhibition of growth due to size effects is probably negligible.

After vacuum sealing, each sample was placed into a furnace at temperature and at the completion of the run was quenched into a mercury bath. The growth temperatures used were 1700°, 1800°, 1900°, and 2000°F controlled to ±10°F. Growth times were varied from 10 to 240 hr. The long times were used in order to eliminate the nucleation and growth effects occurring during the initial transformation. Time was measured from the introduction of the capsule into the hot furnace to the time of quench. Grain-size measurements were made with the use of a grain-size eyepiece of a microscope. By determining the number of grains per square millimeter at X100 and taking the square root of the reciprocal of this number, the average linear dimension of the grains was determined. Figs. 1 and 2 are plots of these data as a function of time and temperature for the various conditions investigated.

The variation of D, the linear dimension of the grains, was assumed to follow the equation[4]

$$D = A\,t^n.$$

The curves of Fig. 1 were obtained from the data by the use of the least-squares method of analysis. Fig. 1 is for the growth of the as-received stock and Fig. 2 is for growth after prior treatments. Differentiating

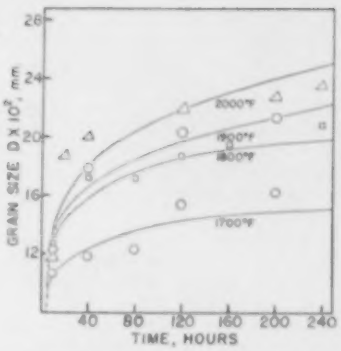

Fig. 1—Austenite grain size as a function of time and temperature. As-received material.

the foregoing equation gives an expression for the rate of growth

$$dD/dt = G = nAt^{n-1} = nD/t.$$

Both D and G as functions of t are given in Table I. It should be noted that G is a function of time; the growth rate is rapid at early stages and decreases with increasing time. Since increasing temperature increases the growth rate, it has been common practice to use the empirical relationship

$$G = G_0 e^{-Q/RT}$$

to relate temperature to growth rate. The growth rate customarily has been taken at constant values of D on the basis that the rate of growth is related to the boundary surface tension and this is measured by the curvature of the boundary. At constant D values, the growth rate is a function of time and temperature. The growth rate can be related however to temperature at constant time, and this has the advantage that under these conditions the growth rate is a function only of temperature. Obviously the Q values, activation energies, obtained for each assumption will not be the same and the question of which is the more correct is a moot one, since the assumed exponential relationship in either case has no particular theoretical significance.

By plotting G, at constant grain size, vs $1/T$, the activation energy over the temperature range of 1800° to 2000°F is found to vary from 30,000 cal per mol at the smaller grain sizes to 50,000 cal per mol at the larger grain sizes. The 1700°F data do not correlate with the data at higher temperatures. The activation energies for the 1200° and 1600°F prior annealed materials were calculated as 50,000 and 62,000 cal per mol, respectively, using the reciprocal time to a given grain size as a measure of the growth rate.

Plotting G, at constant times, vs $1/T$ yields an activation energy of 12,300 cal per mol for the tem-

H. B. PROBST and M. J. SINNOTT, Member AIME, are Graduate Student and Associate Professor of Metallurgical Engineering, respectively, University of Michigan, Ann Arbor, Mich.

TN 242E. Manuscript, Jan. 22, 1954.

Table I. Grain Diameter and Growth Rate as Time Functions (As-Received Iron)

Temperature, °F	$D = f(t)$	$G = f(t)$
1700	$0.1t^{0.50}$	$0.011t^{-0.50}$
1800	$0.1t^{0.50}$	$0.012t^{-0.50}$
1900	$0.1t^{0.50}$	$0.015t^{-0.50}$
2000	$0.1t^{0.50}$	$0.016t^{-0.50}$

perature range from 1700° to 2000°F. The pretreated irons gave values of 12,600 and 10,800 cal per mol for the 1200° and 1600°F treatments, respectively.

The data follow the assumed dependence on time reasonably well in most cases. The constant A in the grain-size equation appears to be independent of temperature in the range investigated. This is at variance with the generally accepted idea that this constant is a function of temperature, grain-boundary energy, grain size, and radius of curvature.[4] These factors may have combined in the present investigation in such a fashion so as to negate any temperature dependency. Its value is also probably due to the type of reaction that is occurring. Growth follows a phase transformation in the present investigation and at zero time the grain size is zero. This is not the case in the previous studies that have been made on grain growth. The theoretical value of the exponent n is 0.5, but this value is rarely attained in metals due to the difference between the growth mechanism upon which the equation is based and the actual growth mechanism. The value of n increases with increasing temperature, an effect which has been noted in grain-growth studies on high purity aluminum.[4]

The significance of the activation energies computed is difficult to assess. Because of the variation in "n," the activation energies computed at constant grain size necessarily will vary. The values reported are considerably less than values reported for steels and are of the order of magnitude reported for other metals.[5-9] The value for steel is of the order of 100,000 cal per gram-atom; commercial brass, as 60,000 cal per gram-atom; high purity brass, 40,000 cal per gram-atom; and nickel, 82,500 cal per gram-atom.[10] The higher purity of the iron used as compared to the steel would account for the decreased activation energy, but the grain sizes obtained on growth are of the same magnitude as those obtained in steel.[4]

Since activation energies based on growth rates at a given time are not usually determined, these were computed from data in the literature where possible.

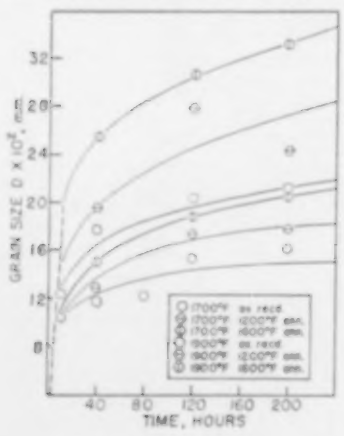

Fig. 2—Austenite grain size as a function of time and temperature.

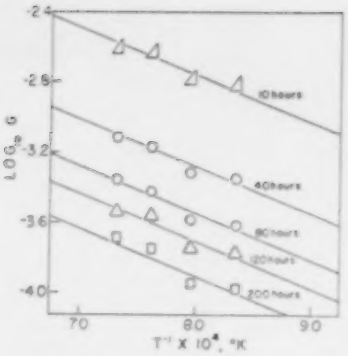

Fig. 3—Log of growth rate vs $1/T$. As-received material.

For brass,[2, 7] values of 15,000 to 25,000 cal per gram-mol were obtained. For steel,[4] values of 45,000 to 55,000 were obtained; for α iron, values of 25,000 to 35,000 calories per gram-mol were calculated.[11] No more significance can be assigned to these values than that given the activation energies obtained from growth rates taken at constant grain size, since, as stated previously, there appears to be no theoretical basis for the exponential dependency observed.

While there will probably be disagreement as to the meaning of activation energies as applied to grain growth, there is no doubt that the prior annealing treatments given the iron produced coarser grains of austenite. It appears that the coarser the ferrite grain size, the coarser will be the resulting austenite grain size. The as-received material on heating undoubtedly recrystallized to produce the finest grain size of ferrite of the three that were studied, and thus subsequently produced the finest austenite grains. Since the austenite nucleates at the α grain boundaries, it follows that the smaller the α grain size, the greater will be the number per unit area of austenite nuclei and this leads to a smaller grain size on impingement and subsequent growth after a given time at temperature. Undoubtedly, the changes that occur during the period of α to γ transformation have a pronounced effect on subsequent growth of the γ grains and should be more thoroughly investigated.

Acknowledgments

The work reported is a portion of a program supported by the Michigan Memorial Phoenix Project of the University of Michigan.

References

[1] J. H. Whitely: *Journal* Iron and Steel Institute (1943) **148**, p. 513.
[2] M. J. Day and J. B. Austin: *Trans.* ASM (1940) **28**, p. 354.
[3] J. E. Burke: *Atom Movements.* (1951) Cleveland. ASM.
[4] P. A. Beck, J. C. Kremer, L. J. Demer, and M. L. Holzworth: *Trans.* AIME (1948) **175**, p. 372.
[5] J. E. Burke: *Trans.* AIME (1949) **185**, p. 73; JOURNAL OF METALS (February 1949).
[6] C. S. Robinson: *Journal of Applied Physics* (1942) **13**, p. 647.
[7] P. A. Beck, J. Towers, Jr., and W. D. Manly: *Trans.* AIME (1948) **175**, p. 162; METALS TECHNOLOGY (February 1948).
[8] J. E. Burke: *Journal of Applied Physics* (1947) **18**, p. 1028.
[9] O. O. Miller: *Trans.* ASM (1951) **43**, p. 260.
[10] G. W. Wensch and H. L. Walker: *Trans.* ASM (1952) **44**, p. 1186.
[11] G. Wiener: *Trans.* ASM (1952) **44**, p. 1169.

DISLOCATIONS IN METALS

Based On An Institute of Metals Div. Symposium

Edited by

Morris Cohen
Massachusetts Institute of Technology
Cambridge, Mass.

Chapter Headings and Authors:

The Nature of Dislocations in Ideal Single Crystals, by

J. S. Koehler and F. Seitz
University of Illinois
Urbana, Ill.

Role of Dislocations in Crystal Growth and Grain Boundary Phenomena, by

W. T. Read, Jr., and W. Shockley
Bell Telephone Laboratories
Murray Hill, N. J.

Dislocations and Mechanical Properties, by

E. Orowan
Massachusetts Institute of Technology
Cambridge, Mass.

1954 **$5.00**

AIME Members will receive a
30 pct discount on the book

Published By

The American Institute of Mining & Metallurgical Engineers, Inc.
Institute of Metals Div.
29 West 39th St.
New York 18, N. Y.

AIME 29 W. 39th St., New York 18, N. Y.
Please send me the books listed below. Enclosed is Check ☐; Money Order ☐
for $..... (AIME members may be billed.)
• AIME Members, 30% Discount on All Books.

1. ..... 3. .....

2. ..... 4. .....

Name .....

Address .....

City and Zone ..... State .....

Nonmember Foreign Orders, Add 30c for Mailing.